Solar fuels via two-step thermochemical redox cycle for power and fuel production

Original
Solar fuels via two-step thermochemical redox cycle for power and fuel production / Uddin, Azhar. - (2019 Jul 23), pp. 1-394.

Publisher:
Politecnico di Torino

Published
DOI:

Doctoral thesis

SOLAR-FUELS VIA TWO-STEP THERMOCHEMICAL REDOX CYCLES FOR POWER AND FUEL PRODUCTION

-Azharuddin

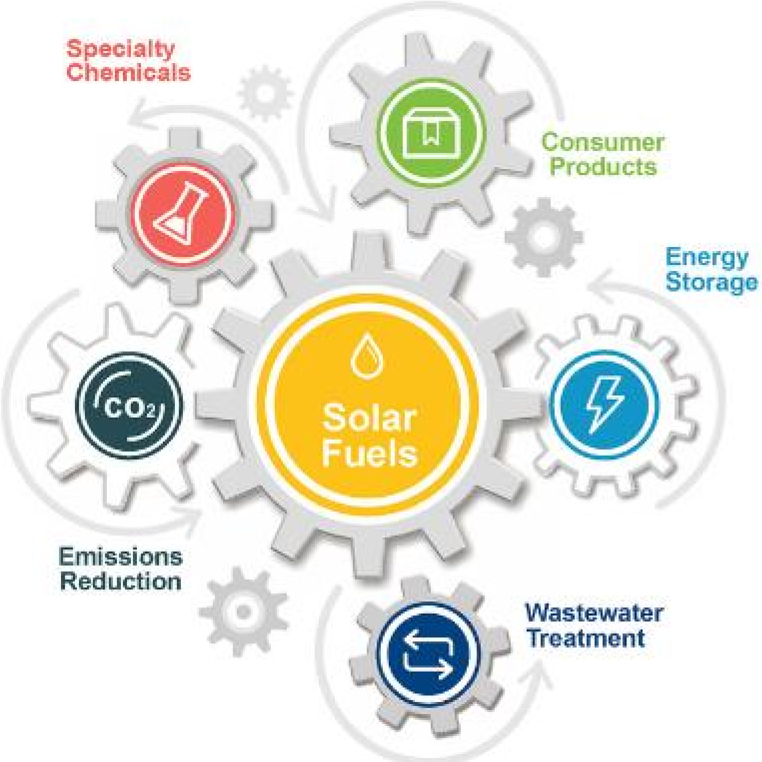

POLITECNICO
DI TORINO

UNIVERSITAT POLITÈCNICA
DE CATALUNYA
BARCELONATECH

ScuDo
Scuola di Dottorato ~ Doctoral School
WHAT YOU ARE, TAKES YOU FAR

Doctoral Dissertation
Doctoral Program in Energy Engineering (31th Cycle)

Solar fuels via two-step thermochemical redox cycles for power and fuel production

Azharuddin E Farooqui

* * * * * *

Supervisors
Prof. Massimo Santarelli, Politecnico di Torino, Italy
Prof. Jordi Llorca, Universitat Politècnica de Catalunya, Spain

Doctoral Examination Committee:
Prof. Marta Boaro, University of Udine, Italy
Prof. Björn Laumert, KTH Royal Institute of Technology, Sweden
Prof. Lluís Soler, Universitat Politècnica de Catalunya, Spain
Prof. Raffaele Pirone, Politecnico di Torino, Italy
Prof. Emilio Paolucci, Politecnico di Torino, Italy

Politecnico di Torino
February 14, 2019

The research presented in this dissertation is performed at the Synergies of Thermochemical and Electrochemical Power Systems (STEPS) group of the department of Energy at Politecnico di Torino (Polito) in Italy and Nanoengineering of Materials Applied to Energy (NEMEN) group of Department of Chemical Engineering and Institute of Energy Technologies, at Universitat Politècnica de Catalunya (UPC), Spain.

The research is primarily funded by the Erasmus Mundus joint doctorate SELECT+ programme (WP 2 Waste to Valued Added Services and Optimization with Environmental Improving Technologies). Additional research and mobility funding is provided by Polito, UPC and InnoEnergy PhD school.

Cover page is taken from Chem, 2017, 3, 3-7 with permission from publisher Elsiever.

I hereby declare that, the contents and organisation of this dissertation constitute my own original work and does not compromise in any way the rights of third parties, including those relating to the security of personal data.

……………………………………......
Azharuddin E Farooqui
Turin, December 17, 2018

Summary

With the issue of the rise of anthropogenic CO_2 with lead to global warming and rise of the primary energy demand, it requires strong measures for the energy transition and the diversification with renewables and existing fossil-based infrastructure. Prior to call for measures for carbon capture and sequestration, utilization of CO_2 would also be needed. In that sense, thermochemical redox cycles gained particular interest to produce synthetic fuel which leads to the production of other chemicals. Chemical looping CO_2/H_2O splitting (CL) via a two-step thermochemical pathway is composed of two redox reactions with a metal oxide. The first step is the reduction of metal oxides by losing oxygen and creating vacancies in the lattice at a higher temperature and becoming lower valence metal oxide. During the oxidation step, the reactant gases CO_2/H_2O reacts with the reduced metal oxide forming CO and H_2. A detailed mapping of different metal oxides has been investigated based on their oxygen carrying capacity and properties to under continuous redox cycles at temperature and pressure swing operation. After careful examination, ceria was selected for the application that can be available for large-scale CO_2/H_2O splitting.

In this present work, solar-driven thermochemical CO_2/H_2O splitting and methane-reduced chemical looping for CO_2/H_2O splitting for syngas production are investigated with the focus on non-structured reactors.

For solar-driven thermochemical looping cycle, an assessment of counter-current flow based moving bed reactor and fluidized bed reactors operating in different fluidizing regimes are assessed. It is moving bed reactor for both reduction and oxidation yield in high selectivity of the CO and H_2 with optimum reactor volumes

while the similar yield could be achieved for bubbling fluidized bed reactor but the reactor volume required would be very high making it unfeasible. The reactor models were developed in Aspen plus and are validated from the literature. A sensitivity analysis revealed the CL unit is highly dependent on the reduction temperature and pressure. The analysis was extended by integrating the developed CL unit as an add-on unit to a 100 MW oxy-fired power plant with carbon capture. The efficiency of the plant was investigated considering only CO_2 splitting, only H_2O and mixture of CO_2 and H_2O as feed to the oxidation reactor of the CL unit. It resulted in maximum power output of 12.9 MW with solar to electricity efficiency of 25.4%. This additional power would bring down the efficiency loss due to carbon capture from 11.3 to 6%. To achieve this, the reduction reactor of CL unit need to operate at 1600ºC and 10^{-7} bar pressure. These conditions would need a huge solar field and the operation would be limited to only a few hours during the day without thermal storage integration. Techno-economic analysis revealed that the levelized cost of electricity 1100 \$/MWh without including incentives or carbon taxation.

Subsequently, methane reduction of ceria as an alternative to thermal reduction was considered. At first, thermodynamic analyses of methane-driven CL unit were performed. From the analysis, it showed that the minimum temperature required was 900 with 50% excess of methane for reduction which yielded a CL unit efficiency of 62% with an optimum yield of CO and H_2. The CO_2/H_2O splitting in oxidation reactor was highly exothermic complete oxidation of ceria, whereby a higher outlet temperature would considerably benefit the energetic efficiency of the complete redox CL cycle. The variation of H_2/CO ratio at the output with respect to varying input parameters including the composition of the gas to the oxidation reactor was studied to specify the necessary operating conditions, while combined to subsequent chemical production from the generated syngas.

Subsequently, methane-driven CL unit was integrated as an add-on unit to a 500 MW oxy-fired power plant. A comparative system performance with conventional natural gas combined cycle, oxy-fired power cycle with carbon capture and the proposed plant was investigated. A system efficiency and exergetic efficiency of 50.7% and 47.4 % were obtained respectively. The system efficiency could be improved to 61.5%, subject to system optimization with pinch analysis. A detailed techno-economic assessment revealed a specific overnight capital cost of 2455\$/kW, the levelized cost of CO_2 savings of 96.25 \$/tonneCO_2, and an LCOE of 128.01 \$/MWh. However, with carbon credits of 6 \$/tonneCO_2, the LCOE would drop below 50 \$/MWh.

The methane-driven CL unit is later integrated as an add-on unit to a polygeneration plant that produces electricity and dimethyl ether. The results showed that the plant can produce 103 MWe and 2.15 kg/s of DME with energy and exergy efficiency of 50% and 44% respectively. The capital investment required for the plant of \$534 million. With the carbon credit price of \$40/tonne of CO_2, the current DME price of \$18/GJ and the electricity price of \$50/MWh would be achieved. The costs resulted are due to air separation unit required for the oxi-fired power plant and it can be reduced by replacing the air separation unit with oxygen transport membranes technology.

Since no comprehensive solid-state kinetic model exists in literature to describe the methane reduction of commercial ceria, experiments were performed in a packed bed horizontal tubular reactor within a temperature range of 900-1100ºC. CO_2 splitting, being a more complex reaction than water splitting was chosen to be studied for kinetic assessment as well, while water splitting kinetics was obtained from the literature. Avrami-Erofe'ev (AE3) model was found to fit best to both the cases, with respective activation energies being obtained as 283 kJ/mol and 59.68 kJ/mol respectively. The order of the reaction was found as a relation between temperature and concertation of the reactants. Since the analysis was performed based on thermodynamic approach, but the heterogeneous reaction of metal oxide and reactant gases would limit to reach the equilibrium during the reaction and would always depend on the type of reactor system chosen for the CL application. Therefore, a moving bed reactor model developed considering the experimentally obtained methane reduction and CO_2 splitting kinetics was incorporated to evaluate the proposed power plant and polygeneration plant. A drop of 20% in the efficiency of the CL unit was observed. However, due to thermal balance within the system, a similar thermal efficiency of the overall plant was achieved as 50.9%. However, unlike the thermodynamic layout, no excess heat was available to improve the system efficiency further. Besides CO_2 recycling and utilization, the land and water footprint as a sustainability assessment criteria were analyzed for the proposed layout. Both the land and water requirements increase by 2.5 times compare to conventional natural gas combined cycle based power plant.

Furthermore, a polygeneration plant with power and dimethyl ether (DME) production has been investigated with kinetics based CL unit and found that the production of DME would drop from 2.15 kg/s to 1.48 kg/s and power from 103 to 72 MW. Therefore, kinetics has strong dependence and would reduce the production of power and DME by around 30% and it cost would increase by 30%.

Overall, integration of the CL unit as an add-on unit to the power plant is more suitable than polygeneration with respect to the cost compared to the existing market price.

Sommario

Con l'aumento delle emissioni di CO_2 antropogenica che contribuiscono al riscaldamento globale e l'incremento della domanda mondiale di energia primaria, sono richieste significative misure per favorire la diversificazione delle fonti e la transizione energetica tramite fonti rinnovabili a partire dalle infrastrutture esistenti basate su combustibili fossili. Prima ancora degli interventi per la cattura e il sequestro dell’anidride carbonica, anche l’utilizzo della CO_2 rappresenta una misura necessaria al raggiungimento degli obiettivi di decarbonizzazione. In questo senso, i cicli redox termochimici hanno acquisito particolare interesse per la produzione di combustibile sintetico da utilizzare come intermedio nella produzione di altri prodotti chimici. La separazione chimica di CO_2/H_2O attraverso un ciclo termochimico – chemical looping splitting (CL) – in due fasi è composta da due reazioni redox con un ossido di metallo. La prima fase del ciclo avviene alla temperatura più elevata e consiste nella riduzione dell’ossido di metallo, che cede ossigeno creando vacanze nel reticolo e diventando ossido di metallo a bassa valenza. Durante la fase di ossidazione, i gas reagenti CO_2/H_2O reagiscono con l'ossido di metallo ridotto che forma CO e H_2. Una mappatura dettagliata dei diversi ossidi di metallo è stata effettuata in base alla loro capacità di trasporto dell’ossigeno e alle proprietà nei cicli di ossido-riduzione a funzionamento continuo in condizioni di variazione di temperatura e pressione. Dopo un attento esame, l’ossido di Cerio - ceria - è stato selezionato per l'applicazione che può essere disponibile per la scissione CO_2 / H_2O su larga scala.

In questo lavoro, sia la separazione termochimica di CO_2/H_2O alimentata tramite energia solare, sia i cicli con riduzione tramite metano, entrambi finalizzati alla produzione di syngas sono stati studiati con particolare attenzione ai reattori non strutturati.

Per il ciclo termochimico basato su energia solare, è stata effettuata la valutazione dei reattori a letto mobile a flusso in controcorrente e a letto fluido che operano in diversi regimi di fluidizzazione. Il reattore a letto mobile è stato individuato come il più performante sia per la riduzione che l'ossidazione, con elevate selettività verso CO e H_2 e volumi ottimali del reattore, mentre una resa analoga con reattori a letto fluidizzato potrebbe essere ottenuta solo con volumi di reattore molto alti, rendendo questa scelta irrealizzabile nella pratica. I modelli di reattore sono stati sviluppati in Aspen plus e sono stati validati dalla letteratura. Un'analisi di sensitività ha rivelato che la performance dell'unità CL è in larga misura dipendente dalla temperatura e dalla pressione di riduzione. L'analisi è stata estesa integrando l'unità CL sviluppata come unità aggiuntiva di una centrale elettrica a ossicombustione da 100 MW con cattura di carbonio. L'efficienza dell'impianto è stata studiata considerando di alimentare il reattore di ossidazione dell'unità CL sia con CO_2, sia con H_2O, sia con una miscela di CO_2 e H_2O. I risultati indicano una potenza massima di 12,9 MW con un rendimento da solare a elettricità del 25,4% generabile grazie all'unità di CL. Questa potenza aggiuntiva ridurrebbe la perdita di efficienza dovuta alla cattura di carbonio dall'11,3 al 6%. Per ottenere ciò, il reattore di riduzione dell'unità CL deve operare a 1600 ° C con una pressione di 10^{-7} bar. Queste condizioni avrebbero bisogno di un enorme campo solare e l'operazione sarebbe limitata a poche ore durante il giorno senza l'integrazione di un accumulo termico. L'analisi tecno-economica ha rivelato che il costo livellato (levelizad cost) dell'elettricità era di 1100 $ / MWh, senza includere incentivi o tassazione sul carbonio.

Successivamente, è stata considerata la riduzione della ceria con metano come alternativa alla riduzione termica. Inizialmente, sono state condotte analisi termodinamiche dell'unità CL con riduzione a metano. Dall'analisi è emerso che la temperatura minima richiesta era 900 °C per la riduzione con un eccesso di metano del 50%, che ha prodotto un'efficienza dell'unità CL del 62% con una resa ottimale di CO e H_2. In questo caso, la scissione di CO_2/H_2O nel reattore di ossidazione consisteva nell'ossidazione completa esotermica della ceria, per cui una temperatura di uscita più elevata avrebbe notevolmente migliorato l'efficienza energetica del ciclo CL redox completo. La variazione del rapporto H_2 / CO all'uscita rispetto ai vari parametri di input, compresa la composizione del gas inviato al reattore di ossidazione, è stata studiata per specificare le condizioni operative necessarie.

Successivamente, l'unità CL a metano è stata integrata come unità aggiuntiva in una centrale elettrica a ossicombustione da 500 MW. Sono state studiate le prestazioni del sistema in una valutazione comparativa con un ciclo combinato convenzionale a gas naturale, un ciclo a ossicombustione con cattura di carbonio e l'impianto proposto. Sono stati ottenuti per l'impianto rispettivamente un rendimento del sistema e un'efficienza energetica del 50,7% e del 47,4%. L'efficienza del sistema potrebbe essere migliorata fino al 61,5% tramite l'ottimizzazione del recupero termico del sistema, valutata attraverso la pinch analysis del sistema. Una dettagliata valutazione tecno-economica ha rivelato un costo specifico del capitale di 2455 $ / kW (overnight cost), un costo livellato delle emissioni di CO_2 evitate 96,25 $ / tonnellata di CO_2, e un costo dell'elettricità (LCOE) di 128,01 $ / MWh. Tuttavia, considerando un incentivo di 6 $ / tonnellata di CO_2 evitata, il LCOE scenderebbe sotto i 50 $ / MWh.

L'unità CL a metano viene successivamente integrata come unità aggiuntiva in un impianto di poligenerazione che produce elettricità e dimetil-etere. I risultati hanno mostrato che l'impianto può produrre 103 MWe e 2,15 kg/s di DME con un'efficienza energetica ed exergetica del 50% e del 44% rispettivamente. L'investimento di capitale richiesto per l'impianto ammonta a 534 M$. Con un valore per la carbon tax di $ 40 / tonnellata di CO_2, il DME e l'elettricità raggiungerebbero la parità con gli attuali prezzi di mercato, pari a $18/GJ per il DME e $50/MWh per l'elettricità. I costi risultanti sono dovuti all'unità di separazione dell'aria richiesta per la centrale elettrica a ossicombustione e può essere ridotta sostituendo l'unità di separazione dell'aria con una tecnologia a membrana per la separazione dell'ossigeno.

Poiché in letteratura non esiste un modello completo per cinetica dello stato solido che descriva la riduzione con metano della ceria, esso è stato ricavato per via sperimentale. Sono stati condotti esperimenti in un reattore tubolare orizzontale a letto fisso in un intervallo di temperatura di 900-1100 °C. E' stata studiata la cinetica della scissione della CO_2, essendo una reazione più complessa rispetto alla scissione dell'acqua, la cui cinetica è stata invece ottenuta dalla letteratura. In base all'analisi sperimentale condotta, il modello cinetico Avrami-Erofe'ev (AE3) è risultato essere il migliore per entrambe le reazioni, con le rispettive energie di attivazione ottenute rispettivamente come 283 kJ/mol e 59,68 kJ/mol. L'ordine della reazione è stato ricavato come relazione tra temperatura e concertazione dei reagenti.

L'analisi è stata effettuata seguendo un approccio termodinamico, ma la reazione eterogenea dell'ossido di metallo e dei gas reagenti limita il raggiungimento dell'equilibrio durante la reazione e dipende sempre dal tipo di reattore scelto per l'applicazione. Pertanto, un modello di reattore a letto mobile è stato sviluppato considerando la riduzione del metano ottenuta sperimentalmente e la cinetica di splitting della CO_2 è stata incorporata per valutare i due impianti proposti: la centrale elettrica e l'impianto di poligenerazione. È stata osservata una riduzione del 20% nell'efficienza dell'unità CL. Tuttavia, grazie all'integrazione termica interna al sistema, l'efficienza termica dell'impianto complessivo è molto simile a quella raggiunta nell'analisi termodinamica, con un valore del 50,9%. Tuttavia, a differenza del layout termodinamico, non è disponibile calore in eccesso per migliorare ulteriormente l'efficienza del sistema. Oltre al riciclo e all'utilizzo della CO_2, come criteri di valutazione della sostenibilità per il layout proposto sono stati analizzati anche l'occupazione del suolo terreno e il fabbisogno idrico. Sia il fabbisogno di terra che di acqua aumentano di 2,5 volte rispetto ad una centrale convenzionale a ciclo combinato a gas naturale.

Inoltre, anche l'impianto di poligenerazione con produzione di energia elettrica e dimetil etere (DME) è stato studiato considerando un modello dell'unità CL basato sulla cinetica e ha rilevato che la produzione di DME scenderebbe da 2,15 kg/s a 1,48 kg/s e la potenza elettrica prodotta da 103 a 72 MW. Pertanto, la cinetica ha una forte influenza sulla prestazione complessiva del sistema, e considerarla nell'analisi porta a ridurre la produzione di energia e DME di circa il 30% con un aumento di costo del 30%.

Complessivamente, l'integrazione dell'unità CL come unità aggiuntiva ad una centrale elettrica a ossicombustione risulta più adatta rispetto alla poligenerazione, considerando il prezzo di mercato attuale per le commodities prodotte.

Resumen

El aumento del CO_2 antropogénico y el calentamiento global y el aumento de la demanda de energía primaria hace que se requieran medidas para la transición energética y la diversificación con energías renovables e infraestructuras existentes basadas en combustibles fósiles. Además de implementar medidas para la captura y el secuestro de carbono, también se necesita desazrrollar métodos para la utilización de CO_2. En ese sentido, los ciclos redox termoquímicos son particularmente interesantes para producir combustible sintético que, a su vez, pueden utilizarse para la producción de otras substancias químicas. La rotura de CO_2 / H_2O (CL) mediante una vía termoquímica de dos pasos está compuesta por dos reacciones redox con un óxido metálico. El primer paso es la reducción de los óxidos metálicos al perder oxígeno y crear vacantes en la red a una temperatura más alta y convertirse en óxido de metal de valencia más baja. Durante la etapa de oxidación, los gases reactivos CO_2 / H_2O reaccionan con el óxido metálico reducido formando CO y H_2. Se ha investigado el uso de diferentes óxidos metálicos en función de su capacidad de transporte de oxígeno y sus propiedades para realizar ciclos redox continuos a distintos valores de temperatura y presión. Después de un examen cuidadoso, se ha seleccionado a la ceria para la división de CO_2 / H_2O a gran escala.

En el presente trabajo, se investigan las divisiones termoquímicas de CO_2 / H_2O impulsadas por energía solar y la reducción de metano para la producción de gas de síntesis, con especial atención a su aplicación en reactores no estructurados. Se evalúa el uso de reactores de lecho móvil basado en flujo contracorriente y reactores de lecho fluidizado que funcionan en diferentes regímenes de fluidización. Es un reactor de lecho móvil tanto para la etapa de reducción como para la etapa de oxidación se obtienen altas selectividades de CO y H_2 con volúmenes óptimos del reactor, mientras

que en un reactor de lecho fluidizado el volumen requerido es mucho más alto, lo que lo hace inviable. Los modelos de reactor se han desarrollado en Aspen plus y se validan a partir de la literatura. Un análisis de sensibilidad ha revelado que la unidad CL depende en gran medida de la temperatura y la presión. El análisis se ha ampliado integrando la unidad desarrollada de CL como una unidad adicional a una central eléctrica de 100 MW con captura de carbono. La eficiencia de la planta se ha investigado considerando sólo la división de CO_2, sólo la del H_2O y la mezcla de CO_2 y H_2O como alimentación al reactor de oxidación de la unidad CL. El resultado es de una potencia máxima de 12.9 MW con una eficiencia de energía solar a eléctrica de 25.4%. Esta potencia adicional reduciría la pérdida de eficiencia debido a la captura de carbono de 11.3 a 6%. Para lograr esto, el reactor de reducción de la unidad CL debe funcionar a 1600 ° C y 10^{-7} bar de presión. Estas condiciones necesitarían un enorme campo solar y la operación, en ausencia de almacenamiento térmico, se limitaría a unas pocas horas durante el día. El análisis técnico-económico ha revelado que el coste nivelado de la electricidad es de 1100 $/MWh sin incluir incentivos ni impuestos sobre el carbono.

Posteriormente, se ha considerado la reducción del metano como una alternativa a la reducción térmica. Al principio, se realizaron análisis termodinámicos de la unidad de CL impulsada por metano. A partir del análisis, se ha demostrado que la temperatura mínima requerida es de 900°C con 50% de exceso de metano para la reducción, lo que supone una eficiencia de la unidad CL de 62% con un rendimiento óptimo de CO y H_2. La división de CO_2/H_2O en el reactor de oxidación a una mayor temperatura de salida beneficiaría considerablemente la eficiencia energética del ciclo redox CL completo. La variación de la relación H_2/CO en la salida con respecto a los parámetros de entrada variables que incluyen la composición del gas al reactor de oxidación se ha estudiado con el fin de especificar las condiciones operativas idóneas.

Posteriormente, la unidad CL impulsada por metano se ha integrado como una unidad adicional a una central eléctrica de 500 MW alimentada por oxígeno. Se ha investigado el rendimiento de un sistema con un ciclo combinado de gas natural convencional con o sin captura de carbono. Se ha obtenido una eficiencia de sistema y eficiencia exergética de 50.7 y 47.4%, respectivamente. La eficiencia del sistema podría mejorarse a 61.5%, sujeto a la optimización del sistema. La evaluación tecno-económica ha revelado un coste de capital durante la noche de 2455 $/kW con un coste de ahorro de CO_2 de 96.25 $/tonelada CO_2 y un LCOE de 128.01 $/MWh. Sin embargo, con créditos de carbono de 6 $/tonelada CO_2, el LCOE caería por debajo de 50 $/MWh.

La unidad CL impulsada por metano también se ha integrado como una unidad adicional a una planta de poligeneración que produce electricidad y éter dimetílico (DME). Los resultados han mostrado que la planta puede producir 103 MWe y 2.15 kg/s de DME con una eficiencia de energía y exergía del 50 y 44%, respectivamente. La inversión de capital requerida para la planta es de $ 534 millones. Con el precio del impuesto al carbono de $ 40/tonelada de CO_2, se lograría el precio DME actual de $ 18/GJ y el precio de la electricidad de $ 50/MWh. Los costes resultantes se deben principalmente a la unidad de separación de aire requerida y se puede reducir reemplazando la unidad de separación de aire con tecnología de membranas de transporte de oxígeno.

Dado que no existe un modelo cinético completo en la literatura para describir la reducción de metano con ceria comercial, se han realizado una serie de experimentos en un reactor tubular horizontal de lecho empaquetado dentro de un rango de temperatura de 900-1100 °C. Se ha elegido la división de CO_2, al ser una reacción más compleja que la división de agua, para estudiar la cinética, mientras que la cinética de división de agua se ha obtenido de la literatura. Se ha encontrado que el modelo de Avrami-Erofe'ev (AE3) se ajusta mejor a ambos casos, obteniéndose energías de activación de 283 y 59.68 kJ/mol, respectivamente. Dado que el análisis se realizó sobre la base de un enfoque termodinámico, la reacción heterogénea entre el óxido de cerio y los gases reactivos se limitan a alcanzar el equilibrio durante la reacción y siempre en función del tipo de sistema de reactor elegido. Así, se ha incorporado un modelo de reactor de lecho móvil teniendo en cuenta la cinética de la división de metano y la división de CO_2 obtenida experimentalmente para evaluar la planta de energía y la planta de poligeneración propuestas. Se ha observado una caída del 20% en la eficiencia de la unidad CL. Sin embargo, debido al equilibrio térmico dentro del sistema, se logra una eficiencia térmica similar de la planta del 50.9%. Además del reciclaje y la utilización del CO_2, se ha analizado la sostenibilidad para el diseño propuesto. Finalmente, se ha investigado una planta de poligeneración con producción de energía y DME con una unidad CL basada en la cinética estudiada y se ha encontrado que la producción de DME se reduciría de 2.15 kg/s a 1.48 kg/s y la potencia de 103 a 72 MW. En general, la integración de la unidad CL como una unidad adicional a la planta de energía es más adecuada que la poligeneración con respecto al coste en comparación con el precio de mercado existente.

Acknowledgment

All praise belongs to Almighty Allah (s.w.t.) for bestowing me with courage and perseverance to carry out this work sincerely. I thank Almighty Allah for giving me chance to do my Ph.D. successfully at Politecnico di Torino (PoliTo), Italy and Universitat Politècnica de Catalunya (UPC), Spain under SELECT+ Erasmus Mundus Joint Doctoral (EMJD) program. I am happy to have had a chance to glorify His name in the sincerest way through this small accomplishment and ask Him to accept my efforts.

Acknowledgement is due to European Union initiative of Erasmus Mundus Joint Doctoral program and KIC InnoEnergy Ph.D. School for providing me financial support and good academic environment during the course of my Ph.D. Special thanks is also due to the STEPS research group at Department of Energy, PoliTo and people at Institute of Energy Technologies in UPC.

My deep gratitude and appreciation go to my thesis advisor, my mentor Prof. Massimo Santarelli for his constant endeavor, guidance, and motivation during the course of my study and research. His valuable and priceless suggestions made this work interesting and challenging for me. I also wish to express my deep appreciation to Prof. Jordi Llorca for his help, guidance, and constant encouragement during my Ph.D.

I am greatly indebted to Dr. Domenico Ferrero for the valuable time spent together throughout my thesis work and also for always being supportive and helping me during difficult times. I wish to thank Dr. Andrea Lanzini and Dr. Davide Papperallu for their constant help with the research activities and motivation.

I am thankful to Prof. Martin Vincent Annaland and Prof. Fausto Gallucci for giving the opportunity to carry out part of the work at Eindhoven University of Technology, Eindhoven, Netherlands and the entire SPI group for making my stay at Eindhoven a memorable one.

I would also like to acknowledge Prof. Marek Sciazko of AGH University of Science and Technology who helped me a lot, guided me and encouraged me in the field of chemical looping technologies.

I am also grateful to Prof. Torsten Fransson and Ms. Chamindie Senaratne of the KTH to help me settle at DENERG at Polito. I would like to thank my friends in Torino: Dr. Rajat Srivatsava, Dr. Praveen Jagdale, Arpit Maheshwari, Hoeshang Wu, Marta

Gandiglio, Davide Drago, Alicia Soto, Archishman Bose, Felice Di Tomaso, Prudwee and all fellow mates of SELECT+ and InnoEnergy Ph.D. School. The life would be much harder if there were not you.

At last, I would like to thank my parents, who have always been a strong back for me. The family is the most precious thing in a person's life. Besides, I would like to thank the most special person in my life: my wife Tooba. She encourages me in a special way all the time when I lose my direction.

To *Ammi*…

Contents

List of Tables

List of Figures

List of publications

Journals:

1. Azharuddin, Archishman Bose, Jordi Llorca, Massimo Santarelli, Kinetic assessment of methane-driven non-stoichiometric ceria redox cycle and its effect on system analysis of an oxi-fired power plant fuelled by syngas produced by CO_2/H_2O splitting (*submitted to Applied Energy, under review*).
2. Azharuddin Farooqui, Felice Di Tomaso, Domenico Ferrero, Archishman Bose, Jordi Llorca, Massimo Santarelli, Techno-economic, energy, and exergy analysis of polygeneration scheme for power and DME production with the integration of CO_2 and H_2O dissociation through chemical looping (*submitted to Energy Conversion and Management, under review*)
3. Azharuddin Farooqui, Archishman Bose, Jordi Llorca, Massimo Santarelli; Simulation of two-step redox recycling of non-stoichiometric ceria with thermochemical dissociation of CO_2/H_2O in moving bed reactors --Part I: Model development with redox kinetics and sensitivity analysis (submitted to *Chemical Engineering Science*, under review).
4. Azharuddin Farooqui, Archishman Bose, Jordi Llorca, Massimo Santarelli; Simulation of two-step redox recycling of non-stoichiometric ceria with thermochemical dissociation of CO_2/H_2O in moving bed reactors --Part II: Techno-economic analysis and integration with 100 MW oxyfuel power plant with carbon capture (submitted to *Chemical Engineering Science*, under review).
5. A Bose, Azharuddin Farooqui, D Ferrero, J Llorca, M Santarelli, Thermodynamic analysis of syngas production by methane reduction and CO_2 + H_2O oxidation of ceria, *Materials for Renewable and Sustainable Energy*, 8:5, 1-15.
6. Azharuddin Farooqui, Archishman Bose, Domenico Ferrero, Jordi Llorca, Massimo Santarelli, Techno-economic and exergetic assessment of an oxy-fuel power plant fueled by syngas produced by chemical looping CO_2 and H_2O dissociation, *Journal of CO_2 utilization* 27 (2018) 500-517.
7. Azharuddin Farooqui, AM Pica, P Marocco, D Ferrero, A Lanzini, S Fiorilli, J Llorca, Massimo Santarelli, Assessment of a kinetic model for ceria oxidation

for chemical-looping CO_2 dissociation, *Chemical Engineering Journal* (2018) 346, 171–181.

8. Azharuddin, Massimo Santarelli, Thermodynamic analysis of solar beam down gas turbine power plant with CSP, *Journal of Physics: Conference Series* 745 (2016), 032011.

Conferences contribution:

1. Azharuddin Farooqui, Archishman Bose, Jordi Llorca, Massimo Santarelli, System analysis of natural gas combined cycle (NGCC) integrated with kinetics-based chemical looping syngas production, International conference on Innovative Applied Energy, 14-15 March 2019, UK.
2. Azharuddin Farooqui, W Jaroszuk, D Ferrero, M Santarelli, J Llorca, System efficiency analysis of dual interconnected bubbling fluidized bed reactors for solar fuel production, 31st International conference on efficiency, cost, optimization, simulation and environmental impact of energy systems (ECOS-2018), June 17-21, 2018 Guimares, Portugal.
3. Azharuddin, Archishman Bose, Massimo Santelli, Jordi Llorca, Thermodynamic analysis of Ceria for partial oxidation of methane and syngas production, International Conference On Renewable Energy (ICREN-2018), April 25-27, 2018, Barcelona, Spain.
4. Azharuddin, Domenico Ferrero, Massimo Santarelli, Jordi Llorca, Two-step solar thermochemical CO_2 splitting via ceria redox reactions: Synthetic fuel production, 3rd fundamental and application of cerium dioxide in catalysis, June 25-28, 2018, Barcelona, Spain.
5. Azharuddin, Massimo Santarelli, Thermodynamic analysis of solar beam down gas turbine power plant with CSP, 7th European Thermal-Sciences Conference. 19-23 June 2016, Krakow, Poland.

Nomenclature

Abbreviation	
NG	Natural Gas
NGCC	Natural gas combined cycle
VLS	Vapor Liquid Seperator
CLN	Column
SRC	Steam Rankine Cycles
MR	Methane Reduction
WS	Water Splitting
CDS	Carbon dioxide Splitting
DME	Dimethyl Ether
ASU	Air Separation Unit
TURBOEXP	Turbo Expander
RED	Reduction Reactor
OXI	Oxidation Reactor
LHHW	Langmuir-Hinshelwood Hougen-Watson
ST	Steam Turbine
GT	Gas Turbine
PHX	Preheater
TPC	Total Project Cost
BEC	Bare Erected Cost
EPCC	Engineering, Procurement, Construction Cost
TOC	Total Overnight cost
TASC	Total As-spent cost
TPC	Total Project cost
NETL	National Energy Technology Laboratories
CEPCI	Chemical Engineering Plant Cost Index
OPEX	Operational Expenditure
CAPEX	Capital Expenditure
DCF	Discounted Cash Flow
NPV	Net Present Value
HR	Heat Rate
CSP	Concentrating Solar Power
CCS	Carbon Capture and Sequestration
AIC	Akaike information Criterion
RSS	Residual Sum of Squares

SB	Sestak-Berggren model
AE	Avrami Erefe'ev model
CCS & U	Carbon Capture and Sequestration and Utilization
RWGS	Reverse water gas shift
CL	Chemical looping CO_2/H_2O splitting unit
IPCC	International Panel on Climate Change
GTL	Gas to Liquid
EOR	Enhanced oil recovery
FCC	Fluid Catalytic Cracking
MEA	Monoethanolamide
CLC	Chemical Looping Combustion
SRM	Steam Reforming of Methane
CPOM	Catalytic Partial Oxidation of Methane
OC	Oxygen Carrier
SMC	Stationary Monolith Cavity
CFD	Computational Fluid Dynamic
CFB	Circulating Fluidized Bed
TR	Thermal Reduction
MR	Methane Reduction
WS	Water Splitting
CDS	Carbon dioxide Splitting
SCM	Shrinking Core Model
RCSTR	Rigorous continuous stirred reactor
COMB	Combustor
HSRG	Heat Steam Recovery Generator
VACPMP	Vacuum pump
SYNCOMP	Syngas compressor
TIT	Turbine inlet temperature
LCOE	Levelized cost of electricity
O&M	Operational and Maintenance
LCOA	Levelized Cost of CO_2 Savings or Avoided
DME	Dimethyl Ether
MeOH	Methanol
POM	Partial Oxidation of Methane
TGA	Thermogravimetric Analyzer
SS	Solid-state kinetic model
QMS	Quadrupole Mass Spectrometer

MFC	Mass Flow Controller
PT	Prout-Tompkins Model
RPM	Random Pore Model

Symbols	
$\dot{m}$	Mass flow rate (kg/s)
LHV	Lower heating value (MJ/kg)
W_{NET}	Net power produced inside the plant (MW)
W_{ST1}	Power produced in steam turbine of SRC1 (MW)
W_{ST2}	Power produced in steam turbine of SRC2 (MW)
W_{GT}	Power produced in gas turbine (MW)
$W_{COMP,tot}$	Auxiliary compression power in compressors (MW)
W_{COMP-3}	Auxiliary compression power for recycling CO_2 (MW)
$\dot{W}_{el,net}$	Net electric power output (MW)
Q	Work obtained from heat flux (MW)
Q^*	Exergy obtainable using the heat of the selected stream (MW)
$I_{destroyed}$	Irreversibility generated (MW)
Ex	Total exergy (MW)
$Ex_{,k}$	Kinetic exergy (MW)
$Ex,_{ph}$	Physical exergy (MW)
$Ex,_{pot}$	Potential exergy (MW)
$Ex,_{ch}$	Chemical exergy (MW)
e_{ch}	Specific chemical exergy (kJ/kg)
X	Relative irreversibilities (MW)
$\dot{Q}_L$	System thermal energy loss (MW)
$\dot{Q}_{sol}$	Rate at which solar power provided to CL (MW)
$\dot{Q}_{RED}$	heat requirement at the reduction reactor (MW)
$\dot{Q}_{OXI}$	Heat released from the oxidation reactor (MW)
$\dot{Q}_{sld}$	Heat recovered from the solids (MW)
$\dot{Q}_{sphtr}$	Heat delivered to the solids for preheating (MW)
W_{VAC}	Pumping work resulting from vacuum generation (MW)
ΔH_{mix}	Enthalpy change due to mixing (kJ/kg)
ΔS_{mix}	Entropy change due to mixing (kJ/kg-K)
$Ex_{destr,i}$	Exergy destruction of i^{th} component (MW)
ΔG^0	Gibbs free energy (kJ/kg)
$CO_{2,DME}$	CO_2 embedded in DME (%)
X	Mass fraction (-)

H	Enthalpy (kJ/kg)
S	Entropy (kJ/kg-K)
R	Ideal gas constant (8.314 J/mol-K)
p_{00}	Partial pressure of the i-th component (Pa)
P	Density (kg/m^3)
T	Temperature (^{o}C)
C_{equ}	Equipment cost ($)
$C_{equ,actual}$	Actual component cost ($)
$C_{equ,ref}$	Reference component cost ($)
M	Scaling factor (-)
L	Number of years (-)
I	Discounted factor (-)
P	Pressure (bar)
θ	Fuel depletion rate (%)
Ξ	Productivity lack (%)
Ψ	Exergetic factor (%)
P_0	Pressure at environment state of 1 atm
T_0	Temperature at environment state of 20^{o}C
$\ddot{K}$	Equilibrium constant (m^3/kmol)
k_i	Arrhenius rate constant
R	Reaction rate (kmol/kg$_{cat}$-s)
Π	Concentration expressed (kmol/m^3)
Pre	Pre-exponential factor in chapter 6
A	Pre-exponential factor in chapter 5
Λ	Heat losses during the process (kJ/kWh)
Ω	Constant for water need for the cooling system per unit of energy that has to be rejected (dm^3/kJ)
Γ	Parameter for make-up water (dm^3/kWh)
B	Level of risk (%)
γ or δ_{max}	Maximum non-stoichiometry achievable for ceria (-)
x_1,y_1	Sestak-Berggren (SB) model parameters (-)
F-ratio	F ratio (-)
θ*	Braggs angle (^{o})
β^*	Line broadening at half the maximum intensity (FWHM)
λ^*	X-ray wavelength (Å)
D^*	Grain size (nm)
N	Avrami exponent (-)
g(X)	Integral function of f(X) (-)
K	Reaction rate constant in chapter 7
E_a	Activation energy (kJ/kg-K)

n_{CeO2}	Moles of ceria (mole)
M_{CeO2}	Molecular weight of ceria (g/mol)
n_{oxygen}	Accumulated intake of oxygen ions
Δ	Bulk-phase non-stoichiometry change (-)
δ_1	Non-stoichiometry reached after the reduction step (-)
δ_2	Non-stoichiometry reached after the oxidation step (-)
m_{CeO2}	Mass of the ceria sample used (mg)
$\dot{V}^0_{ox,in}$	Total volumetric inflow rate at standard temperature and pressure (STP) (ml/min)
$\dot{n}_{ox, out}$	Total molar outflow rate of the gas mixture (mol/s)
K_1	Number of parameter of the model (-)
$\hat{L}$	Likelihood function of the model (-)
n_1	Dimension of the data set (-) in chapter Appendix A.3.1
$\hat{u}_i$	Residual, the difference between the real values and the values from the regression model (-)
[Ce]	Cerium concentration
$[O_{Ce}]$	Oxygen that can be released from ceria
$[O_{vac}]$	Vacancies of the oxygen
$[O_{gas}]$	Oxygen gas concentration that is released
k_f	Forward reaction rate constants
k_b	Backward reaction rate constants
X	Conversion (-)
$X_{CO, out}$	Mole fraction of CO at the exit of the reactor (-)
X_M	Conversion value at the maximum (dX/dt) (-)
X_{OXI}	Solid conversion in oxidation (-)
X_{RED}	Solid conversion in reduction (-)
η_{th}	Thermal efficiency
η_{sol-e}	Solar to electricity efficiency
$\eta_{sol-field}$	Solar field efficiency
$\eta_{reciever}$	Receiver efficiency
η_1	System efficiency for the two-step chemical looping syngas production via methane reduction in chapter 4
η_2	System efficiency considering only the syngas produced in the oxidation reactor in chapter 4
η_{ex}	Exergy efficiency (-)
η_c	Energy efficiency (-) in chapter 6
A_k	Spatial footprint of the capture components for plant scale k (m^2)
S_i	Capacity of component i for plant scale k
$S_{i,ref}$	Reference capacity of component i for plant scale k

$\mathfrak{N}$	Calibration factor (-)
$\dot{R}$	Raw peak counts (a.m.u)
$\dot{B}$	Background reading counts arise due to background noise (a.m.u)
x_i	Mole fraction (-) in chapter 7 and weight fraction of fine particles (-) in Appendix A.1
N	Number of gases (-) in chapter 7
A	Reaction coefficient (-) in chapter 7 and decay constant (1/m) in Appendix A.1
$Re_{,p}$	Reynolds number of the particles
Ar	Archimedes number (-)
μ_g	Viscosity of the gas (Pa.s)
δ^*	Bubble volume fraction (-)
ε_s	Solids volume fraction (-)
ε_e	Emulsion volume fraction (-)
$V_{b,0}$	Maximum bubble volume before it detaches orifice surface (m^3)
N_{or}	Number of orifices (-)
d_{bm}	Maximum bubble diameter (m)
d_p	Diameter of the particle (μm)
u	Velocity (m/s)
$K_{i\infty}$	Elutriation rate (kg/(m^2-s))
A_{cs}	Bed cross-section area (m^2)
E_{ih} (t)	Entrainment flux of particles with diameter d_{pi} at time t and height h
F_∞	Elutriation rate above TDH (kg/(m^2-s))
F_o	Elutriation rate at the surface (kg/(m^2-s))
F	Entrainment rate in the freeboard zone (kg/(m^2-s))
D_c	Diameter of the reactor (m)
Λ	Specific water needs in (L/kWh) in chapter 5 and 6 and frictional coefficient due to particle collisions in Appendix A.1

Subscripts	
Ph	physical
Ch	chemical
Vap	vapor state
Liq	liquid state
COMP	compression work
P	product stream
Bm	maximum bubble

F	resource stream
Is	isentropic
mech	mechanical
comp	compressor
Turb	turbine
Ex	exergy
TURBEXP	work by turbo expansion
in,i	contribution to inlet mass flows
out,i	contribution to outlet mass flows
Tot	total or cumulative
COND	condenser
REB	reboiler
K	k-th component
S	solid
G	gas
B	bubble
b0	initial bubble
Mf	minimum fluidization
Br	bubble rise
E	emulsion
O	superficial
T	terminal

Chapter 1

Introduction

1.1 Background

Burning fossil fuels, resulting in anthropogenic carbon dioxide (CO_2) emissions are presently recognized as the primary contributor to climate change, with 35.2 Gt being emitted in 2017 [1]. Notwithstanding substantial investment and a decline in the prices of renewable energy, fossil fuels continue to play an indispensable role in the World's energy landscape [2]. Indeed, even though the trend is on a decline, such technologies continue to play a major role as the primary energy source, especially in developing countries. Hence, it is expected that the relevance of fossil fuels in the primary energy mix will continue to a significant extent in the considerable future. It is reported that one of a major source of the increase of carbon dioxide emissions are from power plants and followed by the transportation sector.

In a recent report by International Energy Agency (IEA), the estimated global energy demand grew by 2.1% in 2017 which was the twice the growth rate in the previous year. Fossils such as natural gas demand grew by an unprecedented value of 3% followed by oil which rose by 1.6%. It is also important to mention electricity demand increased by 3.1%. Even though renewables have seen the highest growth which accounted for $1/4^{th}$ of global energy demand in 2017. Overall, 70% of global energy demand was met by fossil-based fuels, out of which natural gas share was of 22% [1]. Therefore, the demand for hydrocarbons as primary fuel will continue to grow as shown in Figure 1. This will eventually lead to an increase in carbon dioxide emissions unless measures of fast transition are not adopted [3].

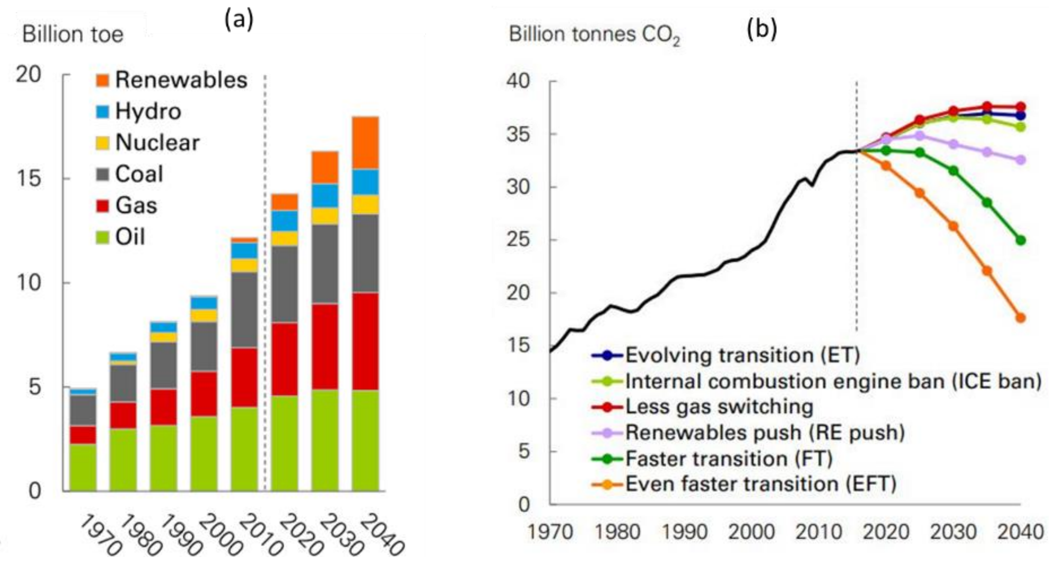

Figure 1. (a) Fuels as primary energy demand and (b) CO_2 emission forecast with different scenarios [3].

In the recent report of International Panel on Climate Change (IPCC) which pave the path of changing, the goal of restricting the global warming rise of 2°C to 1.5°C within by 2040 has been posted as mandatory. This leads to a global call to make some stringent efforts in changing energy policies to reduce further the usage of fossil fuels [4] otherwise consequences will be irreversible in terms of ecological imbalance and environmental damage. Primarily apart from renewable energy based power production, there was an extensive drive for carbon capture and sequestration (CCS) based power plants and call for retrofitting the existing power plants to adopt CCS. Since adopting CCS based power generation system would not solve the problem as the amount of CO_2 generation from them is so huge that it is not possible to store all of it in a depleted oil well or geological formations which also has safety implications to store in a long-term basis. Other alternatives such as the use of CO_2 in enhanced oil recovery also has limitations as the recovery rates are as low as 10% [5].

In this perspective, efforts to sequestrate CO_2 emissions should proceed together with a policy of re-utilization of the high amount of recovered CO_2. In terms of re-utilization, one possibility is to produce synthetic fuels from carbon dioxide emissions. Syngas is considered the target fuel because there is a large availability of CO_2 and H_2O from the flue gases of carbon capture based power plants, available for its production. Secondly, the syngas serves as the feedstock for multiple chemical productions such as methanol, dimethyl ether (DME), ethanol to just name two fuels [6]. The downstream possibility of usage of syngas is shown in Figure 2. At the moment syngas is produced using biomass, natural gas, and coal commercially. The natural gas to syngas by steam reforming, partial oxidation, autothermal reforming, and two-step reforming are the well-known technologies to produce syngas [7].

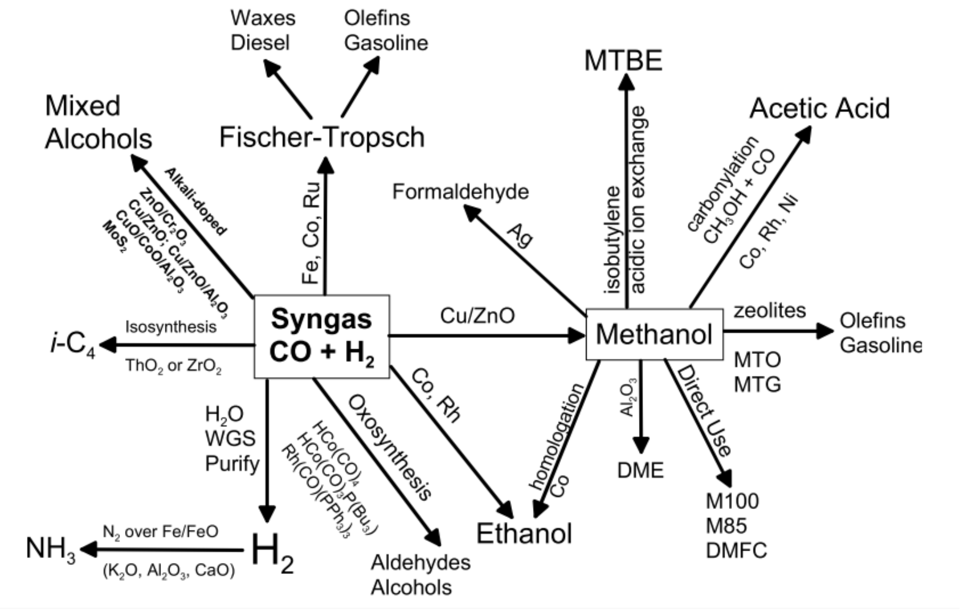

Figure 2. Syngas as feedstock for different chemical products [6].

Since the reforming reactions for syngas production are endothermic in nature and require external heat, their combination with solar energy is an attractive option to improve such processes [8]. What makes solar energy even more attractive to the production of fuels or chemicals, is the fact that solar energy is readily available almost everywhere. When a fuel (syngas, H_2, or any chemical based fuel) is produced by combining solar energy is termed solar fuel [9,10].

Conversion of solar energy and CO_2 by thermochemical processes to produce solar fuels was initially investigated to produce hydrogen as it was considered as the fuel of the future. Further processing can lead to the production of methanol, gasoline diesel, and kerosene, which are the liquid hydrocarbon feedstock for chemical processes, contributing to a sustainable circular economy in fuel and power industry as shown in Figure 3 [11]. Therefore, solar fuels considered as carbon neutral if they are produced from waste gas (a mixture of H_2O and CO_2), represent a viable way of storing intermittent renewable energy.

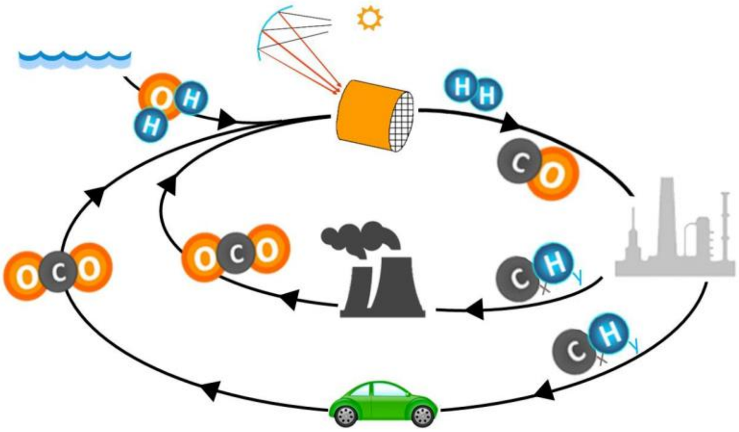

Figure 3. Circular economy by solar fuels from renewable energy. CO_2 and H_2O are captured from power plants and fed to a solar thermochemical process and converted to hydrocarbons in chemical plants [11].

There are many pathways suggested for solar fuels based on the mechanism, process and temperature range required (Figure 4). The processes are broadly classified as a photochemical or photobiological, electrochemical and lastly thermochemical group, which requires a very high temperature that can be attained by concentrated solar power technologies. Photochemical and photobiological pathway requires photon energy from solar energy, but the scale of the process is very small. In the electrochemical pathway, the solar energy is initially converted to electricity, which by electrolysis produces hydrogen or syngas depending on the feed.

Thermochemical cycles associated with concentrated solar energy constitute one of the cheapest solutions in terms of cost among those mentioned above to produce syngas and hydrogen [12]. It is comparable with the most developed and widespread process which is Steam Methane Reforming. The problems related with steam methane reforming (SMR) are the degree of development of the technology which does not allow to reach higher efficiency and the use of a fossil fuel as raw material, which is a greenhouse gas emitting process [13]. Anyway, the demand for clean and cheap hydrogen is pushing the research towards the development of alternative technologies [14,15].

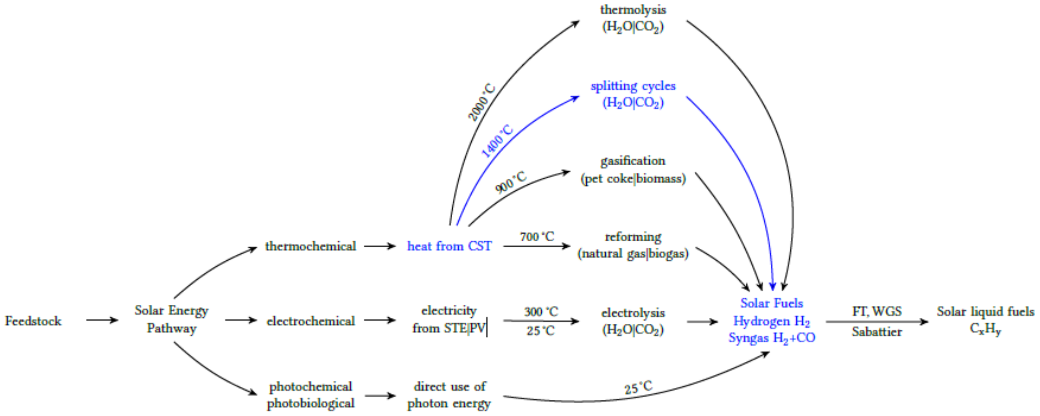

Figure 4. Solar fuels major pathways [16].

Theoretically, the simplest reaction to obtain syngas from the mixture H_2O/CO_2 is the direct thermal splitting. Unfortunately, the temperature needed of 2400°C is not achievable with the current technology and the problem of the separation of H_2 and O_2 to avoid explosive mixtures is a major issue. Alternatively, the process of thermochemical dissociation is carried out in two steps (reduction and oxidation) by using metal oxides, which tremendously lower the temperature required for syngas production.

In two-step thermochemical redox cycles heterogeneous chemical reactions take place. The solid reactant is usually a metal oxide (also called an oxygen carrier) that changes its oxidation state stripping and releasing oxygen in a cyclic way. Many materials have been investigated to maximize the syngas production, minimize the degradation and to reduce the operating temperature. The most interesting was found to be ferrites, ceria-based materials, and perovskites. For all these materials there is the possibility of tuning their redox properties and improve their behavior thank to an appropriate doping of their lattice. [16].

1.2 Motivation

In the last two decades, a number of oxygen carriers have been investigated for two-step thermochemical dissociation of H_2O and CO_2. Initially, the focus was on volatile oxygen carriers but the challenges associated with quenching and sublimation of this type of carriers led the researchers to develop non-volatile metal oxides [17]. The initial focus was on iron oxide-based ferrites and hernicytes [18,19]. In the last decade, the research was more focused on non-stoichiometric carriers such as ceria and doped ceria oxides which showed high reactivity and splitting rates at lower temperatures. In parallel, perovskites were explored due to very high reported oxygen storage capacities.

In order to make the concept of thermochemical solar fuel production to a pilot or demonstration stage, large-scale availability of the oxygen carrier is essential [20–23].

Ceria is abundant in nature, with properties such as non-toxic, environmentally friendly and economically cheap. Therefore, in the non-stoichiometric non-volatile category, it may be the best candidate for an industrial scale-up of the process.

Most of the experimental investigation reported in literature about this oxide was focused on enhancing the reactivity by different synthesis methods, different level of doping, and different type of dopants. However, since the non-stoichiometry during the reduction and oxidation steps varies due to temperature and pressure, it is very difficult to draw a mapping of the thermodynamic properties of all the developed materials [24]. As for any chemical process, the thermochemical redox cycles have been investigated thermodynamically by considering different swings of temperature and pressure between reduction and oxidation [25–30]. The literature also explored the different techniques by which reduction via vacuum pressure can be achieved and system analysis of solar thermochemical units for power plants have been reported. [31–33].

Un till now all the demonstrated setup built to show the proof of concept of two-step thermochemical dissociation for syngas production have been structured reactors which are characterized by a very low efficiencies, in which ceria has been used in the form of reticulated, foam, monolith or honeycomb structures and the inert or oxidizing gases passed through it [34].

Only a few studies reported about moving bed and fluidized bed reactors with the focus on whether the redox cycling can be achieved even using these configurations [35,36]. In this case, selection of the volume of the reactors is highly depended on the CO_2/H_2O feed and ceria recirculation rate between the oxidation and reduction reactors. However, reported investigations did not estimate the volume of each reactor for achieving an appreciable amount of conversion and selectivity in each cycle. Therefore, the design of such type of reactors requires further studies.

Also, it would be of utmost importance to know whether such a chemical looping unit (solar thermal reduction and CO_2/H_2O splitting) can be integrated to an oxy-fired power plant, which can provide CO_2/H_2O at industrial scale. In addition, taking into account that the solar thermochemical redox cycles are highly dependent on the availability of irradiance, it is essential to investigate the system based on the capacity factor on which these cycles could operate annually. Therefore, a feasibility study would help in determining the bottleneck of the process to make it commercially viable.

Ceria is also investigated for partial oxidation of methane in the literature [37]. Therefore, the solar thermal reduction step which needs endothermic heat and high vacuum pressures (or a huge volume of inert gas to maintain the very low partial pressure of oxygen) can be replaced by a methane-driven reduction of ceria. Methane-driven redox cycle is able to operate at atmospheric pressure. This eliminates the pressure swing between the two-step redox recycling. It also gives the freedom to run isothermal redox cycles with heat recuperation between oxidation and reduction. However, few experiments have reported the reactivity of methane reduction followed by H_2O splitting [38]. Studies were focused on the reactive behavior of the ceria-based oxygen carriers during redox cycles and on the ability to reach the large extent of reduction and oxidation. Apart from the morphological investigations, synthesis methods, doping characteristics of different oxygen carriers, the research extended even to characterize mechanical mixing of two oxygen carriers [39–43]. Very few groups reported on the kinetic assessment, determination of reaction mechanism or fitting of semi-empirical kinetic models for methane driven redox cycles. It is essential to investigate the temperature range at which redox cycles can be performed to avoid methane cracking during reduction and at the same time achieving appreciable non-stoichiometry. Moreover, as the exothermicity and reaction rates for CO_2 and H_2O splitting are different with H_2O being the faster, it would be relevant to consider how CO_2 splitting may influence the complete re-oxidation of ceria when comes in contact with H_2O. The fuel reduction in redox cycles has more benefits compared to the solar thermochemical reduction, which gives a new area to explore for the recycle/conversion of CO_2 at large scale in power plants and gas to liquid (GTL) plants.

The challenges described above in thermochemical redox cycles based on ceria oxides for syngas production allow framing the following objectives to understand the fundamentals and limitations of these systems and also to explore their feasibility to recycle/convert CO_2 at large scale with a beneficial environmental impact.

1.3 Objectives

The objectives of the present work are to investigate ceria driven chemical looping syngas production systems and are listed as:

- To provide the state of the art about the technologies and the reactors that have been explored into two-step thermochemical conversion of CO_2 and H_2O for syngas production.
- To develop a moving bed reactor model for reduction and oxidation of a chemical looping CO_2/H_2O splitting (CL) unit and to explore the effect of temperature and pressure in the reduction step and in the efficiency of whole CL process.
- To investigate the effect of adding the solar thermochemical CO_2/H_2O splitting unit to an oxy-fired power plant, focusing especially on the effect of reduction temperature and pressure on an integrated power plant, this to determine the optimum operating conditions. Moreover, the economic viability of the proposed plant and determination of bottleneck components that may limit the integration of CL unit to the oxy-fired power plant will be considered.
- To investigate the thermodynamics of methane reduction by ceria followed by CO_2/H_2O splitting for syngas production and to derive the temperature and flow limits for optimal conditions.
- To investigate the feasibility of adding a methane-driven CL unit to a 500 MW oxy-fired power plant with 100% carbon capture and to draw the operating

conditions to provide an efficiency gain compensating what was lost due to carbon capture.

- To make a comparative investigation of a conventional oxy-fired and oxy-fired power plant with the chemical looping CO_2/H_2O splitting unit about techno-economics, water-energy nexus, and the land requirement finalized to draw an overall conclusion of syngas production at large scale with CL processes.
- To investigate the feasibility of adding a methane-driven CL unit to a polygeneration plant that produces power and dimethyl ether and to carry out a techno-economic, energy and exergy analysis for maximum power dimethyl ether production along with power production.
- To determine the kinetic assessment of methane reduction for syngas production and CO_2 splitting for a suitable temperature, i.e. to provide an evaluation of the kinetic model along with kinetic parameters such as activation energy and pre-exponential factors.
- To investigate the effect of solar thermal reduction and methane reduction kinetics on the overall system efficiency when CL is integrated into the power plant
- Lastly to draw recommendations and give direction for further research to make the technological CL concept a reality for large-scale power and fuel production plant.

1.4 Thesis structure

The thesis is organized as per the objectives listed in the above section. Firstly there is an investigation of the solar thermochemical dissociation of CO_2/H_2O using a moving bed model for reduction and oxidation reactors. The scope is to validate the model and determine the selectivity of the syngas at the different operating conditions. The study extends the scope of integrating the solar thermochemical splitting unit to a power plant to foresee the benefits and challenges from a technical and economic point of view. In the second part of this analysis, the solar thermal reduction is replaced by methane reduction to gain the benefit of producing syngas in both reduction and oxidation reactors. Methane-driven chemical looping syngas unit is then integrated into the power plant to investigate the efficiency gain with 100% carbon capture. The analysis is then extended to fuel production (dimethyl ether) along with power generation to define the feasibility of a polygeneration system.

Chapter 1 gives a general introduction to the topic followed by a detailed literature review in Chapter 2.

Chapter 2 describes carbon capture and sequestration technologies, and the solar thermochemical redox cycles investigated in the current literature. Different reactors and their classification based on different oxygen carrier materials are presented. Different modeling efforts by many research group and methodologies adopted are described in detail.

Chapter 3 is divided into two sections. The first section presents a moving bed model used for reduction and oxidation reactors for solar thermochemical CO_2/H_2O splitting. The model includes non-stoichiometric redox cycling considering reaction kinetics. The second section presents a techno-economic study of the solar thermochemical looping unit integrated with a 100 MW oxy-fired power plant.

Chapter 4 presents a detailed thermodynamic methane driven chemical looping redox cycle. The reduction and oxidation reactors considered are based on Gibbs minimization principle to investigate the parameters such as methane to ceria ratio, reduction temperature, and metal oxide and gas inlet temperatures. For the oxidation reactor, CO_2/H_2O composition, excess flow required and endothermicity and exothermicity heat are explored.

Chapter 5 describes the techno-economic, energy and exergy analysis of a methane-driven chemical looping unit integrated with a 500 MW power plant with 100% carbon capture. The study includes a detailed sensitivity analysis of the major performance indicators that affect power production. A comparative evaluation is done for the conventional natural gas power plant, an oxy-fired power plant with 100% carbon capture and oxy-fired power plant integrated with chemical looping CO_2/H_2O splitting unit with 100% carbon capture. Lately, economic analysis of the plant is investigated for main economic indicators contributing to capital investment. Finally, the water-energy nexus of the power plant proposed along with the land requirements is presented.

Chapter 6 describes a polygeneration plant that produces power and dimethyl ether. The plant includes a 100 MW oxy-fired power plant with 100% carbon capture integrated to the methane-driven chemical looping unit considered in chapter 4. The study involves a detailed sensitivity analysis to derive operating conditions to maximize power and dimethyl ether production. The analysis includes an economic investigation to identify the costs of each section of the plant that may limit its application.

Chapter 7 presents a reactivity and kinetic assessment of two sets of experiments obtained in a horizontal tubular packed bed reactor. The first set of experiments were performed by considering hydrogen reduction followed by a CO_2 splitting oxidation step to evaluate the CO production. In the second set of experiments, methane reduction of ceria followed by CO_2 splitting was tested.

Chapter 8 investigates the effect of the kinetics which was developed in chapter 7 and integrated into a moving bed reactor model for a redox chemical looping unit for a power plant.

Chapter 9 compiles the conclusions of this study and recommendations for future work.

Chapter 2

Literature review

2.1 Carbon capture and sequestration

Carbon capture was proposed in the late 1970s, after the global crisis, to enhance the oil recovery. Later, the use of CCS was shifted to capture CO_2 emitted from fossil fuel for tackling climate change. At the current status, there are 26 facilities integrated with CCS technology, which account for more than 30 Mtpa of CO_2 emission avoided [44]. The CO_2 produced in a power or industrial plant is previously captured, conditioned, transported through pipeline, railways or roadways and stored in a suitable body for several decades. According to the point where CO_2 is separated CCS is referred to as pre-combustion, oxi-fuel or post-combustion as can be seen in Figure 5.

In post-combustion CCS, CO_2 is separated downstream from the flue gases after the combustion of fossil fuel [45]. The main advantage of this technology is that can be adapted to retrofit existing fossil fuel plant such as a coal power plant. However, its use implies a plant efficiency penalty and cost addition due to the fact that CO_2 is present in the flue gases with a low partial pressure, since the use of air in the combustion. In addition, flue gases coming from the combustion chamber are at ambient pressure, making the CO_2 separation highly energy inefficient [46]. The most used separation process are physical and chemical absorption in which CO_2 is scrubbed through a liquid solvent. In physical adsorption, CO_2 is physically captured at the surface of the solvent, which has an increased absorption ability at high pressure [47]. In general physical absorption is used when CO_2 content in flue gas is higher than 15% vol. [48]. In chemical absorption process, the flue gases are scrubbed through an aqueous alkaline solvent (MEA, DEA, MDEA etc.) in an absorber, where CO_2 is captured by the solvent via chemical reactions. A subsequent stripper column is used to regenerate the rich-in CO_2 solvent through heating up and release a high content CO_2 stream (>85%) [49]. When the flue gas from fossil fuel power is at ambient pressure and CO_2 content is lower than 15% vol, chemical absorption is preferred.

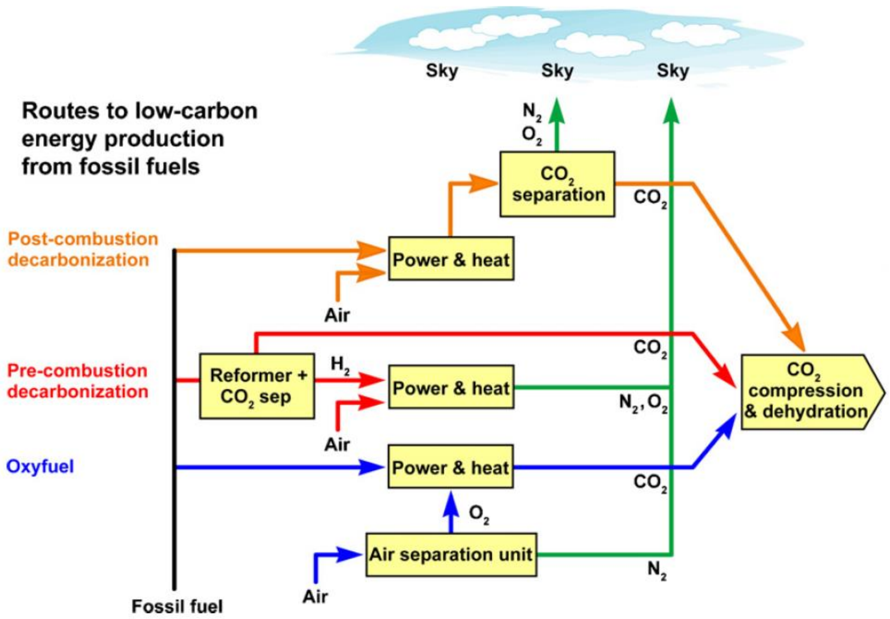

Figure 5. Main route for carbon capture [46].

An oxyfuel CCS based process consists in burning the fuel in a pure oxygen atmosphere (>95%) so that the flue gas is not diluted in nitrogen but is only composed by CO_2 and water which can be easily separated by condensation. For this reason, oxyfuel-combustion permits to achieve a 100% CO_2 capture. In addition, since N_2 is present in low amount, NO_x production is limited [50]. Differently, from air combustion plant, where N_2 absorbs the heat of combustion, in oxyfuel combustion plant, in order to control the adiabatic flame temperature, a recirculation of the exhausted gases is required (>80%) [50]. This technology can be used for novel plants or can retrofit existing power plants with few modifications [51]. The main drawback is the energy required to produce a pure oxygen stream in an air separation unit (ASU); it is estimated a consumption of 0.16-0.25 kWh per kg of O_2 for the production of a 95% pure O_2 stream [52]. Separation of oxygen from nitrogen can be either obtained by cryogenic and non-cryogenic processes. For industrial process where a high amount of O_2 is required, cryogenic separation is used. Nevertheless, most of the research is direct to non-cryogenic technology, such as membrane separation, whose adoption will reduce the energy penalty [48,51]. Cryogenic separation takes advantage of the different condensation temperatures of gases. The air is firstly compressed (4-6 bar), cooled down to its condensation temperature (-172°C at 6 bar) and sent continuously to two stripper columns where N_2 and O_2 are separated [53]. The energy cost of this cycle is due to the air compression, which is required to have an appropriate level of cooling power to drive the separation [54]. In the current state of the art, big scale oxyfuel combustion is not yet in the commercial status, most of the projects are pilot or demonstrative plants based on coal combustion [55]. As shown in Figure 6 after the construction of pilot plants of 1 MWe and lower size in the first decade of 2000s, larger size demonstration plants such as White Rose in the UK [56] or Shenhua in China [57] are now in the phase of projection and construction. Regarding the oxyfuel combustion process integrated with the natural gas-driven cycle, they are in a lower stage of development with respect to above-listed coal fed projects. Few proposed plants such as the one from Allam et al. [58] or Anderson et al. (CES) [59] have reached the demonstrative phase.

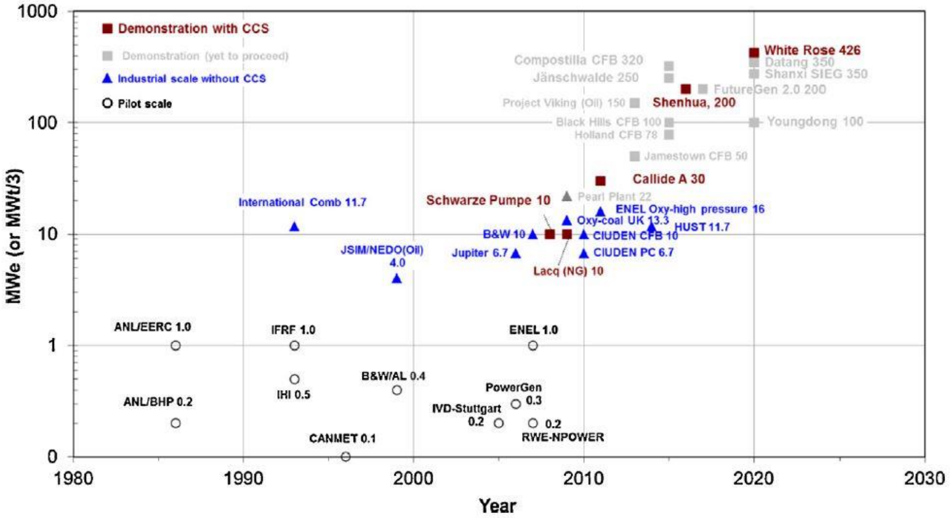

Figure 6. Historical progression of oxyfuel combustion technology [60].

In pre-combustion CCS process, pre-treatment of the fuel such as coal or natural gas is necessary. For coal, it firstly undergoes low-O_2 gasification process which produces a syngas mainly composed of H_2 and CO. A water gas shift (WGS) reaction is secondly used to increase the H_2 content converting CO in CO_2 (reaction (2.1)). In the case of methane, which is in gaseous form, it undergoes steam reforming (reaction (2.2)) and then the H_2 content is increased by a WGS reaction [45].

$$CO + H_2O \leftrightarrow H_2 + CO_2 \tag{2.1}$$

$$CH_4 + H_2O \leftrightarrow 3H_2 + CO \tag{2.2}$$

Finally, CO_2 and H_2 are separated via physical, chemical absorption or using membrane separation and H_2 is burnt producing as a product just water [61]. After sequestration, CO_2 is dehydrated, conditioned, pressurized at a pressure of 110 bar and sent to storage location via pipeline, railways or roadways [62]. Especially for large plants, pipeline transportation is the main solution, since it has been used for decades, especially in the USA, for oil recovery (EOR)[63].

There are several options for CO_2 storage. At present, the most corroborate option is the storage in geological bodies such as deep saline aquifers, unmined coal bed or oil and gas depleted reservoir [44,64]. A suitable geological site can hold a million tonnes of CO_2 for several decades or centuries by different physical and chemical mechanism [65]. An alternative is to store CO_2 in the oceans. Injecting carbon monoxide at depths higher than 3 km, it is demonstrated that it can be stocked for several centuries due to the CO_2 higher density with respect to the surrounding [66]. Moreover, oceans cover 70% of the earth's surface, so they can represent a sink for a huge amount of CO_2. However, there is some controversy about the potential risk of acidification of water due to CO_2 storage that would be disastrous for the marine ecosystem [66]. For this reason, although the high potential, ocean storage is not considered in the near term.

To conclude, CCS is one of the most attractive solutions to climate change tackling, especially in the middle term where fossil fuel is still the main source for power generation. However, it presents many drawbacks such as energy efficiency drop for the power plant when it is integrated. It is estimated that the energy penalty might range from 7-15% drop in efficiency depending on the carbon capture technology [45]. In addition, storage due to potential leakage, earthquakes, global capacity, engineering feasibility, and economic expenditure issues are a controversial and critical part of the CCS chain [67,68]. For this reason, rather than a pollutant to be stored, CO_2 can be seen as a carbon feedstock for the production of new chemicals and fuels [69]. This concept opens to a new branch referred to as Carbon Capture and Utilization (CCU), which will be discussed in the following subsection.

2.2 Carbon capture and utilization

As an alternative to storage, CO_2 utilization has achieved a great attention in the scientific and industrial field in last years [70]. In fact, the concept of CCU not only permits to make fuel exploitation cleaner but also gives the opportunity for a more sustainable energy economy [71]. CO_2 can be recycled and used as a product directly or converted into a new one. Several industries use directly CO_2 for their applications. For example, in the food and beverage sector, it is used as a carbonating agent, packaging gas or in the pharmaceutical sector as an intermediate for drug synthesis [72]. However, these market do not have a potential size to be considered a valid solution in limiting CO_2 emissions in a crucial way. Viceversa, the conversion of CO_2 to chemicals and fuels is a promising and attractive market as it allows to cut a portion of the capture cost and create a closed-loop carbon cycle [73]. CO_2 conversion into fuel or chemicals initially received criticism for various reasons. Since the CO_2 embedding time into fuel is not so long as it will eventually get from fuel to CO_2 and then again into the atmosphere if it is not captured again. Other reasons being the stringent conditions such as very high temperatures for thermochemical dissociation. With scientific advancement capturing CO_2 and retrofitting existing plants would solve the issue of emitting CO_2 directly to the atmosphere.

It is estimated that the CO_2 recycle can contribute to a 7% reduction in overall emissions [74]. The main drawback of CO_2 is that it is thermodynamically highly stable and so its conversion requires high energy input, active catalyst, and optimum reaction conditions [75]. CO_2 can be used as co-reactant in carboxylation reactions, in which the all carbon dioxide molecule is built into products without entirely cut the C=O bonds [76]. Among carboxylation processes, mineral carbonation and utilization of CO_2 as a precursor to organic carbonates, carbamates, acrylates, carboxylic acids, and polymers can be cited [77]. For example, the production of urea, for fertilizers and polymers synthesis, is an organic carboxylation reaction that is already present at industrial scale (more than 100 Mt of urea are produced yearly) [70]. Alternatively to carboxylation, CO_2 can be reduced, breaking one or both the C=O bonds and used for the synthesis of new species like syngas. Syngas, a mixture of H_2 and CO, is one of the most valuable resources in the industry field since its versatility. As shown in Figure 7 the syngas can be used in multiple processes for either chemical, fuel and power generation.

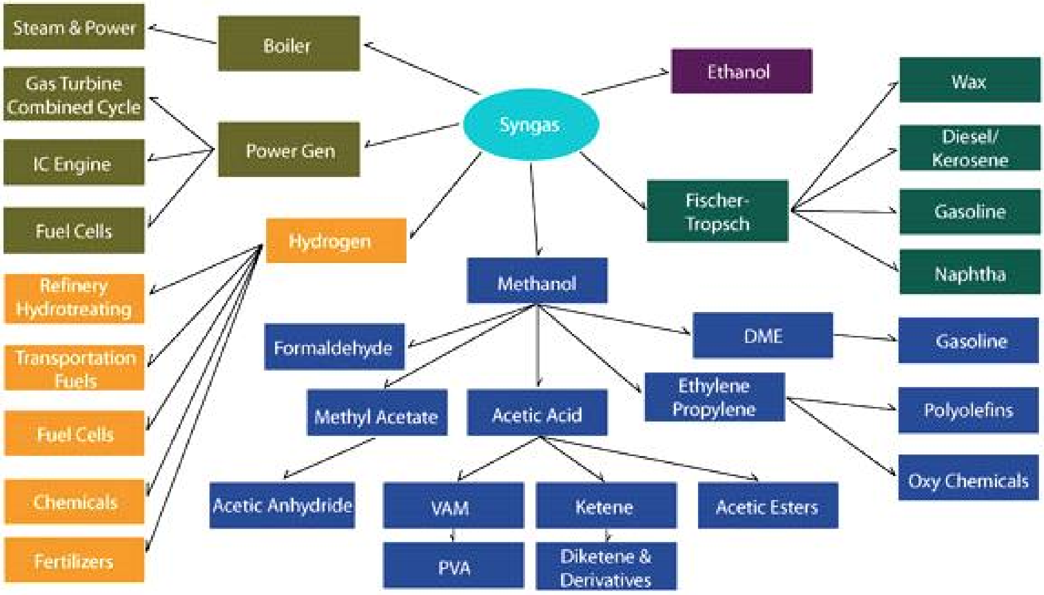

Figure 7. Syngas utilization routes in the industrial sector.

Nevertheless, as already stated, CO_2 is a highly stable molecule, so in order to break one of the C=O bonds a high energy carrier is required. Of great interest, it is when this energy vector, either heat, electricity, high-energy reactants (H_2, CH_4 etc.) are produced by renewable resources. This rends the reaction of dissociation a chemical storage of a renewable source [76]. Several processes have been proposed for CO_2 dissociation, one that has received great consideration in the research, especially for its application at a large scale, is the chemical looping [41,78]. In the following, a detailed description of the state of the art of this technology is presented.

2.3 CO_2 utilization using chemical looping processes

Due to the limitation of electrochemical or photochemical or other modes of conversions of CO_2, thermochemical conversions of CO_2 are being currently studied as cheaper alternatives. There are primarily two methods for such thermochemical conversions of CO_2, namely: (a) Direct dissociation (b) Chemical Looping.

Direct dissociation of CO_2 at extremely high temperatures of 1900˚C-2400˚C has been investigated by Traynor and Jensen in USA [79]. The process yielded around 6% of CO_2 into CO. Multiple other studies have been conducted to define the working parameters of such thermo-chemical conversions [80,81]. However, due to the requirements for high reaction temperatures and extra quenching processes, direct dissociation of CO_2 have so far been considered as difficult and unprofitable.

Chemical looping process is based on the principle of a set of chemical reactions occurring in multiple reactors, whereby, one of the reactants constantly circulates between reactors forming a closed loop as shown in Figure 8

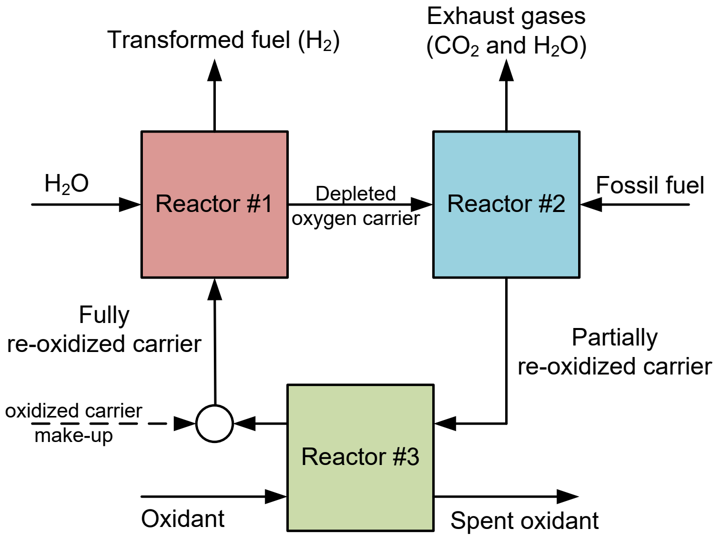

Figure 8. Chemical looping diagram of a three-reactor set–up for fuel decarbonization.

Indeed, for practical application, losses occur, requiring make-up of the reactants into the closed-loop system, as indicated by the dashed lines in Figure 8. In general, depending on the individual reactions being either endothermic or exothermic, such systems do not operate in isothermal conditions. Temperature swings between the reactors often over hundreds of degrees, requiring regenerative heat exchangers to be frequently incorporated into the system.

A wide variety of processes in the power engineering and petrochemical engineering currently use chemical looping as their main principle of operation, one of the most mature processes being the Fluid Catalytic Cracking (FCC). In this process, the catalyst is first used in the cracking reactor to break up higher order hydrocarbons to shorter chains, however, by losing its own potential, requiring regeneration. Therefore, it is sent to a regeneration reactor and back to the cracking process, thereby completing a chemical loop. In this process, the regenerator reactor is of a circulating fluidized bed type, whereby the catalyst resides for a couple of cycles in the regenerator (Figure 9). This configuration of the system helps in temperature control of the regeneration process which otherwise is highly exothermic [82].

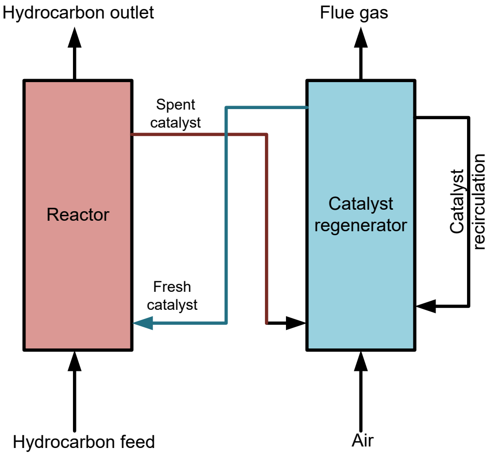

Figure 9. FCC process chemical loop with indicated recirculation of part of the catalyst in the regenerator.

Another example of an industrial chemical looping process is the monoethanolamine (MEA) reactor for Carbon Capture and Storage (CCS) systems. Though used in relatively small scale due to primary reason of lack of economic feasibility of the CCS process in current market condition, the technology is well developed. A general layout of the amine-based capture systems is presented in Figure 10. In this process, the exhaust gas is rinsed with chilled monoethanolamine in the counter-flow reactor, where the amines absorb the CO_2, SO_2 and other oxides available in the flue gas. Later the lean mixture is heated up, releasing the absorbed gases. Amines leaving desorption reactor are cooled down, first in the regenerative heat exchanger and in the additional cooler and then they are directed into the scrubber. The MEA system is used as a post-combustion method of the CO_2 separation, by which existing plants can be retrofitted to incorporate it.

However, new approaches are being developed for carbon capture, one of the recent developments being the separation of the exhaust gases from the oxidant through the Chemical Looping Combustion (CLC) process [83,84]. In such a system as opposed to the concept of direct interaction between oxidant and fuel, the oxygen required for the combustion process is transported in between them by metal oxides. In fact, Figure 8 represents diagrammatically a CLC system layout. Even though it is not necessary to have the three-reactor setup, some of the oxygen carriers might not be re-oxidized to their initial state within the first oxidation reactor (reactor #2, Figure 8) thus requiring additional oxidation reactor, fed with air or pure oxygen. Such a process has also been proposed to be used for fuel decarbonization.

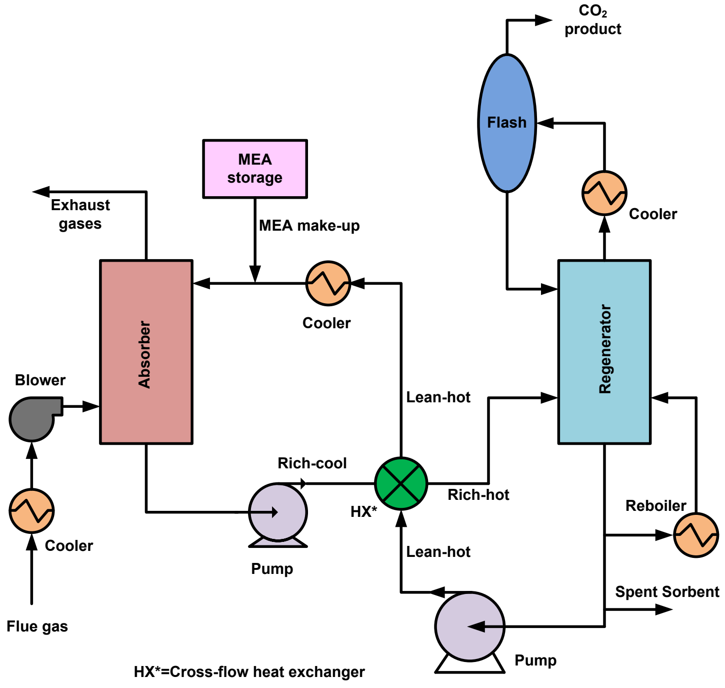

Figure 10. Monoethanolamine based carbon capture chemical loop diagram.

In the CLC, the chemical energy of a carbonaceous fuel (coal, hydrocarbons, etc.) is converted to chemical energy of hydrogen, as reported in processes studied by Chiesa et al. [47]. In the study by Chiesa, iron oxide-based redox pair (hematite–wustite–magnetite) was considered as the oxygen carrier in three reactors configuration as can be visualized from Figure 8. The complete reaction chain is exothermic, allowing the production of high-quality steam. Chemical looping CO_2 or H_2O splitting investigated in this work has similar configuration, though energy required to drive the process is not strictly limited to being from fossil fuel combustion, it can come from absorption of the solar irradiation or reduction via methane.

2.3.1 CO_2/H_2O dissociation by chemical looping

Chemical looping (CL) syngas production is an innovative fuel production technology based on splitting CO_2 and H_2O, for production of CO and H_2 respectively. In the most common two-reactor set-up of the CL, two interconnected reactors (reduction reactor and oxidation reactor), containing metal oxides particles, form a circulating closed loop, being alternately reduced and oxidized respectively. The principle of its operation is based on the spontaneous release of oxygen from the metal oxide's crystalline lattice either by thermal reduction at high temperatures (above 1300ºC) or by fuel reduction, which leads to the creation of oxygen vacancies in the material. Subsequently, this reduced metal oxide is re-oxidized in the low-temperature oxidation reactor (around 1000°C) with use of water vapor or carbon dioxide. It is important to mention that the thermal reduction is favourable at a very low partial pressure of oxygen (vacuum pressures). Therefore, in the solar thermochemical redox cycle, there would be a pressure and temperature swing between the two-steps unlike fuel-reduction redox cycles can operate at near atmospheric pressure as well as at isothermal mode.

Indeed, as mentioned, two fundamentally different pathways of the reduction reaction are possible. Thermal reduction using concentrated solar energy is one of the most studied processes. The energy required to sustain the otherwise endothermic reduction reaction and to maintain such high temperatures is derived from the concentrated solar radiation. The complete reaction chain occurring via thermal reduction of metal oxide can be presented as per equations (2.3) and (2.4). A schematic of solar based thermochemical and fuel-driven chemical looping CO_2/H_2O splitting redox cycle is shown in Figure 11(a).

$$\text{Thermal}-\text{reduction}:\ \text{MeO}_x \rightarrow \text{MeO}_{x-\delta} + 0.5\delta\text{O}_2 \tag{2.3}$$

$$\text{Water}-\text{splitting(WS)}:\ \text{MeO}_{x-\delta} + \delta\text{H}_2\text{O} \rightarrow \text{MeO}_x + \delta\text{H}_2 \tag{2.4a}$$

$$\text{CO}_2-\text{splitting(CDS)}:\ \text{MeO}_{x-\delta} + \delta\text{CO}_2 \rightarrow \text{MeO}_x + \delta\text{CO} \tag{2.4b}$$

However, an intriguing approach to operating the cycle at a lower temperature, thereby decreasing the temperature swing between reduction and oxidation, is to combine the redox cycle with the methane reforming [85,86] according to the equations (2.5) and (2.4). Several sources of methane, a primary constituent of natural gas can be identified. Besides the abundant supply of locally available natural gas, increased access to natural gas reserves, through technological innovations like hydraulic fracturing has resulted in an increased access to methane for multiple industrial processes [87]. Additionally, current development in power to gas (P2G) technologies, with a well-established natural gas network, can be speculated to provide an abundant supply of synthetic methane in the future. Moreover, also considering the importance of bio-methane in the renewable energy mix, the utility of methane would increase in the future. Apart from lowering the temperature of the entire cycle, this approach also enables the production of parallel streams of syngas from both the reduction and the oxidation reactors steps as shown in Figure 11, together with the possibility of the system to operate round the clock, without the need of the fluctuating renewable resource like the sun.

$$\text{Methane}-\text{reduction}:\ \text{MeO}_x + \delta\text{CH}_4 \rightarrow \text{MeO}_{x-\delta} + \delta\left(\text{CO}+2\text{H}_2\right) \tag{2.5}$$

In both the schemes, either a thermal reduction of fuel reduction, the oxygen carrier is often reduced to a non-stoichiometric extent (δ). Meaning that 0.5δ moles of oxygen is released from the oxygen carrier during thermal reduction which should be taken away by a vacuum pump. Similarly, by partial oxidation of CH_4 forming CO and H_2 (equation 4). For oxidation reaction, $Me_{x-\delta}$ would reaction with incoming CO_2 and H_2O forming CO and H_2 by reincorporating oxygen into the lattice of the oxygen carrier.

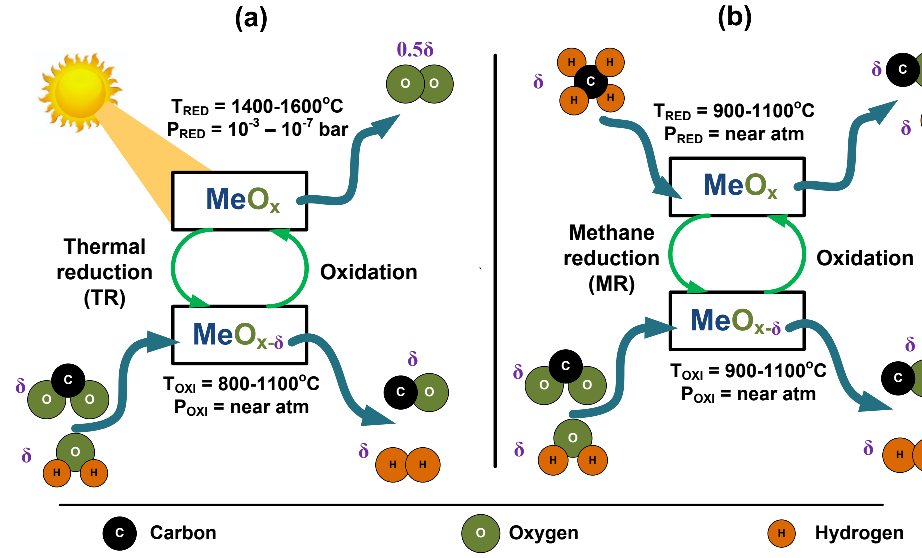

Figure 11. (a) Solar thermochemical redox cycle for syngas production (b) methane-reduction chemical looping CO_2/H_2O splitting for syngas production

In addition, the chemical looping partial oxidation of methane over metal oxide provides multiple benefits listed as follows:

i. It provides an alternative to the current high energy-intensive industrial process of steam reformation of methane (SRM) for syngas generation for subsequent chemical production.
ii. It also provides an alternate to catalytic partial oxidation of methane (CPOM), which, even though advantageous compared to SRM, suffers from the drawback of direct contact of fuel and oxidant near the auto-ignition temperature of the fuel, raising safety concerns [88]
iii. It also negates the need for a separate Air Separation Unit (ASU) for pure oxygen requirement in the CPOM process, whereby, the oxygen is supplied by an oxygen carrier directly during the partial oxidation process, simplifying the entire chemical cycle greatly.
iv. Since thermal reduction requires vacuum pressures and fuel reduction is possible to reduce the metal oxide at atmospheric pressure, this would eliminate the pressure swing between the thermally reduced two-step redox cycles.

2.4 Oxygen carriers used in CO_2 and H_2O splitting

Oxygen carriers are essentially the species of metal oxides which has at least two states of oxidation or one metallic and oxidized state. Examples include ZnO/Zn, Fe_3O_4/FeO, etc., that has the ability to release oxygen during high-temperature reduction process [22]. Numerous studies exist on the determination of the suitable metal oxide for the chemical lopping splitting cycle, the overview of which can be found in the literature [22,24,83,89]. Such wide variety of metal oxides require them to be categorized specifically, based on the temperature of the reduction and oxidation reactions, the potential for oxygen storage or whether the metal oxide undergoes phase transformation during the redox cycle.

2.4.1 Volatile oxygen carriers

Among the different categories that exist, the oxygen carriers for the two-step chemical looping applications can be technically classified into volatile and non-volatile oxygen carriers (also referred as metal oxides). Volatile redox usually exhibits a phase transition in the reduction step, especially during thermal reduction. The metal produced due to the reduction of the metal oxide is usually in a vapor state, due to the lower boiling temperatures than the corresponding metal oxides, thus requiring rapid cooling to avoid recombination of oxygen [24]. The most common volatile oxygen carriers (OCs) include ZnO/Zn, GeO_2/GeO, CdO/Cd and SnO_2/SnO as metal oxide/ metal redox pair [90].

The thermal reduction of the volatile metal oxides are usually highly endothermic, with the ΔG of reaction going below zero only at temperatures above 1723ºC, for instance, zinc dissociation from zinc oxide, the temperature is 1980ºC [24]. However, at this high temperature, the recombination of the reduced volatile metals with the released oxygen is the major problem. Therefore, a quenching process to fast cool the metal is an indispensable step for such redox pairs. Nevertheless, during the quenching process, a certain amount of oxygen recombines with the metal oxide reducing the overall effectiveness and efficiency of the cycle [22]. Multiple studies have focussed on the research and development of working with the volatile metal [91–93]. However, the drawback of the quenching remains as the major issue for such redox pairs. Hence, this type of metal/metal redox pairs was not further considered in recent times.

2.4.2 Non-volatile oxygen carriers

Non-volatile oxygen carriers, unlike the volatile oxygen carriers, do not undergo phase transformation upon reduction, either thermally or chemically, i.e., they remain solid during the entire thermochemical cycle. Hence, no quenching step is necessary. Most often, specifically for thermal reduction, the non-volatile carriers are carried out from the reactor via sweep gases only as solids. Therefore, the separation of the reduced metals, usually in a cyclone is much easier, lowering the system complexity and also system losses. Nevertheless, non-volatile cycles usually utilize those metal oxides having a lower storage capacity than their volatile oxygen carrier (OC) [22]. It is worth mentioning that due to the lower molecular weights of the volatile OC, they tend to have a larger share of oxygen atoms by weight. Thus, often, the storage capacity of the volatile metal oxides are 2 to 5 times higher than in the case of magnetite/wustite or ceria/Cerium Oxide (III) pairs.

Several non-volatile OCs were investigated in the literature including ferrites with different valences, Co_3O_4, Nb_2O_5, WO_3, SiO_2, Ir_2O_3, CdO to name few [21,94–97]. The magnetite/wustite redox cycle was firstly proposed in 1977 by Nakamura [98], while Roeb et al. [99], in 2006, was one of the first to propose the same metal pair for the water dissociation. In this redox cycle, the magnetite was first thermally reduced to wustite by simultaneously releasing oxygen, while the water reacted back with the wustite (FeO) to form magnetite (Fe_3O_4) and H_2, as per the following equation (2.6) and (2.7).

$$Fe_3O_4 \rightarrow 3FeO + 0.5O_2 \tag{2.6}$$

$$3FeO + H_2O \rightarrow Fe_3O_4 + H_2 \tag{2.7}$$

Iron oxides have been historically investigated as oxygen carriers for Chemical Looping Combustion (CLC) initially. However, unlike the three-step CLC, the iron oxide-based cycles used for water and carbon dioxide splitting are two-step cycles, whereby, the Oxygen Carrier (OC) goes through the magnetite/wustite cycle, without being fully reoxidized to hematite. In his work, which essentially was a thermodynamic analysis, Nakamura [100] developed the reaction system for alternate reduction and oxidation at temperatures of 2200°C and 1000°C respectively. The thermal reduction was evaluated to occur in air. However, the thermal reduction temperature, being higher than the melting point of the component metal oxides, limits the applicability of this process. Multiple strategies, however, can be used to improve the benefit of the cycle that included: decreasing the cycle operation pressure [100]; doping of the iron oxide either with transition metal such as manganese (Mn), cobalt (Co), nickel (Ni) or zinc (Zn) forming a ferrite oxide $(Fe_{1-x}M_x)_3O_4$ or with a reduced form $(Fe_{1-x}M_x)_{1-y}O$ with the aim of decreasing the reduction temperature [22,101]. All the alternatives were studied with relative advantages and disadvantages and have been extensively reported in the literature [91,99,102–104]. However, as can be noticed from the reactions (2.4) and (2.5), this redox pair OCs essentially operates between two thermodynamically stable stoichiometric conditions (FeO and Fe_3O_4). Hence such non-volatile oxygen carriers can be also be referred to as stoichiometric oxygen carriers as a sub-category.

Indeed, there exists one other sub-category within non-volatile OCs. This is formed by those oxygen carriers, which usually release oxygen, often up to a non-stoichiometric extent. One of the most studied metals in this category is cerium oxide. Cerium (Ce^{+4}) oxide has been extensively studied for different application as a catalyst for being structurally stable due to its elevated optical and electrochemical properties [105]. Furthermore, the crystallographic stability of CeO_2, even after several redox cycles are well documented [106]. Rapid kinetics, together with the very minimal effect of sintering at high temperature with good attrition resistance and mechanical strength makes ceria one of the most interesting materials for the chemical looping CO_2/H_2O splitting applications [86].

Indeed, temperature plays one of the most important roles in determining the stoichiometric extent of reduction. Abanades and Flamant [107] have reported almost stoichiometric reduction of cerium (Ce^{+4}) oxide to cerium (Ce^{+3}) oxide at very high temperatures of around 2000ºC, however, often leading to problems of sublimation of the reduced OC. Nevertheless, the focus in the later stages of material development was shifted too much lower temperatures, around 1300 to 1500ºC, even though this yielded non-stoichiometric reduction of ceria. Both the stoichiometric and non-stoichiometric thermal reduction reactions, followed by the splitting with CO_2 and H_2O, are shown in the following equations (2.8) and (2.9) respectively.

$$2CeO_2 \rightarrow Ce_2O_3 + 0.5O_2 \tag{2.8}$$

$$CeO_2 \rightarrow CeO_{2-\delta} + 0.5\delta O_2 \tag{2.9}$$

$$CeO_{2-\delta} + \delta CO_2 \rightarrow CeO_2 + \delta CO \tag{2.10}$$

$$CeO_{2-\delta} + \delta H_2O \rightarrow CeO_2 + \delta H_2 \tag{2.11}$$

As can be understood, at lower temperatures and at non-stoichiometric conditions, the removal of the oxygen by thermal or chemical reduction is essential while ensuring no change in the crystalline structure even after repeated cyclic redox operation. Therefore, this results in a limiting non-stoichiometric parameter δ, which has been reported in the literature to be 0.35 by Buffin et al. [108], Kümmerle et al [109] and Knoblouch et al [36]. The corresponding maximum available oxygen storing capacity of CeO_2, therefore, can be calculated as 0.033 $kgO_2/kgCeO_2$ before the material loses its lattice configuration.

The performance of pure and doped ceria has been extensively studied in the literature. Gokon et al. [112] evaluated the comparative performance of ceria and $NiFe_2O_4$, both supported and unsupported on ZrO_2. Results showed a superior thermal stability and yield rates of ceria over six consecutive cycles. Better ceria oxygen was reported with a non-stoichiometric coefficient (δ) varying between 0.034 to 0.11 at a thermal reduction temperature of 1450°C. However, no significant improvement was observed as the temperature was raised to 1550°C [112].

Doping ceria has been investigated for improving the extent of reduction by increasing the intrinsic vacancies that affect its electronic structure which in turn influences the ionic conductivity resulting in the redox cycle to be achieved at lower temperatures. Abanades et al. [113] reported significant improvements in the thermal reduction behavior of zirconia doped ceria, $Zr_{0.5}Ce_{0.5}O_2$ powder, in comparison to pure Ceria. It was obtained that the reduction started already at 900ºC in comparison to 1150ºC for pure ceria with a 70% increase in yield of oxygen release from the doped

OC. However, this increases the oxidation temperature, with water splitting reactions starting in temperatures above 800ºC [113]. In a second study performed in 2011, the same research group reported the rapid decrease in the performance of the doped metal oxide for re-oxidation [114]. Sheffe et al. [115] carried out thermodynamic analyses for CO_2/H_2O splitting on differently doped ceria oxides. The general trend showed a reduction reaction starts at temperatures of 930°C with simultaneous enhancement of oxidation reactions with an increase in the dopant concentration. Results from the evaluation of thermochemical cycles for CO_2 dissociation utilizing doped ceria were also reported by Jiang et al. [42]. Similar improvement to the thermal reduction as obtained by Abanades et al. [113], was reported utilizing $Ce_{0.75}Zr_{0.25}O_2$ [42]. A doubling of the CO yield from splitting of CO_2, from 4.5 ml/g for CeO_2 to 10.6 ml/g for $Ce_{0.75}Zr_{0.25}O_2$ was obtained [42]. The temperature range for redox cycles for some of the volatile and non-volatile OCs are listed in Table 1. Redox temperature range for general OCsTable 1.

Table 1. Redox temperature range for general OCs.

Material cycle	**Temperature range (ºC)**
Tin cycle	600-1600
GeO_2/GeO cycle	1400-1800
CdO/Cd cycle*	1150-14-1723
Ferrite cycle	927-1327
Zinc cycle	1127-1727
Ceria	700-1600
Perovskites	1000-1600

*Cd is toxic and has very few studies

Otsuka et al. [116] first investigated the δ phase of ceria i.e., nonstoichiometric ceria for water splitting application. Non-stoichiometric reduction of ceria ($CeO_2 \rightarrow CeO_{2-\delta}$) occurs at a relatively lower reduction temperature of 1400ºC. Panlener et al. [117] carried out a thermodynamic analysis of oxygen non-stoichiometry of ceria at various oxygen partial pressures and temperatures. The thermal reduction of CeO_2 at 1500ºC and oxygen partial pressure of 10^{-5} bar results in non-stoichiometry of 0.066 which produces a nearly stoichiometric quantity of H_2 [106]. Ceria is reported to have a favorable oxidation kinetics but it has the drawback of poor reduction ability. CeO_2 is doped by several metal cations and metal oxides improve its reactivity and kinetics. Divalent such as Ca, Sr, Mg [118] and trivalent cations such as La, Sc, Gc, Y, Cr, Sm [119–124] have been doped in the fluorite lattice to create intrinsic vacancies. This promotes oxygen diffusion and in turns oxidation rate. For instance, La^{3+} doped with ceria improves thermal stability during multiple redox cycles. Doping of Cr^{3+} produces H_2 at very low temperatures. Ca and Mg cations doping will increase the ability of fuel production and lower the thermal reduction temperature. Tetravalent cations such as

Zr, Ti, Hf, Sn-doped with ceria facilitates reduction [121]. Doping of Zr^{4+} cation deforms the lattice structure of CeO_2 by reducing the partial oxygen molar enthalpy [119] and thereby increasing the reduction capability. Thermodynamic data calculations were confirmed with experimentation performed by Hao et al. [125] on oxygen non-stoichiometry in $Zr_xCe_{1-x}O_2$ (x=0-0.2), which shows the increasing extent of reduction with increasing Zr content at 1350ºC. Another study conducted for doping of tetravalent and trivalent cations to ceria [126] $Ce_xM_{1-x}O_{2-\delta}$ ($M=Ti^{4+}$, Sn^{4+}, Hf^{4+}, Zr^{4+}, La^{3+}, Sm^{3+}, Y^{3+}; x=0.75-0.95) was performed for CO_2 splitting. The tetravalent cations $M=Ti^{4+}$, Sn^{4+}, Hf^{4+}, Zr^{4+} doping shows higher oxygen production rates when tested at 1400ºC and the order of oxygen release was evaluated as CeO_2 (2.5 ml/g) < $Ce_{0.75}Zr_{0.25}O_2$ (6.5 ml/g)< $Ce_{0.75}Hf_{0.25}O_2$ (7.2 ml/g) < $Ce_{0.8}Sn_{0.2}O_2$ (11.2 ml/g) < $Ce_{0.8}Ti_{0.2}O_2$ (13.2 ml/g). Similarly, CO production is increased from 4.5 ml/g for CeO_2 to 10.6 ml/g for $Ce_{0.75}Zr_{0.25}O_2$. The release of both CO and O_2 simultaneously was also reported for $Ce_{0.75}Hf_{0.25}O_2$ and $Ce_{0.75}Zr_{0.25}O_2$ when the temperature exceeds 1100ºC. For $Ce_{0.8}Sn_{0.2}O_2$ and $Ce_{0.8}Ti_{0.2}O_2$, the oxygen release was increased several times, but CO production rate is low due to the formation of stable compounds, $Ce_2Sn_2O_7$, and $Ce_2Ti_2O_7$ respectively, after high-temperature reduction reaction. The trivalent cations M= La^{3+}, Sm^{3+}, Y^{3+} doping to ceria shows a negative impact for both O_2 release and CO production. In another study reported by G.Takalkar et al. [127] on doped ceria $Ce_xM_{1-x}O_{2-\delta}$ (M = Ni, Zn, Mn, Fe, Cu, Cr, Co, Zr) considering thermal reduction at 1400ºC and CO_2 splitting at (1000ºC) to investigate the effect of doping transition metals to the ceria using thermogravimetric analyser (TGA). It is reported that the doping of Zn and Fe showed the higher capability to release O_2/g of oxygen carrier during thermal reduction Similarly the CO splitting rates were higher for the reported doped oxygen carrier. The O_2 release rate for these doped ceria are reported as $Ce_{0.9}Zr_{0.1}O_{2-\delta} < Ce_{0.9}Mn_{0.1}O_{2-\delta} < Ce_{0.9}Cu_{0.1}O_{2-\delta} < Ce_{0.9}Co_{0.1}O_{2-\delta} < Ce_{0.9}Ni_{0.1}O_{2-\delta} < CeO_2 < Ce_{0.9}Cr_{0.1}O_{2-\delta} < Ce_{0.9}Fe_{0.1}O_{2-\delta} < Ce_{0.9}Zn_{0.1}O_{2-\delta}$ for the average values for ten cycles. Similarly the CO production ability reported are as follows: $Ce_{0.9}Zr_{0.1}O_{2-\delta} < Ce_{0.9}Mn_{0.1}O_{2-\delta} < Ce_{0.9}Cu_{0.1}O_{2-\delta} < Ce_{0.9}Cr_{0.1}O_{2-\delta} < Ce_{0.9}Co_{0.1}O_{2-\delta} < Ce_{0.9}Ni_{0.1}O_{2-\delta} < CeO_2 < Ce_{0.9}Fe_{0.1}O_{2-\delta} < Ce_{0.9}Zn_{0.1}O_{2-\delta}$. The results for CO_2 splitting rate are higher for doping of Zn and Fe which is higher than undoped ceria with highest being $Ce_{0.9}Zn_{0.1}O_{2-\delta}$ with CO/O_2 of 2.31 ratio of release for oxidation and reduction step. Ni and Co doping showed not much effect giving similar CO_2 splitting rates as that of undoped ceria.

2.4.3 Perovskite oxygen carriers

Besides metal oxides, perovskites, as alternative OCs have gained significant research interest in recent years. Even though the most significant share of the research for the applicability of such OCs is in the CLC and methane reforming processes [21,60], many studies have reported the outcomes of the use of perovskite in chemical looping CO_2/H_2O splitting [128]. Much better oxygen capacities at lower temperatures in comparison to both pure and doped metal oxides have been reported. Perovskites with general formula $ABO_{3-\delta}$ have large non-stoichiometry at high temperatures and also the oxidation reversibility, which is considered as an essential criterion for a material to be useful for thermochemical application of H_2 production with high solar to fuel conversion efficiency. Perovskites have been popular as oxygen separation membranes in the last decade, with multiple options of substituting A and B sites to tune the properties of the final material.

$La_{1-x}Sr_xMO_3$ (M=Mn, Fe) were investigated for syngas production with methane and H_2O as reactants at around 1000°C [126]. Substitution of transition metals such as Cr, Co, Ni, Cu in $La_{1-x}Sr_xFeO_3$ has significantly improved performance. $La_xA_{1-x}Fe_yB_{1-y}O_3$ (A=Sr, Ce; B = Co, Mn; $0\leq x, y\leq 1$) perovskites with different supports were tested for different temperatures [129]. For unsupported perovskites, there is no significant CO production reported even with a higher O_2 release during reduction cycle at a lower temperature. Different supports such as ZrO_2, Al_2O_3, and SiO_2 were tested and found SiO_2 to be the best candidate. By substituting A site and B site the reduction temperature i.e., O_2 evolution temperature is reduced by 200-300°C and fuel production is increased by 2-3 times. $LaFe_{0.7}Co_{0.3}O_3/SiO_2$ shows 4 times higher CO production compare to un-doped $LeFeO_3/SiO_2$ at a reduction temperature of 1300°C.

A-site substitution by alkaline earth ions

For $La_{1-x}Sr_xMnO_3$ (LSMx) perovskites high-temperature non-stoichiometry is investigated by extrapolating the low temperature experimental non-stoichiometry data using a defect model. Higher oxygen non-stoichiometry of LSM perovskites were observed compared to ceria under similar oxygen partial pressures and reduction temperatures (1500°C) for LSM35 ($La_{0.65}Sr0._{35}MnO_3$). It was also reported that the Gibbs free energy for LSM is more negative than ceria at similar temperature conditions. A study of LSMx (x=0-0.5) by Yang et al. [130] results in an H_2/O_2 ratio of 2, but increasing Sr increases the extent of reduction simultaneously decreasing the oxidation capability, thereby reducing the H_2 production. A new class of perovskites $La_{1-x}Ca_xMnO_3$ (LCMx, x=0.35, 0.5, 0.65) have been tested for WS and CDS [131]. The extent of reduction increases with the increase of Ca and there is a decrease in the reduction temperature by a significant margin. The reduction temperature was set to 1400°C and O_2 production was calculated for LCM35 (109 µmol/g), LCM50 (315 µmol/g) and LCM65 (653 µmol/g). LCM50 produces 1.6 times more oxygen than LSM50 (201 µmol/g) and 5 times more oxygen than ceria (112 µmol/g) under similar conditions.

With increasing of Ca percentage the oxidation ability decreases. At the oxidation temperature of 1373 K LCM50 undergoes oxidation stoichiometrically by 40% CO_2. Thus, LCM50 (525 µmol/g) produces 1.6 times than LSM50 (325 µmol/g) and 5 times more than ceria (112 µmol/g). Similar is the case of H_2 production and the WS was shown at 1273 K with LCM50 (272 µmol/g), which is lower than LSM50 (308 µmol/g) [130]. In both WS and CDS, reaction kinetics for oxidation was little slower. Similarly

$La_{1-x}Ba_xMnO_3$ (LMBx, x=0.35, 0.5) were tested for two-step CO_2 [132]. O_2 production is in the following order: LCM50 > LSM50 > LBM50. The CO production with LBMx did not show improvement. LCM50 has an orthorhombic atomic structure and LSM50 has a rhombohedral structure. The difference is due to the smaller size of Ca than Sr. Though the stoichiometry is the same for both LSM50 and LCM50, the difference in the activity is due to the structural difference which is indicated by tolerance factor (τ). The smaller value of the tolerance factor (0.978) of LCM50 compared to that of LSM50 (0.996) is responsible for the different splitting action.

A-site substitution by rare earth ions

Two perovskites families with rare earth ions were tested – $Ln_{0.5}Sr_{0.5}MnO_3$ and $Ln_{0.5}Ca_{0.5}MnO_3$ (Ln = La, Nd, Sm, Gd, Dy, Y) – for WS and CDS in two-step thermochemical decomposition [131]. It was reported that from La to Y, the oxygen production increases with the reduction of the size of the rare earth ion, with yttrium yielding the highest oxygen amounts. This is due to the decrease of tolerance factor with the smaller size of the rare earth ion. The oxygen production by YSM50 (481 µmol/g) is higher than LSM50. It was also reported that YCM50 even produces more oxygen (575 µmol/g); the oxygen release temperature decreases with the smaller size of rare earth ion from La to Y order. The size difference in Ln and A cations is described by a size variance factor σ^2 which creates disorder in the perovskite motif, which effects the reduction temperature of $Ln_{0.5}A_{0.5}MnO_3$. The variance factor of $Ln_{0.5}Sr_{0.5}MnO_3$ is significantly larger compared to $Ln_{0.5}Ca_{0.5}MnO_3$ and therefore $Ln_{0.5}Sr_{0.5}MnO_3$ has lower reduction temperature [131]. YSM50 has a higher variance factor and begins to release O_2 around 860°C and YCM50 at 970°C. Similar to O_2, CO production also increases with decreasing the rare earth ion size. Yttrium based perovskites show the highest CO production (671 µmol/g) at 1100°C. It was also reported that YSM50 produces fuel production in constant levels with multiple cycles, making it one of the promising perovskite for energy applications. The reduction and oxidation temperature reported being low as compared to other perovskites. Table 2 lists temperatures and performances of several perovskites and, for comparison, of ceria-based materials.

Table 2. Perovskites and ceria and doped ceria oxygen carriers and their operating conditions.

Oxide	T_{RED}(°C)	T_{OXI}(°C)	O_2 (µmol/g)	$CO(H_2)$ (µmol/g)	Ref
$Y_{0.5}Sr_{0.5}MnO_3$(YSM50)	1400	800	483	757^a	[97]
$Y_{0.5}Sr_{0.5}MnO_3$(YSM50)	1300	800	389	624^a	[97]
$Y_{0.5}Sr_{0.5}MnO_3$(YSM50)	1200	800	258	418^a	[97]
$Y_{0.5}Ca_{0.5}MnO_3$(YCM50)	1400	1100	575	671^a	[97]
$La_{0.5}Ca_{0.5}MnO_3$(LCM50)	1400	1100	315	525^a	[96]
$La_{0.5}Sr_{0.5}MnO_3$(LSM50)	1400	1100	201	325^a	[96]
$La_{0.5}Sr_{0.5}MnO_3$(LSM50)	1400	1000	298	298^b	[98]
$La_{0.5}Sr_{0.5}MnO_3$(LSM50)	1400	873	236	224^a	[99]
$La_{0.6}Sr_{0.4}MnO_3$(LSM40)	1400	700	205	397^c	[95]
$La_{0.6}Sr_{0.}Al_{0.6}Mn0_{.4}O_3$	1350	1000	120	247^a	[100]

CeO_2	1400	1000	53	105[a]	[114]
$Ce_{0.75}Zr_{0.25}O_2$	1400	1000	193	241[a]	[101]
$Ce_{0.75}Zr_{0.25}O_2$	1400	1000	179	323.9[b]	[101]

[a] TGA study for CDS

[b] TGA study for WS

[c] Alumina tube reactor was used for WS with an infrared furnace heating rate of 500°C/min.

B-site substitution

Apart from perovskites, ceria was reported to have the highest fuel production rate and conversion efficiency, therefore all the comparisons of new material were reported to compare with ceria for non-stoichiometric and non-volatile redox cycles. Aluminum was substituted in LSMx, and the material showed 9 times more H_2 and 6 times more CO production compared to CeO_2 with no change in reaction kinetics [133]. In $La_{0.5}Sr_{0.5}Al_{1-x}Mn_xO_3$ with an increase of Al content, there is an increase of O_2 release, which reaches 322 µmol/g for x=0.5. Similar is the case with the $La_{0.5}Ca_{0.5}Al_{1-x}Mn_xO_3$ increase in Al content, for which the O_2 release increases as well as CO production. It was also reported that Al doping reduces the formation of carbonate on the surface, which deactivates the perovskites characteristics [134]. Mg was also doped in LSMx which exhibits high resistance to sintering, but the fuel production was not improved compared to LSMx. [135]. Other transition metals such as Fe, Co, Cr were also tested for B-site substitution [126,129,136]. Ga and Sc substituted LSMx showed higher CO production rate [136].

Using $Sr_{0.4}La_{0.6}Mn_{0.4}Al_{0.6}O_3$, McDaniel et al.[137] obtained an increase of 8 times the yield of hydrogen at 1350°C than pure Ceria, with a subsequent higher yield of H_2 and CO from the H_2O/CO_2 split reactions respectively. A high cyclic stability of the perovskite was also reported, with no noticeable decrease in performance after 80 redox cycles. These results were subsequently confirmed through the studies by Jiang et al. [138], in 2010, where the performance of lanthanum–ferrite based perovskites doped with Co and Mn on the ferrite side were evaluated. Experimental results on the thermal reduction of both $LaFe_{0.7}Co_{0.3}O_3$ and $LaFe_{0.7}Mn_{0.3}O_3$ revealed the high oxygen carrying capacity of such materials. However, a poor performance of the CO_2 splitting was reported, which were considerably improved by the addition of supporting materials like SiO_2 [138]. Another study by Galinsky reported significant improvements to the reduction rate utilizing iron oxide supported $La_{0.8}Sr_{0.2}FeO_{3-d}$ (LSF) as a supplement to iron oxide [139].

2.4.4 Spinel structured oxygen carriers

Recent studies have also focused on the development of the spinel structured oxygen carriers for the chemical looping splitting application through the modification of physical and chemical properties. The selection of the right cation enables the synthesis of an OC, optimized for the selected application, with a high structural and mechanical stability under high-temperature operations [140,141]. Aston et al. [142] reported the performance of two mixed metal oxide spinels, $NiFe_2O_4$ and $CoFe_2O_4$ prepared by the incipient wetness method, with ZrO_2 as substrate. Results indicated a high yield of hydrogen through water splitting (7-9 times per gram of OC than iron oxide), however, at a much lower rate compared to that of iron oxide. Similar studies were performed on $CoFe_2O_4$ by Cocchi et al. [143]. Even though a faster reaction rate was seen, there was significant carbon deposition for CO_2 splitting, which would often limit the applicability of the tested material over several cycles. Also, due to the corresponding oxidation and reduction reactions, the applicability of this metal oxide to a two-step cycle is limited, with a three-step cycle being a more preferred solution [128].

With the in-depth review of different oxygen carriers for thermochemical redox application, it is evident that there is huge interest in the material development with respect to its reactivity, stability to operate at high temperature and pressure swing. Apart from these important aspects, other physical properties need attention, such as attrition rate, agglomeration and sintering behavior due to continuous cyclic redox operation. The reactivity properties of the oxygen carrier can be improved by finding ways to improve the oxygen carrying capacity by means of doping or with appropriate supports, which needs further research on new materials. At present, if the CO_2/H_2O dissociation could be implemented at industrial scale, then it could only be possible by an oxygen carrier which has good properties and at the same time, it is abundantly available. Out of the above mentioned OCs, ceria stands as reliable and good candidate showing good splitting ability and stability. The next section describes the reactors that have been tried and investigated for CO_2/H_2O splitting application.

All the oxygen carriers reported in the literature demonstrated the redox ability of CO_2/H_2O splitting as well as O_2 release during the reduction step. The broad classification of metal oxides into volatile and non-volatile and the sub-category of non-volatile into stoichiometric and non-stoichiometric redox metal oxides have shown a broad mapping of the suitable metal oxides that could lower the reduction temperatures. Volatile metal oxides have the issue of quenching and sublimation and therefore, the research for the quest of most suitable oxygen carrier is drifted to non-volatile oxygen carrier category. Ferrites and hercynite have been investigated with different doping and supports. The slow kinetics and lower oxygen carrying capacity has motivated researchers to investigate the non-stoichiometric metal oxides such as ceria which showed higher ability to participate in redox reactions with mechanical stability and maintaining the uniformity in the structure. Ceria has been studied with different doping and supported for the benefit of H_2O and CO_2 splitting along with O_2 release rates during the reduction step. Of all the metal oxides, even though doped ceria and perovskites have shown very high reaction kinetics for redox recycling CeO_2 is the only commercially available oxygen carrier at a cheaper price and could satisfy the need to an industrial scale plant that undergoes ceria redox recycling. Therefore, commercial ceria has been selected for the analysis of the future study in the present thesis.

2.5 Reactors for CO_2/H_2O splitting

Based on the type of reduction mechanism, the reactor design can be fundamentally different between the concentrated solar driven cycle and the methane driven cycle. Also, based on the two reactors or three reactor design (splitting or CLC cycle), the reactor designs change significantly. In order to present a state of the art of the reactor designs, studied and/or operated for chemical looping CO_2/H_2O splitting for the two reactor design model, the typology is divided between reactors for solar thermochemical cycles and those for fuel reduction cycles.

2.5.1 Reactors for solar thermochemical splitting cycles

The most commonly used technique to achieve the high temperature of thermal reduction required is the use of concentrated solar energy. Most often, the conventional forms of concentrated solar power generation systems, as used for electricity generation, are employed, which includes: the linear Fresnel (line focus), parabolic trough (line focus), heliostat field (point focus) and the parabolic dish (point focus) solar concentrators. A detailed discussion of the solar thermal reactors is provided in the subsequent section [144].

The four reactors above mentioned have been listed in the increasing order of achievable concentration ratio, and thereby of maximum operating temperatures. Obviously, the concentrators with line focus are unable to generate a high temperature due to a much lower concentration ratio. Since a temperature of over 1200°C is usually employed for thermal reduction of OCs, heliostat field or central tower systems and parabolic dish technologies are the preferred choices. However, due to the limitation of the scale of parabolic dishes, state of the art of solar concentrators for thermal reduction of OCs have focused on the central tower as the most suitable technological alternative. In addition to the type of concentrators, many other categories of reactors exist and are discussed below.

Based on the mechanism of heat transfer from the concentrated solar heat generator to the working fluid and the reactor, the solar reactor configurations can be categorized as a) Direct Process and b) Indirect Process [145]. For the direct process, the reactor forms a single unit with the receiver. They are the so-called volumetric receivers, and volumetrically absorb the solar radiation on the oxygen carriers. On the other hand, the indirect process employs an additional thermal fluid that exchanges heat with the receiver (usually in a tubular receiver).

Since the primary reaction occurs on a solid (the OC) in presence of a gas (usual fuel for fuel-reduction or vacuum created in the reactor), reactor's classification can be based on the arrangement of the metal oxide in the reactor. Accordingly, two reactor types can be defined [145]:

- **a. Structured reactors –** In the structured reactors, the metal oxides are most often arranged in a particular ordered structure within the reactor. The reactor design ranges from a single reactor chamber to a modular dual chamber reactor for the simultaneous production of O_2 and H_2 [146]. The most common type of reactors belonging to this category is the honeycomb, foam or membrane reactor [34,145].
- **b. Non-structured reactors –** In these type of reactors, the metal oxide is distributed randomly without a particular order, with the fluidized bed, moving bed and packed bed reactors being the most common reactors of this category [145].

Indeed, yet another classification exists for the reactor based on the possibility to perform the two-step cycle in a single reactor or separate reactors for the reduction and the oxidation reactions. As mentioned, structured reactors can usually be designed to perform simultaneously the two reactions of the two-step cycle.

The efficiency of the reactor is an important parameter, which might limit the productiveness of the entire cycle, even with a very active OC. To maintain optimal thermodynamics, kinetics, and durability, together with economic and efficient design for the production of the desired product, the reactor must be able to deliver solar thermal heat and reactant gases to the oxygen carrier without dissipating heat energy which may need external work, by maintaining structural integrity [146]. For any high-temperature process to be efficient, heat losses have to be minimal. The primary necessities to ensure an adequate system design while minimizing system heat losses can be summarized as follows [147]:

- a. To limit the number of solar reflections, due to the limited efficiency of commercially available reflectors.
- b. To minimize heat loss by re-radiation or convection from the light absorbing material.
- c. A rapid transfer of heat from the solar radiation to the active material.
- d. By maintaining the temperature of the reactor system and the oxygen carrier material to avoid inefficient heat recuperation between solids.
- e. By efficient removal of all reactants and products to ensure that there is no back reaction.
- f. By ensuring an effective transport of solids and at the same time maintaining the structure of active oxygen carrier.

Besides efficient management of parasitic losses from mass transport and heat transfer, there are several other parameters which are considered essential to ensure adequate system performance of the entire cycle. These factors can be summarized after Muhich et al. as follows [146]:

- i. The reactor should be modular and scalable to ensure the economy of the scale.
- ii. The reactors should be able to effectively decouple the reduction and oxidation reactor times since the kinetics and reaction rates are not identical.

iii. The reactors should be able to effectively decouple the reduction and oxidation steps, both spatially or temporally to separate the O_2 and the product gases (H_2 and CO).
iv. The design should minimize moving parts, thereby also preventing high-temperature operation failure of the reactors.
v. Reactor materials should be compatible with the OCs, as well as be stable under the high temperature operating conditions.
vi. The reactors should be designed in such a way that it minimizes the attrition of the OC and should have sufficient residence time in both reactors.

Based on such design goals, significant work has been performed and the reactors can be broadly classified into monolithic (structured) or particle systems based (non-structured) reactors. A brief discussion on some of the developed reactors for the solar thermochemical cycle for two-step CO_2/H_2O splitting syngas production follows.

2.5.2 Monolith or structured reactors

The basic feature of this type of solar thermal reactors is that the design is based on a self-supported active material. In addition to this, the reduction and the oxidation steps are spatially separated [146]. This is made possible either by mechanical motion (e.g., rotation) of the material or redirection of the solar beam. Many designs of the monolithic reactor have been proposed.

The simplest of the monolithic or structured reactors is the stationary monolith cavity (SMC), as proposed by Chueh et al. in 2010 [148], a schematic representation of which is provided in Figure 12. Here, the active material, present in a porous cavity, was irradiated from the top through a quartz window. The gases were proposed to be introduced radially, flowing through the OCs and exiting from the bottom. The tested metal oxide was monolithic porous ceria collected in cylinder form. The peak solar to fuel efficiency obtained was 0.8%, without any heat recovery [148]. In further experiments by Furler et al [149] the monolithic ceria was replaced by porous ceria felt, which led to the doubling of the solar to fuel efficiency. An energy balance was performed to evaluate the efficiency of the proposed reactor. It was found that around 50% of the energy losses came from conduction through the reactor wall, while 41% from the re-radiation of the windows [148]. Even though the first loss can be decreased by improving the reactor insulation, the losses through the windows are limited by the current technology of window materials. However, a good cyclability of the reactor was obtained, where, the reactor was able to operate continuously for 500 cycles, the steady state being achieved after 200 cycles.

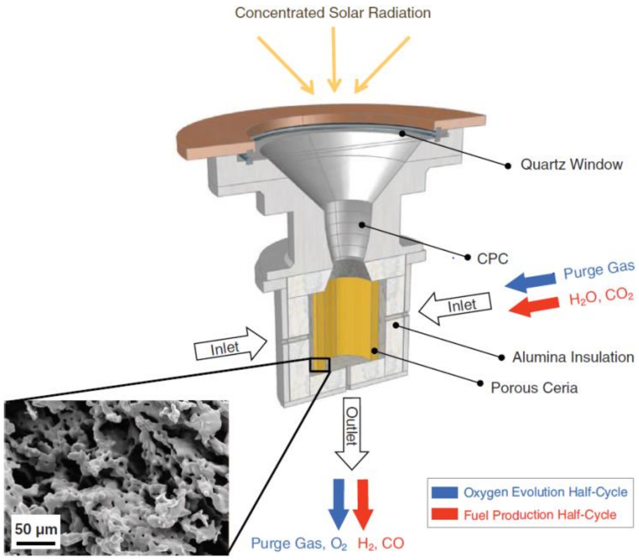

Figure 12. Stationary monolith cavity (SMC) reactor by Chueh et al. [148] for H_2O-CO_2 dissociation.

Other types of monolithic cavity reactors have been proposed with one or more reaction chambers for the alternate reactions of the redox cycle to occur. Houaijia et al. [150] in 2013 proposed a multi-cavity reactor, while at the same time aiming to improve the thermal performance of the reactor. A modular reactor design for 1MW thermal output was proposed with conical and spherical geometries being obtained as the most promising absorber geometries. However, spherical geometry was simulated as the most suitable and the design of the reactor developed is presented in Figure 13. A net cycle efficiency of 0.88% was obtained for the complete solar receiver-reactor system including hydrogen production. Radiation losses predominated the overall losses, contributing to over 50% of the net thermal losses, close to 100 kW. Windows continued to play a major role in the overall system losses, resulting in the poor system efficiency of such reactor designs.

Depending on the design of the solar cavity reactors, the reactive material is either free-standing or supported on a scaffolding, like a honeycomb structure [20]. In addition, the active metal can also be directly heated by the concentrated sunlight through a quartz window or indirectly heated using a containment structure. Even though the simplicity of design makes such cavity reactors less prone to mechanical failure, they lack in having an inherent way to recuperate the heat released during the temperature swing between the reduction and oxidation steps, unless the reduction and oxidation reactors are contained within a single cavity. This leads to the lowering of the system losses. Additionally, the use of a quartz window to introduce solar radiation into the reaction chamber limits the potential size of the reactor, which means that these reactor types cannot fully exploit the economies of scale.

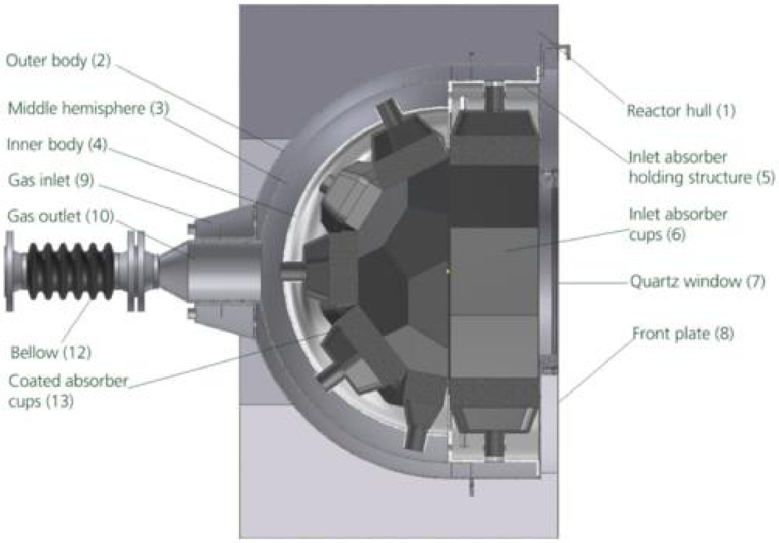

Figure 13. Sectional view of the Spherical Stationary monolith cavity (SMC) reactor as proposed by Houaijia et al. [150].

As opposed to a cavity reactor, the rotating piston reactor has been proposed. Even though the primary principle of the reactor design is the same as that of the cavity reactor, this reactor design particularly suits well for application to volatile stoichiometric reaction chemistries [151] (Figure 14). For volatile metal oxides, as the OC involves volatilization during reduction which swept to quenching in a separate chamber by an inert gas, while the fresh material is continuously fed into the reactor. The rotating monolith reactors have similar advantages and disadvantages as SMC reactors, however, enabling the use of volatile OCs [146].

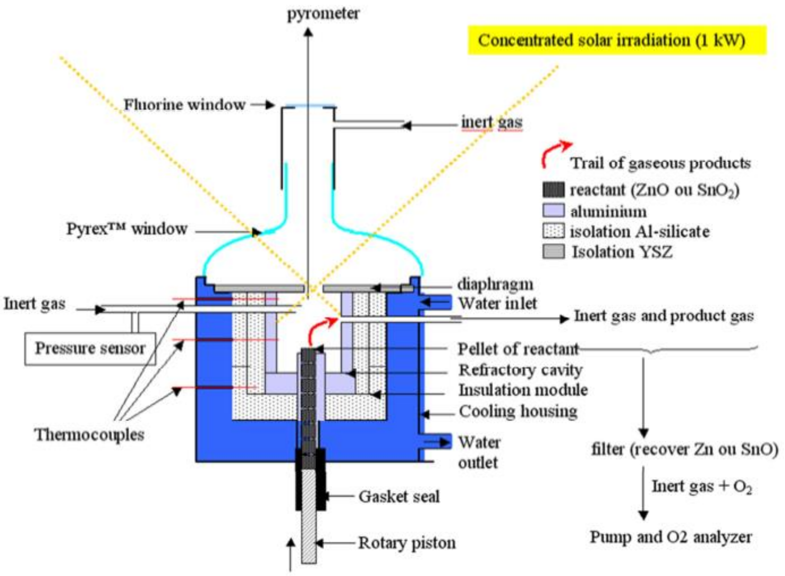

Figure 14. The rotating piston reactor as proposed by Chambon et al. [151].

The Counter-Rotating-Ring-Receiver-Reactor-Recuperator (CR-5) was proposed by Diver et al. [152], where, a stack of counter-rotating rings with metal oxide fins along the circumference will be irradiated in the upper part by solar beams. In this reactor, the active OC is fed into the hot zone of the reactor by a piston in the form of pallets as shown in Figure 15. As explained for SMC reactors, OC reduced by getting volatilizing and swept to quenching chamber [151]. Each ring rotates in the opposite direction to that of its neighbor at a speed less than 1 rpm to enhance the heat recovery. As the ring rotates, the metal oxide alternately passes from the high-temperature reduction zone to the lower temperature oxidation regime and back again to form a continuous cycle. The calculated solar to fuel efficiency was 29% [152]. The scalability of such reactors was also evaluated, as Kim et al. [153] proposed the use of the CR5 reactor for H_2O/CO_2 splitting for liquid fuel generation within the "Sun to Petrol" (S2P) project.

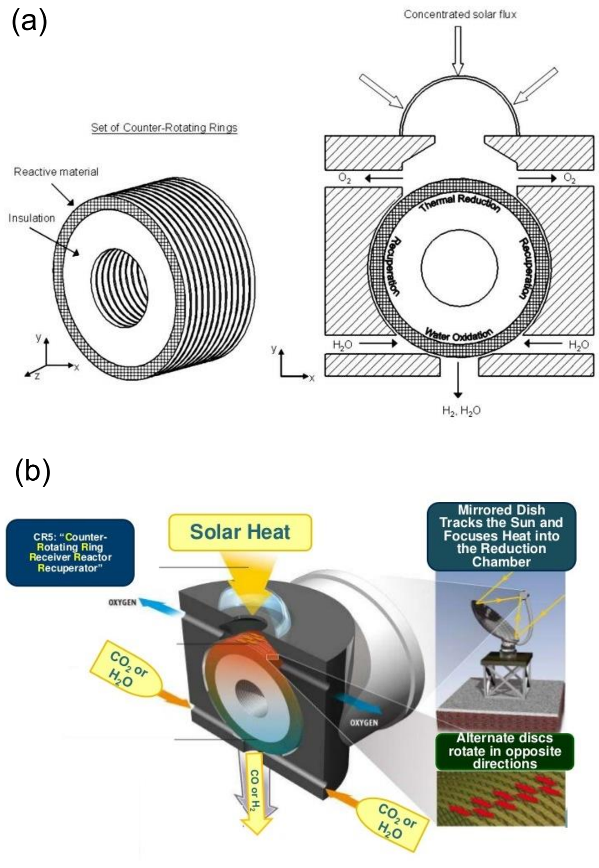

Figure 15. CR5 reaction proposed by Diver et al. [152].

Yet another reactor design for structured reactors was developed as the Surround-Sun reactor, using a 'tube within a tube' design, could potentially avoid the use of a quartz window, which by far was found to be one of the most inefficient components of such solar reactors [146]. As proposed by Melchior et al. [154], and followed by other studies by Martinek et al. [155], one or more tubular reactors packed with the OC housed in an insulated cavity similar to shell and tube format. The concentrated sunlight would enter through an open aperture and the overall operation would occur in a temperature swing mode. While half of the tubes would be subject to concentrated solar energy, thereby undergoing reduction, the other half would be exposed to steam or CO_2 to undergo oxidation. The reactor operation and geometry are pictorially depicted in Figure 16. Additionally, the reactor gives the flexibility to operate in an isothermal mode with all the tubes being continually illuminated, and the reduction and oxidation cycles are subject to controlling the respective sweep ad reactant gas flow. Not having a transparent material, in the form of a window, nor having rotating mechanical parts represent significant advantages in such reactor designs, allowing them to be potentially scalable, subject to the availability of a suitable containment materials [146]. However, one serious drawback of this type of reactor design is the uneven radial illumination of reactor [155] and poor thermal transport within the bed of OC. This results in lower reaction rates in both reduction and oxidation leading to lower CO and/or H_2 production rates [154]. Other problems like pumping gases through the packed bed, development of hot spots within the reactor bed, poor heat conductivity, etc. poses challenges to the commercial scale development of this type of reactors [146].

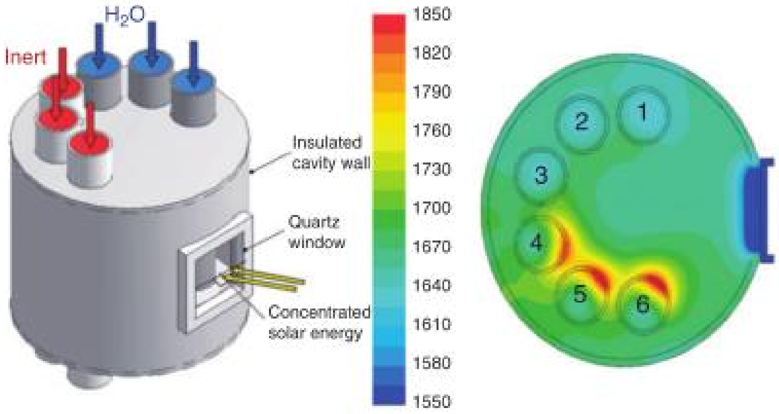

Figure 16. The Surround-Sun reactor design proposed by Melchior et al. [154].

Different prototype reactors incorporating fixed coated ceramics in a structured reactor form have been developed within the HYDROSOL project. Roeb et al. [99], proposed a structured solar reactor for simultaneous reduction and dissociation, implementing a honeycomb monolith reactor made by a plurality of channels. As can be seen from Figure 17, each of the channels was coated by a surface of the active metal oxide compound and comprises a siliconized silicon carbide (SiSiC) coating with ferrite oxide. The metal oxide has been chosen to be directly irradiated by the concentrated sun rays. The reactor was tested within a solar furnace, under a reduction temperature of 1200°C, and the corresponding water dissociation temperature of 800-1200°C for six cycles [99]. A better output from oxidation reactions was obtained at a high temperature of 1200 °C, which, nevertheless, results in precipitation, leading to a faster degradation of the support material. Around 80% productivity of the water-splitting reaction was obtained, at an efficiency of 40%, however, producing hydrogen intermittently.

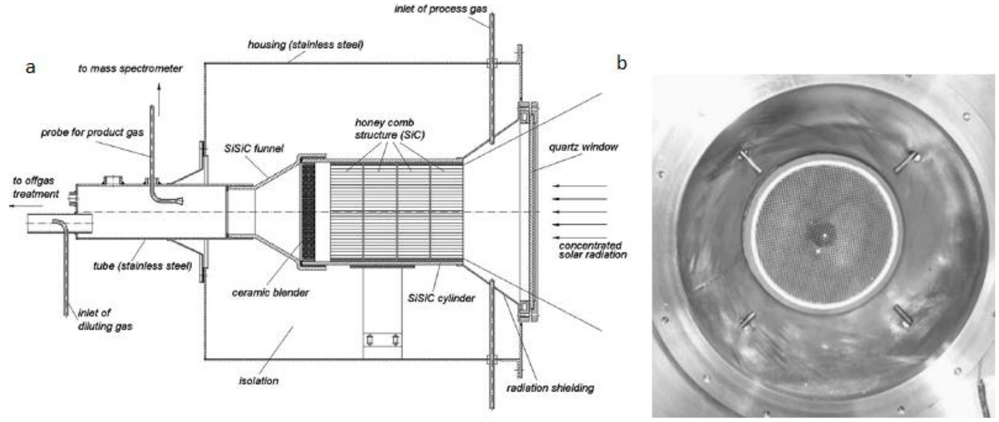

Figure 17. Honeycomb multi-channels Solar Reactor as proposed by Roeb et al. [99].

To improve on the discontinuity in the production of hydrogen, due to the application of the same reactor for alternate reduction and oxidation, Roeb et al. 2009 [156] further proposed a quasi-continuum reactor for hydrogen synthesis. The honeycomb structures developed in their previous study were used, but employing two parallel chambers that made it possible to perform reduction and oxidation together (Figure 18(a)). Similar to the previous study, they were assessed at 1200°C and 800°C for reduction and oxidation, utilizing a lamellae shutter to regulate the different temperatures in the respective reactors, as shown in Figure 18(b).

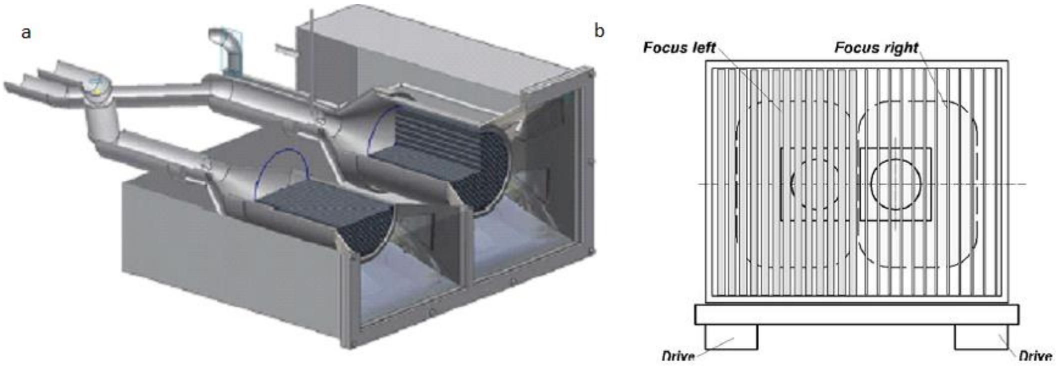

Figure 18. (a)multi-chambers reactor proposed by Roeb et al. [156], (b) lamellae shutter for temperature regulation.

A scale-up plant of 100 kW, based on the multi-chamber reactor design with the honeycomb structure, as proposed by Roeb et al. [156], with a solar tower as a concentrator was installed on the Plataforma Solar de Almeria [157]. About 35 g per cycle of H_2 was measured which resulted in the production of around 500 grams of hydrogen per day, even though the objective was set at a daily production of 3 kg. Deactivation of the metal oxide during the cycles and non-homogeneous temperature distribution inside the coated channels were some of the challenges observed.

As an alternative to the design of Roeb et al. [156], for the continuous production of hydrogen in a honeycomb monolith structure, Kaneko et al. [158] proposed a rotary reactor which would be able to perform both reduction and oxidation continuously. A rotating reactor between two chambers was proposed, where, water splitting was simultaneously performed in one reactor, to that of reduction in another, as shown in Figure 19. Like the previous study by Roeb et al. [156], both lab and pilot scale applications were studied using a Ni-ferrite oxide coated reactor [158]. At the reported optimum temperatures for oxidation and reduction (900°C and 1200°C respectively), 2.1 cm^3 of O_2 was produced in 30 minutes [158].

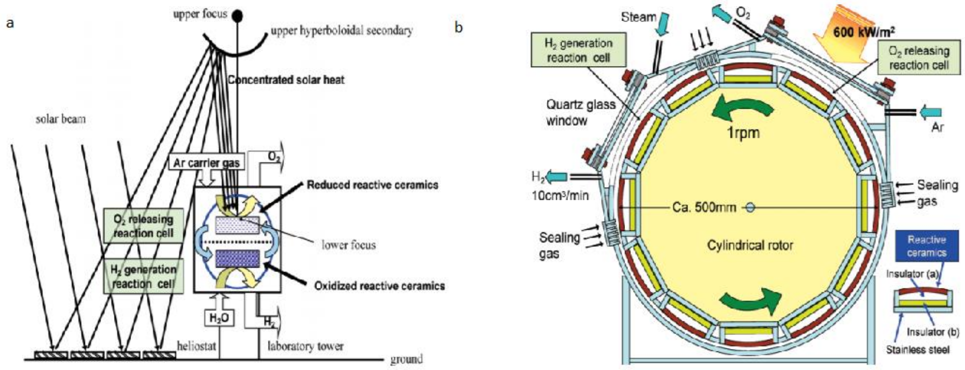

Figure 19. (a) Rotary reactor concept proposed by Kaneko et al. [158], (b) pilot scale rotating reactor.

2.5.3 Particle or non-structure reactors

This category of reactors essentially utilizes the movement of particles (i.e., the OCs), rather the reactor itself. This results in the reactors to be non-structured, in relation to the arrangement of the metal oxides within the reactor [145,146]. Such movement of the OCs enables the easy decoupling between the oxidation and reduction reactions, which, often have much dissimilar reaction kinetics.

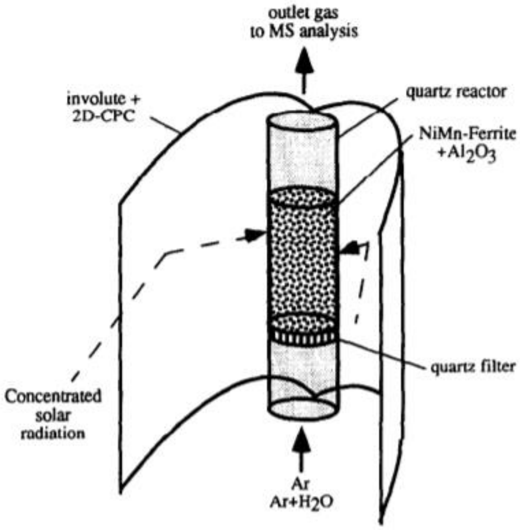

Figure 20. Tubular packed bed solar reactor for H_2 production proposed by Tamaura et al.[159].

One of the first reactors to be proposed of this kind was a tubular packed bed reactor in 1995 by Tamaura et al. [159]. It comprised a 2 cm diameter quartz tubular packed bed reactor heated by a solar furnace. As can be seen from Figure 20, secondary concentrator was placed behind the solar reactor to ensure a uniform irradiation of the external surface. The performance of the reactor was evaluated by using an OC that comprised 5 gm of $Ni_{0.5}M_{0.5}Fe_2O_4$ powder mixed with 7.5 gm of Al_2O_3 support. Alternate streams of argon and water were used for reduction and oxidation respectively [159]. Low amount of oxygen produced, together with the limitations with respect to the use of oxygen free atmosphere for reduction step was reported as significant disadvantages.

A comprehensive reactor design, overcoming multiple challenges of the non-structured class of reactors is the rotating cylinder type reactor by Müller et al. [160]. In this reactor design, sunlight would enter the rotating cylinder, where the OCs are contained along the main axis, as shown in Figure 21. The design of such reactors has specifically focused on the use of volatile stoichiometric oxygen carriers. Therefore, the reduced material is removed via a vacuum pump and transported to the quenching and oxidation units. Screw feeders are employed for the feeding in fresh OCs [161]. Even though a good mass and heat transport properties are obtained, due to the use of direct radiation, these types of reactors often suffer from scale limitations with the use of quartz windows. Moreover, the presence of the rotary elements at high temperatures of more than 1500°C creates significant operational challenges to the proposed design. Nevertheless, a reactor efficiency of 14% and a process efficiency of 12% was obtained by employing ZnO as the OC. Optimal operating conditions and feed conditions were also studied and reported in the same study [160].

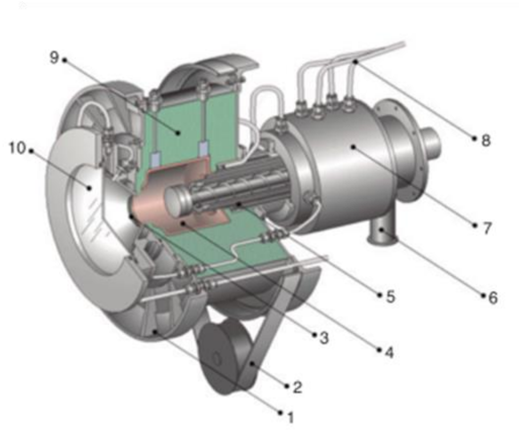

Figure 21. The Rotating particle flow reactor proposed by Muller et al. [160].

To overcome the issues of a mechanically moving reactor, several different reactor designs, especially relating to material feeding has been proposed. Initially, a simple beam down reactor was developed on an experimental scale, which was further aimed to improve by incorporating vortex flow in a two-chambered solar beam-down thermochemical reactor by Koepf et al. [162,163]. Abbreviated as the GRAFSTRR (Gravity-Fed Solar-Thermochemical Receiver/Reactor) consist of inverted conical-shaped reaction surface, as shown Figure 22. The OCs were fed from the top and the particles were gravitationally transported through the incident concentrated solar radiation, essentially depicting a moving bed. A highly concentrated sunlight is achieved in the reaction cavity for a thermochemical reaction where the particle residence time is based on the inclination of the surface. A good reactor design and stability was obtained with ZnO as the OC.

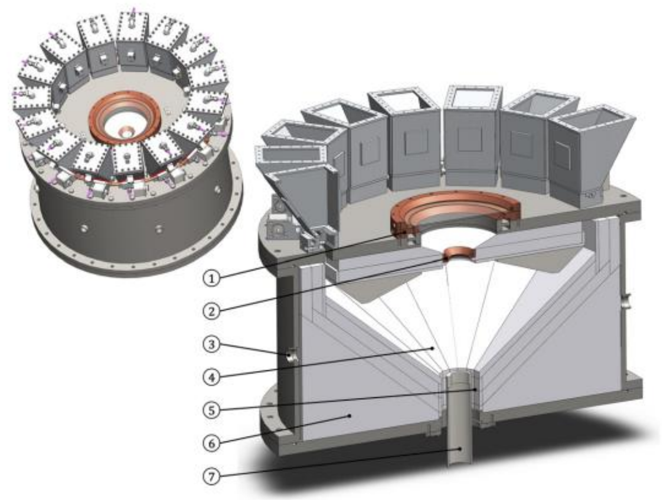

Figure 22. The proposed beam-down solar thermochemical reactor by Koepf et al [162].

Particle reactors, essentially focusing on non-volatile metal oxide redox pairs have also been developed in recent years. Scheffe et al. [164] proposed an aerosol-based reactor design, in which the particles were proposed to be loading from the top of a long tubular reactor, which would be subsequently gravity fed through the hot zone of the reduction chamber, as shown in Figure 23. It essentially resembles a moving bed reactor. The inert sweep gas in the reduction reactor is fed from the bottom, countercurrent to the reducing particles to increase residence time and mass transfer [146,164]. For volatile metal oxide redox pairs, the released oxygen and metal oxide vapor transferred from the top of the reactor to the quenching chamber. However, for non-volatile OCs, the reduced metal oxide is accumulated at the bottom and transferred to the oxidation reactor through a conveying arrangement [164]. This reactor type essentially employs the indirect heating of metal oxide particles, where the heat is conducted and radiated onto the metal oxide particles from the walls of the reactor, which directly absorb the concentrated solar radiations. Ceria was employed as the OC and the entire set up was tested at a temperature range of 1500 to 1600ºC and very low partial pressure of O_2 of the order of 5 -12 pa. A very high yield of ceria reduction was obtained but low mass flow with respect to the reactor size. An isothermal operation of the reactor has been envisaged, and together with effective decoupling of the reduction and oxidation reactors, would result in a potential twenty four hour syngas generation from CO_2/H_2O splitting [164].

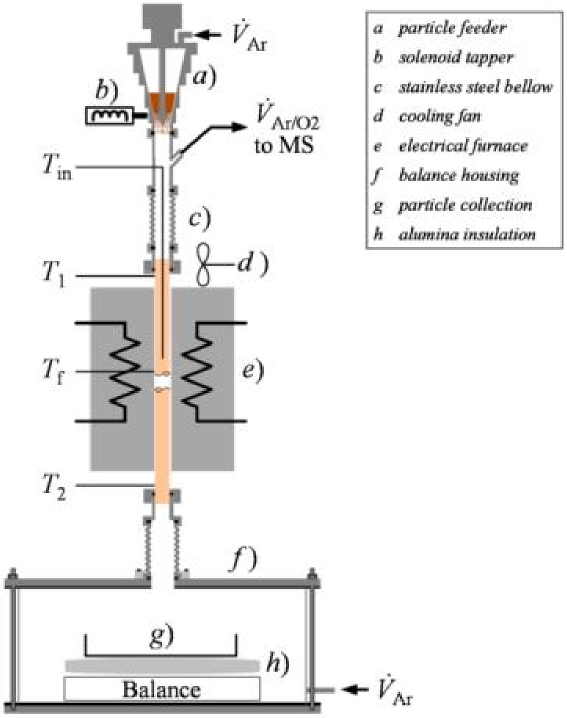

Figure 23. The schematic of the aerosol reactor, as proposed by Scheffe et al. [164].

Even though the above model of reactor design would benefit in terms of lower mass transfer limitation, the essential drawback is there is no direct connection to the oxidation reactor or heat recuperation heat exchanger from solids for temperature swing redox reactions and the metal oxide conveyor system to return the oxidized OC to top of the aerosol reactor [146]. To overcome such barriers, the internally circulating fluidized bed reactors were proposed by Gokon et al. [165] combined with a beam-down solar concept, as shown in Figure 24. The reactor design attempts to have the same benefit of the aerosol reactor of maintaining low mass transfer limitation with both the redox reactions occur in the same chamber. [165]. The OCs are loaded into a reaction chamber making it a fluidized bed with a draft tube in the center to enhance intermixing, while the inert sweep gases are fed at the bottom through a distributor. This fluidizes the particles and forces them to rise through the center and afterward, fall through the annulus. A quartz window at the top of the reactor bed is employed to directly irradiate the particles from the top, while the circulating bed facilitates the heat transfer along the entire length of the fluidized bed. The reactor performance was evaluated with unsupported $NiFe_2O_4$ and supported $NiFe_2O_4/ZrO_2$ on a lab scale, using a high-powered sun-simulator equipped with three 6 kW Xenon lamps. Non-uniform heat distribution within the reactor was obtained, with only the upper part of the draft tube measuring sufficient temperatures required for the reduction step [165]. On an overall 30 minutes cycle, a 35% reduction of the supported ferrite oxide was obtained, however, with a subsequent complete re-oxidation for H_2 production from water splitting reaction. The need for a quartz window, and presence of the oxidation reactor within the same chamber, limiting the space for reduction reactor and unequal heat distribution are the primary disadvantages for efficient use of concentrated sunlight.

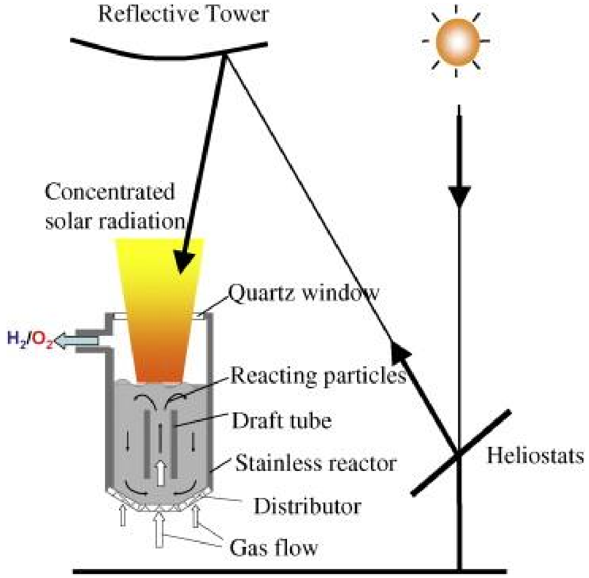

Figure 24. Internally circulating bed proposed by Gokon et al. [165].

A moving bed reactor for thermochemical redox cycle was patented by Sandia laboratories developed by Ermanoski et al. [35] that decouple the reduction and oxidation reactions, also capable of solid heat recuperation between the redox steps [35]. The reactor comprises a reduction chamber which can be directly illuminated. A schematic diagram of the proposed configuration is shown in Figure 25(a).

The fully oxidized OCs are lifted to the bottom of the reduction chamber via a screw elevator, after which a rotating casing conveying the OC particles up to a stationary ceramic screw which also serves as a heat exchanger. The reduction step occurs at the top of the reactor, where the OC particles are heated with the concentrated solar light before dropping through the hollow center of the screw elevator [35]. The O_2 released would be taken away by a vacuum pump. As the reduced OC fall through the center of the stationary screw they would be able to exchange heat with the oxidized particles moving up the outer section of the reactor. The oxidation zone is roughly atmospheric, while the reduction zone would operate at a low pressure, the screw acting as a pressure buffer between the two. The oxidation chamber forms a secondary moving bed through which H_2O/CO_2 can be pumped, thus oxidizing the OC, thereby generating syngas. While decoupling the oxidation and reduction reactions, this reactor design also simplifies the solid-solid heat transfers, provides co-location of both the redox steps, enabling continuous reaction. A design update has also been proposed by Ermanoski et al.[166] (Cascading Pressure Receiver Reactor, CPR2) at Sandia laboratories, US, whereby a staged pressure reduction has been proposed to facilitate oxygen removal while de-emphasizing the heat exchange through solid/solid heat recuperation. However, the use of the quartz window presents the familiar drawback, which, in addition to limiting the reactor size based on the size of available quartz windows would also increase the probability of attracting fine particles through thermophoretic deposition. This could potentially result in a diminished transparency of the window. The heated particles may come in contact with the window producing hot spots leading to catastrophic failure. Moreover, the rotating parts at high temperatures are also a negative aspect, straining the vacuum seals and stressing the casing the of the reactor [146].

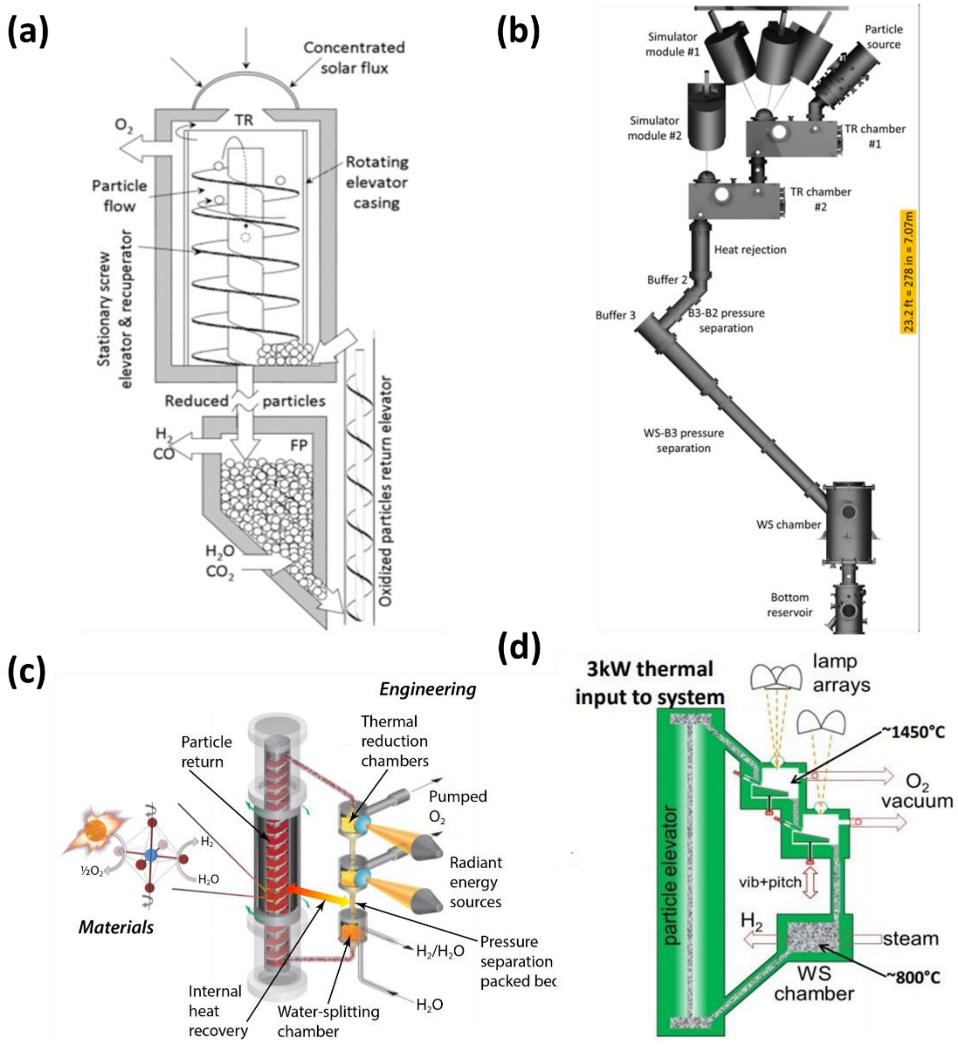

Figure 25. Moving bed reactors proposed by Sandia laboratories [35,166,167].

Another recent development in reactor configuration was the *"Solar Thermal Particle Flow Reactor"* proposed by Muhich et al [146]. The design is based on a beam-up approach and comprises of multiple reduction/oxidation reactors are arranged in an inner and outer periphery. The reduction chambers have been designed to form the inner ring of the reactor, while the oxidation chambers are on the outside. The reactor is proposed to be placed on a central tower, with concentrated sunlight being directed up through the gap in the bottom of the receiver, as illustrated in Figure 26. Due to the need of only one reflection by the downward-facing cavity receiver, a minimal convective heat loss from the hot gas rising out of the aperture is envisaged.

The reduction reactor forms a moving bed reactor, indirectly heated through the reactor wall, and oxygen is evacuated by a vacuum pump. The reduced OCs, forming a pseudo packed bed, before entering the oxidation reactor would also provide a pressure buffer, enabling simultaneously a low pressure in the reduction reactor and a higher partial pressure in the oxidation reactor [146]. The oxidation reactor is essentially a fluidized bed reactor, the particles being transported up by steam entrainment, which enables the oxidation time to be decoupled from the height of the steam conveyance tube. The design claims the possibility to run in near-isothermal temperatures for redox reactions eliminating the heat of solid to solid heat recuperation which in turns eliminates the thermal stresses in the OC due to temperature swing. Use of the fluidized bed results in a better heat distribution and gas/solid heat recuperation, resulting in a potential increase in the overall reactor and system efficiency. However, key challenges like the development of high-temperature ceramic heat exchangers, reactor material which is thermal shock resistant also compatible with reactive OCs and the highly capable oxygen carrier apart from the efficient solar tower, heliostat and receiver system remains an open area for research [146]. It is worth noting that the selectivity of the products in these type of reactors are limited to the fluidization regime in which the reactor operates and by the downstream usage of the product gas.

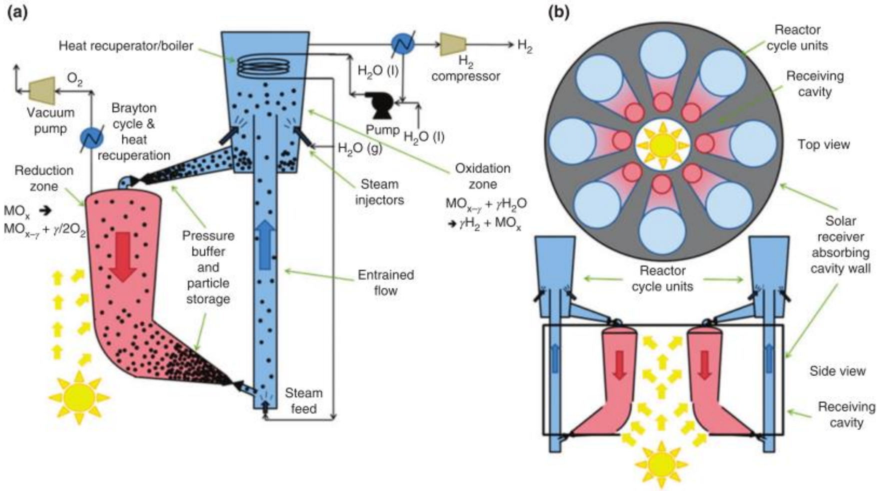

Figure 26. Interconnected solar based particle flow reactor based on fluidized bed and moving bed reactor by Muhich et al. [146] (a) Single unit of reduction and oxidation reactor with a vacuum pump system for the removal of oxygen from the reduction reactor and (b) Multiple oxidation and reduction reactor configuration with solar receiver concept. Reactors are not shown to scale.

2.5.4 Reactors for CO_2/H_2O splitting cycles with carbonaceous fuels

Experimental set-up using fixed bed reactors for studying the behavior of methane partial oxidation using metal oxides have been made and reported in multiple studies in the literature [87,88]. Solar aided methane reforming using ceria as the OC has been proposed and studied by Welte at al. [86]. The reactor design concept is a particle transport reactor, whereby the heat required for the endothermic reaction has been proposed to be supplied via a solar concentrator. The schematic of the reactor, as proposed by Welte et al. is shown in the following Figure 27. Both counter and co-current configurations have been evaluated. The maximum non-stoichiometry obtained was 0.25 with a solar to fuel efficiency of 12%. Indeed, the primary concept of the reactor was to use methane as an aid to enhance the thermal reduction and not as a primary reactant. The authors also reported the simultaneous upgrade of the calorific value of methane by 24% through the use of concentrated solar energy.

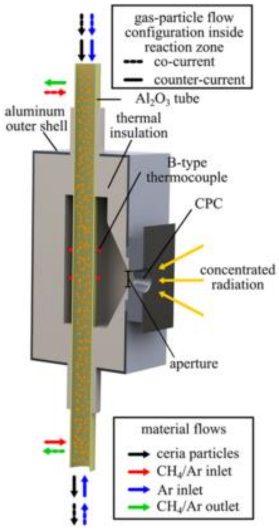

Figure 27. Schematic of the proposed solar particle-transport reactor by Welte et al. [86] showing both counter current and co-current gas-solid flow configurations.

However, unlike thermal reduction of metal oxides for chemical looping cycles, no commercial-scale reactor design exists for methane partial oxidation coupled to CO_2 and H_2O splitting. Multiple reactor designs based on the fluidized or moving bed have proposed reactors for three-step chemical looping combustion cycles with complete combustion of methane aiming to produce CO_2 and H_2O [128]. However, being a fundamentally different process to what the present study aims to explore, such reactors have not been further elaborated in detail.

2.6 Modelling of reactors

Fundamental to the efficiency and reliability of the chemical looping process, irrespective of the type of reduction, is the type, behavior and performance of both the reduction and oxidation reactors. It is necessary to not only determine the possible losses and limitations of the reactor design, but also to improve the understanding of the selection of the reactor design based on the peculiar downstream applications of the generated products. Therefore, modeling the reactors would aid the design, optimization, and scale-up of the process, so as to obtain high metal oxide reduction and gas conversion rates in both the reactors, together with identifying the challenges deriving from the scale-up of such proposed reactor systems. Most of the advanced reactor design modeling has been performed for chemical looping combustion [168,169]. As mentioned, non-structured reactors have shown the highest potential for scale-up, of which moving bed and fluidized bed reactors are the most commonly studied [170].

2.6.1 Fluidized bed reactors

Fluid bed reactors is an industrially commercialized technology being used in the industry for many years now [171], with the first industrial scale devices developed for coal gasification, known as the Winkler's coal gasifier. Since then, the concept has been expanded to different catalytic processes and synthesis of the hydrocarbon-based fuels in the Fischer–Tropsch process [171]. A significant development in scaling up of the reactor has taken place, especially for coal combustion and metallurgical processes. Commissioned at the end of the 2000s, the newest unit of Łagisza power plant in Poland uses the Circulating Fluidized Bed (CFB) boiler that supplies supercritical steam to the 480 MWe turbine.

Modeling of fluidized bed reactors can be categorized into three categories after Abad et al. [168], based on the fundamental principles followed for the respective design and evaluation.

- Simplistic models neglecting the complex fluid dynamic behaviors taking place in the fluidized bed [172,173];
- Macroscopic models considering experimentally developed semi-empirical correlations for the hydrodynamics of a fluidized bed [174]; and
- Multiphase computational fluid dynamic (CFD) models [175,176].

Each of the different principles followed have their individual advantages and disadvantages. While the simplistic models lack accuracy, they provide relatively faster results in comparison to CFD models that are restricted from the large computational power necessary for evaluating the same.

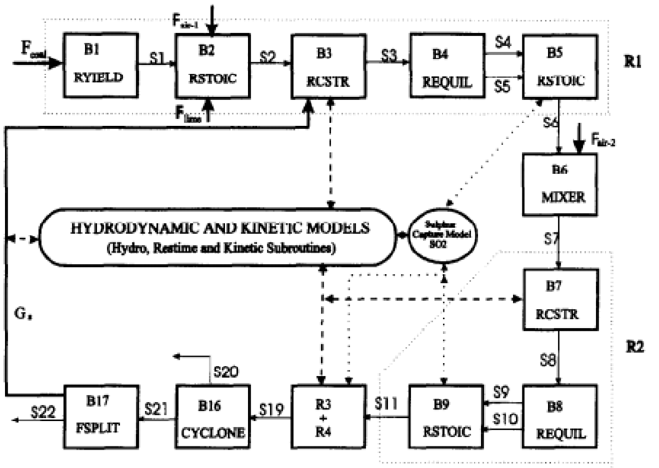

Figure 28. Proposed hydro-dynamic and kinetic model of a circulating fluidized bed reactor in ASPEN Plus as proposed by Legros et al [177].

To reduce the complexity of the mechanistic modeling approaches, the development of simplistic models incorporating the principles of the chemical reactions occurring in the reactors (e.g., chemical equilibrium or reactions kinetics) is necessary. Such an approach may be conveniently realized using the process simulator Aspen Plus, a chemical design tool. It is widely used and accepted in the industry for its versatility, ease of use and ability to simulate a wide range of steady-state processes ranging from single unit operation to complex processes involving many units [178]. Legros et al. [178] studied the modeling of circulating fluidized bed reactors for coal combustion in ASPEN Plus, by essentially utilizing the first principle of the reactor modeling stated above. Since no in-house fluidized bed model existed at that time in the ASPEN Plus reactor directory, a model of a circulating fluidized bed, using conventional reactor models of ASPEN Plus integrating Fortran blocks and user kinetic subroutines were used to develop the desired model with satisfactory results. The proposed model is shown in Figure 28. Similar models have been extensively used for modeling coal and biomass gasification or combustion processes, with results being reported in the literature [179].

However, with the addition of the in-house fluidized bed model to the ASPEN Plus directory (v8.8), the need to develop own model to replicate fluidized bed hydrodynamics would no longer be there. Of course, kinetic modeling for reactions in the reactor is essential to be included to obtain accurate results. Indeed, the present in-house fluidized bed model in ASPEN Plus, that is simulated as a series of stirred reactors (RCSTR), utilizes the second principle of modeling fluidized bed reactors using empirical relations for the hydrodynamics of the fluidized bed [180]. It is understood that the fluidized bed reactors for CO_2/H_2O dissociation could be questionable with respect to the selectivity of the syngas produced as it requires a huge amount of reactant gases for the fluidized bed to operate. Another issue is the mode of fluidization regime in which it could operate as it is inherently linked with the solid inventory of the bed. CO_2/H_2O gas at the inlet distributor cannot be diluted with an inert such as in case of CLC due to the limitation of the downstream usage of the syngas. The separation of the inert would increase tremendous effort and decrease the efficiency as a whole.

2.6.2 Moving bed reactors

Similar to the fluidized bed, moving bed reactors have been extensively used in the chemical industry. One of the most used is the countercurrent moving bed reactor comprising two different phases moving countercurrent to each other and thereby transferring mass and/or energy between the phases accompanied by a chemical reaction in one or both phases [181]. The most famous example is the blast furnace, followed by calcination of limestone, etc. [181]. In spite of the economic and operational benefits of the moving bed reactors, it received relatively less attention in comparison with the packed or fluidized bed reactors due to non-availability of general model to solve the governing equations considering heat and mass transfer in these systems.[182].

Most of the studies for modeling moving bed reactors have focussed on selecting the ideal reaction mechanism to increase the accuracy of prediction of the products from the designed reactors [182]. While Parisi and Laborde [183] and Negri [184] studied the applicability of the shrinking core reaction model, Dussoubs et al. [185] extensively analyzed the additive characteristic times model for formulating accurately the gas-solid reaction rates. Another kinetic model, the extended grain model was adopted and extended for the moving-bed reactor introduced by Niksiar and Rahimi [182]. Nonetheless, Rahimi et al. [182] developed and reported a comprehensive numerical model of a moving bed reactor for reduction of Fe_2O_3 pellets via an in-house methodology developed using fundamental principles of thermodynamics and chemical kinetics. An average error of 1.2% was reported from the obtained results of the simulation [182]. Reactor modeling using commercial software ASPEN plus provides multiple benefits and advantages, as already mentioned earlier. Since no moving bed reactor model exists in Aspen Plus, similar to past modeling of Fluidized bed reactors, the development of a comprehensive model using the available in-built reactor models of Aspen Plus is necessary. Benjamin, 1985 [186] proposed a built-in model for a counter-current moving bed coal gasifier. However, the results showed that the solution was time-consuming and an analysis of the proposed model can be found in the Aspen plus guide to moving bed gasifier modeling [187]. An alternative, as proposed by Aspen Plus [187], to utilize multiple RCSTRs in series, results in a considerably simpler model. This also allows the direct use of the built-in algorithms of Aspen Plus.

Such a reactor model for the thermodynamic assessment of the moving bed reactor was implemented by Tong et al. [188] for a moving bed in a chemical looping combustion cycle with Fe_3O_4/Fe redox pair and methane as fuel. Five RGIBBS reactors were modeled in series to replicate the counter-current moving bed reactor model, employing minimization of the Gibbs free energy for thermodynamic analysis. A good match for both the solid and gas conversion was obtained with respect to the experimental results conducted and reported in the same literature [188]. He et al. [189] developed a steady state kinetic model of a moving bed gasifier using a similar technique in Aspen Plus, however, to model a Lurgi Coal Gasifier for Synthetic Natural Gas (SNG) production. In the same study, he went on to demonstrate the methodology of optimizing the number of RCSTRs in series, necessary to provide a convergence to the obtained results. The results were also compared with industrial data, with good agreement.

A similar modeling approach for chemical looping CO_2/H_2O splitting has been conducted for both the reactors in the present study, using a kinetic approach for the reactions. A detailed discussion is subsequently followed at the corresponding chapter 3 of the thesis.

2.7 System modelling

Besides generating CO or H_2 from splitting CO_2 or water respectively, system modeling for further use of the proposed chemicals is crucial not only to study the probable integration of the individual units like the chemical looping unit but also to identify the need of advancement for the balance of plant for effective integration. Integrating the chemical looping unit effectively within process layouts design for power or chemicals production has been studied mostly for the chemical looping combustion technology [190,191].

Nevertheless, two-step water and CO_2 splitting cycles have been simulated for integration into industrial-scale processes by Gencer et al. [192], whereby the Fe_3O_4/FeO redox pair was used for water splitting in a solar-driven cycle for round the clock power generation. An average efficiency of 35% was obtained including energy storage. Calle and Bayon [193] modelled 1 MW solar thermochemical redox cycle plant that produces H_2 based on the solar tower with a heliostat based field of 2.7 km^2 could reach 1850-1950°C reduction temperature and oxidation temperature of 1000-1100°C with peaking non-stoichiometry of 0.25. Besides water splitting, also CO_2 splitting provides considerable opportunities for carbon dioxide utilization (CCU) as an alternative to CCS with potential system integration for chemicals or electricity production.

2.8 Concluding remarks

The thermochemical process of dissociation of carbon dioxide and water into CO and H_2 is a relatively easy way to produce fuel. It will certainly help in a way of CO_2 utilization of the ever-increasing carbon emissions and will help in reducing the carbon credit. The process has many important factors, being one of the most important the metal oxide or the material which undergoes reactions with CO_2 and H_2O for their splitting, another is the reactor design.

During the two-step cycles, the thermal reduction is thermodynamically favored at high temperature and low oxygen partial pressures and the oxidation step i.e., the splitting step is favored by low temperature and high partial pressures of CO_2/H_2O. In order to achieve high reaction rates, high temperatures are needed but not so high to induce thermal reduction simultaneously during oxidation or splitting reactions. There is a cyclic temperature swing with a parallel swing of CO_2/H_2O with inert gas during the thermal reduction process. This was a common problem reported for single and mixed metal oxide pairs. These heat rejection at thermal reduction are associated with heat losses and lowers the efficiency of the system. Also due to the high specific heat of metal oxides, and continuous swing of temperatures creates thermal stress on the reactive substrate.

The reactor design is essentially important as it has to handle very high temperatures. In the past, many directly radiated solar reactors have been designed and tested and still, significant improvement are needed to implement these reactors for large-scale applications. Reaction kinetics also play an important role in designing material oxide for the process which includes supports.

Since the materials tested in the past are classified into volatile and non-volatile, the research is driven towards non-volatile and non-stoichiometric material oxides due to their higher valence characteristics which exhibit high oxygen evolution and higher splitting efficiency. Volatile materials listed in the above sections have the issue of reactions occurring above the melting points and have issues with recombination. The potential candidate for the metal oxide redox cycles later shifted to ceria, as it has higher conversion efficiency and operates at lower temperatures relative to other materials. The efficiency is generally improved by doping ceria lattice with trivalent and tetravalent cations. The increasing interest in perovskites in the last decade for many different applications drew also attention in the thermochemical application as well. Many perovskite families were tested with many substitutions of A sites and B sites. Perovskites showed very high oxygen release and CO_2 and H_2O splitting efficiency and it was reported to have 6 times higher than ceria for CO_2 splitting and 9 times for O_2 release. Of all the oxygen carriers tested, even though other materials such as perovskites and doped metal oxides showed high oxygen carrying capacity, ceria is one of the most suitable candidates for large-scale industrial application for the CO_2/H_2O splitting. Therefore, further investigation is based on the commercial ceria for system analysis and kinetics study for both solar thermochemical power production and fuel-reduced power and fuel production.

Of all the reactor concepts, the reactor which would be considered industrially developable for both reduction and oxidation steps will be a moving bed reactor. This because in this reactor, it is relatively easy to control the residence time of the oxygen carrier that is an important parameter due to the different reaction kinetics of reduction and oxidation. The analysis also aims at developing schemes for an industrial scale power plant and performs a feasibility study for percentage efficiency again after a solar based (or fuel reduced) CO_2/H_2O splitting unit.

Chapter 3

Solar-thermochemical dissociation of CO_2/H_2O in moving bed reactors system

3.1 Model development with redox kinetics and sensitivity analysis

Chemical looping syngas production is a two-step process that produces CO and H_2 from water and CO_2 splitting in one step by exploiting a metal oxide as oxygen carrier material, which is thermally reduced and releases oxygen in a second step. The core-process layout is composed of two reactors (oxidation reaction and reduction reactor) and oxygen carriers (metal oxides) circulating between the two reactors. A comprehensive moving-bed reactor model is developed and applied to simulate both the syngas production from water and carbon dioxide by ceria oxidation and the thermal reduction of metal oxide. An extensive FORTRAN model is developed to appropriately simulate the complexities of ceria reaction kinetics and implemented as subroutine into an Aspen plus reactor model. The kinetics has been validated with the model developed by comparing experimental and simulated data on the reduction reactor. The sensitivity of both the reduction and oxidation reactors have been performed. The reduction reactor temperature and pressure were varied between 1200-1600ºC and 10^{-3}-10^{-7} bar, respectively. The oxidation reactor was evaluated by varying the inlet temperatures of the reactants as well as the relative gas composition between CO_2 and H_2O. The results show the maximum achievable non-stoichiometry to the temperature and vacuum degree at 1600ºC and 10^{-7} respectively. Water splitting yields significantly better solid conversion (metal oxide conversion) in the oxidation reactor, with 97% conversion, compared to 91% by CO_2 splitting with around 5% excess gas flow with respect to stoichiometric requirements. The metal oxide inlet temperature significantly improves the yield of the oxidation reactor, in contrast to the minimal impact of variation of gas inlet temperature. A selectivity of over 90% can be achieved irrespective of gas composition with over 90% metal oxide conversion in the oxidation reactor.

3.1.1 Introduction

In recent years, the direct use of non-fossil fuels synthetically developed starting from CO_2 has been explored as a contribution to the mitigation of fossil carbon emissions. One of the easiest ways of dealing with this issue is to use carbon dioxide as a reactant into catalytic processes to prepare hydrocarbons and alcohols, to be used in industrial applications [72,194]. Another promising method to use carbon dioxide as a feedstock for fuels production is thermochemical processes, which harness the solar energy by concentrated solar power systems (CSP) supplying high-temperature reactions (usually, chemical looping cycles) that produce syngas [195,196].

A high number of thermochemical cycles have been proposed with multiple steps; among those, two-step based on oxide redox pair systems have shown great potential for synthetic solar fuel generation [197]. These thermochemical cycles operate on the principle of transition between higher valence oxidized (MeO_{oxd}) and lower valence reduced (MeO_{red}) form of the oxide of a metal having multiple oxidation states [1]. The first higher temperature endothermic step requires a higher valence oxide of a metal oxide to undergo a thermal reduction (TR), i.e., to release oxygen upon supply of external heat to form a lower valence oxide of the metal oxide. In the second step, the reduced metal oxide is oxidized back to higher valence state by taking oxygen from water and/or CO_2, then resulting in H_2 and CO production in splitting water (WS) and carbon dioxide (CDS) reactions, respectively [20,21]. The partial pressure of reactants during the oxidation and reduction affects the process drastically, and especially the reaction kinetics play a role in determining the overall efficiency of the process.

Many metal oxide pairs have been exploited in recent years to investigate the behaviour and the reactivity of materials for enhancing splitting reactions. The investigated metal oxides, also called oxygen carriers, were mostly ZnO, SnO_2, Fe_3O_4, and CeO_2 [23]. Doped ceria and perovskites are of particular interest as they exhibit high oxygen storage capacity which enhances the splitting reactions and thereby improve the process by working at relatively lower temperatures [198]. It is observed that ceria has shown excellent optical and electrochemical properties, making it a very good candidate as an oxygen carrier for thermochemical dissociation of CO_2/H_2O [199]. In the reduction phase of the cycle, ceria undergoes a non-stoichiometric reaction from ($CeO_2 \rightarrow CeO_{2-\delta}$) which helps to lower the reduction temperature to less than 1600°C. In the present study, ceria is selected as an oxygen carrier for the process.

For solar thermochemical dissociation, few reactor concepts have been reported [30,200–202]. Most of them are small stationary reactors and the metal oxides are often arranged in a particular ordered geometry. The reactor design ranges from a single reactor chamber to a modular dual chamber reactor for the simultaneous production of O_2 and H_2 for water splitting [146]. The most common type of reactors belonging to this category is the honeycomb, foam or membrane reactor [145]. Another category of the reactors investigated contains the metal oxide distributed randomly without a particular order, with a fluidized bed, moving bed and packed bed reactors being the most common reactors of this category as presented in chapter 2 [145].

Similar to the fluidized bed, moving bed reactors have been extensively used in the chemical industry. One of the most used is the countercurrent moving bed reactor, comprising two different phases moving countercurrent to each other and thereby transferring mass and/or energy between the phases accompanied by a chemical reaction in one or both phases [181,200] The most famous example is the blast furnace, followed by calcination of limestone [181]. For reduction reaction in fluidized bed reactors, a huge amount of sweep gas would be necessary to maintain a low oxygen partial pressure for forward reaction. Therefore, application of fluidized bed reactor for reduction reactor is limited. It is also reported that for pressure lower than 0.5 bar there was no fluidization for reduction making the use of fluidized bed reactor for reduction step less efficient [203]. However, Muhich et al. [146] proposed the use of fluidized bed reactor for oxidation reactor but the process would yield a very low selectivity of CO and H_2 with a huge volume of the reactor would be necessary for achieving good non-stoichiometry. In order to quantify this claim an assessment of fluidized bed reactor and moving bed reactor model for chemical looping unit is presented in Appendix A.1.

In spite of the simplicity of operation and major economic advantages of moving-bed operations, the main aspects of heat and mass transfer in these systems have received less attention in comparison with the fixed or fluidized bed reactors due to the absence of a general model and numerical techniques in solving the governing equations [182].

Most of the studies for modelling moving bed reactors have focussed on selecting the ideal reaction mechanism to increase the accuracy of prediction of the products from the designed reactors [182]. While Parisi and Laborde [183] and Negri [184] studied the applicability of the shrinking core reaction model, Dussoubs et al. [185] extensively analysed the additive characteristic times model for formulating accurately the gas-solid reaction rates. Another kinetic model, the extended grain model was adopted and extended to the moving-bed reactor introduced by Niksiar and Rahimi [182]. Nonetheless, Rahimi et al. [182] developed and reported a comprehensive numerical model of a moving bed reactor for reduction of Fe_2O_3 pellets via an in-house methodology developed using fundamental principles of thermodynamics and chemical kinetics. An average error of 1.2% was reported from the obtained results of the simulation [182]. Li et al. [200] developed a thermodynamic model of the counter-current flow reactor considering Gibb's criterion and neglecting the effect of kinetics on water splitting working at atmospheric pressure for both reduction and oxidation reaction. The methodology adopted can be valid only for stoichiometric oxygen carriers such as ferries.

In the literature, there is heterogeneity in the simulated reduction extent (for non-stoichiometric oxygen carriers) for different temperatures and oxygen partial pressures at which the reduction reactor is operating, along with the oxidation kinetics, but it prevails that redox kinetics has a significant effect on the chemical looping cycle performance [204,205].

A common approach to the modelling of moving bed reactors is to use commercial process flowsheet simulators, implementing thermodynamics or kinetics models for the reactions in various types of reactor models, which can be integrated into system models for the simulation of complete processes. In the literature, the most common commercial software applied for reactor modelling is Aspen plus. Since no moving bed reactor model exists in Aspen Plus, the development of a comprehensive model using the available in-built reactor models of Aspen Plus is necessary. Benjamin, 1985 [186] proposed a built-in model for a counter-current moving bed coal gasifier, an analysis of the proposed model can be found in the Aspen guide to moving bed gasifier modelling [187]. However, the results showed that this solution was time-consuming. An alternative, as proposed by Aspen plus user guide [187], is to utilize multiple RCSTRs (continuous stirred bed reactors) in series, resulting in a considerably simpler model. This also allows the direct use of the built-in algorithms of Aspen plus. Such a reactor model for the thermodynamic assessment of a moving bed configuration was assessed by Tong et al. [188] for a chemical looping combustion cycle based on a moving bed reactor with Fe_3O_4/Fe redox pair and methane as fuel. Five RGIBBS reactors were modelled in series to simulate the counter-flow moving bed reactor, employing minimization of the Gibbs free energy for thermodynamic analysis. A good match for both the solid and gas conversion was obtained with respect to the experimental results reported in the same literature [188].

Chang et al. [189] developed a steady state kinetic model of a moving bed gasifier using a similar approach in Aspen plus to simulate a Lurgi Coal Gasifier for Synthetic Natural Gas (SNG) production. In the same study, the methodology for optimizing the number of RCSTRs in series – necessary to provide a convergence to the obtained results – was demonstrated. The results were also compared with industrial data, with good agreement. Besides reactor modelling, also system modeling for further use of the syngas produced in the reactors from WS and/or CDS is crucial not only to study the reactors integration within individual units, like the chemical looping unit, but also to identify the need for advancements of the balance of plant for effective integration. Integrating the chemical looping unit effectively for power or chemicals/fuels production has been studied mostly for utilizing the chemical looping combustion technology [206,207].

Addressing a gap in the literature, a moving bed reactor model with detailed kinetics has been developed, validated by comparison with experimental data and applied to the case of industrial-scale solar-driven chemical looping CO_2/H_2O splitting using ceria as a metal oxide. The moving bed reactor model has been applied for the simulation of both the reduction and oxidation reactors of a generic chemical looping unit layout based on the thermal reduction of the metal oxide, as shown in Figure 29.

The reduction reactor has a supply of heat from solar energy and the oxygen carrier (metal oxide) is recirculated between the two moving bed reactors. A model of the reaction kinetics is necessary within the overall reactor model; for this reason, a detailed analysis of the kinetics of WS, CDS and ceria thermal reduction has been performed and suitable kinetics models have been selected (Section 3.1.2). The kinetics implemented in a FORTRAN sub-routine has been included in the reactor model. Commercial software ASPEN Plus has been utilized for this purpose, modelling the moving bed reactor as a series of RCSTR reactors (Section 3.1.3).

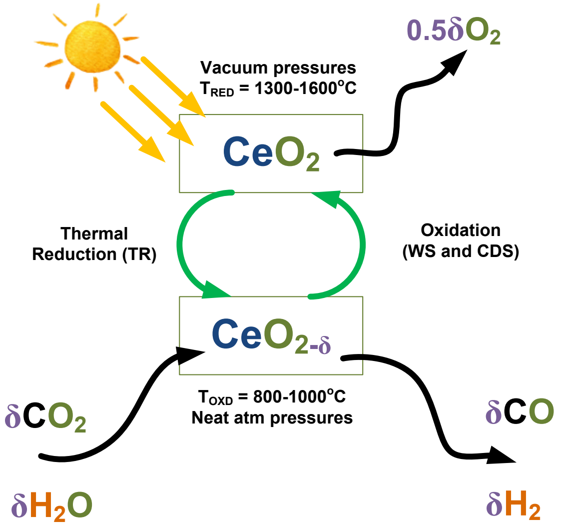

Figure 29. Schematics of interconnected solar-driven thermochemical CO_2 and H_2O dissociation using non-stoichiometric ceria.

The reactor model is then evaluated by sensitivity studies on relevant parameters (temperature, pressure, reactor volume, inlet gas composition) of the reduction and oxidation reactors, and validated for the reduction application by comparing simulations with experimental results (Section 3.1.4).

3.1.2 Reaction kinetics

Multiple materials of distinct categories have been studied to select the most suitable oxygen carrier (OC). However, none of them has yet been recognized as the ideal one. Non-stoichiometric ceria has shown higher oxygen storage capacity at relatively lower reduction temperatures, with added advantages of good mechanical and physical properties. The typical reactions taking place in the reduction and the oxidation reactors are shown below in equations (3.1) and (3.2), in which, ceria releases oxygen and undergoes thermal reduction, in turn, to be oxidized by the incoming carbon dioxide and water producing carbon monoxide and hydrogen in the two reactors respectively.

$$\text{Reduction reactor : } CeO_2 \xrightarrow[T_1]{\Delta H_1} CeO_{2\text{-}\delta} + 0.5\delta O_2 \tag{3.1}$$

$$\text{Oxidation reactor : } CeO_{2\text{-}\delta} + \delta CO_2 \xrightarrow[T_2]{-\Delta H_2} CeO_2 + \delta CO \tag{3.2a}$$

$$\text{Oxidation reactor : } CeO_{2\text{-}\delta} + \delta H_2O \xrightarrow[T_2]{-\Delta H_2} CeO_2 + \delta H_2 \tag{3.2b}$$

Reduction and oxidation reactions are fundamentally different from the energy perspective, with the former being endothermic and the latter, an exothermic reaction. Hence, the two reactors are operated at different temperature levels, with the reduction reactor being at a higher temperature.

Due to the limited availability of the thermodynamic properties of non-stoichiometric ceria, a different approach was used to describe the reactions, using the fully reduced and stable form of ceria, Ce_2O_3, whose properties are widely available in the literature. The above reaction set (equation 3.1 and 3.2) was therefore re-written as the follows:

$$CeO_2 \xrightarrow{k_{RED}} (1\text{-}2\cdot\delta)CeO_2 + \delta Ce_2O_3 + 0.5\delta O_2 \tag{3.3}$$

$$(1\text{-}2\cdot\delta)CeO_2 + \delta Ce_2O_3 + \delta CO_2 \xrightarrow{k_{OXI}} CeO_2 + \delta CO \tag{3.4}$$

$$(1\text{-}2\cdot\delta)CeO_2 + \delta Ce_2O_3 + \delta H_2O \xrightarrow{k_{OXI}} CeO_2 + \delta H_2 \tag{3.5}$$

The non-stoichiometry factor δ has been proposed to be defined as the ratio between the completely reduced form, Ce_2O_3, and the still unreacted ceria. Equation (3.3) represents the reduction reaction, while the CDS and WS reactions can be modelled as per the equations (3.4) and (3.5) respectively. The non-stoichiometry factor (δ) can hence be evaluated following equation (3.3) and can be written as per the following equation (3.6), whereby the value of δ varies between 0 and 0.5, the later corresponding to a fully reduced state of CeO_2.

$$\delta = \frac{\dot{m}_{Ce_2O_3}}{2\times\dot{m}_{Ce_2O_3} + \dot{m}_{CeO_2}} \tag{3.6}$$

Nevertheless, a complete removal of all the available oxygen would cause the fluorite phase of CeO_2 to destabilize, making phase transition inevitable beyond a certain degree of reduction [108]. The crystal structure of CeO_2 and Ce_2O_3 is shown in Figure 30 [208,209]. Bulfin et al. [108] developed an analytical thermal reduction model and in their study maximum δ_{max} reported to be 0.35 with a least standard deviation below 1600°C. Although the maximum non-stoichiometry without changing the fluorite structure of CeO_2 for redox recycling of ceria is limited to 0.286 ($1.714 \leq (2\text{-}\delta) \leq 2.0$) at 1000°C [106]. Thus, due to the limited availability of the thermodynamic properties of non-stoichiometric ceria at different δ values, the degree of advancement of the reaction has been used in the kinetics model developed instead of the non-stoichiometry coefficient. Therefore, a separate parameter X was defined for all the reactions in terms of the relative content of Ce_2O_3 and CeO_2 in the solid mixture after respective reactions.

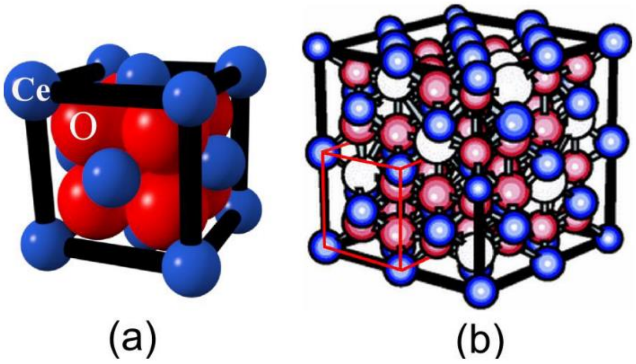

Figure 30. Crystal structure of cerium dioxide (a) CeO_2 (b) Ce_2O_3 [208].

For the reduction of CeO_2, the degree of advancement of reaction X_{RED} primarily describes the performance of the reduction reaction in terms of degree of reduction of the ceria powder is represented by equation (3.7). The equation is based on its relationship with the non-stoichiometry coefficient δ, whereby a maximum extent of reaction is obtained at δ_{max} of 0.35. The numerator represents the current non-stoichiometry after reduction, while the denominator indicates the maximum possible non-stoichiometry.

$$X = X_{RED} = \delta/\delta_{max} \tag{3.7}$$

A detailed discussion on the calculation of the degree of advancement of reaction is done in the following subsections. Indeed, such a formulation of the degree of advancement of thermal reduction reaction (X_{RED}) agrees with the reduction kinetic model developed by Bulfin et al [108]. On the other hand, the oxidation of the reduced ceria inherently moves in the opposite direction to reduction, whereby, the extent of oxidation (X_{OXI}) can be written according to the following equation (3.8).

$$X_{OXI} = 1 - X_{RED} \tag{3.8}$$

Before delving into detail at the individual reaction kinetics, the pathways of reaction are worth discussing. Two primary pathways of reaction for the solid-gas systems have primarily been used in the literature [210]. In one reaction mechanism, the solid particle decreases in size as the reaction moves forward and leaves only a small portion containing impurities that are not able to react. An example being coal combustion, where the unreacted fraction of the initial fuel remains as ash. Another example of such a mechanism might be a reduction of volatile OCs, whereby the metal oxide gets vaporized after the removal of oxygen by thermal reduction. The second mechanism assumes a constant reaction particle size during the entire reaction, even though the composition changes. The non-volatile OCs can essentially be considered to follow this reaction approach when the temperatures are low enough not to cause sublimation of the outer layers of the solid [211,212].

The thermal reduction of metal oxides comprises a number of reaction steps. Of the five reaction steps of thermal reduction, as proposed by Levenspiel [210], these steps can be limited to three, since there is no additional reactant transport towards the reaction surface. The steps can be elaborated as i) the release of oxygen particles from the surface of the ceria; ii) the diffusion of oxygen vacancies towards the particle core and iii) the diffusion of oxygen particles through the gas film.

On the other hand, the oxidation reaction can also be fully described through four steps as i) the transport of oxygen vacancies towards the reaction surface, ii) the diffusion of oxidant through the gas film towards reaction surface, iii) the filling the vacancies with oxygen and iv) the diffusion of the spent oxidant through the gas film. The additional step of oxidant (CO_2/H_2O) diffusion towards reaction surface needs to be considered for the oxidation reaction. The second and fourth steps of the oxidation reaction are much faster with respect to the other reactions. Literature reveals that studies in the related field primarily focused on expanding the reaction mechanism associated with filling the vacancies of the OC by oxygen (Step 3) through multiple reaction pathways [213,214] and on the transport of oxygen vacancies in the particle [215].

Shrinking core model (SCM) can be used to model the redox kinetics of ceria, though is not often used due to its complexity. Most of the studies focused on the kinetics of the OCs tend to describe possible reaction pathways for the material and later try to fit experimental data into various reaction models, based on the rate-limiting step in the reaction. Thus, the rate-determining step of the reaction pathway is included in the general formulation of the reaction rate. Between the two reactions, the reduction reaction is inherently slower, resulting to be the rate-determining step for the entire cycle. This also directly influences the yield from the oxidation step. Therefore, based on the above discussions, as well as considering that the crystal structure of the OC, especially for non-volatile and non-stoichiometric ceria remains constant throughout the redox cycle, a simplified approach was considered for modelling the reaction kinetics for the solar thermochemical cycle as described in the following sub-section.

Reduction kinetics

Bulfin et al. [108] investigated ceria reduction kinetics for a wide range of temperature, between 1000°C and 1900°C and a wide range of oxygen partial pressures from 10^{-2} to 10^{-8} bar. The partial pressure of oxygen derives from the presence of removable oxygen produced by the reduction of CeO_2 as per equation (3.3). The proposed reduction kinetic model by Bulfin et al. [108] is essentially based on the Arrhenius equation, assuming an equilibrium reaction. This causes both forward and backward reactions, i.e. the release of oxygen and the recombination of released oxygen, to occur together ($CeO_2 \leftrightarrow CeO_{2-\delta} + 0.5\delta O_2$). The oxygen vacancy concentration change during the reduction reaction is the rate at which oxygen departing (forward) from CeO_2 subtracting the rate at which it again combines (backward reaction) which is given by equation (3.9).

$$\frac{d[O_{vac}]}{dt} = [O_{Ce}]k_f - [O_{vac}][O_{gas}]^{n_b} k_b \tag{3.9}$$

The equation (3.9) can be rewritten to non-dimension form as equation (3.10).

$$\frac{1}{[Ce]}\frac{d[O_{vac}]}{dt} = \frac{[O_{Ce}]}{[Ce]}k_f - \frac{[O_{vac}]}{[Ce]}[O_{gas}]^{n_b} k_b \tag{3.10}$$

Where [Ce], $[O_{Ce}]$, $[O_{vac}]$, $[O_{gas}]$ are the cerium concentration, oxygen that can be released from ceria, vacancies of the oxygen and oxygen gas concentration that is released respectively; k_f and k_b are forward and backward reaction rate constants. It is also mentioned that the rate constants were based on Arrhenius based equation which relates temperature with activation energy and pre-exponential factors. Unlike the previous argument of measuring the extent of non-stoichiometry, it was proposed that moles of oxygen vacancies $[O_{vac}]$ per mole of cerium [Ce] per second or simply per second to be used as the measure of the non-stoichiometry of the reduced ceria, as shown in the following equation (3.11).

$$\frac{[O_{vac}]}{[Ce]} = \delta \tag{3.11}$$

The forward reduction reaction is driven by the concentration of oxygen removal, while the backward recombination (or oxidation) reaction is influenced by the concentration of both the vacancies and the oxygen [108]. Thus, the rate of the total change of the non-stoichiometry, which in other terms is also the rate of change of the oxygen vacancy concentration can be written as difference of the rate at which oxygen leaves CeO_2 (forward reaction) and the rate at which it recombines (backward reaction) as per the following equation (3.12) and can be seen in Figure 31.

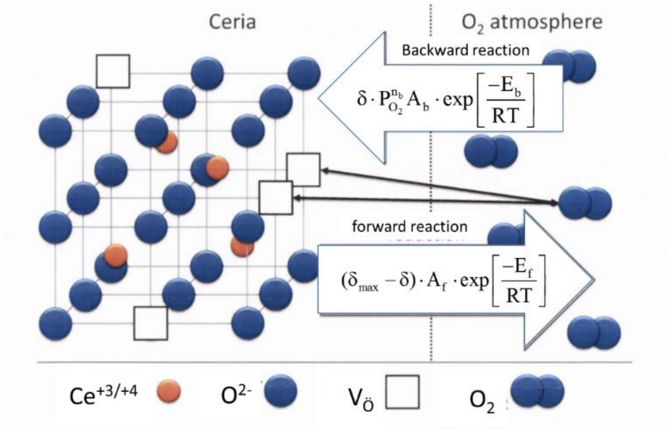

Figure 31. Reduction equilibrium reaction considering forward and backward reaction [216].

$$\frac{d\delta}{dt} = (\delta_{max}\text{-}\delta) \cdot A_f \cdot \exp\left(-\frac{E_f}{RT}\right) - \delta \cdot P_{O_2}^{n_b} \cdot A_b \cdot \exp\left(-\frac{E_b}{RT}\right) \tag{3.12}$$

Where A represents the Arrhenius constant, E is the activation energy in kJ/mol/K, P_{O_2} is the partial pressure of oxygen, n_b is the reaction order, R is the universal gas constant and T is the absolute temperature in Kelvin with subscript f and b as forward and backward reaction respectively.

Assuming ideal gas behaviour, the concentration of O_2 is directly proportional to the partial pressure of O_2 (P_{O_2}) or the vacuum pressure of the total reactor, if a sweep gas is not used, as applicable based on the reactor design. Based on the works of Panlener et al. [217] and Dawicke et al. [218] and through the plotting of log(δ) against log(P_{O_2}) with certain assumptions, the authors developed a reaction kinetic model for the net thermal reduction reaction of ceria. To fit the developed kinetic model with the experimental results, the shrinking core model was used. Considering a surface reaction to be the rate-determining step there would be a shrinking sphere of vacancies resulting in a restriction on the reaction rate with the advancement of the reaction. A third order model for the rate equation was found to be the best fit and the overall rate equation for the reduction reaction, based on X_{RED} is obtained as per the following equation (3.13). The values of the parameters of the rate equation are summarized in Table 3.

$$\frac{dX_{RED}}{dt} = \frac{d\delta}{dt} \cdot (1\text{-}X_{RED})^{-1/3} \tag{3.13}$$

Table 3 Ceria reduction rate equation coefficients presented by Bulfin et al. [214].

Parameter	Value
δ_{max}	0.35
n_b	0.218 ± 0.0013

E_f (kJ/mol)	232 ± 5
E_b (kJ/mol)	36 ± 4
A_f (s^{-1})	720,000 ± 360,000
A_b ($s^{-1}bar^{-nb}$)	82 ± 41

However, the transition from the rate equation to the reaction rates of the concerned chemical species is done as per the equations (3.2) and (3.13) together with the available chemical species. Three distinct chemical species take part in the above reaction. For each mole of cerium (III) oxide (Ce_2O_3) generated, two moles of ceria (IV) oxide (CeO_2) are consumed and half a mole of oxygen gets released. Aside from stoichiometric coefficients, knowledge of reaction time step is important. In the discrete kinetic model, the particle residence time is used as the time parameter, in terms of Δt, as can be seen from equations (3.14) to (3.16). The thermal reduction reaction rates for the three species taking part in the reaction are shown below.

$$k_{RED\text{-}CeO_2} = -2 \cdot \dot{m}_{CeO_2} \frac{dX_{RED}}{dt} \Delta t \tag{3.14}$$

$$k_{RED\text{-}Ce_2O_3} = 1 \cdot \dot{m}_{CeO_2} \frac{dX_{RED}}{dt} \Delta t \tag{3.15}$$

$$k_{RED\text{-}O_2} = 0.5 \cdot \dot{m}_{CeO_2} \frac{dX_{RED}}{dt} \Delta t \tag{3.16}$$

where $k_{RED\text{-}i}$ is rates of reduction species i listed as CeO_2, Ce_2O_3, O_2.

Oxidation kinetics

The oxidation kinetics for ceria for H_2O and CO_2 splitting has been investigated by several research groups [197,219,220]. The initial reduction state of the sample has been reported to strongly influence the subsequent oxidation reaction. A significant drop in the reaction rates was noticed when non-stoichiometry factor exceeded 0.18-0.2 values in the temperatures below 820°C [219]. High variations in the reaction activation energies are reported with non–stoichiometry of the sample in higher concentrations of the oxidizing gas. As reported, the activation energy varied in the range of 160-200 kJ/mol for non-stoichiometry between 0.01 and 0.09. For oxidation kinetics, Arifin [214] and Arifin and Weimer [220] investigated a redox kinetics of ceria for water and carbon dioxide splitting reaction. The reaction mechanism has been proposed in the general formulation for the reaction rate as equation (3.17) with the corresponding coefficients being listed in Table 4.

$$\frac{dX_{OXI}}{dt} = A_0 \cdot \exp\left(-\frac{E_0}{RT}\right) \cdot y_i^{n_o} \cdot (1 - X_{OXI})^{\psi} \tag{3.17}$$

where A_0 is the Arrhenius constant, E_0 is the activation energy degree and n_o is the order of the oxidation reaction and y_i is the oxidant molar fraction.

The oxidation reaction of the reduced ceria with water vapour and CO_2 splitting was found to behave similarly to a homogeneous reaction, i.e. its rate decelerates proportionally to the depletion of the reactants ($1-X_{OXI}$). However though, unlike the water-splitting reaction, that presents a relatively faster reaction with a low activation energy of 45 kJ/mol, the CO_2 splitting reaction is a more complex phenomenon based on surface mediation.

However, similar analyses revealed the dependence of the rate-determining step of the carbon dioxide splitting reaction on the temperature of the process [214]. It was also observed that with the increase in temperature, carbon site blocking, and subsequent surface recombination stops. At 875ºC the only reaction pathway is the direct desorption of carbon monoxide from the particle surface, which might result in significant changes to the reaction coefficients ψ and n_o as indicated in Table 4. It is worth noticing that in the discussed research, ceria sample was constantly cycled and reused in different conditions. Nevertheless, Arifin [214] noted that the overall production of the fuel from the sample remained almost constant, though reaction times varied because of varying temperatures and molar fractions of reactants.

Table 4. Kinetic parameters of the oxidation reaction of reduced ceria obtained by Arifin and Weimer [220].

Oxidant	Temp (ºC)	A_0 (1/s)	E_0 (KJ/mol)	ψ (-)	n_o(-)
CO_2	750-950	1	29	0.89	1
	650-725	4.2	47	0.53	1
H_2O	750-800	3.4	45	0.65	1.2
	825-875	2.5	41	0.7	1.7

To determine the reaction rates for splitting reactions, the degree of advancement of oxidation reaction was calculated as per mentioned in equation (3.8). Following the aforementioned equation, independent to the use of CO_2 or H_2O, when one mole of each species is consumed, it leads to simultaneous consumption of each mole of Ce_2O_3 with the corresponding generation of two moles of ceria and one mole of CO and H_2 respectively. Taking this into account, the reaction rates for each species, in terms of the available solid reactant quantity (molar flow) are listed as per the following equations (3.18-3.23).

$$k_{OXI\text{-}CeO_2} = 2 \cdot \dot{n}_{Ce_2O_3} \left\{ \frac{dX_{OXI\text{-}H_2O}}{dt} + \frac{dX_{OXI\text{-}CO_2}}{dt} \right\} \Delta t \tag{3.18}$$

$$k_{OXI\text{-}Ce_2O_3} = -1 \cdot \dot{n}_{Ce_2O_3} \left\{ \frac{dX_{OXI\text{-}H_2O}}{dt} + \frac{dX_{OXI\text{-}CO_2}}{dt} \right\} \Delta t \tag{3.19}$$

$$k_{OXI\text{-}H_2O} = -1 \cdot \dot{n}_{Ce_2O_3} \frac{dX_{OXI\text{-}H_2O}}{dt} \Delta t \tag{3.20}$$

$$k_{OXI\text{-}H_2} = 1 \cdot \dot{n}_{Ce_2O_3} \frac{dX_{OXI\text{-}H_2O}}{dt} \Delta t \tag{3.21}$$

$$k_{OXI\text{-}CO_2} = -1 \cdot \dot{n}_{Ce_2O_3} \frac{dX_{OXI\text{-}CO_2}}{dt} \Delta t \tag{3.22}$$

$$k_{OXI\text{-}CO} = 1 \cdot \dot{n}_{Ce_2O_3} \frac{dX_{OXI\text{-}CO_2}}{dt} \Delta t \tag{3.23}$$

where $k_{OXI\text{-}j}$ is rates of oxidation species j listed as CeO_2, Ce_2O_3, H_2O, H_2, CO_2, CO.

3.1.3 Model development

Based on work of Panlener et al. [217] and following the kinetics developed by Bulfin et al. [108], which has also been used in the present study, it can be concluded that a very low partial pressure of oxygen is necessary to have an acceptable reduction of ceria, often lower than 10^{-5} bar [108], working at temperatures of around 1300ºC and above. This can be achieved either by operating the reactor in vacuum conditions or by sending sufficiently high sweep gas flow to maintain the desired level of oxygen partial pressure in the reduction reactor. The later, however, requiring more than 10^5 times the sweep gas flow with respect to the oxygen delivered, is often limited due to the scale of the amount of inert gas flow [202]. The moving bed aerosol reactor, proposed by Scheffe et al. [164], acknowledges this fact, which would lower the effectiveness of the entire cycle. Indeed, such a requirement of low pressure for direct reduction limits the use of sweep gas, which in turn would limit the application of fluidized bed reduction reactors. On the other hand, non-structured reactors working under vacuum can essentially be referred to as equivalent to moving bed reactors, where the particles undergo reduction while moving through the reactor. Reactor design concepts by Muhich et al. and Ermanoski among many other similar reactor designs proposed are essential of this type [35,146,221,222].

On the other hand, it is essential to maintain higher pressure to perform the oxidation. With CO and H_2 being the primary products, this would considerably decrease the work needed for the compression of the products, especially H_2, essentially for their use in downstream industrial applications. In this regard, both fluidized bed and moving bed reactor configurations can be applicable, both with relative advantages and disadvantages. While employing a circulating fluidizing bed configuration solves one of the major problems of metal oxide transport in a redox cycle, considerable disadvantages also exist related to the selectivity of the products and fluidization regime the reactor operates. Fan et al. [170] studied and reported the relative advantages of a moving bed reactor over a fluidized bed reactor for reduction of oxygen carriers with methane. Besides a more homogeneous reduction of the OCs, reactions in a moving bed reactor result closer to thermodynamic equilibrium, rather than in fluidized bed reactors.

In a fluidized bed reactor, due to the requirement of desired flows for fluidization, this often results in a low gas or metal oxide conversion (transport reactors for smaller configurations) or would require sufficiently large reactors with a very high oxygen carrier inventory (bubbling bed reactors). Additionally, for transport reactors, the relative gas conversion is very low with a low-pressure drop, while for a bubbling bed, even though the conversion is higher, would result in a higher pressure drop. A low gas purity would then require downstream purification before the use of the generated product for the subsequent industrial application. However, the effectiveness of the cycle decreases. Moving bed reactors, on the other hand, do not experience such limitations and hence are more flexible in design and operation. Such a moving bed reactor system is also patented by Ivan Ermanoski [222] which consist of two reactors that work at pressure swing as well as temperature swing with both the reactors are coupled with heat exchangers which are analytically studied without specific kinetics involved. Most of the studies addressing the analysis of the chemical looping systems presented reactor models are based on thermodynamics and Gibbs minimization principle, while reaction kinetics are often not included.

Hence, following the above discussion relating to both the reduction and the oxidation reactors, moving bed reactors are considered in the present study. While the reduction reactor would operate at vacuum, the oxidation reactor would operate at near atmospheric conditions. This resembles the reactor concept proposed by Muhich et al. [146], with the only essential difference being that the oxidation reactor is a moving bed reactor instead of a bubbling bed reactor. The transport of the oxidized metal oxide particle can be performed by a screw-conveyor.

The present study has been focused on the development of the reactor model using commercial software ASPEN Plus to predict the results reported in literature and to investigate the performance of each reactor for different operating conditions in order to have a high selectivity of the syngas produced and to see the effect of composition of mixture (CO_2 and H_2O) on the conversion within the oxidation reactor. The following section details the development of such reactor models and the obtained results are discussed in Section 3.1.4.

Moving bed reactor model

A general schematic of the countercurrent moving bed reactor is shown in Figure 32. In the reduction reactor, the metal oxide is thermally reduced, as it is fed from the top operated in a vacuum. Hence, there exists no gas inlet. However, the generated oxygen flows up to the top of the reactor in a counterflow with respect to the metal oxide, wherefrom it is connected to a vacuum pump that drives it away and maintains the necessary vacuum (not shown). In the oxidation reactor, the reduced metal oxide is fed from the top as well and reacts with the gas (CO_2/H_2O) moving up. Since the splitting reaction is exothermic, a temperature gradient exists along the length of the reactor for non-isothermal operations. The reduced metal oxide is removed from the bottom (e.g., by a rotating grate, not shown in the figure), while the produced gas exists the reactor from the top. The oxidized metal oxide is transported back to the reduction reactor. The pressure swing between the two reactors for the metal oxide has been proposed to be performed similarly to the one proposed by Muhich et al. in their reactor design concepts [146]. At the bottom of the reduction reactor, the particles would be stored, in a form replicating a pseudo packed bed, before being transmitted into the oxidation reactor via a constricted passage. This pseudo-packed bed moving storage, together with a gradually decreasing flow area would provide the necessary pressure buffer, so as to increase the pressure from the vacuum in the reduction reactor to nearly atmospheric pressures in the oxidation reactor. However, since it is a physical process, it would not lead to additional mechanical work being expended.

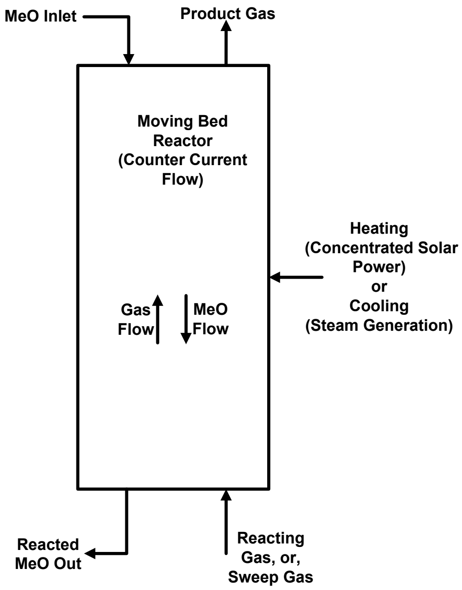

Figure 32. Schematic diagram of a generic moving bed reactor

A counter-current reactor model was thereafter simulated for the thermal reduction and CDS and WS reactions respectively, using ASPEN Plus incorporating set of RCSTR reactors in series. The RCSTR reactor has the characteristic that all phases have the same temperature, which means the temperatures of solid and gas phases in the reduction and oxidation processes are equal in each RCSTR model. Also, it is modelled so that each RCSTR has the same volume, equal to the whole gasifier volume divided by the number of RCSTRs in series. The reaction kinetics described were written in an external user kinetic subroutine in FORTRAN, which is compiled and hooked up with each of the RCSTR reactors in the moving bed model. Specific assumptions with respect to the oxidation and reduction reactors were individually considered and summarized below:

1. All the RCSTRs in the reduction reactor were at the same temperature, to simulate an isothermal reactor for the reduction.
2. All the RCTSRs in the oxidation reactor were simulated as adiabatic reactors, and the heat losses of RCTSRs were neglected (i.e., heat loss factor set to 0). This drives the temperature of the products and the reactor in some cases quite high. If not controlled, this might lead to the change of crystal structure of the oxygen carrier in actual practice. However, such considerations were not taken into account during the present simulation.
3. A single-entry, counter-current moving bed reactor was simulated for the oxidation reactor, where the oxygen carrier is fed from the top and the reactant gas flows upward from the bottom inlet as shown in Figure 32. However, the scope for optimization to enhance the reaction rates, together with performing temperature control within the reactor by multiple gas inlets is possible. Nevertheless, it was not included in the present study.
4. The residence time in the reactors was calculated based on the bed volume with respect to the inlet oxygen carrier volumetric flow rate neglecting the changing volume flow due to change in composition from reactions.
5. No change in oxygen carrier structure and hence the change in reactions kinetics was considered during the course of the reactions.

Modelling a moving bed reactor with a series of RCSTRs is like discretizing the reactor volume in a finite number of smaller volumes. Indeed, the higher the number of RCSTRs in series, the higher is the accuracy of the estimation of the yields from the reactor. But an excessive number of reactors would increase the iterative calculations resulting in a time-consuming simulation. Also, such configurations exhibit slow solution convergence because of the form of the mathematical model of counter-current moving bed reactor, that is a two-point boundary value problem [189]. Hence, the selection of the number of RCSTRs in series is crucial to the net evaluation of the system in order to realize the goal of minimizing simulation errors and at the same time limiting the computation time as much as possible. To evaluate the number of RCSTRs in series that would result in the minimization of error from approximation, an iterative calculation procedure is applied, as described in Section 3.1.3.

The hook-up logic between the in-built ASPEN Plus model and the external FORTRAN code for user kinetics, together with the use of calculator blocks for calculating the necessary external heat requirement for the isothermal reduction reactor is shown in Figure 33. Each RCSTR block is linked up with the user kinetic model and the resulting output is fed to the successive reactor. There will be an exchange of variables from each RCSTR providing temperature, pressure and molar flow of each gaseous and solid species, along with the volume of each RCSTR, which are used in the

FORTRAN subroutine to calculate non-stoichiometric parameter and metal oxide conversion. User-kinetic subroutine calculates the instantons rate of reaction (equation (3.13) and (3.17) for reduction and oxidation respectively) together with residence time. From the instantaneous rate of reaction, the rate of reaction of specific species is evaluated by equations (3.14-3.16) for reduction reaction and equation (3.18-3.23) for oxidation reaction, which are reported back to RCSTRs in Aspen Plus, as it can be seen in Figure 33(b).

Unlike the reduction reactor, it is interesting to note that for the oxidation reactor, since two inlets (i.e., ceria and H_2O/CO_2 streams) at two different points in the reactor system are provided, the convergence is essentially a two-point convergence. This requires to provide an estimation of the yields in each stream to facilitate convergence, and estimations too far off from the results often lead to increased convergence time and in some cases, failure of convergence. Calculator blocks were added to calculate the heat need of each reactor for both the reduction and oxidation reactors. Then, besides the heat requirement, the need to calculate the non-stoichiometry (δ) generated along the length of the reactor, together with other parameters, might necessitate the addition of more calculator blocks for both the set of reactors. Indeed, based on the following Figure 33, the need to optimize the number of RCSTRs in series so as to predict well the net output from the RCSTR is essential and is conducted accordingly. The Broyden Solver was used as per the suggestion of ASPEN Plus model already developed for moving bed coal gasifier [187] and 500 iterations were provided for both the mass and energy solvers. The relative tolerance of errors was set at 10^{-3} to decrease the computation time while minimizing errors in the overall results of the simulation. Usually, for gas processing, it is recommended to use the PR-BM method which utilizes the Peng-Robinson cubic equation of state with the Bostone Mathias alpha function [223]. Therefore, the PR-BM method was selected for the simulations.

The temperature profile for an adiabatic reactor (oxidation) can be obtained through the results of each reactor, retrieved by calculator blocks. The corresponding non-stoichiometry of the input and the output metal oxide to the reactors are also evaluated via calculator blocks, incorporated with each RCSTR as per the coupling of the equations (3.6).

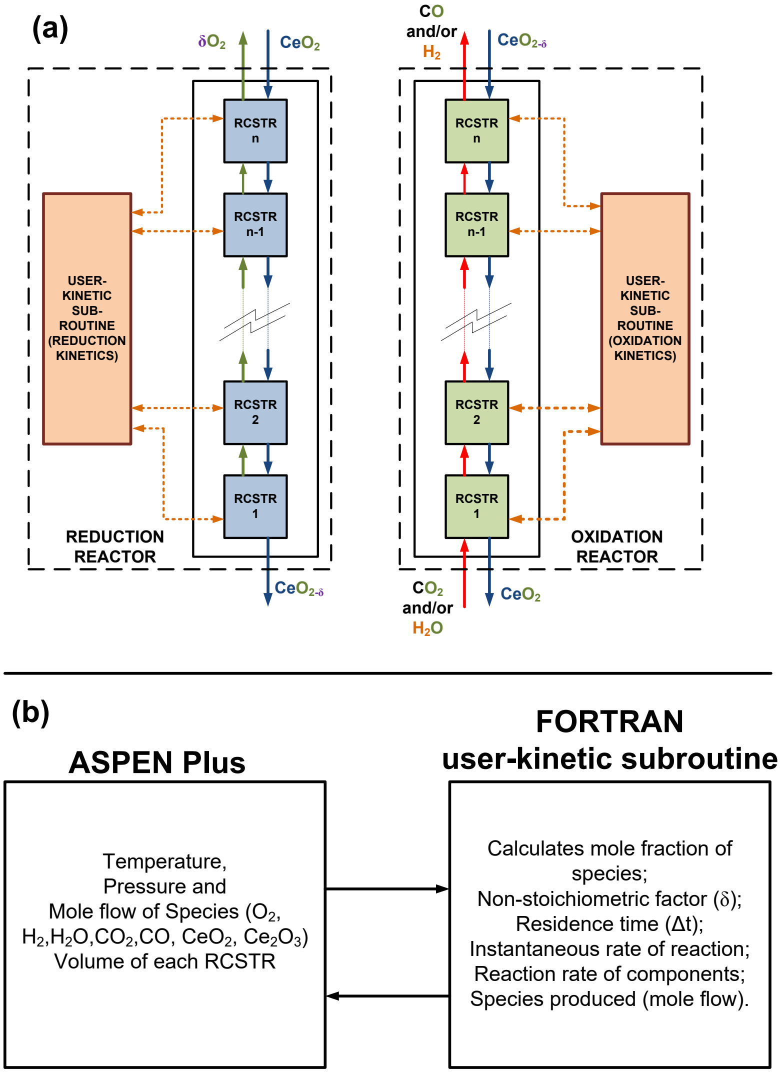

Figure 33. Moving bed reactor model in ASPEN Plus hooked with user-kinetic subroutine written in an external FORTRAN Code.

3.1.4 Evaluation methodology

Industrial-scale evaluation is essential to understand the design perspectives and evaluate the fundamental areas necessary for future focus for practical application of any chosen technology. In this regard, application of the chemical looping technology for CO/H_2 production, coupled to an industrial scale source of the CO_2 or water has been evaluated. The reactor model has been evaluated based on the common aim to provide a 100 mol/s of syngas from either CO_2 or H_2O or CO_2/H_2O mixture. The value suits well with the amount of CO_2 or water available from the state of the art carbon capture power plants [224,225]. As per equations (3.3 and 3.6), the equivalent amount of CeO_2 to be circulated for generating a non-stoichiometry of 0.35 is 285.71 mol/s.

This results in an equivalent Ce_2O_3 stream of 100 mol/s generated during the reduction phase, following the above-mentioned equations.

The reduction temperature was varied between 1000°C and 1600°C following the arguments by Bulfin et al. [108] to allow comparison of the results of the model developed with experimental results available in the literature. Solar tower and parabolic dishes are the technologies of choice to achieve the high temperatures required [22]. In addition, from the limitations of the scale with regards to parabolic dishes, the solar tower has been considered as the most suitable technology for thermochemical cycles. Nevertheless, to date, the highest temperature application for ceria cycles at 1600°C through solar tower technology has been reported by Tou et al. [226]. Hence, a maximum temperature of 1600°C was selected to evaluate the reduction reactor. The base case for this reactor was selected also to be the best case application, with a temperature of 1600°C and a reactor vacuum pressure of 10^{-7} bar, in order to obtain an acceptable reduction extent. Such low reduction pressures can be achieved by multiple cascading pressure chambers to achieve high reduction efficiency as suggested by [31,32,166].

On the other hand, the oxidation reactor was evaluated separately from the reduction reactor. As has already been discussed, based on a maximum achievable δ of 0.35 [199], the oxidation reactor was supplied with a maximum reduced ceria. This was to ensure the study of the oxidation reactor, irrespective of the limitation to the reduction technologies. Furthermore, the kinetics of the oxidation reactor used in the present study had been evaluated at atmospheric conditions. However, by Le-chatelier principle, the oxidation reaction is preferred at higher pressures. Nonetheless, due to the uncertainty of the kinetics of reaction with pressure variation, a small pressure rise has been considered for the oxidation with respect to that at which the kinetics were developed. Hence, an oxidation pressure of 2 bar was selected for the simulation study. This would also be advantageous through the decrease in the subsequent compression work associated with H_2 and CO compression for downstream applications. The gas flow rate was varied according to the need of the reactor design. This also results in the assessment of the product purity in the generated stream from the splitting oxidation reactor, better known as the selectivity. The selectivity of CO and H_2 via three different splitting reactions (only CO_2, only H_2O, and CO_2/H_2O mixture) is written as per the following equations below (3.24a and 3.24b).

$$S_{CO} = \frac{\dot{m}_{CO}}{\dot{m}_{CO_2} + \dot{m}_{CO}} \tag{3.24a}$$

$$S_{H_2} = \frac{\dot{m}_{H_2}}{\dot{m}_{H_2O} + \dot{m}_{H_2}} \tag{3.24b}$$

Here $\dot{m}$ represents the molar flow of the components in the outlet product gas from the splitting reactor (oxidation reactor) and the subscript represents the components for which the molar flows are considered.

In addition, the inlet temperature of the oxygen carrier into the reduction reactor was fixed at 1300ºC for the base case scenario. As for the oxidation reactor, the oxygen carrier and gas inlet temperature was fixed at 800ºC for base case simulations. Further sensitivity studies to evaluate the impact of the variation of these temperatures have been carried out and commented accordingly. Based on such assumptions and considerations, the following section details the results and the design aspects of the moving bed reactor for application to an industrial scale solar CO_2/H_2O splitting using ceria as the OC.

Model convergence

To evaluate the number of RCSTRs in series that would result in the minimization of error from approximation, an iterative calculation procedure was adopted after He et al. [189]. The reduction and the oxidation reactors have been considered separately for the optimization. Each RCSTR have been sequentially arranged along the height of the reactor, with an equivalent volume of 0.5 m^3 and 4 m^3 for the reduction and the oxidation reactor, respectively. An iterative procedure, with increasing the number of the RCSTRs (with the total volume of reactor fixed) is carried out until the relative change would result in a value lower than 0.25% change of the output (O_2 or H_2/CO flows) of the moving bed reactor. The value of 0.25% was considered a good approximation to the reactor convergence while ensuring minimization of computation time by unnecessarily increasing the number of reactors in series. The schematic of the algorithm followed for the iterative simulation is shown in Figure 34.

Figure 35 shows the relative changes of the outputs from the reduction and the oxidation reactors respectively while varying the number of RCSTRs in series (n). To evaluate the relative change, the oxygen released from the reduction of ceria was obtained for an isothermal reduction reactor at 1600ºC and a vacuum pressure of 10^{-7} bar. The amount of CeO_2 sent for reduction was 285.71 mol/s. As can be seen, beyond n = 4, the relative change in the results drops below 0.25% and beyond n = 7, the relative change becomes negligible. Therefore, the optimum number of RCTRs in the reduction zone is considered as n = 7.

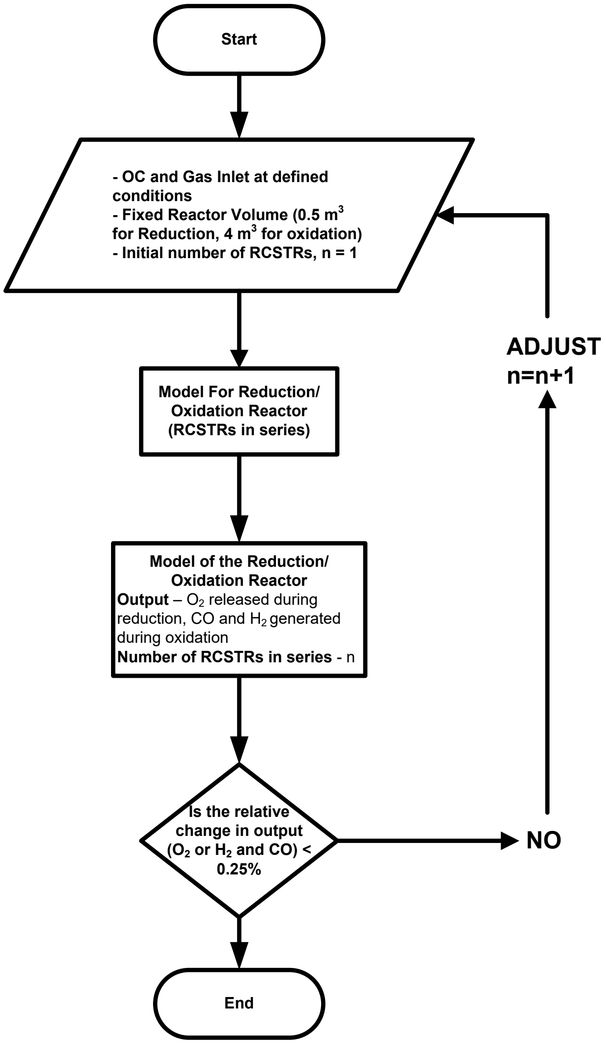

Figure 34. Iterative calculation procedure for determining RCSTRs numbers, n.

For the oxidation reactor, the H_2 and CO yield were considered to evaluate the convergence of the number of RCTRs. An equimolar mixture of CO_2/H_2O was sent to oxidize the reduced ceria with a maximum non-stoichiometric factor limit of 0.35, at a constant gas and metal oxide inlet temperature of 800°C. The reactors were considered adiabatic. As can be seen from the results shown in Figure 35(b), due to slower CO_2 splitting kinetics, a larger number of RCSTRs in series is required to obtain the necessary convergence. Hence, while after 8 RCSTRs in series the relative change in H_2 yield drops below 0.25%, the corresponding value is obtained with 10 RCSTRs in series for the CO yield. Hence, an n = 10 was found to result in minimal relative error while simulating the oxidation reactor.

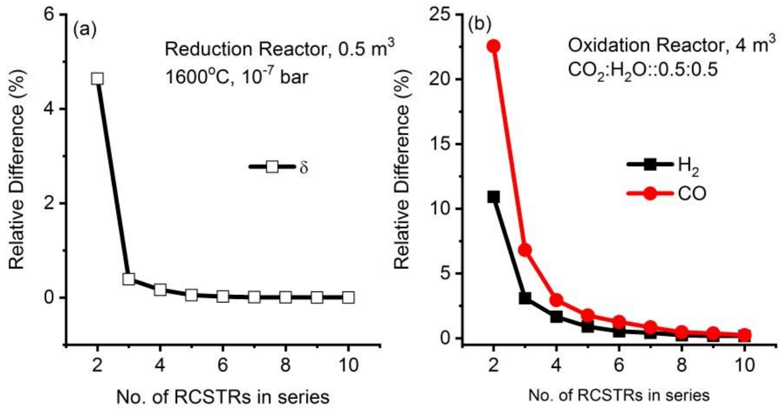

Figure 35. Relative changes in the output from increasing the number of RCSTRs in series for (a) reduction reactor (b) oxidation reactor.

3.1.5 Results and discussion

Reduction reactor

The impact of the different operating parameters on the performance of the moving bed reduction reactor is described in the following section.

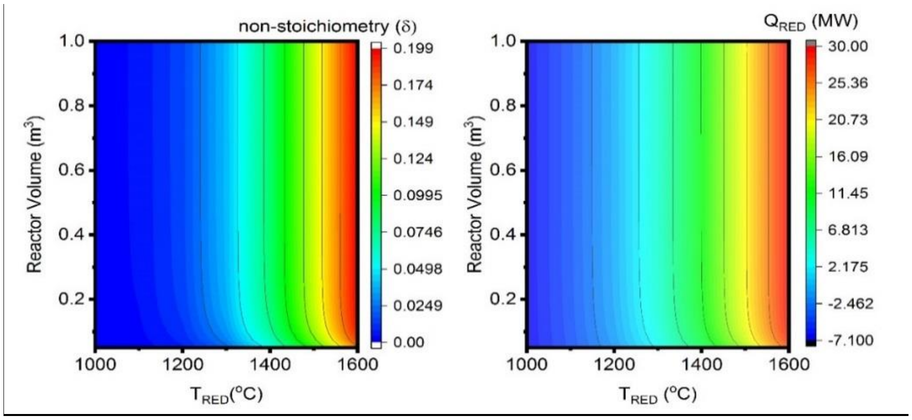

Figure 36. Variation of (a) Non-Stoichiometry (δ) and (b) heat requirement of the reduction reactor (Q) with temperature and reactor volume of the reactor at a constant vacuum pressure of 10^{-7} bar, CeO_2 molar flow of 285.71 mol/s and metal oxide inlet temperature of 1300°C.

The first sensitivity assessment was performed to evaluate the variation of the non-stoichiometry (δ) with respect to both the reactor volume and temperature of the reactor, as shown in Figure 36. Due to the increased rate of oxygen recombination reaction with an increase in the non-stoichiometry factor, a fast initial reaction is seen, especially at higher temperatures. However, the increase rate is slower for lower temperatures, where, the kinetics of the global reduction reaction is considerably slow. Nevertheless, to comment on the reactor volume to suffice for the complete reduction regime, between 1000ºC and 1600ºC, the relative change in the non-stoichiometry factor based on the two temperature regimes is plotted in Figure 37. As can be followed thus, no change in the reduction extent of ceria from a non-stoichiometry factor of 0.1982 is noticed at 1600ºC beyond a reactor volume of 0.4 m^3, also signifying an approximate residence time of the metal oxide of 1.2 minutes within the reactor. Nonetheless, even though much smaller, at 1000ºC the reduction continues to occur with an increased volume of the reactor up to 1 m^3. This corresponds to an approximate metal oxide residence time in the reactor of 3 minutes. Beyond 0.4 m^3 however, the relative increase in yield is significantly small as well.

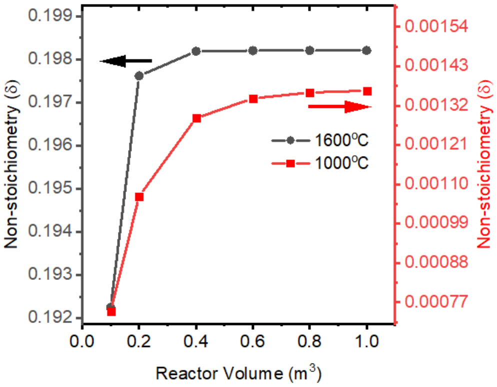

Figure 37. Variation of non-stoichiometry (δ) at 1600ºC and 1000ºC with the reduction reactor volume at a constant vacuum pressure of 10^{-7} bar, CeO_2 molar flow of 285.71 mol/s and constant metal oxide inlet temperature of 1300ºC.

On the other hand, a higher reduction extent would result in a higher heat of reaction (Q_{RED}) in the reduction reactor. This is clearly depicted in Figure 36(b), whereby a maximum Q_{RED} of 30 MW is needed to ensure the maximum yield of ceria reduction. Interesting to note is the negative heat required for operating at temperatures lower than 1200°C. Indeed, since the metal oxide inlet is fixed at 1300°C and no significant reaction is observed, a net cooling effect can be seen within the reactor, with the metal oxide releasing heat to reach 1200°C. However, above that temperature, a higher reaction extent occurs with high endothermicity, and this results in the net heat requirement for the reaction to increase and become positive. Nonetheless, an unnecessarily high reactor volume would require excess heating to the reactor, with minimal increase in the reduced ceria yield. Thus, choosing an optimal reactor volume would not only ensure an almost maximization in the desired yield over a wide range of temperatures but at the same time optimize the heat requirement of the reactor.

Hence, based on the above discussions, a reactor volume of 0.5 m^3 was selected to perform the subsequent sensitivity studies. Accordingly, the temperature of the reduction reactor was varied between 1000ºC and 1600ºC, while the vacuum pressure was varied between 10^{-3} and 10^{-7} bar to study the impact of temperature and pressure on the reduction of pure ceria. Figure 8 shows the obtained results, which are plotted together with the experimental data obtained from Bulfin et al. [108]. As can be seen, a good agreement is obtained between the experimental results and the developed moving bed model in ASPEN Plus. Hence, a validation of the present model in predicting the non-stoichiometric reduction of ceria is obtained.

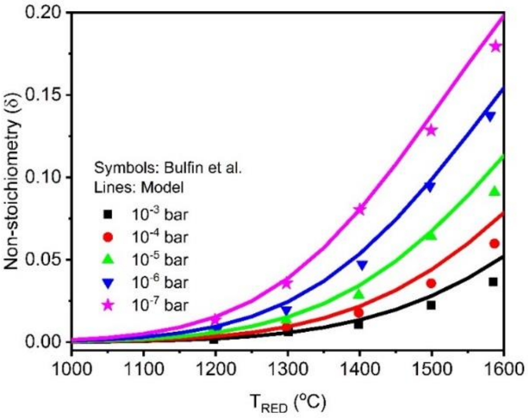

Figure 38. Variation of non-stoichiometry (δ) generated in the reduction reactor with temperature and reactor vacuum pressure at a constant reactor volume of 0.5 m^3, CeO_2 molar flow of 285.71 mol/s and constant metal oxide inlet temperature of 1300ºC. Symbols represent results of Bulfin et al. [108], lines represent the simulation model results.

Figure 38 shows that the profile of the non-stoichiometry (δ) with temperature is similar irrespective of the pressure variation. Below 1200ºC no significant reduction of ceria is noticed, even at a vacuum pressure of 10^{-7} bar. A steep increase in the non-stoichiometry (δ) of the reduction reaction is only noticed beyond 1300ºC. However, the rate of increase is enhanced at lower pressures, whereby the non-stoichiometry obtained at 1400ºC and 1500ºC being around 0.08 and 0.138 respectively for a pressure of 10^{-7} bar. Indeed, at the same two temperatures, the non-stoichiometry drops to 0.05 and 0.09 respectively at a lower vacuum pressure of 10^{-6} bar. The maximum non-stoichiometry of 0.199 was obtained at 1600ºC and a pressure of 10^{-7} bar. On the other hand, at lower vacuum pressure, the reduction reaction becomes extremely limited, even at very high temperature, whereby only around 0.025 of δ was obtained at around 1475ºC. The corresponding δ becomes around 0.06 and 0.124 at pressures of 10^{-5} and 10^{-7} bar respectively. Alternately, this also implies that to operate the reduction reactor at a lower vacuum condition, a higher temperature range needs to be maintained to have acceptable reduction yields. Therefore, the claim of the necessity to operate the reduction at high vacuum conditions, or, in other words, at very low partial pressures of oxygen is reinstated. This, however, provides an energy penalty from vacuum creation even though the corresponding yield increases.

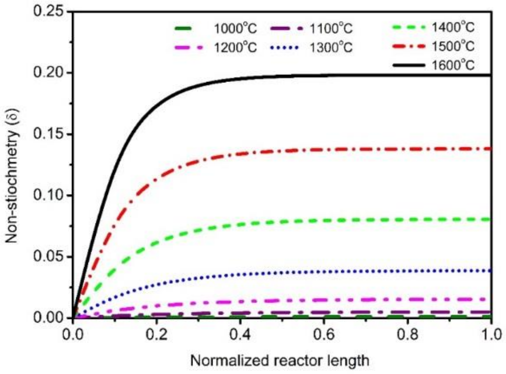

Figure 39. Variation of Non-Stoichiometry (δ) along the length of the reactor at a constant reduction reactor volume of 0.5 m^3, a constant CeO_2 flow of 285.71 mol/s and a constant reactor temperature and a vacuum pressure of 1600ºC and 10^{-7} bar respectively.

The variation of the non-stoichiometry along the normalized length of the reactor is shown in Figure 39. For lower temperatures, below 1200ºC, the evolution of δ along the length of the isothermal reactor is mostly linear. However, for temperatures of 1300ºC and higher, most of the reaction occurs before half the reactor length. This can directly be followed from the discussed reactor kinetics, whereby the rates of the backward and the forward reaction becomes almost equal after an initial reduction of the ceria. Therefore, this implies that the reactor can either be made smaller in size, or the focus volume of the solar concentrator can be more concentrated to ensure the desired reaction while minimizing the solar energy input to perform the same.

In the end, the variation of the heat of reaction at a constant reduction temperature of 1600ºC and pressure of 10^{-7} bar (plotted as the negative logarithm of the vacuum pressure) with a variable oxygen carrier inlet temperature is shown in Figure 40. Since the reactor has been modelled as an isothermal reactor, no change in the non-stoichiometry of the reduced metal oxide would occur with respect to the variable oxygen carrier inlet temperature to the reactor. As can be followed from previous arguments, at higher oxygen carrier inlet temperatures with a corresponding lower operating temperature of the reduction reactor, the net heat requirement for the reaction to occur decreases. Indeed, for a metal oxide inlet temperature of 900ºC, the heat requirement increases by almost 20 MW to around 39.3 MW in relation to the base case oxygen carrier inlet temperature of 1300ºC. Therefore, the importance of the metal oxide inlet temperature to the reduction reactor, which in other terms is the metal oxide outlet temperature from the oxidation reactor, on the overall system performance is crucial, with a higher metal oxide inlet temperature resulting in a lower heat requirement in the reduction reactor.

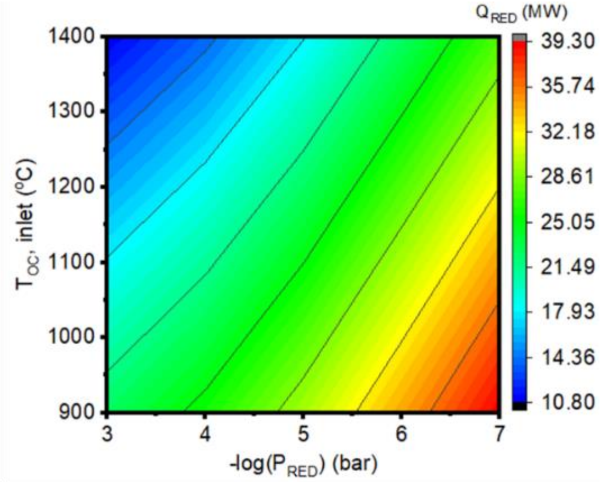

Figure 40. Variation of the heat of reaction (Q_{RED}) with metal oxide inlet temperature to the reduction reactor ($T_{oc,\ inlet}$) and reactor pressure for a constant reduction temperature of 1600ºC for a constant reactor volume of 0.5 m^3 and CeO_2 molar flow 285.71 mol/s.

Oxidation reactor

After the sensitivity assessment on the reduction reactor, a complete set of sensitivity studies were performed on the moving bed oxidation reactor, as modelled in ASPEN Plus. As discussed in the previous methodology section 3.2, a constant non-stoichiometry factor of 0.35 was assumed for the inlet to the reactor. For a CeO_2 flow of 285.71 mol/s, as assumed previously for the reduction reactor, this leads to the production of an equivalent of 100 mol/s of Ce_2O_3, as per discussed in equation (3.6). Besides, a constant metal oxide and gas feed temperature to the oxidation reactor (OXI) of 800ºC was also assumed. A 5% excess of CO_2 or H_2O or CO_2/H_2O mixture was sent for CO or H_2 production respectively. The composition of the mixture was varied between five mixture compositions, more specifically 100% CO_2, 75% CO_2 and 25% H_2O, 50% each of CO_2 and H_2O, 25% CO_2 and 75% H_2O, 100% H_2O.

The solid conversion (from a non-stoichiometry factor of 0.35 of the reduced metal oxide state to fully oxidized state) – X_{OXI}, was evaluated with a variation of the reactor volume and of the composition of the inlet gas. As can be followed from the oxidation kinetics discussion in the reaction kinetics section, due to the relatively faster kinetics of water splitting, a higher conversion is achieved at a similar reactor volume as opposed to CO_2 splitting. As can be seen from the following Figure 41, with 5% excess flow with respect to the stoichiometry and at reactor volumes below 4 m^3 for water splitting, a lower solid conversion (X_{OXI}) is noticed (around 95%) due to insufficient reactor volume. However, for volumes larger than 4 m^3, the rate of solid conversion (X_{OXI}) is very slow making the complete conversion of the reduced ceria much difficult within acceptable reactor volumes for the given scale of application.

For pure water splitting, the maximum solid conversion achieved for a 5 m^3 reactor volume was 98%, while for a reactor volume of 4 m^3, the corresponding conversion was 97.5%. The selectivity of the splitting product would follow the same profile as the metal oxide conversion and hence not plotted separately. Nevertheless, the selectivity of hydrogen for water splitting for a 4 and 5 m^3 reactor volume was obtained as 93.2% and 93.6% respectively, indicating the necessity of trade-off for selecting the moving bed reactor volume.

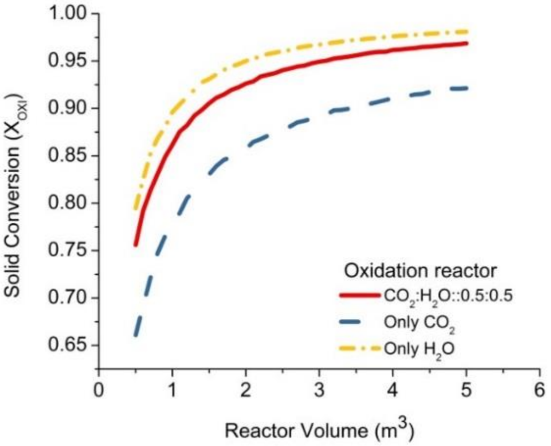

Figure 41. Impact of variation of the reactor volume on the solid conversion (X_{OXI}) in the oxidation reactor (OXI) with a variation of the inlet gas mixture composition, all other parameters, and molar flows being constant.

On the contrary, CO_2 splitting kinetics being slower than water splitting kinetics results in the solid conversion to be lower than that for water splitting, even though the variation of X_{OXI} with reactor volume follows a similar profile to that of water splitting. Corresponding to the 4 and 5 m^3 reactor, the solid conversion with CO_2 splitting was found to be 91% and 92% respectively, showing a higher relative increase in the yield with the same change in reactor volume as compared to water splitting. The corresponding CO selectivity is respectively 86.3% and 87.7%. All the mixtures of CO_2 and H_2O for co-splitting lie within the two limits whereby CO_2 provides the lower bound and H_2O the upper bound of the conversion. Nonetheless, the presence of water (steam) in the mixture enhances the reaction rate significantly, being not only more exothermic but also due to faster kinetics. Therefore, as can be followed from Figure 12, the co-splitting of an equimolar mixture of CO_2 and H_2O yields almost 96.2% solid conversion at a reactor volume of 4 m^3, a significant increase from stand-alone CO_2 splitting. The H_2/CO molar ratio was calculated as 1.06, showing similar selectivity of H_2 and CO, a major benefit of a moving bed reactor.

Indeed, a sensitivity to evaluate the solid conversion (X_{OXI}) with an increased flow of steam, together with an increased reactor volume was performed and the results are shown in Figure 42. The flow of steam was varied between 100 mol/s (stoichiometric) to 200 mol/s (stoichiometric excess 100%). As can be followed from Figure 42(a), a moderate increase in the solid conversion of 0.4% can be seen up to 20% excess of flow for a reactor volume of 4 m^3, while the corresponding increase in yield is 0.6%

and 0.2% for reactor volumes of 3 and 5 m^3 respectively. Nevertheless, beyond 20% of excess flow to the reactor, the relative increase in the metal oxide conversion becomes smaller, while the selectivity of the H_2 would drop proportionally because of the excess of reactant. Another disadvantage of sending much excess flow to the reactor, together with having a higher reactor operating volume can be concluded from Figure 42(b) a linear drop in the oxidized metal oxide outlet temperature is observed, with a drop of over 100ºC for a 100% excess flow. Also, for more than 50% excess flow of steam and for a higher reactor volume, the outlet temperature is even lower, signifying a relative cooling of the oxidized metal oxide inside the reactor. Being a counter-current reactor, a higher reaction extent is seen for a larger reactor, which in turn lowers the oxidation reaction rate further. This results in minimal reaction and hence a lower exothermicity of the reaction and a lower temperature of the outlet solid product is observed even though the conversion is higher. A higher temperature of the outlet metal oxide being always desired for decreasing the heat requirement for reduction as described in an earlier section and this would require a reactor design optimization while performing the entire system in a redox cycle of thermal reduction of ceria with CO_2 and water splitting.

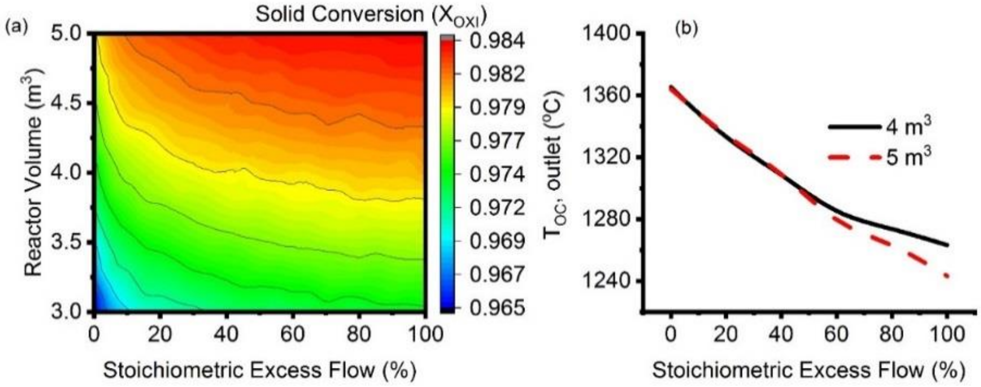

Figure 42. (a) Variation of the reactor volume and excess flow of (CO_2/H_2O) on Solid Conversion (X_{OXI}) and (b) the variation of the metal oxide outlet temperature (Toc, outlet) with the flow of steam (stoichiometric excess) on the Solid Conversion (X_{OXI}) and (b) Variation of the metal oxide outlet temperature ($T_{OC,}$ outlet) with the excess flow on the Solid Conversion (X_{OXI}) in the oxidation reactor (OXI) for water splitting for an inlet non-stoichiometry of 0.35, completely oxidized CeO_2 flow rate of 285.71 mol/s and pressure of 2 bar.

Based on the above discussion, a reactor volume of 4 m^3 was fixed to evaluate the variation of the solid conversion (X_{OXI}), and the metal oxide temperature (T_{OC}) along the length of the reactor for the five different gas compositions. As can be seen from Figure 43(a), a similar reaction extent is noticed until around midway through the reactor length irrespective of the gas mixture composition. However, beyond that, with 50% or more fraction of water in the gas mixture, a considerable increase in the reaction extent occurs which results in the final solid conversion to be 97.6%, similar to that of only water splitting. However, below 50% water content in the inlet gas flow, the reaction rate drops, resulting in a slower reaction along the length of the reactor after midway through the reactor. The corresponding impact on the metal oxide temperature variation along the length of the reactor is evident as well. A higher exothermicity of water splitting results in proportionally higher metal temperatures attained within the reactor with an increased content of steam in the inlet gas mixture to the oxidation reactor. Indeed, both the reaction extent along the length of the reactor and the relative proportion of CO_2 and H_2O plays a crucial role in the metal oxide temperature within the reactor. For a faster water-splitting reaction, a maximum metal oxide temperature within the oxidation reactor of about 1460°C is reached at about 80% of the reactor length, while a maximum reactor temperature of 1275°C was achieved at similar stages along the reactor length for only CO_2 splitting. The drop in the metal oxide outlet temperature is due to a counterflow reactor configuration, whereby the cooler reactant gas being supplied results in cooling down of the metal oxide temperature by ~100°C towards the end of the reactor length, as shown in Figure 43(b). Also, at such later stages, due to the advanced condition of the oxidation, the reaction rate is much slower, resulting in lower exothermicity of the reaction. This lowering of the metal oxide temperature would result in the requirement of higher heat in the reduction reactor as discussed earlier following Figure 36. One possible alternative can be a multi-entry reactor design whereby the gases can be fed in stages along the length of the reactor. This alternative was studied in brief and not reported in detail in the present work since the net outcome was found to decrease the metal oxide conversion in the OXI, even though the outlet metal oxide temperature from the OXI increased. Nevertheless, the benefit of working with water in splitting, even to lower extents over pure CO_2, can be emphasized through the following Figure 43. Even a presence of 50% of water in the CO_2/H_2O mixture ensures similar solid conversion to that of water splitting together with increasing the metal oxide outlet temperature from the OXI by almost a 100°C from around 1150°C to around 1300°C for the same fixed reactor volume and fixed molar reactant gas flow.

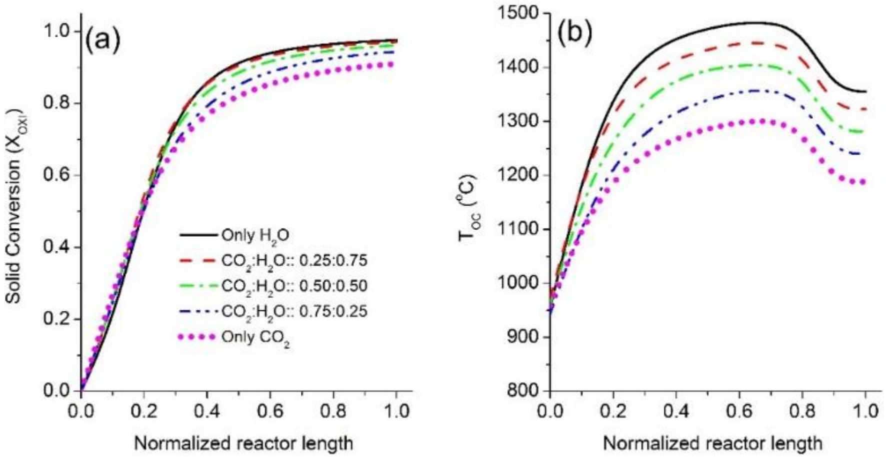

Figure 43. Variation of the Solid Conversion (X_{OXI}) (left) and metal oxide temperature (right) in the oxidation reactor with variable inlet gas mixture composition, at a constant oxidation reactor volume of 4 m^3, a constant non-stoichiometry factor of 0.35 and a constant inlet molar flow of reactant of 110 mol/s, with a fixed oxygen carrier and gas inlet temperature of 800°C.

The impact of the variation of inlet temperatures of reactants and reduced metal oxide into the oxidation reactor (OXI) on the outlet temperature of the oxidized metal oxide and solid conversion have been investigated for a constant reactor volume (4 m^3) and fixed molar flows of both the solid and gaseous reactants. The two temperatures have been varied separately, maintaining the non-varying one at the constant value of 800°C during the simulations. Figure 44(a) and (b) represent the impact of the gas inlet temperature on the outlet temperature of the oxidized metal oxide and the solid conversion, respectively. Irrespective of the variation of the metal oxide or gas inlet temperature, the impact of the relatively slower kinetics of the CO_2 compared to the water-splitting reaction is evident. A linear increase in the outlet metal oxide temperature of about 100°C is noticed with an increase in the gas inlet temperature of 500°C (from 500 to 1000°C), which can be argued from the perspective of a counter-current flow in the reactor. No notable change in the relative solid conversion is however obtained, as can be followed from the previous discussions. A linear relation exists between the temperatures and the percentage of water in the inlet gas mixture. While a maximum $T_{OC,outlet}$ of 1398°C was obtained for water splitting at a steam inlet temperature of 1000°C, the lowest temperature of 1114°C was found to occur for only CO_2 splitting for a CO_2 inlet temperature of 500°C.

Indeed, the metal oxide inlet temperature has also been varied and the results are reported by considering a constant gas inlet temperature of 800°C, all other parameters being constant (Figure 44(c) and (d)). In fact, the results indicate this to be a better choice, since a significant increase in the metal oxide outlet temperature, as well as the overall solid conversion is noticed. For a variation of 400°C of the reduced metal oxide inlet temperature a corresponding variation of 300°C in the outlet temperature of the metal oxide is noticed, irrespective of the composition of the inlet gas. It is noticed that for a metal oxide inlet temperature of 1000°C, the outlet temperature of the oxidized metal oxide increases to almost 1350°C, significantly improving the slower CO_2 splitting kinetics and hence the net metal oxide conversion (from 87% at 600°C to 92% at 1000°C of metal oxide inlet temperature). The relative impact of solid conversion decreases with the increase in the water content in the inlet gas mixture due to inherently faster water splitting kinetics and a more advanced oxidation condition (with the solid conversion of 97% for water splitting). Nonetheless, a high metal oxide outlet temperature of around 1500°C from the oxidation reactor can be seen, which would significantly reduce the heat requirement for reduction of ceria in the reduction reactor. However, whereby due to counter-current configuration, a very high metal oxide temperature within the reactor might occur. Thus, adequate reactor design optimization from multiple aspects is necessary to develop a moving bed oxidation reactor for CO_2 and H_2O splitting for a two-step chemical looping cycle with ceria. The results presented further motivate in developing a closed loop reduction and oxidation moving bed reactor cycle and integrate into an oxyfuel power plant to investigate the efficiency of the solar thermochemical power generation, which is presented in a next section [227].

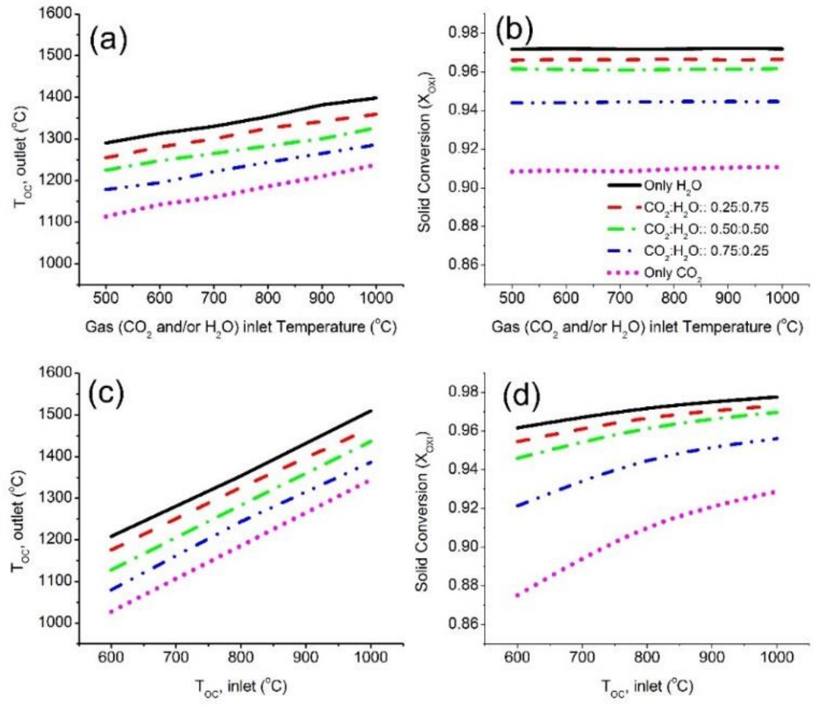

Figure 44. Variation of (a) metal oxide outlet temperature from the oxidation reactor and (b) solid conversion (X_{OXI}) in the oxidation reactor with variable gas inlet temperature; Variation of (c) metal oxide outlet temperature from the oxidation reactor and (d) solid conversion (X_{OXI}) with variable metal oxide inlet temperature ($T_{OC, inlet}$) in the oxidation reactor for a variable gas mixture composition at a constant oxidation reactor volume of 4 m^3, a constant inlet metal oxide non-stoichiometry factor of 0.35 and a constant molar flow of 105 mol/s of gas in the oxidation reactor.

3.1.6 Concluding remarks

A comprehensive model was developed in Aspen Plus to simulate the chemical looping syngas fuel generation from water and carbon dioxide splitting in a dual moving bed reactor with redox cycling through ceria oxides. An extensive FORTRAN subroutine was developed to appropriately model the complexities of the reaction kinetics. The kinetics subroutine was implemented in the Aspen Plus moving bed reactor model. The entire set-up was evaluated considering an industrial scale application for the generation of 100 mol/s of syngas fuel. An isothermal reduction reactor and an adiabatic oxidation reactor model was developed and evaluated.

The sensitivity of the reduction reactor was studied by varying the temperature and pressure between 1200-1600ºC and 10^{-3} and 10^{-7} bar respectively. Close agreement with experimental data reported in the literature was obtained for the reduction non-stoichiometry of ceria. A maximum reduction non-stoichiometry of 0.198 was obtained in the reduction reactor at 1600ºC and 10^{-7} bar pressure. The optimal residence time obtained was around 1.5 minutes, an increase in residence time will not yield any further benefit due to a faster backward reaction rate of recombination of the released oxygen in the reduction reactor.

For the oxidation reactor, system parametric sensitivity was studied considering maximum non-stoichiometry extent achievable for ceria of 0.35, as reported in the literature. The volume of the oxidation reactor to achieve a 90% conversion of the reduced metal oxide was 8 times higher to that of the reduction reactor. The impact of the variation of the gas inlet temperature was found to be minimal, while an increase in the metal oxide inlet temperature would significantly increase the solid conversion and selectivity of the generated syngas fuel. A faster water splitting kinetics would result in not only a higher solid conversion and selectivity but also in a higher product outlet temperature due to higher exothermicity. Indeed, a relatively substantial increase in the yields from the oxidation reactor with 25% water in the gas mixture is noticed compared to working with pure CO_2. Nevertheless, similar selectivity from co-splitting of CO_2 and H_2O would allow generating an H_2/CO ratio similar to the input H_2O/CO_2 ratio. A large temperature variation along the length of the adiabatic oxidation reactor is also noticed, which would thus require further reaction design optimization of the moving bed oxidation reactor for CO_2 and/or H_2O splitting. This gives the motivation to further investigate the reactor model as a chemical looping syngas production unit as an add-on unit to the power plant and investigate the efficiency of the system which is presented in a next section.

3.2 Techno-economics analysis of oxy-fired power plant integrated with solar thermochemical CO_2/H_2O splitting unit

This section presents the model of a solar thermochemical looping CO_2/H_2O dissociation unit (CL) with commercial ceria as redox oxygen carrier which is integrated to a 100 MW oxy-fuelled natural gas combined cycle with carbon capture to investigate the efficiency benefit obtained. The moving bed counter-current reactor model and the kinetic subroutine developed in section 3.1 is used. It is found that the efficiency of the chemical looping unit varies widely with reduction reactor temperature and operating pressure. Chemical looping unit efficiency is obtained for three conditions: considering feeding the oxidation reactor with CO_2 only and H_2O only, the efficiency is found to be 35.41% and 30.84% respectively, and for a mixture of them (86% CO_2, 14% H_2O) it is 35.26%. The lower efficiency for H_2O-only operation is due to the heat needed for water vaporization and the higher vacuum degree required for the reduction compared to CO_2-fed cycle. The maximum solar to electrical efficiency for the whole system layout is found to be 25.4% with a reduction reactor operating at a temperature of 1600ºC and 10^{-7} bar vacuum pressure. With 0.5 m^3 reduction reactor volume and 5 m^3 oxidation reactor volume, the maximum net electricity produced by the CL add-on unit is 12.9 MW_e. Economic analysis revealed that the major contributors to total plant cost are the hydrogen compressor and solar field and tower, which are the 19% and 39% of the total equipment cost, giving a specific overnight capital cost of 12136 \$/kW with an LCOE of 1100 \$/MWh.

3.2.1 Introduction

In the present section, the reactor type considered in the analysis of the CL unit for both reduction and oxidation steps is a moving-bed reactor, modeled by multiple RCSTRs in series implemented in Aspen Plus with kinetic subroutines for the calculation of reaction rates (see the previous section). The thermal reduction kinetics considered is that reported by Bulfin et al. [108] for non-stoichiometric ceria, while kinetics of CO_2 and H_2O splitting presented by Arifin [228] was utilized for the oxidation reactor. The reactor's model has been validated against experimental results and is presented in a parallel paper [229]. In principle, the end use of the CO/H_2 produced in the CL unit can vary ranging from power production to the synthesis of fuels like methane, methanol and advanced Fischer Tropsch liquids or chemicals. However, for such polygeneration systems, no direct definition of efficiency exists [230]. Hence to evaluate the primary benefits of the excess fuel generation by chemical looping splitting, a solar thermochemical cycle dedicated to power generation from the excess fuel produced was conceived. Therefore, the reactor model applied to reduction and oxidation steps has been implemented in a system model of a CL unit connected to an oxy-fuel power plant with 100% carbon capture. The goal of the chemical looping thermo-chemical dissociation of the captured CO_2 is to produce a syngas fuel from H_2O and recycled CO_2 by using solar energy as input, with the aim of improving the system efficiency by providing additional fuel to the power plant.

The oxy-fuel combustion is currently one of the most promising alternatives among the portfolio of all the low-emission technologies (LETs) [231,232]. In this technology, the fuel (coal or natural gas or bio-methane) is burnt in an oxygen (O_2) rich environment (near stoichiometric O_2 flows), instead of air, thereby improving combustion efficiency [233] and eliminating NO_x emissions and generating only CO_2 and H_2O as the product of the combustion unit. The oxygen is supplied via an air separation unit (ASU). Burning fuels under these conditions generate combustion gases, which, after condensation yields a very high purity of CO_2 exhaust. Oxy-combustion can also be applied to natural gas combined cycle (NGCC), however, subject to the redesign of gas turbines. This is due to the alternation in the physical properties of the metal occurs from an increased CO_2 concentration in the flue gas [233,234]. Nevertheless, ease and ability to retrofit existing systems at low cost are the primary attractions [232], together with the high efficiency of 96-99% carbon capture [235] of such systems.

Similar to LETs, technical challenges exist for the oxy-fuel combustion process. The most critical limitations lie in the higher energy penalties associated with air separation unit (ASU) for O_2 production and CO_2 processing unit (CPU) for CO_2 purification and compression [52,236,237] after the combustor unit. The existing commercialized technology for air separation for utility-scale application is the cryogenic air separation process (CASU). It works on the principle of the cryogenic distillation via compression of air to its liquefaction stage, followed by the fractional distillation of its constituent components, such as N_2, O_2, Ar and other rare gases. The primary advantage is that this process can produce liquid or gaseous streams of N_2 and O_2 as per the specification of the end user and for large-scale requirements also. Indeed, O_2 production, via such a process of cryogenic distillation of air, demanding 160 to 250 kWh per ton of O_2 produced [238,239] is acknowledged as the bottleneck [232,237]. State of the art of ASU can consume between 10 and 40% of the gross power output after retrofitting a conventional coal-fired power, resulting in a net energy penalty as high as 8-13 percentage points [240,241]. The efficiency penalty from integrating the ASU to a conventional NGCC unit without carbon capture for oxy-fuel combustion could be as much as 13% [242]. The penalties incurred by the use of the ASU would, therefore, offset any advantages gained by oxyfuel combustion. This has prompted many researchers to investigate the use of alternative air separation systems. However, to date, none of the alternative technologies for air separation have been able to produce high purity oxygen at large utility scale, either due to high costs, such as for adsorption processes, or the technology is still under development or in demonstration stage, as for membrane technologies such as oxygen transport membranes [243,244]. True, with a lower purity of O_2 of about 95%, if acceptable for such oxy-fuel applications, the energy requirement for oxygen production with ASU can be further reduced, together with the energy penalty [232].

Correspondingly, the specific CO_2 emissions are low as well compared to other fossil fuel power generation units, at around 350 gCO_2/kWh, besides having much less SO_x and NO_x emissions due to the lower sulphur and nitrogen content of the fuel [60]. Addition of CCS units to considerably decrease the specific CO_2 emissions to much below 100 gCO_2/kWh have therefore been studied and presented in multiple times in the literature via diverse technologies [60,245,246]. Like solid fuel power units, the primary motivation of such studies included the decrease in the energy penalty of the capture process, thereby increasing the efficiency of the power plant alongside keeping the capture efficiency to its maximum potential.

Several studies have addressed solar-assisted chemical looping combustion cycles for the integration with power plants [247–249], in which the metal oxide is reduced by methane with the solar source only providing a fraction of the required heat of reaction, and the oxidation is performed with air. Kong et al. [250] investigated a polygeneration system that operates a solar-driven isothermal redox cycle of ceria at 1600ºC with reduction reactor operating at 10^{-5} bar and oxidation reactor at 1 bar considering Gibbs minimization. The downstream process from an oxidation reactor, either a CO/CO_2 or an H_2/H_2O stream, undergoes a methane reforming followed by power and methanol production. The solar to syngas efficiencies (η_{SCL}) reported for the chemical looping unit of this polygeneration system is 45.7% with only CO_2 splitting and 38.1% for water splitting. Kong et al. [251] also studied a comparison of temperature swing and isothermal redox cycle considering at the 1650ºC and 10^{-5} bar. The argument presented raised the issue of heat recovery system between a two-temperature swing redox cycle and concluded that a trade-off is needed between thermal recovery and operating conditions acceptable by materials, presenting an efficiency for CO_2 splitting of 28%. However, the analysis of a completely solar-driven CL cycle for syngas production integrated with an oxyfuel power-plant with CCS has not been presented in the literature.

The study in this section aims at investigating with a techno-economic analysis a complete plant based on solar-driven CL cycle integrating an oxy-fuel power plant. In this regard, considering chemical looping syngas production still a developing technology, the CL has been included as an add-on unit to an existing 100 MW Oxyfuel NGCC power plant with CCS, considering a simple power plant model to evaluate the net CO_2 and water generated. The primary aim of the present study is to develop the feasibility investigation of the integration of the splitting cycle in an add-on unit and to evaluate the net benefit from the generation of additional electricity from the produced syngas. Multiple sensitivity analyses of the CL unit were performed varying different operating parameters, including the composition of the gas feed to the oxidation reactor, and the conceptual layout developed has been studied in a techno-economic feasibility assessment of such integration.

3.2.2 Power plant layout and configuration

The most efficient conventional fossil fuel power plant is considered to be a natural gas combined cycle (NGCC) with its efficiency reaching 57% based on lower heating value [60]. Integrating a carbon capture and sequestration (CCS) to the conventional NGCC plants decreases the CO_2 emission to a level less than 100g CO_2/kWh from different technologies reported in the literature [60,245,246]. Among all the CCS technologies, oxyfuel combustion requires minimum modification with respect to the layout of a conventional plant without CCS and has the capability of capturing 100% CO_2, but leads to a high energy penalty due to air separation process for O_2 production, which decreases the plant efficiency to a large extent [244]. Hence, an add-on unit, utilizing the thermal reduction of ceria by concentrated solar power and performing the splitting of a part of the gaseous exhausts (CO_2 and/or H_2O) of the power plant has been proposed to produce syngas (fuel) and increase the power output of NGCC with the aim to balance the suffered energy penalty from carbon capture. A part of the stream of pure CO_2 and wastewater generated in the CCS unit has been proposed to be utilized within the add-on unit. Figure 45 below shows the plant layout and configuration of the proposed solar thermochemical power system to be set as an add-on unit to the oxyfuel plant. It needs to be clarified that the add-on unit is not limited to integration with only NGCC. Indeed, the availability of pure CO_2 and H_2O also from other types of oxyfuel power plants with different feedstock (coal and oil) would allow the proposed add-on unit to be integrated into the plants.

The add-on plant primarily comprises the chemical looping (CL) unit consisting of reduction and oxidation reactor, the second for the generation of syngas from the splitting of recycled CO_2 and/or H_2O. The reduction reactor would be operated under vacuum as the solar thermal reduction is favoured at a very low partial pressure of oxygen. Several heat exchangers need to be employed for heat integration within the system for CO_2 heating or generation of the steam delivered to the oxidation reactor, as well as steam generation from the excess heat to be expanded in the steam turbine. Indeed, all the excess heat in the present layout has been integrated into a heat recovery steam generator (HRSG) for subsequent steam production and use in a single bottoming steam cycle. Irrespective of the gas composition, an additional oxyfuel combustion chamber for the produced syngas has been considered. The exhaust gases deriving from the additional oxy-combustion would then be treated for CCS, either by employing a dedicated condenser unit or through minor modifications to the existing condenser of the CCS unit. Since the reduction reactor is operated under vacuum conditions, pure oxygen is produced, which has been proposed to be utilized in the oxy-combustor. This would decrease the need for oxygen from an additional air separation unit, which is nevertheless needed – or a size increase of the existing ASU is needed – to supply all the oxygen required for the combustion. The oxidation reactor would be operated at 2 bar pressure instead of atmospheric conditions, with the aim of decreasing the compression work on the produced CO and/or H_2 that is needed for increasing the syngas pressure to the operating one of the combined cycle.

The solar field can either be a central tower configuration, or a beam down configuration. Indeed, the reactor design concept presented by Muhich et al. [146] utilizes a beam-up reactor concept via a central tower, where the oxidation reactor is a fluidized bed reactor. With regards to the understanding of operability of fluidized bed reactors, a huge volume of gas is required for the fluidization, and this would certainly decrease the selectivity of the CO and H_2 produced to very low values, which limits the application of fluidized bed reactor for oxidation. Therefore, in the present layout, a moving bed reactor has been considered for the oxidation (as reported in [229]). The beam down reactor configuration seems to be easier to operate, especially with regards to solids handling between the reduction and the oxidation reactor. Nevertheless, solar field design considerations have not been included in the present study, except for the necessary performance evaluation of the proposed add-on unit, though the assumption of solar field efficiency.

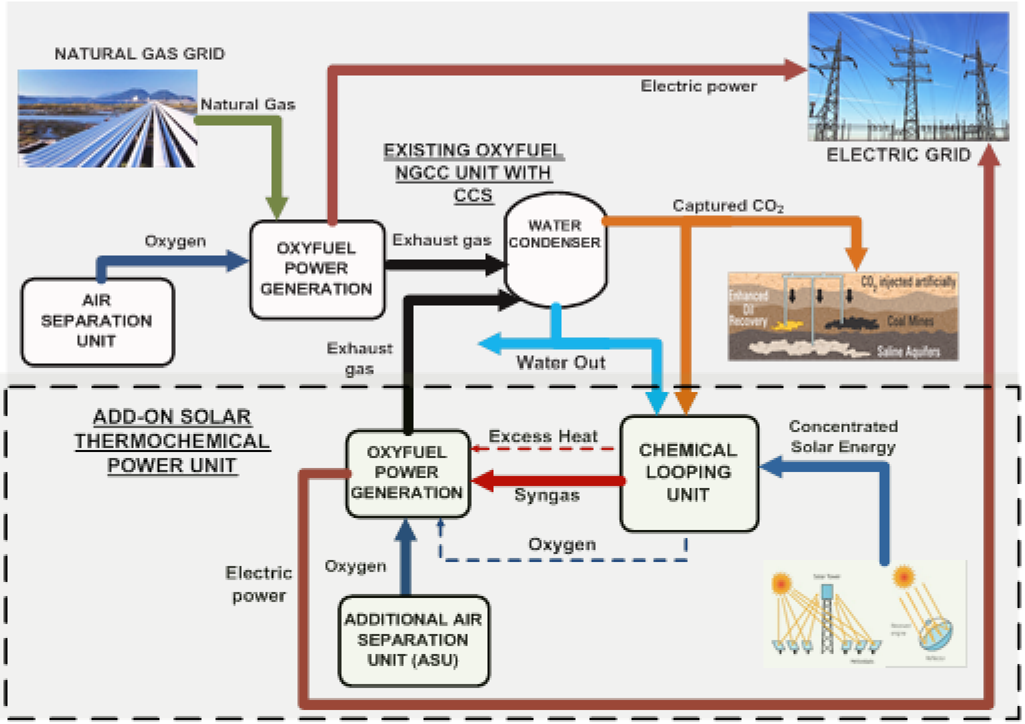

Figure 45. Solar thermochemical plant conceptual layout with CO_2 and/ or H_2O recycling for power generation.

3.2.3 System analysis in Aspen plus

The plant model of the Solar Chemical Looping Power Generation add-on unit with oxyfuel combustion involving CO_2 and/or H_2O dissociation and carbon capture (SCLP-OXY-CC) is presented and discussed in this Section. Subsequent evaluation of the proposed add-on unit is carried out in Aspen plus and the results are presented in Section 3.2.4.

Assumptions

The generic assumptions used in the simulations are listed below:

1. Steady-state simulations were performed, hence the results obtained are not applicable to start-up or transient operations.
2. Reduction (RED) and oxidation reactors (OXI) are modelled as moving bed reactors as presented in our parallel work [229].
3. The maximum Turbine Inlet Temperature (TIT) of 1377ºC was considered, within the range of maximum TIT of commercially available gas turbines [252].
4. The maximum pressure ratio for a single stage expansion in a stationary gas turbine is 18:1 as of commercial gas turbines [253]. This limit was respected within the present layout as well.
5. No heat loss and inefficiencies are considered within in the lines connecting plant components.
6. The ambient condition was assumed as 25ºC and 1.013 bar. Also, the composition of air was assumed to comprise 79% N_2 and 21% O_2 on a volume basis.
7. Minimum approach temperature in heat exchangers was taken as 10ºC [223].
8. The isentropic efficiency and mechanical efficiency for compressors and turbines were considered as 0.9 and 0.98, respectively. The pump efficiency was assumed to be 0.85 and 0.9, for isentropic and mechanical efficiency respectively.
9. The primary objective of the present study is to recognize the potential efficiency gain from the addition of the chemical looping and a downstream power generation unit in a conventional oxyfuel plant. Hence the turbines and the HSRG were modelled as simple units, without reheating or multi-pressure systems. Indeed, by increasing the model complexity, together by performing design optimization, the net efficiency can be improved considerably by process optimization studies.

Moreover, design assumptions with respect to individual units of the respective layouts are listed in Table 5.

A simplistic model of a 100 MW power NGCC and a corresponding oxyfuel NGCC power plant of the same capacity with CCS was developed in ASPEN Plus, incorporating all the necessary assumptions stated above. This was necessary to evaluate the performance of the base case power plants, together with the availability of CO_2 and H_2O necessary for the added fuel generation step via CL splitting. Since the primary aim of the present study is to develop the feasibility investigation of the integration of the splitting cycle in an add-on unit and to evaluate the net benefit from the generation of additional electricity, the need for detailed modelling of the base case without CL integration was not considered crucial. The net molar flow of CO_2 to the carbon capture and sequestration unit from the base case of 100 MW oxyfuel NGCC with CCS obtained was around 330 mol/s. The corresponding water released from the condenser of the exhaust gas was 550 mol/s. The layouts of the base case oxyfuel power plant without CL unit, with and without CCS integration, as modelled in ASPEN Plus can be seen in Farooqui et al. [254].

Due to the limitation of the present technology development, not only for the CL unit but also for concentrated solar technology on the perspective of providing high-temperature heat over a large control volume, a limited size of the add-on solar-CL unit has been assumed. For this reason, the use of only 20% of CO_2 from the CCS unit was considered for splitting in the base case scenario. The molar flow of gas for splitting thus would be 66 mol/s. Corresponding water utilization for the base case scenario is 12%. The ceria flow was calculated accordingly and has been discussed in subsequent sections.

Simulation description

A common configuration of the add-on unit, applicable irrespective of the gas mixture fed into the oxidation reactor, was modelled and simulated in ASPEN Plus. Figure 46 shows the system configuration developed.

Table 5. Design assumptions used for developing the process flowsheet models in ASPEN plus.

Unit	Parameters
ASU	• O_2 purity: 99.9% (by volume); ASU O_2 and N_2 delivery pressure: 1.2 bars; O_2 compression pressure: 18 bars; A small fraction of the N_2 was used as sweep gas in CL unit.
Solar Field	• A generic solar field efficiency of 75% was assumed based on the consideration of a central receiver configuration [255]; • Thermal Receiver efficiency was assumed as 89% [256].
Reduction Reactor (RED) and Thermal Receiver	• An isothermal reactor at 1600ºC and a vacuum pressure of 10^{-7} bar was considered for the base case scenario; • Continuous metal oxide transportation between the oxidation reactor (OXI) and reduction reactor (RED) reactors was assumed, neglecting work expended in metal oxide handling.
Oxidation reactor (OXI)	• An adiabatic reactor with adequate insulation to ensure no heat loss was considered; • The oxygen carrier outlet temperature from OXI was considered as the oxygen carrier inlet temperature to RED.
Vacuum Pump (VACPMP)	• Modelled as a four-stage compressor with inter-cooling; • Isentropic efficiency: 90%; • Mechanical efficiency: 98%; • Discharge pressure: 1 atm.
Compressors	• Isentropic efficiency: 90%; • Mechanical efficiency: 98%.

Combustor (COMB)	• Excess oxygen factor of 1.05 for CO and/or CO and H_2 mixture combustion considered; • Pressure drop within combustor: 0.2 bar; • Heat loss from combustor: 0.2 MW.
Gas Turbine	• Isentropic efficiency: 90%; • Mechanical efficiency: 98%.
Steam Turbine and HRSG	• Single stage expansion in the steam turbine was considered; • Turbine isentropic efficiency: 90%; • Mechanical efficiency: 98%; • Steam Pressure: 150 bars; • Live steam temperature for steam turbine inlet: 600ºC; • Condenser pressure: 0.04 bar; • Pump isentropic efficiency: 0.8.

For the reduction reactor (RED), a vacuum pump (VACPMP) is necessary to maintain the vacuum pressure and has been modelled as a four-stage compressor with inter-cooling. The oxygen from the RED (Stream 14) is first cooled and then released at atmospheric pressure by the vacuum pump. The heated and reduced metal oxide from the RED (Stream 25) is then cooled in steps, modelled as two heat exchangers (METHX-1 and METHX-2) for simplicity. The first heat exchanger would conceptually be used to heat up the inlet gas mixture to the oxidation reactor (OXI) in the form of steam generation or CO_2 heating. METHX-2 would then ensure the necessary metal oxide inlet temperature to the OXI via steam generation (for power generation). This would, however, limit the plant operation at lower temperatures of the reduction reactor due to the chances of temperature cross-over for a constant feed temperature to the OXI.

The product gas from the OXI (Stream 6) is first cooled against steam generation for power generation till ambient temperature and subsequently passed through a condenser to remove the moisture (COND-1). However, this becomes a redundant unit while working with the only CO_2, wherein no water is present in the product gas. Subsequently, the syngas (Stream 9) is compressed in SYNCOMP to a pressure of 18.2 bar and fed into the combustor. Since the exhaust gas needs to be fed back to the CCS stream, an oxyfuel combustion is necessary. Excess O_2, as required for the combustion (Stream 18) is sourced from an additional air separation unit and compressed together with the oxygen from the RED to the combustor. Since near stoichiometric oxygen necessary for the combustion of syngas is produced from the reduction reactor, the size of the ASU required is significantly small in comparison to the scale of the add-on unit. Thus, a significant energetic benefit from the internal use of the generated oxygen can be obtained, countering the energy penalty of vacuum generation for reduction.

In the combustion chamber (COMB), a pressure drop of 0.2 bar results in the inlet pressure to the gas turbine (GT) of 18 bars. The temperature at the combustor outlet, or in other words, the turbine inlet temperature (TIT) is maintained at 1377ºC by recycling CO_2 from the CCS stream (Stream 29) via a CO_2 compressor (CO2COMP). The exhaust gas from the combustion chamber (COMB) is expanded in a gas turbine

(GT) up to a pressure of about 1.04 bar and further subsequently fed to an HRSG for steam generation to be used in the bottoming steam cycle. Due to the absence of SO_x, the gas can be expanded to temperatures as low as 50°C. The exhaust gas, after water condensation, comprises almost pure CO_2 (Stream 13). Therefore, it would be sent back to the CCS stream from where it was originally sourced from. Thus, the zero-emission system of the original plant is maintained, as can be visualized in the plant layout detailed in Figure 46. A major advantage of the proposed cycle working with or without CO_2 is the fact that the entire cycle continues at the same molar flow of the sourced CO_2 from the CCS stream, with no additional product being generated to that of the recycled CO_2. This simplifies the integration of the add-on unit to the original power plant significantly, by requiring minimum additions or changes for the necessary retrofit. Indeed, a direct utilization of the exhaust of the original Oxyfuel power plant, which essentially is a mixture of approximately 86% of CO_2 and about 14% of H_2O would be of significant interest. Hence, analyses with three possible gas mixtures, only CO_2, only H_2O and a CO_2/H_2O mixture replicating the typical exhaust of an oxyfuel power plant were performed to evaluate the performance of the SCLP-OXY-CC add-on unit with respect to the inlet gas composition to the OXI.

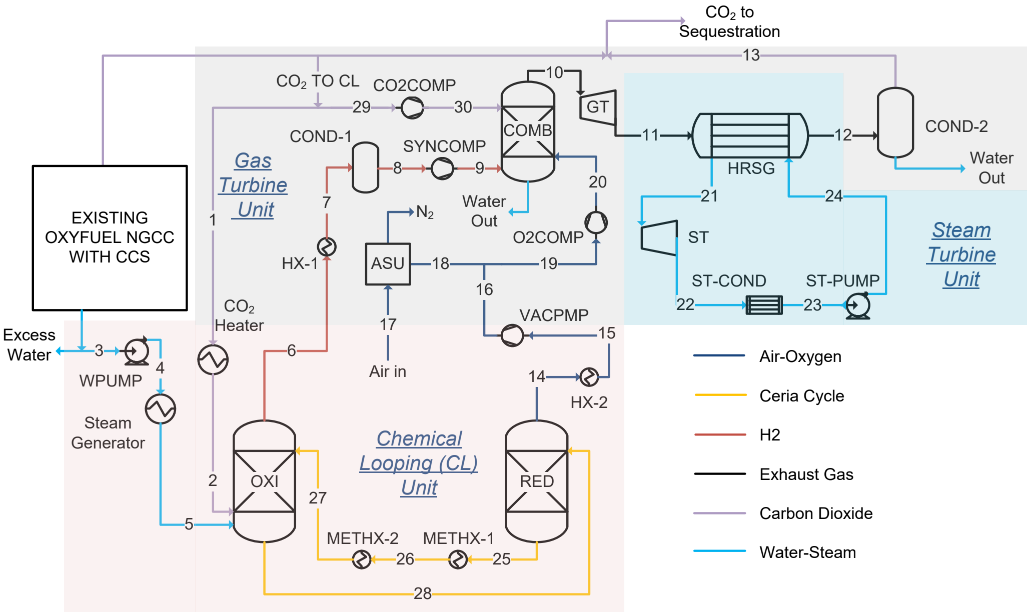

Figure 46. Conceptual layout of the SCLP-OXY-CC add-on unit utilizing CO_2 and/or H_2O splitting with thermal reduction of ceria recycling for power generation via oxy-fuelled combustion.

Energy performance evaluation

To obtain the comparative thermodynamic system performance of the add-on solar thermochemical power plant with respect to the efficiency of the unit and with respect to the combined efficiency with the oxyfuel power plant, an energy analysis is performed.

The energy analysis is based on the first law of thermodynamics and considers the principle of conservation of energy applied to a system. The thermal efficiency of the proposed add-on plant, directly determined on the basis of the first law of thermodynamics, is therefore evaluated in terms of the rate at which solar power ($\dot{Q}_{sol}$) provided to the CL unit is converted to the net electric power output ($\dot{W}_{el,net}$) [257], as defined by the following equation (3.25):

$$\eta_{th} = \dot{W}_{el,net}/\dot{Q}_{sol} = 1- (\dot{Q}_{L}/ \dot{Q}_{sol}) \qquad (3.25)$$

where $\dot{Q}_L$ is the system thermal energy loss.

In the plant simulations, for components such as pumps or compressors, where the thermal efficiency is not possible to be evaluated in terms of useful energy output, the thermodynamic performance is assessed via the concept of 'isentropic efficiency'. By this, a comparative analysis is developed between the actual and ideal performance of a device. The ideal conditions are related to no entropy generation, together with negligible heat transfer between the device and the surrounding [258]. The isentropic efficiency is further corrected by the mechanical efficiency of the components, as shown in Table 5. Nevertheless, beyond the thermal efficiency of the power plant, the efficiency of the receiver and the solar field play a crucial role in the overall solar to electricity of the proposed add-on unit. Indeed, this limits the overall performance of the proposed SCLP-OXY-CC unit. For a solar field efficiency of $\eta_{sol\text{-}field}$, and a receiver efficiency denoted by $\eta_{reciever}$, the solar to electricity efficiency of the proposed add-on unit ($\eta_{sol\text{-}e}$) can be written as per the following equation (3.26). In the following analysis, the solar-to-electricity efficiency has usually been referred to describe the SCLP-OXY-CC plant efficiency, unless otherwise mentioned.

$$\eta_{sol-e} = \eta_{th} \times \eta_{sol-field} \times \eta_{receiver} \qquad (3.26)$$

However, in addition to the net plant efficiency of the add-on unit, interest lies in the study of the CL unit efficiency in itself. The efficiency is derived based on the similar principle described above, however, the output being the net chemical potential in the split gas in terms of its lower calorific value (LHV). The definition of efficiency for the CL unit has been defined as follows by equation (3.27).

$$\eta_{SCL} = \frac{(\dot{m}_{H_2} LHV_{H_2} + \dot{m}_{CO} LHV_{CO})_{oxy}}{(\dot{Q}_{RED} - \dot{Q}_{OXI}) + \dot{Q}_{CO_2/H_2O} + (\dot{Q}_{sphtr} - \dot{Q}_{sld}) + W_{VAC}} \qquad (3.27)$$

Where, $\dot{Q}_{RED}$ is the heat requirement at the reduction reactor, $\dot{Q}_{OXI}$ is the heat released from the oxidation reactor. Since the OXI is an adiabatic reactor, $\dot{Q}_{RED}$ would be zero. $\dot{Q}_{CO2/H2O}$ is the net heat needed for the system operations, including that needed for heating up the sweep gas and the inlet CO_2 and/or H_2O before the splitting reaction in

OXI. $\dot{Q}_{sld}$ represents the heat recovered from the solids from the reduction reactor before it enters oxidation, while $\dot{Q}_{sphtr}$ is the heat delivered to the solids for preheating. However, in the present layout, no pre-heating was employed and hence would be equal to zero as well. Heat losses from system components were neglected in the efficiency assessment. Finally, W_{VAC} represents the pumping work resulting from vacuum generation for the removal of generated oxygen from the reduction reactor.

3.2.4 System evaluation

In this Section, the results of the system evaluation of the proposed SCLP-OXY-CC unit are reported. The metal oxide flow rate was first fixed for performing the simulations. As explained before, for the base case add-on unit, the imposed flow to the OXI was 66 mol/s of total reactant (CO_2 and/or H_2O). This would ideally require 66 mol/s of equivalent Ce_2O_3 flow into the oxidation reactor. A 20% excess gas flow in the oxidation reactor was chosen based on the results of sensitivity studies, and the corresponding maximum non-stoichiometry of 0.198 was fixed for a reduction temperature and pressure of 1600ºC and 10^{-7} bar respectively, and a CeO_2 recirculation rate of 275 mol/s in the CL unit. Indeed, the value closely follows the mole flow of CeO_2 used for the previous sensitivity analysis presented in [229]. Additionally, the reduction temperature range within which the proposed add-on unit was analysed was 1300 and 1600ºC, to obtain a considerable reduction extent. The reduction reactor volume of 0.5 m^3 was selected to minimize the heat requirement for the reduction by avoiding unnecessary heating of a large volume of the reactor without significant reaction described in [229]. However, the oxidation reactor volume needs to be decided separately due to a maximum reduction extent of 0.198 as opposed to 0.35 considered for the sensitivity studies. In this regard, a sensitivity analysis to decide upon the oxidation reactor volume was performed by comparing two extreme cases of water splitting and CO_2 splitting. The results are shown in Figure 47.

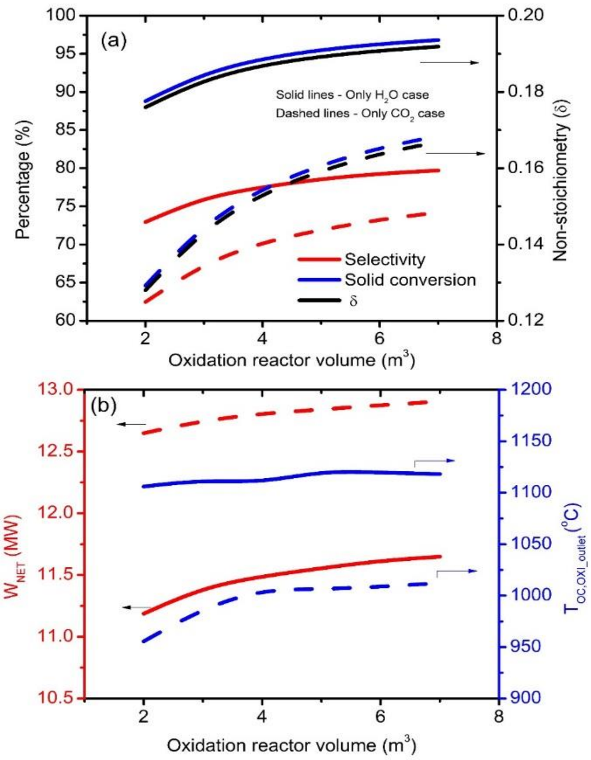

Figure 47. Impact of the variation of the oxidation reactor volume with water splitting (solid lines) and CO_2 splitting (dashed lines) on the specific system performance of the proposed SCLP-OXY-CC add-on at a constant RED temperature and pressure of 1600°C and 10^{-7} bar respectively, a constant molar flow rate of CeO_2 and CO_2/H_2O of 275 mol/s and 66 mol/s respectively, and a constant metal oxide and gas inlet temperature of 800°C to the OXI (solid lines are only H_2O case and dashed lines represent only CO_2 case).

The oxidation reactor volume was varied between 2 and 7 m^3. Due to the faster kinetics of water splitting yielding to the selectivity of H_2 shown in Figure 47(a) (red solid line), a reactor volume of 4 m^3 results in a minimum enhancement to the system performance. However, for the slower CO_2 splitting reaction, a larger reactor volume is required. Indeed, the highest impact of the variation of the reactor volume is seen on the solid conversion (metal oxide conversion, Figure 47(a)), whereby for CO_2 splitting it increases from 65% for a 2 m^3 reactor to 80.4% for a 5 m^3 reactor and 84.2% for a 7 m^3 reactor. This also results in the net reduction extent in the reduction reactor (RED) to increase, due to a higher number of oxygen vacancies in the oxidized metal oxide. Nevertheless, besides the CL unit itself, a reactor volume of more than 5 m^3 is seen to have a lower impact on the overall system performance (see Figure 47(b)). While a rise of 0.2 MW of the net power production is noticed irrespective of the gas composition, the relative variation in the oxidized metal oxide outlet temperature from the oxidation reactor (OXI) is minimal beyond a reactor volume of 5 m^3. A combined effect of such variation of the system operating parameters results in a stable solar-to-electricity efficiency of the system of about 24.2% for working with the only H_2O while the corresponding efficiency is 25.4% for only CO_2 splitting. Accordingly, 5 m^3 was selected as the reactor volume of the oxidation reactor (OXI). In the end, it can be claimed with confidence that such a conservative design would also ensure an operational flexibility with respect to available feedstock.

Sensitivity analysis

To decide on the operating parameters and hence evaluate the achievable system efficiency, a comprehensive set of sensitivity studies was performed. The first set of sensitivity was performed to determine the impact of the inlet temperature of the gas and metal oxide into the oxidation reactor (OXI), all other parameters remaining constant. Following the discussions of the individual reactor sensitivity presented in [229], a minimal variation of the system performance was noted with varying the gas inlet temperature to the OXI, irrespective of the gas composition. A net increase in the net power output of 0.5 MW is obtained for decreasing the gas inlet temperature from 1000ºC to 500ºC due to a decrease in the steam available for expansion in the steam turbine, irrespective of the OXI inlet gas composition. However, with the rise in the gas inlet temperature, a rise in the metal oxide temperature at the OXI outlet is also observed, which would decrease the heat requirement for the same extent of reduction. Thus, no significant impact on system efficiency is obtained by varying the gas inlet temperature to the OXI, with an average efficiency of 24.2% and 25.4% being achieved for the only CO_2 and the only H_2O cases respectively (Figure 48(b)). Furthermore, for lower reduction temperatures, a gas inlet temperature beyond 800ºC would result in temperature cross-over between STEAMGEN and METHX-1 for water splitting, due to a higher heat requirement to evaporate water in comparison to sensible heat requirement for CO_2 heating. Hence, to ensure a flexible system operation irrespective of gas composition to the OXI, a gas inlet temperature of 800ºC was set.

Thereafter, by fixing the gas inlet temperature to the OXI at 800ºC, the reduced metal oxide temperature (T_{OC,OXI_inlet}) to the OXI as varied between 600 and 1000ºC. A discussion on the variation in the individual power generation from the GT and ST, as well as the auxiliary power requirement, while working with either CO_2 or H_2O is necessary. This can be followed from the results plotted in Figure 48(b) and (c) with varying the metal oxide inlet temperature to the OXI. A solid conversion (X_{OXI}) between 93% and 96.7% is noted between 600 and 1000ºC of T_{OC,OXI_inlet} for water splitting, while the corresponding values for CO_2 splitting yields and X_{OXI} between 74.3% and 86%. This higher impact of T_{OC,OXI_inlet} on the CO_2 splitting reaction results in significant improvement to the reduction reaction extent as well for the only CO_2 case, whereby the non-stoichiometry (δ) generated from reduction increases from 0.147 to 0.171. However, with a higher and a more constant solid conversion for water splitting, more oxygen is available to be removed via reduction, resulting in the net δ generated to be improved from 0.184 at 600ºC to 0.191 at 1000ºC of T_{OC,OXI_inlet} (Figure 48(c)). For the same molar flow of gas to the OXI, a higher reduction extent in the RED results in a higher selectivity of H_2 (79.9% at T_{OC,OXI_inlet} 1000ºC) in comparison to the selectivity of CO (51.17% at T_{OC,OXI_inlet} 1000ºC), as can be seen from Figure 48(b).

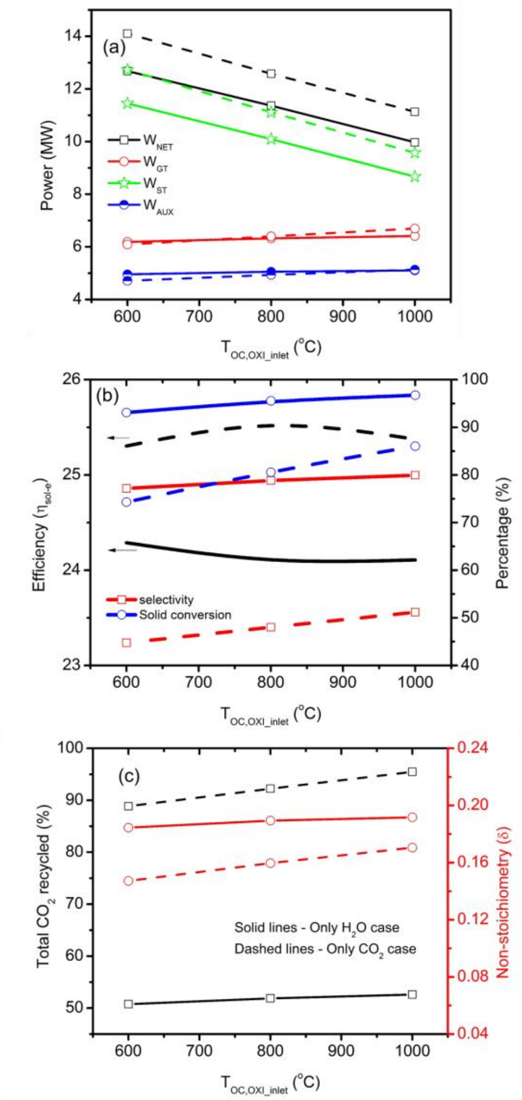

Figure 48. Impact of the variation of the reduced metal oxide inlet temperature to the OXI on the operating parameters of the SCLP-OXY-CC at a constant RED temperature and pressure of 1600ºC and 10^{-7} bar respectively, a constant molar flow rate of CeO_2 and gas to the OXI of 275 mol/s and 66 mol/s respectively and a constant gas inlet temperature to the OXI of 800ºC (solid lines are only H_2O case and dashed lines represent only CO_2 case).

Based on the selectivity, excess CO_2 is circulated to the combustion chamber to maintain the TIT at 1377ºC (1650K). For water splitting, the excess water is removed from the H_2O/H_2 stream exiting the OXI reactor in the condenser before compression and combustion with recycled CO_2. For a lower variation in the selectivity of H_2, this results in similar molar flow to be expanded in the GT irrespective of T_{OC,OXI_inlet} . On the other hand, for CO_2 splitting the final CO_2 expanded is balanced by the recirculated carbon dioxide into the combustor. Hence, the GT output remains constant at 6.3 MW irrespective of the gas composition used for splitting. However, a higher heat is required to heat water from 25°C to 800°C than CO_2 due to the requirement of latent heat for the former. This would result in a lower heat availability in METHX-2 for steam generation causing a lower steam to be expanded in the steam turbine for the water only scenario. A drop of almost 1 MW in the power output from the ST is observed hence. As for the auxiliary power demand, no significant effect is noticed from the variation of the T_{OC,OXI_inlet}. Therefore, a drop in the net electricity output from 14.1 MW to 11.1 MW is observed with an increase in T_{OC,OXI_inlet} from 600°C to 1000°C for working with the only CO_2, with the corresponding output with the only H_2O being always about 1.2 MW lower.

A combined impact of the individual variations is obtained in the plant efficiency ($\eta_{sol\text{-}e}$). Indeed, to comment on the plant efficiency, the impact of the metal oxide and split gas temperature from the oxidation reactor is crucial to be considered as well. As can be followed from the previous sensitivity results, an increase in the T_{OC,OXI_inlet} significantly increases both the T_{OC,OXI_outlet} and the gas outlet temperature from the OXI. While the former decreases the thermal requirement in the RED, the cooling of the gas from higher temperature results in a larger steam generation. Indeed, being the exothermicity of water splitting higher, a higher temperature of both metal oxide and the product gas from the OXI is obtained for water splitting than for CO_2 splitting. Thus, a constant lower heat (around 1.5 MW) would be required in the RED to maintain the temperature while working with only water as opposed to working with CO_2 only. Notwithstanding this fact, due to a relatively higher net electricity output, the overall efficiency for a pure CO_2-operated SCLP-OXY-CC unit is higher by one percentage point than for a pure water operating cycle. Based on the relative impact of all the parametric variations resulting from the variation of the T_{OC,OXI_inlet}, the optimum efficiency is reached (25.5%) at 800°C of T_{OC,OXI_inlet} for CO_2 only operation (Figure 48(b)).

A variation in the reduction temperature between 1300 and 1600°C was performed and its impact on the system performance was evaluated. Similar logical reasoning can be followed from the discussions of the previous sections. A lower reduction temperature results in a lower non-stoichiometry (δ), which significantly increases with temperature (Figure 49(a)). A constant molar flow in the OXI reactor would therefore significantly decrease the selectivity of the product gas in the OXI. The reduction is so high that, for CO_2 splitting with no separation of the product and reactant gas, the TIT would not be possible to be maintained with a constant molar feed rate of gas to the OXI from around a RED temperature of 1400°C. This is shown in Figure 49(b), whereby the molar flow sent to the OXI corresponds to only 15% and 2.5% of the total CO_2 molar flow sent for CCS from the original Oxyfuel power plant. This, however, results in the selectivity of CO to be higher for a reduction temperature of 1300°C than for 1400°C. On the other hand, even though the H_2 selectivity drops to almost around 2%, the presence of the condenser ensures a stable TIT to be maintained by varying the flow of the recycled CO_2 in the combustor accordingly. Nevertheless, with the decrease in the production of H_2 with reduction temperature, the overall CO_2 recycled would drop as well from around 52% at T_{RED} of 1600°C to lower than 2% for a T_{RED} of 1300°C, as shown in Figure 49(c). A maximum CO_2 recycling rate of about 65% is obtained for working with the only CO_2 at a reduction temperature of 1600°C.

As can be followed from the kinetic discussions, a lower non-stoichiometry in the reduction reactor would also significantly decrease the reaction rate of the oxidation reaction. Due to slower kinetics resulting from a smaller number of vacancies in the reduced metal oxide, the solid conversion drops as well with a decrease in the reduction temperature. This effect can be seen in Figure 49(b) on the blue coloured lines. The solid conversion with water splitting is inherently higher than that with CO_2 splitting, yielding a conversion of over 96% at T_{RED} of 1600°C, while the corresponding value with CO_2 splitting is 80%. Indeed, it needs to be clarified that a higher solid conversion does not imply a higher H_2 or CO generation since the conversion fraction essentially indicates the relative change in the oxidation state of the ceria between the inlet and outlet of the reduction reactor, irrespective of the absolute value of non-stoichiometry (δ) generated.

The impact of the absolute amount of H_2 or CO generated in the OXI, directly proportional to the net non-stoichiometry generated in the RED, can be visualized through the relative power outputs from the GT and ST and the auxiliary consumptions within the proposed unit (Figure 49(a)). A higher δ at a higher T_{RED}, results in higher H_2 and CO yield, leading to a higher power output from the GT, the maximum being around 6.3 MW. On the other hand, a higher T_{RED} leads to greater heat availability and steam generation from MET-HX2, increasing the output from the ST as well. The power of the ST in the only-water cycle is lower due to reasons already discussed previously. The auxiliary power requirement is primarily due to the CO_2 recycle compressor and product gas compressors necessary prior to the combustor. Additional power needs for ASU operation and pump work are, however, much smaller in the proposed plant design. Therefore, with the drop in the overall CO_2 recycled in the add-on unit, as well as because of less product gas generated with a drop in the temperature of reduction, the auxiliary power requirement drops as well for a lower T_{RED}. A combined effect is seen on the net power output from the system, whereby only around 4.5 MW of electric power output is achieved at a T_{RED} of 1300°C irrespective of gas composition for the OXI. However, for a higher T_{RED} resulting in greater solid conversion, the net power output from the H_2O-only cycle is lower due to the higher power requirement for hydrogen compression than CO compression, and a corresponding lower output from the ST. For a T_{RED} of 1600°C, thus, around 11.6 MW of electric power is obtained, compared to 12.8 MW from the CO_2-only cycle (Figure 49(a)).

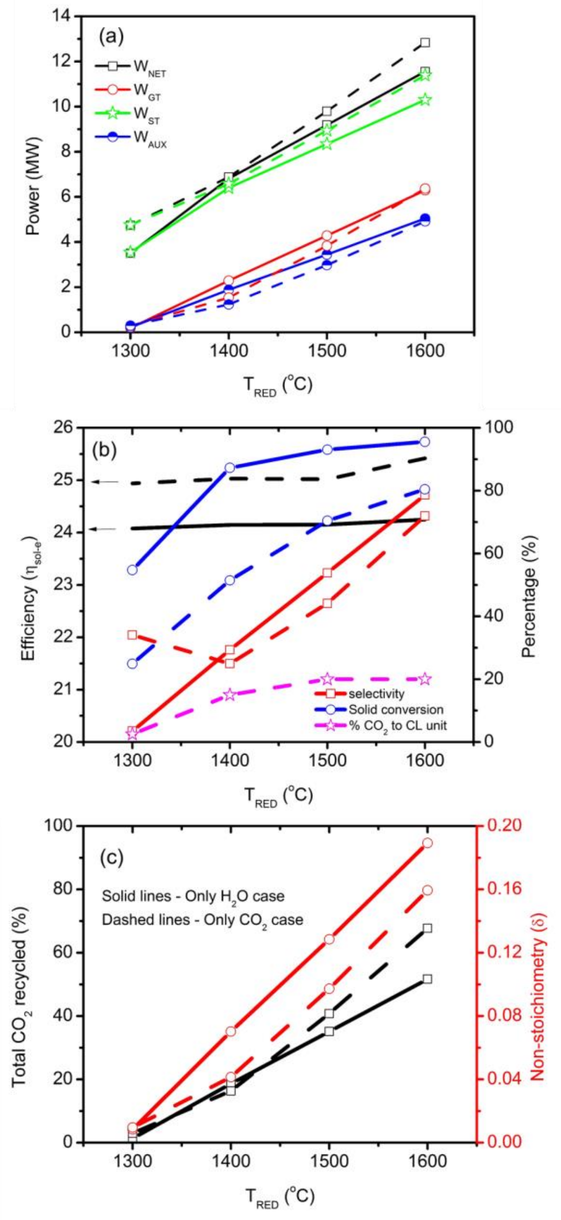

Figure 49. Impact of the variation of the reduction temperature on the operating parameters of the SCLP-OXY-CC at a constant pressure of 10^{-7} bar respectively, a constant molar flow rate of CeO_2 and gas to the OXI of 275 mol/s and 66 mol/s respectively and a constant gas inlet temperature to the OXI of 800°C (solid lines are only H_2O case and dashed lines represent only CO_2 case).

Indeed, similar to the discussions and conclusion of the previous sensitivity analysis, the impact of T_{RED} on the efficiency of the power plant is shown in Figure 49(b). No notable change in the efficiency is seen for a cycle operating with the only H_2O, whereby the efficiency remains constant at around 24.2%. On the other hand, a maximum efficiency of 25.4% is obtained with the only CO_2 and T_{RED} of 1600°C, which becomes constant at 25% below a T_{RED} of 1500°C.

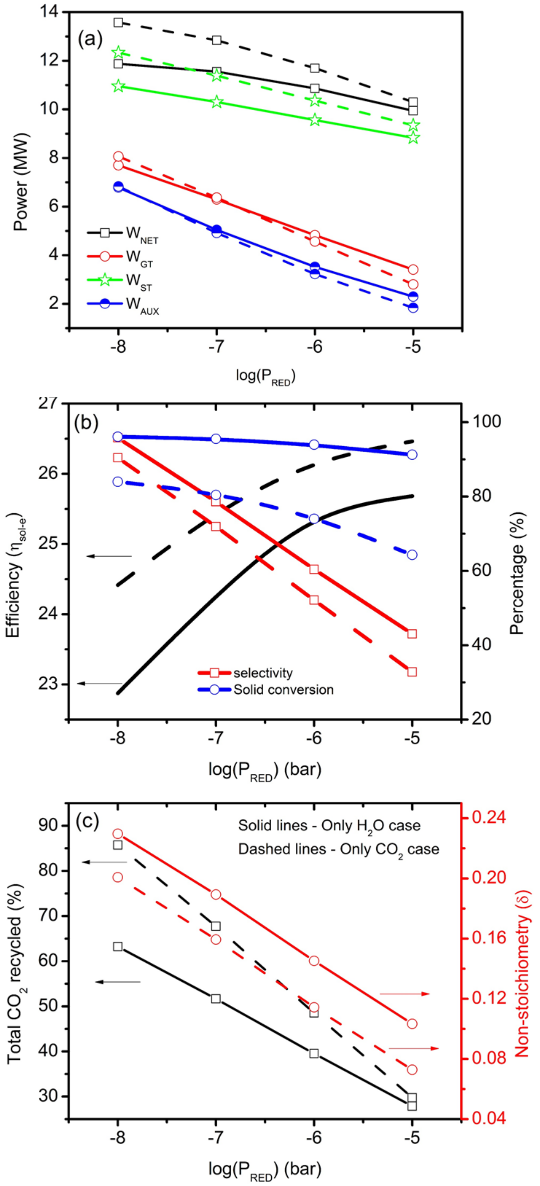

Figure 50. Impact of the variation of the reduction vacuum pressure on the operating parameters of the proposed SCLP-OXY-CC add-on unit at a constant RED temperature of 1600ºC, a constant molar flow rate of CeO_2 and gas of 275 mol/s and 66 mol/s respectively and a constant gas and metal oxide inlet temperature to the OXI of 800ºC (solid lines are only H_2O case and dashed lines represent only CO_2 case).

The impact of the variation of the reduction vacuum pressure is shown in Figure 50. Similar to the variation of the T_{RED}, a higher vacuum degree (i.e., lower pressure) increases the system yield significantly, in terms of the generated non-stoichiometry, as well as the selectivity for a constant molar flow of the gas to the OXI. As discussed before, due to a lower solid conversion in the OXI from CO_2 splitting, the resulting δ in the RED for the CO_2 only cycle is lower by about an average of 0.03. The corresponding selectivity of CO is also lower by 5 to 10% compared to that of H_2, which varies between 43% and 95.8% for a reduction vacuum pressure of 10^{-5} and 10^{-8} bar, respectively.

A higher selectivity would hence imply a higher net CO_2 recirculation within the add-on unit, which is indeed the case, as shown in Figure 50(c). For the lower vacuum conditions of 10^{-5} bar, the selectivity of the CO generated is lower, requiring around 10% of the total flow of CO_2 to be recirculated in the combustor while maintaining the desired TIT. The net CO_2 recycled was then 30% (20% CO_2 being sent previously directly to the OXI). As for the operation with H_2O, around 30% of CO_2 is necessary to ensure the desired TIT with H_2 combustion. Nonetheless, for higher vacuum pressures and with an increase in the selectivity, the overall CO_2 circulated in the add-on unit increases, whereby a maximum recirculation of 85.7% is seen at a pressure of 10^{-8} bar. The corresponding value at 10^{-7} bar was 51.7% and 67.7% for working with only water and CO_2 respectively.

Similar trends in the power generation from the GT and the ST, together with the auxiliary power requirement and the net power produced in the add-on unit, as was previously seen by varying T_{RED} is shown in Figure 50(a). Besides all previous discussions, it is important to mention that a higher vacuum degree, even though would ensure a higher reduction extent of ceria, and hence a higher selectivity, for a constant reactant gas molar flow, would also result in an increased auxiliary consumption from vacuum pumping. Also, the heat of reaction increases with the reduction extent, requiring more heat to be supplied. These factors, therefore, offset the net gains of the productivity of OXI and consequently the increased power output from the proposed layout at increased vacuum conditions of reduction. Thus, even though a decrease in the operating pressure of the RED from 10^{-7} bar to 10^{-8} bar operation would increase the W_{NET} by 0.3 to 0.7 MW (for H_2O and CO_2 respectively), the net system efficiency drops by over 1% in both the cases (Figure 50(b)). Hence a trade-off in the reduction reactor pressure with respect to system optimization is necessary for the proposed add-on unit.

The impact of the flow rate of water and CO_2 into the OXI for a constant ceria recirculation rate was performed subsequently. A reduction temperature of 1600°C with a metal oxide and gas inlet temperature of 800°C was fixed. Indeed, interesting to note is the maximum flow of water that can be utilized within the plant without temperature cross-over. Though not shown explicitly in Figure 51, it can be understood that a maximum of around 42% of the available water (230 mol/s) could be utilized at the set temperature configuration of the system. This would allow further scale-up of the system.

Nevertheless, as can be seen from Figure 51(a), around 10% of the flow (55 mol/sec) corresponds to the stoichiometric amount of water necessary to oxidize the non-stoichiometry of ceria. Below this, a sub-stoichiometric flow would cause an incomplete reaction in the oxidation reactor, and hence a significant drop of the system effectiveness, as well as the efficiency. Beyond the stoichiometric flow (10% of H_2O

from the CCS unit), the selectivity of hydrogen drops without any significant benefit to the solid conversion or to the reduction extent, i.e. δ, of the oxidized metal oxide (Figure 51(a)). By increasing the fraction of H_2O to CL, a peak of the oxidized metal oxide outlet temperature from the OXI ($T_{OC\_OUT,\ OXI}$) of 1120ºC is seen at around stoichiometric flow rates. Indeed, it needs to be mentioned that unlike the sensitivity study performed in [229], where a δ of 0.35 was assumed at the OXI inlet, in the present layout, the δ is 0.198. Hence, a much lower temperature of both the gas and the metal oxide from the outlet of the OXI is obtained. This considerably limits the overall performance of the CL unit while operating in a closed cycle. Nevertheless, at lower flow fraction of H_2O, the product outlet temperature (both gas and metal oxide) is lower due to unreacted metal oxide, while at higher flow, the cooling from the excess gas flow lowers the metal oxide outlet temperature. However, with a higher flow rate, due to the counterflow reactor configuration, a paradigm difference in the temperature of the gas outlet at the OXI is noticed, with a rise in almost 150ºC between before and after the stoichiometry flow respectively (Figure 51(c), red curve).

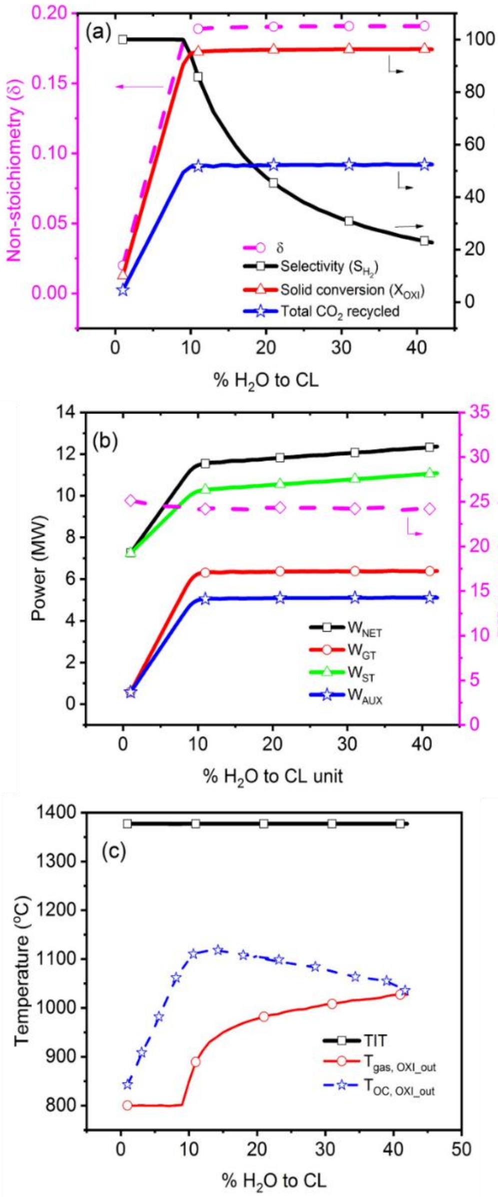

Figure 51. Impact of the variation of the water flow rate (% H_2O to CL) on the parameters of the proposed SCLP-OXY-CC unit working with only water at a constant molar flow rate of CeO_2 and water of 120 mol/s, a constant gas and metal oxide inlet temperature of 800°C to the OXI and a constant reduction temperature and pressure of 1600°C and 10^{-7} bar.

However, since a higher amount of steam is sent for splitting, a larger heat content in the gas exiting from the OXI allows the generation of more steam from cooling the larger volume of gas, thus increasing the power output from the steam turbine. The auxiliary power need being almost constant (notwithstanding the minimal power increase from pumping additional water), the net power output from the system increases up to 12.35 MW for an H_2O to CL fraction of 0.42. Nevertheless, an increase in the heat requirement in the RED reactor from lowering the metal oxide inlet temperature to the RED bypassing excess steam in the OXI results in no net benefit to the system efficiency beyond 10% of H_2O to CL. A maximum average system efficiency with water at the proposed operating conditions can hence be said to be 24.2% as seen in Figure 8b. Interestingly, such excess steam flow would often be limited to operating power cycles only, which do not require a high purity product gas from the OXI. For chemical processes like Fischer-Tropsch synthesis, the need for high purity product would limit the excess of steam into the OXI reactor to around 5% excess to the stoichiometry, posing a limit to the attainable system performance.

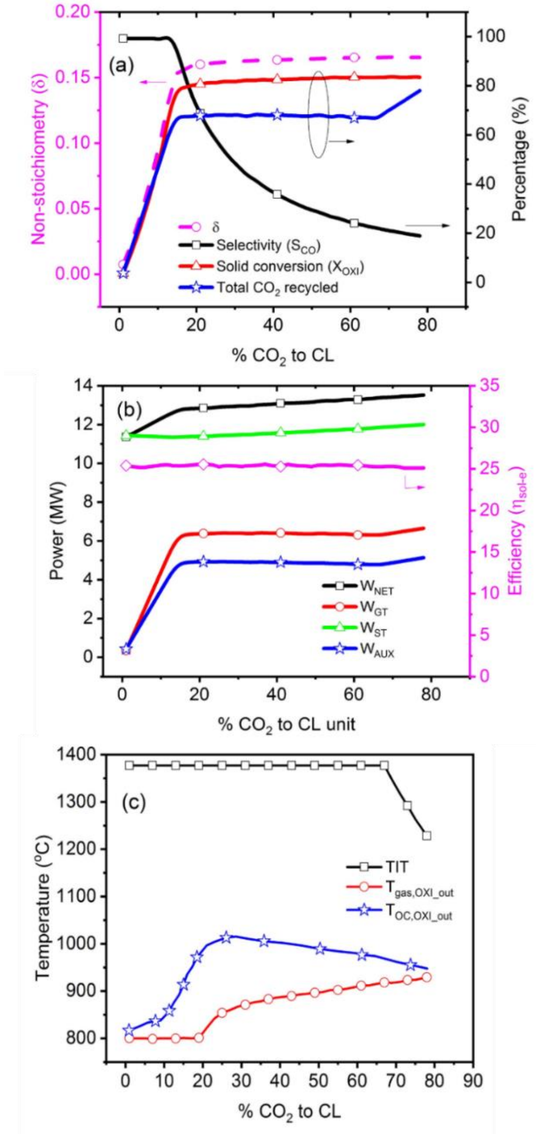

Figure 52. Impact of the variation of the CO_2 flow rate (% CO_2 to CL) on the parameters of the proposed SCLP-OXY-CC unit working with only water at a constant molar flow rate of CeO_2 and water of 120 mol/s, a constant gas and metal oxide inlet temperature of 800°C to the OXI and a constant reduction temperature and pressure of 1600°C and 10^{-7} bar.

On the other hand, the impact of the variation of the CO_2 flow provided to the CL unit on the different system operating parameters, together with the individual outputs of the turbine, as well as the auxiliary power input to the system and the net system efficiency is plotted in Figure 52. The reduction temperature was fixed at 1600ºC for the assessment of CO_2 flow variation, together with the gas and reduced metal oxide inlet temperature to the OXI at 800ºC. No temperature cross-over was noticed until 78% of recycling fraction of the CO_2 to the CL unit. This occurs because, unlike water, the CO_2 does not change phase, and hence the sensible heat required to heat up the CO_2 is much lower.

Similar profiles to that of water-only splitting are observed in all cases. At around 16.7% of the CO_2 fraction to the CL unit, which corresponds to the stoichiometric flow, a complete conversion of the gas (Figure 52(a)), together with a stable solid conversion of 83% is obtained. Being an exothermic reaction, this also results in the highest output temperature to the metal oxide from the OXI, around 1020ºC, about 100ºC lower than the maximum temperature achieved in the case of water splitting. All the related arguments of obtaining a lower temperature are valid for CO_2 as well, and hence not discussed separately. However, the gas outlet temperature rises gradually, being a counterflow reactor. However, no significant benefit is gained, since the metal oxide outlet temperature drops, signalling a higher thermal requirement in the reduction reactor. Due to a high conversion rate in the OXI for the gas at stoichiometry, the corresponding requirement of the CO_2 in the combustor for maintaining the TIT also peaks at 15% of CO_2 to CL unit, (not shown). With a further rise in the CO_2 fraction to CL, the selectivity starts to drop lower, and beyond 65%, the excess CO_2 in the product gas results in a drop in TIT without additional need of CO_2 to be recycled, as can be seen in Figure 52(c).

Figure 52(b) shows the net power output, together with the outputs from the GT and the ST and the auxiliary power requirements with the variation of the CO_2 flow to the splitting unit. As can be seen, after the 16% CO_2 from the CCS stream to CL, the GT power remains constant, since the total gas expanded is constant following previous arguments. However, with a higher flow of the CO_2 to the CL unit, and with a rise in temperature of the outlet gas from the OXI, as seen in Figure 52(a), the net steam generation increases, resulting in the increase of the net power output from the system. Beyond the 65% of CO_2 to CL, the net gas compressed for the COMB increases to a limit that decreases the TIT. This results in a steady rise in the auxiliary power demand. Even though the TIT decreases, the gas turbine sees a slight increase in power output due to the expansion of a larger volume of gas. The ST power increases, however, at a lower rate, since the temperature of the GT exhaust decreases, even though the net volume of the gas flow increase. Combining all these factors, a linear increase in the net power output from the system is noticed beyond 65% fraction of the CO_2 to CL unit. However, due to the lowering in the metal oxide outlet temperature from the OXI, leading to an increased heat load in the RED, the net system efficiency remains unaffected throughout at around 25.4%, as can be seen in Figure 52(b).

3.2.5 Comparative evaluation

A comparative evaluation of the performance of the proposed SCLP-OXY-CC add-on unit was performed by utilizing three different gas mixtures (only CO_2, only H_2O, and 86% CO_2 and 14% H_2O as replication of the composition of an Oxyfuel NGCC exhaust), fixing the operating conditions, based on the above sensitivity analyses. The reduction reactor temperature and operating pressure were chosen as a 1600ºC and 10^{-7} bar, together with the metal oxide and gas inlet temperature to the OXI at 800ºC. Since the primary aim of the proposed layout was power generation, the net molar flow of the gas was kept constant at 66 mol/s (equivalent to the utilization of 20% of CO_2). With regards to the product gas, no limit to the purity of the gas produced in the OXI is necessary as it will be fed to the combustor for power generation. The chosen operating pressure of reduction reactor is optimistic with respect to the vacuum technology available (and may require turbo vacuum pump) as it would suggest the maximum limit of feasibility integration with the power plants for viability investigation with respect to economic reasons. There have been many methods reported in the literature to reach low vacuum pressures for thermochemical dissociation application and the problems associated with it [9,31,32,259].

Table 6. Comparative performance evaluation of the proposed SCLP-OXY- CC, add-on unit with varying gas compositions to the OXI at equivalent operating conditions of 1600ºC and 10^{-7} bar reduction temperature and pressure respectively, metal oxide and gas inlet temperature to the OXI of 800ºC, 275 mol/s flow of CeO_2 and gas flow to the OXI of 66 mol/s.

Plant data	Units	Only CO_2	CO_2-H_2O mixture	Only H_2O
Solar Energy Input (A)	MWth	33.72	31.76	31.81
Net GT Output	MWe	6.30	6.30	6.30
ST Output	MWe	11.380	10.512	10.30
Gross Electric Power Output (B)	MWe	17.68	16.812	16.596
ASU Consumption + O_2 compression	MWe	0.024	0.024	0.024
Recycled CO_2 Compression	MWe	1.754	1.659	1.877
Compressor/ Pump Work for OXI Feed	MWe	0.324	0.319	0.353
Power Cycle Pumps	MWe	0.130	0.119	0.117
Syngas Compressors	MWe	0.562	0.552	0.455
Vacuum Pump	MWe	2.033	1.997	2.216
Total Auxiliary Power Consumption (C)	MWe	4.827	4.67	5.041
Net Electrical Power Output (D=B-C)	MWe	12.853	12.142	11.555
Gross Electrical Efficiency (B/A*100)	%	52.43%	52.93%	52.17%
Net Electrical Efficiency (excluding solar field and receiver efficiency) (D/A*100)	%	38.12%	38.23%	36.32%
Net System Efficiency (Solar to Electricity)	%	25.44%	25.52%	24.25%
Non-Stoichiometry yield (δ)		0.165	0.170	0.189
Metal oxide inlet temperature to RED	ºC	1006.17	1032.26	1121.36

Metal oxide conversion (solid conversion) in the OXI	%	80.43	86.09	95.53

Table 6 lists the comparative plant performance of the proposed SCLP-OXY-CC add-on unit with the three different gas mixtures discussed above. As can be observed, working with only water forms the lower bound to the system performance, while that with CO_2 provides the upper bound to the system performance in terms of the solar-to-electricity efficiency of the proposed add-on unit.

From the previous discussions, even though the power generated in the gas turbine is almost constant irrespective of the gas composition, the steam turbine output decreases significantly with increased water content in the gas mixture to the OXI. Additionally, a higher vacuum pumping power is necessary due to a higher yield of non-stoichiometry for H_2O splitting, which significantly increases the overall auxiliary power requirement as well. Even though this results in a higher yield of product from the system, indicated by a higher non-stoichiometry obtained by working with only water, as compared to working with CO_2/CO_2-H_2O mixture. Furthermore, a higher temperature of the solid outlet from water splitting reactor would result in the net heat required for reduction to decrease, which is a significant benefit in deriving from the increase of the amount of water in the gas mixture entering the OXI. Also, the solid conversion increases significantly with the increase in water content of the mixture, whereby, even with 14% water content, a 5.5% increase in the solid conversion is noticed, while the corresponding increase is 15% between working with only CO_2 and only H_2O.

Indeed, a maximum thermal efficiency of 38.12% of the proposed layout is obtained while working with only CO_2 splitting. This also provides the simplest among the possible configurations, without the need of HRSG for steam generation and additional condensers for water removal from the different streams of the power plant. Nevertheless, the overall solar-to-electricity efficiency drops to 25.4% due to the efficiency penalties arising from the solar field losses and the losses in the receiver, which, in fact, is the heat inlet to the reduction reactor. The maximum net electricity yield of 12.9 MW is obtained correspondingly.

Table 7. Comparative performance evaluation of the CL unit of the proposed SCLP-OXY-CC with varying gas composition to the OXI at fixed operating conditions of reduction (1600°C and 10^{-7} bar), metal oxide and gas inlet temperature to the OXI of 800°C, 275 mol/s flow of CeO_2 and gas flow to the OXI of 66 mol/s.

Description	Only CO_2	CO_2-H_2O mixture	Only H_2O
Solar Energy Input (A)	33.72	31.76	31.81
H_2 Flow (mol/s)	0	8.946	51.81
CO Flow (mol/s)	47.47	37.96	0
Energy yield rate (MW)	13.48	12.85	12.02
Vacuum pump work in RED (MW)	2.033	1.997	2.216

Heat Need for CO_2/H_2O Heating (MW)	2.329	2.7	4.947
Efficiency of CL Unit (η_{SCL})	35.41%	35.26%	30.84%

In addition to evaluation of the solar-to-electricity efficiency of the entire layout, the efficiency of the CL unit alone is also of interest. The corresponding evaluation results are shown in Table 7. As can be seen, at similar operating conditions, due to a higher metal oxide inlet temperature to the RED, the solar energy input for operating with only water is the minimum. However, due to latent heat requirement in heating water, the heat need for the water heating is significantly higher than the corresponding for CO_2, by more than 2.5 MW. In addition, a higher δ with water results in an increased requirement of vacuum pump work to maintain the necessary vacuum pressure in the reduction reactor. Thus, similar to the trend of results obtained for the overall plant efficiency, the efficiency of the CL unit decreases proportionally with increased water content in the gas mixture to the OXI as well. A maximum CL unit efficiency without considering heat recuperation is therefore obtained as 35.4% while working with the only CO_2.

3.2.6 Comments and discussions

A comprehensive evaluation of the proposed SCLP-OXY-CC add-on unit was performed, varying multiple operating conditions and also the gas composition to the OXI. Based on such analyses, operation strategies and issues with the two extreme mixture compositions (only CO_2 and only H_2O) have been described and evaluated. The net efficiency obtained was found to vary between 24.5% and 25.7%. This can, however, be sought to be increased via further system optimization. The net power generated was correspondingly found to be between 11.5 and 12.9 MW with the add-on unit. Considering the solar energy to be free, the power generation from the combined 100MW CCS and the SCLP-OXY-CC add-on unit would result in a maximum net system efficiency of about 49.72%, a 5.7% rise to the original efficiency of 44% of the Oxyfuel with CCS unit, as described above. Besides, the variability in the power output, without a significant drop in the system efficiency would aid flexible operations with the necessary control system. However, a significant drop in the power output at low reduction reactor temperature would often limit the operation of the cycle throughout the day without integrating adequate thermal storage. This becomes increasingly more significant since at start-up conditions, occurring every day, a temperature of 1600°C could seldom be reached. This would, therefore, limit the system performance to achieve its maximum potential only during a few hours around mid-day. Thus, a further complex system design with the integration of storage would be necessary for the resilient operation of the proposed layout and would form part of future work.

3.2.7 Economic evaluation

Further to the technical assessment of the system, economic assessment is crucial as well to comment on the overall feasibility of the proposed layout. Capital cost (including specific investment costs), Operational and Maintenance (O&M) costs and levelized cost of electricity (LCOE) were considered as the primary economic indicators to the proposed SCLP-OXY-CC system. The costs of the different components were obtained from the literature, either directly, or after suitable assumptions. In this regard, the costs were updated for the present day through chemical plant cost indices [260]. Besides, a currency conversion factor of 1.23 USD/EUR was used.

The Capital cost of the plant (CAPEX), included the capital cost of each module or equipment and was estimated by the utilization of the component scaling factor exponent, which is shown as the following equation.

$$C_{equ}=C_{equ,ref}(J/J_{ref})^{M} \tag{3.28}$$

C_{equ} and $C_{equ,ref}$ represent the equipment cost with a capacity of J and J_{ref}, respectively. M is the equipment scaling factor exponent, ranging between 0.6 – 1 [261,262]. The summary of the scale factors for the different components of the plant can be found in Table 8 [254] and scaling factor for the solar tower and its component with reflectors are considered as a unity. All the estimated equipment costs were converted to the year 2017 US dollar using the chemical engineering plant cost index (CEPCI) using equation (3.29).

$$C_{equ,actual}= C_{equ,ref}\frac{\text{CEPCI 2017}}{\text{CEPCI at the time of original cost}} \tag{3.29}$$

Table 8. Summary of the different plant component scale factors [207,254,263–265].

Plant Component	Scale factor M
Gas turbine, generator and auxiliaries	1
HRSG, ducting and stack	0.67
Steam turbine, generator and auxiliaries,	0.67
Cooling Water System and Balance of Plant	0.67
CO_2 Compressor and Condenser - Compressor 1	0.67
Chemical Looping, Combustor and Oxy Reactor	1
Turbo Expander	0.67
Other Heat Exchangers	1

To assess costs beyond equipment costs, that is, costs associated with plant installation and other direct and indirect costs related to the project development, a bottom-up approach adopted in the CAESER project [263] was used and is described below and the assumptions are summarized in Table 9.

The *Total Equipment Cost (TEC)* is the sum of all module costs in the plant. Besides this, additional *installation costs* are incurred due to expenses being required while integrating the individual modules into the entire plant, comprising costs for piping or valves, civil works, instrumentations, electrical installations, insulations, paintings, steel structures, erections and other outside battery limit (OSBL) activities.

Total Direct Plant Cost (TDPC) is then calculated as the sum of the Module/Equipment Costs and the Installation Costs. *Indirect Costs* have been fixed to 14% of the TDPC for all the three technologies [263], which include the costs for the yard improvement, service facilities and engineering costs as well as the building and sundries.

Engineering, Procurement and Construction Cost (EPC) was calculated as the sum of the Total Direct Plant Cost and Indirect Costs. Finally, the *Owner's Costs and Contingencies* (OCC) were included as the owner's costs for planning, designing and commissioning the plant and for working capital, together with contingencies, and were fixed to 15% of the total EPC cost for all the technology options as per literature [263]. In addition, the cost of initial metal oxide loading was also accounted for, which led to the overall CAPEX or *Total Plant Cost (TPC)* of the project to be obtained as per the following equation.

$$\begin{aligned}\text{TPC} = {} & \text{EC} + \text{Installation Costs} + \text{Indirect Costs} \\ & + \text{OCC} + \text{Metal oxide loading costs}\end{aligned} \tag{3.30}$$

In parallel, the O&M costs mainly comprise two aspects, namely fixed O&M costs and variable O&M costs. Fixed O&M costs comprise five components, i.e. general annual maintenance cost including overhead cost, property taxes and insurance and direct labour cost. On the other hand, variable costs are connected with the costs associated with power generation, include the cost of water (including both process water and make-up water), cost of a metal oxide for make-up, and fuel costs [263]. In the present calculation, solar energy was assumed to be available for free and no fuel cost was considered.

Table 9 presents the basic parameters used for calculating the economic indicators of the proposed power plant including those discussed in the previous sections. Based on the literature, erected cost of most of the equipment was obtained [266]. However, for the rest, the erection, piping and other added costs were also considered.

Table 9. Basic economic assumptions [262,267,268].

Item	Assumption
Ceria oxide price	49 \$/kg
Process Water	7.43 \$/m^3

Make-up Water	0.43 $/m^3
Erection, Steel structures and Painting	49% of Equipment Cost
Instrumentation and Controls	9% of Equipment Cost
Piping	20% of Equipment Cost
Electrical Equipment and Materials	12% of Equipment Cost
Indirect Costs, including Yard Development, Building, etc.	14% of TDPC
Owner's Costs	5% of EPC
Contingencies	10% of EPC
Annual operational time	1862 hours
Property Taxes and Insurance	2% of TPC
Maintenance Cost	2.5% of TPC
Labour Cost (Million Euro)	$100 per kW
Operational Life of Plant	30 years
Interest Rate	10%
Carbon credits	Not considered
Electricity Price	50 $/MWh

The levelized cost of electricity (LCOE) was considered to assess the economic performance of the system, where, the "break-even" value for producing a unit of electricity is often employed as a parameter to compare different electricity production technologies from the economic point of view. The LCOE is expressed as the following expression (equation 3.31), based on the investment cost at time period t (I_t), O&M Costs at time period t (M_t), Fuel Cost at time period t (F_t), the electricity generated at time t (E_t) and the interest rate r.

$$\mathrm{LCOE} = \frac{\sum \frac{I_t + M_t + F_t}{(1+r)^t}}{\sum \frac{E_t}{(1+r)^t}} \tag{3.31}$$

3.2.8 Capital cost and operation expenses

As developed from the process simulations, it can be easily concluded that the SCLP-OXY-CC provides a clear technical benefit to a conventional oxyfuel NGCC system with carbon capture. However, the most critical component of the SCLP-OXY-CC unit can be related to the solar field and tower, together with the need for new system additions including solid handling units, reactors for reduction and oxidation, and an additional power generating station among others. This would incur considerable capital investments for the necessary retrofit. Table 10 represents the cost breakdown of the proposed SCLP-OXY-CC unit. The cost of the solar fields was obtained from a recent study by Falter et al [269], which was then modified to the necessary scale.

Table 10. Capital cost breakdown of the proposed SCLP-OXY-CC unit.

Plant Component	Values (million)	% Contr
Primary Gas turbine, generator and auxiliaries	$1.33	0.88%
HRSG, ducting and stack	$2.47	1.64%
Steam turbine, generator and auxiliaries,	$5.74	3.82%
Cooling Water System and Balance of Plant	$6.35	4.22%
CO_2 Recycle Compressor	$3.16	2.10%
Pump for H_2O	$0.02	0.01%
CO_2 Compressor for CL Unit	$0.97	0.65%
Syngas Compressor (H_2)	$28.54	19.00%
ASU (Complete CAPEX)	$0.15	0.10%
Other Heat Exchangers	$0.04	0.03%
Solar Reactor	$7.08	4.71%
Reflectors	$20.60	13.71%
Receiver Cost	$7.08	4.71%
Solar Tower	$0.83	0.55%
Total Equipment Costs (TEC)	$84.21	56.05%
Cost of metal oxide loading	$0.01	0.01%
Total Installation Costs	$34.00	22.63%
Total Direct Plant Cost (TDPC)	$118.37	78.78%
Indirect Costs	$16.57	11.03%
Engineering Procurement and Construction Costs (EPCC)	$134.94	89.81%
Owner’s Costs	$1.66	1.10%
Contingencies	$13.49	8.98%
ASU (Complete CAPEX as an add-on unit)	$0.15	0.10%
Total Project Costs (TPC)	$150.25	100.00%

The ASU was assumed as an add-on unit, with a CAPEX of $150,000 based on cost proposed by Berghaut el al [265] as 51 million per kilotonne of O_2 per day. The cost of separation of oxygen for oxyfuel combustion could be reduced by replacing it with more advanced technologies, such as ion transport membranes, which could also increase the efficiency of the system as well as reduce the total equipment cost. However, the major contributor to the overall CAPEX is from the solar field and its associated components. The reflectors form the costliest of all the equipment, accounting for over 13.7% of the total plant CAPEX and 29.2% of the TEC. The combined solar field, including the reflectors, receiver, tower and reactor account for almost 36% of the overall equipment costs. However, the costliest equipment is the hydrogen compressor, which accounts for 19% alone of the TPC. This is due to its high cost of equipment working under pure hydrogen environments [270]. The net project CAPEX was obtained at around \$150 million, which amounts to around 12,136 \$/kW, a cost, much higher than the present day specific cost of electricity producing units, and especially for traditional solar tower based concentrated solar power producing plants [271,272].

In addition, the operational expenses were calculated based on the assumptions mentioned in the earlier section. A capacity factor of 25% was assumed for a CSP without storage based on literature [272]. The net fixed OPEX was obtained as \$7.02 million, while the variable cost was calculated as 1.42 \$/MWh of gross power generation. Hence a net annual operating cost of \$15.05 million was calculated to run the proposed 12.8 MW SCLP-OXY-CC unit.

3.2.9 Levelized cost of electricity (LCOE)

LCOE calculations were hence developed based on equation (3.31) with assumptions listed in Table 9 to perform a comparative evaluation of the system economic performance. As mentioned, no carbon credits were assumed. Correspondingly an LCOE of 1,100 \$/MWh was obtained. The cost attained is well over current technologies and hence incentives or carbon credits are crucial to making such a system economically competitive. In addition, economies of scale can be understood to play a severe role, a higher capacity would tremendously benefit the specific CAPEX of the proposed unit, allowing the technological breakthroughs needed to make this type of systems economically attractive. However, it is to be mentioned, that if CO_2 would be utilized only and no water for splitting purposes, the cost of the components can be decreased further, that can result in significant economic benefits of the proposed system.

3.2.10 Concluding remarks

The techno-economic performance of a solar thermochemical looping CO_2/H_2O splitting plant with moving bed reactors has been assessed for the integration with a 100 MW oxyfuel power plant with carbon capture. In section 3.1, a moving bed reactor model was developed in ASPEN Plus including kinetic models that simulate both the step of thermal reduction of ceria and the water and/or carbon dioxide splitting on reduced ceria. The CL unit model was then integrated into a power plant layout to be implemented as an add-on unit to an existing Oxyfuel power plant with CCS. Retrofitting a 100 MW Oxyfuel NGCC was thus evaluated with multiple sensitivity studies varying different operating parameters and composition of the gas to the oxidation reactor of the CL unit. Utilizing 20% of the CO_2 generated for CCS, a maximum of 12.85 MW of electricity can be generated, which can be improved subject to system optimization. A maximum solar to electricity efficiency of 25.4% was obtained while working with CO_2 only and operating the reduction reactor at 1600^{o}C and 10^{-7} bar vacuum pressure. The oxidation reactor was operated at 2 bar pressure. Considerable variation in the output of the system is noticed with the variation of the reduction temperature, which would often limit the steady operation of the system to only a few hours of the day without a thermal storage. Economic analysis has been carried out and found that the major contributor to CAPEX of the plant is solar field related components and equipment accounting to nearly 36% of the cumulative equipment costs. Besides that, hydrogen compressor cost is 19% of total plant cost. The specific overnight capital cost is 12136 $/kW, which is very high compared to traditionally produced by solar tower technology. The levelized cost of electricity evaluated to be 1100 $/MWh, without including incentives or carbon taxation in the analysis. The CAPEX could be reduced if CO_2-only splitting is carried out through thermochemical looping, as the cost of hydrogen compressor is determinant, resulting in significant economic benefits to the proposed system.

The economic evaluation reveals that the cost of electricity production by add-on of the chemical looping syngas unit to an oxy-fuelled power plant is very high compare to the existing electricity price and the capital investment is huge. The challenges in the solar-thermochemical splitting unit are majorly due to pressure swing and temperature swing between the reduction and oxidation reactor, very high temperatures of reduction to attain the reaction extent. Therefore, one of the possible solutions suggested is to replace the solar thermal reduction by fuel reduction which can operate at the atmospheric pressure which gives the opportunity to operate both the reactors at same pressure and temperature.

Chapter 4

Thermodynamic analysis of syngas production by methane reduction and CO_2 + H_2O oxidation of ceria

As obtained from the previous analyses of solar thermochemical CO_2/H_2O splitting, even though technologically attractive, multiple practical limitations exist and especially restrictive are the need for a high temperature of reduction and a very high vacuum conditions, indicating a high temperature and pressure swing between the two reactors. This is considerably limiting to the flexible operation of the system, as well as increasing its complexity by requiring additional components like the vacuum pump, heat recuperators, etc. Additionally, the variation of output with the available solar flux throughout the day is of considerable concern to the stable output from the system. In this regard, the use of methane as the reducing agent can be considered as an interesting alternative.

This chapter focussed on to study the thermodynamic performance of methane reduction of ceria with subsequent oxidation of the reduced metal oxide. Since a thermodynamic study has been considered, this would provide the maximum yield from an idealistic performance from the proposed metal oxide, in the present case, ceria.

4.1 Introduction

Unlike iron oxide, which has received wide attention for thermodynamic analysis for redox chemical looping cycles [99,273,274], that for ceria is limited in literature, especially for methane reduction. Bader et al [275] reported a thermodynamic analysis of isothermal redox cycling of ceria at 1500°C, achieving efficiencies of up to 10% and 18% for hydrogen and carbon monoxide production, respectively. The efficiencies were considerably improved to over 30% for hydrogen production by introducing a temperature swing of 150°C between the reduction and the oxidation reactors. A similar investigation for non-stoichiometric ceria cycle by Furler et al. [276] in a thermally reduced cycle reported much lower solar-to-fuel energy conversion efficiency using sweep inert gas as 1.7% with peak achieved as 3.5%. The lower efficiencies are due to no pressure swing between the two steps. In order to improve the system with respect to the scale and efficiency, a moving packed bed of reactive particle reactors have been employed to investigate and analyse the efficiency [221]. Indeed, the scope for increasing the energy efficiency through multiple processes including heat recovery was suggested, enabling the conversion efficiency of solar energy into H_2 and CO at the design point to exceed 30%. It is worth mentioning that non-stoichiometry (δ) never reaches 0.5 for thermal reduction (without changing its fluorite-related structure having α-phase below 0.286[277]), similarly with methane reduction, δ reported as 0.378 [278,279] at 1000°C, 0.21 at 1035°C by Warren et al [280] but the same group conducted packed experiments of ceria with methane reduction and reported that δ of 0.5 (meaning Ce_2O_3 is reached during reduction) is reached above 900°C by using Pt crucible instead of alumina [87]. Ce_2O_3 is considered as the end member in the reduction reaction because there is a lack of data for $CeO_{2-\delta}$ thermodynamic parameters.

In the present study, thermodynamic analysis for stoichiometric reduction of ceria for maximum redox pair utilization was performed. Accordingly, the redox pair considered was CeO_2/Ce_2O_3 with a reduction in the presence of methane, as described by the equations (4.1-4.2).

$$\text{Methane reduction: } 2CeO_2 + CH_4 \rightarrow Ce_2O_3 + CO + 2H_2 \quad (4.1)$$

$$\text{WS: } Ce_2O_3 + H_2O \rightarrow 2CeO_2 + H_2 \quad (4.2a)$$

$$\text{CDS: } Ce_2O_3 + CO_2 \rightarrow 2CeO_2 + CO \quad (4.2b)$$

In the reduction reactor, the methane reduces the metal oxide at a higher oxidation state (CeO_2) to a lower completely oxidation state (Ce_2O_3), while itself getting oxidized to CO and H_2 via reaction (4.2). The reduced ceria oxide is then recycled back to the higher oxidation state through reactions (4.2a) and (4.2b). In both the reactors, syngas can be generated, however, with varying H_2/CO fractions. While, from thermodynamic and mass conservation conditions, the H_2 to CO ratio of the syngas from the reduction reactor is mostly 2:1, the ratio in the oxidation reactor can be varied based on the inlet gas feed mixture, and other thermodynamic parameters.

Multiple studies, mostly based on iron oxide-based redox metal pairs have reported the conversion efficiencies and operating conditions for conversion of methane into syngas over metal oxides [281–283]. Such studies also include the limiting operation range based on the need to prevent carbon deposition reactions as crucial for the system operation. Thermodynamics of ceria reduction with hydrogen have been investigated to explore the maximum extent of reaction and reported in the literature [284]. Solar-driven thermal reduction for ceria coupled with either CO_2 or H_2O splitting has been studied extensively by Welte et al. [164,285] and other researchers [89,275]. However, limited literature on the thermodynamic assessment regarding methane reduction of ceria followed by splitting of waste gas (a mixture of CO_2 and H_2O) is available [85].

Additionally, the need to identify the regimes for carbon formation is crucial to identify the suitable operation regimes of the reaction system further.

Within the reduction reactor, carbon deposition, through Boudouard reaction (4.3) and methane dissociation mechanisms (4.4) is important. This carbon is subsequently transported into the oxidation reactor along with the reduced ceria. Within the oxidation reactor, even though the carbon does not directly inhibit any reaction, it forms its own set of reaction towards syngas production with H_2O (Water Gas Reaction) and CO_2 (Reverse Boudouard Reaction) as given by reactions (4.5) and (4.6) respectively. Therefore, the presence of carbon results in competitive reactions against the reduced metal oxide for the subsequent oxidation, which would cause the metal oxide to remain at a reduced state, while the solid carbon takes preference in oxidation. This would become more critical under a stoichiometric quantity of reactants, lowering the utilization of the metal oxide.

$$2CO \rightarrow C(s) + CO_2 \tag{4.3}$$

$$CH_4 \rightarrow C(s) + 2H_2 \tag{4.4}$$

$$C(s) + H_2O \rightarrow CO + H_2 \tag{4.5}$$

$$C(s) + CO_2 \rightarrow 2CO \tag{4.6}$$

Besides carbon formation, the oxygen released from the reduced metal in the reduction reactor has the potential to react with the produced CO and H_2 to form CO_2 and water and respectively at suitable thermodynamic conditions, as per the equations (4.7) and (4.8). This would considerably reduce the effectiveness of the entire system by lowering the calorific value of the syngas produced in the reduction reactor, thereby decreasing the system efficiency.

$$CO + 0.5O_2 \leftrightarrow CO_2 \tag{4.7}$$

$$H_2 + 0.5O_2 \leftrightarrow H_2O \tag{4.8}$$

Based on the present chemical components, the water gas shift reaction (4.9) and the methane reforming reaction (4.10) can also occur. However, the thermodynamic and chemical conditions would render such reactions unfavourable from being primary contributors to system thermodynamics.

$$CO + H_2O \rightarrow CO_2 + H_2 \tag{4.9}$$

$$CH_4 + H_2O \rightarrow 3H_2 + CO \tag{4.10}$$

Therefore, the aim of the present study is to perform thermodynamic and process simulation studies to obtain the ideal operating conditions, close to equilibrium, avoiding carbon deposition, of the CeO_2/Ce_2O_3 redox pair chemical looping syngas production via methane reduction. The analysis has been performed by evaluating the thermodynamic equilibrium composition of the reaction system, the impact of the reactant feed molar ratios and temperature on the product compositions for the reduction and oxidation reactors, respectively. Furthermore, the system efficiency regarding the redox cycle performance was assessed.

4.2 Thermodynamic model

The thermodynamic simulation of methane reduction and water and CO_2 splitting was performed in Aspen Plus®. Gibbs free energy minimization principle (GFEM) was used to perform the thermodynamic calculations. For a reaction system, where multiple simultaneous reactions take place, equilibrium calculations are often performed through the GFEM approach, details of which can be found in the literature [286,287]. For the entire set of reactors and components modelled, the gaseous species included were: CH_4, CO, CO_2, H_2, and H_2O; while the solid species were: C, Ce_2O_3, and CeO_2.

The process layout of the simulation system is shown in Figure 53. The Aspen plus® RGIBBS reactor model was used to simulate both the reduction and oxidation reactors, using the Peng Robinson equation of state. Within the RGIBBS reactor, the equilibrium composition of all feasible combination of reactions within the thermodynamic domain was considered. The RGIBBS reactor calculates the most stable phase combination obtained through chemical reactions where the Gibbs free energy of the reaction system reaches its minimum at a fixed mass balance, constant pressure, and temperature. Besides the RGIBBS module, the other components simulated were cyclone units to separate solid and gas streams, and heat exchangers, in which steams are preheated to reach the temperatures of reaction and heat is removed from the reaction products.

For the reduction reactor, the temperature was varied in the range of 500-1000ºC, at a constant pressure of 1 atm. The CH_4/CeO_2 feed molar ratio was varied from 0.4 (sub-stoichiometric value according to equation (4.1)) to 4. The solid product of the reduction reactor was fed to the oxidation reactor after cyclone separator. The oxidation reactor was modelled by a series of two RGIBBS reactor. The oxidation of CO_2 and H_2O over Ce_2O_3 is a highly exothermic reaction. Therefore, two rectors with an intercooler were modelled to simulate an ideal isothermal reactor. The first reactor was modelled as an adiabatic reactor, while the second reactor was an isothermal reactor, set at the temperature of the reaction. In the oxidation reactor, the Ce_2O_3 was reacted with a mixture of steam and carbon dioxide according to equation (4.2a) and (4.2b). Similar to the reduction reactor, the oxidation reactor temperature was varied between 500-1000^{o}C at a constant pressure of 1 atm. The feed flow of the mixture was varied in the range of 0.5 to 2 kmol/h (stoichiometric to excess flow). The study corresponding to the oxidation reactor was performed to obtain the quantitative H_2 and CO produced at multiple regimes and hence identify the conditions of operations for different H_2/CO ratio requirements for subsequent downstream processes. Additionally, determination of the minimum amount of gas flow and the corresponding composition to regenerate completely the reduced ceria was also aimed for within the regime of favourable reaction thermodynamics. However, it should be noted that, in the present study, all the simulation calculations performed were based on theoretical thermodynamic considerations, since no heat and mass diffusional limitations along with kinetics effects were considered for the confirmation of the present thermodynamic analysis. This corresponds to the theoretical limits that must be considered during further experimental evaluations of the reaction systems.

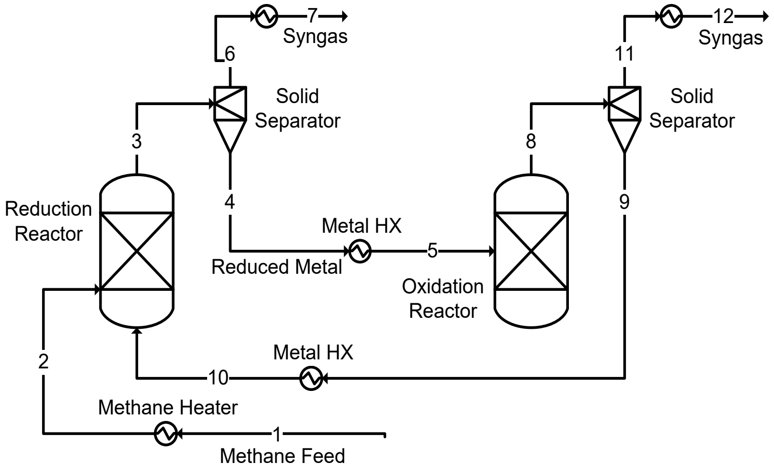

Figure 53. Process simulation flowsheet of interconnected reduction and oxidation reactors.

4.3 Results and discussion

4.3.1 Reduction reactor

The equilibrium composition of H_2, CO, CO_2, H_2O, O_2 and CH_4 and C, CeO_2 and, Ce_2O_3 obtained from the reduction of methane over CeO_2 in a temperature range of 500 to 1000°C and CH_4/CeO_2 feed molar ratios from 0.4 to 4 are discussed in the following section.

Figure 54 shows the equilibrium production of H_2 and CO within the reduction reactor (dry basis) as the molar fraction of the outlet product gas stream with respect to temperature and CH_4/CeO_2 feed molar ratio, together with the methane molar fraction at the outlet of the reactor. Oxygen, being always present as trace gases were not depicted separately. Additionally, the reduced CeO_2 as a solid fraction is also plotted with respect to the mentioned conditions, as shown in Figure 54(d). Within the conditions investigated, the methane reduction reaction initiates over 600°C. Lower methane to ceria ratios yielded lower products than higher feed ratios at same temperatures. At stoichiometric conditions, that is with 0.5 mole CH_4 per mole of CeO_2, 50% of CeO_2 conversion occurs around 800ºC, while the reaction yielded 99.9% conversion at temperatures over 900ºC. This can be attributed to the intrinsic reactivity of solid CeO_2 with respect to the gaseous fuel, methane, and availability of the metal oxide lattice oxygen into the gas phase for partial oxidation reactions. At lower temperatures (500 to 600ºC) and for a lower CH_4/CeO_2 feed ratio (below 0.5), the availability of oxygen and temperature is limited to drive the reaction towards the production of syngas (CO + H_2), resulting in the metal oxide to be poorly active for reaction (4.1). In any case, even with higher CH_4/CeO_2 feed ratio, the complete reaction occurs at temperatures over 700ºC, providing a thermodynamic limit to the reduction temperature of pure CeO_2 over methane.

Nevertheless, as can be visualized from Figure 54, an operation with 0.7 to 0.8 mole of CH_4 per mole of CeO_2 at around 900-950ºC would provide the ideal operating conditions with respect to methane utilization, without the need to feed a high fraction of methane. A syngas stream of 31% CO and 63% H_2 can be obtained (balance 1% H_2O, 0.4% CO_2 and 4.6% CH_4) at around 950ºC and a CH_4/CeO_2 feed ratio of 0.7 to 0.8. Indeed, for higher methane flows, the excess methane at the outlet of the reduction reactor would decrease the effectiveness of the chemical looping system.

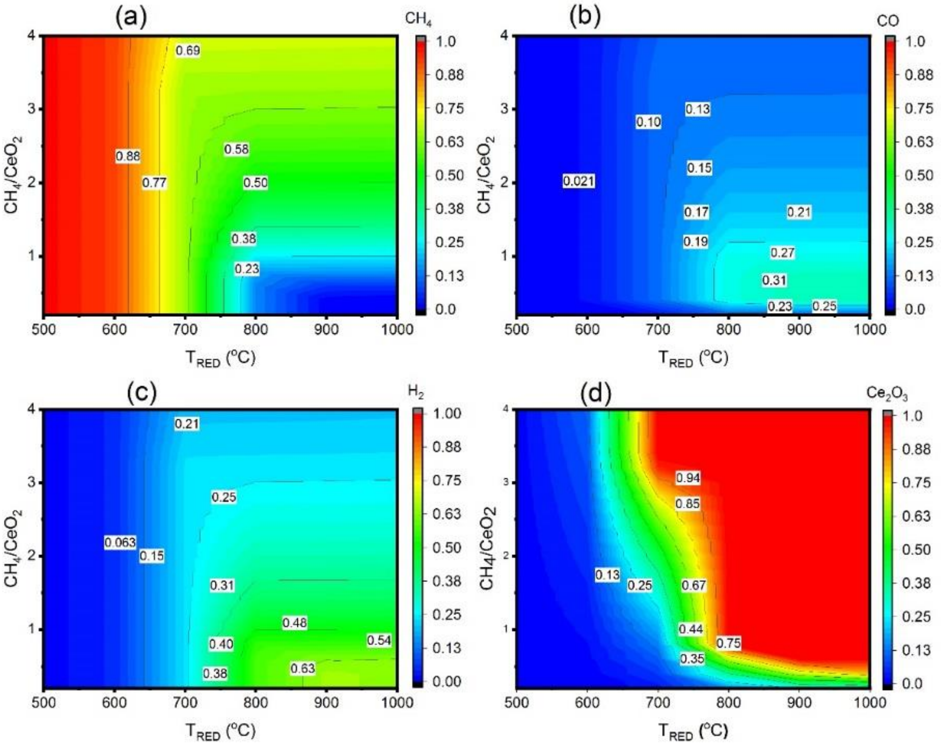

Figure 54. Impact of the variation of the CH_4/CeO_2 ratio and temperature on the yield of the following chemical species as molar fractions of outlet streams within the reduction reactor: (a) CH_4; (b) CO; (c) H_2; (d) Ce_2O_3 (solid).

Figure 55 shows the molar fraction of unwanted chemical species in the outlet gas of the reduction reactor, produced within the studied conditions, namely elementary carbon, CO_2 and H_2O resulting from the reactions (4.3-4.4) and (4.7-4.8), occurring alongside the primary reaction, represented by equation (4.1). It can be observed that, at a higher temperature, and especially at the content of methane, there is a considerable increase in CO_2 formation. A similar trend is observed for H_2O formation, even though the yield of H_2O is considerably higher than CO_2, at corresponding temperature and pressure. Together, they make up about 4% of the product gas flow for near stoichiometric operations. The primary reason for the initiation of reactions given by equation (4.7) and (4.8) can be attributed to the lower availability of methane for reaction at higher temperatures. The oxygen released from the metal lattice reacts instead with the produced CO and H_2 to oxidize them further into CO_2 and H_2O.

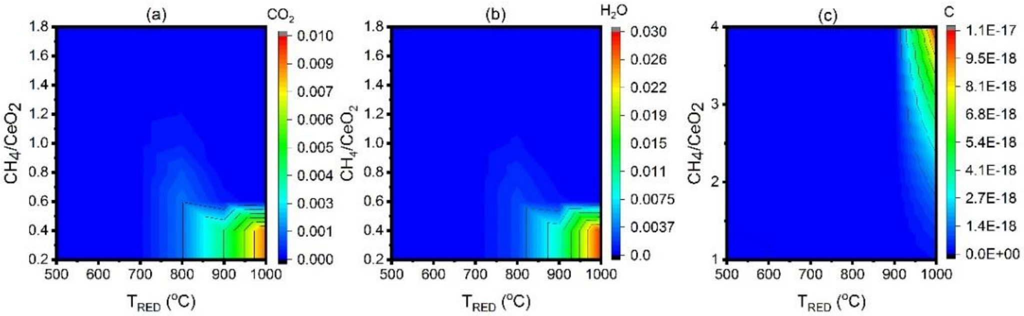

Figure 55. Impact of the variation of the CH_4/CeO_2 ratio and temperature on the yield of the following unwanted chemical species as molar fraction of the outlet product streams within the reduction reactor: (a) CO_2; (b) H_2O; (c) elementary carbon (solid).

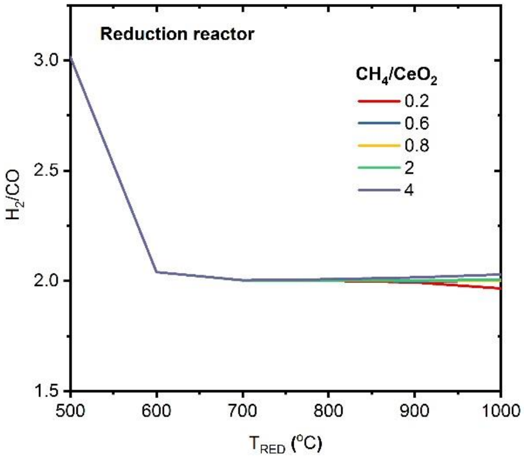

Figure 56. H_2/CO ratio at the exit of the reduction reactor for different reduction temperatures for various CH_4/CeO_2.

It can be observed from that the carbon formation starts at temperatures over 900°C and higher feed ratios. As indicated in Figure 55(c) the carbon deposition initiates at a methane to ceria feed ratios above 1.0, and subsequently increases with higher molar flows of methane and temperature. This is because the thermodynamics for either the Boudouard and/or the methane decomposition reactions (equation (4.3) and (4.4)) are not favourable at other conditions. As discussed before, the production of carbon in the reduction reactor has considerable influence on the system efficiency due to competitive reactions with Ce_2O_3 in the oxidation reactor. Even though the fraction of carbon content is exceedingly low, this would restrict the working conditions with methane reduction to around 900ºC, and the molar feed ratio, to around 1.0. These results agree well with the experimental results reported by Welte et al. [86].

Combining all factors, as discussed above, it can be concluded that favourable operating zone of the reduction reactor has to be limited to around 900-950ºC with 0.7-0.8 mole of CH_4 per mole of CeO_2 to ensure complete reduction of CeO_2, without the need of high methane content and avoiding unwanted reactions from taking place. Moreover, in this operating range, the syngas obtained has the desired ratio of H_2/CO equal to 2, as shown in Figure 56. Hence, in the subsequent analysis of system efficiency and sensitivity studies, the regime of over 900-950ºC was used for the reduction reactor to evaluate the system performance.

4.3.2 Oxidation reactor

The equilibrium amounts of H_2 and CO obtained by splitting CO_2 and H_2O over reduced Ce_2O_3 within the oxidation reactor is presented in the following section. The parametric study was carried out within a temperature range of 500 to 1000ºC, considering completely reduced Ceria (Ce_2O_3) being fed into the oxidation reactor. A variation of H_2O/CO_2 mixture composition (from 5% to 95% CO_2) and the molar flow rate of the mixture from 0.5 to 2 kmol/h was also performed. In all the cases the flow of Ce_2O_3 was kept constant at 0.5 kmol/h, being considered to be completely reduced from 1 kmol/h of CeO_2 in the reduction reactor as per equation (4.1).

For the base case study, an equimolar mixture between H_2O and CO_2 was fed into the oxidation reactor at varying feed rates and temperatures. Figure 57(a) and (b) presents results from the oxidation reactor at the described conditions as the mole fraction of the products in the outlet gas stream from the reactor. It is observed that hydrogen production was obtained as a function of temperature and the feed molar flow to the reactor. Therefore, the region of maximum hydrogen production can be identified, varying between 600 to 700ºC, depending on the molar feed flow rate. With higher feed flow rate, the peak of hydrogen shifts towards a lower temperature. More specifically, for a waste gas flow rate of 1 kmol/h, for an equimolar mixture between CO_2 and H_2O, with each 0.5 kmol/h, the peak hydrogen production occurs around 650ºC, which shifts to 600ºC with an increase of the molar feed rate of 2 kmol/h.

On the other hand, the CO yield increases at a higher rate till around 650ºC, after which the rate of increase of CO yield drops considerably. Higher the flow of the waste gas, lower is the difference in the rate of yield increase between the two temperature ranges (below and above 650ºC). For molar flows higher than stoichiometry (0.5

kmol/h), the yield becomes stable at about 0.28 kmol/h with a further rise in temperature irrespective of the increase in molar feed flow.

The yield variations based on the thermodynamic conditions play a critical role in varying H_2/CO ratio obtained at the outlet of the oxidation reactor, which therefore can be controlled to obtain the H_2/CO ratios required for specific processes. Combining the yields of the two gases, for the stoichiometric flow of waste gas (1 kmol/h and equimolar mixture), a syngas stream of 45% H_2 and above 40% CO could be obtained. The remaining fraction of the gas is composed of un-reacted species. However, sending above-stoichiometric flows, even though would result in complete oxidation of Ce_2O_3 and providing maximum yield, would result in syngas fraction to drop considerably. This would decrease the effectiveness of the process by requiring additional downstream processes to separate CO_2 and water for obtaining pure syngas.

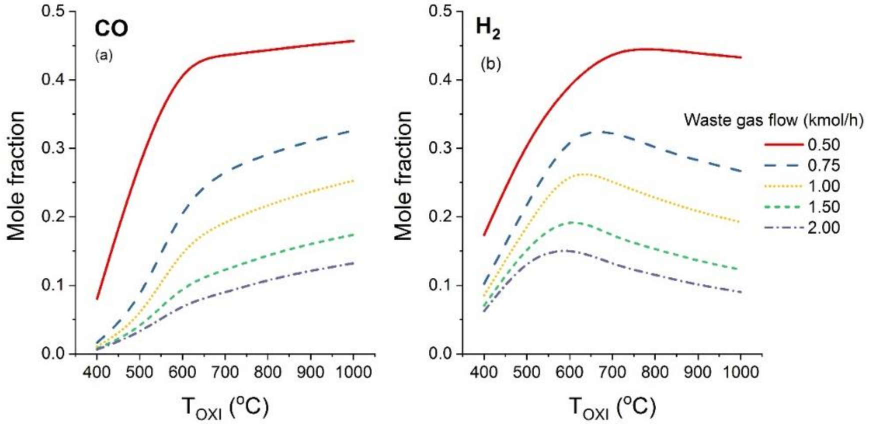

Figure 57. Impact of the variation of the waste gas (equimolar mixture of CO_2 and H_2O) flow rate and temperature on the yield of the (a) CO and (b) H_2 as the molar fraction of the product gas of the oxidation reactor.

The H_2 and CO results can be combined to obtain the H_2/CO ratios at the outlet of the oxidation reactor with varying molar feed flows of the equimolar mixture of H_2O and CO_2 as presented in Figure 58(a). At lower temperatures, the formation of H_2 is thermodynamically favourable over that of CO. Additionally, with increase in molar feed rate, the preferential splitting of water over carbon dioxide increases the H_2/CO ratio further at lower temperatures. The H_2/CO ratio decreases considerably with increase of temperature to around a constant 0.6 at 1000°C, irrespective of the waste gas feed flow, as H_2 formation peaks around 600-650°C, while there is no specific peak for CO formation that constantly increases with the temperature. Also, interestingly, at a lower flow of 0.5 kmol/h of the waste gas, when neither of the chemical species can completely oxidize the reduced metal, the H_2/CO ratio remains constant at around 0.6 irrespective of the temperature variation. This can be concluded from the fact that the H_2O and CO_2 split can then occur simultaneously, since the individual gases are lower than the stoichiometric quantity necessary to oxidize the reduced metal by themselves as per reaction (4.2). However, it needs to be kept in mind that the complete oxidation of the Ce_2O_3 to CeO_2 was ensured within the defined conditions, and the produced CeO_2 was recirculated back to the reduction reactor.

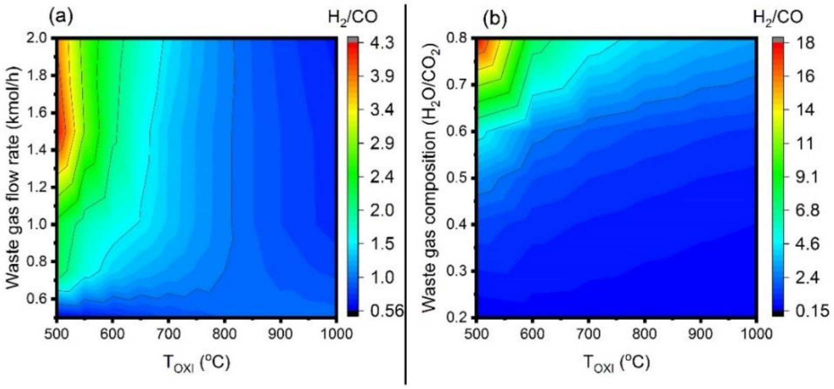

Figure 58. Impact of the variation of the waste gas flow parameters and temperature on the H_2/CO yield ratio in the oxidation reactor: (a) variation of flow of waste gas with an equimolar mixture of CO_2 and H_2O; (b) variation of the composition of the waste gas at a constant waste gas feed rate of 1kmol/h.

The variation of the ratios H_2/CO from the oxidation reactor, based on varying compositions of H_2O and CO_2 at a constant waste gas feed flow of 1 kmol/h of the mixture is presented in Figure 58(b). The formation of H_2 is 18 times more than that of CO for a waste gas containing 80% of water vapour and 20% of CO_2 at a temperature of 500°C. However, at the same temperature, for a gas containing 80% CO_2, the H_2/CO ratio is about the same ratio as H_2O/CO_2. Indeed, as can be followed from the previous discussions, with the formation of H_2 peaking at around 600°C, with the corresponding increase in the CO yield, the ratio of H_2/CO decreases to about 2.5 even with 80% H_2O at the feed stream. This would result in the outlet gas to contain a significant fraction of unreacted H_2O, while all the CO_2 would have been converted to CO. At higher fractions of CO_2, higher temperatures would yield better result from the conversion perspective of the waste gas feed. It needs to be mentioned, that higher flow rates were also studied for variation of composition with similar trends. By such consideration, therefore, the need for determining the operating temperature of the oxidation reactor, depending on the composition of the waste gas, would play a crucial role in determining the most effective conversion, besides ensuring complete oxidation of the reduced metal. Also, the importance of the requirement of the H_2/CO ratio for subsequent downstream processes is to be given importance. Nonetheless, it can be concluded that for waste gases, with large fractions of water content, it is preferable to maintain the oxidation reactor at a temperature about 600 to 700°C to ensure maximum reactivity of H_2O. However, for higher CO_2 content, typically occurring for exhaust of power plants, the temperature of the oxidation reactor can be set at higher temperatures of around or above 900°C, thereby ensuring high conversion of CO_2, and also presenting the possibility to operate the redox cycle at isothermal conditions.

4.3.3 Heat balance

The heat necessary for the reactions to occur in the reduction reactor and the heat that must be removed from the oxidation reactor to ensure the isothermal operation is plotted in Figure 59(a) and (b) respectively. The methane reduction reaction is endothermic over the entire thermodynamic conditions studied. Interesting, however, is to note the similarity of the heat demand curve with the reaction extent plot, as in Figure 59. The lower heat rates at lower temperatures and molar feed ratio can be attributed to the lower reactivity between ceria and methane. However, with complete reactivity, the heat requirement stabilizes to 50kW per mole of CeO_2 reduced. Indeed, for complete conversion of methane, with a molar feed rate ratio of over 0.7 to 0.8, and above 900°C, the heat required for the reaction to occur stabilizes.

On the other hand, the oxidation reaction is exothermic over the entire thermodynamic conditions considered in the paper. As follows from thermodynamic laws, an exothermic reaction is favoured at lower temperatures. This is indeed represented in Figure 59(b), where, at lower temperatures, the heat released from the reaction is much more pronounced, than the heat released at higher temperatures. Additionally, at lower temperatures, the heat released is primarily from the splitting of water, which is much more exothermic than the corresponding CO_2 splitting reaction, which gains predominance at higher temperatures. However, the overall reaction continues to be exothermic. Indeed, the drop of exothermicity at higher temperatures impact on the overall system efficiency and thermodynamics and has been subsequently discussed in the following sections.

As discussed, the advantage of ceria reduction by methane is the lowering of the reduction temperature. Therefore, as can be deduced from the present analysis, an isothermal system with complete reduction and oxidation of ceria in the respective reactors can be obtained via the present layout. This, however, would limit the isothermal operation zone to between 850-950°C, since this would ensure the complete reduction and corresponding oxidation of CeO_2 with the selected flow of methane as discussed earlier. In fact, it is interesting to note, that even though the oxidation reactor is exothermic, the exothermicity is lower than the endothermicity of the reduction reactor within the defined range of isothermal operations. Hence, external heat would be required for driving the system. Often, due to elevated temperatures of 900°C or 1000°C, concentrated solar is implemented to provide the necessary heat, more specifically required for the reduction reaction.

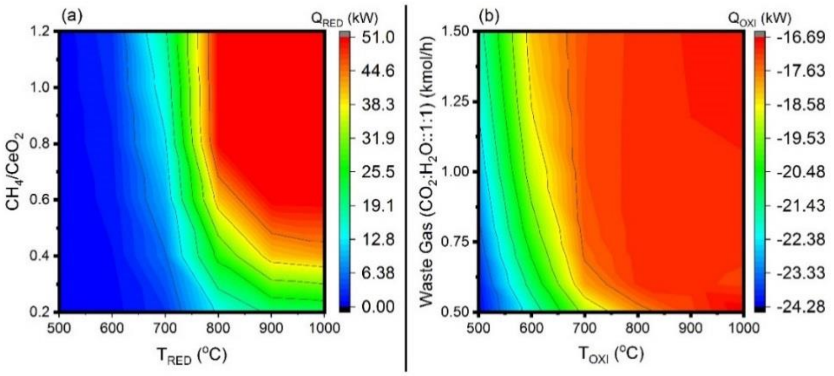

Figure 59. Heat need/release from the reduction and oxidation reactions as per: (a) with a variation of CH_4/CeO_2 feed ratio and temperature in the reduction reactor; (b) with a variation of the waste gas flow at an equimolar mixture composition and temperature in the oxidation reactor.

4.4 Efficiency assessment

To evaluate the system performance and identify the scope of improvement, the efficiency of the system plays a significant role. As the case, two parallel streams of syngas are produced, of which, however, the syngas from the oxidation reactor is the main aim of such thermo-chemical cycles, as the goal of the system is to produce a syngas from waste streams of CO_2 and H_2O. In the reduction reactor, methane is converted to syngas to drive the redox cycle with the methane content in the syngas varying significantly depending on the operating conditions of the reactor (i.e., temperature and CH_4/CeO_2 fraction). Even with high fractions of unreacted CH_4, this syngas can be utilized for multiple purposes as well. Besides being further upgraded to syngas by chemical conversions via steam reforming reactions, it can be utilized directly for combustion. However, efficiencies of such conversions are directly dependant on the downstream conversion process required and hence was left out of scope within the present definitions. In the case that the methane is fully converted, and the reduction syngas composition matches with the one of the syngas obtained in the oxidation reactor, the two syngas flows can be mixed for a subsequent use in the same process.

Therefore, considering the diverse opportunities, two efficiencies were defined for the proposed system considering the performance of both the reactors, the preheating requirements of the solids and gas reactants in both the reactors, as well as the heat recuperated from solid. The first efficiency takes into account the syngas produced in both the reactors, while the second efficiency is defined considering only the syngas from the splitting of CO_2 and H_2O in the oxidation reactor.

Based on the described conditions, equation (4.11) depicts the system efficiency for the two-step chemical looping syngas production via methane reduction and subsequent CO_2 and H_2O splitting considering syngas produced in both the reactors, while equation (4.12) depicts the system efficiency considering only the syngas produced in the oxidation reactor.

$$\eta_1 = \frac{(\dot{m}_{H_2} LHV_{H_2} + \dot{m}_{CO} LHV_{CO})_{RED} + (\dot{m}_{H_2} LHV_{H_2} + \dot{m}_{CO} LHV_{CO})_{OXI}}{(\dot{m}_{CH_4} LHV_{CH_4} + (\dot{Q}_{RED} - \dot{Q}_{OXI}) + \dot{Q}_{\text{need, net}}\ ) + (\dot{Q}_{\text{sphtr}} - \dot{Q}_{\text{sld}})} \tag{4.11}$$

$$\eta_2 = \frac{(\dot{m}_{H_2} LHV_{H_2} + \dot{m}_{CO} LHV_{CO})_{OXI}}{(\dot{m}_{CH_4} LHV_{CH_4} + (\dot{Q}_{RED} - \dot{Q}_{OXI}) + \dot{Q}_{\text{need, net}}\ ) + (\dot{Q}_{\text{sphtr}} - \dot{Q}_{\text{sld}})} \tag{4.12}$$

Where $\dot{Q}_{RED}$ is the heat requirement at the reduction reactor, $\dot{Q}_{OXI}$ is the heat released from the oxidation reactor, $\dot{Q}_{\text{need,net}} = (\dot{Q}_{\text{need,CH4}} + \dot{Q}_{\text{need,waste gas}}) - (\dot{Q}_{\text{syngas,OXI}} + \dot{Q}_{\text{syngas,RED}})$ is the net heat needed for the system operations, including the heat needed for methane and waste gas heat-up and the heat recovered from the syngas product streams, that are directly used to pre-heat the inlet gases, and hence included in the defined manner. ($\dot{Q}_{\text{sphtr}}$- $\dot{Q}_{\text{sld}}$) represents the net heat required to preheat the solids in case of the operation of the two reactors at different temperatures, with the reduction reactor at a higher temperature due to thermodynamic considerations. $\dot{Q}_{\text{sld}}$ represents the heat recovered from the solids from the reduction reactor before it enters oxidation, while $\dot{Q}_{\text{sphtr}}$ is the heat delivered to the solids for preheating. Heat losses from system components were neglected in the efficiency assessment.

4.4.1 Efficiency evaluation

To illustrate the benefits of the proposed cycle as per the definition of efficiency, the results of the effect of the operating parameters on the efficiency of the system are presented in the following section. The impact of the variation of the feed flow rate of the oxidation reactor, as well as the variation of the gas composition on the overall system efficiency, for constant methane to ceria feed ratio of 0.8 to the reduction reactor is shown in Figure 60. The impact on the combined efficiency definition, considering both the reactors have been discussed since a constant CH_4/CeO_2 ratio of 0.8 would yield a fixed output from the reduction reactor above 900°C. The optimal temperature of operation of the reduction reactor being identified as 900°C, the efficiency study has been carried out at temperatures of 900°C and 950°C. It is seen that neither the variation of the flow of the waste gas nor the composition of the gas has a significant impact on the net system efficiency. A slight decrease in the efficiency is however noticed for an increased water content for the waste gas flow. Acknowledging the fact that the minimum flow, that is 0.5 kmol/h of waste gas, corresponds to the stoichiometric conditions, and that the present thermodynamic conditions are feasible for the splitting reactions, (4.2a) and (4.2b), the results indicate the complete oxidation of the reduced metal. Indeed, with an increase in the flow of waste gas, stoichiometric fraction of the CO_2 and H_2O takes part in the reaction, with the excess gases remaining unreacted.

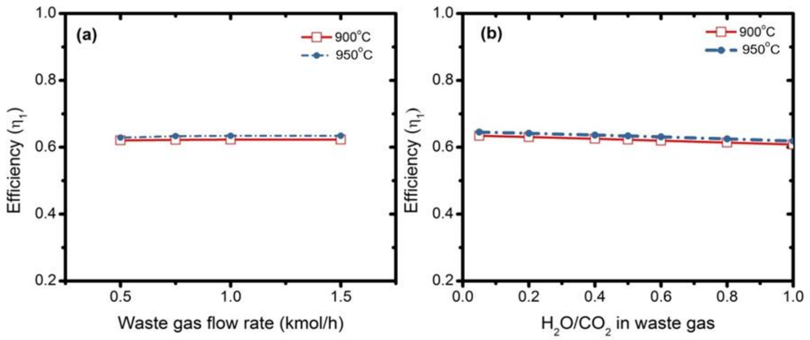

Figure 60. Variation of system efficiency considering syngas from both the reactors based on the parametric variations within the oxidation reactor, at a constant CH_4/CeO_2 flow ratio of 0.8 in the reduction reactor based on: (a) variation of waste gas flow rate at a constant equimolar mixture of CO_2 and H_2O and temperature; (b) variation of waste gas composition and temperature.

The impact of the variation of the methane to ceria feed flow in the reduction reactor on the system efficiency considering syngas from both the reactors is shown in Figure 61, together with the corresponding total CO and H_2 yield as obtained from both the reactors. The feed flow in the oxidation reactor was kept constant at 1 kmol/h, and an equimolar flow of CO_2 and H_2O was considered, with an isothermal redox cycle operation between 800ºC and 950ºC. At 800ºC and with a CH_4/CeO_2 flow ratio of up to 0.8, the metal oxide remains largely unreacted, leading to system efficiencies of about 60%, always lower than that of the system working at higher temperatures of 900ºC and 950ºC. At temperatures over 850ºC, the methane conversion becomes 99%, even at lower than stoichiometric flow rates. However, with lower than stoichiometric flow rates of methane to the reduction reactor, even though methane conversion is maximum, a part of the ceria remains unreacted. By definition of efficiency, this leads to a high system efficiency of around 90%, even though the total yield of CO and H_2 is considerably less than the maximum potential. At a methane to ceria flow ratio of 0.5 and below, the yield corresponds to only around 50% of the maximum potential yield of the redox system, which starts occurring at CH_4/CeO_2 flow ratios of 0.7 at temperatures over 850ºC and 0.8 for a temperature of 800ºC. Indeed, once the yield of the system becomes comparable irrespective of temperature at CH_4/CeO_2 flow ratio over 0.8, the system efficiency starts becoming comparable irrespective of the working temperature of the system.

Based on the defined efficiency η_1 the excess methane plays no significant role in increasing the H_2 and CO yield of the system, however, it decreases the system efficiency. Following the discussion, to ensure high system efficiency together with maximum possible system yield, the system should operate with a CH_4/CeO_2 molar feed ratio between 0.7 and 0.8 at a temperature of 900ºC or higher. In these conditions the efficiency is around 70%, yielding 1.2 kmol/h of H_2 and 0.8 kmol/h of CO from a stream of 1 kmol/h (CO_2/H_2O ratio equal to 1).

Corresponding to the definition of the system efficiency with only the yield from the splitting reaction, an overall system efficiency of 16%, corresponding to the maximum system yield is obtained, as can be visualized from Figure 62. This result, indeed, is comparable to solar thermochemical cycles, showing similar efficiency trends where only syngas from splitting reaction is prevalent. The trend of both the efficiencies is similar, further justifying the need to operate within the specific region as already discussed in the previous sections for maximum system effectiveness and resource utilization.

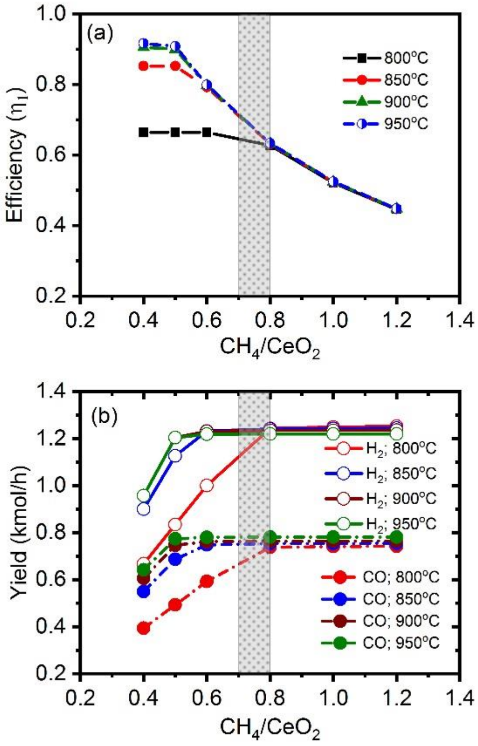

Figure 61. Impact of the CH_4/CeO_2 molar feed ratio and temperature, based on an isothermal system operation and a constant flow of 2 kmol/h of waste gas at equimolar composition within the oxidation reactor on (a) the system efficiency, η_1 (b) net H_2 and CO yield from the redox cycle, considering both the oxidation and reduction reactors.

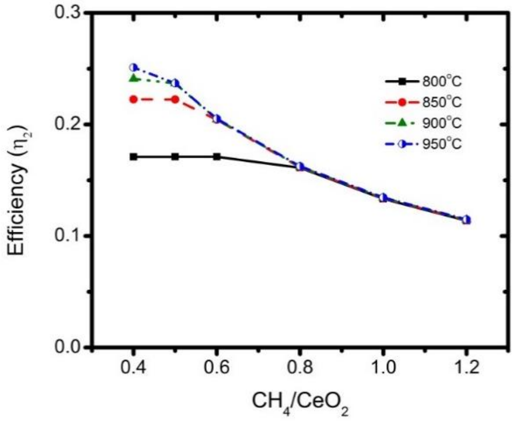

Figure 62. Impact of the CH_4/CeO_2 molar feed ratio and temperature, on the system efficiency considering only the yield from CO_2 and H_2O splitting (η_2), based on an isothermal system operation and a constant flow of 1 kmol/h of waste gas at equimolar composition within the oxidation reactor.

4.5 Pinch analysis

The pinch analysis has been also performed to evaluate the thermal integration within the thermochemical cycle for an isothermal operation at 950°C. Results are shown in Figure 63.

As can be seen, the amount of high-temperature heat needed is significant due to the highly endothermic reduction reaction. Such heat, however, can be provided either through concentrated solar energy – even if this option could not allow the continuous operation of the system – or by burning a fuel, for example, additional methane or renewable fuels, thereby enabling the system to run continuously. Even combined solutions can be proposed, by providing heat from burning fuels only to integrate the solar heat flux when it is not sufficient. The analysis of these solutions is outside of the scope of the present work.

Indeed, as can be seen, due to the considerable amount of heat content from the exiting product gas streams from both the reactors, a considerable amount of heat is available at lower temperatures, increasing the system efficiencies as per the defined efficiencies. Integration to larger systems, therefore, would yield benefits through the availability of significant amounts of low-temperature waste heat.

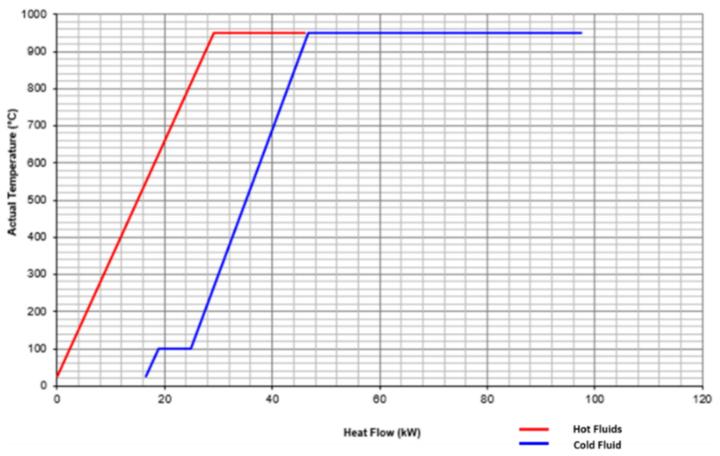

Figure 63. Pinch Analysis of the methane driven chemical looping cycle at an isothermal temperature of 950ºC.

4.6 Concluding remarks

In this chapter, the performance of the CeO_2/Ce_2O_3 redox pair was evaluated for chemical looping syngas production through methane reduction and carbon dioxide and water splitting using thermodynamic analysis. Process simulation was performed to identify the most favourable working conditions with corresponding efficiency evaluation. In the fuel reactor, syngas production was studied via reduction of the metal oxide by methane. For the primary aim of the reduction reactor to produce syngas, methane to CeO_2 feeding ratio of 0.7 to 0.8 at a temperature of 900ºC was obtained as the most suitable condition, resulting in a complete reduction of CeO_2 to Ce_2O_3 while avoiding the formation of CO_2 and carbon deposition. The temperature and composition of waste gas (a mixture of CO_2 and H_2O), coupled with the end use of produced syngas would govern the operating conditions of the oxidation reactor. However, water splitting reaction peaks at temperatures between 600-650ºC, while a monotonic increase of CO production with the temperature was obtained for CO_2 splitting reaction. A minimum molar flow of 0.75 kmol/h of waste gas at the equimolar composition of CO_2 and H_2O would be required to oxidize a flow of 0.5 kmol/h Ce_2O_3 completely to CeO_2 to close the redox cycle. This corresponds to a flow of 50% excess than the stoichiometric quantity. Further, the system efficiency was evaluated based on two defined efficiency terms for the chemical looping configuration. It is observed that the variations of the flow of waste gas (a mixture of CO_2 and H_2O), as well as the composition had little or no impact on the overall system efficiency. Nevertheless, for lower flows of methane, high system efficiency was obtained, however with lower yields of H_2 and CO. A system efficiency of around 70%, considering syngas from both the reactors, with a production of syngas composed by 60% H_2 and 40% CO was obtained for an isothermal operation at 900ºC or higher, as the optimum for the entire chemical looping cycle. However, the value drops to 16% while considering only the syngas from splitting of CO_2 and H_2O. The corresponding isothermal system temperature needs to be 900°C between the reduction and oxidation reactor. In the end, it can be concluded that these results can be taken as a limiting basis for techno-economic assessment studies in determining the feasibility of adding the chemical looping splitting unit to the power plant and investigating its efficiency, CAPEX and LCOE.

Chapter 5

Techno-economic and exergetic assessment of an oxy-fuel power plant fueled by syngas produced by chemical looping CO_2 and H_2O dissociation

The major challenge of implementing carbon capture and sequestration is the impact of energy penalty and loss of efficiency points even though it ensures lower emissions of the power plant from fossil fuels. Plant scale configurations integrating chemical looping for power production has been carried out, however, utilizing thermal reduction through concentrated solar power. Even though Gencer et al [192] proposed a system for solar hydrogen generation with subsequent round the clock power production at an average efficiency of 35% with ceria as the oxygen carrier [192], till date, no complete system analysis of the NGCC power production with the chemical looping CO_2/H_2O splitting unit with methane reduction of ceria has been studied for utility-scale applications. Furthermore, comparative evaluation of individual capture technologies from the existing literature is difficult due to variations in modelling assumptions regarding the type of fuel used, the scale of power output and efficiencies of individual process units. In the previous section, an add-on unit with solar reduction of ceria has been proposed and evaluated, however, with limitations of optimal operation round the clock, variation of yield with the availability of solar energy and need for operation under very high vacuum conditions. Indeed, unlike the previous plant layout design, the present design focuses on a new NGCC power plant integrated with the CL unit, rather than retrofitting existing power plant. This is because the methane reduction of ceria would necessitate considerable system design changes to the original plant. In the present chapter, a 500 MW Oxy-fuel combustion power plant integrated with a chemical looping CO_2/H_2O dissociation with methane reduction of ceria (OXY-CC-CL) unit has been proposed and evaluated.

5.1 Introduction

Of all the existing carbon capture technologies in power plants, oxyfuel power plants are considered as the most easiest and efficient technology as it can capture CO_2 100% within minimal modification. Several studies have alternately proposed to increase the efficiency for carbon capture. Improving efficiency through a novel chemical looping air separation technology has been proposed by Moghtaderi [239]. From a system perspective, chemical looping combustion has been shown to have considerable potential for a relatively high efficiency of power production together with carbon capture. For a pulverized coal power plant, around 39% efficiency was calculated while ensuring a CO_2 capture efficiency of almost a 100% [288]. Innovative system integration has shown the further possibility to decrease the energy penalty of carbon capture. From the chapter 3 it can be deduced that the solar thermochemical looping operation is limited to the availability of solar energy and that can reach too high temperatures for longer period meaning that capacity factor of the solar based plant is around 25% only, Solar field and other optical systems that are required to attain high temperatures and few hour operations lead to high capital investment and localized cost of electricity. One of the alternatives to the high-temperature reduction, temperature and pressure swing between reduction and an oxidation step is to replace thermal reduction to fuel (methane) reduction to lower reduction temperature and can be able to operate at near atmospheric.

Plant scale analysis of chemical looping combustion coupled with NGCC for carbon capture has been analysed with a net electrical efficiency of 43%, an energy penalty of 14%-points with respect to the NGCC plant without capture [289]. However, till date, no complete system analysis of the NGCC power system with the chemical looping (CL) CO_2/H_2O splitting has been studied for utility-scale applications. Furthermore, comparative evaluation of individual capture technologies based on existing literature is difficult due to variations in modelling assumptions regarding the type of fuel used, the scale of power output and efficiencies of individual process units. In the present work, an Oxy-fuel combustion power plant integrated with a chemical looping CO_2/H_2O dissociation (OXY-CC-CL) unit has been proposed. The objective of this work is to analyze the techno-economic, exergetic and environmental performance of the OXY-CC-CL unit compared to traditional NG-fueled power cycles. The results have been compared with a conventional NGCC without carbon capture and an Oxyfuel-combustion power plant (OXY-CC) with carbon capture technology through simulation studies via common modelling assumptions and considerations. The two capture technologies were analysed against a conventional NGCC process without carbon capture to estimate and compare, besides the energy penalty associated with CO_2 capture, economic and other environmental impacts as well. An overall exergetic performance comparison was also performed for the NGCC, OXY-CC and OXY-CC-CL processes. A detailed exergetic study was carried out for the proposed

OXY-CC-CL layout to identify the sources of irreversibility, and hence, the scope for improvement and optimization. Power production, power consumption, electrical efficiency, CO_2 capture efficiency, exergy, economic performance, land and water footprint are the key parameters investigated and their variation is reported in the present work.

5.2 Methodology

The present study performs a techno-economic and sustainability assessment of the proposed Oxyfuel power plant with Carbon Capture integrated with chemical looping CO_2 and H_2O splitting (OXY-CC-CL) compared to state of the art NGCC and Oxyfuel NGCC with carbon capture. Based on the literature reported CeO_2 is selected as an oxygen carrier.

In this process, to integrate the system with a traditional oxyfuel power plant, methane reduction of ceria has been considered as an alternative to thermal reduction. Recently one experimental study reported that CeO_2 reduced to Ce_2O_3 above 900°C completely when reduced with methane [87]. However, this claim is subject to investigation based on the size of the material and quantity of the material chosen and microstructural studies need further investigation to support the claim. In the present study, a thermodynamic redox pair of CeO_2/Ce_2O_3 for stoichiometric reduction of ceria for maximum redox pair utilization was considered to evaluate the highest possible performance of the integrated system as described in chapter 4. Accordingly, the CeO_2/Ce_2O_3 redox pair with reduction of CeO_2 by methane, and subsequent oxidation with CO_2/H_2O was utilized, as described by the equations (4.1-4.2).

The system performance and techno-economic assessments of the OXY-CC-CL power plant were carried out as per the methodology depicted in Figure 64. It should be stressed that several alternative plant configurations, differing in strategies for integration of the CL unit to the traditional system and subsequent mode of utilization of the syngas generated from the oxidation reactor were conceptualized and examined. However, all possible combinations of interest could not be presented within the scope of the present work. The assessments presented herein were performed using a combined Aspen Plus model and an in-house spread-sheet developed specifically for the current study.

The process evaluation, techno-economic study and sustainability assessments summarized in this paper does not include considerations of retrofitting existing state of the art NGCC or oxyfuel NGCC power plants. This is due to the considerable complexity identified for such integrations, which can be found within the explanation of the subsequent sections.

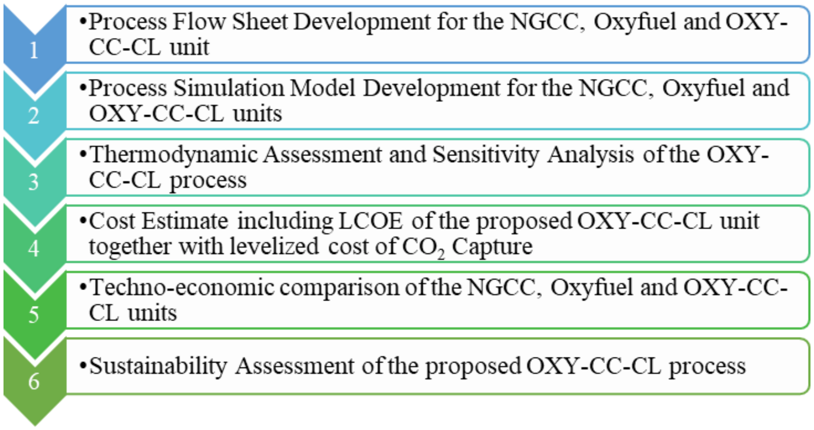

Figure 64. Methodology for techno-economic and sustainability assessment.

The process simulation models and corresponding technical analyses were developed in Aspen Plus®, version 8.8 to investigate the performance of the proposed system (OXY-CC-CL) in comparison to the traditional plant configurations (NGCC and oxyfuel combustion based NGCC with carbon capture (OXY-CC)). The key technical performance indicators evaluated are (i) plant thermal efficiency, (ii) plant thermal efficiency penalty, (iii) relative efficiency gain, (iv) plant exergetic efficiency and (v) plant-specific emission savings.

The economic assessment of the proposed OXY-CC-CL unit with the corresponding comparison with NGCC and OXY-CC with Carbon capture was performed based on the different cost data available in the literature. The key economic performance indicators evaluated are (i) power plant capital cost, (ii) operating costs, (iii) Levelized Cost of Electricity (LCOE) and (iv) cost of CO_2 avoided as Levelized Cost of CO_2 Savings. Besides techno-economic assessment, sustainability assessment through water and land footprint assessment was performed based on existing methodologies available in the literature.

5.3 Process description and plant configuration

Figure 65 presents the block diagrams of the conventional NGCC, OXY-CC and the novel CL coupled Oxyfuel (OXY-CC-CL) process. The process description of the traditional NGCC and OXY-CC are outside the scope of this work and can be found in the literature [245,289]. A complete CL integrated novel Oxyfuel NGCC power plant (OXY-CC-CL), comprising several operating units including the reduction reactor (RED) and the oxidation reactor (OXI), as integral parts of the CL unit, together with traditional units of an oxyfuel power plant including the cryogenic ASU has been proposed and described in the following section.

The heart of the proposed OXY-CC-CL plant is the chemical looping CO_2/H_2O splitting unit (CL). The CL unit works at a considerably lower pressure than that of the natural gas supply of around 70 bar from the gas networks from the outside battery limit (OSBL). Therefore, the gas needs to be expanded to the working pressure of the CL unit. Pre-heating of the inlet natural gas by the process heat of the power plant can considerably improve the net work obtained by such expansion. Also, it would prevent the expanded natural gas from going to sub-zero temperatures after expansion. The expanded methane is further pre-heated and supplied to the reduction reactor (RED) where it is partially oxidized into CO and H_2, producing syngas, while reducing the cerium (IV) oxide to cerium (III) oxide a. The selection of the operating temperatures is crucial to prevent the complete oxidation of the methane to CO_2 and water, simultaneously preventing carbon deposition through methane cracking.

The reduction reaction is highly endothermic, requiring a large amount of supplemental heat to maintain the reforming temperature and drive the reaction forward. The metal oxide reduction by methane is preferably operated at elevated temperatures of above 900^oC to ensure more than 99% conversion of the methane to CO and H_2. However, it has been observed from thermodynamic study carried in chapter 4 that around 40% to 60% excess flow of methane is necessary to ensure complete reduction of metal oxide at temperatures below 950^oC. As also deduced from the same study the most suitable methane to ceria (CH_4/CeO_2) flow ratio was 0.7, higher than the stoichiometric ratio of 0.5, and was hence selected for the present system deployment. As for the pressure, multiple advantages and disadvantages exist for systems working at higher pressures. While solids handling is a major challenge for higher pressure, the previous study by Harrison [290] revealed the economic advantage of methane conversions at a higher pressure between 5-25.3 bar. Also, from Le-Chatelier's principle, the reduction reaction is preferred at a lower pressure while the oxidation reaction is favoured at a higher pressure. Nevertheless, commercial relatively low-cost technologies were found to increase the metal oxide pressure to 6 bar [291], together with the thermodynamic constraints limiting the very high operating pressures for reduction step of thermochemical redox cycle.

In the present power plant, instead of combusting the natural gas directly, the combustion of syngas produced by partially oxidized methane has been proposed. Being an oxyfuel power plant, the combustion is done by near stoichiometric oxygen (5% excess) generated via a cryogenic ASU, that adds to the considerable power penalty to the conventional NGCC. A part of the captured CO_2 is re-circulated back to the combustor to maintain the temperature of the outlet combustion gases into the gas turbine.

The partial oxidation of methane in reduction reactor (RED) is highly endothermic, requiring around 50kW of heat per mol of Ce_2O_3 reduced. A large amount of heat has been proposed to be supplied by heat integration with the combustor of the gas turbine cycle as shown in Figure 65. An annular rector design is hence necessary whereby, the inner reactor would be the reduction reactor of the chemical looping unit, while the outer reactor would perform the work of the combustor. Such a reactor design exists in literature, wherein the detailed information on such reactor design concept can be obtained [292]. Modulating the quantity of CO_2 for recirculation within the reduction reactor, the net duty of the reduction reactor can be controlled, so as to provide the necessary heat required to drive the reduction reaction.

A part of the exhaust from the gas turbine has been proposed to be utilized for CO_2/H_2O splitting within the oxidation reactor (OXI) of the CL unit. A complete reaction would not only generate additional fuel in the form of syngas which will then be utilized to produce additional power but also oxidize the metal oxide back to the higher valence state (CeO_2). The oxidized metal oxide can then be recirculated back to the reduction reactor (RED) to continue the chemical looping cycle. However, auxiliary consumptions from compression for syngas and CO_2 for recycling would necessitate system optimization and identify suitable operating conditions. The oxidation reactions are essentially exothermic, which provides benefits of system control and improvement of efficiency by allowing generation of additional steam, as shown in Figure 65(c). This would also simplify the recycling of the metal oxide between and RED and OXI reactors by eliminating the need of an additional heat exchanger for heating the oxidized metal oxide, and hence requiring lower heat duty for the reduction step. Higher the metal oxide temperature lower would be needed for supplementary heating. Therefore, an outlet temperature of around 1300-1400°C from the oxidation reactor (OXI) would provide a significant advantage, requiring no intermediate heating needs for the oxidized metal oxide and increasing the mass flow of the exhaust gas due to higher recirculation of CO_2.

The exhaust gases from the gas turbines at elevated temperatures of over 800°C would then be utilized for steam generation within the heat recovery steam generator (HRSG). Being an oxyfuel power plant and having natural gas as fuel, the impurities in the exhaust gas, especially SO_x, NO_x and particulates are negligible, allowing the gas to be cooled down to near ambient temperatures of around 50°C, providing considerable advantages to the system efficiency, unlike traditional NGCC, where it is limited to about 140°C to prevent acid condensation. Carbon capture methodologies are followed from traditional oxyfuel units, where, due to the high purity of the flue gas, simple water condensation leads to more than 99% pure CO_2. Following the recirculated fraction of CO_2, the rest is sent for storage after compressing to a pressure of 110 bar.

In general, due to the addition of the CL unit, that recycles and utilizes a part of the exhaust gases within and for the system, a net improvement of the system efficiency has been envisaged. The novelty of this layout is, therefore, to improve the efficiency penalty through the addition of the CL unit to the conventional oxyfuel NGCC with carbon capture while maintaining the same effectiveness of carbon capture by a typical oxyfuel unit of close to 100%.

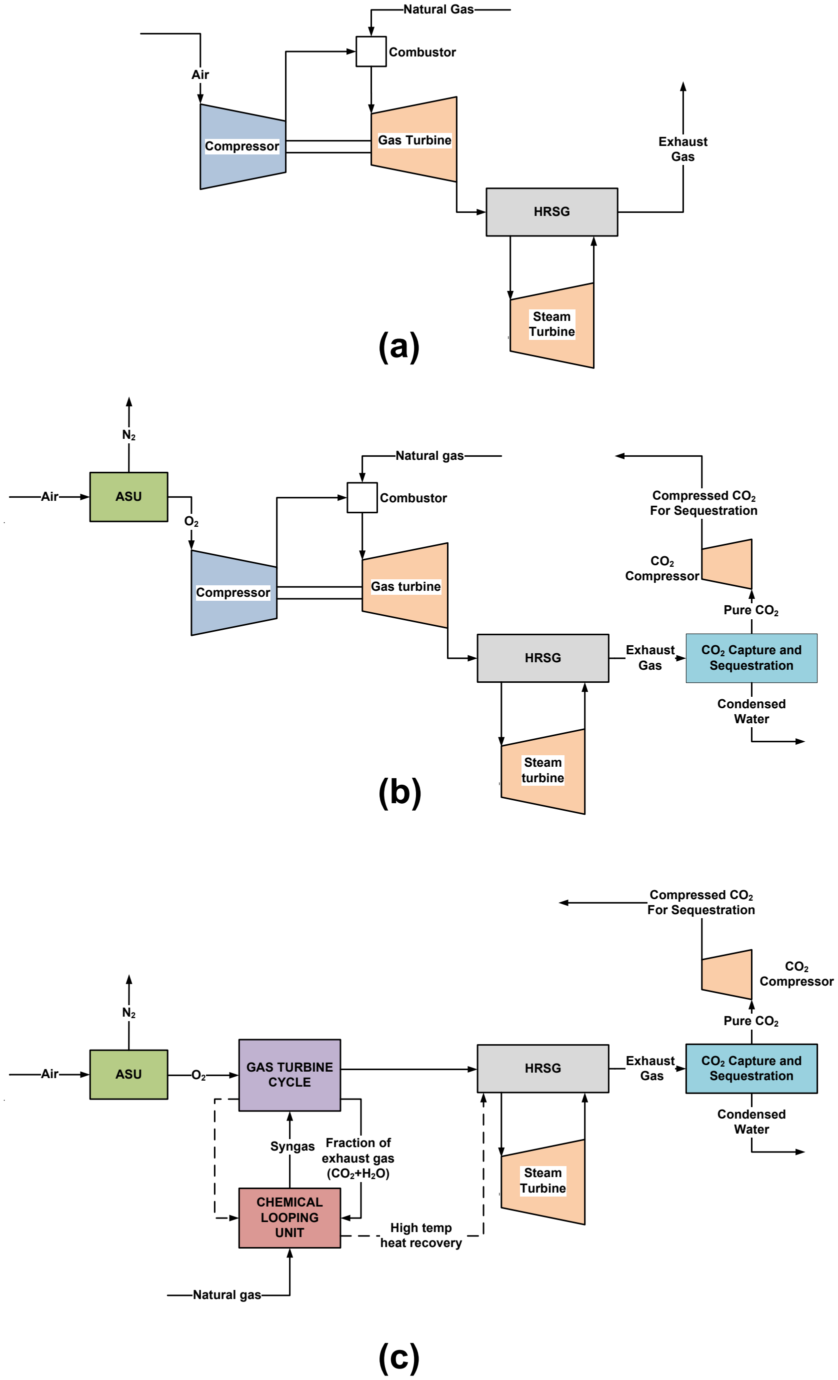

Figure 65. Block diagram of (a) NGCC, (b) OXY-CC and (c) the proposed OXY-CC-CL process.

5.4 Process simulation and assumptions

In this section, the detailed schematic of the conventional NGCC, OXY-CC and the proposed novel OXY-CC-CL are simulated using Aspen Plus® (v 8.8) and its corresponding existing functions and built-in modules. To predict the thermodynamic data and phase behaviour of a material stream, especially for systems for gas processing, it is recommended to use the PR-BM method which utilizes the Peng-Robinson cubic equation of state with the Boston- Mathias alpha function [223]. Therefore, in all the three processes, the PR-BM method was selected for the simulations. The assumptions considered in the three processes for simulation in Aspen Plus are summarized below:

1. The heat losses in the RED and combustion process were neglected, while a pressure drop of 0.1 bar was considered in the combustion chambers (COMB1 and COMB2).
2. A loss of 1% in the high-temperature gas lines were considered, especially for gases being transferred between components.
3. Equilibrium reactions have been considered in the RED and the OXI, as well as the combustion chambers COMB1 and COMB2, where the reaction residence time was long enough to achieve chemical and phase equilibrium.
4. Steady-state simulations were performed, and the results hence obtained are not applicable to start-up or transient operations.
5. Ambient temperature was assumed as 25°C. Also, air was assumed to comprise 79% N_2 and 21% O_2 on a volume basis.
6. Minimum approach temperature in heat exchangers was taken as 10°C [223].
7. The isentropic efficiency and mechanical efficiency for compressors and turbines were considered as 0.9 and 0.98, respectively. The pump efficiency was assumed to be 0.85 and 0.9, for isentropic and mechanical efficiency respectively.
8. In actual scenario, natural gas instead of pure methane would be fed to a reduction reactor (RED). Even though the purity of natural gas with respect to the sulphur content is considerably high, typical clean-up processes would be required. However, the removal of sulphur was not considered within the specific layout. Nevertheless, since no catalyst exists within the entire process, the purity on natural gas would not be a major concern, especially with respect to the operation of the CL unit.
9. The primary objective of the present study is to recognize the potential efficiency gain from the combination of the chemical looping unit in a conventional oxyfuel plant. Thereby, the turbines and the HSRG were modelled as simple units, without reheating or multi-pressure systems. Indeed, by increasing the model complexity, the net efficiency can be gained considerably by process optimization for all three cycles.

Moreover, specific design assumptions with respect to individual units of the NGCC, OXY-CC and OXY-CC-CL units, that were considered, have been shown in Table 11. Indeed, it has to be mentioned that the proposed system is not a retrofit, but a separate entity. Hence, limitations by parameters of a conventional NGCC was not considered applicable to the OXY-CC-CL unit.

Table 11. Design assumptions used for developing the process flowsheet models in Aspen plus.

Unit	Applicable to	Parameters
ASU	OXY-CC and OXY-CC-CL	O_2 purity: 99.9% (by volume); O_2 and N_2 delivery pressure: 1.2 bars; O_2 compression pressure: 26 bars; No use of N_2 was considered.
Turbo Expander	OXY-CC-CL	Feed Pressure of Natural Gas from OSBL: 70 bars; Expansion Ratio: 35; Inlet Temperature of NG: 325° C.
Combustion Chamber	All	Excess Air factor: 182%; Excess Oxygen factor: 5%; Combustor Pressure Drop: 0.1 bar; Combustor working pressure: 18 bars.
Reduction Reactor (RED) and Combustion Chamber, COMB-1	OXY-CC-CL	Reactors were modelled separately with complete heat integration; Working pressure: 26 bars in Combustor Side and 2 bars in Reducer Side; Methane Conversion: 99%.
Oxidation reactor (OXI)	OXY-CC-CL	Reactor Type: Adiabatic, jacketed for high-temperature steam generation; Outlet Product Temperature: 1380°C; Working Pressure: 2 bars
CO_2 Drying and Compression	OXY-CC and OXY-CC-CL	Delivery pressure: 110 bars; Delivery temperature: 40°C Compressor isentropic efficiency: 90%; Compressor mechanical efficiency: 98%
Gas Turbine/ Expander	All	Isentropic efficiency: 90%; Maximum pressure ratio: 18:1; Discharge pressure: 1.04 bar; Turbine inlet temperature (TIT): 1273°C (1550K) for NGCC and Oxy-CL and 1373°C (1650K) for OXY-CC-CL
Steam Turbine and HRSG	All	Single Stage Expansion; Turbine Isentropic efficiency: 90% IP; Steam Pressure: 120 bars for NGCC and OXY-CC and 150 bars for OXY-CC-CL; Condenser pressure: 0.04 bar; Pump Isentropic Efficiency: 0.8; All of the steam generated in gasification island, chemical looping and syngas cooling unit was expanded together; Minimum Approach Temperature: 10°C, no pressure drop

A detailed description of the OXY-CC-CL cycle as simulated within the ASPEN Plus environment is described as per depicted in Figure 66. Natural Gas (as per composition shown in Table 12) is fed into the system at 20°C and 70 bar pressure from outside battery limit (OSBL)[293].

Table 12. NG Composition Assumed.

Component	**Value (% Mole Fraction)**
Methane	94.00%
Ethane	4.20%
Propane	0.30%
CO_2	0.50%
N_2	1.00%
Total	100.00%

This natural gas is preheated with the syngas from the reduction reactor (Stream 4) before being expanded through a turbo-expander (TURBO-EXP) to the operating pressure of the CL unit of 2 bars. The natural gas is then further pre-heated, where it is then fed to the RED at a temperature of approximately 890ºC. The oxidized ceria, in the form of ceria (IV) oxide, CeO_2, (Stream 44), is fed at a temperature of 1375ºC to the reduction reactor. Based on the thermodynamic results, the methane to ceria (CH_4/CeO_2) feed flow ratio of 0.7 is maintained for complete reduction of metallic ceria, to increase its effectiveness as an oxygen carrier. The heat of the reaction in the RED is provided directly by the heat of oxy-combustion of the syngas. The syngas, after exiting the reduction reactor at around 906ºC, is used for methane heating, as well as, preheating of oxygen to around 140ºC before entering the combustion chamber (COMB-1). The cooled syngas, compressed to 26 bars by COMP-1 is fed to the COMB-1. The Combustion outlet temperature and hence the Turbine Inlet Temperature (TIT) is directly regulated by the flow of recycled CO_2, which, however, is also dependant on the heat needed to carry the reduction reactor forward in the RED. The oxygen supplied for combustion is produced via a cryogenic air separation unit (ASU). A cryogenic pump was employed (O-PUMP) to increase the pressure of liquid oxygen removing the need for oxygen compression, thereby significantly reducing the plant auxiliary power consumption.

A turbine inlet temperature (TIT) of 1377ºC was assumed, within the limits of TIT of commercial gas turbines. To take advantage of the fact that the CL unit operates at a pressure of 2 bars, the turbine inlet pressure to the primary gas turbine was set at 26 bars to maximize the system outputs. The expanded gas (Stream-10) from the first gas turbine (GT1-1), around 1115ºC is split into two streams. One stream is fed to the oxidation reactor (OXI) for CO_2 and H_2O splitting to produce syngas as a fuel, while the remaining flue gas (Stream-12) is fed into the second gas turbine (GT1-2), where it is expanded to a near atmospheric pressure of 1.04 bar.

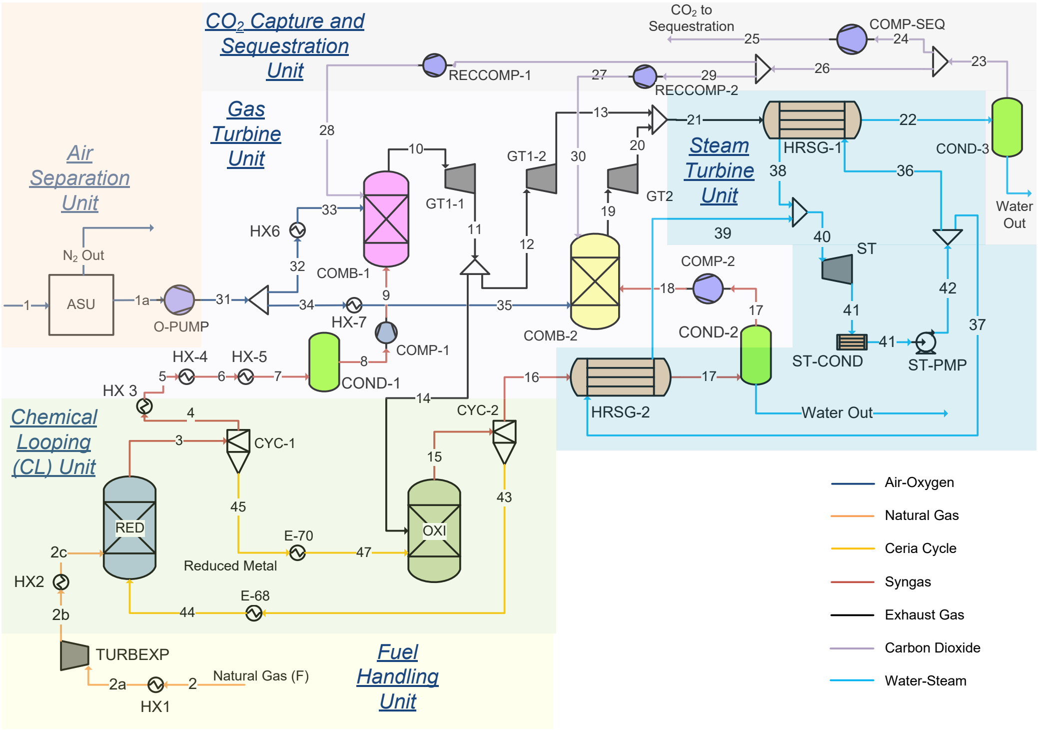

Figure 66. Process simulation flowsheet of OXY-CC-CL unit.

The CO_2/H_2O splitting reactions are highly exothermic, and the metal oxide exit temperature is controlled via jacketed cooling. The product exit temperature of the oxidation reactor (OXI) is set as being equal to the feed temperature of the RED, which is around 1380ºC. The hot raw syngas at around 1380ºC from OXI (Stream-16) is cooled to around 50ºC in a heat recovery steam generation unit (HRSG-2). The cooled raw syngas is compressed to 18 bars (COMP-2) before being fed into the second combustion chamber (COMB-2) and subsequently into the GT2 at 1377ºC, 18 bars (Stream 19). The exhaust gases from the two combustion chambers (Streams 13 and 20) are then mixed and fed into the HRSG (HRSG-1) for heat recovery steam generation by the downstream steam cycle. Being high purity gas, composed primarily of CO_2 and water, the gas was cooled down to near ambient temperatures of 50ºC. A live steam of 150 bars and 596ºC was generated for power production via the steam cycle from both the HRSGs (Stream-38 and 39). The flow of steam was calculated accordingly. As mentioned, a simple single turbine Rankine cycle was modelled. The expanded steam at 0.4 bars is passed through a condenser (ST-COND) and pump (ST-PUMP) to subsequently complete the steam cycle.

The clean and cool exhaust gas from HRSG-1 (Stream-21), at 50ºC and 1.04 bar is passed through a flash chamber (COND-3), where the water is separated and almost 99% pure CO_2 is obtained. This CO_2 is then split into two streams. One stream (Stream-26) is further compressed and recycled back into the combustion chambers for temperature control. However, the other stream (Stream-24) is compressed to 110 bars by COMP-SEQ and sent for sequestration outside the battery limit of the designed power plant. Besides the discussed heat exchangers, no additional heat integration was considered. Indeed, a pinch analysis would be necessary thus to understand the heat availability in the unit and subsequently an improved design with the better and improved location of heat exchangers can be developed in future.

The syngas composition exiting the two reactors of the chemical looping unit is shown in Table 13. The noticeable differences lie in the relative fraction of the H_2 and CO compositions of the two streams. While the H_2/CO ratio in the RED is 1.9, the corresponding value for the OXI is 0.16. Due to the supply of excess methane to the RED, the methane content in the outlet stream of the Reduction reactor is considerable. However, no methane is produced during the splitting reaction in the OXI. The content of water and CO_2 forms about 1.2% in the reduction reactor, while the corresponding value is higher in the OXI since excess reactants were passed to ensure complete reaction.

Table 13. Syngas composition from the Reduction Reactor (RED) and the Oxidation Reactor (OXI) of the Chemical Looping Unit.

Mole fraction (%)	from RED	from OXI
CO	28.43	61.4
H_2	54.23	9.84
CO_2	0.85	18.87
H_2O	0.35	9.63
CH_4	15.71	Trace
N_2	0.43	0.26
Total	100	100

5.5 System evaluation and performance

5.5.1 Thermodynamic performance

To obtain the comparative thermodynamic system performance of the proposed power plant with respect to the traditional power plants, the present analysis has been performed based on both the first and second laws of thermodynamics.

Energy analysis

The energy analysis is based on the First Law of Thermodynamics and considers the principle of conservation of energy applied to a prescribed system. Assuming steady-state operations, together with kinetic and gravitational potential energies being negligible, the energy balance can be written as a rate equation [257] as per the following equation (5.1).

$$\dot{Q}_{CV} - \dot{W}_{CV} + \sum_i m_i h_i - \sum_e m_e h_e = 0 \quad (5.1)$$

where $\dot{Q}_{CV}$ and $\dot{W}_{CV}$ are the specific heat required and work output from the selected control volume respectively, while the following two terms represent the net change in enthalpy between the outlet and the inlet streams of the same.

Nonetheless, this simplified approach fails to provide appropriate system evaluation, especially concerning the correct evaluation of heat flows (in heat exchangers and other components where significant heat transfer is designed to occur).

Exergy analysis

Exergy analysis or availability analysis, based on the second law of thermodynamics, is used to measure the maximum theoretical work [294–297]. The exergy value, unlike the energy value of a stream, is based on its temperature, pressure and compositions as the stream passes from a given state to a state in equilibrium with the environment. Therefore, exegetic evaluation of each material or energy stream is directly related to the assumed environmental state, which, in the present study was considered as T_0=25°C and P_0=1 atm.

For steady state operations of an entire process, the total exergy destruction (Ex_{destr}) can be calculated via exergy balance as written by the following equation (5.2):

$$Ex_{destr} = Ex_{in} - Ex_{out} \tag{5.2}$$

Ex represents exergy, the subscripts 'in' and 'out' representing the inlet and outlet, respectively. The overall inlet exergy is derived directly from the exergy contained within the fuel (Ex_F). For the OXY-CC-CL plant, for the individual components like the compressors and the pumps, the energy required is derived directly from the energy generated within the system. As for heat needed for the reduction reactor of the CL unit, the system is designed to be self-sufficient due to the integration of the RED and the COMB-1. Therefore, no additional external input is necessary for the proposed system in terms of exergy besides the fuel. The outlet exergy including the desired output in the form of electricity (W), material streams in the form of exhausted gas ($Ex_{exhaust}$) and available heat ($Ex_{Q,av}$), can be represented as per equation (5.3).

$$Ex_{out} = W + Ex_{exhaust} + Ex_{Q,av} \tag{5.3}$$

The un-used exergy of the system (Ex_{loss}) is defined as the sum of the amount of exergy destroyed (Ex_{destr}) and the amount of exergy wasted in the exhaust stream ($Ex_{exhaust}$) as shown in the following equation (5.4).

$$Ex_{loss} = Ex_{exhaust} + Ex_{destr} \tag{5.4}$$

A considerable amount of heat might also be available (based on system optimization and pinch analysis) from the proposed system, which adds benefits over the traditional NGCC or the oxyfuel unit ($Ex_{Q,ph}$). Hence, the net system output from the proposed OXY-CC-CL unit can be written as per the following equation (5.5).

$$\mathrm{Ex}_{\mathrm{destr}} = \mathrm{Ex}_{\mathrm{in}} - \mathrm{Ex}_{\mathrm{out}} \tag{5.5}$$

In general, the heat exergy is obtained as per the temperature of the available heat, given by the following equation (5.6).

$$\mathrm{Ex}_{\mathrm{Q}} = \mathrm{Q}(1-(\mathrm{T}/\mathrm{T}_0)) \tag{5.6}$$

where Q is the amount of heat and T represents the temperature at which the heat is available.

For a multicomponent material stream, the exergy (Ex_m) is often divided into three components of exergy, namely, the physical exergy (Ex_{ph}), chemical exergy (Ex_{ch}) and mixing exergy (Ex_{mix}) and written as per the following equation (5.7).

$$\mathrm{Ex}_{\mathrm{m}} = \mathrm{Ex}_{\mathrm{ph}} + \mathrm{Ex}_{\mathrm{ch}} + \mathrm{Ex}_{\mathrm{mix}} \tag{5.7}$$

The physical exergy is defined as the maximum work that can be extracted from a stream when it is made to pass from its current working conditions to the state of equilibrium with the environmental atmosphere [298,299]. The physical exergy is, therefore, dependent on the physical parameters, primarily temperature and pressure and can be calculated by equation (5.8), as obtained through the simulation results.

$$\mathrm{Ex}_{\mathrm{ph}} = (\mathrm{H}-\mathrm{H}_0) - \mathrm{T}_0(\mathrm{S}-\mathrm{S}_0) \tag{5.8}$$

where H and H_0 are the enthalpy flow and S and S_0 are the entropy flow of a material stream at working and environmental state respectively.

Chemical exergy is defined as the maximum work which can be obtained when a substance is brought from the environmental state (physical equilibrium) in a state of further chemical equilibrium with the so-named “dead state” by a reversible process which involves only heat transfer and exchange of substances with the environment [300]. The chemical exergy of pure components can be obtained from Bejan’s reference environmental model [258], where the chemical exergy of a material stream is given by equation (5.9) as follows.

$$Ex_{ch} = \dot{m}\left(y_{0,L}\sum_{i=1}^{n} y_{0,i} Ex_{ch,i}^{0,L} + y_{0,V}\sum_{i=1}^{n} y_{0,i} Ex_{ch,i}^{0,V} \right) \tag{5.9}$$

where $\dot{m}$ is the molar flow rate of a material stream, $y_{0,L}$and $y_{0,V}$ denote the liquid and vapour mole fractions, respectively, $y_{0,i,L}$ and $y_{0,i,V}$ denote the mole fraction of component 'i' in the liquid and vapour phases, respectively and denote the standard chemical exergy of component 'i' in liquid and vapour phases, respectively.

The standard chemical exergies of pure solids, on the other hand, are mostly covered by the values provided by Kotas [297] and Szargut [298] in their respective works. Even though the standard chemical exergy of elementary Cerium (Ce) and CeO_2, as the most abundant form of ceria available in nature is available, the standard chemical exergy of Cerium (III) oxide (Ce_2O_3) is not a reference subject in any readily available literature. However, it can be formed through the reaction of two moles of Ce and 1.5 moles of O_2 with known chemical exergies according to the reaction between Ce and O_2 as per the following equation (5.10).

$$2Ce + 1.5O_2 \rightarrow Ce_2O_3 \tag{5.10}$$

Subsequently, the chemical exergy of Ce_2O_3 can be calculated as per the following equation (5.11).

$$Ex^0_{ch,Ce_2O_3} = 2Ex^0_{ch,Ce} + 1.5Ex^0_{ch,O_2} + \Delta G^0_{Ce_2O_3} \tag{5.11}$$

where Ex^0_{ch,Ce_2O_3}, $Ex^0_{ch,Ce}$ and Ex^0_{ch,O_2} are the standard chemical exergy of Ce_2O_3, Ce and O_2, respectively; $\Delta G^0_{Ce_2O_3}$ represents the Gibbs free energy for the formation of Ce_2O_3 as per Ce/O_2 reaction shown in equation (5.11).

Finally, the mixing exergy, which always has a negative value, and can be estimated by equation (5.12) as per the following equation [223].

$$Ex_{mix} = \Delta H_{mix} - T_0 \Delta S_{mix} \tag{5.12}$$

where ΔH_{mix} and ΔS_{mix} is the enthalpy and entropy change due to mixing respectively. Hence, the common exergetic efficiency (η_{ex}) of the power plants is given as the ratio of the useful exergy output from the system and the necessary exergy input to the process as follows from equation (5.13). On the other hand, the total exergy destruction from the individual components of the overall system is given as the summation of all the individual component exergy destruction as per equation (5.14).

$$\eta_{ex} = \frac{W + Ex_{Q,av}}{Ex_F} \tag{5.13}$$

$$Ex_{destr} = \sum_i Ex_{destr,i} \tag{5.14}$$

Here, $Ex_{destr,i}$ refers to the exergy destruction of i^{th} component.

5.5.2 Economic performance

To evaluate the economic performance of the proposed OXY-CC-CL unit, the most important economic parameters such as the capital cost (including specific investment costs), Operational and Maintenance (O&M) costs, levelized cost of electricity (LCOE) and levelized cost of CO_2 savings/avoided have been considered. In addition, not all the costs of all component were available up to date. In this regard, the chemical plant cost indexes were employed to transfer the literature values to present day values [260]. The basic assumptions presented in Table 9 will be applied to the evaluation except for the annual operation time of 7450 hours considering the capacity factor of 0.85. The cost of the natural gas considered as 0.04 \$/kWh [254]. Other details of economic assumptions are presented in chapter 3.2.7. The levelized cost of electricity is evaluated as per equation (3.31) of chapter 3.

The levelized cost of CO_2 capture (LCOA), on the other hand, is calculated based on the corresponding formula as presented by the equation (5.15). The calculation is based on the discounted expenses of operating the power plant including the investment costs with respect to the emissions saved in comparison to a conventional NGCC.

$$\mathrm{LCOA} = \frac{\sum \frac{\mathrm{I_t + M_t + F_t}}{(1+\mathrm{r})^{\mathrm{t}}}}{(\mathrm{CO_2\ abated / yr}) \times \mathrm{t}} \tag{5.15}$$

5.5.3 Environmental performance

The environmental performance of the OXY-CC-CL in comparison with the conventional NGCC and the oxyfuel combustion units was evaluated based on multiple criteria. The fundamental criteria selected were the CO_2 savings. Indeed, this forms the single most interesting criterion for such assessments. However, other criteria were studied to observe the broader picture with respect to the sustainability of a technology.

Water availability will become a critical issue in the future and especially for plants with carbon capture [301]. In this regard, an analysis of the water requirement with respect to conventional technologies was evaluated after the method proposed by Martin, 2012 [302]. The specific water needs (λ) for the present system in terms of L/kWh was calculated based on the following equation (5.16) accounting for the water needed for both cooling and process applications [302]. An assumption of employing wet cooling tower was considered and corresponding values were selected from the literature.

$$\lambda = \Omega \times (\mathrm{HR} - \Lambda) + \Gamma \tag{5.16}$$

Where Ω is a constant depending on the type of cooling = 5.03×10^{-4} L/kJ based on wet cooling [302]; HR represents the heating rate and Λ represents the net output of the system, both with respect to useful energy in electricity or heat and system losses. Hence, (HR-Λ) represents the amount of cooling load necessary. Γ represents the process water needed by the system other than the cooling system. It is to be noted that the chemical looping unit demands no additional water beside cooling. Therefore, the water need for a conventional NGCC with CCS remains constant also in this case is 0.2 L/kWh [302].

Land footprint assessment is another sustainability criterion, important to analyse the system viability. Indeed, additional systems with increased system complexity would increase the need for space required to accommodate additional units. Florin and Fennel [303] proposed an alternative to the linear model of spatial footprint assessment due to its over-simplistic approach leading to inaccurate evaluations. A suggestion was made to take a modular approach and scale footprint with respect to the number of capture trains. Berghout et al [265] proposed to evaluate the capacity increase of process equipment as the third power of the size (determined by volume) while the capital costs would increase in a quadratic way (based on the surface area). Therefore, the spatial footprint of the capture components for plant scale k (m^2) was assessed as follows from the following equation (5.17).

$$A_k = \sum_i [A_{i,ref} \times (\tfrac{S_i}{S_{i,ref}})^M] \tag{5.17}$$

where $A_{i,ref}$ represents the space requirement for component i for the reference capacity (m^2), S_i refers to the capacity of component i for plant scale k (unit as per the component), $S_{i,ref}$ being the reference capacity of component i for plant scale k (unit as per the component), and M_i refers the scaling factor for component i. After Berghout et al [265], a scaling factor of 0.67 (or 2/3) was used. An additional 20% margin was added to the computed physical footprints considering space requirements for installation and maintenance.

5.6 Thermodynamic evaluation of OXY-CC-CL plant

5.6.1 Energy analysis of OXY-CC-CL plant

Table 14 lists the detailed technical assessment results for the proposed OXY-CC-CL power plant. The results are expressed in terms of power generation from the gas and the steam turbine, overall plant thermal efficiency, total energy penalty, net CO_2 emission savings and relative efficiency gain.

Table 14. Global Energy Flow and Energetic Efficiency of the Proposed OXY-CC-CL Unit.

Plant data	Units	OXY-CC-CL
Fuel Energy Input, LHV (A)	MWth	990.71
Net GT Output	MWe	484.23
GT Output from CO_2 recycling	MWe	110.04
ST Output	MWe	255.94

Gross Electric Power Output (B)	MWe	750.20
ASU Consumption + O_2 compression	MWe	63.38
CO_2 Capture and Compression	MWe	19.22
Power Cycle Pumps	MWe	3.287
Air/ Recycled CO_2 Compression	MWe	142.88
Syngas Compressors	MWe	17.18
Total Parasitic Power Consumption (C)	MWe	245.96
Net Electrical Power Output (D=B-C)	MWe	504.25
Gross Electrical Efficiency (B/A*100)	%	75.72%
Net Electrical Efficiency (D/A*100)	%	50.7%
CO_2 Capture Efficiency	%	100%
CO_2 captured	t/h	178.66
Electric Power Output per tonne of CO_2 Captured	MWh/t	2.822

As can be observed from Table 14 a considerable share of the generated electrical energy is used up for oxygen separation in the ASU and also for recycling the carbon dioxide for being fed into the combustion chamber for temperature control. Some fraction, around 3.8% is also used for compressing the captured CO_2. The extra energy needed for carbon capture and storage is known as the energy penalty with respect to the conventional base case NGCC without carbon capture. These, in addition to the auxiliary power requirement, become the two major penalties for the conversion of energy from the chemical energy of natural gas to electricity. However, generation of around 110 MW of electricity from the recycling of the exhaust gas via splitting of CO_2 and H_2O in the CL unit to produce syngas results in considerable improvement of the net power output, even with almost 100% carbon capture. An impressive energy efficiency of about 51% with carbon capture is obtained. The higher efficiency is achieved due to addition CL unit addition which lowers the energy penalty of carbon capture compared to conventional oxyfuel power plant. Additionally, generation of heat by integration of the power plant units might result in energy savings and decrease the overall penalty by working the power plant on a combined heat and power mode.

5.6.2 Exergy analysis of OXY-CC-CL plant

The exergy flow of the proposed OXY-CC-CL unit is depicted in Table 15. As can be clearly observed, due to both electricity and heat self-sufficiency of the system, the input fuel, namely natural gas contributes entirely (100% of the total exergy input) to the net exergy input to the system. The work consumed for compressors and pumps comprise a relatively small contribution to the entire input exergy (4.83%). However, the ASU alone consumes around 3.04% of the net input exergy of the entire system. The exergy consumed for capturing CO_2 represents a large fraction of the total exergy input (7.27%), which includes the net exergy destruction related to water condensation and compressing the CO_2 to 110 bars for the sequestration.

On the other hand, the majority of the system output is electricity (393.75 kJ/mol of CH_4). The exergy exhausted through the exhaust gas measures 24.4% of the process inlet exergy. Approximately 28.5% of the exergy is destroyed due to irreversibilities within the system. Indeed, the system optimization would considerably improve upon the net exergy destroyed by decreasing the unused fraction of exergy amounting to 52.9% of the net input exergy.

Table 15. Global Exergy Flow and Efficiency of the OXY-CC-CL unit.

	Exergy (kJ/mol CH_4)	% of total Ex_{in}
Net Exergy into the Plant	835.34	100
Exergy in Methane	835.34	100
$W_{compressors}$	40.31	4.83
W_{pump}	0.23	0.03
W_{ASU}	25.43	3.04
CO_2 Capture including CO_2 compression	60.73	7.27
Exergy Out	597.66	71.55
Exhausted gas	203.92	24.41
Exergy destroyed	237.68	28.45
Exergy un-used	441.59	52.86
Exergy efficiency (η_{ex})	-	47.14

To evaluate the primary reasons of exergy destruction in the proposed OXY-CC-CL process, an exergy analysis of each component was performed. The results are listed in Table 16. The methane preheating, occurring between HX-1 and HX-3 before the turbo-expander and HX-2 and HX-4 (hot side and cold side respectively) after the turboexpander is referred to as FPH-1 and FPH-2 respectively as two separate heat exchangers. Also, for physical processes occurring in heat exchangers, pumps, compressors, etc., the chemical exergy is not involved in the energy transformation process, and the component exergy efficiency $\eta_{ex,comp}$ can be predicted by equation (5.13). The final column depicts the relative irreversibility of each component with respect to the net irreversibility of the entire process, that is, reports the component exergy destruction percentage ($Ex_{destr,i}$) with respect to the total exergy destruction (Ex_{destr}).

Clearly, compressors (COMP-1, COMP-2 and RECCOMP 1 and 2) and pump work represent a minor fraction of total Ex_{destr}. Turbines, heat exchangers and the reactors contribute a higher percentage of exergy destruction. The heat exchangers contribute 21.27% of Ex_{destr}, whereby the primary reason for exergy destruction is the heat transfer across a finite temperature difference [304]. However, the exergy destruction from the mixing of the gases from the two turbine outlets plays the most significant role in the net exergy destruction of the proposed power plant, contributing to over 37% of the same.

A significantly high exergetic efficiency can be observed in the combustion chamber due to oxyfuel combustion and also the assumptions of no heat losses. The CO_2 separation unit in the form of the water separator and corresponding CO_2 compression contributes to a significant fraction of the total exergy losses, accounting for over 8% of the total Ex_{destr}.

Therefore, as can be observed from the exergy analysis of each of the component of the OXY-CC-CL a better integration of the entire power plant through design optimization would lead to a considerable decrease in net exergy losses.

Table 16. Exergy balance in OXY-CC-CL break-down by component.

Type	Component	$Ex_{in,i}$(MW)	$Ex_{out,i}$(MW)	Ex_{dest},(MW)	Component η_{ex} (%)	Ex_{destr} % of Total
Physical process	FPH-1	2043.98	2031.8	22.47	99.40	1.33
	TURBEXP	1082.35	1078.34	12.18	99.63	0.438
	FPH-2	2138.06	2089.36	4.01	97.72	5.31
	CMP-1	976.05	975.76	48.7	99.97	0.031
	RECCOMP-1	323.83	303.55	0.29	93.73	2.21
	GT1-1	1007.57	932.69	63.05	92.57	8.17
	GT1-2	859.54	848.36	74.87	98.70	1.22
	HRSG-2	292.64	254.88	36.59	87.10	4.12
	COMP-2	222.67	221.8	37.76	99.61	0.094
	RECCOMP-2	125.54	95.38	0.86	75.97	3.292
	GT2	319.38	287.27	3.17	89.95	3.50
	HRSG-1	628.37	547.73	343.82	87.17	8.80
	ST-COND	25.78	9.63	80.65	37.37	1.76
	ST-PUMP	12.90	12.60	16.14	97.70	0.032
	COND-3	351.95	301.19	0.30	85.58	5.54
	COMPSEQ	73.87	46.87	50.76	63.45	2.95
Physical and Chemical Processes	ASU	63.19	40.73		64.45	2.45
	RED & COMB-1	2653.46	2590.42	20.29	97.62	6.88
	OXI	561.58	524.99	11.18	93.48	3.99
	COMB-2	322.55	319.38	30.17	99.02	0.346
	Mixture	960.75	616.93	32.11	64.21	37.52
	Total	1069.55	501.65	27	7	100

5.6.3 Effect of key operating parameters

The impact of key process variables, viz., temperature, pressure, system size, etc. on the process performance characteristics of the OXY-CC-CL process was systematically examined through a comprehensive series of simulations using the proposed power plant integration scheme. The variation of the outputs from the gas turbines, the steam turbine, the net power output, and the system efficiency have primarily been analysed. Results of these analyses are presented in this section from Figure 67 to Figure 70.

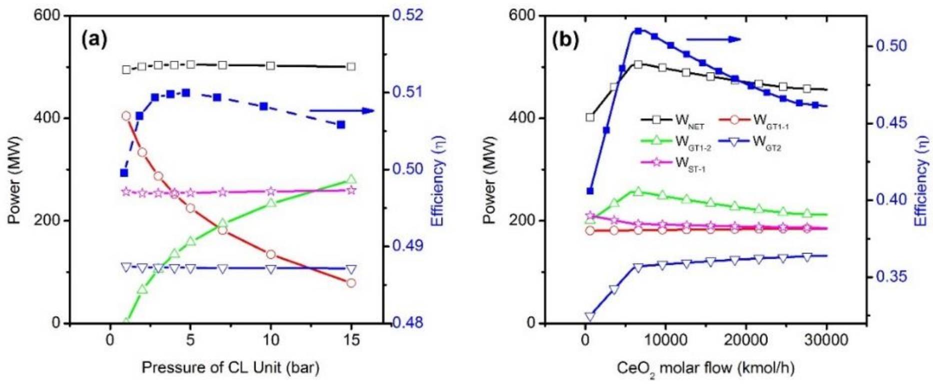

Figure 67. Impact of the variation of a) pressure of the CL unit and b) molar flow rate of cerium oxide (CeO_2) on the power generating components, the net power produced and the efficiency of the OXY-CC-CL power plant at a constant natural gas input flow.

Figure 67(a) represents the effect of operating pressure of the CL unit on the defined parameters. A minimal rise in the net power output from the entire plant is observed with the increase of pressure in the CL unit. While there are a proportional increase and decrease of the power output from GT1-1 and GT1-2 respectively due to varying pressure ratios, the power outputs from the steam turbine and that of WGT2 remains constant. However, at a pressure of 1 bar, the compression ratio of the produced syngas from the CL unit for power generation is the highest, 26, leading to the efficiency recorded as lower than 50%. Indeed, with a rise in the operating pressure of the CL unit, the compressor work for syngas compression decreases considerably. However, beyond 5 bars, the conversion of methane in the reduction reactor drops, together with a relatively lower decrease in the compression ratio of syngas and a low power output from the turbo-expander. These factors combined lead to a drop in the efficiency of the power plant beyond 5 bars to around 50.5% at 15 bars operation pressure of the CL unit.

The performance study of the system with respect to the variation of the circulating metal oxide indicated similar trends in the efficiency of the plant. At lower CeO_2 flowrates in the CL unit, the combustion in the COMB-1 is with natural gas, since no partial oxidation takes place in the reduction reactor (RED). All other parameters remaining constant, this results in a power output similar to traditional OXY-CC, and hence a corresponding low efficiency. However, with the higher CeO_2 flow in the CL unit, the production of syngas in the OXI and subsequent power production through exhaust gas recycling increases not only the efficiency but also the net power output of the system. However, with higher CeO_2 flow rates, and therefore, with a correspondingly higher fraction of exhaust being sent to the OXI, the net yield from WGT1-2 decreases, with no net increase in the efficiency. This leads to a drop in efficiency at very high CeO_2 flow rates (5 times the CH_4/CeO_2 stoichiometry for metal oxide reduction) to as low as 46%. Interestingly, the highest efficiency, around 51% occurs at a CH_4/CeO_2 stoichiometric ratio of around 0.8.

The variation of the fraction of exhaust gas (a mixture of CO_2 and H_2O) from the WGT1-1 to the OXI for syngas production through splitting was investigated. It was observed that a peak system efficiency of 50.7% occurs at a split fraction of 0.1. At lower split fractions, the net utilization of the circulating CeO_2 is low, thereby producing low syngas for power production in WGT2. However, a higher split fraction, even though increases the power generated from WGT2, lowers the power output from WGT1-2. Nonetheless, this simultaneously increases the auxiliary power consumption of COMP-2. This results in the net efficiency to be lowered to around 48.5% with 25% recycling of exhaust gas to the oxidation reactor as seen in Figure 68(a).

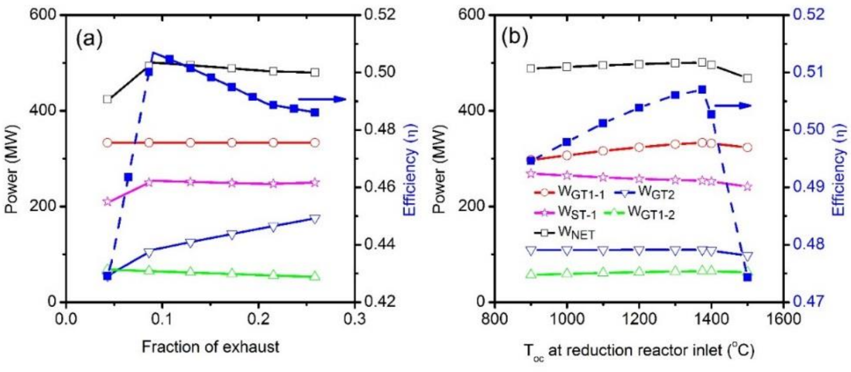

Figure 68. Impact of the variation of a) fraction of the exhaust gas from GT1-1 recirculated into the oxidation reactor (OXI) of the CL unit for production of syngas and b) temperature of the CeO_2 at the inlet of the reduction reactor (RED) of the CL unit on the power generating components, the net power produced and the efficiency of the OXY-CC-CL power plant at constant natural gas inlet flow.

The temperature of the CeO_2 (oxygen carrier) inlet to the reduction reactor (T_{oc}) has a significant impact on the system efficiency as shown in Figure 68(b). An optimal value of about 50.7% is reached at a temperature of around 1375°C. This is directly related to the fact that the endothermicity of the reaction needs to be maintained through variation of the recycled CO_2 in the combustor (COMB-1). This is because, at higher oxygen carrier temperature, the endothermicity of the reaction (equation (4.1)) drops, requiring more carbon dioxide to be recycled to the combustor to maintain the TIT to its desired level. Consequently, an increase in the GT1-1 output power is noticed. However, beyond 1375°C, due to a much lower CO_2 need for recycling, the power output from GT1-1, GT1-2 and ST drop, while the auxiliary power need by COMPSEQ increases significantly, resulting in a steep drop in the system efficiency. Therefore, an efficiency, as low as around 47.5% is obtained at a T_{oc} of 1500°C.

The variation of the Turbine inlet pressure of the Gas turbines was also studied. Commercial scale stationary gas turbines are usually limited to a working pressure ratio of 18:1 [253]. Considering an operation pressure of the CL unit of 2 bars, the inlet pressure of GT1-1 was varied between 15 bars and 30 bars. As can be seen from Figure 69(a), the inlet pressure primarily increases the power output from GT1-1, and therefore, the net system power output, and the efficiency. However, it correspondingly also increases the compression ratio of COMP-1, lowering the net benefit of increased power output to some extent. At a turbine inlet pressure of GT1-1 of 30 bars (pressure ratio 15) an efficiency of 51.2% was obtained.

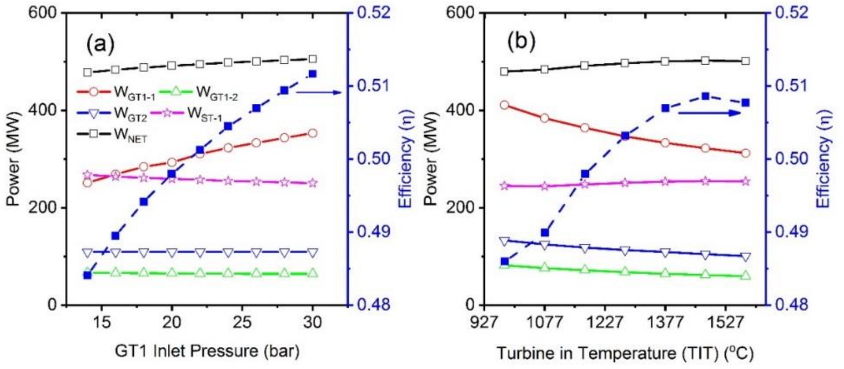

Figure 69. Impact of the variation of a) GT1-1 inlet pressure and b) Turbine Inlet Temperature (TIT) for both the turbines (GT1-1 and GT2) on the power generating components, the net power produced and the efficiency of the OXY-CC-CL power plant at constant natural gas input flow.

Turbine Inlet Temperature (TIT) of the gas turbines critically impacts the system efficiency. All the gas turbines have been assumed to be kept at the same TIT. A lower TIT results in a lower efficiency, more specifically, around 48.5% at 977°C, which is subsequently improved to around 51% for a TIT of 1477°C as shown in Figure 69(b). Hence, the efficiency of the OXY-CC-CL unit, proposed for operation at 1377°C TIT, can be increased further by increasing both the TIT and GT1-1 inlet pressure. Interesting to note, that even if the absolute power output from the individual turbines, besides the steam turbine, decreases, the net power output and the efficiency increases. This can be explained by the fact, with a higher TIT the CO_2 recycled into the combustion chambers (COMB-1 and COMB-2) decreases, thereby considerably improving the overall power output from the system. However, at temperatures beyond 1477°C, due to lower CO_2 recirculation the power output from the all the gas turbines (GT1-1, GT1-2 and GT2) decreases, together with the power output of the ST, while a higher CO_2 compression results in power need of COMPSEQ to increase. This results in a drop of efficiency to about 50.75% at a TIT of 1577°C.

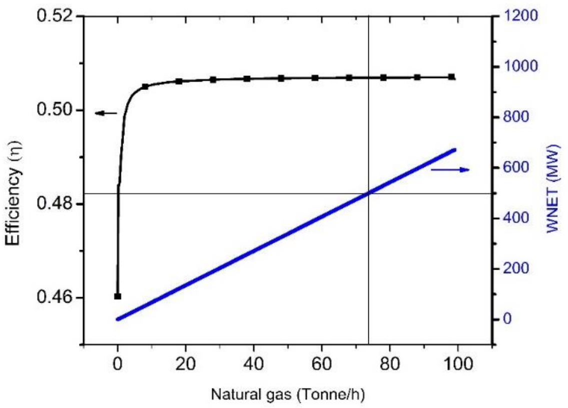

Figure 70. Impact of the variation of natural gas flow rate on the system capacity (net power produced) and the efficiency of the OXY-CC-CL power plant.

Finally, the impact of scale on the system efficiency is depicted in Figure 70. For a 500MW power plant, the efficiency obtained was 50.7% corresponding to a natural gas flow rate of 73.75 tonnes per hour. Indeed, the impact of the scale was obtained to be limited towards the net system efficiency till around 10 MW. As can be seen, the efficiency of the system above 10 MW is constant around 50.7%. However, below such size, the efficiency drops significantly to about 46% for a size of 1MW, limiting downsizing of such systems beyond certain limits as shown in Figure 70.

5.7 Comparative evaluation of the performance of NGCC, Oxy-fuel NGCC with carbon capture and OXY-CC-CL

The performance of the NGCC, OXY-CC and OXY-CC-CL plants are compared on the basis of net electrical efficiency and CO_2 emissions for thermodynamic evaluation. Detailed simulation results for both cases are summarised in Table 17. The base case, without any CO_2 capture, emits 178.65 t/h of CO_2. In contrast, both the OXY-CC and the OXY-CC-CL provides a near 100% capture of CO_2. As per the developed ASPEN plus model, the non-optimized base case NGCC has an efficiency of 54.65%, agreeable to efficiencies of state of the art NGCC, as available in the literature [245,305]. However, this considerably drops due to the addition of the ASU and CO_2 sequestration compressor for the OXY-CC power plant, which has a much lower efficiency of 43.25%. Therefore, an efficiency penalty of more than 11 percentage points can be seen. Indeed, as predicted with the above analysis, the novel OXY-CC-CL unit, with an efficiency of 50.7% was able to improve the efficiency of the power plant by around 7.5 percentage points due to internal recycling of a part of the exhaust gases that can be termed as CO_2 recycling. This also decreases the corresponding relative parasitic load of the power plant due to a relative increase in the net work output from the proposed unit.

Table 17. Plant performance indicators for State of the Art NGCC, oxy-fuel NGCC, and the oxyfuel NGCC with CL unit (OXY-CC-CL) processes obtained by Aspen plus simulations.

Plant data	Units	NGCC	OXY-CC	OXY-CC-CL
Fuel Energy Input, LHV (A)	MWth	910.76	1155.27	990.71
Net GT Output	MWe	693.33	570.37	484.23
ST Output	MWe	160.40	259.04	255.94
Gross Electric Power Output (B)	MWe	853.73	829.41	750.20
ASU Consumption + O_2 compression	MWe		113.51	63.38
CO_2 Capture and Compression	MWe		26.52	19.22
Power Cycle Pumps	MWe	1.88	3.06	3.29
Air/ Recycled CO_2 Compression	MWe	351.75	186.66	142.87
Syngas Compressors	MWe			17.18
Total Parasitic Power Consumption (C)	MWe	353.63	329.76	245.95
Net Electrical Power Output (D=B-C)	MWe	500.09	499.65	504.24
Gross Electrical Efficiency (B/A*100)	%	93.74%	71.79%	75.72%
Net Electrical Efficiency (D/A*100)	%	54.91%	43.25%	50.70%
CO_2 Capture Efficiency	%		100%	100%
CO_2 Emissions	t/h	178.65		
CO_2 specific Emissions	t/MWh	0.505		

Figure 71 shows the relation between power produced and consumed in different units for three cases studied. The net power output from the three cases was kept constant to develop a comparative evaluation. The net thermal energy input from the natural gas is however different in the three different cases resulting in a variation of the net energy efficiency from the three units. In the base case NGCC, the overall heat is completely generated in a single combustion chamber, whereby, the natural gas is combusted with an excess of air. The exhaust gases are then first expanded in the gas turbine for electricity generation and then passed through the HRSG for heat recovery. Similar to this, the OXY-CC also combusts the natural gas in a single step, however, with 5% excess of oxygen and recycled CO_2, resulting in the GT power output to reduce by 77 MW. Unlike the previous two cases, a mixture of CO, H_2, and CH_4 is combusted in the OXY-CC-CL with 5% excess oxygen and over 90% recycled CO_2, lowering further the net power output from the gas turbine. Indeed, for the OXY-CC-CL, the net power output from the gas turbines include two-step expansion, one from 26 bars to 2 bars and subsequently up to 1.04 bar after exhaust gas separation for splitting, together with the gas turbine output from the split exhaust gas containing syngas. This lowers the contribution from the gas turbine, however, increasing the contribution from the steam cycle, comparable to that of OXY-CC unit. Nevertheless, the gross power of the OXY-CC-CL unit is significantly lower by around 100 MW from the base NGCC and 80 MW from the OXY-CC power plant. However, interestingly, the parasitic load of the proposed OXY-CC-CL unit decreases by more than 105 MW and 85 MW respectively than base NGCC and OXY-CC unit, thereby showing better energy performance than the traditional OXY-CC system.

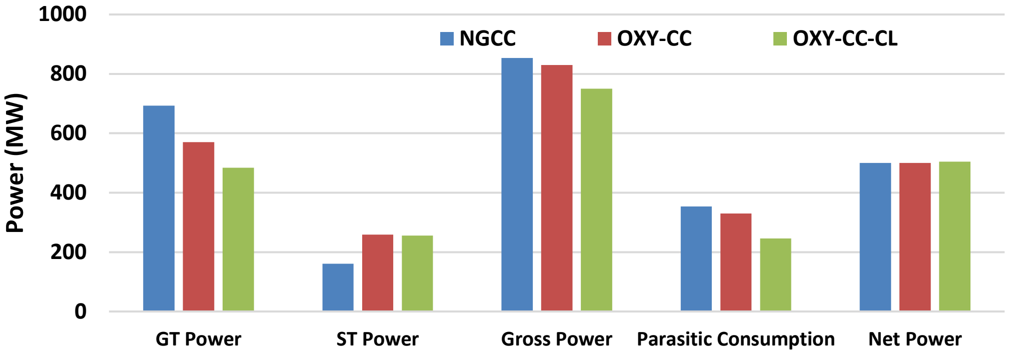

Figure 71. Comparison between GT, ST, gross, parasitic and net power output for base NGCC, OXY-CC and OXY-CC-CL.

Table 18 depicts the comparative energy and efficiency penalty associated with CO_2 capture between the reference base case NGCC, OXY-CC and the proposed novel OXY-CC-CL unit. The relative decrease in net electrical efficiency from the NGCC and the OXY-CC and the OXY-CC-CL units is around 11.4% and 4% respectively. Therefore the proposed new system performs better than Oxyfuel-CC with carbon capture as reported in the CAESER project [263]. The CO_2 captured per MWh of energy expended in the OXY-CC-CL (11.34 t/MWh) is therefore significantly higher than the corresponding energy expended for CO_2 capture in the OXY-CC process (4.35 t/MWh). These results suggest that OXY-CC-CL unit is a more favourable option from the energetic point of view (without economic considerations) to capture CO_2 from NGCC power plants compared to simple Oxyfuel unit. Indeed, a much lower relative efficiency decrease, by about 4 percentage points, with respect to the base case NGCC makes the proposed technology highly interesting for future NGCC power plants with CCS, especially while striving for higher efficiencies. However, the OXY-CC power plant is a practically proven and commercially available technology, while the OXY-CC-CL unit requires considerable further research and optimization to be available for commercial use.

Table 18. CO_2 Captured per unit energy and efficiency penalty with reference to conventional Oxyfuel NG Power Plant.

Plant data	Units	NGCC	Oxyfuel-CC with CCS	OXY-CC-CL with CCS
Energy Penalty (A)	MW		57.63	18.45
CO_2 Captured (B)	t/h		251.01	209.3
CO_2 captured per MW decrease in energy Production than Base Case NGCC (C=B/A)	t/MWh		4.35	11.34
Net Electrical Efficiency (D)	%	54.91%	43.25%	50.7%
Net Electrical Efficiency Penalty Compared to Base Case NGCC, E=(54.65-D)	%		11.52%	3.69%
Relative Decrease in Net Electrical Efficiency Compared to Base NGCC F=E*100/54.65	%		21.08%	6.75%

CO_2 Captured per unit decrease in net electrical efficiency from Base Case NGCC (B/E)	t	21.78	56.72

5.8 Economic analysis

5.8.1 Capital cost and operational expenses

As developed from the process simulations, it can be easily concluded that the OXY-CC-CL unit has a clear technical edge over conventional and advanced NGCC system with and without carbon capture. However, for integration purposes, the OXY-CC-CL unit needs considerable new system additions including solid handling units, reactors for reduction and oxidation, an additional combustion chamber among others. This would incur additional capital investments. Therefore, an economic analysis was performed to find the economic feasibility of the proposed OXY-CC-CL systems and is presented in detail in this section.

Table 19. Capital Cost Breakdown of the proposed OXY-CC-CL unit.

Plant Component	Values (million $)	% Contribution
Primary Gas turbine, generator and auxiliaries	76.09	6.20%
Primary Low-Pressure Gas turbine, generator and auxiliaries	14.79	1.20%
Secondary Gas turbine, generator and auxiliaries	25.1	2.05%
HRSG, ducting and stack	21.39	1.74%
Steam turbine, generator and auxiliaries,	49.76	4.05%
Cooling Water System and Balance of Plant	63.26	5.15%
CO_2 Compressor and Condenser - Compressor 1	16.27	1.33%
Chemical Looping, Combustor and Oxy Reactor	48.72	3.97%
Turbo Expander	2.93	0.24%
Other Heat Exchangers	1.73	0.14%
Total Equipment Costs (TEC)	320.04	26.07%
Cost of Metal Loading	0.01	0.00%
Total Installation Costs	309.1	25.18%
Total Direct Plant Cost (TDPC)	624.48	50.87%
Indirect Costs	87.43	7.12%
Engineering Procurement and Construction Costs (EPC)	711.91	57.99%
Owner's Costs	8.74	0.71%
Contingencies	71.19	5.80%
ASU (Complete CAPEX as an add-on unit)	435.7	35.49%
Total Project Costs (TPC)	1,227.55	100.00%

Table 19 represents the cost breakdown of the proposed OXY-CC-CL unit. The ASU was assumed as an add-on unit, with a CAPEX of $435.70 million, contributing to about 35.5% of the entire plant cost. The net project CAPEX was obtained at around \$1227 million, which amounts to around 2455 \$/kW, a relatively high cost than the present day NGCC power plants without carbon capture, with overnight capital costs reported as 978 \$/kW [271]. On the other hand, the capital costs become comparable to advanced NGCC with carbon capture, quoted around 2050 \$/kW as per the 2016 study by the US Department of Energy [271].

In addition, the operational expenses were calculated based on the assumptions mentioned in the earlier section. The net fixed OPEX was obtained as \$62.58 million, while the variable cost was calculated as 50.15 \$/MWh of gross power generation. Hence a net annual operating cost of \$347.1 million was calculated to run the proposed 500 MW OXY-CC-CL unit.

5.8.2 LCOE and LCOA calculation

LCOE calculations were further developed based on equation (3.31) of chapter 3.2 to perform a comparative evaluation of the system economic performance. As mentioned, no carbon credit was assumed. Correspondingly an LCOE of 128.01 \$/MWh was obtained. However, as depicted in Figure 72, with a carbon credit of 6 \$/tonne CO_2, the LCOE would drop to comparable prices of the average wholesale market price of electricity [306]. Therefore, the importance of carbon credits for such systems to be economically competitive is most crucial.

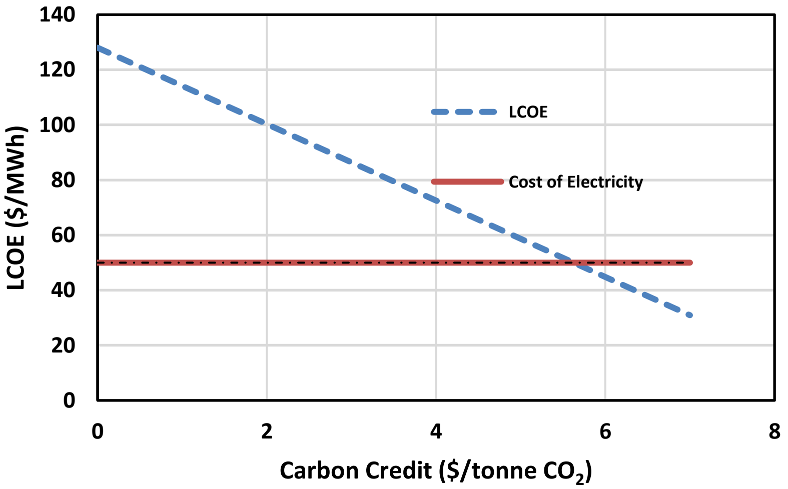

Figure 72. Impact of carbon tax on the levelized cost of electricity of the proposed OXY-CC-CL unit

Additionally, levelized cost of CO_2 savings (LCOA) was calculated to obtain the economic performance of carbon capture. Indeed, as can be seen in Figure 73, the levelized cost of carbon capture for the proposed OXY-CC compares well to those of already available technologies. Indeed, with an LCOA of 96.25 \$/tonne of CO_2, the cost is lower than that of the oxyfuel power plant with carbon capture, reported as 104

$/tonne of CO_2 by Khorshidi et al., 2012 [307]. A higher efficiency, lowering the need for fuel consumption for similar power production is a considerable benefit. As for post-combustion capture, the value is on the higher side, being needed to be integrated for a new and much-complicated power plant, increasing the costs. Also for the OXY-CC power plant, an LCOA of 104 $/tonne CO_2 captured was reported by the study by Rubin et al 2015 [308], higher than that of the OXY-CC-CL unit proposed.

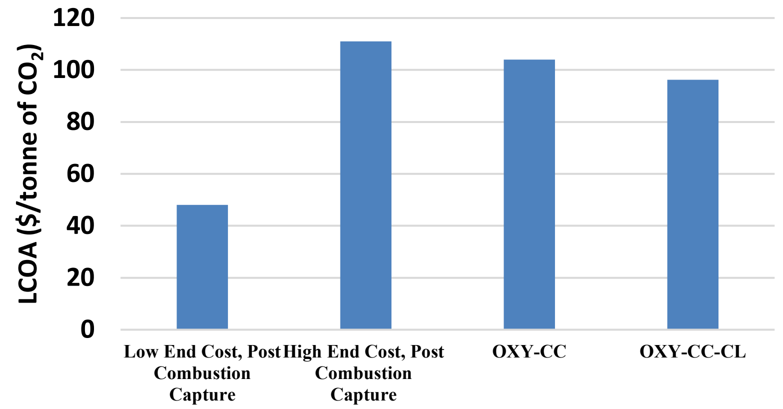

Figure 73. Comparative Evaluation of the Levelized Cost of Carbon Capture between OXY-CC-CL and post-combustion capture at new NGCC power plants [254].

5.9 Pinch analysis

The optimization for the proposed OXY-CC-CL plant concept with CCS was performed through heat and power integration analysis (via pinch technique), often used for maximization of power generation [309,310]. A value of 10°C was assumed for the minimum approach temperature, necessary for the pinch assessment [310]. As assumed in the methodology, a simple steam cycle was modelled with the primary aim to obtain the relative efficiency gain from integrating the CL unit to a conventional oxyfuel power plant with CCS. A self-sustained system with regards to thermal integration was obtained. Furthermore, as illustrated from the hot and cold composite curve in Figure 74, a strong potential for system optimization to improve the efficiency further was identified through the production of steam for power generation.

About 350 MW thermal of high-temperature heat can be seen to be available for optimized use. Assuming a conservative system efficiency of 30% for electricity generation via steam an additional 105 MW of electricity can be generated by the proposed layout. This would increase the system efficiency to 61.4%, higher than the state of the art base case NGCC without CCS.

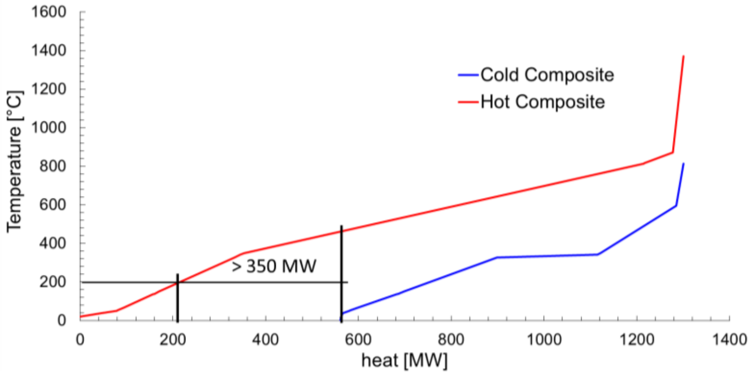

Figure 74. Pinch Analysis of the proposed OXY-CC-CL unit.

5.10 Environmental evaluation

5.10.1 Water footprint analysis

Following the methodology presented in the earlier section, a detailed water demand was calculated for the proposed OXY-CC-CL system. The net specific water footprint was calculated to be 1.893 L/kWh and more detailed results for water need analysis is summarized in Table 20. As can be seen from Figure 75, the net specific water need of the proposed OXY-CC-CL system is comparable to existing commercial power plant technologies [311]. However, compared to an NGCC, the increase of water need is almost 2.5 times. Considering water sustainability, hence the proposed system lags behind and a system optimization focusing on lowering the specific water requirement hence is necessary.

Table 20. Summary of water footprint analysis of the OXY-CC-CL unit.

Description	Unit	Values
LHV of NG	MJ/kg	48.3
Flow of NG	tonne/hr	73.75
Plant Capacity	MW	500.69
Heat Rate (HR)	kJ/kWh	7114.43
Electricity produced	kJ/kWh	3600
Other Heat Losses	kJ/kWh	355.72
Net Energy Out (B)	kJ/kWh	3955.72
Water needed for cooling using tower cooling (A)	L/kJ	0.001
Specific Cooling Water Requirement	L/kWh	1.589
Plant Capacity Factor		85%
Net Energy Generated	MWh	3.73E+06
Total Cooling Water Requirement	m^3	5.92E+06
Process Water (gross)	L/kWh	0.2
Gross Plant Capacity	MW	761.74

Gross Energy Generated	MWh	5.67E+06
Excess Water need for Chemical Looping	L	0
Total Process Water Requirement	m^3	1.13E+06
Total Water Footprint	m^3	7.06E+06
Net Specific Water Footprint	L/kWh	1.893

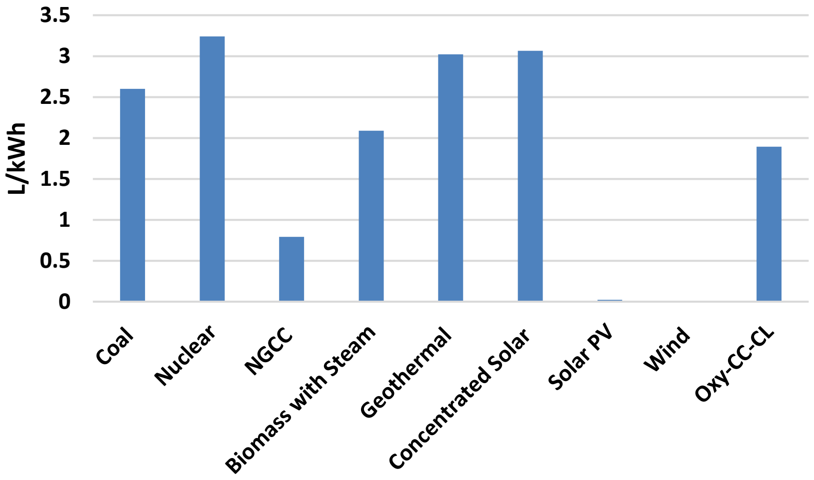

Figure 75. Comparison of specific water need of power production of the proposed OXY-CC-CL and commercial technologies with cooling tower based cooling.

5.10.2 Land footprint analysis

Comparative Land Footprint Analysis, as presented in Table 21, clearly indicates the larger area needed for similar power production from the three units. The proposed OXY-CC-CL unit, comprising of ASU, CL units and additional metal handling units, with a higher number of turbines, would require a much higher land area. Indeed, it would need as much as 2.5 times the land area than a simple NGCC power plant without carbon capture. The CO_2 drying and compression unit accounts for the largest share of the increased area, followed by the chemical looping unit, accounting for about 15% of the total land area needed for the proposed power plant. The ASU, on the other hand, takes up around 7% of the total land area, is considered as a separate unit to the NGCC, connected through pipelines supplying oxygen for combustion.

Table 21. Comparative land area requirement in m^2 for NGCC, OXY-CC and OXY-CC-CL unit for a net power output of 500MW.

Component	NGCC	OXY-CC	OXY-CC-CL
NGCC (Combustion Turbine)	1690	1690	1690
ASU		324	287
CO_2 Drying and Compression		1289	1289
Chemical Looping Unit - Included as Boiler Units			583

Solids Handling Units - Included as equivalent to Coal Handling Plants			211
Net Spatial Footprint	1690	3303	4060

5.11 Concluding remarks

Thermochemical looping of ceria for splitting CO_2/H_2O in a methane-driven redox cycle producing syngas is integrated with oxyfuel-combustion natural gas combined cycle (OXY-CC-CL). Except for the chemical looping CO_2/H_2O dissociation unit (consisting of two interconnected reactors), which is still under technological development, the remaining process design comprises already existing industrial components. The resulting improvement in the system efficiency, even with carbon capture and storage is observed. A system design and simulation were performed in Aspen plus to evaluate the thermodynamic performance of the proposed system. An energetic efficiency of 50.7% and an exergetic efficiency of 47.4% was obtained. Sensitivity analysis with different operating parameters of the system showed scopes for improvement, however, subject to development of corresponding technologies. Comparison with natural gas oxyfuel power plant with carbon capture (OXY-CC) revealed a net efficiency gain of around 7.5 percentage points even with 100% CCS, making this technology promising for subsequent applications in the future. An economic analysis was performed and compared with the existing technologies for power production. Even though the specific overnight capital cost was high, at 2455\$/kW, the levelized cost of CO_2 savings was obtained at 96.25 \$/tonneCO_2, well within limits of commercial technologies. An LCOE of 128.01 \$/MWh was calculated without carbon credits, which, however, would drop to the rates of existing wholesale electricity prices with a carbon credit of around 6 \$/tonneCO_2. However, as per the pinch analysis performed, with better heat integration, the system efficiency can be improved to almost 61.4%, resulting in a much-improved performance of the proposed system. In comparison to NGCC without carbon capture, both the water and land footprints for the proposed technology was obtained to be more than 2.5 times higher for the same scale.

Chapter 6

Techno-economic and exergy analysis of polygeneration plant for power and DME production with the integration of chemical looping CO_2/H_2O splitting

In this chapter, a novel polygeneration plant with carbon capture for the combined power and dimethyl ether (DME) production has been investigated. The plant layout integrates a chemical looping CO_2/H_2O splitting (CL) unit that produces syngas (CO and H_2) for the DME synthesis by using the exhaust gases of an oxy-fuel power plant. This latter plant is fed with a syngas stream generated during the reduction step with methane of the metal oxide in the CL redox cycle. The oxyfuel power plant also generates steam for combined power production with two streams Rankine cycles. The aim of the present work is to assess the process on the basis of energy and exergetic efficiency and economic performance of the integrated CL unit for the industrial scale DME production plant. The economic analysis was also carried out to derive information on the main economic drivers associated with high capital investment in the process plant with individual sub-systems. The analysis highlighted the strong potential of integrating chemical looping CO_2/H_2O splitting processes for the production of syngas with polygeneration systems that can produce power, DME and methanol, thus increasing the overall efficiency with a reduced cost of carbon capture processes.

6.1 Introduction

The quest to meet the never-ending energy demand and the rise of emissions is leading to the search for innovative technologies and non-petroleum based alternative fuels which would help in restricting the global warming to 1.5ºC above the pre-industrial temperatures (new target set by the recent report by Intergovernmental Panel on Climate Change (IPCC) as of 2018) [4]. Among the multiple pathways proposed for the reduction of anthropogenic emissions of CO_2, Carbon Capture and Utilization technologies (CCU) to convert captured CO_2 into valuable products have recently gained much focus as an alternative to Carbon Capture and Storage processes (CCS).

[225,237,240]. This is due to CCU is not only complementary to CCS in some respects but also providing multi-product outputs through the recycling and reuse of the captured CO_2 in several synthesis processes [312–315]. As described earlier in previous chapters carbon capture in power plants comes with huge energy penalty and loss of efficiency points. Many studies have been proposed to gain the loss of efficiency due to carbon capture by alternate methods [244]. Polygeneration systems, which can efficiently combine multiple utility outputs (e.g., electrical power, chemicals, fuels etc.) from one or more input in a single system, provide an interesting option for alternative use of captured CO_2 [316]. Besides the potential to gain significant efficiency and local use of the captured CO_2, suitable integration and synergy between different processes also ensure higher flexibility of operation, allowing to vary the share of products according to their value, for example, related to fluctuating market prices [317]. Multiple configurations of polygeneration systems integrated with CO_2 capture processes have been reported in the literature [318]. Li et al. [319] modelled a polygeneration plant with CO_2 capture for production of power and synthetic natural gas, the proposed arrangement achieving a lower life-cycle energy use and GHG emission with respect to the ultra-supercritical coal power plant. Bose et al. [312] studied a cost-effective production of urea and power combined with CCS using coal gasification. Jana et al reported the improved sustainability through life cycle assessment for a proposed rice-straw based power, ethanol, heating and cooling polygeneration power plant [320].

Most polygeneration systems designed or proposed till date have employed coal as the fuel [316]. However, oxyfuel combustion using gaseous fuel like natural gas and biomethane has been shown to be the most promising among the low emission technologies (LETs) [321]. Above such, innovative methods for the use of natural gas are being proposed to improve upon the efficiency of natural gas combined cycle power plants, which can reach an efficiency of as high as 57% [322]. One such innovative technology is the chemical looping CO_2/H_2O splitting cycle using methane reduction, to produce CO and H_2 respectively [321]. This indeed forms an interesting alternative to the solar thermochemical redox cycle, which has gained attention for CO_2/H_2O splitting to produce syngas (CO/H_2) after the successful demonstration of water-splitting by oxygen carriers [323–325]. Chemical looping (CL) cycle driven by methane reduction using ceria as oxygen carrier is explained in detail in chapter 4.

Ceria reduction by methane has been investigated by Warren and Scheffe [87] and the results showed that CeO_2 undergoes complete reduction to Ce_2O_3 above 900°C. Accordingly, the CeO_2/Ce_2O_3 redox pair with reduction of CeO_2 in the presence of methane and subsequent oxidation with CO_2/H_2O can be described by the equations (4.1-4.2) in reduction and oxidation reactor respectively.

By optimally combining the ratio of water and CO_2 in the inlet gas mixture to the oxidation reactor and the temperature of reaction, the desired composition of syngas can be obtained, to be subsequently utilized for production of chemicals ((H_2/CO: 1.79) methanol [326,327], (H_2/CO: 2.1) jet fuels [269] and naphtha [269,328,329], (H_2/CO: 1.76) kerosene and gasoil [329] etc.) through industrial processes.

Dimethyl Ether (DME) is one of the most attractive candidates as a synthetic fuel due to its similarity with diesel. Even though DME has a lower LHV than conventional diesel and its use requires pressurization to maintain it in a liquid state at ambient conditions, its physical properties and chemical structure make it a very interesting fuel. Low NO_x, limited hydrocarbon (HC) and almost no SO_x and particulate emissions during the combustion [330], are added advantages of its use. In this regard, DME has been investigated in the literature as raw material for the synthesis of aromatics, gasoline, olefins and other chemicals besides direct use as an alternative fuel [331]. It is to highlight that DME also gained attention in recent times due to its physicochemical properties are similar to liquid petroleum gas (LPG) giving the chance to retrofit the LPG based automotives [332]. DME synthesis is generally classified as i) two-step process (indirect) which uses hydrogenation to produce methanol and then dehydration to DME ii) the second method is one-step (direct) process reported to be more efficient which uses bi-functional catalysts. Both the pathways are commercially viable technology and invested by companies such as Haldor Topsoe, Korea Gas Corporation, Air products, JFE Holdings, Toyo, MGC, Lurgi and Udhe [333,334]. Synthesis of DME using syngas (CO and H_2) from CO_2/H_2O splitting can, therefore, present an interesting pathway for the production of clean fuels using an unconventional process [40,335].

Alternative methods to produce syngas by the chemical looping processes have been reported such as chemical looping reforming (CLR), autothermal reforming and chemical looping partial oxidation of methane (CLPOM) [7,336]. CLR and autothermal reforming usually operate at a lower temperature of 800-900°C that produces H_2/CO ratio of 2.8-4.8 and 1.8-4.0 respectively with a higher concentration of CO_2/H_2O at the outlet stream. While syngas production by CLPOM needs a temperature above 1300°C with H_2/CO of 1.7-1.8 and also has lower H_2O/CO_2 in the product [337]. This makes CLR more suitable for Fischer-Tropsch synthesis for methanol or hydrogen production. However, a novel process of generation of syngas from the exhaust stream and re-use within the power plant for producing additional power has been shown to be a viable alternative to improve the efficiency with 100% carbon capture [254]. Indeed, within a polygeneration scheme, the use of syngas for synthetic fuel production becomes an imperative option. Hankin and Shah [338] in a study explored the process of DME and methanol synthesis from CO_2 and H_2O. Syngas is produced by water electrolysis and solid oxide electrolysis for CO where all the processes such as DME, methanol synthesis, electrochemical electrolysis and solid oxide electrolysis for CO are investigated by the assumption of chemical equilibrium. Salkuyeh and Adam II [339] proposed a polygeneration scheme which combines the coal gasification, natural gas reforming by chemical looping processes such as gasification and combustion to produce power, methanol, and DME. The system was tested with iron oxide and nickel oxide oxygen career for chemical looping processes with different gains based on the operability of the system. The path for syngas production as feedstock DME was investigated.

However, till date, no polygeneration system which integrates the chemical looping CO_2/H_2O splitting (CL) with fuel reduction step and DME and power production have been studied for utility-scale. In this work, an oxyfuel natural gas combined cycle power plant integrated with CL CO_2/H_2O splitting and DME production has been proposed (OXYF-CL-PFG) with a detailed techno-economic, exergetic and environmental assessment. The exergetic study was carried out for the proposed OXYF-CL-PFG layout to identify the sources of irreversibility, with which the proposed layout could be improved and optimized. The analysis includes power production, fuel production, and power consumption, exergy analysis, economic estimation along with the net present value (NPV) with different carbon credit scenarios, as well as efficiency and percentage of carbon captured and recycled.

6.2 Process and plant description

The proposed polygeneration scheme is an oxyfuel natural gas fed combined cycle power plant integrated with a chemical looping CO_2/H_2O splitting unit (CL) for power and DME production (OXYF-CL-PFG) shown in Figure 76. To maintain the simplicity of analysis, the gas pre-treatment including sulphur removal has been assumed to have occurred upstream [340] The clean natural gas is sent to the chemical looping (CO_2/H_2O) splitting unit where it is converted into a hydrogen-rich syngas by the simultaneous reduction of ceria. The produced syngas is sent to an oxyfuel unit where it is combusted with pure oxygen from an ASU. The hot combustion products, primarily comprising H_2O and CO_2 are firstly expanded in a gas turbine and then sent in a heat recovery steam generation unit (HRSG). Here, the surplus heat is exploited to produce superheated steam for power production in a bottoming steam cycle. Finally, a water condenser partially separates carbon dioxide and water. The large part of the separated CO_2 can be sequestrated for storage or used in other processes, while another fraction together with steam is sent to the chemical looping CO_2/H_2O (CL) unit. In the CL unit, both H_2O and CO_2 are dissociated to H_2 and CO in an oxidation reactor by the reduced ceria from the reduction reactor. The produced syngas from the oxidation reactor is used for DME synthesis. The diluted DME, resulting thus, is cleaned in a distillation unit (or clean-up unit), additionally producing a secondary fuel stream of methanol. In the following sub-sections, the methodology adopted for the presented work, along with more details on each unit and their integration are described.

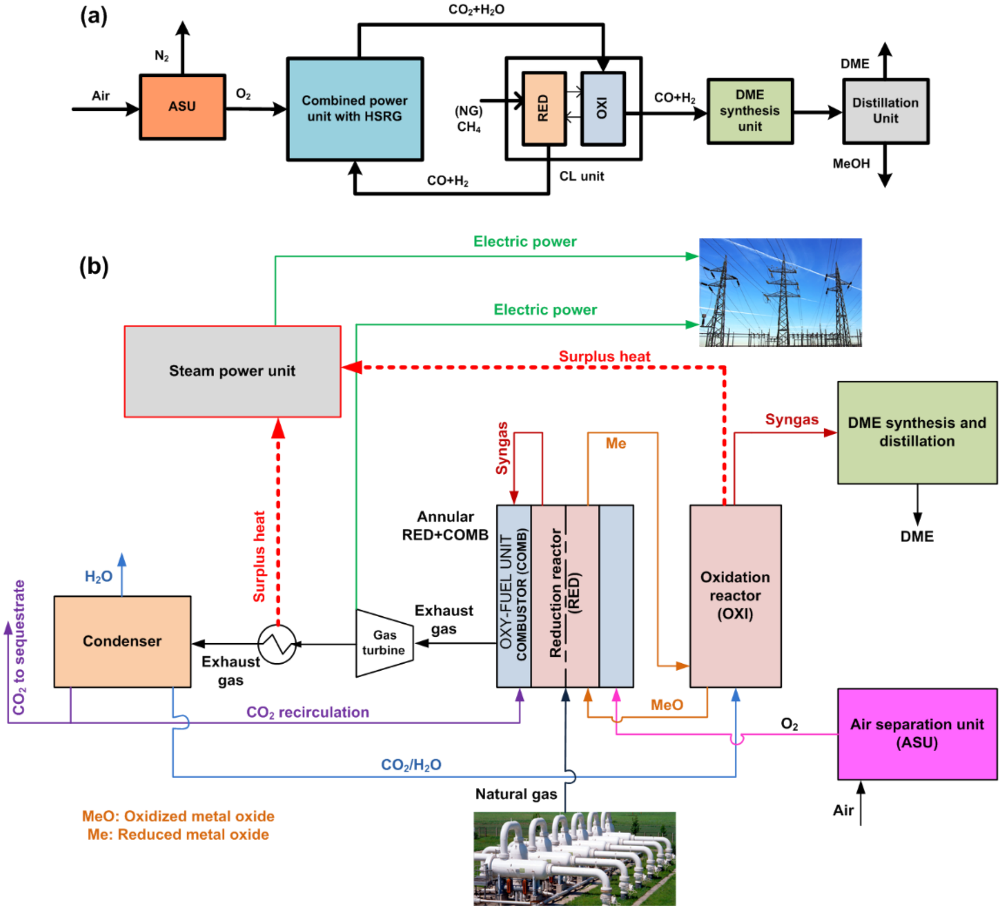

Figure 76. General concept of integration of oxy-fuelled power unit with chemical looping (CO_2/H_2O) splitting unit and DME production process (a) block diagram (b) process flow diagram.

6.3 Simulation methodology

The polygeneration plant has been modelled by combining mass and energy balance equations. As per the detailed plant layout proposed in Figure 77. Simulations were performed using the commercial software Aspen Plus v8.8. The characteristic components of the system are the integrated combustor of the oxyfuel unit and the reduction reactor of the CL unit and oxidation reactor, the DME synthesis reactor, the DME distillation columns, and the ASU apart from the standard components of the plant, such as heat exchangers, pumps, compressors, and turbines. The entire modelling was performed with the assumption of chemical equilibrium with the exception of the DME reactor, for which a kinetic approach has been used. Therefore, RGIBBS reactor blocks were used for modelling the oxidation and reduction reactors of the CL unit, as well as the combustor of the oxyfuel unit. The distillation unit and air separation columns were modelled using the RADFRAC column. The DME reactor was simulated with an RPLUG reactor using the Langmuir-Hinshelwood Hougen-Watson (LHHW) kinetic model. During the simulation of this component, the Soave-Redlich-Kwong (SRK) EOS model was utilized, which is usually applied to binary components

[341]. Graaf et al. [342] demonstrated that the chemical equilibrium of the methanol reaction and water gas shift (WGS) reaction can be well described at high-pressure by using the SRK-EOS model. More details on the modelling approaches followed for the main components of the plant are given in section 6.4-5.

The material streams used in the model involve conventional and solid components. The Peng-Robinson-Boston-Mathias (PR-BM) property method was used for conventional components, as this approach was recommended for hydrocarbon processing applications such as gas processing, refinery, and petrochemical processes [343–345]. This method uses the Peng-Robinson cubic equation of state combined with the Boston-Mathias alpha function for all the thermodynamic properties [344]. The oxygen carriers (CeO_2/Ce_2O_3) used for the chemical looping simulation were implemented as conventional pure solid components. For this type of streams, the Barin equation was used [346,347]. The main hypotheses used in the modelling phase are summarized in Table 22. CLN-CO_2, CLN-DME, and CLN-MeOH are the columns used in the distillation unit.

Table 22. Main assumptions and hypothesis used in the process simulation.

Natural gas	Composition (std.vol%): 93.1% CH_4, 3.2% C_2H_6, 1.6% N_2, 1.1% C_3H_8, 1.0% CO_2; LHV=47.1 MJ/kg [348]; Model: RGIBBS, no heat losses.
Oxidation and reduction reactors	10°C drop for ceria recirculation from OXI to RED was assumed in order to assess heat losses; Model: RGIBBS;
Combustor	Model: RGIBBS; ΔP=0.2 bar, no heat losses;
Compressors, pumps and turbines	$\eta_{is,comp}=0.9$, $\eta_{mech,comp}=0.98$, $\eta_{is,pump}=0.9$, $\eta_{driver,pump}=0.90$, $\eta_{is,turb}=0.9$, $\eta_{mech,turb}=0.98$;
Oxygen carrier	Solid ceria: CeO_2/Ce_2O_3, diameter=100 µm; Temperature drop of 20°C during ceria recycling from OXI to RED;
DME reactor	Model: RPLUG multi-tube reactor, Operation: T=250°C P=50 bar;
Heat exchangers	ΔT_{min}=10°C;
Distillation unit	Model: RADFRAC, Reboiler type: Kettle.

CLN-CO_2	CLN-DME	CLN-MeOH
P=10 bar	P=9 bar	P=2 bar

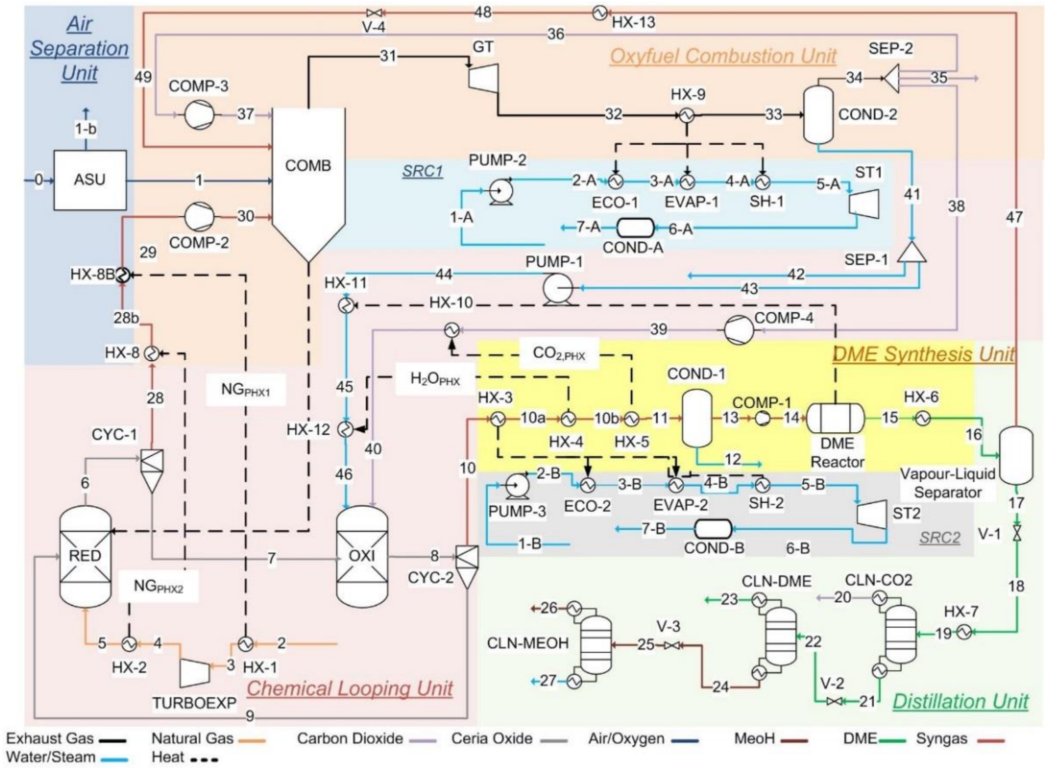

Figure 77. Detailed polygeneration plant layout OXYF-CL-PFG.

6.4 Polygeneration plant units

6.4.1 Chemical looping CO_2/H_2O splitting unit (CL)

The chemical looping unit consists of two interconnected reduction reactor (RED) and the oxidation reactor (OXI) operating at 2 bar with the circulating oxygen carrier pair (CeO_2/Ce_2O_3). The pre-cleaned natural gas, at a grid pressure of 70 bars (stream 2) [293] is heated up at 290°C and expanded to 2 bar via the turbo-expander (TURBOEXP). Table 22 lists the composition of natural gas at the inlet to the plant (without H_2S). The preheating is necessary to prevent an outlet temperature of the natural gas (stream 4) from the turbo-expander lower than 0°C. After the expansion of the natural gas, it is heated to 890°C (stream 5) and fed to the RED. For the endothermic reduction reaction, external heat is mandatory to maintain the reaction temperature. Ceria reduction by methane occurs above 900ºC to achieve full conversion to CO and H_2 as well as a reduction to Ce_2O_3 [87]. From the thermodynamic studies, it was found that 40 to 60% excess flow of methane is required to ensure complete conversion of OC below 950ºC. From the results presented in chapter 4 most suitable methane to ceria flow ratio (CH_4/CeO_2) for the reduction reactor was 0.7 instead of the stoichiometric ratio of 0.5. Here CeO_2 (stream 9), at an inlet temperature of 1312°C as a result of the exothermic oxidation reaction, is completely reduced with natural gas, producing a syngas in a 2:1 H_2/CO ratio (equation (4.1)) and unreacted natural gas [321]. As for the external heat source to sustain the reaction in the RED, it has been proposed to use a part of the heat generated in the oxyfuel combustion chamber. To this end, a reduction reactor thermally integrated with the oxyfuel combustion chamber was proposed utilizing an annular combustion chamber design already analyzed by Khan and Shamim [349].

The hot syngas (stream 6) produced in RED exits it at 900°C and is separated from the solid (stream 7) by a cyclone (CYC-1), cooled and sent to the oxyfuel unit. The reduced ceria is fed, without an intermediate heat recovery, into oxidation reactor (OXI) where it is then oxidized (equation 4.2(a) and (b) of chapter 4) by a mixture coming from the oxyfuel unit of 60% H_2O-40% CO_2 (stream 40 and 46) to have at the outlet the ideal H_2/CO ratio of 1 for DME production, as described in section 6.5. It is observed (from chapter 4) that in order to achieve a full oxidation of Ce_2O_3, a 60% excess of water and carbon dioxide mixture is required.

Before the oxidation, both water and carbon monoxide are compressed at the operating pressure of OXI (2 bar), respectively with a pump (PUMP-1) and a compressor (COMP-4), and heated up at 500°C. Since the reactions in the oxidation reactor are exothermic and the reactor itself is set as adiabatic, the outlet temperature of the reactor goes to 1322°C. The hot syngas produced is separated from the oxidized ceria by the cyclone separator (CYC-2), cooled down (stream 10, 10a, 10b, 11) and sent to the DME unit, while the solid stream is re-circulated back for a new reduction cycle (stream 9).

6.4.2 Air separation unit (ASU)

The air separation unit consists of a cryogenic distillation unit able to produce 99.99% pure O_2. The schematic of the ASU layout is shown in Figure 78. The air is separated into two thermally interconnected distillation columns, HP-COL and LP-COL, which work at 5 and 1.2 bar respectively [350–352]. The overall refrigeration is driven by the expansion from high pressure (30 bar) of the compressed air (stream 6-C and 7-C, which become 14-C and 16-C respectively, after cooling down in HX-2C) through the VALVE-2 and the TURBOEXP-2C. The inlet air (1-C) is compressed at 6.3 bar by the compressor COMP-1C and separated in two streams (4-C and 8-C) by the splitter SPLIT-1C. The stream 8-C is cooled down (becoming 9-C in Figure 78) in the exchanger HX-2C by the cold products (steam 19-C) of the LP-COL and then is sent to the HP-COL. The HP-COL is a 40 stages distillation column which produces as a top product a gaseous rich-in N_2 (stream 12-C) and as a bottom product a liquid rich-in O_2 stream (stream 10-C). The latter stream is further cooled down through Joule-Thomson effect in the valve VALVE 1-C and fed in the 56 stages low-pressure column. The low-temperature air streams 15-C and 17-C, together with the rich-in O_2 liquid stream 11-C, provide the necessary refrigeration in the LP-COL to obtain as top-product a pure N_2 stream (20-C), while as a pure O_2 stream (18-C) is produced from the bottom of the condenser. The latter stream is pumped by the PUMP-1C at the operational condition of the combustor in the oxyfuel unit and heated in the HX-2C to 80°C with pressure 26 bar. The ASU block can be seen in Figure 78 and stream data is listed in table A1 in the appendix.

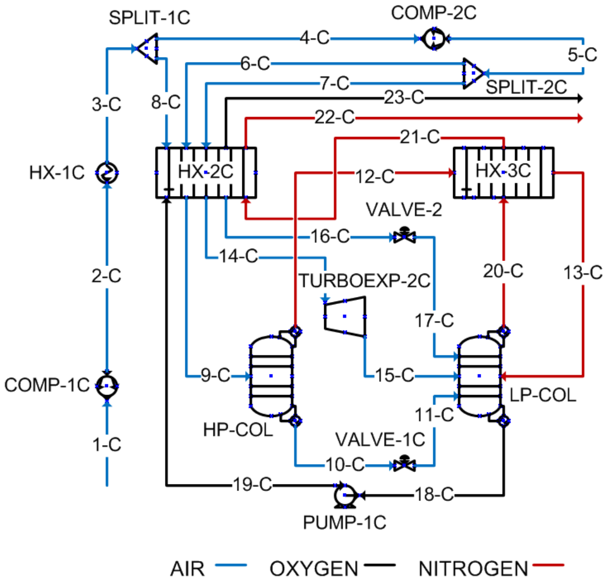

Figure 78. Detailed layout of the air separation unit (ASU).

6.4.3 Oxy-fuel combustion unit

In this unit, combustion of syngas is performed with oxygen instead of air. This eliminates the presence of nitrogen in the exhaust gases that would have affected the subsequent CO_2 separation process. Another advantage is a substantial reduction in thermal NO_x due to the absence of nitrogen [353].

The oxyfuel unit consists of a combustor (COMB), where the syngas from the reduction (stream 30) and the non-condensable gases from the clean-up unit (stream 49, mainly CO_2 with CO and H_2) are burnt with a 5% excess oxygen stream derived from the air separation unit (ASU) (stream 1). Stream 36 represents the part of the captured CO_2 that is re-circulated to the combustor to control the combustion temperature in the chamber. The recirculation ratio was set such as the total combustion heat was sufficient to have a combustor outlet syngas temperature of 1377°C (keeping the limits of TIT of commercial gas turbines) and the required heat to carry on the reduction of the ceria in the reduction (RED) reactor. The CO_2 and syngas streams entering COMB are compressed to 26 bar with two two-stage compressors (COMP-2 and COMP-3). Then, the flue gas exiting the combustion chamber is firstly expanded in a two-stage gas turbine GT (26 bar to 5 bar and 5 bar to 1.05 bar) and then sent to the heat recovery steam generator (HX-9) for the generation of steam for the steam power cycle SRC1. More details on the steam power cycle are given in section 6.4.4.

Finally, the CO_2 is separated from the water in a condenser (COND-2) and the stream is split into three parts. One part is recirculated to the combustor (stream 36), one is sent for sequestration or other applications (stream 35) and the last part (stream 38) is sent to the oxidation reactor for dissociation (OXI).

6.4.4 Steam power cycles

Two steam Rankine cycles (SRC1 and SRC2) are included in the system layout. The extra heat available within the polygeneration system is exploited to produce steam by heat recovery steam generators (HRSGs), which expands in steam turbines to generate power. The turbines and the HRSGs were modelled as simple units, without reheating or multi-pressure systems. In fact, as the primary objective of the present study is to understand the benefits deriving from polygeneration by integration of a chemical looping unit in a conventional oxyfuel plant, the optimization of the system was not in the scope of the present study. The SRC1 uses the heat of the flue gases from the oxyfuel unit (stream 32) to produce super-heated steam (125.59 tonne/h) at 150 bar and 550°C (stream 5A), generating an electrical power of around 44 MW while expanding in the turbine (ST1). The SRC2 uses the extra heat from the chemical looping unit to produce a smaller flow of steam (8.3 tonne/h) at the same condition of stream 5A (stream 5B), generating 3 MW in ST2. The reason for the choice of two HRSGs connected to two different steam cycles is to ensure flexible operation by minimizing the influence of DME and power production over each other.

6.4.5 DME synthesis unit

In this unit, the syngas produced in the oxidation reactor (stream 10) is converted into liquid fuel within the catalytic reactor. Before the syngas is fed to the DME reactor, it undergoes condensation (COND-1) to remove H_2O at atmospheric pressure. The operating conditions of the DME reactor have been selected from the work of Pozzo et al. [354] fixing the pressure at 50 bar and the temperature at 250°C. In order to reach the operating pressure of the reactor, the dried syngas (stream 13) is compressed by a three-stage compressor at 50 bar (COMP-1). The DME reactor is kept at a constant temperature of 250°C by a water-jacket cooler used for saturated steam generation at 2 bar (stream 44) for the oxidation (OXI) reactor.

The DME reactor was considered as a multi-tube fixed bed reactor. Each tube contains the dual catalyst (physically mixed) with a bed voidage of 0.45. The total density of the catalyst particles is an average of the density of the two catalysts, $Cu/ZnO/Al_2O_3$, and γ-Al_2O_3, used in the 1:2 optimal ratio. The parameters used for the DME reactor are listed in Table 23.

Table 23. Fixed parameters for DME reactor design.

N° tubes	Diameter [m]	Bed voidage	density $Cu/ZnO/Al_2O_3$ [kg/m^3]	density γ-Al_2O_3 [kg/m^3]	ρ average [kg/m^3]	Temperature (°C)	Pressure (bar)
5000	0.02	0.45	1200	1470	1380	250	50

6.4.6 DME distillation unit

The produced DME contains significant impurities, requiring a separation or distillation unit to obtain pure dimethyl ether. The distillation plant comprises a cooling and a gas-liquid separation unit. The cooling unit, represented in the layout by a vapour-liquid separator (VLS), is used to produce chilled streams at -40°C resulting in a liquid stream of DME with dissolved CO_2 and MeOH (stream 17) and a gas stream of incondensable gases, namely, H_2, CO, undissolved CO_2 and traces of other diluents (steam 47). The gas stream is re-circulated into the oxyfuel unit and burnt, while the liquid stream is further processed in the gas-liquid separation unit. The gas separation unit is composed of three different distillation columns: CLN-CO_2, CLN-DME, and CLN-MEOH (Table 24). The first one is used to separate the dissolved CO_2, the second to produce a pure 99% DME and the last one to separate the methanol from the water. Thus, an additional fuel as methanol is generated as a by-product of DME distillation. A valve and a heat exchanger are placed before each column in order to adjust the pressure to the optimal value and to have 50% of vapor in the inlet stream [354]. The number of stages used in the distillation columns was estimated by increasing them until a certain change in composition was detected.

Table 24. Distillation unit operation parameters**.**

Column	T_{REB} [°C]	Q_{REB} [MW]	T_{cond} [°C]	Q_{cond} [MW]	Number of stages	Feed-in stage	Purity of the product [%]
CLN-CO_2	45.87	1.12	-40.83	-0.64	25	10	-
CLN-DME	150.99	0.93	42.57	-0.55	30	24	99.1
CLN-MeOH	101.53	0.03	66.36	-0.05	24	18	94.1

6.5 Synthesis of DME

6.5.1 Reaction scheme

DME production can be realized in two steps (methanol and DME are produced in two different reactors) or in a single step adopting a dual catalyst. The disadvantage of the two-step process is that syngas conversion to methanol is significantly limited by equilibrium and thermodynamic constraints [355]. Consequently, the further conversion of methanol to DME in the single step process shifts the equilibrium toward more methanol production. For that reason, the direct DME synthesis is thermodynamically and economically preferable than the two steps process [356–358]. Therefore, the single-step DME synthesis with a dual catalyst has been selected in the present study. The overall process can be described by three main reactions: the syngas conversion to methanol (reaction (6.1)), water gas shift (reaction (6.2)) and methanol dehydration to DME (reaction (6.3)).

$$CO_2 + 3\ H_2 \leftrightarrow CH_3OH + H_2O \quad -\Delta H_{298\ K;0.1\ MPa} = 49.2\ kJ/mol \tag{6.1}$$

$$CO + H_2O \leftrightarrow CO_2 + H_2 \quad -\Delta H_{298\ K;0.1\ MPa} = 41.2\ kJ/mol \tag{6.2}$$

$$2\ CH_3OH \leftrightarrow CH_3OCH_3 + H_2O \quad -\Delta H_{298\ K;0.1\ MPa} = 24.0\ kJ/mol \tag{6.3}$$

The overall reaction to synthesize the syngas to DME route is represented by the combination of reactions (6.1), (6.2) and (6.3) into reaction (6.4):

$$3H_2 + 3CO \rightarrow CH_3OCH_3 + CO_2 \quad -\Delta H_{298\ K;0.1\ MPa} = 246.0\ kJ/mol \tag{6.4}$$

The overall reaction is exothermic and generates two molecules of products from six molecules of reactants. Hence, according to the Le Châtelier principle [359], conversion is favoured working at high pressure and low temperature.

6.5.2 Reaction kinetics

The DME reactor was simulated in Aspen plus with an RPLUG reactor combined with a Langmuir-Hinshelwood Hougen-Watson (LHHW) kinetic model based on three simultaneous reactions (6.1-6.3). Bi-functional catalyst $Cu/ZnO/Al_2O_3$:γ-Al_2O_3 with a loading ratio of 1:2 has been selected from the literature, with the $Cu/ZnO/Al_2O_3$ active for the methanol synthesis, while the γ-Al_2O_3 component catalyses the methanol dehydration [355] among the other presented in the literature the selected catalyst is most investigated [360]. The details of the catalyst properties are reported in Table 23. The kinetic model adopted is described in Pozzo et al.[354]. The rate expression for CO_2 hydrogenation, RWGS and methanol dehydration are given by equations (6.5-6.7) [355,361,362].

$$r_{CO_2\ hydrogenation} = \frac{k_1\left(p_{H_2} \cdot p_{CO_2}\right)\left[1-\left(\frac{1}{\ddot{K}_{eq,1}}\right)\frac{p_{CH_3OH} \cdot p_{H_2O}}{p_{CO_2}\, p_{H_2}^3}\right]}{\left(1+k_2\frac{p_{H_2O}}{p_{H_2}}+\sqrt{k_3 \cdot p_{H_2}}+k_4 \cdot p_{H_2O}\right)^3} \tag{6.5}$$

$$r_{RWGS} = \frac{k_5 \cdot p_{CO_2}\left[1-\frac{1}{\ddot{K}_{eq,2}}\frac{p_{CO} \cdot p_{H_2O}}{p_{CO_2} \cdot p_{H_2}}\right]}{1+k_2\frac{p_{H_2O}}{p_{H_2}}+\sqrt{k_3 \cdot p_{H_2}}+k_4 \cdot p_{H_2O}} \tag{6.6}$$

$$r_{MeOH\ dehydration} = \frac{k_6 \cdot \ddot{K}_{CH_3OH}^2\left[[\Pi]_{CH_3OH}^2-\left(\Pi_{H_2O} \cdot \frac{\Pi_{DME}}{\ddot{K}_{eq,3}}\right)\right]}{\left(1+2\sqrt{\ddot{K}_{CH_3OH} \cdot \Pi_{CH_3OH}}+\ddot{K}_{H_2O} \cdot \Pi_{H_2O}\right)^4} \tag{6.7}$$

Reaction rates of equation (6.5-6.7) are expressed in kmol/kg$_{cat}$ s; p is the partial pressure of the gases in Pa and Π the concentration expressed in kmol/m^3. The equilibrium constant ($\ddot{K}_i$) and constant rate (k_i) values used to determine the reaction rates are shown in Table 25.

Table 25. Kinetic parameters used in DME synthesis.

	Pre	unit	E_a	unit
k_1	1.07×10^{-13}	(kmol/(kg-sPa^2))	36,696	(J/mol)
k_2	3450	-	0	(J/mol)
$k_3^{0.5}$	1.578×10^{-3}	Pa$^{-0.5}$	17,197	(J/mol)
k_4	6.62×10^{-16}	Pa^{-1}	124,119	(J/mol)
k_5	122	(kmol/(kg s Pa))	-94,765	(J/mol)
k_6	1.486×10^{11}	(kmol/(kg s))	-143,666	(J/mol)
$\ddot{K}_{CH_3OH}$	5.39×10^{-4}	m^3/kmol	70,560.92	(J/mol)
$\ddot{K}_{H_2O}$	8.47×10^{-2}	m^3/kmol	42,151.98	(J/mol)

These parameters refer to the Arrhenius equation shown by equation (6.8):

$$k_i = (\mathrm{Pre})_i \times \exp\left(\frac{E_{a,i}}{RT}\right) \tag{6.8}$$

where E_a represents either the activation energy or the reaction enthalpy or a combination of both [361] as in LHHW kinetic mechanism the rate constants are represented as a combination of rate constants and equilibrium constants. Following were the expressions used to determine the equilibrium constants [342,361,363]:

$$\log_{10} \ddot{K}_{eq,1} = \frac{3066}{T} - 10.592 \tag{6.9}$$

$$\log_{10}(1/\ddot{K}_{eq_2}) = -\frac{2073}{T} + 2.029 \tag{6.10}$$

$$\ln \ddot{K}_{eq,3} = \frac{3220}{T} - 1.7 \tag{6.11}$$

The model was used to perform a sensitivity analysis of methanol and DME yield using the equations (6.12) and (6.13) varying the composition of the inlet stream, H_2/CO ratio, and the amount of the diluent H_2O and CO_2.

$$DME_{yield} = \frac{DME_{out}}{\left(CO + CO_2\right)_{in}} \tag{6.12}$$

$$MeOH_{yield} = \frac{MeOH_{out}}{\left(CO + CO_2\right)_{in}} \tag{6.13}$$

where DME_{out} and $MeOH_{out}$ are the DME and methanol molar flow at the outlet of the reactor (stream 15) and CO and CO_2 the molar flow at the inlet (stream 14).

As shown in Figure 79 the highest DME yield is obtained by feeding a syngas with an $H_2/CO = 1$ with a positive effect of having the main byproduct of the reaction as CO_2 which can be easily separated from the DME and MeOH in the separation unit which is verified from the results reported by Ogawa et al [332] . At $H_2/CO=1$, the DME yield was 38.6% and MeOH yield was 0.8% which are similar to the results reported by Pozzo et al [354]. It is observed that with increasing the CO_2 content at the inlet feed, the DME yield decreases. This is attributed mainly to two factors. Firstly, the methanol synthesis is retarded with the increase of CO_2 content [364] as CO_2 molecules are absorbed by the methanol catalyst by occupying the active sites quicker than CO and H_2, affecting the MeOH production and consequently also the DME synthesis [365] as shown in Figure 80(a). Secondly, with a high CO_2 concentration in the feed of the DME reactor, the beneficial effect of the water gas shift reaction would get decreased. The water formed is removed by WGS producing hydrogen which kinetically advances the methanol production. Therefore, the higher CO_2 favors the reverse-water gas shift that reduces the hydrogen content and produces more water. The effect of higher water content at the inlet is even worse than CO_2 and it can be seen in Figure 80(b). The high water percentage shifts the methanol dehydration towards the reactants, increasing the MeOH yield while reducing the DME yield. With a water percentage higher than 20%, also methanol production is penalized. In addition, the water tends to deposit near the catalyst accelerating the catalyst degradation [332]. Therefore, to increase the DME production it is necessary to have at the inlet of the DME reactor a syngas composed by an equimolar H_2-CO mixture, reduce the CO_2 percentage (molar fraction) in the 0-5% range and remove as much as possible the water content.

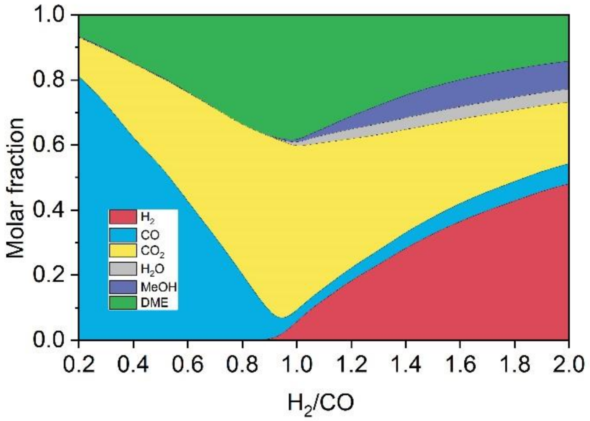

Figure 79. Effect of H_2/CO ratio on the equilibrium synthesis of DME at T=250°C and p=50 bar.

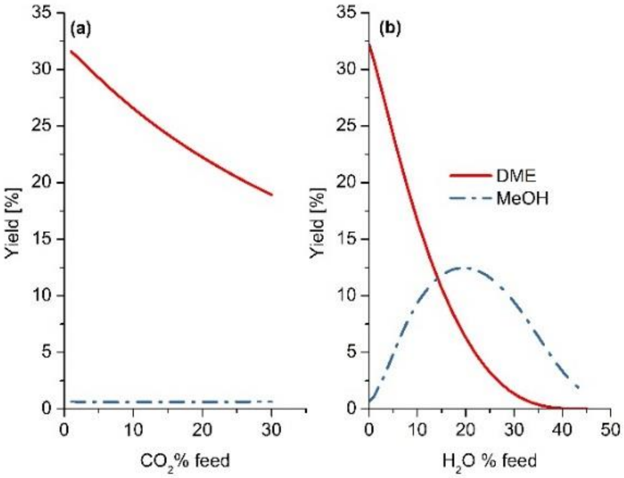

Figure 80. Effect of (a) CO_2 and (b) H_2O on the equilibrium synthesis of DME at T=250°C and p=50 bar.

6.6 Results

6.6.1 Effect of operating conditions

A sensitivity analysis of the most affecting parameters – namely: operating pressure of chemical looping H_2O/CO_2 splitting unit, outlet temperature of reduction reactor, H_2O/CO_2 composition in the oxidation reactor of the CL unit, and turbine inlet temperature – was performed to maximize the global efficiency of the plant (Eq. 6.14) and the DME production.

$$\eta_c = \frac{\dot{m}_{DME} \cdot LHV_{DME} + \dot{m}_{MEOH} \cdot LHV_{MEOH} + W_{NET}}{\dot{m}_{NG} \cdot LHV_{NG}} \tag{6.14}$$

where: $\dot{m}_{DME}$, $\dot{m}_{MeOH}$ represent the DME and MeOH streams produced (kg/s), while LHV_{DME}, $LHV_{MeOH,}$ and LHV_{NG} are the lower heating value (MJ/kg) of DME, MeOH and natural gas respectively, and W_{NET} is the net power (MW) produced inside the plant with $\dot{m}_{NG}$ being the natural gas stream feed into the plant (kg/s).

6.6.2 Chemical looping (CO_2/H_2O) splitting (CL) unit pressure

Figure 81 shows the effect of varying the pressure of the chemical looping unit, where both oxidation and reduction reactors work at the same pressure. With the increase of pressure of CL unit, an efficiency gain is observed from 49.4% at 1 bar to 51.1% at 5 bar. This can be attributed to the fact that a significant saving of the auxiliary power compression ($W_{COMP,tot}$ in Figure 81) is obtained by reducing the pressure ratio of syngas compression. However, with a further increment of the pressure, the efficiency decreases, dropping down to 43.6% with 20 bar of pressure. Based on the Le Châtelier principle, it can be understood that the reaction in the RED reactor is not thermodynamically favoured at high pressure since the reduction reaction has three moles of reactants and four moles of products. In fact, it can be seen that over 5 bar the amount of reduced ceria (Ce_2O_3 line in Figure 81) at the outlet of the reactor decreases. This results in a lower syngas production from OXI reactor, as less reduced ceria is available, and consequently in DME production and eventually in the overall plant efficiency. DME production drops after 5 bar pressure and it does not vary between 1 to 5 bar while the W_{NET} increases very slowly from 1 to 5 bar from 100 to 105 MW. The CL unit pressure can be fixed to 2 bar as the benefit of working at higher pressure is offset by the power required to maintain pressure drop while working with solids.

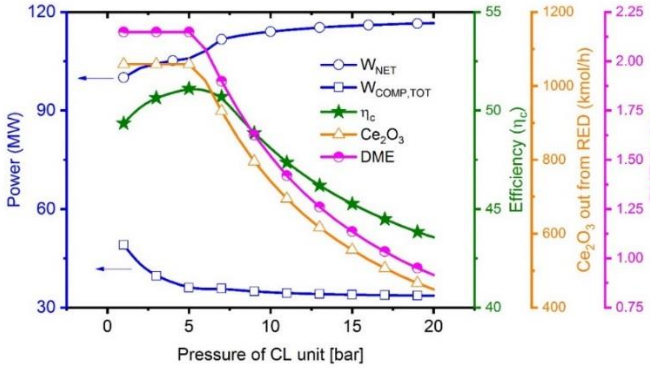

Figure 81. Effect of of chemical looping unit pressure on efficiency η_c, W_{NET}, Ce_2O_3 outlet from RED and $W_{COMP,tot}$ (=$W_{COMP\text{-}1}$+ $W_{COMP\text{-}2}$+ $W_{COMP\text{-}3}$).

6.6.3 Output temperature of the reduction reactor

Another fundamental parameter is the outlet temperature of the metal oxide from the reduction reactor. It is found that below 900°C there is no complete metal oxide conversion similar to the results observed by Warren and Scheffe [87]. Therefore, all the analysis were performed considering reduction temperature above 900ºC. A higher OC temperature at the outlet of the reactor, inherently demands more heat supply. Since this heat is derived from the heat of combustion, to have higher RED temperature, less CO_2 needs to be recirculated to the combustion chamber. This, even though results in a corresponding drop in the power spent for recycling CO_2, also implies a lower mass flow through the GT, producing less power, as shown in Figure 82. Such would then lower the power produced by the ST1 as well, notwithstanding the higher temperature of the GT outlet, and hence decreasing the net power output. In addition, a higher outlet temperature of RED also restricts the effective operation of the OXI. In fact, since both the CO_2 and H_2O splitting reactions are exothermic, by principle, this requires the reactions to take place at a lower temperature. Moreover, the water-splitting reaction has a higher exothermicity than CO_2 splitting with Ce_2O_3; thus, a higher temperature would result in a slower reaction rate for H_2O splitting, resulting in a CO-rich syngas. The effect of this is evident in Figure 82, in which a significant drop in the DME production can be seen beyond 1000°C (from 2.15 kg/s for 900°C to 2.13 kg/s at 1000°C and to 1.99 Kg/s at 1100°C) due to a deviation from the ideal H_2-CO ratio and higher concentration of CO_2 in the produced syngas stream (Figure 83).

DME is one of the primary products of the proposed polygeneration system, a decrease in the DME production has a dramatic impact on the plant efficiency, as clearly observed in Figure 82, where the drop in the DME yield drives the trend of the decrease in the overall plant efficiency. To be more specific, a relative drop of 10.5% in efficiency is observed between 1000°C and 1300°C, corresponding to an in DME production of 24% and a relative net power output drop of 2%.

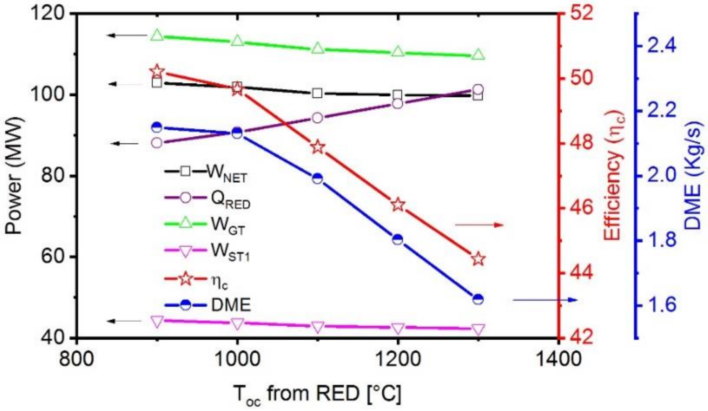

Figure 82. Influence of the metal oxide outlet temperature of RED on efficiency (η_c), W_{NET}, W_{ST1}, W_{GT} Q_{RED}, and DME production.

Figure 83 shows the effect of the metal oxide inlet temperature of the OXI on the H_2/CO ratio in the syngas and on the CO_2 content in the syngas after water removal. As mentioned before, water splitting is favored at a lower temperature compared to CO_2 splitting due to the higher exothermicity of the reaction. Hence, in order to have the ideal H_2/CO =1 for DME production, it is necessary to send an increasingly rich-in H_2O mixture with the higher temperature to the oxidation reactor. In fact, with the increase of the metal oxide temperature, the water splitting is further penalized and consequently, a higher H_2O content is necessary at the inlet. As shown in Figure 83(a), the amount of water needed ranges from 60% to 74% with a metal oxide temperature inlet from 900°C to 1300°C. In addition, as already explained in section 6.4.5, the dilution of syngas with CO_2 has to be avoided in order to enhance DME production. As shown in Figure 83(b), even if it might be possible to produce the ideal composition of syngas (i.e., H_2/CO = 1 ratio) for any metal oxide temperature inlet, the CO_2 content increases at higher temperatures. For this reason, it is suitable to work with lower ceria inlet temperature (900-1000°C) to avoid CO_2 dilution.

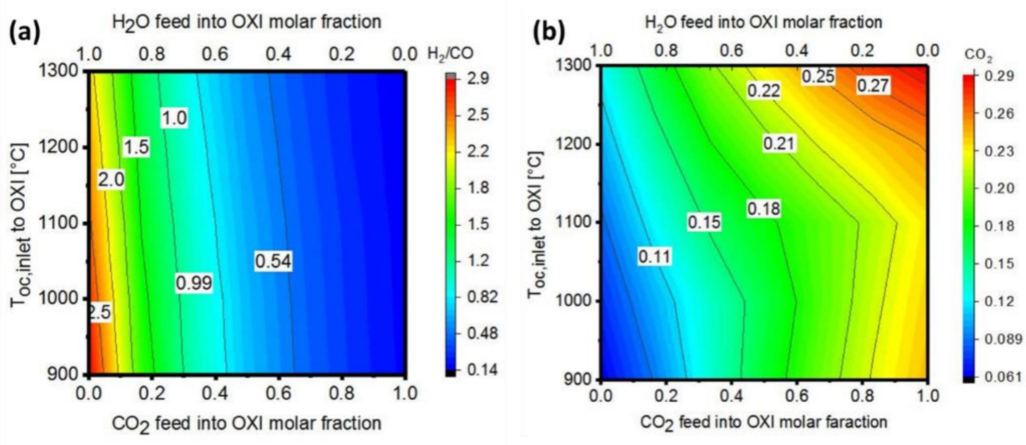

Figure 83. Effect of the initial gas mixture composition fed into OXI on (a) final syngas H_2/CO ratio, (b) CO_2 content (molar fraction) in the syngas after water removal.

6.6.4 Composition of inlet OXI mixture

Figure 84 describes the effect of the variation of the gas mixture composition at the inlet of the OXI on plant performance. The maximum efficiency of 50% is achieved with an OXI inlet mixture of 60% of H_2O and 40% CO_2, with the outlet OXI mixture has the equimolar H_2:CO ratio (i.e., H_2 and CO curves intersect) which reflects the maximum DME production.

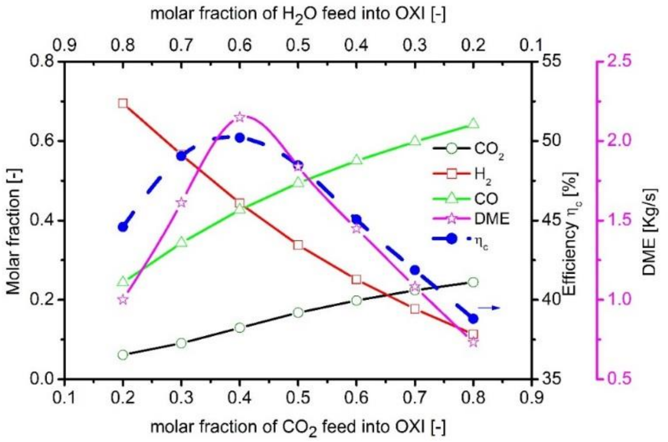

Figure 84. Effect of the gas mixture composition at the inlet of the OXI on the plant performance by considering a metal oxide outlet temperature from the RED of 900°C.

Increasing the water content in the feed to OXI reactor increases outlet metal oxide temperature (Figure 85(a)) as water splitting is more exothermic than CO_2 splitting reaction. In the proposed OXYF-CL-PFG plant layout, the oxidized ceria is recirculated back to the reduction reactor without intermediate heat recuperation. Hence, a higher temperature of oxidized ceria at the outlet of OXI results in a higher inlet temperature of OC to the RED which thereby reduces the heat requirement for the reduction reaction. Due to inlet higher temperature of OC to the RED reactor, the heat requirement from the combustion chamber reduces and therefore, the recirculation of CO_2 to the combustion chamber to maintain the temperature of the outlet would be increased. With this, the power output from the gas turbine (GT) increases as higher flow expands which increases the net power production, as seen in (Figure 85(d)). As stated earlier, this can be possible with the higher H_2O concentration in the feed of OXI which increases the H_2/CO ratio more than unity leading to the drop in DME production and overall efficiency (see Figure 85(b)-(c)). Therefore, an ideal H_2/CO ratio feed to DME reactor, even though leads to lower overall net power, however, ensures the highest efficiency of the polygeneration unit, as can be understood from Figure 85(d). In the case of a non-ideal H_2/CO ratio being fed to the DME reactor, it leads to a lower conversion with unreacted syngas in the product stream. Even though after distillation, this is recycled to the combustor increasing the power, but reduces the DME production and thus, the overall efficiency of the plant.

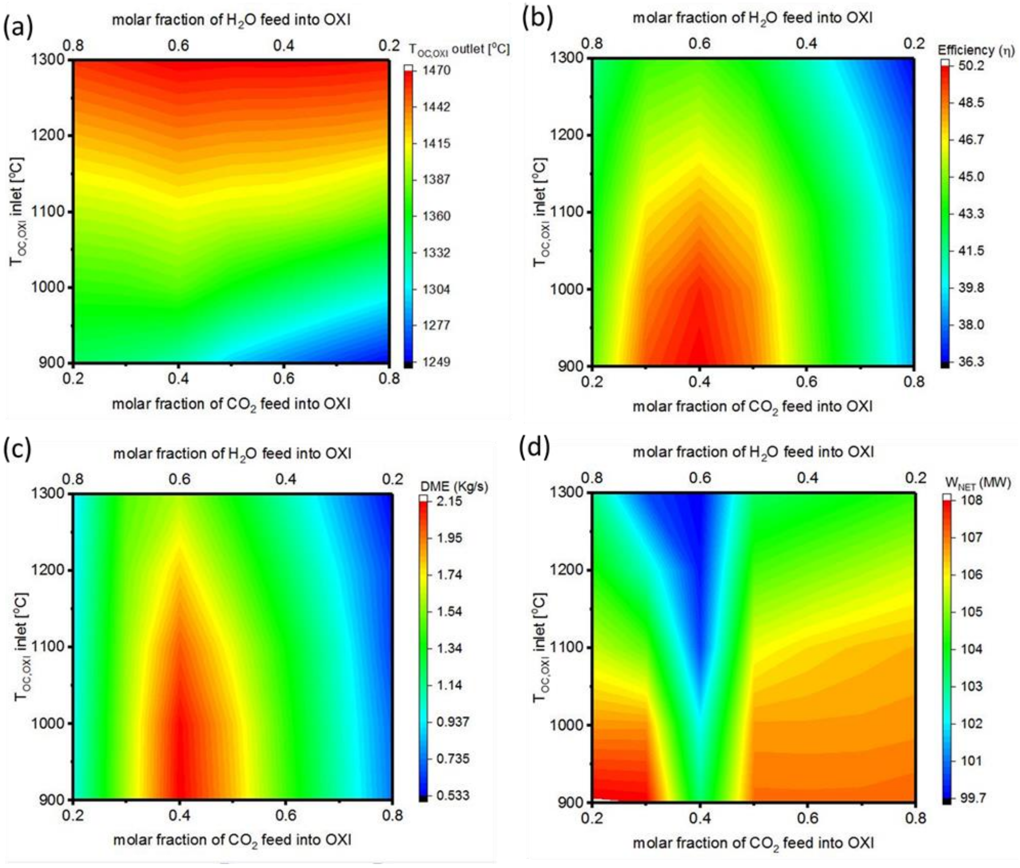

Figure 85. Effect of the gas mixture inlet composition and metal oxide inlet temperature ($T_{OC,OXI}$ inlet) on (a) the temperature of the metal oxide outlet, (b) plant efficiency, (c) DME production, and (d) net power.

6.6.5 Gas turbine inlet temperature

Finally, the impact of the gas turbine inlet temperature (TIT) was analysed. It can be said from Figure 86 that with an increase of TIT the efficiency and net power produced are positively influenced. Nevertheless, the output from the GT drops, which is the result of a lower recirculation of CO_2 to the combustor, needed to ensure a higher combustor exit temperature and consequently a higher TIT. This also causes a lower gas volume to be expanded within the GT, resulting in a lower power output, even though a partial compensation of the lost work is obtained by the lower compression work for the recirculated CO_2 in COMP-2. The power produced by the steam turbine ST1 increases slightly due to a higher exhaust temperature from the GT, overcoming the lower overall gas flow rate. For a TIT of 1100°C, the efficiency of 47.6% was obtained, which increases to 50.7% for a TIT of 1450°C.

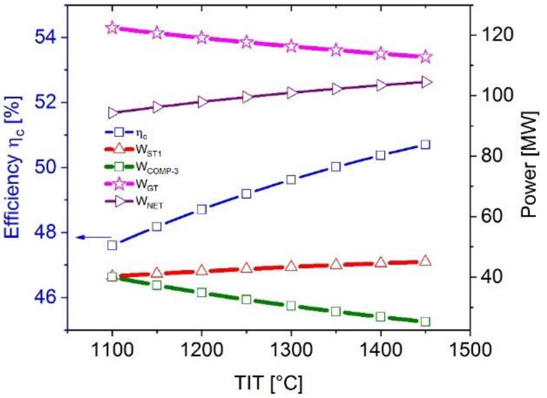

Figure 86. Effect of the gas turbine inlet temperature TIT on the efficiency of the plant (η_c), power produced by the steam turbine (W_{ST1}), by the gas turbine GT (W_{GT}) and the power absorbed by the COMP-3 (W_{COMP-3}).

6.6.6 Plant performance

Based on the sensitivity analysis the following operating parameters were chosen:

- chemical looping operation pressure of 2 bar;
- 40% CO_2 and 60% H_2O feed in the oxidation reactor with an excess of 60% with respect to the stoichiometric value based on the Ce_2O_3 inlet to OXI;
- reduction reactor temperature outlet equal to 900°C;
- TIT of 1377°C.

The plant performance based on the listed parameters is summarized in The total CO_2 produced in polygeneration plant is 3.36 million tons per year out of which 3.4% is converted to the DME ($CO_{2,DME}$). The recirculation streams of CO_2 ($CO_{2,REC}$) in the combustor accounts for the 85% produced CO_2 from the exhaust (2.86 million tons per year), while the one sent into OXI for dissociation is 6.54% (220.4 kilotonne per year) and 283.73 kilotonne of CO_2 per year is sent for sequestrations. In addition, a polygeneration scheme ensures the ability to produce DME within the same system, thus cutting emissions from stand-alone DME production. Conventional DME production via a stand-alone steam methane reforming process results in an equivalent CO_2 emission of 51.1 kgCO_2/GJ of DME [340]. Therefore, an equivalent of an additional 85.65 kilotonne of CO_2 was saved by the polygeneration scheme accounting of total 589.15 kilotonne of CO_2 avoided annually if the CO_2 recirculated is not accounted.

Table 26. Overall, the plant produces 102.90 MW_e, 185.6 ton/day (2.15 kg/s) of DME and 2.59 ton/day (0.03 kg/s) of methanol with a total efficiency of 50.21% and a DME yield of 24.9% (as per equation (6.5)). The highest power consumption is represented by the COMP-3 for the recycle of the CO_2 followed by the compression work in the ASU which accounts for 17% and 11.5% of the gross power generated

respectively. Table 27 gives the composition and main thermodynamics parameters of major streams.

The inlet stream to the DME reactor (stream 14) has the ideal H_2/CO =1 ratio, while the CO_2 content is 13%. However, it can be seen in Figure 85(b), that the minimum CO_2 percentage which can be achieved from the oxidation reactor is near 6%, even though not producing the equimolar mixture of H_2/CO. Therefore, the actual plant configuration allows producing a syngas with a composition which diverges from the ideal H_2/CO ratio of syngas. A solution might be to propose two distinct oxidation reactors, one for the CO_2 splitting and another for the water-splitting. However, this will lead to two different oxidized metal oxide temperatures, complicating the system design dynamics and operations.

An encouraging result is that the proposed oxyfuel-NGCC cycle with the chemical looping and DME unit permits to cut the efficiency penalty of CCS. In particular, compared with results from literature [62], it is possible to achieve a gain of 4 percentage points with respect to a stand-alone Oxyfuel-NGCC process[1].

The total CO_2 produced in polygeneration plant is 3.36 million tons per year out of which 3.4% is converted to the DME ($CO_{2,DME}$). The recirculation streams of CO_2 ($CO_{2,REC}$) in the combustor accounts for the 85% produced CO_2 from the exhaust (2.86 million tons per year), while the one sent into OXI for dissociation is 6.54% (220.4 kilotonne per year) and 283.73 kilotonne of CO_2 per year is sent for sequestrations. In addition, a polygeneration scheme ensures the ability to produce DME within the same system, thus cutting emissions from stand-alone DME production. Conventional DME production via a stand-alone steam methane reforming process results in an equivalent CO_2 emission of 51.1 kgCO$_2$/GJ of DME [340]. Therefore, an equivalent of an additional 85.65 kilotonne of CO_2 was saved by the polygeneration scheme accounting of total 589.15 kilotonne of CO_2 avoided annually if the CO_2 recirculated is not accounted.

Table 26. Plant results with selected parameters.

NG feed	25.2 ton/h
W_{GROSS}	167.61 MW
W_{NET}	102.90 MW
η_c	50.21%
W_{COMP-1}	3.76 MW
W_{COMP-2}	10.67 MW
W_{COMP-3}	28.29 MW
W_{ASU}	19.34 MW
W_{GT}	114.42 MW
W_{ST1}	44.30 MW
W_{ST2}	2.96 MW

---

[1] considering 0.09 kWh/Nm^3 energy requirement for CO_2 compression [488].

$W_{TURBEXP}$	4.37 MW
$\dot{m}_{DME}$	2.15 kg/s
$\dot{m}_{MeOH}$	0.03 kg/s
$CO_{2,REC}$	85%
$CO_{2,DME}$	3.4%

Table 27. Thermodynamics properties and composition of selected streams.

Stream	28	10	14	15	17	20	31	37	38	43	47	7	9
T (°C)	900	1322	200	250	46	43	1377	80	40	40	-41	900	1322
P (bar)	2	2	5	50	10	9	26	26	1	1	10	2	2
Mole flow (kmol/s)	1	0.47	0.34	0.15	0.05	0.04	3.67	2.44	0.19	0.28	0.09	0.59	0.29
Molar fraction													
H_2	0.57	0.32	0.44	0.04	0	0	0	0	0	0	0.01	0	0
H_2O	0	0.28	0	0.01	0.03	0	0.22	0	0	0.99	0	0	0
CO_2	0	0.09	0.13	0.6	0	0	0.77	0.99	0.99	0	0.96	0	0
CO	0.29	0.30	0.43	0.03	0	0	0	0.01	0	0	0.03	0	0
CH_4	0.12	0	0	0	0	0	0	0	0	0	0	0	0
other gases*	0.02	0.01							0.005	0.01			
MeOH	0	0	0	0.01	0.02	0.01	0	0	0	0	0	0	0
DME	0	0	0	0.31	0.95	0.99	0	0	0	0	0	0	0
CeO_2	0	0	0	0	0	0	0	0	0	0	0	1	0
Ce_2O_3	0	0	0	0	0	0	0	0	0	0	0	0	1

6.7 Pinch analysis

The thermal integration of the proposed polygeneration plant was performed using the pinch point analysis [366]. The highest temperature found is 1322°C, which corresponds to the oxidation reactor outlet, while the lowest is -40°C and correspond to the DME condensation temperature. Figure 87 shows the hot and cold composite curve indicating a good thermal integration between cold and hot utilities, without the use of an external heat source. Therefore, the scope for a further increment in the efficiency of the power plant through optimized heat integration is limited. Starting from the hotter utilities, the profile can be interpreted as the following.

- The cold utility curve from 50°C to 550°C represents the steam generation (stream 2A-5A and 2B-5B) driven by the exhaust gas from GT (stream 32) and the hot syngas from the oxidation (stream 10). It also represents the CO_2-H_2O preheating before the dissociation (stream 39 and 45) driven by stream 10a and 10b (hot syngas) in the HX-5 and HX-10 (for CO_2 preheating) and HX-4 and HX-12 (for H_2O preheating);
- The steep part of the curves, from 550° to 900°C for the cold utilities, represents the of natural gas preheating before the reduction in RED (stream 5) taking place in the heat exchangers (HX-1 and HX-8B) and (HX-2 and HX-8);
- The part of the curves near and below zero is mostly related to the distillation unit and the condensation up to a temperature of -40°C of the DME;

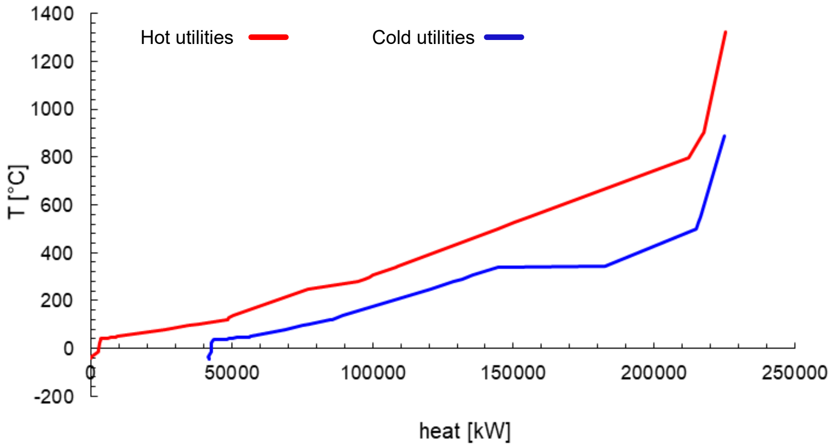

Figure 87. Pinch analysis with hot and cold composite curves.

6.8 Exergy analysis

Exergy of a steady stream of matter is defined as the maximum amount of work obtainable when the stream is brought from its initial state to the dead state by processing during in which the stream may interact only with the environment [367]. As described in chapter 5 related to exergy, similar equations were used for exergy evaluation. The exergy analysis is based on the second principle of thermodynamics, thus permits to evaluate the so-called ‘‘destroyed’’ exergy ($I_{destroyed}$ or Ex_{destr}). Destroyed exergy represents the real loss in the quality of energy that cannot be identified by means of a simple energy balance because the conservation of energy will always apply.

In order to estimate the exergy efficiency (or efficiency of the second principle) of a system is necessary to define the resource exergy flow of the process (Fuel) and which is the final product of the process (Product). The exergy efficiency is shown by the equation (6.15).

$$\eta_{ex} = E_{x,P}/E_{x,F} \qquad (6.16)$$

Where $Ex_{,P}$ represents the exergy of the product streams and $Ex_{,F}$ the exergy of the resource streams. However, the only exergy efficiency does not give a complete framework of the plant or subsystem. For this reason, an additional exergetic factor and other parameters were adopted [300]:

- Relative irreversibilities: $\chi_i = \frac{I_{i,destroyed}}{I_{tot,destroyed}}$ (6.16)
- Fuel depletion rate: $\theta_i = \frac{I_{i,destroyed}}{Ex_{F,plant}}$ (6.17)
- Productivity lack: $\xi_i = \frac{I_{i,destroyed}}{Ex_{P,plant}}$ (6.18)
- Exergetic factor: $\psi_i = \frac{Ex_{F,i}}{Ex_{F,plant}}$ (6.19)

A reference state was selected for the analysis shown in Table 28. For the environmental state, a pressure (P_0) of 1 atm and a temperature (T_0) of 20°C were selected, while for the dead state the reference environment of Szargut [298] was chosen.

Table 28. Chemical exergy of species used.

Environmental state: P_0=1 atm T_0=20°C

Dead State Chemical exergy E_{ch} (kJ/mol)											
H_2	CO	CO_2	H_2O_{vap}	H_2O_{liq}	N_2	CH_4	O_2	CeO_2	Ce_2O_3	DME	MeOH
236.09	275.1	19.2	9.18	0.87	0.696	853.36	3.8	33.8	384.7	1414.5	715.5

Since in the proposed layout there are several chemical reactions, which change the composition of the gaseous streams, the first step was to evaluate the reference chemical exergy of the multiple mixture streams using the dead state of the reference elements. The results are shown in Table 29.

Table 29. Specific chemical exergy of the gas mixture streams.

Stream	31	28	10	15	13	47
$e_{ch,i}$ [kJ/kg]	389	27110	7391	11287	11919	6225

The exergetic performance of the overall plant has been assessed by evaluating its efficiency (equation (6.20)) and the total irreversibility generated (equation (6.21)). As can be clearly observed, due to both electricity and heat self-sufficiency of the system, the input fuel, namely natural gas, contributes entirely to the net exergy input to the system (i.e., it is 100% of the total exergy input) and the products are the total DME, MeOH and the net power produced by the plant.

$$\eta_{ex} = \frac{\dot{m}_{DME} \cdot Ex_{DME} + \dot{m}_{MEOH} \cdot Ex_{MEOH} + W_{NET}}{\dot{m}_{CH_4} \cdot Ex_{NG}} \tag{6.20}$$

$$I_{tot,\, destroyed} = \dot{m}_{CH_4} \cdot Ex_{NG} - \dot{m}_{DME} \cdot Ex_{DME} - \dot{m}_{MEOH} \cdot Ex_{MEOH} - W_{NET} \tag{6.21}$$

As expected, since it is related only to natural gas input and DME, MeOH and net power production, the exergy efficiency trend is specular to the thermodynamic efficiency previously described. The energetic and exergetic efficiency with respect to pressure of CL unit and metal oxide inlet temperature to reduction reactor and turbine inlet temperature are presented in Figure 88 and effect of molar composition of CO_2 and H_2O in OXI is presented in Figure 89. Finally, also a detailed exergy analysis of the components of the layout operating at the conditions described in section 6.6 was performed. Chemical, physical and total exergy values of all streams are reported in Table 30.

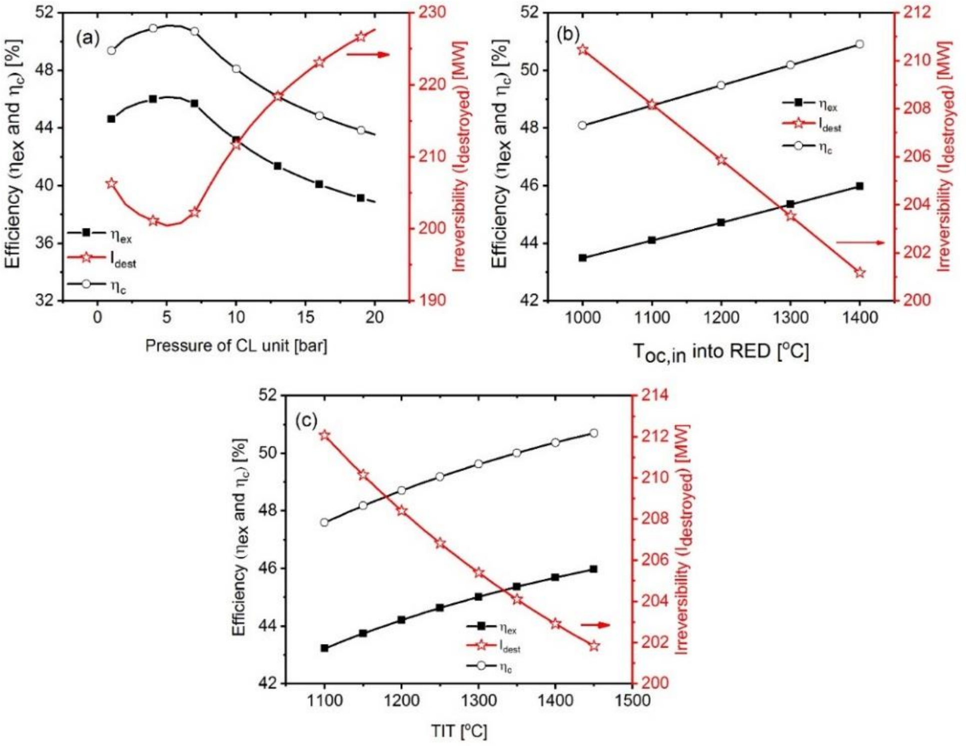

Figure 88. Exergetic efficiency and total irreversibilities ($I_{destroyed}$) generated varying a) the operating pressure of the CL unit, b) the temperature of the inlet metal into the reduction reactor ($T_{OC,in}$) c) the temperature inlet into the gas turbine (TIT).

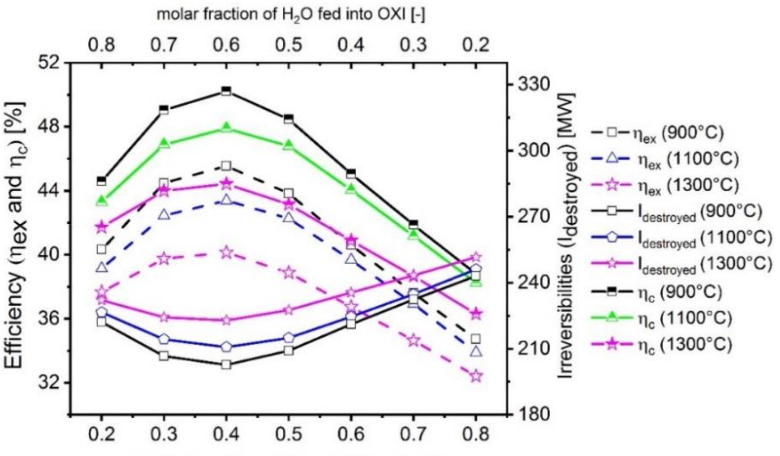

Figure 89. Effect of the gas mixture composition feed into the OXI on the exergetic efficiency η_{ex} and irreversibilities ($I_{destroyed}$).

Table 30. Chemical, physical and total exergy of the plant streams.

State	Specific Physical Exergy [kJ/kg]	Specific Chemical Exergy [kJ/kg]	Specific Exergy [kJ/kg]	Exergy Flow [MW]
0	-	-	-	-
1	247.15	119.91	367.05	7.98
1a	14.72	24.86	39.58	2.83
2	584.21	53201.75	53785.96	376.50
3	806.40	53201.75	54008.14	378.06
4	97.86	53201.75	53299.61	373.10
5	1851.99	53201.75	55053.73	385.38
6	1542.39	27109.67	28652.06	335.37
7	718.95	1172.02	1890.97	182.52
9	599.54	195.24	794.78	80.45
10	1772.70	7416.35	9189.05	79.42
10a	1063.98	7416.35	8480.33	73.29
10b	546.08	7416.35	7962.43	68.81
11	313.68	7416.35	7730.03	66.81
12	3.21	48.33	51.54	0.12
13	90.35	11914.03	12004.38	74.87
14	579.24	11914.03	12493.27	77.92
15	291.85	11273.25	11565.10	72.13
16	198.40	11273.25	11471.65	71.55
17	171.76	11246.12	11417.87	69.93
18	164.88	11246.12	11411.00	69.89
19	127.61	11246.12	11373.73	69.66
20	133.68	436.43	570.11	2.23
21	81.93	30292.33	30374.25	67.05
22	95.62	30292.33	30387.95	67.08
23	109.35	30750.00	30859.35	66.67
24	100.82	9216.04	9316.86	0.44
25	66.65	9216.04	9282.69	0.44
26	4638.21	21603.97	26242.18	0.53
27	43.82	48.33	92.15	0.00
28	357.80	27109.67	27467.47	321.51
28b	189.96	27109.67	27299.62	319.54
29	145.98	27109.67	27255.65	319.03
30	868.38	27109.67	27978.05	327.48
31	1375.23	387,84	1763.06	246.88
32	515.30	387,84	903.14	126.47
33	37.04	387,84	424.87	59.50
34	49.60	436,43	486.04	57.23
35	49.60	436,43	486.04	4.84
36	40.96	436,43	477.40	47.78
37	218.95	436,43	655.38	69.78
38	49.60	436,43	486.04	4.02
39	94.68	436,43	531.11	4.39
40	294.88	436,43	731.31	6.04
41	3.18	48,33	51.52	0.76
42	3.18	48,33	51.52	0.50
43	3.18	48,33	51.52	0.12
44	3.11	48.33	51.44	0.12
45	497.88	48.33	546.21	1.27
46	1022.64	48.33	1070.97	2.48
47	621.44	6044.21	6665.65	0.75
48	607.94	6044.21	6652.15	0.75
49	505.90	6044.21	6550.11	0.74
1-A	19.82	48.33	68.15	2.36
2-A	19.45	48.33	67.78	2.35
3-A	630.56	48.33	678.89	23.51
4-A	1161.85	48.33	1210.18	41.90
5-A	1552.72	48.33	1601.06	55.43
6-A	109.18	48.33	157.51	5.45
7-A	2.06	48.33	50.40	1.74
1-B	19.82	48.33	68.15	0.16
2-B	20.74	48.33	69.07	0.16
3-B	630.56	48.33	678.89	1.57
4-B	1161.85	48.33	1210.18	2.80
5-B	1552.72	48.33	1601.06	3.71
6-B	109.18	48.33	157.51	0.36
7-B	2.06	48.33	50.40	0.12

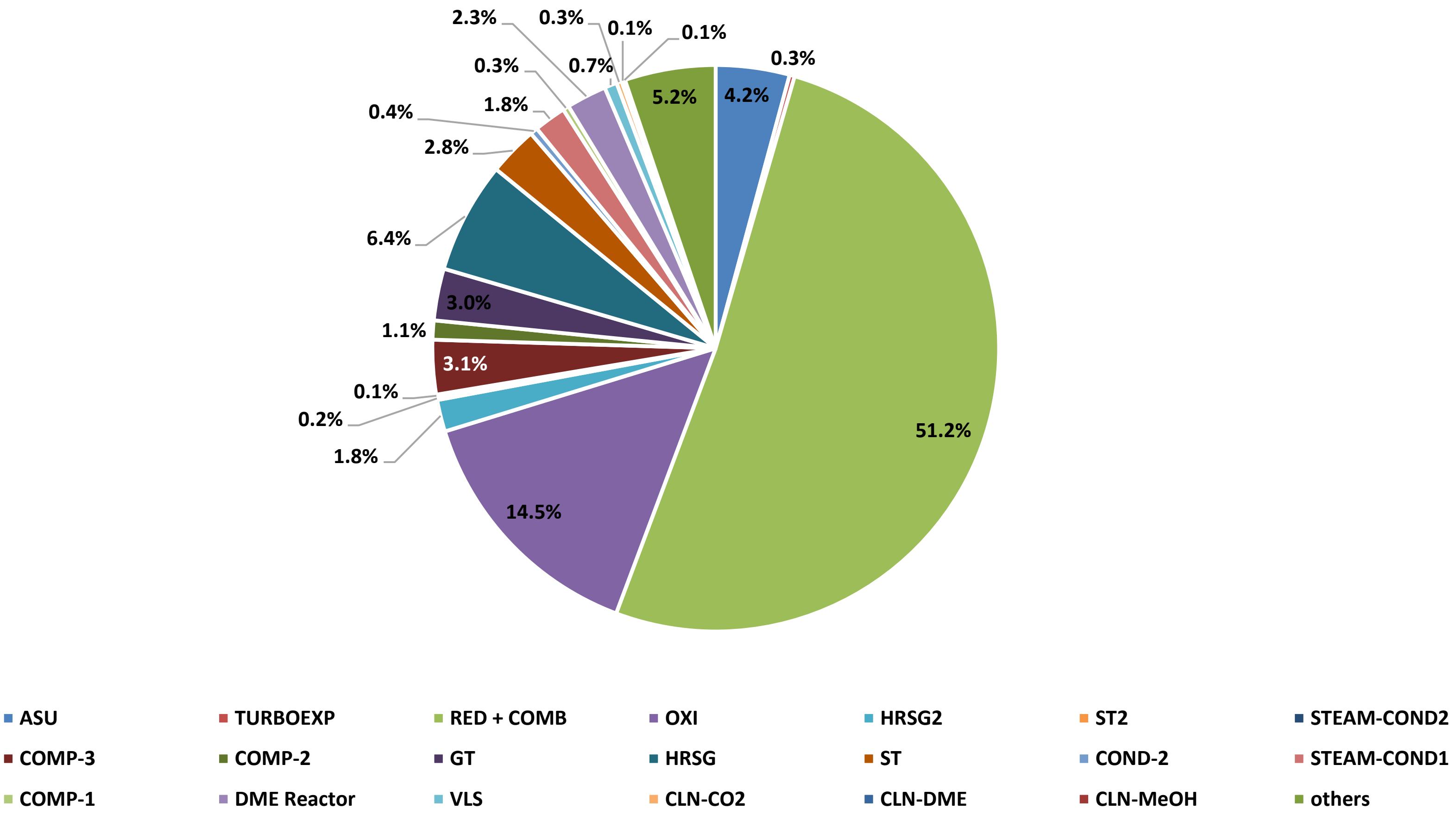

Figure 90. Total irreversibilities distribution.

From the results, the global exergy efficiency (η_{ex}) of the plant is 45.0%, five points lower than the calculated first-law efficiency (η_c). The total irreversibilities generated are 202.72 MW with an overall fuel depletion rate (θ) of 53.84%. All the components present an exergetic efficiency over the 80%, with the exception of the air separation unit (55.9%) and the two condensers for the steam cycle (32%) and the CLN-MeOH (77%). However, the contribution of COND-A, COND-B, and ASU to the overall efficiency is marginal since their relative irreversibilities χ_i do not exceed the 3.9% (Table 31).

The exergy efficiency of the RED+COMB results in 88.1%. Although this value is not extremely low, more than half of the 202.72 MW total irreversibilities are located in this component (Figure 90). As shown in Table 31, the RED+COMB exergetic factor ψ results in 231.3%, so the irreversibilities are not due to the efficiency, but are mainly proportionally correlated to the high exergy of the inlet streams. In fact, the exergy inlet of the RED+COMB ranks first among the components (870 MW), the second is the turbo-expander inlet (378 MW). Moreover, it is worth mentioning that, with the hypothesis of zero heat losses inside the combustor and reduction reactor, the main contributor to the exergy losses are of the chemical form. In fact, the exergy efficiency of the RED+COMB, considering only the chemical exergy of the inlet and outlet streams, results in 70%. This is also verified by exergo-economic analysis reported in Appendix A.2. The oxidation reactor is the second-ranked component for the relative irreversibilities parameter (14.4%) even if the exergy efficiency (83.4%) results in to be lower than the one of the RED+COMB. This is due to the lower exergy factor (50.7%).

The other irreversibilities are mostly located in the HRSG1 of the steam ranking cycle (SRC1) (13.99 MW) and in the compression process (9.3 MW). The DME reactor jacketing for saturated steam production allows increasing the exergy efficiency of the component of 2.2%.

Table 31. Results from the exergetic analysis of the main components.

Component	Exergy balance eq.[1]	I [MW]	$\eta_{ex,i}$ [%]	θ_i [%]	ψ_i [%]	ξ_i [%]
ASU	$E_0 + W_{ASU} = E_1 + E_{1b} + I_{ASU}$	8.53	55.91	2.26	5.14	5.03
TURBOEXP	$E_3 = W_{TURBOEXP} + I_{TURBOEXP}$	0.59	99.84	0.16	100.41	0.35
RED+COMB	$E_{9a} + E_5 + E_{30} + E_1 + E_{49} + E_{37}$ $= E_{31} + E_{28} + E_7 + I_{RED+COMB}$	103.83	88.08	27.58	231.29	61.23
OXI	$E_7 + E_{46} + E_{40} = E_{10} + E_{9a} + I_{OXI}$	29.47	84.57	7.83	50.74	17.38
HRSG2	$E_{10} + E_{2\text{-}B} = E_{10a} + E_{5\text{-}B} + I_{HSRG\text{-}2}$	3.68	97.49	0.98	38.88	2.17
ST2	$E_{5\text{-}B} = E_{6\text{-}B} + W_{ST2} + I_{ST2}$	0.38	89.77	0.10	0.99	0.22
COND-B	$E_{6\text{-}B} = E_{7\text{-}B} + I_{COND\text{-}B}$	0.25	32.0	0.07	0.10	0.15
COMP-4	$E_{38} + W_{COMP\text{-}4} = E_{39} + I_{COMP\text{-}4}$	0.08	98.26	0.02	1.18	0.04
COMP-3	$E_{49} + W_{COMP\text{-}3} = E_{37} + I_{COMP\text{-}3}$	6.29	91.73	1.67	20.21	3.71
COMP-2	$E_{29} + W_{COMP\text{-}2} = E_{30} + I_{COMP\text{-}2}$	2.21	99.33	0.59	87.57	1.30
GT	$E_{31} = W_{GT} + E_{32} + I_{GT}$	6.00	97.57	1.59	65.57	3.54
HRSG1	$E_{31} + E_{2\text{-}A} = E_{33} + E_{5\text{-}1} + I_{HSRG\text{-}1}$	12.88	90.0	3.42	34.21	7.60
ST1	$E_{5\text{-}A} = E_{6\text{-}A} + W_{ST1} + I_{ST1}$	5.68	89.75	1.51	14.72	3.35
COND-2	$E_{33} = E_{34} + E_{41} + I_{COND\text{-}2}$	0.88	98.51	0.23	15.80	0.52
COND-A	$E_{6\text{-}1} = E_{7\text{-}A} + I_{COND\text{-}A}$	3.71	32.00	0.99	1.45	2.19
COMP-1	$E_{13} + W_{COMP\text{-}1} = E_{14} + I_{COMP\text{-}1}$	0.71	99.10	0.19	20.88	0.42
DME Reactor	$E_{14} + E_{44} = E_{15} + E_{45} + I_{DME\ reactor}$	4.64	94.05	1.23	20.73	2.74
VLS	$E_{15} = E_{47} + E_{17} + I_{VLS}$	1.45	97.99	0.39	19.16	0.86
CLN-CO_2	$E_{19} + Q^*_{COND,\ CLN\text{-}CO2} + Q^*_{RED,\ CLN\text{-}CO2}$ $= E_{20} + E_{21} + I_{CLN\text{-}CO2}$	0.60	99.15	0.16	18.56	0.35
CLN-DME	$E_{22} + Q^*_{COND,CLN\text{-}DME} + Q^*_{REB,CLN\text{-}DME}$ $= E_{22} + E_{23} + I_{REB\text{-}DME}$	0.30	99.56	0.08	17.90	0.18

CLN-MeOH	$E_{25} + Q^*_{COND,CLN\text{-}MeOH} + Q^*_{REB,CLN\text{-}MeOH} = E_{22} + E_{23} + I_{REB\text{-}MeOH}$	0.15	77.39	0.04	0.18	0.09
NG_{PHX1}	$E_2 + E_{28} = E_3 + E_{28b} + I_{NG\text{-}PHX1}$	0.41	99.94	0.11	185.39	0.24
NG_{PHX2}	$E_4 + E_{28b} = E_5 + E_{29} + I_{NG\text{-}PHX2}$	1.59	99.78	0.42	188.17	0.94
CO_{2PHX}	$E_{10a} + E_{39} = E_{10b} + E_{40} + I_{CO2\text{-}PHX}$	0.38	99.48	0.10	19.34	0.23
H_2O_{PHX}	$E_{10b} + E_{45} = E_{11} + E_{46} + I_{H2O\text{-}PHX}$	3.26	95.63	0.87	19.80	1.92

[1] The left-side of the equation in the table represents the fuel of the component, while the right side of the equation represents the product and the irreversibilities of the component.

Q^* represents the exergy obtainable using the heat of the selected stream

$$Q^*_{COND,CLN-CO2}{=}Q_{COND,CLN-CO2} \times \left(1 - \frac{T_{COND,CLN-CO2}}{T_0}\right);$$

$$Q^*_{REB,CLN-CO2} = Q_{REB,CLN-CO2} \times \left(1 - \frac{T_0}{T_{REB,CLN-CO2}}\right);$$

$$Q^*_{COND,CLN-DME}{=}Q_{COND,CLN-DME} \times \left(1 - \frac{T_0}{T_{COND,CLN-DME}}\right);$$

$$Q^*_{REB,CLN-DME} = Q_{REB,CLN-DME} \times \left(1 - \frac{T_0}{T_{REB,CLN-DME}}\right);$$

$$Q^*_{COND,CLN-MeOH} = Q_{COND,CLN-MeOH} \times \left(1 - \frac{T_0}{T_{COND,CLN-MeOH}}\right);$$

$$Q^*_{REB,CLN-MeOH} = Q_{REB,CLN-MeOH} \times \left(1 - \frac{T_0}{T_{REB,CLN-MeOH}}\right);$$

6.9 Economic analysis

An economic assessment was performed to calculate the capital cost of investment for the construction of the proposed plant. The National Energy Technology Laboratory (NETL) guidelines for techno-economic analysis for power plants was adopted [368,369]. This methodology defines capital cost at five levels: bare erected cost (BEC), engineering, procurement, and construction cost (EPCC), total project cost (TPC), total overnight cost (TOC) and total as-spent cost (TASC). In the current study, the TOC was considered for the capital investment expenditure. The first four items are "overnight cost" and are expressed in base-year US dollar that is the first year of capital expenditure. The Bare Erected Cost (BEC) comprises the cost of the equipment, facilities and infrastructure, and labour required for its installation. The equipment cost estimation was done using the scaling factor exponent M, is given by (equation (3.28)) [370] and details of the scaling factor can be found in [321]:

To assess further costs related to setting up of the polygeneration plant including installation and other direct and indirect costs related to the project development, a bottom-up approach following the methodology adopted in the CAESER project [263] was selected. The equipment costs were evaluated using equation (3.28) and (3.29) using CEPCI (Table 32) and are shown in Table 33.

Table 32. CEPCI Index.

Year	CEPCI index
2017	572.7
2016	585.7
2008	575.4
2007	525
2006	499.6
2003	402

Table 33. Equipment cost of proposed OXYF-CL-PFG plant.

Equipment	Scaling Parameter	Cost Year	$C_{equ,0}$ [M$]	$C_{equ,actual}$ [M$]
GT [263]	GT Net Power [MW]	2008	$60.99	$25.70
HRSG1, ducting and stack [371]	ST Net Power [MW]	2003	$6.10	$4.55
ST1 and ST2, generator and auxiliaries [263]	ST Gross Power [MW]	2008	$41.60	$15.82
Cooling Water System and Balance of Plant [263]	Q rejected [MW]	2008	$61.23	$24.84
COMP-3 [263]	Compressor Power [MW]	2008	$9.95	$16.77
COMP-2 [372]	Compressor Power [MW]	2003	$4.83	$5.02
COMP-1 [372]	Compressor Power [MW]	2003	$4.83	$2.50

ASU [265]	Oxygen Production [ktO$_2$/day]	2008	\$62.96	\$117.65
RED and OXI [207]	CLC Plant, (150MW)	2016	\$48.72	\$14.55
TURBEXP [373]	MW Power Produced	2008	\$0.73	\$1.32
DME reactor and BOP [372]	Inlet gas [kmol/s]	2007	\$21.00	\$5.16
DME cooling system [372]	Electrical power [MW]	2007	\$1.70	\$0.73
Clean-Up unit [372]	inlet DME [kg/s]	2007	\$28.40	\$13.33
HRSG2, ducting and stack [371]	ST Net Power [MW]	2003	\$6.10	\$13.23
COMP-4 [263]	Compressor Power [MW]	2008	\$9.95	\$0.74
Exchangers [372]	Heat exchanged [MW$_{th}$]	2007	\$52.00	\$1.32

The cost of the cooling tower system was included in the cost of the four condensers (COND-1, COND-2, SRC1, and SRC2 condenser). The overall cost was subdivided between the four components proportionally to the calculated rejected heat. The cost of the two condensers (COND-A and COND-B) of the two HRSG was included in the HRSG investment cost. The most expensive equipment is the ASU, followed by the GT. The RED+COMB unit accounts for 5.2% of the total expenditure. The individual contribution of the respective equipment to the total overnight cost is shown in Figure 91. The bare erected cost (BEC) of each equipment was given summing all the installation costs (see Table 34 for assumptions of CAPEX estimation) to the equipment cost is given by equation (6.22).

$$BEC = C_{equ,actual} + \text{Installation Cost} \tag{6.22}$$

Table 34. Main assumption in CAPEX estimation [263,267,268].

Installation Cost	
Accessory Electrical Plant	16,93 M\$
FO Supply System and Natural Gas Supply System	10,04 M\$
Erection, Steel Structures and Painting	49% of equipment cost
Piping	9% of equipment cost
Indirect cost	
Yard improvement	2% BEC
Services facilities	2% BEC
Engineering/consulting costs	5% BEC
Building	4% BEC
Miscellaneous	2% BEC
Owner's cost	5% EPCC
Contingency [369]	30% EPCC

The engineering, procurement and construction cost (EPCC) comprises the BEC plus the costs of all services provided by the engineering, procurement and construction contractor (equation 6.23). These items include detailed design, contractor permitting and project management costs.

$$\text{EPCC} = \text{BEC} + \text{INDIRECT COST} \tag{6.23}$$

The total project cost (TPC) takes into account the EPCC plus the contingencies cost (equation 6.24). Contingencies are added to account for unknown costs that are omitted or unheralded due to lack of complete project definition or uncertainties with the development status of a technology. In the present case, since the proposed plant is based on a novel technologies arrangement, a high contingency cost of 30% was selected (Table 34).

$$\text{TPC} = \text{EPCC} + \text{CONTINGENCIES} \tag{6.24}$$

The total overnight cost (TOC) comprises the TPC plus other overnight costs (Table 35), owner's cost included (i.e pre-production, inventory capital, land, financing), it was calculated as:

$$\text{TOC}=\text{TPC} + \text{OWNER'S COST} \tag{6.25}$$

Table 35. Main assumption in OPEX estimation [263,267,268].

Variable costs	
Process Water	7.41 $\$/m^3$
Make-up water	0.41 $\$/m^3$
Fuel cost [268]	0.04 $/kWh
Ceria oxide cost ([374])	49 $/kg
Yearly Ceria oxide make-up	30% of the total
Fixed costs	
Property, Taxes and insurance	2% TOC
Maintenance cost	2.5% TOC
Labour cost	1% TOC

From the assumptions of Table 35, the total overnight cost (TOC) of the plant resulted in 537.45 $million. Figure 91 represents the contribution to the total overnight cost of the different equipment. The most expensive equipment resulted in the ASU, followed by the GT. The RED+COMB unit accounts for 5.2% of the total expenditure. For the economic analysis, all assumptions are listed in Table 35 and Table 36 for OPEX estimations.

Table 36. Economic assumptions.

Life of the system (t)	30 years
Discount rate (i)	10%
Capacity factor (CF)	85%
Debt	60%
Equity	40 %
Cost of debt	2.4 %
Inflation	1.5%
Project financing	10 years

TASC	7.8% TOC
Construction	3 years

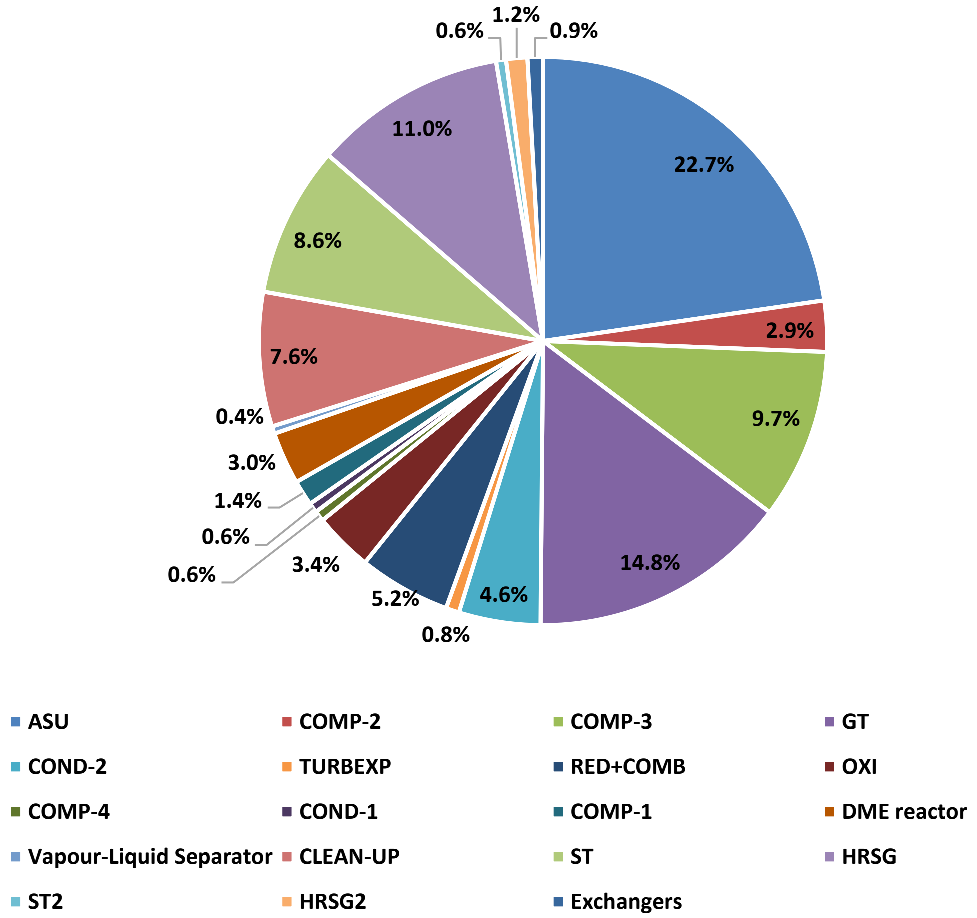

Figure 91. Contribution of the component to the TOC.

Finally, to evaluate the profitability of the plant during its lifetime a discounted cash flow analysis (DCF) was adopted. DCF is based on the concept of the time value of money, all the future cash flows are estimated and discounted by a discounted factor (i) (Table 36), obtaining their present value [375]. The sum of the all discounted cash flows, both positive (revenues) and negative (based on operation cost, see OPEX assumption in Table 35), gives the net present values (NPV) given as equation (6.26).

$$\mathrm{NPV} = -\mathrm{TASC} + \sum_{l=1}^{\mathrm{t}} \frac{(\text{net cash flows})_l}{(1+\mathrm{i})^l} \tag{6.26}$$

A project is acceptable only if the NPV is at least positive. In this particular case, TASC is used to evaluate the total project cost instead of TOC, in order to asses both escalation and interest during construction (Table 35) [368,369]. A sensitivity analysis was performed to evaluate the effect of the selling price of power and DME on the economic performance of the plant.

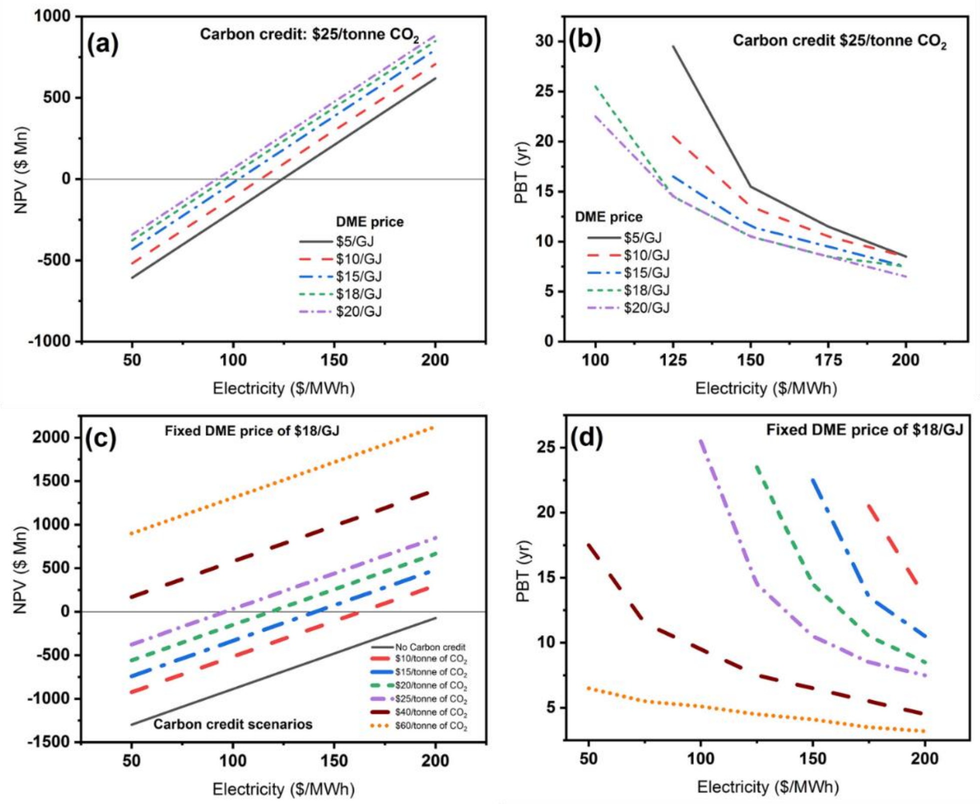

Figure 92. (a), (c) Economic performance varying carbon credits and DME prices for different electricity prices (b), (d) Payback period (PBP) varying DME and electricity price for different levels of carbon credit.

It is observed that a payback period (PBT) of 20 years was obtained with the electricity and the selling price of DME of $20/GJ and $220/MWh respectively which is around 4.4 times the current wholesale electricity price without carbon credits considered.

Figure 92(a) and (b) represents the variation of electricity prices for different DME prices from \$5-20/GJ. It is observed that for the current reported carbon credit price of \$25/tonne of CO_2 [376] the NPV is positive if the electricity price of \$96/MWh (almost twice of the current electricity price) with a payback period of 25.5 years. However, with the stringent carbon credit initiatives and energy policies, the carbon credit have been predicted to be doubled by 2020 and subsequently quadrupled reaching \$60/tonne of CO_2 by 2030 [377] for European markets. Therefore, the NPV values were varied for different scenarios of electricity and DME price based on the carbon credit variation from \$10-60/tonne of CO_2 as per the current carbon prices worldwide [376,377]. Figure 92 (c) and (d) corresponds to the fixed current market DME price of \$18/GJ [340] and varying the carbon credits for electricity pricing. From the Figure 92 (c) it can be said with the carbon credit above \$40/tonne CO_2 would have positive NPV that can be able to match with the current electricity price of \$50/MWh for the proposed polygeneration with a PBT of 17.5 years, with potential to drop further for higher carbon credit scenarios.

However, more strong carbon credit policies and a further development of technologies, such as Oxyfuel combustion, air separation, and chemical looping, will make the proposed polygeneration plant more competitive. By considering oxygen transport reactors that use ion transport membranes, such as perovskites, for oxygen separation at high temperatures (i.e., above 700°C), high-purity oxygen could be produced at a relatively lower price compared to ASU, thereby increasing the efficiency and decreasing the equipment cost. At present, with this technology, it is possible to produce 2000 tonne per day, which is sufficient for an oxyfuel plant of 110 MW capacity. Therefore, with the adoption of the ion transport membrane technology that costs 31% less compared to the ASU, consequently, the cost of DME and power production would decrease tremendously and the overall efficiency of the plant would improve by 2-4% [378].

6.10 Water footprint analysis

An important parameter for an industrial and/or power plant is its water use. A generally accepted indicator of water use is the water footprint [301,379] which measures the volume of freshwater used to produce a product over the full supply chain [380]. In this specific case for water footprint is intended the water exploited during the plant operation, i.e. for cooling and another process. A part of the input fuel energy is lost as waste heat, dissipated to the environment. Of this, the major part is rejected through a cooling system, usually using water as a transfer medium. In general, water use in a polygeneration plant can be really complicated. However, a good estimation of it doesn't require a detailed analysis since according to Gerdes et al[368,369] the cooling process accounts for 73-99% of the water consumption. Therefore, the water need for all other auxiliary purposes except cooling can be neglected with minor errors. However, the knowledge of the heat rate and the type of cooling system is crucial.

The following water withdrawal calculation is based on the model described in [381] as described in equation (5.16).

The heat rate (HR) is defined as the amount of energy required to produce one kW of electricity:

$$\mathrm{HR} = \frac{\text{Heat Input of Fuel}}{\text{Net Power Output}} \tag{6.27}$$

The energy input to the plant can leave it only in two ways, as process heat loss or as electricity. Thus, the heat sent to the cooling system is represented by HR- Λ, where, Λ (kJ/kWh) takes into account all the heat losses during the process, i.e heat losses from the steam turbine, generator, radiation, combustor etc. In general, depending on the technology, they range from 3% to 5% of the total energy input [381]. The parameter Ω (dm^3/kJ) is the constant that takes into consideration the water need for the cooling system per unit of energy that has to be rejected. These parameters depend on many factors such as the type of cooling system (cooling tower, one-trough, dry cooling), the design of the cooling system, temperature and humidity of the air and water. Finally, the parameter Γ (dm^3/kWh), provides the make-up water factor for the two steam cycles. The values of the described parameters are shown in Table 37.

Table 37. Main assumption made in water footprint calculation and results.

Heat Rate (HR)	11523.45 kJ/kWh
Heat losses	5%
Λ	4176.2 kJ/kWh
Ω	0.001 dm^3/kJ
Γ	0.02 $dm^3/kWh_{e,gross}$
Water use for cooling	2834374.4 m^3/year
Water use for the process	24893.7 m^3/year

In order to simplify the comparison to the plant that produces only fuel or only power or polygeneration, the water assessment is converted based on the total m^3/MWh by converting the calorific value of the DME produced and the power Figure 93 illustrates the water consumption of the proposed plant compared with other technologies. It results in the plant with the highest water consumption with 3.65 m^3/MWh, the main reason is that the other fuel power plants considered are without CCS. Moreover, the calculated water footprint is based only on the electrical power production, but since it produces also a liquid fuel, the water footprint can be related also to the MWh produced by DME. In that case, the m^3/MWh is equal to 2.33, comparable to a nuclear power plant. In few studies, the water consumptions were related based on DME production. Therefore based on that DME production, water consumption found to be 73.3 kg/kg_{DME} of water are consumed for the cooling application. It has been observed that for DME polygeneration plants with CSP the water consumption for cooling is 103 kg/kg$_{DME}$, 26.8 kg/ kg$_{DME}$ with PV solar and 1561 kg/kg$_{DME}$ with biomass driven cycle [382]. Hence, the water consumption is lower than the renewable technology is driven polygeneration DME plant, except for PV solar.

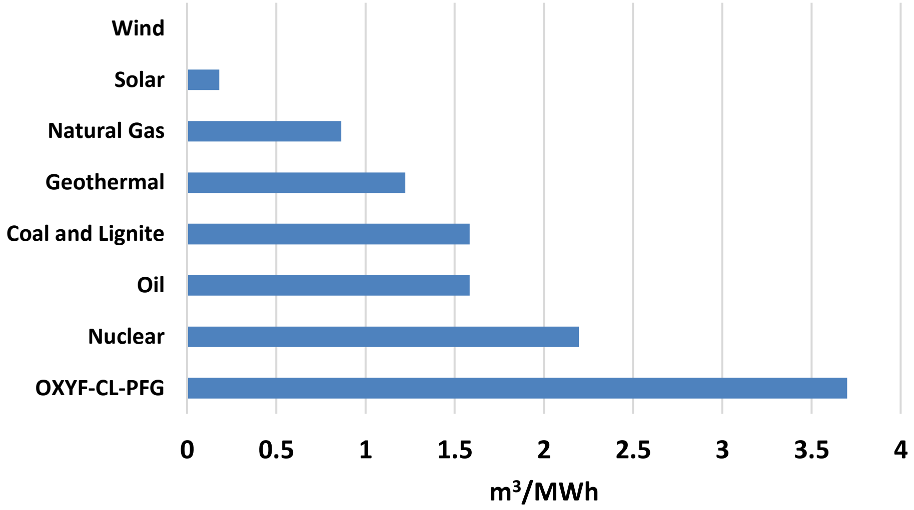

Figure 93. Water footprint comparison between different power plant technology [301] and proposed OXYF-CL-PFG polygeneration plant.

6.11 Concluding remarks

A novel natural gas feed polygeneration plant was proposed that integrates a chemical looping CO_2/H_2O splitting unit with an oxyfuel combustion unit for the production of power, DME and methanol. The results demonstrated the advantages of using a chemical looping CO_2/H_2O process in a polygeneration plant to reduce the efficiency penalty due to the carbon capture. The analysis revealed that the ideal H_2/CO ratio for a single step DME synthesis to be which can be obtained by feeding H_2O/CO_2 ratio of 60/40%. The plant was able to produce 103 MWe and 185.6 ton/day (2.15 kg/s) of DME with an energetic and exergetic efficiency of 50.2% and 45.0%, respectively. Compared to the only power plant with carbon capture the present polygeneration revealed an efficiency gain of 4%. Through an exergy analysis, the main contributors of exergy destruction were identified: the combustor and reduction system resulted to contribute for 51.2% of the total generated irreversibilities (221 MW). The capital investment was estimated to be $534 million. The overall CO_2 avoided was 3.43 million tonne for 7446 hours (with a capacity factor of 0.85) of the annual operation of which approximately 3.4% is contributed by the DME production in a polygeneration scheme. Economic analysis revealed that around 23% of the total equipment costs is attributed by ASU and with the use of more sophisticated technology for producing oxygen at less price would decrease the capital investment. A discounted cash flow analysis revealed that the proposed plant would able to meet the current electricity and DME price of \$50/MWh an \$18/GJ with the carbon credit of \$40/tonne of CO_2, which is projected to be the carbon credit by 2020.

Chapter 7

Reaction kinetic assessment for non-stoichiometric ceria

Oxygen carriers are the fundamental component of a chemical looping process, and the choice of stable and efficient carriers with fast redox kinetics is the key to the successful design of the process. Hence, understanding the reaction kinetics is of paramount importance for the selection of an appropriate oxygen carrier material. This work provides a method for kinetic model selection aimed to identify the reaction mechanism. Therefore in this chapter, we investigate the kinetics and reactivity of ceria for H_2 reduction and then methane reduction considering CO_2 splitting for the oxidation step. Reactivity assessment and the kinetic model selection were performed for different temperature and concentration of oxidizer and reducer. The reactivity data was tested for different semi-empirical kinetic models for the non-catalytic type of reactions and based on the fit of the data with the model, kinetic parameters were evaluated. The fitted model and kinetic parameters are of paramount importance that will help in designing a reactor for large-scale fuel or power production systems.

7.1 Introduction

Solar-thermochemical cycles for syngas production has gained potential interest in recent time and earlier we have investigated the reactor model and its integration to a power plant. It is also observed the challenges associated with temperature and pressure swing between the reduction and oxidation step. For thermal reduction step, reaching a very high vacuum is a very energy intensive and a sophisticated pressure cascading systems were suggested [31,166,329] and the system is not continuous as it depends on the availability of solar energy. Therefore, the solar thermal reduction step is replaced by methane reduction allowing the redox cycle to operate at the same pressure and isothermal condition and its schematic is presented in Figure 94.

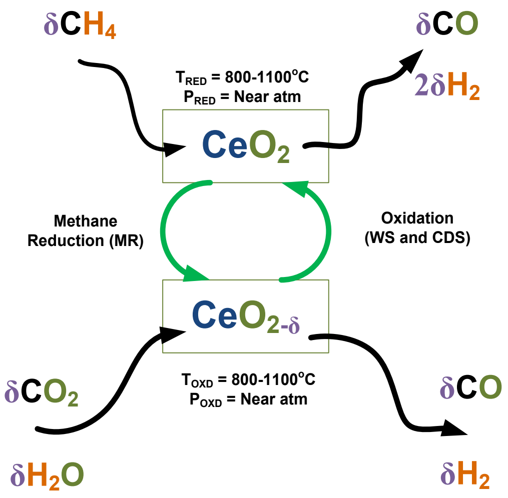

Figure 94. Chemical looping CO_2/H_2O splitting of non-stoichiometric ceria by methane reduction

Literature study on the reduction of ceria through partial oxidation of methane (POM) has largely focused on the characterization of the material performance including the study of the effects of doping through transition metal promoters and/or by addition of different inert support materials [128,383]. The study carried out in chapter 4, 5 and 6 considered the Gibbs minimization principle considering CeO_2 is completely reduced to Ce_2O_3 to investigate the feasibility of the non-structured reactors in CO_2/H_2O splitting (CDS/WS) add-on unit to power and fuel production with respect to scale and economic viability. But it is understood that the non-catalytic heterogeneous reaction of ceria with fuel does not lead to full conversion to Ce_2O_3 and this will affect reactor performance due to parameters, such as particle residence time, reaction time (which are different for reduction and oxidation steps), reaction mechanism, selectivity and composition of the products species. Several experiments were performed to investigate the reactivity of non-stoichiometric ceria with methane. Otsuka et al [384] studied the reaction mechanism between both doped and undoped ceria for POM with Pt as a catalyst, where, the recombination or desorption of the produced H_2 was identified as the rate determining step for the reduction reaction. In a further study, the same author reported activation energy of POM over pure ceria to a value around 160 kJ/mol [37]. Nair and Abanades [279] carried out experiments in a solar assisted reactor between the temperature range of 900-1100°C in a solar assisted thermogravimetric system and reported an activation energy of 109 kJ/mol and a reaction order of 0.62. The maximum non-stoichiometry (δ) obtained for commercial ceria was reported as 0.37 [279]. Warren et al [87], in a recent work published in 2018 reported the kinetic behavior related to POM over pure ceria including studying the impact of different factors like the limitation of gas/solid diffusion, gas composition ratio between the reactant and the product, etc. Through experiments conducted at the range between 750°C and 1100°C and atmospheric conditions, and carrying out measurements through a thermogravimetric analyzer, the activation energy for the reaction was obtained using Arrhenius-type plots [87]. The activation energy reported was much lower, between 20 kJ/mol and 80 kJ/mol, with the higher value being obtained at a δ>0.15. Furthermore, a complete reduction of ceria was reported beyond 900ºC [87] though the study does not infer the sample characterization and microstructure analysis to support the claim, as with the ceria phase diagram the structure does not hold if the ceria loses more than 17% of the oxygen from it. Chauyboon et al [278] investigated solar driven methane reduction and CO_2/H_2O splitting for a temperature range of 950-1050ºC. It is reported that the maximum non-stoichiometry reached is 0.38 and 0.37 for reduction and oxidation respectively. The reactor setup is a structured type with ceria in the reticulated porous foam weighing 18.3 gm. The study reported the stability of the redox cycle is observed at 1000ºC and effect of methane cracking at higher temperature and effect of methane flow rates are linked. The carbon deposition is observed at a temperature above 1000ºC and for methane flow rates greater than 0.1 Nl/min concluding that lower concentration of methane and temperature below 1050ºC is suitable to avoid methane cracking and carbon deposition. Also, none of the studies, have considered a model based kinetic approach to reporting the overall reaction kinetics of POM with ceria reduction. This model specifically benefits in the identification of the rate controlling mechanism, while at the same time assign parameters to the kinetic model, so as to successfully predict the outcomes of the reactions over the entire envelope of the fuel curve [385].

For the oxidation reaction, multiple studies of the kinetics of catalytic oxidation of Ce_2O_3 at low temperatures (below 800ºC) with water or CO_2 have been studied and reported in the literature, especially due to its applications in catalytic converters, fuel cells and other applications [385]. Nevertheless, such low-temperature studies for catalytic reactions are typically not applicable to higher temperature non-catalytic oxidation reactions. Ishida et al [215] studied the kinetic models for water splitting while Le Gal and Abanades [114] studied and reported the kinetics of both water and CO_2 splitting in the context of solar fuel chemistry. For undoped Ceria, Le Gal et al obtained the second-order power law model to best describe the CDS kinetics, through a surface-limited reaction mechanism, even though no kinetic parameters were reported. "Master Plot" approach [386,387] was used in this regard to analyzing the mass gain measured by the thermogravimetric analyzer (TGA) during oxidation. Arifin et al [385], using a similar, but a modified approach, by separating the experimental effects from material specific H_2 and CO curve rates, reported the WS kinetics to be best described by a first-order kinetic model. All model parameters were also reported, whereby, a low apparent activation energy of 29 kJ/mol was obtained in the range of 750-900ºC. On the other hand, carbon dioxide splitting (CDS) kinetics was found to be surface-mediated phenomena with a much higher complexity than the WS reaction, leading to solid-state kinetic model (SS) to accurately predict the product yield over the entire range of experimental conditions, 600-875ºC and 10–40 vol% CO_2. This is due to the fact that the SS models, essentially lumped parameter models with a minimal level of detail about the reaction mechanisms, does not account for the transient phenomena occurring during the CDS reactions. All the experiments were performed with H_2 reduction. It is observed from thermodynamic studies of CO_2 and H_2O splitting, water splitting is favored at a lower temperature and has higher exothermicity than CO_2 splitting which is favored at a higher temperature. Therefore, reactivity studies of water-splitting are studied in large number [97,112,158,213,388–397] and CO_2 splitting is studied relatively less due to vision to adopt hydrogen as proliferant fuel. It is also understood that H_2O reaction kinetics way faster making CO_2 splitting rate determining reaction where the oxidizer is a mixture of CO_2/H_2O. Hence, the CO_2 splitting reaction is considered for the oxidation step.

In order to derive the kinetics, we performed two sets of experiments; first H_2 reduction and CO_2 oxidation experiments and later in the next set of experiments methane reduction followed by CO_2 oxidation. A tubular reactor setup is used for the redox cycle tests and the details of the experimental set-up are described in the next section.

7.2 Experimental system

7.2.1 Setup overview

The experimental setup consists of a horizontal alumina tubular reactor, a control unit, a gas delivery system and a real-time gas analysis system with an online quadrupole mass spectrometer (QMS) as shown in Figure 95. Four Bronkhorst EL-FLOW mass flow controllers (MFCs) are used for the gas flow control. The reactor is made of an alumina tube positioned inside a tubular furnace (Lenton UK) that provides an isothermal environment up to 1600ºC. A quadrupole mass spectrometer (QMS) (Hiden Analytical Inc.) is used to analyze the gas composition. The QMS has a response time of less than 0.3 s and a wide bandwidth of species detection capability. Four Bronkhorst EL-FLOW mass flow controllers (MFCs) are used for the gas flow control. Oxidizer (CO_2) flow is controlled by MFC 1 (0-100 sccm), the purging and sweep (inert Ar) are controlled by MFC 2 (0-500 sccm). MFC 3 (0-100 sccm) and MFC 4 (0-200 sccm) controls the flow of hydrogen and methane respectively.

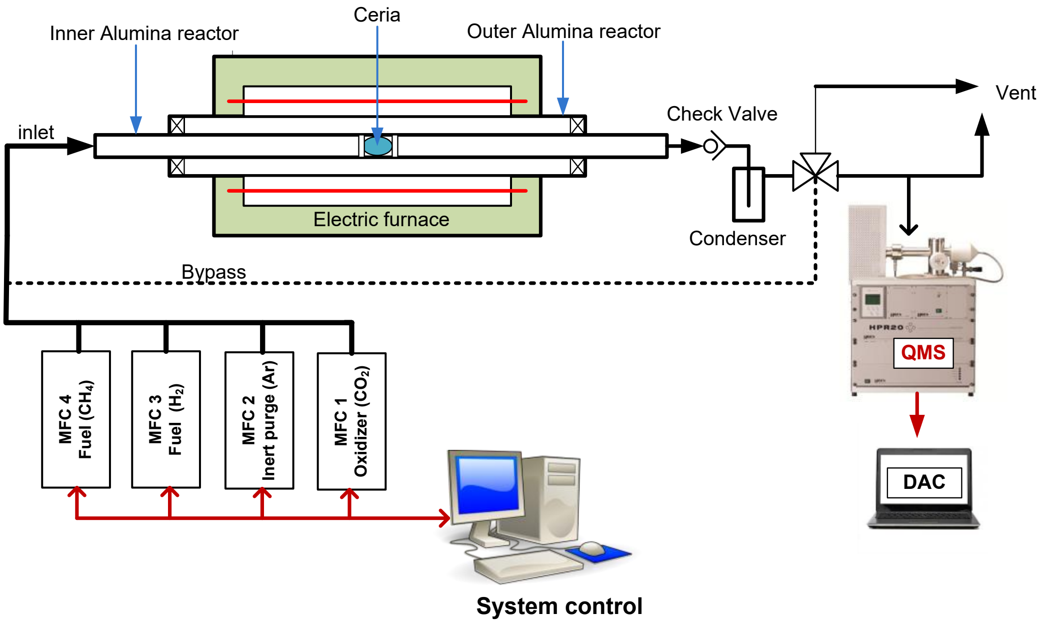

Figure 95. Experimental set-up for testing in micro-reactor configuration

7.2.2 Reactor system

The reactor is made of an alumina tube positioned inside an LTF 16/15/180 horizontal tubular furnace (2.5kW/11.5 A/230 VAC, single phase) that can heat up to 1600ºC. As shown in Figure 95, the reactor consists of an outer alumina tube with 90 cm length, inner diameter (i.d) of 50 mm, an inner concentric 12 mm o.d alumina tube and 10 mm i.d with 1 m length. The gas flow passes through the inner tube where the sample is placed in the center supported by quartz wool. The gas enters from the mass flow controllers and leaves through the other end through the sample which is placed at the center of the reactor. Inlet and exhaust gas streams of the reactor are connected to a 6 mm stainless steel tube. The exhaust gas passes through a needle valve and then through a condenser and a filter before the sample of the gas enters the mass spectrometer. The furnace is equipped with thermocouples and all the control system. Nevertheless, the probes are not placed in the point where the reaction takes place, but outside of the tube that contains the reactor. Hence, there is a ΔT between the measurement point and the fixed bed due to the isolation caused by the alumina tube of the furnace, the air surrounding the reactor and the latter itself (made of alumina) as shown in Figure 96.

In order to control the temperature of the reaction (i.e. in the fixed bed), the temperature set on the controller must take into account the ΔT and the relation is given as equation (7.1):

$$T_{set} = T_{reactor} + \Delta T \tag{7.1}$$

where T_{set} is the temperature to select on the Eurotherm and $T_{reactor}$ is the temperature theoretically needed for the reaction.

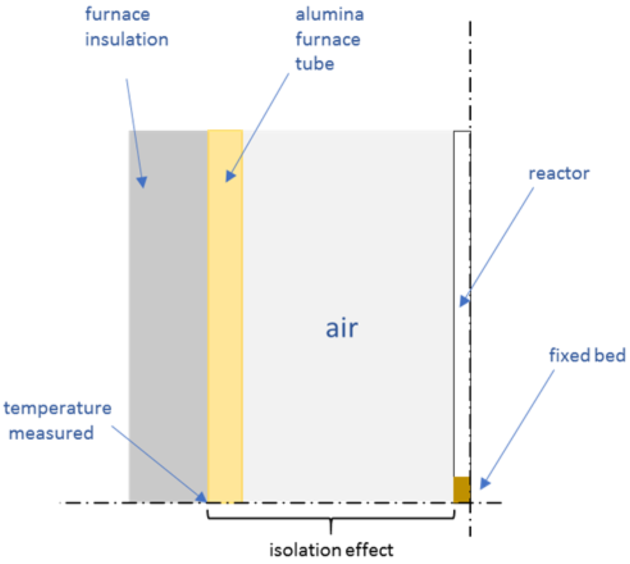

Figure 96. Part of the cross-section of the furnace.

However, the ΔT is not a constant, but a function of the temperature. The problem is solved empirically by constructing a curve of the temperature measured by the furnace thermocouple and the real temperature in the reactor. The curve-building procedure is based on changing the set temperature several times and reading the corresponding temperature in the reactor. The instrumentation employed is composed by the Eurotherm controller and a B-type thermocouple. The thermocouple calibration procedure is equivalent to the one applied in the MFC calibration because also the thermocouple works exploiting the voltage signals and converting them from and to temperatures.

In the procedure, the thermocouple has been placed in an empty reactor tube and the temperature has been gradually increased, up to 1300°. The resulting curve is shown in Figure 97.

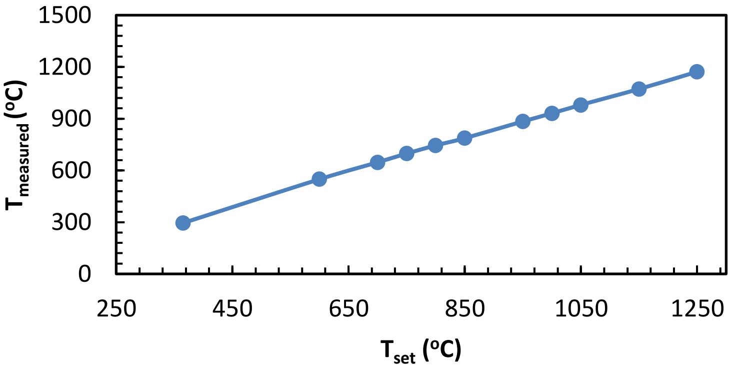

Figure 97. Temperature correspondence curve.

7.2.3 Data acquisition with QMS

In this set-up, the Mass Spectrometer used is the model HPR-20 QIC R&D produced by HIDEN Analytical Inc. It is equipped with both Faraday cup and Secondary Electron Multiplier. It can analyze gases and vapors at a pressure near atmosphere, it has a detectable mass range of 200 AMU and its detection capability is from 100% to less than 500ppb. The core of the instrument is a Hiden HAL 3F Series Triple Filter Mass Spectrometer: an assembly composed by the electron impact ionization source, a pre-filter, the mass selective primary filter (quadrupole type), a post-filter and the detection assembly (dual Faraday and secondary electron multiplier) in series. The species using in the redox experiments with their peaks are listed in Table 38.

Table 38. Peaks for different species for the different experimental scenario.

Experimental conditions	Gas species	Peak for species
H_2 reduction	H_2, Ar	H_2: 2, Ar: 40
CH_4 reduction	CH_4, Ar	CH_4: 15, CO: 28, CO_2: 44, H_2: 2, Ar: 40
CO_2 oxidation	CO_2, Ar	CO_2: 44, CO: 28, Ar: 40

The mole fraction x_i of each species in the flow is calculated by peak counts as:

$$x_i = \frac{\text{Corrected signal of species i}}{\sum_j \text{corrected signal of species j}} \qquad (7.2)$$

where the corrected signal is calculated as = $(\dot{R}-\dot{B})/\Re$; $\dot{R}$ is the raw peak counts, peak reading at the condition of experimental interest, $\dot{B}$ is the background reading counts arise due to background noise. Background reading is evaluated by passing only inert gas. $\Re$ is the calibration factor and it has to be determined before each set of experiments as it accounts for different sensitives of the detector for different species. For an experimental system with N number of gases, N-1 calibration factors would characterize the species sensitivity. But according to the guidelines provided by Hiden Inc, the calibration factor is set to unity for major species (such as Argon in our case). To calculate the calibration factors, the gas mixture is passed through QMS and these factors are then varied to minimize the difference between the measured concentration and the unknown mixture as:

$$x_i = \min_{\Re}\left\{\sum_j (\mathrm{x}_{\mathrm{i,\ measured}} - \mathrm{x}_{\mathrm{i,0}})\right. \qquad (7.3)$$

While calibration, it should be emphasized that fed gas mixture represent well as that of calibration gas. For a gas mixture with multiple species (such as methane reduction step), it would be difficult calibrate. An alternative is that each minor species is calibrated against major species such as argon individually. For conditions of species mixture with peak overlapping, fragmentation factor is evaluated.

For instance, a mixture of CO_2 and CO in which CO_2 has a fragmentation peak reading of 28. Therefore fragmentation factor of CO_2 is determined by first feeding only CO_2 with Argon in the system then compares the peak reading of 28 with respect to reading of 44 and it can be given as equation (7.4).

$$\text{Fragmentation factor of } CO_2 = (\dot{R}_{28}-\dot{B}_{28})/(\dot{R}_{44}-\dot{B}_{44}) \tag{7.4}$$

The corrected signal of CO in a CO/CO_2 is determined by considering the fragmentation factor of CO_2 as equation (7.5).

$$\text{Corrected signal of CO} = ((\dot{R}_{28}-\dot{B}_{28})-(\dot{R}_{44}-\dot{B}_{44})\times\text{Fragmentation factor of } CO_2)/\Re_{CO} \tag{7.5}$$

Here $(\dot{R}_{28}-\dot{B}_{28})$ is peak reading signal from CO and CO_2 environment and equation (7.5) are substituted in equation (7.2) for calculation of mole fraction.

Calibration drift away slowly with time due to degradation of the detector, power supply fluctuation, impurities, etc., therefore it is suggested to perform calibration before starting a fresh set of experiments every time. During all experiments, inert gas (Ar) is used as major species for consistency of the results. The performance of the reactor system was tested for accuracy and flow responses for a wide range of flow rates to check the residence time of gas and to check if there exist any mass transfer limitations.

7.2.4 Measurement procedure

Initially, the experiments will be performed considering H_2 reduction with CO_2 splitting and later with methane reduction considering CO_2 for oxidation. The relevance and details are described in detail in section 7.3 and section 7.4 of this chapter.

Commercial ceria powder from Alfa Aesar (99.95% purity) is used for the reaction study. The sample was crushed and sieved to 32 μm before the tests. A 250 mg amount of ceria powder is embedded in quartz wool and placed at the center of the inner alumina tube. The total flow rate into the reactor during the oxidation step is maintained constant at 120 ml/min (GHSV 28800 ml/g/h).

In H_2 reduction and CO_2 splitting experiment to assess the CO_2 dissociation kinetics, fixed mixture of hydrogen and argon (5% H_2 concentration) is used as a fuel for the reduction step, as this experiment particularly focuses on the oxidation step and the analysis of related kinetics. The CO_2 mole fraction is varied during the oxidation step.

During the methane reduction experiment, since one mole of methane leads to the formation of 2 moles of H_2 and one mole of CO, the molar flow at the outlet is higher than the inlet. However, as the production of 1 mol of CO leads to the consumption of 1 mol of CO_2, the total molar flow rate throughout the control volume remains constant during the oxidation step.

Table 39. Experimental conditions used for reactivity and kinetic assessment.

Experiments	H_2 Reduction/CO_2 splitting	CH_4 reduction/CO_2 splitting
Objectives	CO_2 splitting kinetics assessment	CH_4 reduction and CO_2 splitting reaction kinetics
Reduction temperature (°C)	700-1000	900-1100
Reducer	5% H_2 (in Ar)	20-50% CH_4 (in Ar)
Reducing gas flow rate (ml/min)	120	120
Reduction time (min)	30	75
In between purge (Ar)	10 min	10 min
Oxidizer	20-40% CO_2 (in Ar)	20-50% CO_2 (in Ar)
Oxidation temperature (°C)	700-1000	900-1100
Oxidizing gas flow rate (ml/min)	120	120
Oxidation time	15 min	15 mins
Purge (Ar)	10 min	10 min

Each experiment foresees a cycle of four steps. The first is the ceria reduction step where the mixture of argon and hydrogen (or methane) (based on the type of experiments) was sent for 30 min (75 min for methane reduction) to ensure complete reduction respectively. Then, a purging stream of pure Ar is fed for 10 minutes, to remove the fuel present in the fixed bed. The next step is oxidation reaction where a mixture of Ar and different concentration of CO_2 (as listed in Table 39) are sent for 15 min. The last step was the purging with pure Argon for approximately 10 min or until the mass spectrometer reading was stable enough to begin the next cycle, whichever is earlier.

The measure of H_2 and CO concentrations for the methane reduction cycle and the CO for the oxidation cycle at the outlet flow of the reactor allowed to extrapolate the reaction rate of the reduction and oxidation reactions respectively. However, for the reduction step, the methane splitting reaction (equation 4.4) can occur, which would give erroneous results from the reading of the hydrogen measurements due to the formation of H_2 and elementary solid carbon, which would be deposited inside the reactor. Indeed, this would be reflected by the corresponding oxidation, whereby the reaction kinetics would depend not only on the ceria oxidation but also on the Boudard reaction (equation 4.3).

Nevertheless, for most parts of the methane reduction experiments, no significant carbon formation was noticed on the sample as explained in the microstructural analysis section. In any case, the measurements of CO both during the reduction and the oxidation cycle were considered for developing the necessary kinetics as equation (7.6) and (7.7). Similarly, for H_2 reduction experiments, only the measure of CO concentration was considered for CO_2 splitting reaction as equation (7.7).

$$\dot{\omega}_{\mathrm{CO,\ red}} = \frac{X_{CO,out}\dot{n}_{red,out}}{m_{CeO_2}} = \frac{X_{CO,out,red}}{m_{CeO_2}}\frac{P^0\dot{V}^0_{red,in}}{RT^0} \tag{7.6}$$

$$\dot{\omega}_{\mathrm{CO,\ oxd}} = \frac{X_{CO,ox-out}\dot{n}_{ox,out}}{m_{CeO_2}} = \frac{X_{CO,ox-out}}{m_{CeO_2}}\frac{P^0\dot{V}^0_{ox,in}}{RT^0} \tag{7.7}$$

$X_{CO,out}$ is the measured mole fraction of CO at the exit of the reactor, $\dot{n}_{ox,out}$ is the total molar outflow rate of the gas mixture for the oxidation, which is equal to the inlet molar flow, while P^0, T^0, $\dot{V}^0_{ox}$ are the pressure, temperature and the total volumetric inflow rate at standard temperature and pressure (STP). The reaction rates are normalized by the total ceria sample m_{CeO2} – i.e. 250 mg – used in the measurement. The derivation assumes the quasi-steady-state and neglects the accumulation or depletion effect in the control volume as the residence time of the gases is negligible with respect to the characteristic time of the redox conversion.

The bulk-phase non-stoichiometry change of ceria would be first evaluated through the extrapolated reduction rate, as per the reaction is written in the following equation (7.8) or equation (7.9) based on the reducer fuel. Correspondingly, the bulk-phase non-stoichiometry change of ceria can also be evaluated by extrapolating the oxidation reaction rate based on oxidation with carbon dioxide. The oxidation reaction can be rewritten as per the equation (7.10).

$$\mathrm{\delta_1 H_2O(g) + CeO_2 \rightarrow \delta_1 H_2(g) + CeO_{2\text{-}\delta_1}} \tag{7.8}$$

$$\mathrm{\delta_1 CH_4(g) + CeO_2 \rightarrow \delta_1\left[CO(g) + 2H_2(g)\right] + CeO_{2\text{-}\delta_1}} \tag{7.9}$$

$$\mathrm{CO_2(g) + (1/\delta)CeO_{2\text{-}\delta_1} \rightarrow CO(g) + (1/\delta)CeO_{2\text{-}\delta_2}} \tag{7.10}$$

where the non-stoichiometry reached after the reduction step is represented by δ_1 and δ_2 correspond to the non-stoichiometry at the end of the ceria oxidation step and $\delta=\delta_1-\delta_2$ is the bulk-phase non-stoichiometry change, calculated as per the following equation [197] (equation 7.11):

$$\delta(t) = \frac{n_{\mathrm{oxygen}}(t)}{n_{\mathrm{CeO_2}}} \tag{7.11}$$

$n_{\text{oxygen}}(t)=\int_0^t \dot{\omega}_{\text{CO}_{red}}dt=\int_0^t \dot{\omega}_{\text{CO}_{oxi}}dt$ represents the accumulated release and intake of oxygen ions during the reduction and the oxidation reactions respectively, $n_{CeO2} = m_{CeO2}/M_{CeO2}$ is the moles of ceria used in the experiment, with M_{CeO2} is its molar mass. The non-stoichiometry is calculated by the amount of oxygen that the solid can release and accept when reduced by fuel (H_2 or CH_4) and oxidized with CO_2, starting from a neutral state. Therefore, at the end of oxidation, which also represents the completion of one cycle, oxygen vacancies are depleted, and no more oxygen is incorporated into the material. The maximum non-stoichiometry is affected by the temperature, where, an increase in temperature results in an increased rate of oxygen release and hence, an increased availability of vacancies.

7.3 Assessment of CO_2 splitting kinetics by H_2 reduction

A number of experiments [398–406] have demonstrated the feasibility of CO_2 splitting with ceria, as listed in Table 40. However, only a few studies reported the reaction kinetics, mainly following equilibrium approach, defect model theory, empirical solid state kinetics models [108,213,228,407–412]. Arifin [228] have investigated the kinetics of splitting of water and CO_2 over ceria and found that it is difficult to converge on a single kinetic model that adequately predicts the CO production behavior from thermally reduced ceria over the entire temperature range investigated. To achieve a high quality fit to the data, three separate models had to be used within the F family of models to give the best fit to the CO transient signal with different kinetic parameters. Bulfin et al [108] developed an analytical kinetic model to fit experimental data and found that the R3 model gives the best fit results below 800°C. Ackerman et al[413] reported that the D2 model provides the best-fitting for ceria oxidation at 1400°C. The lack of agreement between the kinetic models based on various experimental studies is a point of observation. The difference of the reaction mechanisms adopted could be a consequence of variations in the experimental conditions or in the morphology and preparation method of CeO_2 samples. Therefore, the present work aims to statistically analyze the solid-state reaction kinetics models that describe the oxidation of non-stoichiometric ceria with CO_2 by comparing their fitting goodness to a broad set of experimental measures. These reaction kinetic models are listed in Table 41 with related detailed formula.

Table 40. Total CO production by CO_2 splitting on CeO_2 for thermally reduced and H_2 reduced Ceria for various redox temperatures cited in the literature.

Temp °C (Red/Ox)	**CO (ml/g)**	**Feed CO_2 (%)**	**Reducer**	**Ref**
1500/800	6.28	50%	thermal	[414]
1400/1000	2.35	50%	thermal	[398]
1400/1000	2.24	50%	thermal	[399]
1600/1000	4.91	60%	thermal	[415]
1527/827	1.99	8.3%	thermal	[416]

1200/850	0.83	25%	thermal	[400]
1500/800	4.03	38.5%	thermal	[401]
1500/1500	2.02	100%	thermal	[402]
1400/1000	1.23	100%	thermal	[403]
1100/500	13.45	0.5-40%	H_2	[404]
827/827	20.93	4%	H_2	[406]
900/900	22.71	14.30%	H_2	[405]
700/700	4.17	14.30%	H_2	[405]
700/700	7.57-9.19	20-40%	5%H_2/Ar	Present study
800/800	17.73-19.28	20-40%	5%H_2/Ar	Present study
900/900	23.90-28.05	20-40%	5%H_2/Ar	Present study
1000/1000	28.51-33.68	20-40%	5%H_2/Ar	Present study

In this work, CO_2 dissociation over ceria is investigated by experiments and the measured reaction rates are used for kinetic models selection based on a statistical approach to identify the involved reaction mechanism.

The transfer of oxygen between the two redox steps exploits the non-stoichiometric oxygen capacity of the ceria, and the oxygen carrier remains intact at the end of the cycle. Isothermal redox cycles of CeO_2 commercial powders are carried out in a horizontal tubular reactor in the temperature range of 700-1000ºC. H_2 is used for the ceria reduction in order to explore the maximum non-stoichiometric capacity (δ) achieved at a set-point temperature while using a different concentration of carbon dioxide in the oxidation step. The temperature swing is thus replaced by isothermal operation for developing the kinetics. The CO production during the oxidation reaction is measured using an online mass spectrometer. The detailed experimental setup and data acquisition are explained in the following section. Based on the reactivity data from the experiments, many kinetic models based on different reaction mechanisms (i.e., reaction order, geometrical contracting, diffusion, and nucleation models) are compared using statistical criteria –Residual sum of squares (RSS), Akaike information criterion (AICc) and the F-test – and the best-fitting model is selected and the corresponding ceria oxidation mechanism is identified.

7.3.1 Material characterization

To confirm the lattice structure of the samples before and after cycles, X-ray diffraction (XRD) was performed using a PANalytical X'pert MPD Pro diffractometer with Ni-filtered Cu Kα irradiation (wavelength 1.5406 Å). All samples were scanned in the 2θ range from 5° to 80° with a step size of 0.2°/s. For a rough estimation on sintering effect, the crystallite size of samples before and after the test was calculated from the Scherrer equation (equation 7.12) based on the reflection with the highest intensity.

$$D^* = \frac{0.9\lambda^*}{\beta^* \cos\theta^*} \tag{7.12}$$

D^*, λ^*, β^*, and θ^* are the grain size, the X-ray wavelength, the width at half maximum intensity, and the Bragg angle respectively. Crystallite micrographs were obtained through a field emission scanning electron microscope (FE-SEM, JSM7800F) at an accelerating voltage of 5 kV.

7.3.2 Reactivity results

Firstly, the results of the tests have been investigated considering the CO_2 splitting performance in terms of CO production rate (ml/(min-g)) and total CO yield (ml/g). With the purpose to highlight the dependence of the performance of the oxygen carrier on temperature and reactant gas concentration, the tests were carried in different experimental conditions, as described in the following sections.

Effect of temperature

Figure 98 shows the CO production rate as a function of temperature from 700 to 1000°C. In each plot, the reaction rate exhibits a fast initial stage, followed by a decrease. During oxidation, the fast initial CO increase corresponds to the rapid oxygen vacancies ion incorporation. Both temperature and reactant concentration play a role in determining the maximum rate. The peak rate varies nonlinearly with temperature and for temperature lower than 700°C, CO production is limited due to the low oxygen non-stoichiometric factor. The increase of temperature to 800°C showed significant enhancement of peak production rates, nearly 1.5-fold higher. Further increase of temperature from 800°C to 1000°C produces a less marked peak growth. All the peaks occur at around 15-30 seconds, and the peak duration increases with the temperature, due to the higher amount of available oxygen sites. After the peak, CO production rate decreases sharply at all the temperatures and approaches zero between 90 and 110 seconds. This behavior shows the strong temperature dependence of the CO rate profile, which becomes higher and wider at a higher temperature, indicating a high activation barrier associated with the CO_2 splitting process [407].

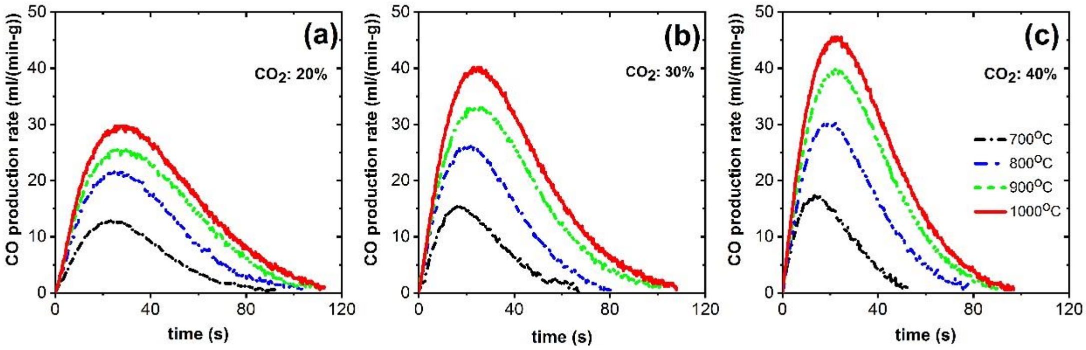

Figure 98. CO production rate (ml/(min-g)) during the oxidation step with (a) 20% mole fraction of CO_2 in the feed, (b) 30% mole fraction of CO_2 in the feed, (c) 40% mole fraction of CO_2 in the feed with Argon. Temperature is varied from 700-1000°C.

Figure 99(a) emphasizes the observed behavior of the peak rates at varying temperature for different CO_2 molar fractions. The production rates exhibit a profile with a fast increase around the temperature of 800°C. Figure 99(b) reports the total CO production during the oxidation step in the redox cycle. In all the cases, arise of total CO production is observed from 9 ml/g at 700°C to 33 ml/g at 1000°C. Figure 99 also shows that the effect of CO_2 concentration on the total production of CO is sensibly lower than that induced by temperature variation. The strong temperature dependence is evident from the earlier studies [402,404,412,417].

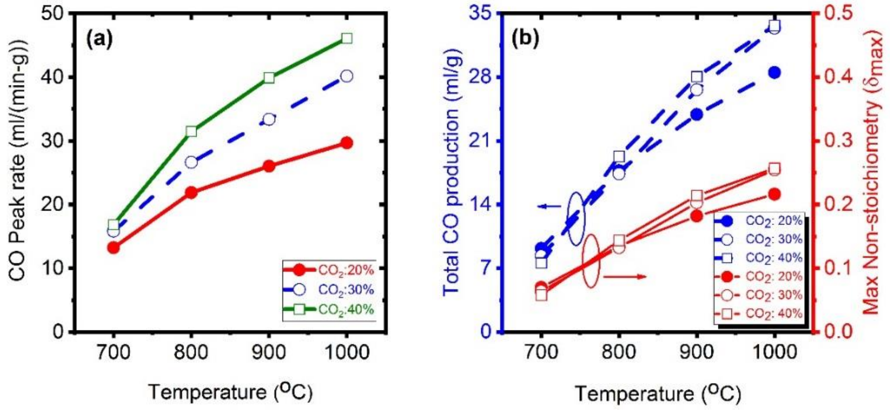

Figure 99. (a) Peak CO rates as a function of temperature and CO_2 mol fraction during oxidation and (b) total CO production and maximum non-stoichiometry δmax attained as a function of temperature and CO_2 mol fraction during oxidation.

Figure 99(b) also shows the maximum non-stoichiometric factor (δ_{max}) of ceria reached during the oxidation step at different temperatures and with different feed CO_2 concentration. The concentration of oxygen vacancies in the ceria slightly increases with an increase of CO_2 concentration in the feed, mainly at the higher temperatures.

Figure 100 compares the difference in profiles of the non-stoichiometry (δ) as calculated in equation (7.11) during oxidation. The initial stage of oxidation ends within 20 seconds but accounts for more than 70% of the overall δ change, while the remaining oxidation leads to a lower change of non-stoichiometry. It is evident that the oxygen-carrying capacity increases due to a higher extent of non-stoichiometry achieved at higher temperatures. It can be noted that the non-stoichiometry increases from 0.07 to 0.21 in the 700-1000°C temperature range for 20% CO_2 mole fraction, and a maximum of 0.25 is reached at 1000°C for 30% CO_2 mole fraction. Similar non-stoichiometry results for oxidation are reported elsewhere [404].

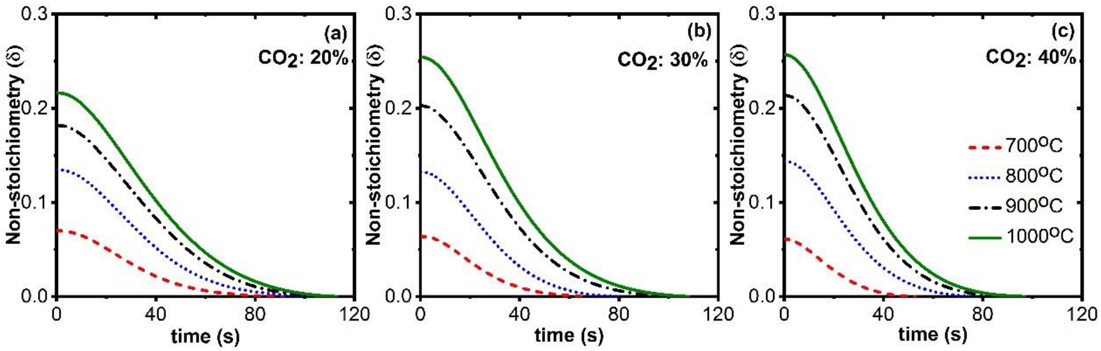

Figure 100. Non-stoichiometry during oxidation step with varying temperature from 700-1000°C for (a) 20% mole fraction of CO_2 (b) 30% mole fraction of CO_2 and (c) 40% mole fraction of CO_2.

Effect of CO_2 concentration

The effect of the oxidant concentration on kinetics and on conversion time was also investigated. Figure 98 shows that the reaction time reduces with the increase of CO_2 partial pressure in the feed. Higher peak rates and reduced time to achieve peak are achieved with higher CO_2 concentration. Similar profiles were reported by Zhou et al [405]. Even if the conversion time reduces with the increase of CO_2 mole fraction in the feed, the growth of CO peak rate with CO_2 concentration balances this effect and the total conversion remains same for that particular point of interest, as shown in Figure 99(b). For instance, the $\delta_{max}$for temperature 700°C is 0.06 for all the CO_2 concentration range, and only at a higher temperature, it varies slightly with the CO_2 fraction. It is evident from the results obtained that the maximum delta increased linearly with temperature, at variance with the effect of CO_2 concentration in the feed, which produced slight variation.

Figure 101(a) shows the effect of concentration within 20-40% concentration (balance Argon) at 900°C: peak rate position shifts from 30 sec to 15 sec with an increase of CO_2 concentration. For higher temperatures, this behavior is not observed and most of the peak rate positions were in the first 20-30 sec range. Figure 101(b) reports the CO peak rate for the three CO_2 concentration investigated for the temperature of 900°C and it reflects that the CO peak rate increases linearly with the CO_2 concentration in feed. The slope of the curve is higher for higher temperature showing a more pronounced influence for temperatures above 800°C (see Appendix). It can be seen that the total CO production with different CO_2 concentration for a particular temperature is minimal and a similar behavior has been observed for all temperatures. It is seen that for CO_2 concentrations of 30% and 40% the maximum non-stoichiometry (δmax) reaches the same value as seen in Figure 99(b) and Figure 100(b) and (c). The relatively lower dependence on CO_2 concentrations have been reported elsewhere [108,400,404,407,414,418].

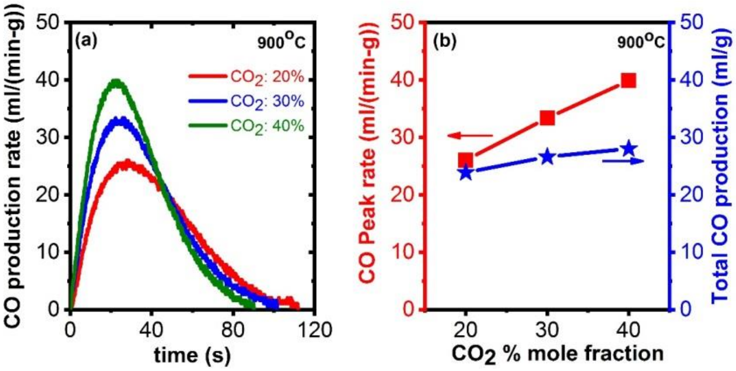

Figure 101.(a) CO production rate versus time for varying concentration of CO_2 in the feed for 900°C (b) CO peak rate and total production as a function of CO_2 concentration

7.3.3. Microstructural analysis

XRD patterns of ceria before and after the reaction cycle, shown in Figure 102, revealed a Cubic fluorite structure in both cases. A minor contamination of silica observed in the sample after the cycle is ascribed to residual quartz wool used to fix the bed in the reactor. Compared to XRD patterns before cycling, the peaks appear more intense after cycling, which indicates a growth of crystalline grains during the high-temperature process. The average crystallite size of ceria before and after cycles was calculated from Scherrer equation based on the strongest reflection peak (111) and resulted in 59 and 63 nm, respectively. FE-SEM images at a high magnification of 25000x show the coexistence of micron-sized particles decorated with much smaller ceria particles. The size of the larger particles is not significantly affected by the reaction, at variance with the smaller ceria particles which, due to sintering, appear larger after the reaction. This is clearly seen in related FE-SEM images and is coherent with the larger average size obtained by Scherrer.

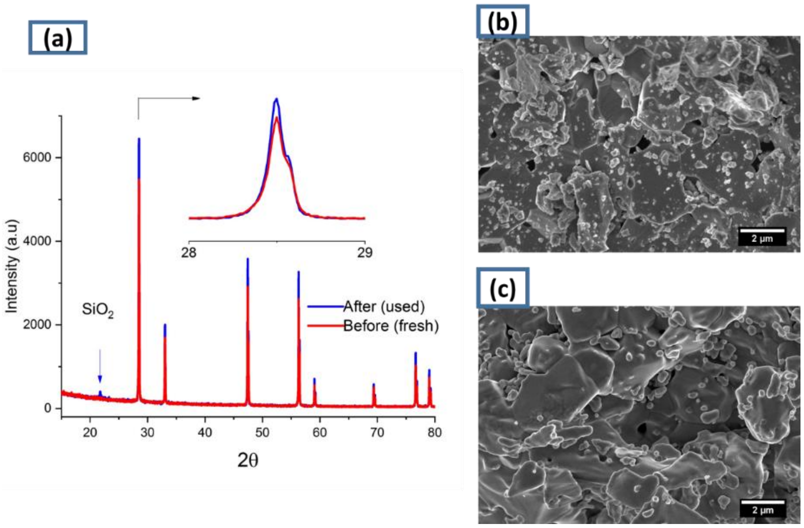

Figure 102. XRD patterns of ceria before and after the reaction cycle (b) FE-SEM images of fresh and (c) cycled ceria.

7.3.4 Kinetic study of CO_2 splitting during ceria oxidation

The mechanism of the reaction kinetics involves a group of individual chemical steps, by which a reactant is converted to product. It is, however, difficult to obtain the information on the mechanism followed during the reaction. Therefore, in gas-solid, solid-solid kinetics, the reaction kinetic determination study involves the application and verification of a derived mechanistic model from the literature based on the process with the experimental data. The schematic description of the general kinetic models is illustrated in Figure 103.

Generally, the reaction mechanism of solid state reactions is described using reaction-order models (F), geometrical contraction models (R), diffusion-limited models (D), nucleation models [419–422] (also called as Avrami-Erofe'ev models, AE), random pore model (RPM) [423], and the Sestak-Berggren (SB) [424], and Prout-Tompkins models (PT) [425].

The reaction order-based models (F in Table 41) assume homogenous reaction process, while geometrical contracting models (R) assume phase boundary reaction control with different geometries with shrinking core mechanism (R2 represents two-dimensional shrinking or growth whereas R3 represents three-dimensional shrinkage or growth [25]). Diffusion models (D1-D4) represent the reaction mechanisms where the rate is controlled by the transport of reactants and products to and from the active interfaces [426]. Nucleation and nuclei growth models also called Avrami-Erofe'ev models (AE) involves the formation of growth of nuclei at the reaction site. The autocatalysis model, the Prout-Tompkins (PT) model, has nuclei growth formation rate and chain breaking rate constants are equal [425]. Bhatia and Perimutter [423] have come up with a new model called the Random Pore Model (RPM) by considering pore growth during the reaction and on the basis of population balance concept. Modifications to RPM based on the material and operating conditions have been reported in the literature. With no literature cited on the applicability of the model for ceria oxidation with CO_2, this model is omitted in the kinetic study. Sestak-Breggen (SB) model is used for more complex crystallization process involving partial nuclei overlapping and growth steps [424].

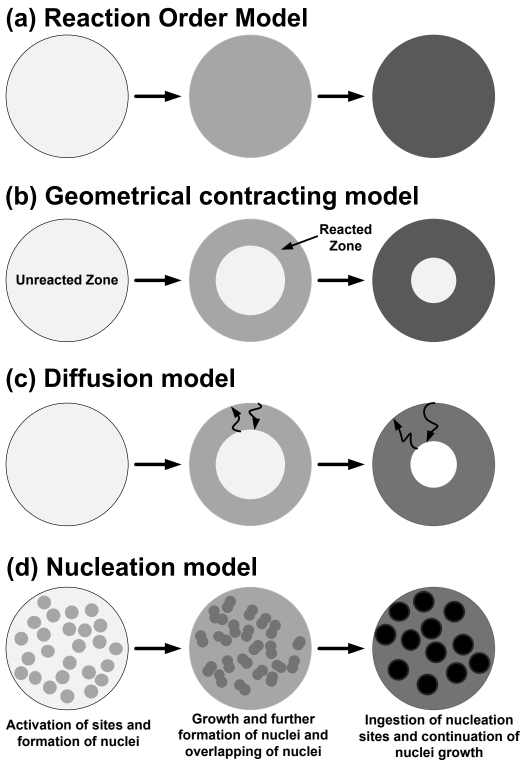

Figure 103. Kinetic models and mechanisms (a) Reaction order model; (b) Geometrical contracting model (c) Diffusion model (d) Avrami-Erofe'ev (nucleation) model applicable for ceria-based oxygen carrier.

Generally, most of the models listed in Table 41 contain one fitting parameter (rate constant, k). Some models with more than one parameter are more complex and allow a better fit for the kinetic data. These models are grouped into three groups based on the number of independent variables i.e., one parameter, two-parameter, and three-parameter models. SB model is a three fitting parameters model, while Avrami-Erofe'ev model with the exponent n, (AEn) and Random pore model (RPM) are two-parameter models. All the other models listed in Table 41 are one-parameter models.

Table 41. Rate and integral expressions for different solid-state kinetic models[a][387].

No	Reaction Model	f(X)=(1/k) dX/dt	g(X)=kt	n
F1.5	*Three – halves order*	$(1-X)^{3/2}$	$2[(1-X)^{-1/2}-1]$	0.91
F2	*Second – order*	$(1-X)^{2}$	$1/(1-X)-1$	0.83
F3	*Third – order*	$(1-X)^{3}$	$(1/2)[(1-X)^{-2}-1]$	0.70
R1	*Zero – order (Polany – Winger equation)*	1	X	1.24
R2	*Phase boundary controlled reaction (contacting area, i.e, bi – dimensional shape)*	$2(1-X)^{(1/2)}$	$1-(1-X)^{(1/2)}$	1.11
R3	*Phase – boundary controlled reaction (contracting volume, i.e, tridimensional shape)*	$3(1-X)^{(2/3)}$	$1-(1-X)^{(1/3)}$	1.07
D1	*One – dimensional diffusion*	$1/(2X)$	X^{2}	0.62
D2	*Two – dimensional diffusion Valensi equation*	$1/[-\ln(1-X)]$	$(1-X)\ln(1-X)+X$	0.57
D3	*Three dimensional diffusion Jander equation*	$3(1-X)^{(1/3)}[2(1-X)^{(-1/3)}-1]$	$[1-(1-X)^{(1/3)}]^{2}$	0.54
D4	*Three dimensional diffusion Ginstling – Brounshtein*	$3/[2(1-X)^{(-1/3)}-1]$	$(1-2X/3)-(1-X)^{(2/3)}$	0.57
AE1	*First – order (Mampel) (F1) or Avrami – Erofe'ev (n = 1)*	$(1-X)$	$-\ln(1-X)$	1
AE0.5	*Avrami – Erofe'ev (n = 0.5)*	$(1/2)(1-X)[-\ln(1-X)]^{-1}$	$(-\ln(1-X))^{2}$	0.5
AE1.5	*Avrami – Erofe'ev (n = 1.5)*	$(3/2)(1-X)[-\ln(1-X)]^{1/3}$	$(-\ln(1-X))^{2/3}$	1.5
AE2	*Avrami – Erofe'ev (n = 2)*	$2(1-X)[-\ln(1-X)]^{1/2}$	$(-\ln(1-X))^{1/2}$	2
AE3	*Avrami – Erofe'ev (n = 3)*	$3(1-X)[-\ln(1-X)]^{2/3}$	$(-\ln(1-X))^{1/3}$	3
AE4	*Avrami – Erofe'ev (n = 4)*	$4(1-X)[-\ln(1-X)]^{3/4}$	$(-\ln(1-X))^{1/4}$	4
AEn	*Avrami – Erofe'ev*	$n(1-\alpha)[-\ln(1-\alpha)]^{(n-1)/n}$	$(-\ln(1-X))^{1/n}$	n
SB	*Sestak – Berggren Function*	$X^{x1}(1-X)^{y1}$		-
PT	*Prout – Tompkins*	$X(1-X)$	$\ln(X/(1-X))$	-

[a] In this table, X is the conversion, f(X) is the differential form of the kinetic model, and g(X) is the integral form of the model.

The evaluation of kinetic model parameters includes isoconversional and isothermal reaction analysis [427]. In the present study, the working envelope of the chemical looping process for narrow temperature range isothermal method was chosen. As reported by Han et al [428] the intra-particle heat gradients can be assumed negligible and thus the particle can be approximated to be isothermal.

In this section, the reaction kinetics study is carried out by fitting different models to the experimental data in order to identify the solid-state reaction kinetic mechanistic model. The metric usually adopted for the comparison of reaction models with experimental evidence is the reaction rate, measured in term of the time profile of reactant conversion or product yield [405]. Three methods are used to compare several solid-state reaction kinetic models against isothermal experimental data. In particular, the methods are: (a) the fit quality of the transient conversion, (X vs. t); (b) the fit quality of the transient time derivative of conversion (dX/dt vs. X).and (c) the Hancock and Sharp Method or model-free method [429]. The model-free method is used to verify the category of the kinetic model is described in the next section.

7.3.5 Hancock and Sharp method

It can be considered as a model-free method as Hancock and Sharp [429] deduced a simple method for identifying the mechanism of isothermal solid-state reaction kinetics. It is based on the nucleation model and can be expressed as equation (7.13):

$$\ln(-\ln(1-X)) = \ln a + n \ln t \tag{7.13}$$

where X is the solid conversion (extent of reaction), t is the reaction time, a is the constant based on the frequency of the nuclei formation and rate of crystallite growth and n is called Avrami-Erofe'ev exponent [430]. This method includes plotting ln(-ln(1-X)) vs. ln(t), and the slope n gives the information of the most suitable kinetic model. Hancock and Sharp [429] illustrated that kinetic data with or without nucleation gives approximately linear plots for ln(-ln(1-X)) vs. ln(t) if the conversion is limited from 0.15 to 0.5. It is also reported that this conversion range is independent of experimental uncertainty and error at t=0 or by geometrical factors. The corresponding values of n for models other than AE models are listed in Table 41. The Hancock and Sharp slopes can be used as a diagnostic tool to preliminary discriminate between the reaction mechanisms. For example, $n<1$ then the mechanism is diffusion controlled and when $n \simeq 1$, the mechanisms approximate phase boundary controlled reaction rate. The disadvantage of this method is that sometimes it is difficult to distinguish between models; for instance, the four diffusion models of different order exhibits slopes of 0.5 to 0.6. Another example of n=1 gives non-conclusive behavior which indicates the suitability of F1.5, R3, and AE1 models. Therefore, Hancock and Sharp method cannot completely be used to discriminate a group of standard models with linear plots of similar n values (slopes). It is recommended also to find the best fit model by plotting dX/dt vs.X and X vs.t over time and wide conversion range.

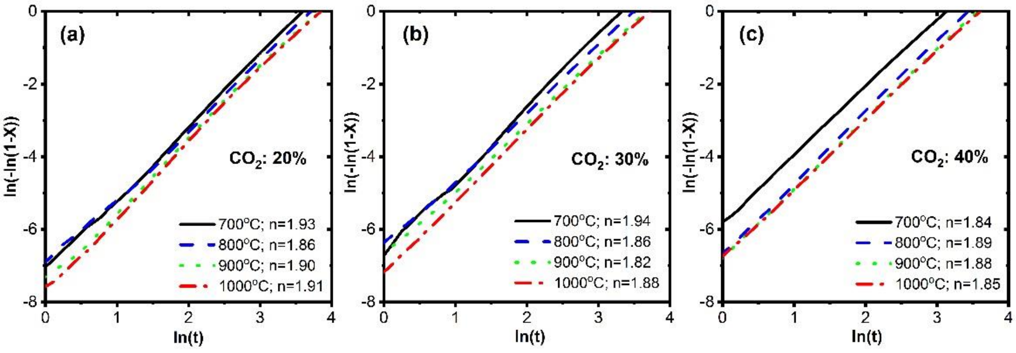

Figure 104 shows the plot between ln(-ln(1-X)) vs. ln(t) for different concentration for varying temperature. The slopes are very similar and they are close to ~1.9. An 'n' value near to 2 identifies a nucleation and grain growth reaction mechanism, which will be validated further in the later section. Both the temperature and the CO_2 concentration seem not to affect the trends so much. The following result means that the reaction mechanism is the same in all operating conditions.

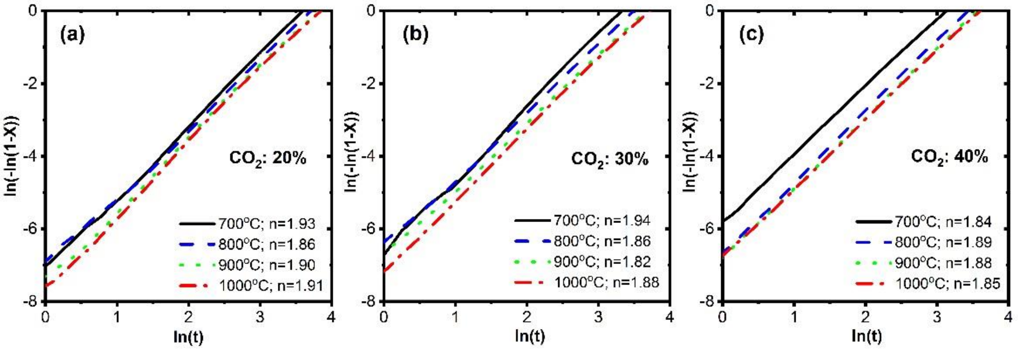

Figure 104. Plot of the Hancock and Sharp method for the ceria oxidation with CO_2 for feed CO_2 concentration (a) 20% (b) 30% (c) 40% for the temperature range of 700-1000°C.

7.3.6 Model fitting method

The kinetic study needs as input data the extent of reaction during the time, which can be derived from the cumulative of the CO produced as equation (7.14).

$$cum\left(\dot{\omega}_{\mathrm{CO,i}}\right)=\sum_{p=1}^{i-1}\left(\dot{\omega}_{\mathrm{CO,p}}\right)+\dot{\omega}_{\mathrm{CO,i}} \tag{7.14}$$

The extent of reaction (X) for each time instant is given by equation (7.15).

$$X(t_i)=\frac{cum(\dot{\omega}_{\mathrm{CO,i}})}{cum(\dot{\omega}_{\mathrm{CO,N}})} \tag{7.15}$$

In other words, the extent of reaction at time t_i is the ratio between the i-th value of the cumulative and the final value of the cumulative. It implies that X varies from 0 to 1. These values are the experimental Xs that should be compared with the Xs coming from the models.

To obtain the kinetic model, a mathematical equation should be developed. The kinetic expression for the gas-solid reaction can be expressed as equation (7.16) [431]:

$$\frac{dX}{dt} = k^1\cdot f(X)\cdot[P]^m \tag{7.16}$$

X is the conversion, $k^1 = A\cdot\exp(-E_a/RT)$ and P is the partial pressure of CO_2, m is the reaction order and f(X) is a function of X depending on the reaction mechanism. The coefficients A and E_a are the Arrhenius parameters; E_a being the activation energy and R is the gas constant that is equal to 8.314 J/mol/K. The first step of calculations was the fitting of the model with the raw data. For this purpose, equation (7.15) was transformed to equation (7.17):

$$\frac{dX}{f(X)} = K \cdot dt \tag{7.17}$$

where $K=k^{1}\cdot P^{m}$ is expressed in terms of partial pressure of CO_2. The integral of the reaction model is expressed by integrating equation (7.18).

$$g(X) = \int_{0}^{X} \frac{dX}{f(X)} \tag{7.18}$$

In other terms, equation (7.18) is also expressed as:

$$g(X) = K \cdot t \tag{7.19}$$

The slope of the curve g(X) vs t is the parameter K. The slope between the natural log of K vs 1/T (Eq. 7.20) gives the activation energy as a negative slope. The intercept will be $\ln(AP^{m})$ where P is the partial pressure of CO_2. The reaction order 'm' was evaluated by plotting $\ln(AP^{m})$ vs. lnP (see Eq. 7.21) and the slope would be the reaction order and the intercept would help in yielding the 'A' value.

$$\ln K = -\frac{E_a}{RT} + \ln A \cdot P^{m} \tag{7.20}$$

$$\ln[A \cdot P^{m}] = \ln A + m \ln P \tag{7.21}$$

The basic procedure here is to utilize the kinetic expressions of the models reported in Table 41 to match the experimental data in the form of dX/dt vs X and X vs t profiles by fitting the value of the K parameter, and then select the models with the smallest residual sum of squares (RSS) among candidate models with the same number of parameters [432]. Two-parameter models (i.e., Avrami-Erofe'ev (AEn)) and three-parameter models (i.e., Sestak-Berggren (SB)) need also the evaluation of additional parameters.

For Avrami-Erofe'ev (AEn) model its exponent n need to be evaluated. The validation of Avrami exponent (n) starts from the identification of a particular value of conversion, X_M, which is evaluated at the maximum dX/dt for each experiment. Then the parameter 'n' comes from the equation (7.22).

$$\text{Avrami exponent } n = \frac{1}{1+\ln\left(1-X_M\right)} \tag{7.22}$$

For SB model, we need to identify the value of the two unknown parameters x_1 and y_1 for evaluating f(X) and g(X). A similar procedure has been adopted, as to evaluate

X_M that comes at maximum dX/dt. For the calculation of the parameters x_1 and y_1, equation (7.23) has been used.

$$p_1 = \frac{X_M}{1 - X_M} \tag{7.23}$$

where $p_1 = x_1/y_1$ in which x_1 and y_1 are evaluated for each individual case.

7.3.7 Statistical methods for model discrimination

Statistical analysis of models

The comparison among the 19 different kinetics models listed in Table 41, beyond a graphical observation, is made using statistical tools. The statistics take in input two sets of data. The reference set is composed by the experimental data of X or dX/dt. This one will be compared with the sets composed by the data obtained with the different models. Two statistical methods are employed in parallel to verify the agreement about the best fitting kinetic model: the Residual Sum of Squares (RSS) and the Akaike Information Criterion (AICc) [432]. Later, if the best-fitting models are characterized by a different complexity (i.e. different number of parameters) an F-test [433] allows selecting the best one, comparing the models two by two. A detailed explanation of the Akaike Information Criterion is stated in Appendix A.3.1.

The model is identified for the best possible accurately using RSS. The two parameter (AEn) or three parameter models (SB) are expected to exhibit better fits for the kinetic data in terms of smaller RSS.

RSS and AICc values are tabulated for all three CO_2 concentrations for the temperature range (700-1000°C) as given in Table 59, Table 60 and Table 61 in the Appendix A.3.1. For each category of models considered in the study, the model which showed the lowest RSS and AICc values for both (X vs. t) and (dX/dt vs. X) was selected. The F1.5 model has the lowest RSS and AICc value in reaction order mechanisms with the reaction order value of n = 0.91 (listed in Table 41). In geometrical contraction models, the R2 model has lower RSS and AICc values with n = 1.11. In Diffusion-based reaction mechanism D1 with n = 0.62 had lowest AICc. Two nucleation models (AE2 and AEn) were selected because showed similar values of RSS and AICc. This is due to the fact that the values of Avrami exponent (n) for AEn – calculated with equation (7.22) – were close to somewhere around 1.9, which is almost the same value of the exponent of AE2. Similar values of n were also predicted from Hancock and Sharp method applied to AEn. Thus, the AEn and AE2 are of same category: the category of nucleation and grain growth.

The results for the selected models are listed in Table 42 and are plotted in Figure 105 for 20% and 40% CO_2 concentration. Similar behavior for the 30% CO_2

concentration is obtained, as can be seen in Appendix A.3.1 (Figure 130 and Figure 131).

Table 42. RSS and AICc values for the 20% CO_2 concentration (lowest in each kinetic model category).

		700°C		**800°C**		**900°C**		**1000°C**	
method	**model**	**RSS**	**AICc**	**RSS**	**AICc**	**RSS**	**AICc**	**RSS**	**AICc**
dX/dt-X	F1.5	0.136506	-4796.81	0.114664	-5586.85	0.099529	-6189.02	0.096052	-6253.45
	R2	0.020423	-5889.13	0.019425	-6735.57	0.016411	-7448.94	0.015734	-7525.22
	D3	0.052743	-5343.6	0.045676	-6182.37	0.041149	-6806.41	0.03937	-6880.45
	AE2	0.000588	-7928.65	0.000535	-9060.22	0.000394	-10055.2	0.000586	-9838.38
	AEn	0.000264	-8387.92	0.000221	-9628.32	0.000155	-10707.2	0.000274	-10371
	SB	0.000271	-8369.78	0.000209	-9665.28	8.94E-05	-11088.6	0.000143	-10826.9
	PT	0.033293	-5608.14	0.026461	-6535.56	0.024524	-7168.17	0.026009	-7171.88
X-t	F1.5	13.77583	-2143.59	14.89744	-2437.94	16.02001	-2637.29	16.04467	-2655.33
	R2	2.669721	-3087.13	5.017568	-3142.03	4.96974	-3455.45	5.038927	-3469.53
	D1	14.30321	-2121.98	15.7158	-2403.34	15.9027	-2642.43	16.0377	-2655.63
	AE2	0.086214	-5061.04	0.18854	-5265.09	0.284452	-5454.98	0.346139	-5352.24
	AEn	0.290962	-4359.64	0.01741	-6804.41	0.071244	-6420.72	0.354522	-5333.42
	SB	0.257819	-4427.17	0.019789	-6719.56	0.05686	-6576.35	0.244802	-5591.75

Figure 105 -i(a) shows that AEn and SB are the closest to X_{exp} at 700°C with RSS of 0.29 and 0.25, and AICc values of -4359.6 and -4427.1 respectively. The graphical visualization shows that R2, AE2, AEn, and SB are fitting well with the experimental conversion (X) values for (X vs. t). For higher temperatures (Figure 105-i(b),(c),(d)), a good fitting of X_{exp} is limited to AEn, AE2, and SB.

Figure 105-ii represents dX/dt vs. X and it shows the R2 model fits well for temperature above 800°C only inthe region ($0.3 < X < 1.0$). Models AE2, AEn and SB were instead in close agreement with dX/dt_{exp} values in all the conditions investigated. Thus, for (dX/dt vs. X) method only AEn, AE2 and SB models fit well with $0 < X < 1.0$.

In conclusion, the nucleation model (Avrami Erofe'ev) and SB model were in close agreement with the X_{exp} and dX/dt_{exp} in all the conditions investigated. These models belong to the same reaction mechanism except that AEn is based on two-parameters (k, n) and SB is an even more complex model based on three-parameters (k, x_1, and y_1). In order to identify the best-suited model describing the mechanism, the authors adopted the F-test method to distinguish between the three models selected (AE2, AEn, and SB) under the same category of the reaction mechanism which is nested within each other based on the number of parameters.

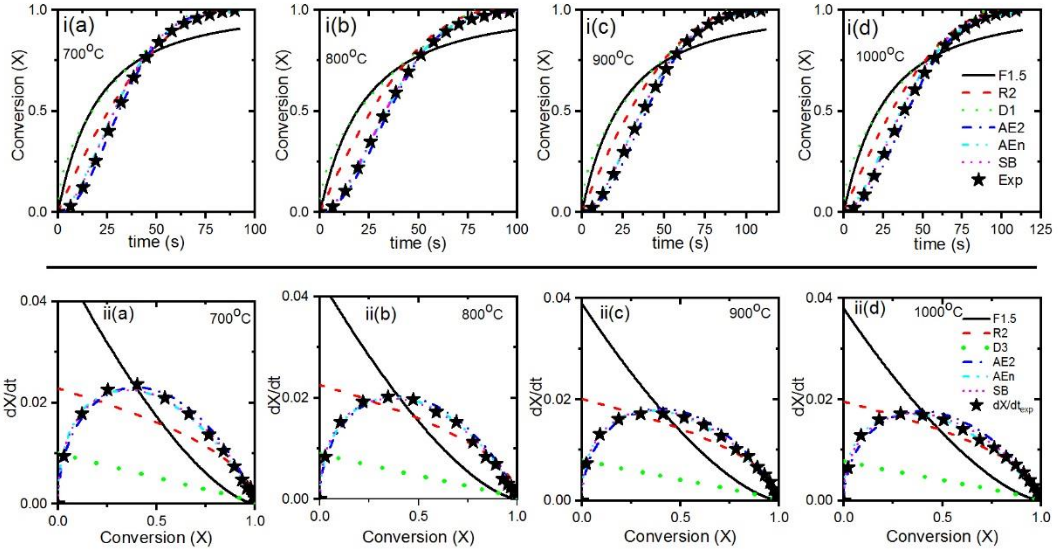

Figure 105. Comparison of X vs. t between the experimental data and models with a concentration of 40% of CO_2 at different temperatures; i(a) T=700°C, i(b) T=800°C, i(c) T=900°C, i(d) T=1000°C; and dX/dt vs. X between the experimental data and models with a concentration of 20% of CO_2 at different temperatures; ii(a) T=700°C,ii(b) T=800°C, ii(c) T=900°C, ii(d) T=1000°C.

F-test

The F-test is the most common method adopted to determine the statistically significant model between different model versions with a varying number of parameters, which are termed as nested. It can happen that sometimes F-test and AICc differ in agreement in their choice of the winner model [434]. The procedure is to select the model with the smallest RSS among all the models with the same number of fitting parameters, and then compare the relative value of the F-ratio, which is evaluated according to the equation (7.24).

$$\text{F-ratio}_j = \frac{RSS_j^2}{RSS_{min}^2} \tag{7.24}$$

RSS_j is the Residual Sum of Squares of model j and RSS_{min} is the minimum RSS between the two models compared. F-ratio follows the Fisher distribution with R and F degrees of freedom (which correspond to the number of parameters). When the models are nested with a different number of parameters, F-ratio is compared with a $F_{critical}$ value (which is the upper quantile of the Fisher distribution evaluated with the different degree of freedoms). The F-ratio in comparing two nested regression models (with a different number of parameters) is the result of a test where the null hypothesis is that all of the regression parameters are equal to zero. In other words, the null hypothesis is that the model has no predictive capability. Basically, the F-test compares the model with zero predictor variables and decides whether the added coefficients (parameters) improved the model.

In order to incorporate the uncertainty, a confidence level defined as 100(1-β)% is selected. Fixing β, which is the level of significance (it is usual to refer to 1-β as the level of confidence), the acceptance limits, called quantiles of order 1-β, can be extrapolated from the table of the Fisher distribution cumulative probability function.

Then, the $F_{critical}$ has been evaluated, which is the upper quantile calculated as qf(1-β, df_R-df_F, df_F) using F-statistic tables, where df_R and df_F are the degrees of freedom of the model with a lower number of parameters and a higher number of parameters, respectively. If F > qf(1- β, df_R-df_F, df_F), then we reject the hypothesis and the model with the higher number of parameter is chosen as the best model[435].

After the identification of models which were with lowest RSS and AICc values, three models AE2, AEn and SB model were in agreement with experimental conversion values and F-test with a confidence interval of 95% has been applied for both the methods adopted (X vs. t and dX/dt vs. X).

The F-test results for 20% CO_2 concentration are listed in Table 43. It depicts that all F-values obtained from the best-approximating models at different temperatures are smaller than the critical value at 95% confidence level (cl) (i.e., significant level $\beta = 0.05$). Therefore, the model predictions and observed values are the same at 95% confidence level. F-test results for 30% and 40% CO_2 concentration (Table S4 and Table S5) can be seen in Appendix A.3.1.

It is yielded that for temperature 700ºC, SB model was the winner for dX/dt vs. t method and AEn for X vs. t. For the dX/dt vs. X method for all concentration of CO_2 in the inlet, SB model is the winner model for temperatures 700ºC, 800ºC and 1000ºC except at 900ºC where AEn model is the winner. For X vs. t method, AEn model is the winner except at 800ºC with 20% CO_2 and 1000°C with 30% CO_2, where SB is the winner model.

Globally, the SB model is the winner in 32 of the F-tests, while AEn in 27 and AE2 only in 13. Therefore, with the methodology adopted both AE and SB model were in agreement with experimental data, but AE2 and AEn pass the F-test in fewer conditions than SB, which revealed to be the winner model for the larger number of conditions in either of the methods adopted. Though it can be seen for few model comparisons where the F values are very close to $F_{critical}$, there may be the chance that the winner model might change depending on the data. It is observed only for 4 cases out of 24 cases reported in Table 43, such as for SB/AE2 in conversion (X) vs.time. Choice of selection the model is subjective and is always taken along with RSS and AICc.

Table 43. F-test for the 20% CO_2 concentration.

Temperature	**Method**	**Cases compared**	**F-ratio**	**$F_{critical}$**	**Winner model**
700ºC	dX/dt-t	AEn/AE2	1.0113	1.1436	AE2
		SB/AE2	0.9627	0.8744	SB
		SB/AEn	0.9519	0.8744	SB

	X-t	AEn/AE2	1.0170	1.1432	AE2
		SB/AE2	0.9224	0.8716	SB
		SB/AEn	1.0198	1.1473	AEn
800°C	dX/dt-t	AEn/AE2	1.0308	1.1341	AE2
		SB/AE2	0.9595	0.8740	SB
		SB/AEn	0.9338	0.8740	SB
	X-t	AEn/AE2	1.0494	1.1334	AE2
		SB/AE2	0.9215	0.8785	SB
		SB/AEn	0.9674	0.8785	SB
900°C	dX/dt-t	AEn/AE2	1.0060	1.1274	AE2
		SB/AE2	1.0699	1.1274	AE2
		SB/AEn	1.0635	1.1274	AEn
	X-t	AEn/AE2	1.0098	1.1266	AE2
		SB/AE2	0.9236	0.8828	SB
		SB/AEn	1.0107	1.1326	AEn
1000°C	dX/dt-t	AEn/AE2	0.9817	0.8893	AEn
		SB/AE2	0.9644	0.8893	SB
		SB/AEn	0.9824	0.8893	SB
	X-t	Aen/AE2	0.9628	0.8894	AEn
		SB/AE2	0.9263	0.8831	SB
		SB/AEn	1.0636	1.1322	AEn

Kinetic parameter evaluation

After the selection of SB as the best-fitting model, the kinetic parameters estimation is done. The ln(K) has been plotted versus the inverse of temperature (1/T) for each concentration of CO_2 as described through equation (7.20). Figure 106(a) represents the ln(K) vs (1/T) plot for the three concentrations. The negative slope yields the activation energy for each concentration. The average activation energy evaluated from the three concentrations is 79.1±6.47 kJ/mol within a 95% confidence level. The intercept of the value would be $\ln(AP^m)$, as described by equation (7.21), which is plotted in Figure 106(b) against natural logarithm of the partial pressure of CO_2.

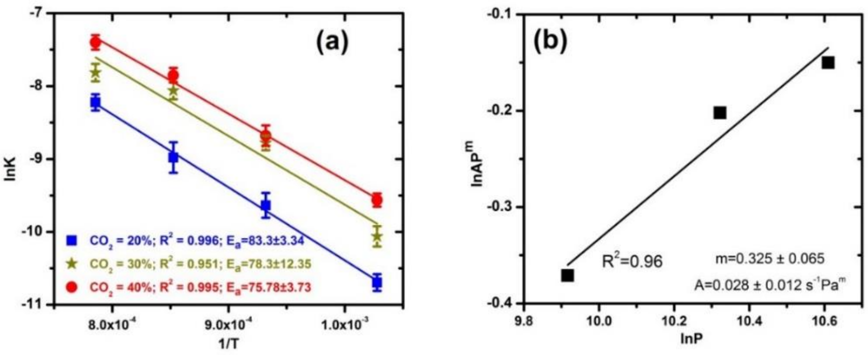

Figure 106.(a) ln(K) vs (1/T) Arrhenius plot of the oxidation reaction for SB model, (b) ln(AP^m) vs ln(P) plot for oxidation reaction order determination.

From Figure 106(b) the reaction order obtained is 0.325±0.06 and the pre-exponential factor is $0.028 \pm 0.012 s^{-1} Pa^m$. The value of activation energy is validated using an analytical model developed by Bulfin et al [108], in which activation energy is obtained by plotting between $\ln(\delta/(\gamma-\delta))$ vs 1/T. Here γ is the maximum non-stoichiometry that an oxygen carrier can reach during oxidation and reduction step. For ceria, the value of γ reported as 0.35[108]. Figure 107 represents the analytical method adopted to verify the activation energy, and it came out as 80±4 kJ/mol which is in-line with the kinetic methodology adopted in the present study.

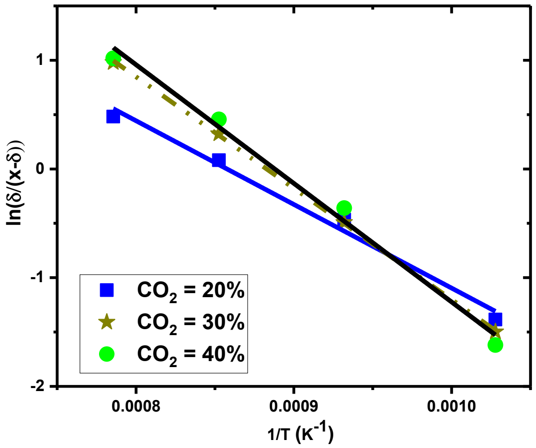

Figure 107. A graph of ln(δ/(x-δ)) vs 1/T for a range of different concentrations. The data was fit linearly and from the slope of each line, we can calculate the activation energy.

7.3.8 Concluding remarks

This work presents a detailed kinetics study of CO_2 splitting on ceria. The time-resolved kinetics were measured in a horizontal tubular reactor at atmospheric pressure. The ceria sample was exposed to 5%H_2 in Argon mixture in the reduction step to remove the lattice oxygen, and CO_2 in the oxidations step to produce CO in the redox cycle. Tests were performed under isothermal conditions (700–1000°C) for multiple redox cycles for three CO_2 concentrations between 20%-40% in Argon. Experiments showed that with an increase in temperature the total CO production increases. For instance, the total CO production at 700°C was 9.2 ml/g and peak production was 13.2 ml/(min-g), and for 1000°C the total CO production was 28.2 ml/g and peak rate was 29.7 ml/(min-g) for the CO_2 concentration of 20%. For higher concentration of CO_2 (40%) the total CO production increased to 33.7 ml/g and the peak rate to 46 ml/(min-g) for 1000°C. The total CO production linearly increased with the increase of temperature, and the effect of CO_2 concentration on total production was minimal. However, the effect of concentration of CO_2 was seen with respect to peak rate signifying the time for conversion reduction.

In order to identify the reaction mechanism and kinetic model, a statistical approach was adopted to select among different reactions models by fitting them to experimental reaction rates. The activation energies, the pre-exponential factors, and the reaction orders were determined. By determining the RSS and AICc values kinetic models were selected, and based on the complexity and the number of parameters the F-test considering upper quantile was used to select the best model. The results showed that the AEn and SB model are both suitable for describing the oxidation reaction, but SB model was the best-fitting one for most of the conditions of temperature and reactant concentration. The activation energy obtained considering the SB model was determined to be ~79±6 kJ/mol, in agreement with the literature. The present study gives a clear understanding in the model selection and mechanism of reaction for the entire range of conversion rate ($0 < X < 1.0$), which would help in designing the chemical looping CO_2 splitting for packed bed or fluidized bed reactors for a large-scale system.

7.4 Assessment of methane reduction and CO_2 oxidation of non-stoichiometric ceria

7.4.1 Introduction

With sufficient experience in assessment of the reaction kinetic models for CO_2 splitting, H_2 is replaced by methane in to investigate the kinetic model for partial oxidation of methane with non-stoichiometric ceria following by CO_2 splitting reaction.

In recent times, the attention to fuel reduction of ceria has increased immensely [383,385,436–439]. Some of them were focused with catalyst promoters such as Pt [436] and Rh [440,441] to enhance the reactivity. Structure of the experimental reactor and material form such as powder, reticulated foam, honeycomb, monolithic structure, etc., with promoters and support, also plays role in achieving higher reaction extent [279,328,383,442–445]. Nair and Abandes [279] investigated the solar methane reforming and H_2O/CO_2 splitting for ceria and ceria promoted with MgO and Al_2O_3 in a solar thermogravimetric device specially designed for particular experiments. The results reported that for CeO_2 part of the sample is completed converted to Ce_2O_3 after reduction with a remaining in non-stoichiometric form with the global $\delta < 0.5$. The maximum δ achieved was 0.37 for pure ceria and with the inert support of MgO, it increased to 0.431. With recent study later in 2017 in Scheffe's group, conducted experiments on solar methane reforming to investigate the performance and extent of reduction along with efficiency with the particle-transport reactor and solar cavity tubular reactor allowing packed bed format for ceria reduction. Both the experiments were testing on different temperature operation with particle reactor being tested 1150-1350°C resulting non-stoichiometry 0.002 to 0.22 [446] while for packed bed setup the

950-1120ºC yielded δ from 0.07-0.24 [280]. Nevertheless, the different experimental conditions, including experimental artifacts significantly affect the overall outcomes and hence the results of the experiments. A detailed discussion in this regard has been reported by Scheffe et al [447]. This not only results in a wide discrepancy in the reported results but also in developing a comprehensive kinetic model to best describe a reaction over a wide range of temperature and operating conditions. Unlike the model developed by Bulfin et al [108] which comprehensively describes the solar thermal reduction of ceria, over a wide range of operating conditions, not one model exists that can accurately predict the reduction of ceria by methane. In addition, all the oxidation kinetics have been studied after thermal reduction of ceria or H_2 reduction. CO_2 kinetics, being so heavily dependent on the surface phenomena, thus needs to be re-evaluated for oxidizing methane-reduced ceria.

Therefore, in this section, the kinetics of methane reduction of commercial ceria with subsequent oxidation with CO_2 was investigated with the semi-empirical solid-state kinetic model assessment. Detailed experimental set-up and kinetic model assessment methodology are already described in section 7.2 and section 7.3.5 respectively.

Isothermal redox cycles of CeO_2 commercial powders were performed in a horizontal tubular reactor in the temperature range of 900–1100°C. The upper range of temperature is selected as methane cracking is reported above 1050ºC with carbon deposition. During the reduction, an online mass spectrometer was used to measure the H_2 and CO production during reduction and CO production during the oxidation reaction. Upon analysis of the reactivity data obtained from the experiments, different kinetic models based on alternative reaction mechanisms (i.e., reaction order, geometrical contracting, diffusion, and nucleation models) were compared for the best-fitting model for selection as described in section 7.3. Hence, the corresponding ceria reduction and oxidation mechanism were identified following the procedure described in section 7.2.5.

7.4.2 Microstructural analysis

XRD patterns of ceria before and after the reaction cycle for different temperatures are analyzed (can be seen in Figure 132 in Appendix A.3.2), revealed a cubic fluorite structure in all the cases of temperature and concentrations. Compared to XRD patterns before cycling, the peaks appear more intense after cycling, which indicates a growth of crystalline grains during the high-temperature process. XRD analysis cannot give information regarding the crystal size (117 nm) because the operating temperature led to a significant growth of crystal size, which resulted higher than 80 nm. In general, for size higher than 80 nm the instrument contribution to the peak width overwhelms the signal from the crystallite size broadening and it is not possible to determine this latter contribution.

SEM characterization helps more to define the splitting processes occurring during the operating conditioning. With 30% CH_4 concentration during reduction at 900°C ceria is present in particles of 60-100 nm that often forms bigger aggregates of 2 microns as shown in Figure 108(a) compare to the structural organization of fresh ceria sample as shown in Figure 102(b). The size of aggregates of ceria at 1000ºC slightly increase with respect to that of the samples treated at 900°C which can be seen in Figure 108(b). At the higher temperature of 1100ºC, the carbon is rarely on the sample as observed but instead coated on the rods of SiO_2 which is from quartz wool sheets which are qualitatively approximated to 10-20%. The ceria aggregates resulted in very compact with size varies from 3 microns to 30 microns. But when the methane is fed in higher concentration the carbon deposit is more evident and cover also the ceria aggregates (Figure 108(c)). The amount of carbon revealed on ceria aggregates is not homogeneous, this is due to small carbon sheet deposited also on ceria which in turns drops the CO production rates at higher concentration of methane during reduction. The carbon formed during methane splitting undergoes reverse bourdard reaction forming CO at a higher temperature.

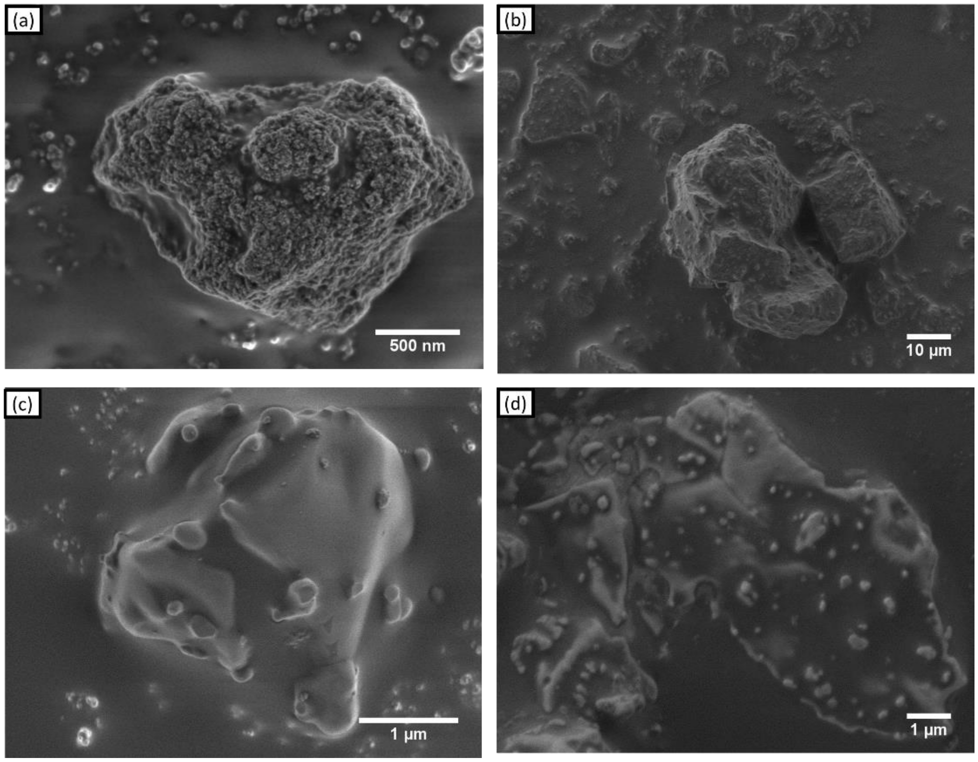

Figure 108. Phases, and compositions in the samples of ceria (a) 900ºC (b) 1000ºC (c) 1100ºC at 30% CH_4 (d) 1000ºC at 30% CH_4.

7.4.3 Reactivity results

The results of the tests for methane reduction and the CO_2 splitting performance in terms of the CO production rate (ml/(min-g)) and the total CO yield (ml/g) were investigated. For each point of observation, five consecutive redox cycles are performed to attain stable results. It is observed besides the first cycle, all the other cycles show a consistent repeatability for both the oxidation and the reduction reactions as shown in Figure 109. For the kinetic analysis, the fifth cycle is taken into consideration. It can also be seen that the H_2/CO ratio for almost 2 for the reported condition but this would increase at a higher temperature accounting for H_2 due to methane splitting. Therefore for developing the kinetic model only CO is considered from both reduction and oxidation step.

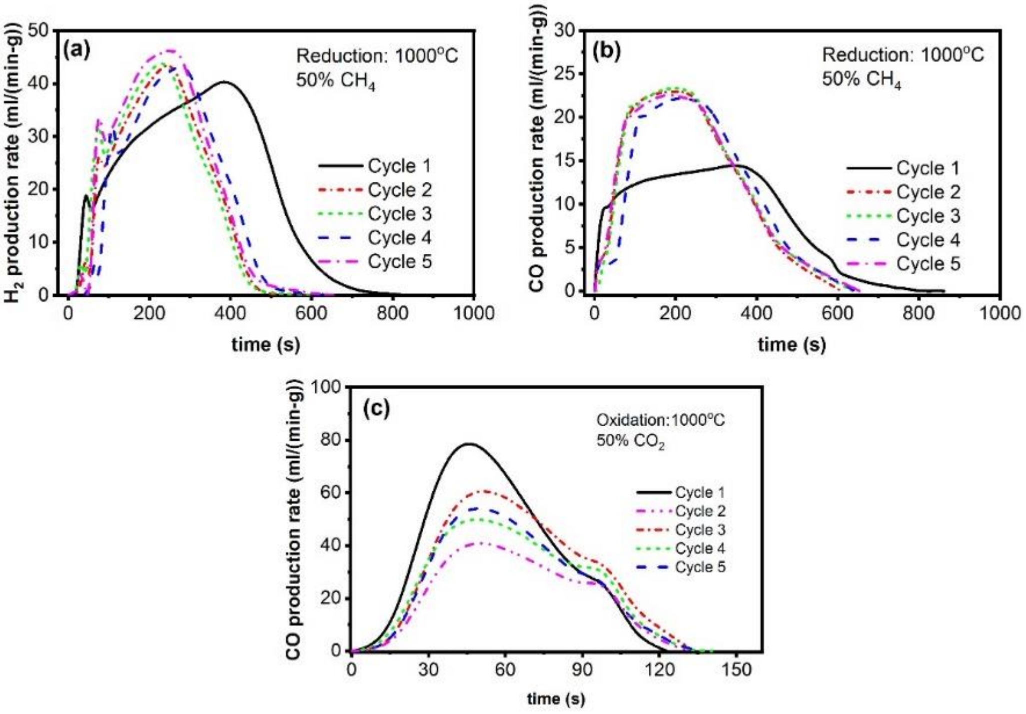

Figure 109. (a) H_2 and (b) CO production rate from the reduction of CeO_2 over 50% CH_4 and (c) oxidation of the reduced metal oxide with 50% CO_2 over five cycles.

The primary motive behind the set of experiments was to evaluate the performance and the dependence of commercial CeO_2 as oxygen carrier on temperature and reactant gas concentration. Hence a series of tests were performed in different experimental conditions and are described in the following sections.

Effect of temperature

Figure 110 shows the CO production rate as a function of temperature for both the oxidation and reduction reactions. For both the reactions, the temperature was varied from 900 to 1100°C. In each plot, the reaction rate is characterized by a slow initial stage, a fast-middle stage, also resulting in a peak reaction rate, and subsequently a decrease.

During reduction, the slow increase in the CO release results from the release of oxygen from the crystal lattice of the metal oxide. Both temperature and reactant concentration play a role in determining the maximum rate. Indeed, the relative length of each of the three phases depends much on the reaction temperature, which is especially significant for the reduction reaction. This, in turn, would lead to a much longer time for completion of the reduction with a subsequent lower yield. As can also be seen for both the reduction and oxidation reactions, the peak rate varies non-linearly with temperature, and for temperatures lower than 900ºC, the reaction becomes slow enough to limit the overall non-stoichiometric ceria yield.

For the reduction reaction, the impact of temperature is much more pronounced on the peak product yield, as can be seen from Figure 110(a). From the increase in temperature from 950ºC to 1100ºC, the peak yield of CO was observed to increase almost six times, with the most marked rise in the yield rate occurring between 1000ºC and 1050ºC, when the production rate almost triples. Also, with temperature, the peak rate becomes faster and quicker to occur (around 600 secs for 950/1000ºC and around 400 secs for 1050ºC. At 900ºC, no significant peak is even noticed, with a flatter trajectory occurring over a larger time due to the lower amount of available oxygen sites. After the peak yield, the production rate drops rapidly, with a complete reaction taking place in around 1000s for all temperatures beyond 900ºC. Thus, a strong temperature dependence of the reduction yield rate profile of methane reduction of ceria, which becomes higher and narrower at a higher temperature.

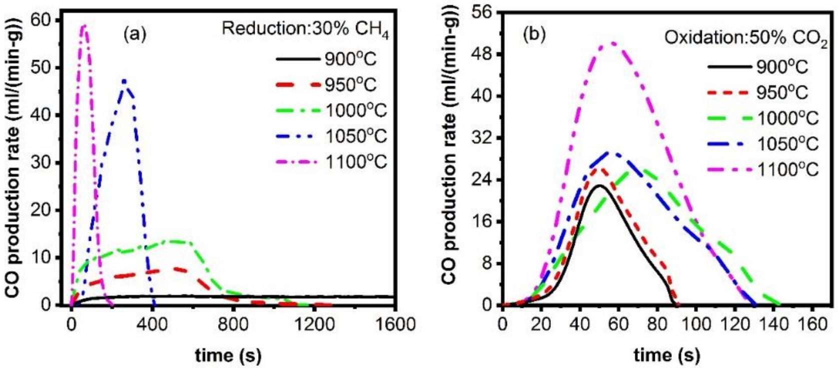

Figure 110. Variation of yield rates of CO in (a) reduction and (b) oxidation of CeO_2 in the redox cycle of methane reduction followed by oxidation with CO_2 with the variation of temperature in the range 900ºC and 1100ºC; Methane concentration during reduction: 30%; CO_2 concentration during oxidation: 50%, baseline reactor pressure: 1 atm.

On the other hand, for the oxidation reaction, a rapid rise in the CO yield is observed due to the rapid oxygen vacancies ion incorporation. Similar to the reduction reaction, after peak CO yield, the yield drops sharply for all temperatures approaching zero in 80-150 secs. It needs to be mentioned here that the oxidation cycles have experimented directly with the reduction cycles. Therefore, the performance of the oxidation reaction is directly influenced by the net non-stoichiometry generated in the reduction step. In this regard, since a lower non-stoichiometry was generated in the reduction reaction ($\delta = 0.10$) for reduction at 900ºC, the net reaction time was lower. However, with an increase in temperature, the peak CO yield becomes higher and wider, indicating a high activation barrier associated with the CO_2 splitting process [407]. Figure 110(b) emphasizes the observed behavior of the peak rates at varying temperature for a fixed CO_2 molar fraction. The strong temperature dependence of CO_2 splitting observed in the present study is evident from the earlier studies as well [161,219,402].

Effect of concentration

The effect of the concentration of the reactants on the reduction and the oxidation kinetics of ceria with methane and CO_2 respectively was also investigated. Figure 111 clearly indicates that for both the reduction and the oxidation reaction, the reaction time decreases with an increase in the partial pressure of CH_4 and CO_2 in the feed for reduction and oxidation respectively, together with a higher peak rate of product yield. Similar effects from lower activation energies at higher CH_4 concentration during CH_4 reduction was reported by Warren et al [87] and Zhao et al [213], while for oxidation, Farooqui et al [197] reported similar reaction profiles. An increase in the conversion rate is counter-balanced by a decrease in the conversion time, and hence the net yield remains fairly constant for the point of interest.

For instance, for the reduction at 1000ºC, the maximum non-stoichiometry generated at lower concentrations (30% CH_4, balance Argon) was slightly higher, 0.20, than for higher methane concentrations (50% CH_4, balance Argon), around 0.184. On the other hand, the overall net yield of the oxidation with CO_2 remains constant, due to a fixed reduction extent of ceria, the result is completely oxidized ceria.

Also, as can be seen from Figure 111(a), the peak shifts considerably to a lower time with higher methane concentrations, with a peak yield being noticed at around 200 secs for 50% concentration of methane, while for 20% methane in feed, a peak was obtained only after 1750 sec. In contrary, the oxidation reaction, even though occurring at a higher temperature, does not show such a significant impact of the variation of concentration, as can be noticed from Figure 111(b). The peak remains constant between 60-70 secs range. In relation to the peak rate variation with temperature, the variation was non-linear for the reduction reaction (Figure 111(a)). However, for the oxidation, the peak rate increases linearly with the concentration of CO_2 in the feed. The lower dependence of CO_2 splitting on the concentration of the CO_2 in the feed in comparison to methane for reduction has been reported elsewhere as well [197,219,400,414].

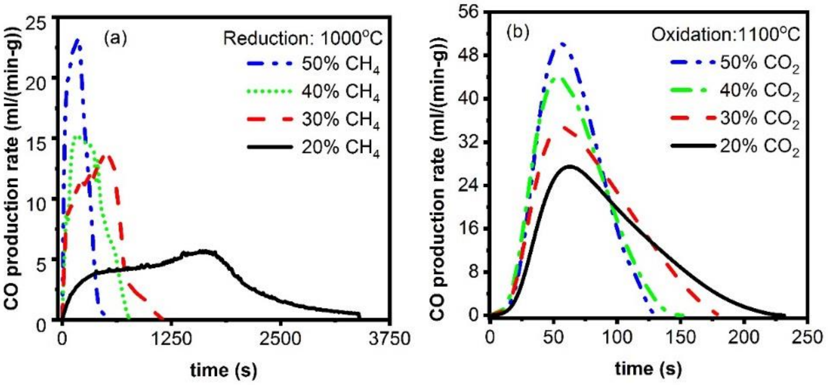

Figure 111. Variation of yield rates of CO in (a) methane reduction of ceria at 1000°C and (b) oxidation of reduced ceria at 1100°C with the variation of concentration of the gaseous reactants at a reactor pressure of 1 atm.

Figure 112 shows the CO peak production rate and total yield of CO from the reduction of ceria by methane and oxidation by CO_2 for different temperature and concentration of interest. The methane flow was kept constant at 20-50% and the total gas flow was maintained at 120 ml/min for reduction. It is observed from Figure 112 (a) the concentration of oxygen vacancies in the ceria increases with increase of temperature from 900-1050°C with total CO production 37.7 – 84.5 ml/g ($\delta = 0.1\text{-}0.23$) but at 1100°C drops to 47.9 ml/g (δ=0.12) reason being is that there is evident methane splitting as shown from the microstructural analysis also. Similar non-stoichiometry is reported by Warren et al [280] δ=0.21 at 1035°C. It is worth mentioning that CO peak rates for lower temperature are very low as 2 ml/(min-g) but making the reduction step long for 62 min comparing to 1000°C making to last for 19.5 min with a peak rate of 14.2 ml/(min-g). Therefore, with an increase in temperature the reaction time drops but it is a trade-off to limit the operating temperature to avoid methane splitting. The initial stage of oxidation ends within the 20s but accounts for more than 70% of the overall δ change, while the remaining oxidation leads to a lower change of non-stoichiometry. It is evident that the oxygen-carrying capacity increases due to a higher extent of non-stoichiometry achieved at higher temperatures. Figure 112(b) represents that total CO production decreases from 90.7-34.0 ml/g (δ=0.24-0.17) with an increase of methane concentration from 20-50% at 1000°C, even though the total CO production drops but the CO peak rate increases from 5.8-23.8 ml/(min-g). The decrease of total CO production is due to a decrease in the oxygen vacancies due to carbon deposition at the surface of the sample at a higher concentration of methane, this is also reported by [205]. Figure 112(c) represents CO peak rate and CO total production increases with an increase in temperature of oxidation. The total CO production rate increases from 12.7-23.8 ml/g (δ=0.1-0.23) from 900-1050°C and there is a sudden rise in total CO production to 37.8 ml/g for 1100°C. This rise is attributed to reverse boudard reaction of carbon which was formed during reduction leading to the higher rise of CO production. Nonetheless, it is worth mentioning that there is the very little effect is observed of CO_2 concentration during oxidation with 33.7-37.8 ml/g for CO_2 concentration from 20-50% even though the peak rate is increased 27-51 ml/(min-g). It can be noted that the non-stoichiometry increases from 0.07 to 0.21 in the 900–1000°C temperature range for 20% CO_2 mole fraction during oxidation, and a maximum of 0.25 is reached at 1000°C for 30% CO_2 mole fraction. Similar non-stoichiometry results for oxidation are reported in our previous results of H_2 reduction and elsewhere [197,219,400,448].

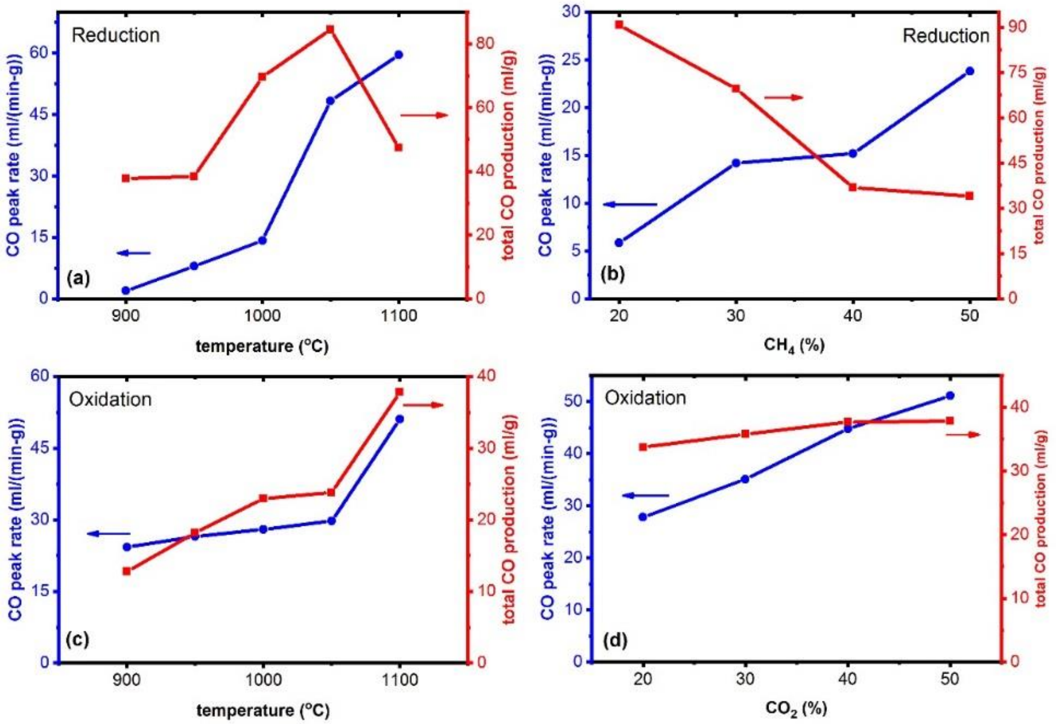

Figure 112. CO peak rate and total CO production for varying temperatures and feed concentrations with CH_4 of 30% and CO_2 of 50% during reduction and oxidation respectively and 1100°C during oxidation.

It is important to mention that methane reduction kinetics is much slower than H_2 reduction and CO production is higher for similar CO_2 concentration during the oxidation step. For instance, in H_2 reduced oxidation step with 20% CO_2 concentration, CO production is 28.5 ml/g compared to 33.7 ml/g when CH_4 is reduced for reduction. Similar results are reported by Zhou [38] for methane reduction for lower temperatures but the oxidation step is replaced by H_2O splitting instead of CO_2.

7.4.4 Kinetic study

Based on the models listed in Table 41, a comprehensive evaluation with all the models was performed, together with finding the least RSS by fitting each model to the experimental results following the procedure described in section 7.3. Nevertheless, the AE3 model was found to fit best with the experimental results for both the reduction and oxidation reactions. The following section summarizes the kinetic results of the two sections of the redox cycle starting from the reduction of ceria with methane.

Ceria reduction by methane

As mentioned, based on the calculation of the least errors of all the models fitted to the experimental results, an average R^2 value of 0.97 was obtained for the AE3 model, showing a good match. After the selection of the kinetic model, the evaluation of the kinetic parameters was carried out.

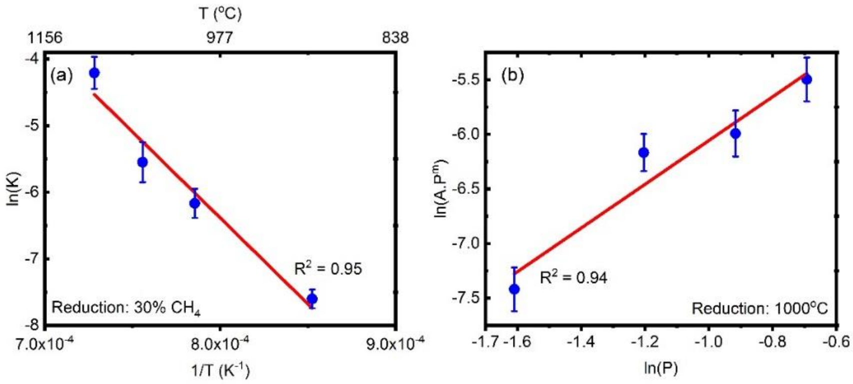

Figure 113. (a) ln(K) vs (1/T) Arrhenius plot of the reduction reaction for AE3 model; (b) $\ln(AP^m)$ vs ln(P) plot for reduction reaction order determination.

The $\ln(A\cdot P^m)$, as obtained directly from the slope of the curve g(X) vs t was plotted first versus log of concentration in terms of partial pressure (ln(P)) to obtain the reaction order, as described in equation (7.20), as shown in Figure 113(b). The reaction order obtained is 2.0 ± 0.36. Correspondingly, ln(K) was plotted versus the inverse of the temperature (1/T) as described through equation (7.19). Figure 113 (a) represents the ln(K) vs (1/T) plot reduction of ceria with 30% methane, the average activation energy was calculated as 283.65 ± 0.66 kJ/mol within a 95% confidence level. The pre-exponential factor, A was calculated as 8.67E9 ± 433 s^{-1}.

Nonetheless, the concentration effect in terms of reactor order was further evaluated through curve fitting and was obtained to vary both with temperature and concentration. In this regard, a regression analysis between m_{RED}, T and P in terms of concentration was carried out for temperatures below 1050°C using statistical methods. The relation obtained is described by the following equation (7.30) and the corresponding R^2 value obtained was 0.98. Beyond 1050°C, the reaction order was found to remain constant at 2.2.

$$m_{RED} = 19.897 - 0.013\times[T] - 1.28\times[P_{CH_4}] \quad (7.30)$$

Where T is in Kelvin and P is the concentration or partial pressure of the gaseous reactant, considering ideal gas laws.

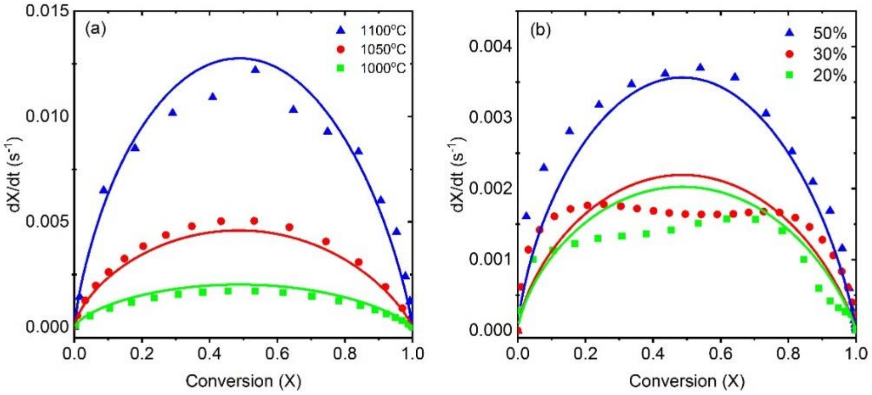

Figure 114. Comparison of the kinetic model and the experimental data for methane reduction of ceria (a) with the variation in temperature, 1000ºC, 1050ºC, 1100ºC and (b) with the concentration of CH_4 of 20%, 30% and 50% for reactor pressure of 1 atm. The symbol represents experimental data and lines represent the kinetic model.

The value of activation energy and the other constants obtained in the model fit well to the experimental results, as obtained through curve fitting using the proposed model, shown in the following Figure 114. A good agreement of the results, both with respect to concentration and temperature variation can be seen. It is observed that there is discrete values of activation energies have been reported which varied from 20 kJ/mol to 334.56 kJ/mol [87,279,413] for a variety of conditions of temperature and concentration of the reducer. Warren et al [87] reported that the activation energy varies from 20-80 kJ/mol as the non-stoichiometry (ranging from 0 to 0.35). Otsuka et al [37] reported 160 kJ/mol of activation of methane reduction by ceria with Pt as a catalyst. A similar value of 165-176 kJ/mol is reported by Ramirez Cabrera et al [449] reported the effect of doping of Gd and Nb over ceria. It is reported that the activation energies are reduced by the doping or by using a catalyst with the ceria. The activation energy evaluated in the present experiments higher than of 221 kJ/mol was reported in the literature [114] but lower than reported 334.56 kJ/mol by Ackermann et al which was evaluated for considering oxygen diffusion in ceria [413]. Even so, no study has reported the complete solid-state kinetic model development for the said reaction. Therefore, no comprehensive comparison with literature data can be done. Nonetheless, a slight over-estimation for lower concentrations are obtained, while for higher concentration, the model slightly underpredicts the yield of the products. Nevertheless, all the results lie within the 95% confidence level and agree well with values obtained in literature, as described earlier.

$CeO_{2-\delta}$ oxidation by CO_2

Like the reduction reaction, a similar curve fitting was performed using least square of errors on all the models listed in Table 41. As like the reduction reaction, the AE3 model fits best with the experimental results and the average R^2 value obtained was 0.98, showing a good match.

A similar procedure, as discussed for the reduction reaction, to obtain the reaction order and the activation energy was carried out. The $\ln(A\cdot P^m)$, as obtained directly from the slope of the curve g(X) vs t was plotted first versus log of concentration (ln(P)) to obtain the reaction order, as described in equation (7.20) (Figure 115(b)). The reaction order obtained is 0.732 ± 0.186. Correspondingly, ln(K), was plotted versus the inverse of temperature (1/T) as described through equation (7.19). Figure 115(a) represents the ln(K) vs (1/T) plot oxidation with 50% CO_2, the average activation energy was calculated as 59.68 ± 6.09 kJ/mol. The pre-exponential factor, A was calculated as $64.48 \pm 1.45\ s^{-1}$.

Nonetheless, the concentration effect in terms of reactor order was further evaluated through curve fitting similarly as before and was obtained to vary both with temperature and concentration. In this regard, a regression analysis between m_{OXI}, T, and P in terms of concentration was carried out for all temperatures and concentrations using statistical methods. The relation obtained is described by the following equation (7.31) and the corresponding R^2 value obtained was 0.985.

$$m_{OXI} = 0.002\times[T]-7.5\times[P_{CO_2}]-1.996 \tag{7.31}$$

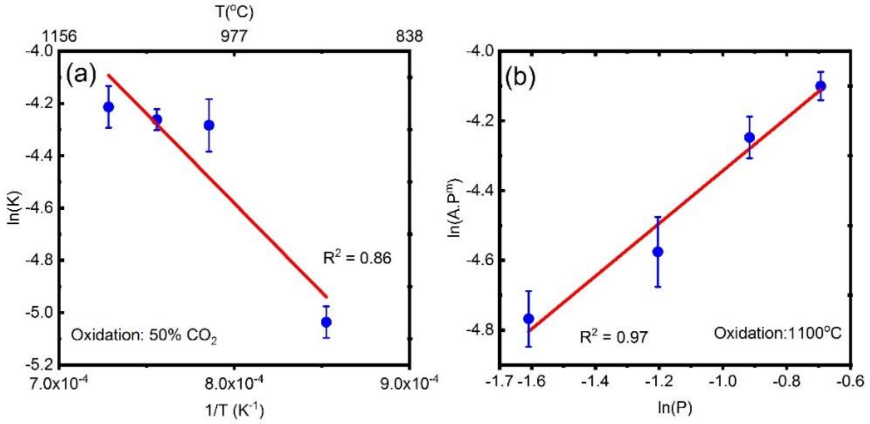

Figure 115. (a) ln(K) vs (1/T) Arrhenius plot of the oxidation reaction for AE3 model; (b) $\ln(AP^m)$ vs ln(P) plot for reduction reaction order determination.

Similar validation studies were performed with the model fit and the experimental results. The values obtained match closely with the results presented by Farooqui et al [197] for oxidation of ceria following hydrogen reduction, where the activation energy obtained was 79 kJ/mol [197]. Nonetheless, curve fitting using the obtained value was performed and presented in the following Figure 116. Since the non-stoichiometry of reduction increases with the increase, it would be empirical to fix non-stoichiometry of a particular value to compare the reaction rate as suggested [450]. Therefore reaction rate data of the model is compared with the experiments for those conditions in which δ_{red} reached 0.22. A good agreement of the results, both with respect to concentration and temperature variation can be seen. A slight over-estimation for lower concentrations are obtained like reduction, however, for higher concentrations a very good fit with is seen. An overall confidence level of the model with respect to experimental results of more than 95% is reached while agreeing well to the values obtained in similar studies performed reported in the literature.

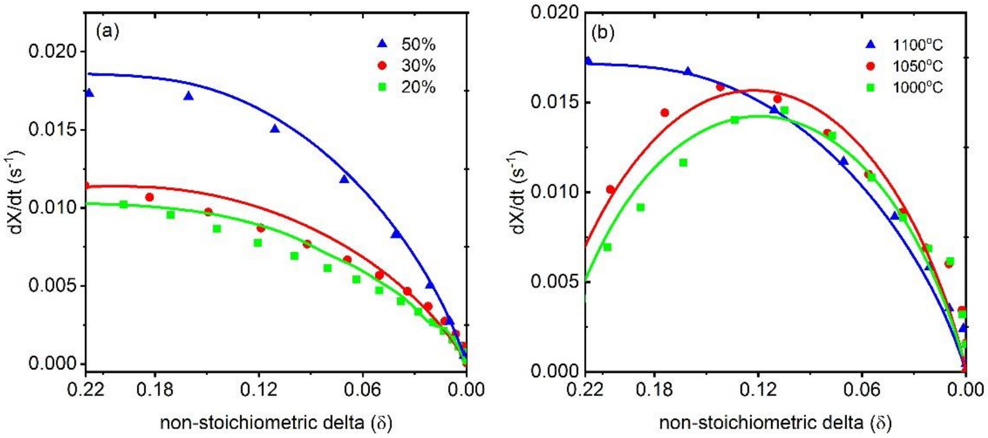

Figure 116. Comparison of the kinetic model and the experimental data for oxidation of reduced ceria with CO_2 (a) with the variation in concentration of CO_2 of 50%, 30% and 20% (b) with temperature of 1000°C, 1050°C, 1100°C for reactor pressure of 1 atm and a constant non-stoichiometric extent of reduced ceria of 0.22. The symbol represents experimental data and lines represent the kinetic model.

7.4.5 Concluding remarks

In the present study, we investigated the redox kinetics for commercial ceria considering methane for reduction that undergoes partial oxidation to syngas. For the oxidation step, CO_2 is used. The produced CO from both reduction and an oxidation step is evaluated for different temperatures (900-1100°C) and methane concentrations (20-50%). It is observed that with an increase of temperature the CO production rate increases from 900-1050°C and drops at 1000°C. Even though at 1050°C reveals to achieve higher CO production rate but the sample shows higher aggregates formation and carbon formation making it prone to deactivation of the sample. Similarly, for higher methane concentration, there is a drop in CO production rate which is also showed by SEM that there is carbon deposition. For oxidation, there is a relative increase in CO production with an increase in temperature but with minimal effect of CO_2 concentration. It is also observed that the reduction and oxidation kinetics paradigm has different reaction rates making methane reduction very slower compare to CO_2 splitting.

Carbon deposition was noticed to small extents at 1050°C, which increased subsequently at 1100°C as evident from reactivity and microstructural studies. However, this can be followed from numerous discussions presented in the literature regarding the same. Carbon deposition for methane reduction of ceria at over 1100°C and for a δ of over 0.2 has been reported by Otsuka et al [37,384]. Furthermore, methane cracking has also been reported to be enhanced at temperatures above 1100°C in the presence of alumina (Al_2O_3) [451], which is also the material of the present reactor. In addition, the passing of excess amount of methane or excessive residence times could also lead to significant carbon deposition, even though not considered as conditions in the present set of experiments [452]. However, Warren et al reported decreased carbon deposition from using platinum crucible as a replacement of alumina or quartz crucible for TGA experimental purpose [87].

Nevertheless, in this study kinetic model fitting is carried out to describe the reaction of methane for syngas production with commercial ceria and corresponding oxidation with CO_2 over a wide range of temperature, 900-1100ºC, and concentration of the reactants. The entire reaction set-up was carried out in atmospheric conditions, indicating the high kinetic potential of the reduction reaction even at such conditions, as opposed to the thermal reduction of ceria, requiring deep vacuum conditions. The AE3 model was found to fit best to the experimental data for both the reduction and oxidation reactions. A varying reaction order with varying reaction conditions was noticed and a relation was obtained for both the cases. Carbon deposition would limit the operation of the reduction at temperatures over 1100ºC, even though a very fast reaction would result.

Chapter 8

Effect of redox kinetics considering moving bed reactor model on the system analysis

8.1 Introduction

Heterogeneous reactions in chemical looping processes are governed by the reaction kinetics as reported by Adanez et al [453]. The maximum non-stoichiometry achieved during reduction is highly depended on the type of reaction environment and the operating conditions such as temperature, the concentration of the reducer and the residence time of the reducer. This lead to exploring the type of the reactor that can lead in achieving maximum utilization of the oxygen carrier producing high selectivity of the products. Different reactors used for thermochemical cycles are described considering different oxygen carriers are described in chapter 2. Based on the product selectivity required, moving bed reactor is suggested to meet the appreciable be highly effective compared to other non-structured reactors. Moving bed reactors for redox cycling considering solar thermochemical reactor system is studied in detail in chapter 3. However, it leads to relatively low system efficiency and, at the same time, it has challenges related to operating conditions such as higher degree of vacuum and higher reduction temperatures leading to huge pressure swing and temperature swing between the two reactors. In order to overcome the stated challenges, the thermal reduction step was suggested to be replaced with methane reduction to lower the reduction temperature and to work at isothermal chemical looping conditions and, at the same time, allowing both reactors to work at the same pressure, which omits the huge vacuum pumps energy for reduction reactor. Chapters 4, 5 and 6 were investigated considering the concept of methane reduction and CO_2/H_2O splitting for power and fuel production but with the assumption that reactions were taking place thermodynamically. In this chapter, the effect of kinetics and the moving reactor model will replace the thermodynamic chemical looping unit considered in chapters 5 and 6. Reactor models are developed similarly to the model presented in chapter 3 except that the kinetics is replaced by the one deduced in chapter 7. Therefore, all the assumptions are the same as listed in chapter 3.

8.2 Moving bed methane-driven chemical looping CO_2/H_2O splitting CL model

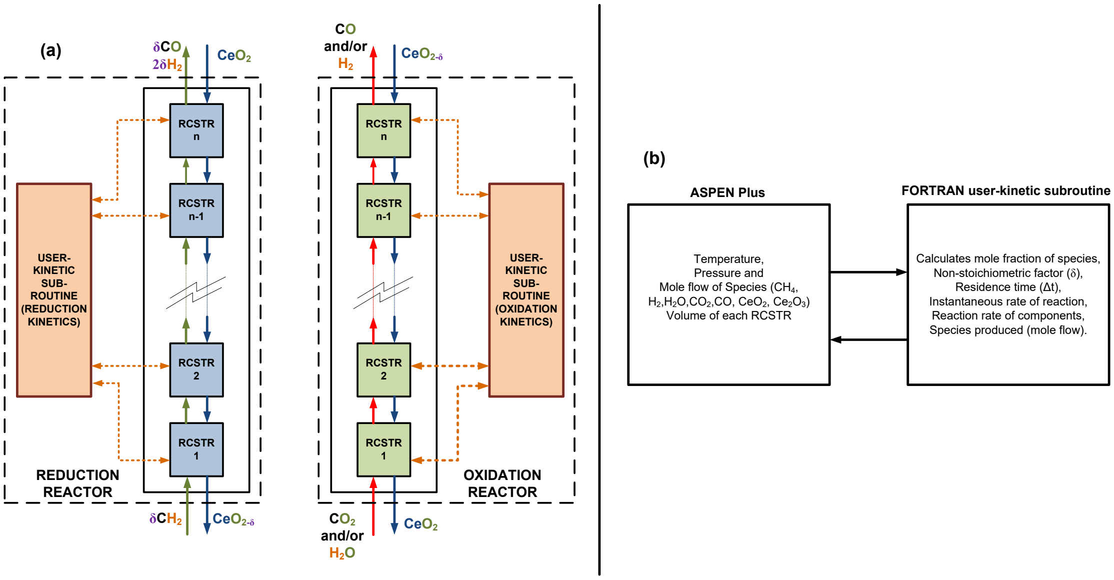

Figure 117. Moving bed reactor model for methane reduction and CO_2/H_2O oxidation reactors in Aspen Plus hooked with user kinetics written in an external FORTRAN Code

Figure 117 represents the schematic of a counter-flow moving bed reactor system for reduction and oxidation reactor. In the reduction reactor (RED), ceria is introduced from the top by a hopper system (not shown) and it is reduced by incoming methane from the natural gas undergoing partial oxidation producing syngas ($CO+H_2$) flowing up to the top of the reactor in a counter-current with respect to ceria flow. In the oxidation reactor, reduced non-stoichiometric ceria is fed from the top and the exhaust gas from the turbine (CO_2+H_2O) is fed from the bottom which moves up reacting with the metal oxide undergoing splitting reaction producing CO and H_2. The oxidized ceria is transported away from the bottom by a rotating conveyor system (not shown) to the reduction reactor. Since the oxidation reaction is exothermic, there will be a ΔT along the length of the reactor.

Each reactor model is as a series of rigorously continuous stirred reactors (RCSTR) interconnected in Aspen Plus. The RCSTR reactor is widely used in the simulation for the multiphase having characteristic of the same temperature for all phases. The total volume of the reactor is a summation of all the RCSTR reactors connected in series. The reaction kinetics developed by model fitting the experimental data is written in FORTRAN as a user-kinetic subroutine for both reduction and oxidation and hooked to each RCSTR reactor in the moving bed reactor model in Aspen plus shown in Figure 117. It has been assumed that the reduction reactor is isothermal and oxidation reactor is adiabatic. The reduction and oxidation kinetic model developed considering all species taking part in reactions are described in the following section. The residence time in each RCSTRs was calculated based on the bed volume with respect to ceria inflow neglecting the volume change due to change in the composition from reactions and lastly there is no change in the phase of ceria during redox recycling in the CL unit.

The number of RCSTRs selected for each reactor model relates to accuracy and time for simulation as described in chapter 3. Considering the similar methodology for optimizing the number of RCSTRs with respect to accuracy and the convergence time, an iterative procedure was adopted and relative change in the output of selectivity of CO and H_2 at both the reactors were observed to be less than 0.25% which resulted in 10 RCSTRs for both reduction and oxidation reactor.

In Aspen plus, Broyden solver was selected with 500 iterations for both mass and energy solvers with a relative tolerance of 0.0001 and the PR-BM method which utilizes the Peng-Robinson cubic equation of state with the Bostone Mathias alpha function [223] is selected for the simulations.

8.3 Reduction and oxidation kinetics

As previously reported in Chapter 7 the non-stoichiometric reaction (δ) of ceria during the methane reduction and oxidation steps follow the equations (8.1) and (8.2a-b):

$$CeO_2 + \delta CH_4 \rightarrow CeO_{2-\delta} + 2 \cdot \delta H_2 + \delta CO \tag{8.1}$$

$$CeO_{2-\delta} + \delta CO_2 \rightarrow CeO_2 + \delta CO \tag{8.2a}$$

$$CeO_{2-\delta} + \delta H_2O \rightarrow CeO_2 + \delta H_2 \tag{8.2b}$$

However, due to limited thermodynamic data available in the literature about the non-stoichiometric form of ceria ($CeO_{2-\delta}$), a different approach was adopted using the fully reduced form of ceria Ce_2O_3, which is completely investigated in the literature. Consequently, the equations (8.1), (8.2a) and (8.2b) were rearranged in a different form:

$$CeO_2 + \delta CH_4 \rightarrow (1-2 \cdot \delta)CeO_2 + \delta Ce_2O_3 + 2 \cdot \delta H_2 + \delta CO \tag{8.3}$$

$$(1-2 \cdot \delta)CeO_2 + \delta Ce_2O_3 + \delta CO_2 \rightarrow CeO_2 + \delta CO \tag{8.4}$$

$$(1-2\delta)CeO_2 + \delta Ce_2O_3 + \delta H_2O \rightarrow CeO_2 + \delta H_2 \tag{8.5}$$

In this case, the non-stoichiometric factor was used as an indicator of the ratio between the reduced ceria (Ce_2O_3) and the maximum amount of Ce_2O_3 achievable as described in equation (8.6).

$$\delta = \frac{\dot{n}_{Ce_2O_3}}{2 \cdot \dot{n}_{Ce_2O_3} + \dot{n}_{CeO_2}} \tag{8.6}$$

Consequently, to a full reduced CeO_2 correspond a δ equal to 0.5. However, since the proposed kinetic is based on the non-stoichiometric reduction of ceria, in order to guarantee the stability of the lattice structure of the metal oxide, a limit to the δ equal to 0.35 (δ_{max}) was selected. Hence, according to the model proposed by Bulfin et al. [108], the degree of advancement of the reduction reaction, X_{RED}, was calculated as follow:

$$X_{RED}=\frac{\delta}{\delta_{max}} \tag{8.7}$$

So the reduction reaction is considered fully completed (X_{RED}=1) when the non-stoichiometric factor reaches the δ_{max}. While the degree of advancement of the oxidation reactor (X_{OXI}), which occurs in the opposite direction of reduction, was calculated as the complementary of X_{RED}.

$$X_{OXI}=1-X_{RED}=1-\frac{\delta}{\delta_{max}} \tag{8.8}$$

No solid-state kinetic model exists for ceria reduction by methane. Correspondingly, a set of experiments were performed as explained in chapter 7 to develop the same. The kinetic model assessment was determined to follow Avrami-Erofe'ev model (AE3) when ceria is reduced with methane. The model was tested for different concentrations and temperatures considering the reduction reaction (Eq 8.3). From the reduction reaction, two moles of CeO_2 consumed to release one mole of Ce_2O_3 and one mole of CO and two moles of H_2.

The same approach reported in chapter 3 was adopted for the reduction kinetics. Hence, considering the reduction reaction (eq. 8.1) and the time-dependent equation for the degree of advancement of the reduction reaction that follows the AE3 kinetic model is given as equation (8.9).

$$\frac{dX_{RED}}{dx}=A_{RED}\cdot\exp(-\frac{E_{0,RED}}{RT})\cdot 3(1-X_{RED})[-\ln(1-X_{RED})]^{2/3}\cdot[CH_4]^{m_{RED}} \tag{8.9}$$

$E_{0,RED}$ is the activation energy, A_{RED} is the pre-exponential constant with m_{RED} is the reactor order and their details are presented in chapter 7. The reaction rate constant for all the species involving in the reaction is represented by equation (8.10). The reaction coefficient (a_{RED}) for the three species taking part in the reaction are Table 44.

$$k_{RED\text{-}i} = a_{RED\text{-}i}\cdot\dot{n}_{CeO_2}\frac{dX_{RED}}{dt}\Delta t \tag{8.10}$$

$k_{RED\text{-}i}$ is rate constants of reduction species *i* listed as CeO_2, Ce_2O_3, CH_4, CO, H_2; Δt is the reaction time step which is calculated based on inlet volume flow of the ceria into the differential volume of the reactor and can be represented as:

$$\Delta t = \frac{\dot{V}_{OC,in}}{\Delta V_{reactor}} \quad (8.11)$$

Table 44. Reduction reaction coefficients.

i	Reduction reaction coefficient (a_{RED})
CeO_2	-2
Ce_2O_3	1
CH_4	1
CO	1
H_2	2

Oxidation kinetics for CO_2 splitting also follow AE3 model as evaluated from the experimental analysis presented in chapter 7 is given by equation (8.12).

$$\frac{dX_{OXI\text{-}CO_2}}{dx} = A_{OXI\text{-}CO_2} \cdot \exp\left(-\frac{E_{0,OXI\text{-}CO_2}}{RT} \right) \cdot 3(1\text{-}X_{OXI\text{-}CO_2})[-\ln(1\text{-}X_{OXI\text{-}CO_2})]^{2/3} \cdot [CO_2]^{m_{RED}} \quad (8.12)$$

A_{OXI} and $E_{0,OXI}$ are the pre-exponential factor and the activation energy as presented in chapter 7 section 2. Methane reduction and consequently H_2O splitting reactivity was investigated earlier [38]. Since the CO_2 splitting reaction is the bottleneck oxidation reaction as it is slower and less exothermic compared to the H_2O splitting reaction, therefore the experimental investigation was done chosen CO_2 as an oxidizer.

For H_2O splitting, reaction kinetics model is adopted from Arifin [214] and Arifin and Weimer [220]. The reaction rate for oxidation reaction is represented as equation (8.13) and coefficients are presented in Table 46.

$$\frac{dX_{OXI\text{-}H_2O}}{dt} = A_{0,OXI\text{-}H_2O} \cdot \exp\left(-\frac{E_{0,OXI\text{-}H_2O}}{RT} \right) \cdot [H_2O]_i^{n_o} \cdot (1 - X_{OXI\text{-}H_2O})^{\psi_0} \quad (8.13)$$

$A_{0,OXI\text{-}H2O}$ is the Arrhenius constant, $E_{0,OXI\text{-}H2O}$ is the activation energy and n_o is the reaction order for the H_2O splitting reaction are listed in Table 45. The reaction rate constant for each species for the CO_2 and H_2O splitting is represented as equation (8.14 and 8.15).

Table 45. Kinetic parameters of the oxidation reaction of reduced ceria obtained by Arifin [220].

Oxidant	T (°C)	$A_{0,OXI\text{-}H2O}$	$E_{0,OXI\text{-}H2O}$ (KJ/mol)	ψ_0 (-)	n_o(-)
H_2O	750-800	3.4	45	0.65	1.2
	825-875	2.5	41	0.7	1.7

$$k_{OXI\text{-}j} = a_{OXI\text{-}j} \cdot \dot{n}_{Ce_2O_3} \frac{dX_{OXI\text{-}j}}{dt} \Delta t \quad (8.14)$$

$$k_{OXI\text{-}l} = a_{OXI\text{-}l} \cdot \dot{n}_{Ce_2O_3} \left\{ \frac{dX_{OXI\text{-}H_2O}}{dt} + \frac{dX_{OXI\text{-}CO_2}}{dt} \right\} \Delta t \quad (8.15)$$

where $k_{OXI\text{-}j}$ rates of oxidation species listed as H_2O, H_2, CO_2, CO and $k_{OXI\text{-}l}$ is for CeO_2,Ce_2O_3 and the reaction coefficient (a_{OXI}) is given in Table 46.

Table 46. Oxidation reaction rate coefficient for water and carbon dioxide splitting.

j	Reaction coefficient (a_{OXI})	*l*	Reaction coefficient (a_{OXI})
H_2O	-1	CeO_2	2
H_2	1	Ce_2O_3	-1
CO_2	-1		
CO	1		

8.4 Effect of kinetics based chemical looping CO_2/H_2O splitting unit integrated to an oxy-fired power plant

The oxyfuel power plant integrated with the chemical looping CO_2/H_2O splitting unit was investigated and presented in detail and the process flow diagram can be seen in Figure 66.

The power plant layout comprises of air separation unit (ASU) that feeds pure O_2 to the combustion chamber that is supplied by natural gas making it an oxyfuel power plant, therefore, a part of CO_2 captured from the exhaust is recirculated back to the combustion chamber to reduce the elevated temperature due to oxy-combustion and maintain outlet gas temperature inlet turbine temperature (TIT). As ASU consume huge power which renders a 13% efficiency penalty. A part of the exhaust gas mixture (CO_2/H_2O) is sent to the oxidation reactor of the CL unit. The oxidation reaction would yield additional syngas fuel which is sent to the combustion chamber for additional power production which would also lower the incoming natural gas requirement. As the exhaust gases from the gas turbines are at high temperatures leading the gases to have a steam ranking cycle with a heat recovery steam generator (HSRG). As the plant is oxy-combustion based there would be minimal SO_x and NO_x, therefore, the exhaust gases can be cooled down to ambient temperature. Apart from two streams, one to oxidation reactor another to the combustion chamber for recirculation, remaining CO_2 is sent for storage after a compression of 110 bar.

Main equipment of the proposed layout is chemical looping (CO_2/H_2O) unit (CL). Natural gas is fed to the combustion chamber of the power plant at a supply pressure of 70 bars that comes from network and expanded to CL unit operating pressure which is near atmospheric. The expanded natural gas is supplied to the reduction reactor (RED) where it undergoes partial oxidation of methane (POM) producing syngas. The operating conditions were selected to avoid complete oxidation or methane cracking.

This reaction is endothermic and needs heat in order to maintain the continuous reaction. Ceria reduction by methane is reported to occur above 900ºC according to thermodynamics [254] studied we carried out and reported in chapter 4. Therefore, the RGIBBS reactor system of CL unit is replaced with moving bed reactors with reaction kinetics with the operating temperature at 1000ºC. Since a supplemental heat is required for reduction reactor an heat integration of combustion chamber of the power plant and reduction reactor is proposed with annular reactor design with inner reactor being reduction reactor of CL unit and annulus being combustion chamber providing excess heat [292]. More details of the system layout equipment operating conditions can be are reported in chapter 5.

Hence, with the integration of CL unit, which recycles and converts a part of the exhaust gases to fuel, a net system efficiency improvement is expected for the conventional oxy-fired natural gas combined cycle with carbon capture of 100%.

8.4.1 Results and discussion

To improve on the thermodynamic evaluations reported by Farooqui et al [254], the GIBBS reactors for the RED and OXI were replaced by moving bed reactors model, as developed in the previous section was integrated into the described OXY-CC-CL-K unit and the energetic performance of the proposed plant layout was evaluated. As for the oxidation reaction, since the primary component of the exhaust comprises over 86% CO_2, the available water splitting kinetics were used alongside the newly developed CO_2 splitting kinetics by in-house experiments described in the previous chapter 7. Based on the experimental results, an isothermal reduction reactor at 1000ºC was considered in the kinetic model. The heat integration and the annular combustion chamber concept was kept unchanged, whereby, the heat needed in the reduction reactor would be supplied from the heat generated in the combustion chamber. Additionally, the oxidation reactor was also considered a well-insulated adiabatic as opposed to a jacketed isothermal reactor at 1380ºC considered during the thermodynamic analysis.

To explain the comparative results of the overall plant performance, the need to understand separately, the efficiency of the CL unit as a separate entity and the efficiency of the entire layout is crucial. In this regard, the efficiency of the CL unit, calculated as per equation (8.16).

$$\eta_{SCL} = \frac{(\dot{m}_{H_2} LHV_{H_2} + \dot{m}_{CO} LHV_{CO})_{RED} + (\dot{m}_{H_2} LHV_{H_2} + \dot{m}_{CO} LHV_{CO})_{OXI}}{(\dot{m}_{CH_4} LHV_{CH_4} + (\dot{\mathrm{Q}}_{RED} - \dot{\mathrm{Q}}_{OXI}) + \dot{\mathrm{Q}}_{\mathrm{NG}}\ ) + (\dot{\mathrm{Q}}_{\mathrm{sphtr}} - \dot{\mathrm{Q}}_{\mathrm{sld}})} \tag{8.16}$$

$\dot{Q}_{NG}$ is the heat necessary for heating the natural gas from after the turbo-expander to the condition necessary for the inlet to the reduction reactor; $\dot{Q}_{RED}$ is the heat requirement at the reduction reactor. Since the OXI is an adiabatic reactor, therefore, $\dot{Q}_{OXI}$ accounts for the net heat needed for the system operations, including the heat needed for heating inlet CO_2 and/or H_2O also the exothermic heat from splitting reactions. $\dot{Q}_{sld}$ represents the heat recovered from the solids from the reduction reactor before it enters oxidation, while $\dot{Q}_{spht}$ is the heat delivered to the solids for preheating. Since the exhaust of the turbine is directly sent to the oxidation unit, no heat-up of the same is necessary. Like before, the heat needed for heating of the solids and the heat required for cooling of the solids was not considered since an isothermal reactor system between the RED and the OXI was considered. However, it was ensured that no temperature cross-over takes place.

The results of the comparative evaluation of the performance of the CL unit from the thermodynamic to the kinetic evaluation is shown in Table 47. As can be seen, all other parameters being constant, the net energy rate content in the syngas formation in both the reactors is much less for the kinetic-based layout. Indeed, for a lower non-stoichiometry, more specifically 0.29 obtained in the reduction reactor of 10 m^3 volume, results in the production of a lower volume of syngas in both the reduction and oxidation reactor (with 6 m^3), unlike in thermodynamics, where a complete reduction of CeO_2 to Ce_2O_3 was assumed with an equivalent non-stoichiometry of 0.5. However, a lower non-stoichiometry also ensures the heating load of the reduction reactor to diminish, as compared to the thermodynamics levels. Nevertheless, the overall efficiency of the CL unit drops from 64% for ideal conditions to 43% for the evaluated operating conditions using developed reaction kinetic models. Also, it should be noted that the outlet temperature of the oxidized metal from the OXI drops to 1350°C as opposed to 1380°C obtained in the thermodynamic evaluation, requiring an additional heat removal of 4 MW. Nevertheless, such a high temperature of metal oxide in the RED, even though will considerably decrease the heat requirement of the reaction, might result in carbon deposition to occur as seen through experimental evaluations. Therefore, a detailed design optimization from multiple design perspectives needs to be assessed in further detail, which is beyond the scope of the present study.

Table 47. Comparison between the layout with thermodynamic and kinetic evaluation of the CL unit.

Parameter	Units	OXY-CC-CL	OXY-CC-CL-K
The rate of Energy Content of Syngas from RED	MW	589.186	375.961
The rate of Energy Content of Syngas from OXI	MW	227.101	134.541
The rate of Net Energy in the Syngas Generated (H_2+CO)	MW	816.287	510.502
$Q_{RED\text{-}IN}$	MW	231.433	149.65
$Q_{OXY\text{-}OUT}$	MW	-4.44	0
Q_{NG}	MW	57.38	51.19
The rate of Energy Content in the Inlet Fuel (NG)	MW	989.667	989.667
η_{SCL}	--	64.07%	42.88%

However, unlike the efficiency of the CL unit, the plant efficiency depends not only on the net syngas generated in the CL unit but also on the total heat balance within the plant. Table 48 lists the comparison of the plant data for the thermodynamic assessment of the CL unit and the kinetic assessment of the same, all other parameters being kept constant. Since the combustion is a very highly exothermic and spontaneous reaction, no kinetic study is necessary to evaluate the reactions occurring in the combustion chamber, and no other chemical reactions occur in the entire plant.

The heat requirement in the reduction reactor decreases due to a lower reaction extent, resulting in a lower non-stoichiometry of the reduced ceria. In addition, based on the concept developed for the oxidation reactor for the solar reduction-based cycle, an excess of exhaust gas was sent to the reduction reactor increase the net power produced from syngas generation via splitting in the OXI. Additionally, being directly from the gas turbine outlet at a pressure of 2 bars, a high gas temperature of 921ºC at the inlet of the OXI was achieved. This results in the oxidized metal oxide temperature from the OXI to be at 1350ºC as opposed to 1380ºC for the thermodynamic layout.

Table 48. Plant Data Comparison of the layout based on thermodynamic (OXY-CC-CL) and kinetic evaluation of the CL unit (OXY-CC-CL-K).

Plant data	Units	OXY-CC-CL	OXY-CC-CL-K
Fuel Energy Input, LHV (A)	MW	990.708	990.708
Net GT Output	MW	484.233	523.488
ST Output	MW	255.937	251.003
Gross Electric Power Output (B)	MW	750.206	774.491
ASU Consumption + O_2 compression	MW	63.383	63.021
CO_2 Capture and Compression	MW	19.222	18.021
Power Cycle Pumps	MW	3.287	3.1
Air/ Recycled CO_2 Compression	MW	142.8797	153.61
Syngas Compressors	MW	17.1881	31.833
Total Parasitic Power Consumption (C)	MW	245.959	269.585
Net Electrical Power Output (D=B-C)	MW	504.247	504.906
Gross Electrical Efficiency (B/A*100)	MW	75.72%	78.18%
Net Electrical Efficiency (D/A*100)	%	50.70%	50.96%
CO_2 Capture Efficiency	%	100%	100%
CO_2 captured	t/h	178.658	178.658
Energy Output per tonne of CO_2 Captured	MWh/t	2.822	2.826

On the other hand, the gas outlet temperature from the OXI drops considerably. Due to a countercurrent reactor configuration, as well as from a lower reduction extent, the net exothermicity dropped considerably in the kinetic-based analysis than in the thermodynamic model based layout. Hence, the gas outlet temperature noted was 1120ºC, as opposed 1380ºC for the thermodynamic layout assessment. This lowers the heat availability within the system. However, the outlet temperature from the RED increases as well from 905ºC to 1000ºC from the thermodynamic to the kinetic model. Besides, the composition of the syngas produced being varying significantly between the two models; the heat transfer characteristics are different as well.

The heat requirement in the RED being significantly lower for the kinetic model (by 80 MW), while the TIT remains constant, the net CO_2 recycled for temperature control in the COMB increases. Thus, the power produced in the GT increases. However, this also increases, accordingly, the auxiliary power consumption in the CO_2 recycling compressor for COMB1. Nonetheless, both the energy production and consumption from auxiliary for the COMB2 cycle decreases due to a lower non-stoichiometry generated from reduction, as can be seen from the results in table 2. Furthermore, a lower temperature of the syngas from the OXI results in a lower steam generation in HRSG-2. Therefore, even though the gas expanded in GT1 and GT1-2 increases, the gas expanded in GT2 falls. The combined effect leads to a net drop in the power generated in the ST.

In summary, as can be followed from table 2, the net efficiency of the power plant is governed by the output from the GT, by far the single largest energy generating unit of the power plant. Even though the auxiliary consumption increases, the net efficiency of the power plant increases slightly for a lower non-stoichiometry resulting from integrating kinetics of methane reduction and corresponding oxidation of the reduced metal oxide by CO_2 and H_2O. Nevertheless, it needs to be highlighted that similar to the thermodynamic system, the kinetic layout is also a non-optimized one. Therefore, to develop a more even comparison between the maximum achievable efficiency by complete heat integration between the two layouts, a pinch analysis for the latter is required as well.

A clear comparison to the pinch analysis of the layout using the thermodynamic assessment and kinetic-based layout, as presented in Figure 118 can be drawn. Unlike the available 350 MW of high-temperature heat above 200°C for the thermodynamic layout, the system with the kinetics of the CL unit seems to be completely optimized without any heat available for further improvement of system performance. Therefore, the maximum achievable electrical efficiency is also limited to the present obtained value of 51%, as opposed to 62% achievable by system optimization of the thermodynamic layout. Nevertheless, even with kinetic limitations of the reduction and oxidation reactions, a reduction in the energy penalty, from 11.6 to only 3.8 percentage points is obtained, which would show the significant benefit of the proposed layout.

In fact, a net economic comparison with the thermodynamic layout was also performed, which are of interest due to the relative change in the sizes of the turbine and the compressors, resulting from a lower non-stoichiometry of ceria reduction. The total TOC of the plant was calculated as $1224 million, around $3 million lower than the corresponding CAPEX calculated using thermodynamic evaluation of the layout. This change is however insignificant with respect to the other operating costs of the power plant as reported by chapter 5 (Farooqui et al [254]).

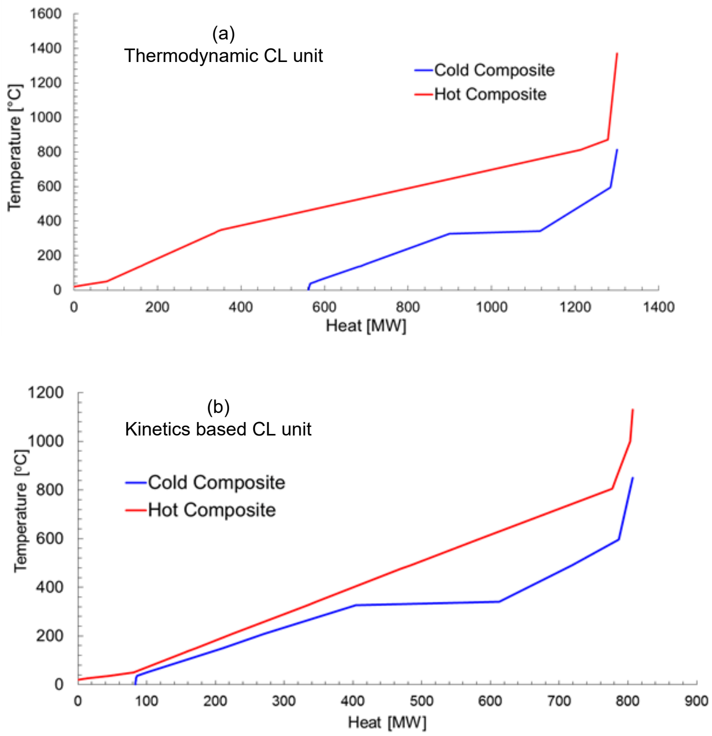

Figure 118. Pinch Analysis of the proposed plant based on (a) thermodynamics model OXY-CC-CL unit and (b) kinetics- based moving bed CL unit (OXY-CC-CL-K).

8.4.2 Concluding remarks

A moving bed reactors system has been developed by considering a number of RCSTRs in series in Aspen Plus to mimic the moving bed behavior of gas and solid in counter-flow direction with kinetics hooked using a user-kinetic subroutine. The developed CL unit has been integrated with an oxy-fueled power natural gas combined cycle power plant and the effect of kinetics on chemical looping unit performance and overall system layout performance has been evaluated. It was found that the CL unit efficiency (η_{SCL}) was reduced from 61% to 42.8% when the thermodynamic model was replaced by kinetic based moving bed CL unit. This decrease is attributed to a decrease in the reduction non-stoichiometry from 0.5 to 0.29. Similarly, the electrical efficiency of the whole plant was 51% with kinetics instead of 61% when thermodynamics is considered. A pinch point analysis has been also performed in order to investigate if the system is tightly integrated for heat balance. From the above analysis, it can be concluded that there is a significant effect of kinetics and the reactor system for chemical looping CO_2/H_2O dissociation integration to power plants. The above analysis is a significant step in retrofitting existing natural gas-fired power plants with the possibility of extending it to other fossil fuel power plants.

8.5 Effect of reaction kinetics of chemical looping CO_2/H_2O splitting unit integrated in a polygeneration plant

The kinetic-based moving bed reactors model for methane-driven chemical looping unit is extended to polygeneration plant described in chapter 6. The polygeneration plant layout shown in chapter 6 (Figure 6.2 and 6.3) considers the chemical looping CO_2/H_2O splitting that is driven by methane-reduction. The analysis carried out was based on RGIBBS reactors for reduction and oxidation. Since the methane reduction of ceria undergoes non-stoichiometric reaction the assumption of chemical equilibrium does not hold good. Therefore, as explained in the earlier section the CL unit based on RGIBBS reactors were replaced to moving bed reactor model for both reduction and oxidation. For the polygeneration plant, reactor sizing would be essential as to meet the need of composition of the H_2/CO ratio to feed the DME reactor.

8.5.1 Reactor sizing

The same approach described in chapter 3.1.3-5 for model description and convergence procedure has been adopted for the present study. A sensitivity analysis was performed to assess the influence of the reactor size and operating conditions on the performance of the reduction reactor. Figure 119 (a) shows the advancement of the reduction reaction (X_{RED}) varying the reactor volume from 1 to 40 m^3 is reported. As seen in chapter 7, the reduction kinetics is slower, hence big volumes are required in order to guarantee a sufficient residence time to the solid to achieve a high degree of reduction extent. However, it is important to underline, that, since the reduction reactor is set as isothermal, one of the most important parameters in the design phase is the volume. In fact, in order to keep the isothermal condition, it is really important to minimize it. Moreover, as previously described, with the integration of the CL unit in the polygeneration plant, the reduction reactor is an annular reactor with the reduction being done in annular section and combustion in the shell side [349]. Hence, it is important to make sure the volume of the reactor is optimum. For this reason, a solution is to work at higher temperatures (1000-1050°C). So that, the volume set for the rest of the analysis is 6 m^3 which allow achieving a reduction extent of 98% and 99.6% at 1000°C and 1050°C respectively. The choice of this values results in a trade-off between volume and advancement of the reaction. Even though it is possible to achieve a higher advancement of the reaction, the more the reaction moves towards the full conversion, the slower it becomes. Hence, at the higher advancement of the reaction, even to achieve a small increase in conversion (X_{RED}) a relatively high increment in volume is required.

Similarly to the reduction reactor, the first analysis performed to assess the effect of the oxidation reactor size. As illustrated in Figure 119, the solid conversion ranged from a minimum of 78.1% to a maximum of 99.5% with a pure stream of CO_2 and a pure stream of H_2O respectively. This is due to the fact that water dissociation results kinetically faster than carbon monoxide splitting, so that, by increasing the water content in the gas mixture, the degree of advancement of the oxidation reaction is enhanced. Based on the analysis, a volume equal to 6 m^3 was selected as optimal for the oxidation reactor, since this value resulted in a good compromise between size and solid conversion. In fact, with the selected volume it is possible to achieve a solid conversion of 94.1% with a pure CO_2 stream while, by increasing the water content, the conversion reaches 97.3% and 98.8% with an equimolar H_2O-CO_2 and a pure water stream respectively. The further increase in the size of the reactor till 20 m^3 would bring the solid conversion to a maximum of 96.4%, 99.1 and 99.5% with respectively a pure in CO_2, equimolar mixture and pure H_2O inlet gas. Hence it is considered not favorable to increase the reactor volume by a ratio higher than two to obtain a few percentage points in conversion.

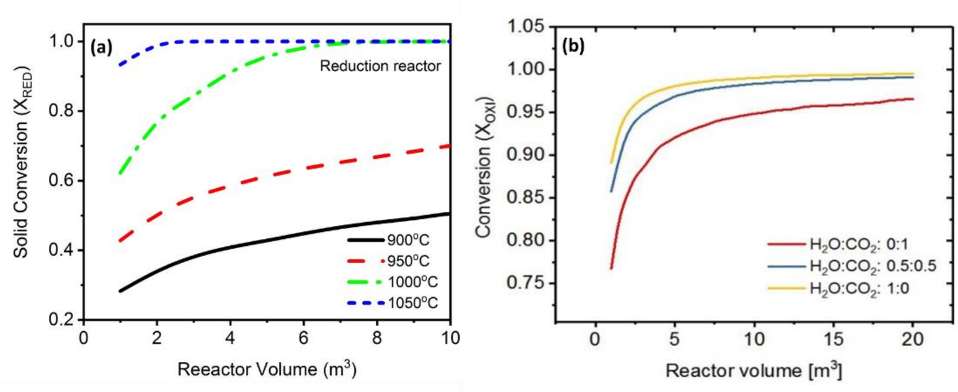

Figure 119. (a) Effect of the reactor volume on the degree of advancement of the reduction reaction (b) effect of the reactor volume on the degree of advancement of the oxidation reaction (X_{OXI}) with different gas mixture (with a 5% excess from the stoichiometric value) at the inlet of the reactor considering a gas temperature inlet of 500°C and a metal oxide inlet temperature of 800°C.

8.5.2 Performance results

A sensitivity analysis was performed to assess the performance of the layout integrated with the counterflow moving bed model for CL unit. The circulating flow of ceria used in chapter 6 was retained (588 mol/s of CeO_2 to reduction reactor (RED)). Moreover, since the main goal of this section is to assess the influence of the moving bed based CL unit integrated within the polygeneration plant, all the operation parameters outside of the CL unit used in chapter 6 are retained (gas inlet temperature, the pressure of the steam in the steam cycle, pressure inlet to the combustor). The effect of the inlet mixture on the H_2:CO ratio of the syngas from the OXI and subsequently its effect on the DME yield has already been discussed in chapter 6. However, the inlet composition mixture of H_2O and CO_2 to the OXI need to be re-evaluated based on the kinetic-based CL unit to obtain an H_2/CO ratio of 1.

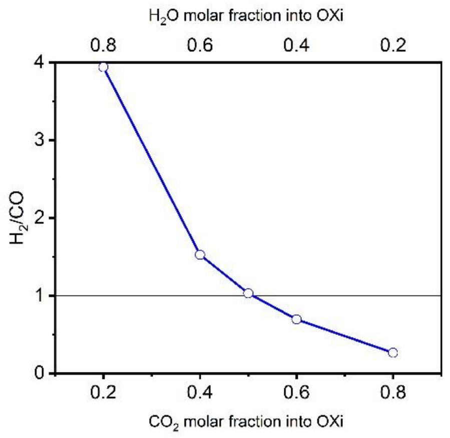

Figure 120. Effect of the gas mixture inlet composition into OXI (with an excess of 5%) on the H_2/CO ratio of the syngas outlet from OXI, considering a gas temperature inlet into OXI of 500°C and metal oxide inlet temperature of 800°C.

Figure 120 shows the effect of both the composition of the gas mixture into the OXI and the temperature of the metal oxide inlet on the H_2/CO ratio of the outlet syngas. As expected by increasing the CO_2 content the H_2/CO ratio decreases. It is observed that the H_2/CO ratio required for DME production is achieved by feeding gas mixture of 52%-48% CO_2-H_2O.

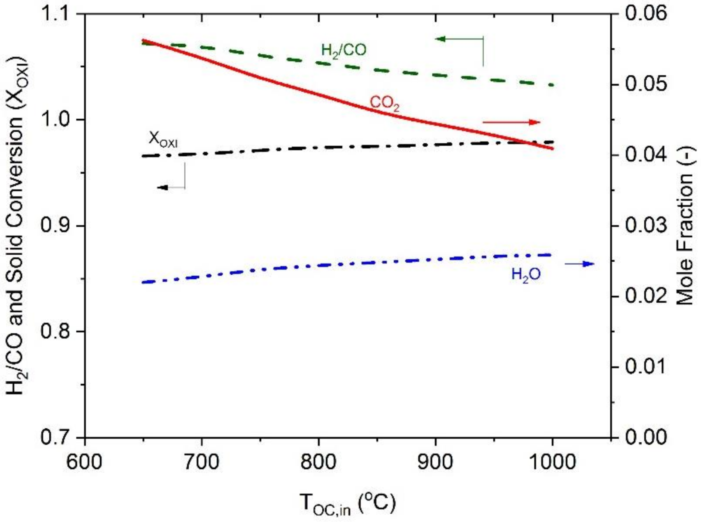

Figure 121. Effect of the inlet temperature of the metal oxide ($T_{OC,\,in}$) and with a mixture composition of H_2O and CO_2 with 5% excess on solid conversion (XOXI) in OXI, H_2/CO ratio and molar composition of CO_2 and H_2O at the outlet of OXI.

Figure 121 shows the effect of the metal oxide inlet temperatures on the degree of the advancement of the oxidation reaction and on the product composition. Differently from the results of the thermodynamics, due to the selected size of the reactor and there is a slowdown of the reaction towards the complete conversion, it is not possible to achieve a fully oxidized ceria due to non-stoichiometric nature and the kinetic dependence on the reaction. However, by increasing the temperatures, the conversion of the oxygen carrier is enhanced. This means that at higher temperature the water and carbon monoxide dissociation are kinetically faster. This results in the opposite of what found by the thermodynamics investigation. Nevertheless, as predicted by the thermodynamics, the H_2O dissociation results penalized with respect to the CO_2 dissociation with the increment of the metal oxide temperature inlet. In fact, as can be seen, the H_2/CO ratio ranges from 1.07 to 1.03 by increasing the temperature inlet of the oxygen carrier from 650°C to 1000°C. This trend is confirmed by molar compositions of H_2O and CO_2 where according to an increment in the metal oxide temperature the water content in the syngas outlet is increased, while at the same time, the CO_2 content is reduced.

The parameters that are varied for the system analysis are the following:

- The temperature of the reduction reactor from 900°C to 1050°C;
- Methane flow from 140 mol/s to 580 mol/s (which gives CH_4/CeO_2 ratio of nearly 0.25 to 1.0).

All the study was conducted fixing an inlet oxygen carrier temperature equal to 800°C and a gas inlet temperature of 500°C to the OXI. The pressure of the CL unit was fixed at 2 bar.

Figure 122(a)-(c) shows the effect of varying the methane flow and the isothermal temperature (T_{RED}) on the plant performance. As already discussed, at lower reduction temperature, the methane reduction kinetics is considerably slow, hence the advancement of the reduction is lower (Figure 122(a)). This results in a higher molar fraction of methane at the outlet of the reduction, hence for low temperature since the less methane is reduced in syngas, more power can be generated in the oxyfuel unit. This trend is confirmed by the 1000°C W_{NET} curve (Figure 122(b)), that starts to coincide with the 1050°C curve once the full reaction is achieved (with a CH_4 flow of 490 mol/s). Furthermore, it can be seen that since with 900°C and 950°C there is no complete conversion, but the net power results always higher as a mixture of unreacted methane and partly produced syngas is combusted but this effect on DME production.

With a lower reduction corresponding to a lower non-stoichiometry of ceria to the oxidation reactor, the syngas produced in oxidation reactor drops. This results in a subsequent drop in the DME production (Figure 122(c)). Being a polygeneration plant, this results in a lower effectiveness of the overall plant output and hence should be avoided as much as possible.

Combining all the individual effects, the overall trend in the efficiency of the power plant can be discussed henceforth. Elaborating, as can be seen from Figure 122(c), the recirculation fraction of CO_2 in the oxidation reactor drops with an increase in methane input to the plant. This indicates a lower recirculation fraction of CO_2, which in turn results in a decrease in the DME production with respect to the methane fed to the power plant. To simplify, with an increase in the methane flow, the plant tends more towards a simple oxy-fuel power plant, whereby the effectiveness of polygeneration decreases. Thus, with the increment of the methane flow, even if the power generation results higher, the relative drop in the DME production results in a drop in the efficiency.

In addition, the effect of the temperature of the reduction reactor on the overall efficiency of the power plant can also be obtained from Figure 122(c). For a lower temperature of the reduction reactor, the degree of advancement of the reduction reaction is decreased. Consequently, a lower non-stoichiometric ceria results, which leads to less syngas being produced and hence, a lower DME. This results in a lower overall efficiency as discussed before the effect of DME drop.

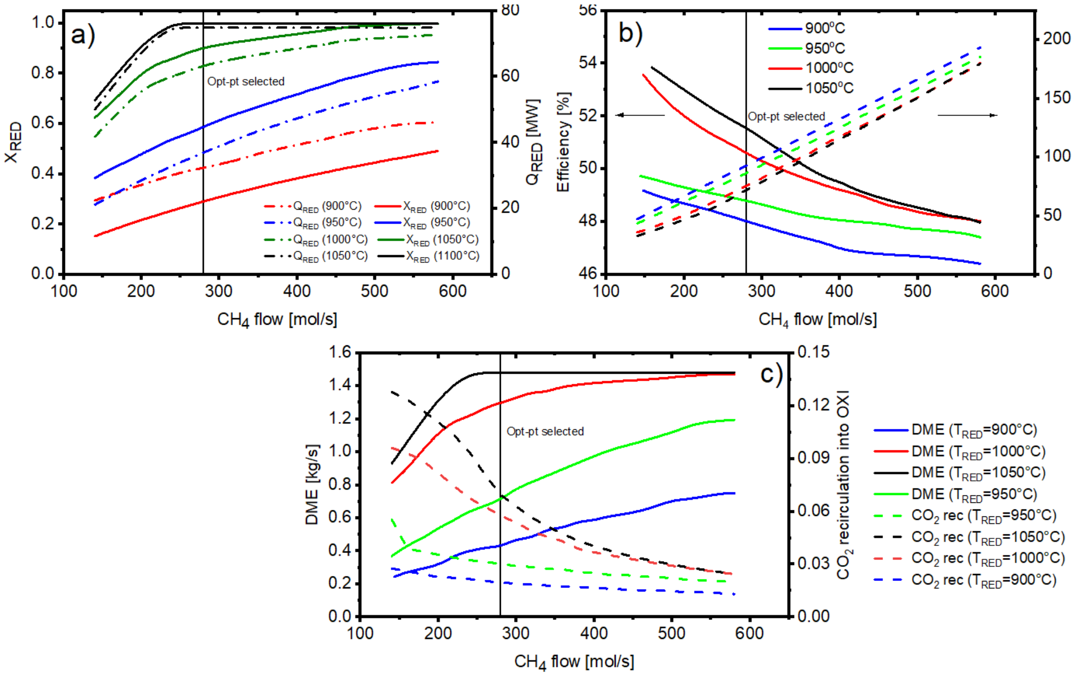

Figure 122. Effect of the operation condition T_{RED} and inlet methane flow on (a) advancement of the reduction reaction (X_{RED}) and hear needed Q_{RED}, (b) efficiency and total power produced W_{NET}, (c) DME production and CO_2 recirculation into OXI.

Considering the sensitivity analysis, the optimum point of operation (Opt-point selected) was set coincident to the reduction reactor temperature of 1050°C and a methane flow of 280 mol/s. With these parameters, the total efficiency results in 51.8% with a power production of 72.2 MW and 1.48 kg/s of DME. For the kinetic model based layout, it is also evident that due to less conversion of the ceria in the reduction reactor it leads to lower production of syngas in the oxidation reactor which in turns reduces the DME production by ~30% compared to thermodynamic study (which was ~2.15 kg/s). Similarly, the power production from the plant is ~30% less. As the basic assumptions for the two layouts are a bit different except the ceria flow by which it is wise to completely compare each parameter rather to just see how the kinetics and reactor selection could influence the overall system performance. Therefore, from the above results, it is found that for heterogeneous non-catalytic gas-solid chemical looping cycles thermodynamic results are overestimated and do not represent a clear picture and a detailed kinetic model inclusion and reactor selection is necessary with optimization. The complete optimization of the whole layout is out of the scope of the present thesis and will be considered in future studies. The present study reports an inclusive moving bed model for chemical looping syngas production which is well integrated for the DME production as well as power production with 100% capture. It is worth pointing that for the same capital investment which was reported in chapter 6 was estimated a price higher than the current market price. With the production of DME and power drops by almost 30% due to the effect of kinetics, the cost may increase by 30% which may hinder the application of CO_2/H_2O splitting for polygeneration plant based on an oxy-fired combined cycle.

Table 49. Results of the best point of operation of the polygeneration plant integrated with the moving bed CL unit (OXYF-CL-PFG-K) compared with the results of the layout with the thermodynamic CL unit (OXYF-CL-PFG).

Parameters	OXYF-CL-PFG-K	OXYF-CL-PFG.
Circulating ceria	588 mol/s	588 mol/s
Excess (CO_2/H_2O) in OXI	5%	60%
CH_4(NG)	16.17 ton/h	25.2 ton/h
W_{GROSS}	110.92 MW	167.61 MW
W_{NET}	72.17 MW	102.90 MW
η_{TOT}	51.80%	50.21%
W_{COMP-1}	2.41 MW	3.76 MW
W_{COMP-2}	6.18 MW	10.67 MW
W_{COMP-3}	15.61 MW	28.29 MW
W_{ASU}	13.89 MW	19.34 MW
W_{GT}	68.45 MW	114.42 MW
W_{ST1}	26.14 MW	44.30 MW
W_{ST2}	13.36 MW	2.96 MW
$W_{TURBEXP}$	2.96 MW	4.37 MW
$\dot{m}_{DME}$	1.48 kg/s	2.15 kg/s
$\dot{m}_{MeOH}$	0.01 kg/s	0.03 kg/s

8.5.3 Concluding remarks

The type of reactors plays a crucial role in the overall performance of the CL unit, which in turn, affects the entire plant to which it is integrated. It has been found that moving bed reactors would yield good conversion of gases and metal oxide in each reduction and oxidation reactor due to its ability to control the residence time within the reactor. Based on the model developed for a redox cycle, the performance of the CL unit has been assessed with a thermodynamic equilibrium model which was developed considered RGIBBS reactors. It has been found that the CL unit based on the kinetics (maximum δ can be achieved 0.35) has 20% less efficiency compared to CL unit based on the thermodynamic model (where the δ considered to be achieved 0.5). Based on the results it is concluded that kinetics has a strong effect on the CL unit performance. Subsequently, the CL unit with the thermodynamic model was replaced with moving bed interconnected model CL unit and overall system performance was re-evaluated. It has been found that the DME production drops from 2.15 to 1.48 Kg/s when kinetics has been considered for the CL unit. Even though the efficiency of the plant layout considering kinetic based CL unit is similar to that of thermodynamic model based CL, there is a drop in the capacity of power production from 103 to 71 MW. This will eventually lead to an increase in costs by approximately 30% which makes it economically challenging unless the earlier proposed modifications (in chapter 6) are not implemented.

Chapter 9

Epilogue: Conclusions and recommendations

9.1 Conclusions

Solar thermochemical redox cycles for syngas production is an attractive pathway foreseen to recycle the CO_2 and utilize it as a reactant for syngas production. Solar energy being readily available is a great source of energy for the reduction step making the process of fuel production a success. According to the initial assessment of solar fuel technology to be a viable process commercially, the solar to fuel efficiency must be at least 20% [147]. The majority of the work reported considered thermodynamic analysis to predict the efficiency of the solar to fuel production via splitting of carbon dioxide and water. It was important also to evaluate the relevance of parameters of the volume of the reactors and residence time of the particles, which in turn affect the recirculation rate of the oxygen carrier and gas feed compositions. Here we have studied temperature and vacuum pressures of reduction and temperatures of gas and oxygen carrier, which have not been considered in prior research for large-scale units. The analyses consider two options for maintaining a low oxygen partial pressure during reduction: using vacuum pressures or coupling methane-driven ceria reduction.

For each study, a detailed parametric study was carried out to investigate the effect of vacuum (and methane flow rate in case of methane reduction), reduction temperatures, composition and flow rate of CO_2/H_2O, non-stoichiometry of reduction extent, oxygen carrier conversion in oxidation step, gas and solid temperatures and the selectivity of products. The study included the efficiencies of the system under investigation considering redox cycling between the reactors. Apart from energy and exergy analysis of the system, an economic analysis was performed to evaluate the feasibility and economic viability of the system based on the capital investment and cost of the product obtained.

9.1.1 Solar thermochemical redox cycle using moving bed reactors considering kinetics

A moving bed reactor for reduction and oxidation reactors was developed in which thermal reduction and CO_2/H_2O splitting kinetics were hooked for syngas production.

The moving bed reactor was developed by considering series of continuous stirred reactors (CSTRs) and the kinetics were provided by extensive user-kinetic subroutine written in Fortran and hooked to Aspen plus. The chemical looping system with reduction and oxidation reactors considered is of industrial scale and more realistic compared to that used in the thermodynamic analysis reported in the literature. Firstly a sensitivity analysis of reduction reactor temperature and vacuum pressures were considered. Based on the literature data, a temperature range of 1200-1600°C and pressure of 10^{-3} to 10^{-7} bar was selected. Validation of the reaction kinetics was performed where the model and the experimental data were in close agreement. Based on the upper limit of ranges of temperature and pressures of reduction a sensitivity analysis of the oxidation reactor was performed to determine the selectivity of the products (CO and H_2). It was found that the oxidation reactor volume needed to achieve more than 90% conversion of non-stoichiometric ceria (OC) is 10 times that of a reduction reactor. It was found that the gas temperature has minimal effect on the selectivity or the solid (OC) conversion whereas the ceria inlet temperature has a linear dependence on solid conversion and selectivity of syngas production. A higher selectivity can be achieved by having a mixture of CO_2/H_2O rather than having separate splitting reactions.

The developed moving bed reactors for reduction and oxidation (CL) unit is integrated as an add-on unit to a 100 MW oxy-fired power plant with 100% carbon capture. A part of the exhaust of power plant which is CO_2 (86%) and H_2O (14%) is considered to be fed to CL unit. A huge sensitivity analysis was performed for the whole system for the parameters mentioned above along with the percentages of CO_2 and H_2O from the exhaust for higher efficiency and to avoid temperature cross-overs. It is found that 20% of CO_2 generated from the power plant can be fed to CL unit, which gives a maximum electricity production of 12.9 MW and lead to maximum solar to electricity efficiency of 25.4% operating at a reduction temperature of 1600°C and at a reduction reactor pressure of 10^{-7} bar.

The oxidation reactor was operated at 2 bar pressure. It is important to highlight that the dynamics of solar energy will affect the efficiency and the selectivity of the products, which is outside the scope of the present dissertation.

It is important to derive the efficiency of only the CL unit apart from solar to electricity efficiency to predict the bottleneck of the process. For doing so, three conditions were tested with only CO_2 feed, only H_2O feed, and a mixture of CO_2 (86%) and H_2O (14%). The results show a higher CL efficiency when pure CO_2 is used (35.4%) or a mixture of CO_2 and H_2O (35.2%) compared to using only H_2O (30.9%). The low efficiency for only H_2O is due to the heat needed for water vaporization. Lastly, an economic analysis showed that the major contributor to capital investment was due to the solar field and component associated with it, which represented about 36% of total equipment costs. The major cost of 19% of total plant cost was found to be the hydrogen compressor when operating with only H_2O or the mixture. Therefore, when operating only with pure CO_2 fed in the oxidation reactor the cost would decrease considerably, which also produces high CL efficiency. The specific overnight capital cost of 12136 $/kW is very high compared to the traditional solar based power plant (such as solar collector (26.1 km^2), CSP (5.3 km^2) or solar tower [379]), mainly due to the large field that would be needed to achieve a reduction temperature of 1600°C. The levelized cost of electricity was found to be 1100 $/MWh without considering the carbon tax incentives. As mention earlier the CAPEX would decrease tremendously if only CO_2 is fed in the oxidation reactor for splitting, which would benefit not only in investment but also the operating and maintenance costs. Apart from technological challenges of chemical looping CO_2/H_2O splitting unit such as achieving very high reduction temperature, vacuum pressure operation of reduction reactor, temperature and pressure swing between redox reactors, the economics also hinders the solar thermochemical dissociation even though the efficiency is comparable to other solar technologies. These challenges can only be tackled by exploring new solar technologies that allow achieving higher temperatures and to use new oxygen carrier materials (such as perovskites which show 8 times higher splitting reaction rates than ceria [137]).

One alternative solution suggested is to replace the thermal reduction by solar technology by fuel reduction. The benefit of that would give liberty to work at the same pressure for both reduction and oxidation reactors eliminating pressure swing. At the same time, the CL unit can work at isothermal temperature due to the lower temperature required for reduction compared to solar-based dissociation.

9.1.2 Methane driven chemical looping syngas production

In order to access the feasibility of methane-driven CL redox cycle, a thermodynamic analysis was performed initially to investigate the temperature and pressure range at which redox cycling can be performed. Also, the methane to ceria ratio and the excess amount required was investigated. The most suitable condition was obtained by using a methane to CeO_2 feeding ratio of 0.7 to 0.8 at a temperature of 900°C, resulting in a complete reduction of CeO_2 to Ce_2O_3 while avoiding the formation of CO_2 and carbon deposition. Results give motivations to investigate the viability of such process, in terms of technical and economic aspects, as an add-on unit to large-scale power plants or polygeneration plants with carbon capture.

Oxy-fuel combustion-based power plants are efficient, have lesser components and easy to retrofit among all the reported carbon capture technologies. They also capture 100% CO_2 as the feed to the combustor is only fuel and oxygen. Therefore, a chemical looping (CL) unit is added the oxy-fired power plant, where the part of the flue gases (CO_2 and H_2O) are fed to the CL unit's oxidation reactor and natural gas is fed to the reduction reactor for syngas production, which is supplied to a combustor of the power plant. It is was found that with carbon capture the power plant achieved nearly 51% energy efficiency and 47.4% exergetic efficiency. A comparative assessment of conventional natural gas combined cycle, oxy-fired power cycle and oxy-fired power cycle with CL unit were performed. The results showed the efficiency loss of conventional natural gas combined cycle due to carbon capture (which was 14%) was regained by 7.5% by adding a CL unit. Moreover, the captured CO_2 is recycled within the system to maintain the temperature of the combustor and to produce syngas. Economic analysis revealed a specific overnight capital cost of 2455$/ kW with a levelized cost of CO_2 saving of 96.25 $/ton of CO_2. The analysis predicted the levelized cost of electricity of 128.01 $/MWh without carbon credits and this would drop significantly to the present electricity prices with carbon credit of 6 $/ton of CO_2. The system analysis showed that there is more than 350 MW of heat available. With heat integration this could be used in applications such as for heat heating and the system efficiency can be improved to 61%, which is more than existing natural gas combined cycle. However, the water and the land requirement for the newly proposed oxy-fired power plant with carbon capture with add-on unit of CL unit would increase by 2.5 times.

The system analysis was extended to investigate the benefit of integrating the CL unit within a polygeneration plant. A novel natural gas feed polygeneration plant is proposed for production of power and dimethyl ether. The plant is designed to produce around 100 MW along with 2.15 kg/s of dimethyl ether. The energy efficiency of the plant was around 50% along with the exergetic efficiency of 44%. The exergy analysis showed that the main contributor of irreversibilities is the proposed combustor-reduction reactor (annulus type of reactor with the core being the reduction reactor and shell being the combustor to supply heat for reduction), which represents 51.2% of the total irreversibilities (221 MW). The total investment of the plant resulted in a huge capital of $534 million. A cash flow analysis predicted a selling price of electricity of $50/MWh and DME of $18/GJ ($577/ton), respectively, which are the current market price, to make a positive NPV at carbon tax of $40/tonne of CO_2. A similar price was obtained by Salkuyeh et al. [454] for polygeneration of DME, methanol and power generation. Even though the integrated unit allows to convert 3.4% of the CO_2 produced to DME with 85% of CO_2 recycling within the system, the capital cost is higher than other technologies if the carbon tax is not considered. But with an increase of scrutiny by implementing carbon tax based energy policies it is expected to reach $60/tonne of CO_2. With this, the cost of producing DME production by considering IGCC-based polygeneration plants is would be similar [455]. From the economic analysis, it was found that 23% of the equipment cost was contributed by ASU for producing oxygen for oxy-combustion. This price could be tremendously reduced by replacing the ASU with ion transport membrane reactor technologies, which at the moment can produce oxygen sufficient for a 100 MW plant. The ITM reactor unit would cost 31% less compared to ASU for the same amount of oxygen production, which in turn reduces the cost of DME and power production. It also benefits for an increase of 2-3% efficiency.

Fuel-driven chemical looping CO_2 and H_2O splitting unit was considered based on RGIBBS reactors in which the chemical equilibrium was considered with non-stoichiometry that can reach 0.5. But in principle, the ceria undergoes non-stoichiometric reduction with a maximum non-stoichiometry reported by different group varied from 0.2 to 0.37 based on the experimental setup and the conditions of the investigation. Therefore, fuel-reduction tubular reactor-based experiments were performed by varying the reduction and oxidation temperature and concentration of reducer (CH_4) and oxidizer (CO_2). It was found that the temperature at which methane reduction can perform is 1050ºC with an appreciable selectivity of the product and avoiding, at the same time, methane cracking and carbon deposition. A model fitting method was adopted to study the kinetics. Among four class of non-catalytic heterogeneous reaction models, 19 models were tested based on its fit and it was found that nucleation and grain growth-based Avrami Erofe'ev model with Avrami coefficient of 3 fits well for both reduction and oxidation. Based on that, the activation energy is found to be 283.65 ± 0.6 kJ/mol and 59.68 ± 6.0 kJ/mol for reduction and oxidation, respectively.

Based on the fuel-reduction, the kinetics of reduction and oxidation is derived. The power plant and polygeneration plant is reassessed by replacing the thermodynamic based CL unit with moving bed reactors for reduction and oxidation.

CL unit efficiency is evaluated considering thermodynamics-based CL model and kinetic-based moving bed CL-model, which was found to be 64% and 42.8% respectively. This shows a significant effect on the CL unit efficiency but overall efficiency of the plant was 50.9% being of 0.29 the non-stoichiometry achieved when kinetics is considered (which was 0.5 for thermodynamic based CL unit). The analysis is a significant step in proposing the addition of a CL unit to recycle CO_2 and converting it to fuel for energy efficiency improvement which can be extended to other fossil-based power plants.

The kinetic-based CL model is also replaced in the polygeneration plant to see the effect of it by keeping the oxygen carrier fixed in the system and to see the effect of non-stoichiometry of methane reduction and CO_2/H_2O splitting on power and DME production. It was found that the CL unit efficiency drops by nearly 20% when the kinetic-based moving bed reactors CL unit is replaced in the polygeneration plant. The drop in the reported CL efficiency affected the power production reduction from 103 to 71 MW and also there is a 30% drop in DME production (from 2.15 to 1.48 kg/s). This eventually led to an increase in costs by almost 30% making integration of CL unit less attractive for polygeneration plants unless higher carbon credits are considered.

9.2 Recommendations

Since there are different aspects of thermochemical cycles were considered in this thesis. In this section, different recommendations and key point guidelines are proposedly.

9.2.1 Reactor perspective

In the present thesis, it was assumed that reduction temperature was attained by CSP or solar tower making it an isothermal reduction reactor. In principle, solar technologies provide heat based on their geographical location, the season of the year and time of the day. Therefore, the available solar heat is varied throughout the day making the maximum temperature attainment possible for few hours only. In order to assess the actual efficiencies of the solar based CL unit, it is important to consider the dynamics of solar irradiance availability. The efficiency of such sub-section can be improved by investigating the solar receiver, optical system etc.

Most of the investigated literature is focused on structured reactors which have the oxygen carrier fixed, like a packed bed reactor, and operations of redox cycling are guided by automation, making it a non-continuous process and highly depended on the size of the reactor. The type of structured reactors is discussed in detail in chapter 2. Only one group from Japan investigated a fluidized bed reactor experimentally, though the numerical work from Sandia labs was presented on moving bed reactor models. Most of the study was focused on solar thermochemical cycles for producing hydrogen. It is highly recommended to investigate the viability of the thermochemical cycles in non-structured reactors as done in chemical looping combustion, gasification and reforming technologies by numerous groups [72,456]. The investigation of solar based CL unit with a reduction reactor and oxidation reactor in chapter 3 was considered hydrodynamic, assuming a homogenous mixture of gas and metal oxides. In the study, a uniform particle size distribution was considered with the assumption that there would be no sintering of the particles at high temperatures of operation, no attrition, and no agglomeration. It is known that the mechanical resilience of the oxygen carrier deteriorates with multiple cycles. Also, it is known the fluidizing behavior change at high temperatures, not only from the gases perspective but also from the metal oxides. In the study performed, the loop seals, valves and the oxygen carrier transportation from reduction to oxidation reactor were not considered.

Therefore, it is highly recommended to investigate the following from the reactor perspective:

-A small-scale pilot experimental set-up to demonstrate the moving bed reactor set-up with reduction, oxidation reactors, cycle separators, and loop seals for the feasibility under cold-run conditions to investigate the behavior of ceria in chemical looping conditions. These experiments also help in determining the hydrodynamic parameters such as mass transfer coefficients, wall effects, the attrition rate, agglomeration behavior and lifetime of the OC.

-Investigate the redox behavior by considering CO_2 and H_2O splitting separately to see the dynamics of each reaction in the oxidation reactor. This also gives the optimum operation range of temperatures and concentration to map the selectivity of the products.

-At high temperature, the gas-solid behavior changes, and it would be empirical to determine the hydrodynamic parameters which would help in scaling up the technology.

-Replicate the process for different fluidized bed reactors and the regime of operation to draw complete mapping of amount of bed mass, oxygen carrier recirculation rate between the reduction and oxidation reactor to successfully operate for the desired selectivity of the product. It is important to mention here, the reaction kinetics play an important role as the reaction kinetics are different for oxidation and reduction (thermal or fuel reduction) reactions.

-As a recommendation, the use of 3D techniques such as X-Ray tomography, Magnetic Resonance Imaging (MRI) or Electrical Capacitance Volume Tomography (ECVT) techniques apart from high-temperature optical technique (HT-PIV) would be proposed to investigate the hydrodynamic behavior of the reactors. Other techniques such as IR transmission technique may help in determining the hydrodynamic emulsion phase behavior. These techniques are using by some of the research groups in Sandia Laboratories, National Energy Technology Laboratories (NETL), SPI group at TU/e to name few.

It is highly recommended to consider the computational fluid dynamic studies, which consider the momentum exchange between particle-particle, particle-wall interactions, to not only design the reactor system efficiently but also from its implication on scaling-up.

9.2.2 Oxygen carrier selection

In this thesis, commercial ceria was selected for kinetic assessment as well as for system analysis. It is relatively cheap and readily available. However, ceria redox activity can be enhanced by doping different transition metals. Ceria doped with tin showed good characteristics for thermochemical redox cycles. Iron oxide is the cheapest among the oxygen carrier. A mechanical mixing of iron oxide with ceria or doped ceria could also be used for pilot scale investigations.

Other materials such as perovskites are reported in the literature to possess good splitting capabilities compare to ceria but their production at a large scale is a question. The main reason being the cost of production, which in turn hinders the usage at large scale.

Oxygen carriers undergo abrasion or fragmentation during particle-particle and particle-wall interaction. Therefore, it is essential to determine the attrition rate by developing models. With steam fed in water splitting experiments and methane reduction experiments, it would be essential to consider agglomeration rate of the particles. Though ceria is reported as agglomeration resistant it would be important to consider this point in future studies.

The reaction kinetics is the key parameter to determine the residence time of the particles in each reactor, therefore, investigation of reaction kinetics for each oxygen carrier is important to design the reactors based on the flow-regime of operation for the desired selectivity of the product. Since the chemical reactions decrease or increase the size of the particle based on the reaction mechanism, the volume of the species changes during the reaction also has an effect on the hydrodynamics. Packed bed microreactor experiments in conjunction with TGA would be sufficient to develop the kinetic model. The developed model would be required in computational studies in determining the feasibility of large-scale application. Lastly, to find the suitable metal oxide for a thermochemical fuel production application, a mapping of the materials need to be done based on environmental issues, economics and reactivity, and availability.

9.2.3 System analysis

As it has been discussed in different sections of the present thesis, the key limitations for further development of chemical looping CO_2/H_2O splitting for syngas production are the pressure and temperature swing between the reduction and oxidation reactors. Maintaining very low pressure is a key limiting factor for structured based solar thermochemical dissociation reactor as the pressure and temperature determine the reaction extent. The potential risk of mixing the gases in oxidation and reduction reactors is a major restriction in pressure swing chemical looping system. From the design perspective, care needs to be taken in designing loop seals as after each reactor there will be pressure buffer and particle storage systems. In the present thesis, the system analysis was focused on the oxy-fuel combined cycle and polygeneration producing power and DME, but the concept can be extended to other power cycles using solid and liquid fuels. The polygeneration plant can be extended to kerosene, jet fuel, and methanol production.

This thesis has introduced the first stage development of a novel moving bed reactor-based chemical looping CO_2/H_2O splitting technology able to produce a syngas of desirable composition. The proposed integration of the CL unit as an add-on to power plant allows to recycle and utilize CO_2 to produce fuel. The development of such a system and its installation in power and hydrocarbon production plants would benefit both the local people and governments as it limits the CO_2 emission by utilization it for fuel production. This in turns helps in the reduction of global warming. Since the flue gases are used as a reactant for fuel synthesis there are economic benefits. In this thesis, natural gas is used as fuel for a methane-driven reduction CL unit. However, the system is flexible to use biomethane which would imply the production of syngas from renewable sources. In this way, the capture of carbon dioxide leads to negative carbon emissions.

Appendices

A.1 Assessment of moving and fluidized bed reactor for solar thermochemical redox cycle

It is observed that the reaction kinetics of CO_2 and H_2O splitting is highly depended on the temperature and residence time of the particles in the reactor. This means that the flow regime at which the reactor operates decides the product selectivity. The higher residence time of the particles in the reactor leads to higher selectivity, but there are issues of oxygen carrier abrasion and fragmentation due to particle-particle and particle-wall interaction at different velocities. Therefore, it is a trade-off between selectivity and oxygen carrier lifetime in practical understanding. Therefore, an assessment is necessary to determine the fluidization regime and the type of reactor for chemical looping CO_2/.H_2O splitting for an industrial scale.

From the literature presented in chapter 2, it can be concluded that much of the research focuses on the structured reactor and only the research group led by Gokon et al [1,2] (Niigata University, Japan) has conducted experiments on solar-based fluidized bed reactors for reduction and CO_2 and water splitting [3,4].

Therefore, an assessment of the type of reactor or regime considered in a moving bed reactor and a fluidized bed reactor operating at different flow regime from bubbling bed to transport zone is investigated. For fluidized bed reactor, an inert gas would be required as fluidizing gas or sweep gas and to also carry away the oxygen released to maintain very low partial pressures of oxygen during reduction. This would need a very high volume of sweep gas of the order of 10^5 times [202], making it very energy intensive. Therefore, a thermal reduction moving bed reactor is selected and the reduced metal oxide is divided into four streams for four fluidized bed reactors. A similar concept is proposed by Muhich et al [146]. For doing so, a fluidized bed reactor model is developed in Aspen plus.

A.1.1 Fluidized bed model

The model developed deals with four fluidized bed reactors operated in different fluidization mode interconnected with metal oxide circulating between with a reduction reactor. Each fluidized bed model developed considers two different zones: the bottom zone, also called as Dense Phase (DP), characterized by high solid volume concentrations, and the upper dilute zone or Freeboard (FB) in which the solid volume concentration decreases with increasing height. The bottom zone is modelled as a bubbling bed according to Werther & Wein [457] and the upper dilute zone follows the approach according to Kunnii & Levenspiel [458]. The void space within the bed can be characterized as having two distinct phases: the bubble and the emulsion. These fluid dynamic models were used with other correlations to describe the distribution of solids along the fluid bed, and for entrainment considerations.

Hydrodynamics

There are a couple of phenomena occurring in the dense phase of the reactor that describes the hydrodynamics in this phase. Arguably the most important set of parameters describing how the bed operates is the minimum fluidization properties—velocity (u_{mf}) and voidage (ε_{mf}). These two properties of the fluidized bed, or more rather particles within it, are used during the whole process of modelling to calculate everything from actual bed voidage (ε_{mf}) to bubble rise velocity (u_b). The parameters have been calculated based on the equations presented by [210] in **Error! Reference source not found.**.

Table 50. Hydrodynamics parameters used in the fluidized bed model.

Reynolds number of the particle	$\mathrm{Re}_p = \sqrt{33.7^2 + 0.04084 Ar_p} - 33.7$
Reynolds number and Archimedes number for minimum fluidization velocity	$\mathrm{Re}_p = \dfrac{u_{mf} \cdot \rho \cdot d_p}{\mu_g}$; $Ar_p = \dfrac{d_p^3 \cdot \rho_g \cdot (\rho_s - \rho_g) \cdot g}{\mu_g^2}$
Maximum bubble volume before it detaches orifice surface as	$V_{bo} = 1.138 \dfrac{v_{or}^{1.2}}{g^{0.6}}$
Initial bubble diameter	$d_{bo} = \dfrac{1.3}{g^{0.2}} \left(\dfrac{u_o - u_{mf}}{N_{or}} \right)^{0.4}$;N_{or} is the number of orifices.
Maximum bubble diameter	$d_b(h) = d_{bm} - (d_{bm} - d_{b0}) \exp\left(-0.3 \dfrac{h}{d_t} \right)$ where $d_{bm} = 0.649\left(A_t \left(u_o - u_{mf} \right) \right)^2$
Bubble absolute rise velocity: general form	$u_b = u_0 - u_{mf} + u_{br}$
bubble rise velocity	$u_{br} = 0.711\sqrt{g d_b}$
absolute bubble rise velocity	$u_b = 1.55 \cdot \left\{ (u_0 - u_{mf}) + 14.1 \cdot (d_b + 0.005) \right\} d_t^{0.32} + u_{br}$
overall voidage of the bed	$\varepsilon_f = \delta^* + (1-\delta)\varepsilon_e$
Solids volume fraction	$\varepsilon_s = 1 - \varepsilon_f$
bubble volume fraction	$\delta^* = \dfrac{u_0 - u_{mf}}{u_b + 2 \cdot u_{mf}}$

Emulsion velocity	$u_e = \dfrac{u_{mf}}{\varepsilon_{mf}}$
Emulsion voidage ε_e	$\left(\dfrac{\varepsilon_e}{\varepsilon_{mf}}\right)^3 \left(\dfrac{1-\varepsilon_{mf}}{1-\varepsilon_e}\right) = \left(\dfrac{u_e}{u_{mf}}\right)^{0.7}$

For small particle size with the momentum that is obtained from bubble coalescence or eruption will be entrained out from the fluidized bed to the freeboard. There are two mechanisms for the particles in a dense bed to freeboard or entrainment [459]. The first one is the eruption of bubbles on the surface of the bed. Particles are entrained into freeboard from the bubble roof or the from the bubble wake with a certain momentum caused by bubble burst. This is due to the different size of particles in the bed and the varying gas velocities. The second mechanism is particle entrainment, for coarse particles and due to the high velocity of superficial gas velocity.

One of the important factors in particle entrainment estimation is the transport disengaging height (TDH) [460–462]. As the reactor of the fluidized bed is divided into two vertical zones in general dense zone and freeboard zone. With the increase of gas velocity, the surface of the fluidized bed gets to loosen up and particles start to project in the freeboard termed as elutriation. Particles having a higher velocity than the terminal velocity gets entrained out. The solid holdup decays along the height from the surface of the fluidized bed i.e. dense zone and becomes constant. The height from the bed surface to the point from where the solid entrainment is constant is called Transport Disengaging Height (TDH). TDH is an important parameter in designing the freeboard height of the reactor. If the system is for gas-solid reactions then the solid particles should not entrain as much as possible, therefore, the height of the reactor should be more than TDH. Many researchers have reported semi-empirical correlations based on a set of experiments by considering a different group of particles for different operating conditions and it reported in Table 51. Of all the reported model George and Grace's model reported to be work for all the Geldart type of particles with higher accuracy [461] as it does not depend on the geometry of the reactor, therefore it is selected for our present investigation.

Table 51. TDH correlations [463–467].

Year	Authors	Correlations	Geldart grp	Particle tested	ρ_s(kg/m^3)	d_{pi}(μm)	u_g(m/s)	D_c(m)
1973	Fournol et al.	$\text{TDH}=1000u_o^2/g$	A	FCC catalyst	830	58	$0.11-0.22$	0.61
1978	George and Grace	$\text{TDH}=18.2d_{bi}$	A, B, D	Coke, FCC catalyst, sand	1900, 2640	$20-500$	$0.4-9.3$	0.108, 0.457
1984	Chan and Knowlton	$\text{TDH}=0.85u_o^{1.2}(7.33-1.2\log u_o)$	A, B	Sand	2595	$37-420$	–	0.3
1991	Sciazko et al	$\text{TDH}=(1500\text{H}_c\,\text{Re}_{pi}/Ar_i)$	A, B, D	Char	1250	$80-2000$	$0.51-1.23$	0.3
1993	Fung and Hamdullapur	$\text{TDH}=(-3d_{bi}\cdot\ln 0.01)$	B	Sand	–	$200-427$	$0.27-0.54$	0.145

The entrainment of particles is mainly affected by the geometry of the vessel (diameter of the bed, the diameter of freeboard, the height of the freeboard), conditions (temperature, pressure), and characteristics of the particles (PSD). It is reported that for Geldart group 'A' particles, as the size of the particles falls below the critical value, for solid entrainment above TDH decreases as the particle size gets increased due to agglomeration. It is because of the high cohesive forces between particles when compared to the gravitational force. Particle entrainment is expressed as the total entrainment flux E_h (kg/m^{2}s) at a height h above distributor. It can also be determined by elutriation rate K_{ih}^* and the relation between entrainment flux and elutriation constant is given below [468].

$$K_{ih}^* = \frac{E_{ih}(t)}{x_i(t)} = \frac{\frac{1}{A_{CS}} \frac{d[x_i(t)m_s]}{dt}}{x_i(t)} \tag{A.1.1}$$

Where A_{cs} is the bed cross-section area in square meter, x_i is weight fraction of fine particles with size d_{pi}; $E_{ih}(t)$ is the entrainment flux of particles with diameter d_{pi} at time t and height h. Therefore, total entrainment flux for all particles sized at height is given as;

$$E_h(t) = \sum_i E_{ih}(t) \tag{A.1.2}$$

The entrainment rate of solids in the freeboard zone is determined by using equation;

$$F = F_\infty + (F_o - F_\infty)\exp(-ah) \tag{A.1.3}$$

Where F is the rate of entrainment in the freeboard zone about height h. F_∞ is the rate of entrainment above TDH, F_o is the rate of entrainment at the bed surface and a is a decay constant and varied between 2 to 12. There are many correlations reported in the literature for entrainment rates but they are mostly determined on certain operating conditions for a set of particles. Therefore, they are either unreliable to calculate the entrainment in the freeboard zone. Wen and Chen [469] correlation have gained a lot of reputation to give good results in determining entrainment rates in the freeboard zone.

$$E_{i\infty} = \frac{1}{A_{CS}} \frac{d[x_i(t)m_s]}{dt} \tag{A.1.4}$$

$$E_{i\infty} = \rho_p(1-\varepsilon_f)(u_o - u_t) \tag{A.1.5}$$

$$\varepsilon_f = \left[1 + \frac{\lambda(u_o - u_t)^2}{2gD_c}\right]^{-1/4.7} \tag{A.1.6}$$

$E_{i\infty}$ is the entrainment flux for particle diameter d_{pi}, m_s is the total mass of solids in bed, $u_{st} = (u_o - u_t)$ is the particle velocity, D_c is the diameter of bed, λ is the frictional coefficient due to particle collisions with each other and with the walls. It can be evaluated with the following conditions [470].

$$\frac{\lambda\rho_p}{d_p^2}\cdot\left[\frac{\mu}{\rho_g}\right]^{2.5} = \begin{cases} 5.17\,\mathrm{Re}_p^{-1.5}\,D_c^2 \text{ for } \mathrm{Re}_p \le \mathrm{Re}_{pc} \\ 13.2\,\mathrm{Re}_p^{-2.5}\,D_c \text{ for } \mathrm{Re}_p \ge \mathrm{Re}_{pc} \end{cases} \tag{A.1.7}$$

$$\mathrm{Re}_{pc} = 2.38 / D_c \tag{A.1.8}$$

$$\mathrm{Re}_p = \rho_g(u_o - u_g)d_p / \mu \tag{A.1.9}$$

Elutriation rate is determined by semi-empirical correlation and the majority of modeling work is based on the following reported correlations as shown in Table 52. Therefore, Aspen plus has incorporated these correlations as user-defined options. Based on the accuracy of the models, Tasirin and Geldart [471] correlation have been selected for our study.

Table 52. Elutriation correlations [466,470–474].

Year	Authors	Correlations	Geldart grp	$H_c(H_s)$(m)	ρ_s(kg/m^3)	d_{pi}(μm) (%wt of fines)	u_g(m/s)	D_c(m)
1958	Zenz and Weil	$K_{i\infty} = 1.26\times10^7 \rho_g u_g \left(\frac{u_g^2}{g d_{pi} \rho_s^2}\right)^{1.88}$ for $\frac{u_g^2}{g d_{pi} \rho_s^2} < 3\times10^{-4}$ $K_{i\infty} = 4.31\times10^4 \rho_g u_g \left(\frac{u_g^2}{g d_{pi} \rho_s^2}\right)^{1.88}$ for $\frac{u_g^2}{g d_{pi} \rho_s^2} > 3\times10^{-4}$	A; multiple species	4.3	–	$10-150$	$0.3-0.72$ (P=7.8 atm)	$2D$; 0.051×0.61
1979	Geldart et al	$K_{i\infty} = 23.7 \rho_g u_g \exp\left(-\frac{5.4 u_{ti}}{u_g}\right)$	A, B; multiple species	3.8 (0.35-0.45)	$706-5000$	$62-219$ $(5-75)$	$0.6-3.0$	0.076
1984	Colakyan and Levenspie	$K_{i\infty} = 0.011 \rho_s \left(1 - \frac{u_{ti}}{u_g}\right)^2$ for $u_{ti} < u_g$	A, B; single species	7.5	$920-5900$	$36-100$ (<10)	$0.901-3.66$	square bed; (0.3×0.3) (0.92×0.92); (0.1×0.1)
1991	Sciazko et al	$K_{i\infty} = 1.6 \rho_g \frac{u_g^2}{u_{ti}} \left(1 - \frac{u_{ti}}{u_g}\right)$	A, B; single species	–	1250	$80-2000$	$0.51-1.23$	0.3
1998	Tasirin and Geldart	$K_{i\infty} = 23.7 \rho_g u_g^{2.5} \exp\left(-\frac{5.4 u_{ti}}{u_g}\right)$ for $\mathrm{Re}_D < 3000$ $K_{i\infty} = 14.5 \rho_g u_g^{2.5} \exp\left(-\frac{5.4 u_{ti}}{u_g}\right)$ for $\mathrm{Re}_D > 3000$	A, B; single species	2.4	$1180-1350$	$30-2000$	$0.1-0.8$	0.15

For determination of the pressure, temperature, and composition of the gas phase, first, all inlet streams (including the streams from the secondary gas supply) are mixed. Then an isobaric, isenthalpic phase equilibrium calculation is performed. From this calculation, the pressure, temperature, and composition of the gas phase are obtained. In addition, the thermodynamic model of the fluidized bed of Aspen plus allow specifying either the temperature or the heat duty. For the reduction reactor we specify the temperature, therefore, an isothermal, isobaric phase equilibrium calculation is performed in order to determine the new composition of the gas phase. If the heat duty (ΔH) is specified as in the case of the oxidation reactor, the enthalpy of the material within the fluidized bed (H_{riser}) is calculated as shown below.

$$\mathrm{Hriser} = H_{in} + \Delta H \qquad (A.1.10)$$

H_{in} is the enthalpy of the mixed inlet streams. Based on the calculated enthalpy an isobaric, isenthalpic phase equilibrium calculation is performed in order to determine the temperature and composition of the vapor phase. More details of the model can be obtained in Aspen plus manual [475,476].

Reaction kinetics that is used in reduction and oxidation reactors are described in chapter 3 and are written in Fortran separately as user-subroutine and hooked in Aspen plus and the of exchange of parameters between Fortran and Aspen plus is also provided [477]. The model allows considering chemical reactions with the assumption that gas in plug flow and solids are ideally mixed. Both dense zone and freeboard are divided number of cells which are considered as CSTRs. For our study, 100 cells for the discretization of the bottom zone and the freeboard. The model also considers the impact of volume production or reduction on the hydrodynamics in the fluidized bed reactor. Minimum fluidization velocity is calculated based on Wen and Yu [478] model stated in Table 50.

Validation

Overall hydrodynamics model has been tested against experimental data provided by Hamzehei et al [479,480]. The experimental results were obtained on Pyrex cylindrical fluidized bed as shown in Figure 123. Neither specific distributor configuration nor pressure drop was reported, thus their values have had to be assumed in the simulation. Validation has been done for the bed filled with spherical glass beads of the density of 1830 kg/m^3. The average particle diameter was 300 μm. Experimental set–up bed dimensions were the diameter of 25 cm and 1 m of height, therefore the same dimensions were selected in fluidized bed model with a distributor pressure drop of $0.3\Delta p_b$ was assumed. Inlet gas pressure was calculated to be higher than atmospheric by this value; in this situation, the dense phase inlet pressure is equal to atmospheric. The mass holdup was calculated based on the data provided by Hamzehei et al. [479]—static bed height of 0.4m and static solids volume fraction of 0.6. Based on the data and on the reactor dimensions solids holdup is calculated as approximately 21.5 kg. Model agreement with the experimental data was checked for different inlet superficial gas velocities from 0.1 to 0.8 m/s. Three parameters have been compared between the simulation and the experimental data. In the experiment bed, pressure drop increased from 4.5 to 5.75 kPa as the superficial velocity increased, in the model this parameter is constant and equal to 4.0 kPa. The result is slightly underestimated mainly due to the difference in bed particle size distribution and difficulty in predicting actual mass holdup in the bed. This is also attributed due to the assumption of a number of orifices calculated based on 80% cross-section area that covers the cumulative orifice area.

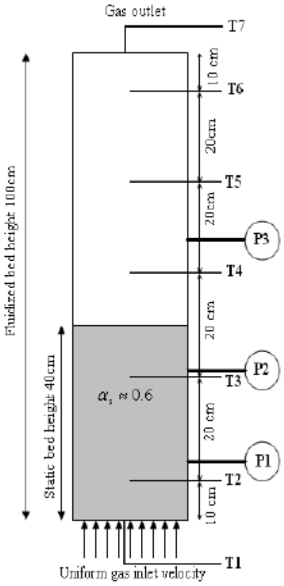

Figure 123. Experimental setup used by Hamzehei et al [479].

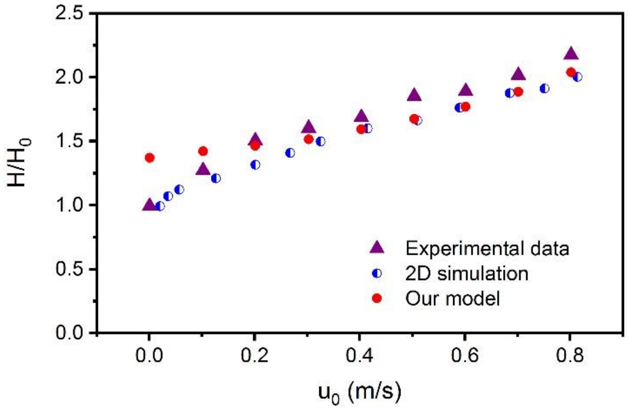

Figure 124. Comparison of the bed expansion coefficients obtained from the simulation and experiment data [479].

From Figure 124, it is shown that hydrodynamic bed model follows the behavior closely. It is noted that for slow fluidizing beds in the area of minimum fluidization and minimum bubbling conditions model predictions are overestimated—relative error of approximately 10%. In the slugging, fast fluidizing regimes and bubbling beds projection of entrainment rate from the dense phase surface fits experimental data with overestimating by a relative error of approximately 2.4%. Hamzehei et al. [480] also reported the computational fluid dynamic model simulation results considering a 2D model of the geometry. The model was based on the Eulerian-Eulerian approach considering the kinetic theory of granular flow. Reported 2D simulation and our model results are in close agreement also.

A.1.2 Assessment and analysis of the reactors

As stated earlier the reduction reactor is fixed as moving bed reactor as described in chapter 3 and oxidation reactors consist of four fluidized bed reactors as shown in Figure 125.

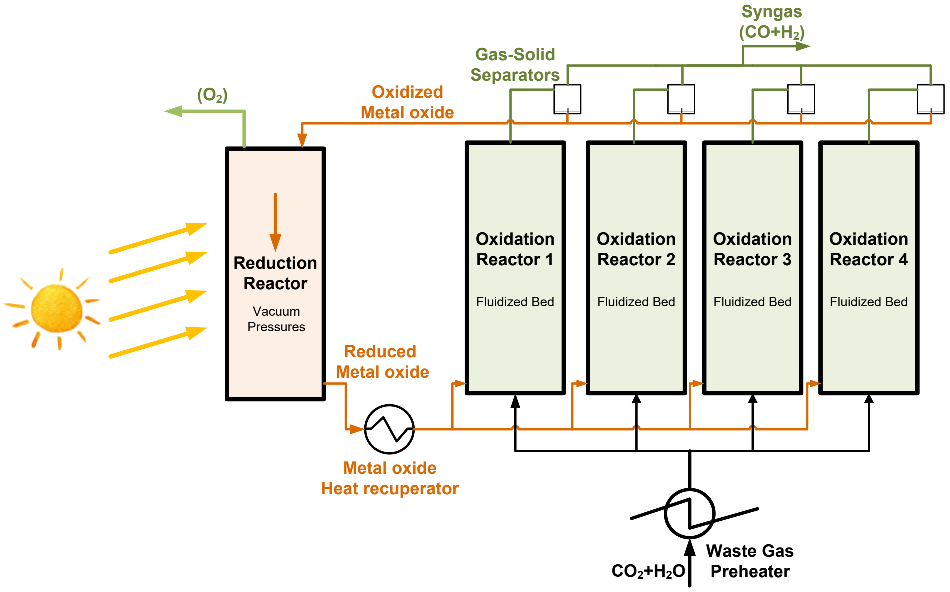

Figure 125. Solar thermochemical redox cycle considering moving bed reduction reactor and fluidized bed oxidation reactors.

For a condition of solar thermochemical reduction temperature of 1500°C with 10^{-7} bar pressure, the non-stoichiometry yielded 0.14. Based on that the volume of the reduction reactor was derived to be 0.4 m^3. A similar procedure is adapted to determine the volume of the moving bed model as described in chapter 3 for an oxidation reactor. For oxidation reactor, the inlet gas and metal oxide temperature are selected as 800°C. Other inlet conditions to the OXI are listed in Table 53.

Table 53. Inlet conditions to the oxidation reactor.

Inlet conditions to OXI	units	value
Ceria flow	kg/h	32942
Non-stoichiometry (δ_{RED})		0.14
Metal oxide temperature	°C	800
Density	kg/m^3	6570.4
Gas temp	°C	800
Gas flow	m^3/h	1666.478
Minimum Fl. Velocity (u_{mf})	m/s	0.004006241

It was found that the reactor volume increases to achieve higher oxygen carrier conversion for moving bed oxidation reactor (Figure 126) for a 5 m^3 reactor volume for three gas composition from CO_2:H_2O from 0 to 100%. For instance, for only CO_2 the solid conversion is minimum at 55% with 71.2% for equimolar CO_2 and H_2O mixture and 80.5% for the only H_2O gas inlet to the OXI. For the higher volume of 8 m^3, the solid conversion is just 85% for only H_2O. The relative increase is just 6% for increase nearly 40% higher volume. Therefore, it is a trade-off between the solid conversion and volume of the reactor. For analysis considering moving bed oxidation reactor volume selected for further study of 5 m^3.

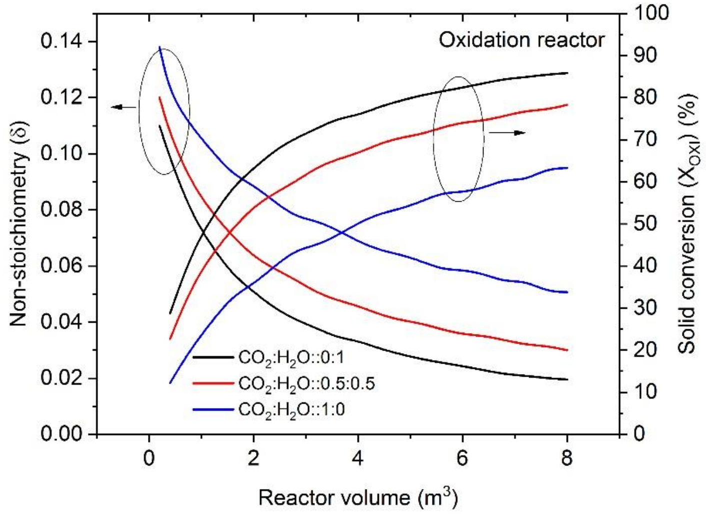

Figure 126. Oxidation reactor volume estimation for moving bed reactor model.

In order to obtain the higher selectivity of the product (S_{CO} and S_{H2}), the ceria flow is divided into four fluidized bed reactor. In order to obtain the geometric conditions of the fluidized bed reactor, four fluidizing regimes were selected based on u_0/u_{mf}. The condition to determine the minimum fluidization velocity and hydrodynamic parameters are presented in Table 50. The condition is determined for three gas compositions from only H_2O, an equimolar mixture of CO_2 and H_2O and only CO_2 as listed in Table 54. Bubble cap gas distributor is selected for the analysis with the assumption that it distributor covers the 80% of the cross-section area of the reactor.

Based on the known gas flow rate and the superficial gas velocity based on the fluidized regime selected, the diameter of the reactor is evaluated.

$$D_c = \sqrt{4A_{CS}/(0.8\cdot\pi)} \tag{A.1.11}$$

Bed mass of the reactor is calculated as considering 10% of the total volume of the reactor and is given as;

$$m_{bed} = 0.1\cdot A_{CS}\cdot L\cdot(1-\varepsilon_{mf})\cdot(\rho_s-\rho_g) \tag{A.1.12}$$

A_{CS} is the cross-section of the bed, L is the length of the reactor, ε_{mf} is the solid void fraction at minimum fluidization condition. The number of orifices for bubble caps required is calculated as equation (A.1.13) with an orifice diameter of d_o=48 mm.

$$N_o = \frac{\text{Cap area (distributor area)}}{\pi d_o^2/4} \tag{A.1.13}$$

Table 54. Parameter determination for fluidized bed for oxidation reactor.

Fluidized bed regimes		Only H_2O	Only CO_2	CO_2:H_2O::0.5:0.5
Velocity Calculation	u_0/u_{mf}	u_0	u_0	u_0
Bubbling bed (BB)	100	0.401	0.362	0.363
Slugging (SFB)	500	2.003	1.808	1.816
Fast fluidizing (FF)	1000	4.006	3.617	3.633
Transport (TR)	5000	20.031	18.083	18.163
Cap Area Calculation (80% of CS Area)	u_0/u_{mf}	m^2	m^2	m^2
Bubbling bed (BB)	100	1.155	3.194	3.224
Slugging (SFB)	500	0.231	0.639	0.645
Fast fluidizing (FF)	1000	0.116	0.319	0.322
Transport (TR)	5000	0.023	0.064	0.064
Diameter Calculation (D_c)	u_0/u_{mf}	D_c (m)	D_c (m)	D_c (m)
Bubbling bed (BB)	100	1.356	2.255	2.266
Slugging (SFB)	500	0.607	1.009	1.013
Fast fluidizing (FF)	1000	0.429	0.713	0.717
Transport (TR)	5000	0.192	0.319	0.320
Length Calculation (L/D_c=3; fixed)	u_0/u_{mf}	L (m)	L (m)	L (m)
Bubbling bed (BB)	100	4.069	6.766	6.798
Slugging (SFB)	500	1.820	3.026	3.040
Fast fluidizing (FF)	1000	1.287	2.140	2.150
Transport (TR)	5000	0.575	0.957	0.961
Bed Mass (m_{bed}) Calculation (10% of RV)	u_0/u_{mf}	kg	kg	kg
Bubbling bed (BB)	100	2316.9	10649.7	10800.5
Slugging (SFB)	500	207.2	952.5	966.0
Fast fluidizing (FF)	1000	73.26	336.77	341.54
Transport (TR)	5000	6.55	30.12	30.54

No. of Caps (orifice dia = 48 mm)	u_0/u_{mf}	N_o	N_o.	N_o
Bubbling bed (BB)	100	638	1766	1782
Slugging (SFB)	500	127	353	356
Fast fluidizing (FF)	1000	63	176	178
Transport (TR)	5000	12	35	35

After the evaluation of all the parameters, the simulation was performed for 5 cases (with reduction reactor fixed as moving bed) in terms of the fluidizing regime for four different gas superficial velocity and moving bed reactor operating in counter-current flow of gas and solids. Based on the conditions discussed above the selectivity of CO and H_2, and the H_2/CO ratios, the heat required for reduction, reactor volume required along with the solid conversion in the oxidation reactor is evaluated. To understand the results of the cases, a representative case with equimolar CO_2 and H_2O feed is considered. For case 1 with both oxidation and reduction as moving bed reactors, the selectivity of H_2 is 0.85 and CO is 0.5 with H_2/CO ratio of 1.72 is obtained. The metal oxide conversion was reported to be 71%. The efficiency of the CL unit was approximately 58% with a heat recuperation of 10.72 MW. For bubbling bed the reactor volume required is the highest 23.5 m^3 with least for the transport regime of 0.05 m^3, the volume of the reactor decreases also the selectivity of the product, solid conversion, also the efficiency. It is clear from the results that for higher selectivity the fluidized bed reactor need to be in bubbling bed mode but the reactor needs large volume which is unrealistic for the scale presented in the study. From the results, it can be observed moving bed for both oxidation and reduction yields higher efficiency with higher yield and selectivity. Similar results were observed for other gas composition of CO_2 and H_2O mixture (CO_2:H_2O ranging from 0:1 to 1.0) as presented in Table 55. Therefore, from the analysis, it can be concluded that the suitable reactor for reduction and oxidation for solar thermochemical redox cycle are moving bed reactor.

Table 55. Results of comparison of fluidized bed reactor and moving bed reactor model for oxidation reactor.

Composition CO_2: H_2O:: 0:0.1

Case	Reduction	Oxidation					Q_{RED}	S_{H2}	S_{CO}	H_2/CO	Total yield	X_{OXI} (%)	δ_{red}	RED VOL	OXI-VOL	ΔP	Elutriation	η_{CL}	$T_{OXIOUT,OC}$	$T_{OXIOUT,gas}$	Heat recuperation
	MB	MB	BB	SFB	FF	TR	MW				mol/s			m^3	m^3	bar	fraction		°C	°C	MW
1	x	x	-	-	-	-	24.84	0.76			31.612	79.779	0.14	0.40	5.000	0.200	0.000	55.08	980.23	857.74	9.971
2	x	-	x	-	-	-	24.31	0.71	-	-	29.555	74.949	0.14	0.40	23.510	0.137	0.000	54.75	970.22	970.22	9.971
3	x	-	-	x	-	-	21.97	0.50	-	-	20.815	52.780	0.14	0.40	1.831	0.067	0.081	49.54	920.09	920.09	9.971
4	x	-	-	-	x	-	20.74	0.39	-	-	16.240	41.177	0.14	0.40	0.647	0.048	0.560	45.43	893.79	893.79	9.971
5	x	-	-	-	-	x	33.47	0.11	-	-	4.385	5.674	0.14	0.40	0.058	0.009	1.000	25.14	813.31	813.31	9.971

Composition CO_2: H_2O:: 0.25:0.75

Case	Reduction	Oxidation					Q_{RED}	S_{H2}	S_{CO}	H_2/CO	Total yield	X_{OXI} (%)	δ_{red}	RED VOL	OXI-VOL	ΔP	Elutriation	η_{CL}	$T_{OXIOUT,OC}$	$T_{OXIOUT,gas}$	Heat recuperation
	MB	MB	BB	SFB	FF	TR	MW				mol/s			m^3	m^3	bar	fraction		°C	°C	MW
1	x	x	-	-	-	-	24.60	0.80	0.51	4.72	30.168	76.415	0.14	0.40	5.000	0.200	0.000	56.28	967.60	850.60	10.366
2	x	-	x	-	-	-	24.12	0.81	0.31	7.94	28.420	72.069	0.14	0.40	23.510	0.137	0.000	55.31	958.64	958.64	10.366
3	x	-	-	x	-	-	21.76	0.56	0.23	7.20	19.711	49.978	0.14	0.40	1.831	0.067	0.127	49.73	909.89	909.89	10.366
4	x	-	-	-	x	-	20.55	0.43	0.19	6.77	15.267	38.709	0.14	0.40	0.647	0.048	0.827	45.38	885.04	885.04	10.366
5	x	-	-	-	-	x	17.38	0.10	0.05	6.10	3.731	9.458	0.14	0.40	0.058	0.009	1.000	20.53	820.76	820.76	10.366

Composition CO_2: H_2O:: 0.5:0.5

Case	Reduction	Oxidation					Q_{RED}	S_{H2}	S_{CO}	H_2/CO	Total yield	X_{OXI} (%)	δ_{red}	RED VOL	OXI-VOL	ΔP	Elutriation	η_{CL}	$T_{OXIOUT,OC}$	$T_{OXIOUT,gas}$	Heat recuperation
	MB	MB	BB	SFB	FF	TR	MW				mol/s			m^3	m^3	bar	fraction		°C	°C	MW
1	x	x	-	-	-	-	24.02	0.85	0.50	1.72	28.040	71.100	0.14	0.40	5.000	0.200	0.000	57.97	956.64	841.22	10.762
2	x	-	x	-	-	-	23.80	0.92	0.36	2.52	26.640	67.553	0.14	0.40	23.510	0.137	0.000	56.03	941.88	941.88	10.762
3	x	-	-	x	-	-	21.38	0.64	0.23	2.75	17.997	45.631	0.14	0.40	1.831	0.067	0.161	49.43	896.32	896.32	10.762
4	x	-	-	-	x	-	20.19	0.48	0.18	2.69	13.721	34.786	0.14	0.40	0.647	0.048	1.000	44.54	873.38	873.38	10.762
5	x	-	-	-	-	x	17.24	0.11	0.04	2.58	3.160	8.010	0.14	0.40	0.058	0.008	1.000	18.57	816.88	816.88	10.762

Composition CO_2: H_2O:: 0.75:0.25

Case	Reduction	Oxidation					Q_{RED}	S_{H2}	S_{CO}	H_2/CO	Total yield	X_{OXI} (%)	δ_{red}	RED VOL	OXI-VOL	ΔP	Elutriation	η_{CL}	$T_{OXIOUT,OC}$	$T_{OXIOUT,gas}$	Heat recuperation
	MB	MB	BB	SFB	FF	TR	MW				mol/s			m^3	m^3	bar	fraction		°C	°C	MW
1	x	x	-	-	-	-	23.52	0.90	0.51	0.59	25.175	63.862	0.14	0.40	5.000	0.200		58.51	928.74	835.08	11.157
2	x	-	x	-	-	-	23.39	0.98	0.45	0.72	24.308	61.638	0.14	0.40	23.510	0.137	0.000	57.56	919.14	919.14	11.166
3	x	-	-	x	-	-	20.87	0.74	0.26	0.96	15.700	39.807	0.14	0.40	1.831	0.067	0.187	48.97	878.41	878.41	11.157
4	x	-	-	-	x	-	19.72	0.56	0.19	0.99	11.684	29.623	0.14	0.40	0.647	0.048	1.000	43.15	858.48	858.48	11.157
5	x	-	-	-	-	x	17.06	0.12	0.04	1.03	2.460	6.235	0.14	0.40	0.058	0.008	1.000	15.81	812.35	812.35	11.157

Composition CO_2: H_2O:: 1:0

Case	Reduction	Oxidation					Q_{RED}	S_{H2}	S_{CO}	H_2/CO	Total yield	X_{OXI} (%)	δ_{red}	RED VOL	OXI-VOL	ΔP	Elutriation	η_{CL}	$T_{OXIOUT,OC}$	$T_{OXIOUT,gas}$	Heat recuperation
	MB	MB	BB	SFB	FF	TR	MW				mol/s			m^3	m^3	bar	fraction		°C	°C	MW
1	x	x	-	-	-	-	22.59		0.52		21.605	54.931	0.14	0.40	5.000	0.200		60.40	907.67	832.56	11.528
2	x	-	x	-	-	-	22.92	-	0.52	-	21.682	54.978	0.14	0.40	23.510	0.137	0.000	59.35	893.51	893.51	11.528
3	x	-	-	x	-	-	20.15	-	0.30	-	12.504	31.701	0.14	0.40	1.831	0.067	0.205	48.16	853.79	853.79	11.527
4	x	-	-	-	x	-	19.01	-	0.21	-	8.749	22.182	0.14	0.40	0.647	0.048	1.000	40.44	837.60	837.60	11.528
5	x	-	-	-	-	x	16.82	-	0.04	-	1.543	3.911	0.14	0.40	0.058	0.008	1.000	11.57	806.62	806.62	11.527

A.2 Techno-economic analysis of polygeneration plant

Table 56. Thermodynamic properties and composition of ASU streams.

	1-C	**2-C**	**3-C**	**4-C**	**5-C**	**6-C**	**7-C**	**8-C**	**9-C**	**10-C**	**11-C**	**12-C**
T [°C]	25	30	20	20	30	30	30	20	-170	-173.4	-189.6	-176.6
P [bar]	1.013	5	6.3	6.3	30	30	30	6.3	6.3	5.1	1.2	5
Molar flow [kmol/hr]	11645.1	11645.1	11645.2	2329	2329	1863.2	465.8	9316.1	9316.1	2279.2	2279.2	7036.8
Mole frac. [%]												
N_2	0.79	0.79	0.79	0.79	0.79	0.79	0.79	0.79	0.79	0.49	0.49	0.884
O_2	0.21	0.21	0.21	0.21	0.21	0.21	0.21	0.21	0.21	0.5	0.5	0.11
	13-C	**14-C**	**15-C**	**16-C**	**17-C**	**18-C**	**19-C**	**20-C**	**21-C**	**22-C**	**23-C**	
T [°C]	-176.8	-146.1	-191.7	-146.1	-191.2	-181.5	-180.5	-194.2	-181.8	-20	0	
P [bar]	5	30	1.2	30	1.2	1.2	26	1.2	1.2	1.2	26	
Molar flow [kmol/hr]	7036.8	1863.2	1863.2	465.8	465.8	2445.4	2445.4	9199.6	9199.6	9199.6	2445.4	
Mole frac. [%]												
N_2	0.884	0.79	0.79	0.79	0.79	4.10E-04	4.10E-04	0.99	0.99	0.99	4.10E-04	
O_2	0.116	0.21	0.21	0.21	0.21	0.99	0.99	1.10E-04	1.10E-04	1.10E-04	0.99	

A.2.1 Exergo-economic analysis of polygeneration plant

Since to obtain a positive NPV high selling costs of the products are required, an exergo-economic analysis was performed to understand which components are the main contributors to the high costs. Exergo-economic relies on the concept that exergy is the only rational basis for assigning monetary costs to the multiple products typical of a polygeneration plant, like the one we are here analyzing, at the same time taking into account the interactions that a system experiences with the environment and the sources of thermodynamic inefficiencies within it [481]. The exergo-economic analysis method was first introduced in 1990 by Tsatsaronis and Lin ([482]) and named SPECO (Specified Exergy Costing) in 1995 by Lazzaretto and Andreatta [483]. For analyzing an energy plant, this method provides an easy and straightforward scheme and it helps in time-saving by employing a compact matrix formulation [484]. So, the SPECO method was adopted in this work. The starting point of this methodology is the exergy analysis of the plant with all the exergy streams and irreversibilities produced during the process (exergy analysis of chapter 6).

Secondly, the productive structure has to be defined, i.e. which are the fuel (F), product (P) and loss (L) for each subsystem. Fuel is defined to be equal as i) all the exergy values to be considered at the inlet of a component, plus ii) all the exergy decreases between inlet and outlet (i.e. the exergy removals from the respective material streams) and minus iii) all the exergy increases (between inlet and outlet) that are not in accord with the purpose of the component. The product is defined to be equal to the sum of i) all the exergy values to be considered at the outlet (including the exergy of energy streams generated in the component) plus ii) all the exergy increases between inlet and outlet that are in accord with the purpose of the component [485]. While all the flows that leave the unit and the plant that are not subsequently used and do not require a special treatment are denominated as losses [486]. Based on the results of the exergy balance of the plant, an exergy cost E^* and unit exergy cost $k^*=E^*/E$ is assigned to each stream. The exergy cost of a physical flow is the exergy spent to produce it, irreversibilities comprised. Therefore, it is completely connected to the production procedure efficiency: the highest is the efficiency, the lowest is the irreversibilities produced, and the lowest is the exergy cost of the stream. The procedure to evaluate the exergetic cost of each stream is described below.

Exergo-economic formulation:

In order to evaluate the exergy cost of each of the ‘m’ flows of a certain plant, it will be necessary to write ‘m’ independent equations. If the plant is sequential, that is all the subsystems are characterized by a single output, since the exergy cost is conservative, it is possible to write as many equations of exergy cost balance as the number of subsystems. Vice-versa, if the subsystems are characterized by multiple outlets (bifurcations), additional equations must be written for each unit equations, equal in number to the outlet streams 'm' minus the fuel F and losses streams L (w=m-F-L). Valero et al. [487] have formulated a rational procedure of exergy cost estimation based on four propositions:

- P1 rule: in the absence of an external assessment, the cost of the inlet flow to the plant is equal to the exergy of the stream: E*i=Ei
- P2 rule: in absence of external assessment, the exergy cost of losses is null: E*i=0
- P3 rule: if an output flow of a device is a part of the fuel, its exergy unit cost is the same of the input flow from which it comes.
- P4 rule: if a unit has multiple outlet flows as a product since their formation process is the same, an equal exergy cost is assigned to all the streams.

The exergy cost assessment can be formulated in a compacted matrix form as:

$$[A_c]\times E^* = Y_e^* \tag{A.2.1}$$

$$\begin{bmatrix} A \\ \alpha_e \\ \alpha_w \end{bmatrix} \times E^* = \begin{bmatrix} 0 \\ \omega_e \\ 0 \end{bmatrix} \tag{A.2.2}$$

$$E^* = [A_c]^{-1} \cdot Y_e \tag{A.2.3}$$

Where:

- A_c is the cost matrix (m×m);
- A(n × m) the incident matrix with as many rows, 'm', as the number of exchanged flows between the components and the environment and as many columns, 'n', as the number of components. It relates to the i-th component with the j-th flow. If the i-j element of the matrix is null, it means there is no correlation between the two elements, if it is equal to –1, the j-th stream is an outlet for the i-th component and, vice versa, if it is equal to 1, the stream is an inlet stream.
- α_e (e × m) is the external and losses assessment matrix. Composed of 'm' columns as the number of components and 'e' rows as the number of the streams coming from the extern plus the plant losses, α_e is the matrix representation of the equations coming from the P1 and P2 rules.
- α_w (w × m) is the bifurcation matrix. Composed of 'm' columns as the number of components and 'w' rows as the number of bifurcations, it is the matrix representation of the equations coming from the P4a, P4b rules.
- Y_e^* (m × 1) is the vector of external assessment, composed of 'n' elements as a result of proposition P1, 'e' elements with the values of the exergies (ω_e)

corresponding to the resources of the plant (P1 rule), and m – n – e null elements corresponding to the losses and product bifurcations (P3 –P4 rule).

- E* is the vector containing the exergy cost of all the streams.

After the calculation of the exergetic cost, it is possible to evaluate the monetary cost (C) of the fuel and products of the plant. The formation of the economic cost of the internal flows and final products is related to both the thermodynamic efficiency of the process and to the equipment and maintenance cost of the plant. Therefore, the exergo-economic cost of a flow, (C_{prod}), can be defined as the combination of two contributions: the first comes from the monetary cost of the exergy entering the plant needed to produce this flow (C_{fuel}), that is its exergy cost, and the second covers the rest of the cost concurred in the production process (Z) (capital cost of equipment, maintenance operating costs, etc.). For a generic component, the cost balance equation can be expressed as:

$$C_{fuel} + Z = C_{prod} \tag{A.2.4}$$

The cost assessing procedure is based on the same principles of the exergy cost estimation and can be carried on with the same listed rules above, replacing the exergy with the monetary cost. Considering the whole plant, the cost accounting equations can be described in a matrix form:

$$[A_c] \cdot C = Z_e \tag{A.2.5}$$

$$\begin{bmatrix} A \\ \alpha_e \\ \alpha_w \end{bmatrix} \cdot C = \begin{bmatrix} -Z \\ C_e \\ 0 \end{bmatrix} \tag{A.2.6}$$

$$C = [A_c]^{-1} \cdot Z_e \tag{A.2.7}$$

C_e is the cost of the external assessment. After obtaining the cost C and relative specific cost (c=C/E), the exergo economic variables, such as the exergo economic factor (f_k) (equation A.2.8) and relative cost difference (r_k) (equation A.2.9), can be calculated. The exergo economic factor permits to evaluate the contribution of the investment cost on the product streams, the highest it is, the bigger is the component investment cost contribution. While the relative cost difference allows locating the component with the highest difference between product and fuel.

$$f_k = \frac{Z_k}{Z_k + C_{D,k}} \tag{A.2.8}$$

$$r_k = \frac{c_{P,k} - c_{F,k}}{c_{F,k}} \quad (A.2.9)$$

where $c_{F,k}$, and $c_{P,k}$ represent the specific cost of the fuel and product of the the k-th component, while $C_{D,k}$ is the cost of the destroyed exergy in the k-th component (equation A.2.10):

$$C_{D,k} = c_{D,k} \cdot I_{destroyed,k} \quad (A.2.10)$$

In the current study, the cost rate (Z) was calculated using the annual capital cost ACC [299]:

$$ACC = TOC \cdot CRF \quad (A.2.11)$$

The annual capital cost is a combination of the total overnight cost and the recovery factor (CRF). CRF is defined as a ratio of constant annuity to the present value at a time (t) with a specified discount rate i.

$$CRF = (i \cdot (1+i)^t)/((1+i)^t - 1)\ \mathrm{c} \quad (A.2.12)$$

The cost rate Z comprises the total overnight cost plus the operational costs. It is given by the overall of this costs divided the annual operational time τ, based on the capacity factor CF (Eq. A.2.13).

$$Z = (\mathrm{ACC} + \text{Fixed costs})/\tau + \text{Variable cost} \ \ [M\$/s] \quad (A.2.13)$$

The process water cost was attributed to the four condensers proportionally to the heat rejected. The analysis was performed considering 64 streams (49 physical streams and 15 energy streams) and 23 components. Hence, 41 auxiliary equations were formulated (Table 57).

Table 57. Productive structure of the plant and auxiliary equations.

Component	Fuel stream	Product stream	Waste	Auxiliary equations
ASU	0+W_{ASU}	1+1_b	-	$P_1: E_1 = E_1^*$ $P_1: E_{ASU} = E_{ASU}^*$ $P_3: k_{1b}^* = k_1^*$
COMP-2	29+W_{COMP-2}	30	-	$P_1: E_{WCOMP1} = E_{WCOMP1}^*$
COMP-3	36+W_{COMP-3}	37	-	$P_1: E_{WCOMP2} = E_{WCOMP2}^*$
GT	31-32	W_{GT}	-	$P_3: k_{31}^* = k_{32}^*$
COND-2	33	35+36+38+43	42	$P_2: k_{42}^* = 0$ $P_4: k_{35}^* = k_{36}^*$ $P_4: k_{36}^* = k_{38}^*$ $P_4: k_{38}^* = k_{43}^*$

NG$_{PHX1}$	28b-29	3-2	-	$P_1: E_2 = E_2^*$ $P_3: k_{28}^* = k_{29}^*$
TURBOEXP	3-4	W$_{TURBEXP}$	-	$P_3: k_3^* = k_4^*$
NG$_{PHX2}$	28-28b	5-4	-	$P_3: k_{28}^* = k_{28b}^*$
RED+COMB	9+5+30+1+37+49	7+28+31	-	$P_4: k_7^* = k_{28}^*$ $P_4: k_{28}^* = k_{31}^*$
OXY	7+46+40	10+9	-	$P_4: k_{10}^* = k_9^*$
LIQPUMP1	43+W$_{PUMP-1}$	44	-	$P_1: E_{WPUMP1} = E_{WPUMP1}^*$
H2O$_{PHX}$	10a-10b	46-45	-	$P_3: k_{10a}^* = k_{10b}^*$
CO2COMP	38+W$_{COMP-4}$	39	-	$P_1: E_{WCOMP4} = E_{WCOMP4}^*$
CO2$_{HX}$	10b-11	40-39	-	$P_3: k_{10b}^* = k_{11}^*$
COND-1	11	13	12	$P_2: k_{12}^* = 0$
COMP-1	13+W$_{COMP-1}$	14	-	$P_1: E_{WCOMP1} = E_{WCOMP1}^*$
DME Reactor	14+44	15+45	-	$P_4: k_{15}^* = k_{45}^*$
VLS	15	17+49	-	$P_4: k_{17}^* = k_{49}^*$
Distillation Unit (only columns)	16+Q$_{COND,CLN-CO2}$ Q$_{COND,CLN-DME}$ + Q$_{REB,CLN-CO2}$ + Q$_{REB,CLN-DME}$ + Q$_{REB,CLN-MeOH}$	26+23+20	27	$P_1: E_{QC1} = E_{QC1}^*$ $P_1: E_{QC2} = E_{QC2}^*$ $P_1: E_{QRB1} = E_{QRB1}^*$ $P_1: E_{QRB2} = E_{QRB2}^*$ $P_1: E_{QRB3} = E_{QRB3}^*$ $P_2: k_{27}^* = 0$ $P_4: k_{20}^* = k_{23}^*$ $P_4: k_{23}^* = k_{26}^*$
ST1	5-A - 6-A	W$_{ST1}$	-	$P_3: k_{5-A}^* = k_{6\_A}^*$
HRSG1	32-33	5-A – 1-A	-	$P_1: E_{1-A} = E_{1-A}^*$ $P_3: k_{32}^* = k_{33}^*$
ST2	5-B – 6-B	W$_{ST2}$	-	$P_3: k_{5-B}^* = k_{6-B}^*$
HRSG2	10-10a	5-B - 1-B	-	$P_1: E_{1-B} = E_{1-B}^*$ $P_3: k_{10}^* = k_{10a}^*$
LOOP FOR CERIA			-	$k_{9a}^* = k_{9b}^*$
			-	$k_{28b}^* = k_{28c}^*$

In Table 58 are reported in detail the main results of the exergo-economic analysis. The exergo-economic factor (f) ranged from 1 to 0.06. The highest exergo-economic factor was observed for the ASU since the power absorbed is self-produced inside the plant. The component with lowest (f) resulted to be the RED+COMB. When evaluating an equipment by an exergo-economic study, a general rule for reducing the final cost of the streams is followed: the subsystems that have the priority for an intervention are the ones with the highest (Z+C$_D$). Among these, the equipment with the highest relative difference cost r$_k$ must be selected. The exergo-economic factor identifies the main causes of cost increase: a high value of this parameter (f) indicates a high influence of the cost of investment, while a low value indicates a high incidence of the thermodynamic efficiency. In the first case, a possible solution could be the use of cheaper components (generally characterized by lower efficiency), in the second case a higher efficiency component could be used with a consequent increase of the investment cost. The component of the polygeneration plant with the highest $Z+C_D$ factor is the RED+COMB. The exergo-economic factor resulted in 0.06, so the exergy destroyed is the main contributor to the product cost. As reported in the exergy analysis section 5, in this element are localized the 51.2% of the overall irreversibilities, so an increase of the efficiency is suggested. For example, a different arrangement between the combustor and the reduction reactor from the annulus might be a solution for proper heat integration. Same consideration for the OXI reactor that has the second highest ($Z + C_D$) factor and a factor (f) equal to 0.09. The HRSG1 has the fourth highest $Z+C_D$, the relative cost difference of 1.77, so the product cost of this unit is bigger than the fuel cost of about 170%. Its exergo-economic factor is equal to 0.6 so the capital cost is the main contributor. The compressors and turbines exergo-economic factor ranged from 0.37 to 0.8. Finally, the overall plant presents a relative cost difference of 1.5 and an exergo-economic factor of 0.37, so a general efficiency improvement is required.

Table 58 Main results of the exergo-economic analysis.

Component	$c_{F,k}$ [\$/MWh]	$c_{P,k}$ [\$/MWh]	r_k	C_D [\$/s]	Z [\$/s]	$Z+C_D$	f_k
ASU	0	163.55	0	0	0.49	0.49	1
COMP-2	78.16	79.37	0.02	0.05	0.06	0.11	0.57
COMP-3	35.32	49.22	0.39	0.06	0.21	0.27	0.77
GT	43.96	56.29	0.28	0.07	0.32	0.39	0.81
COND-2	43.96	56.23	0.28	0.06	0.12	0.18	0.66
NG_{PHX1}	80.77	123.66	0.53	0.01	0.01	0.02	0.5
TURBEXP	32.66	50.61	0.55	0.08	0.02	0.1	0.16
NG_{PHX2}	80.77	565.56	6	0.04	0.04	0.07	0.52
RED+COMB	60.19	80.77	0.34	1.71	0.11	1.82	0.06
OXY	80.77	102	0.26	0.71	0.11	0.82	0.13
$H2O_{PHX}$	102	396.19	2.88	0.09	0.01	0.1	0.06
COMP-4	59.35	62.2	0.05	0	0.01	0.01	0.91
$CO2_{PHX}$	102	149.22	0.46	0.01	0.01	0.02	0.52
COND-1	102	102	0	0.13	0.01	0.14	0.1
COMP-1	86.69	88.91	0.03	0.02	0.03	0.05	0.65
DME Reactor	88.86	97.49	0.1	0.11	0.06	0.18	0.37
Vapour-Liquid Separator (VLS)	98.7	98.7	0	0.02	0.01	0.02	0.38
Distillation Unit (only columns)	97.44	114.38	0.17	0.15	0.17	0.32	0.52
ST1	69.38	93.23	0.34	0.11	0.19	0.3	0.63
HRSG1	43.96	121.79	1.77	0.17	0.25	0.42	0.6
ST2	196.28	236.39	0.2	0.02	0.01	0.03	0.37
HRSG2	102	205.12	1.01	0.1	0.03	0.13	0.22

A.3 Reactivity and kinetic model assessment of non-stoichiometric ceria

A.3.1 Assessment of CO_2 splitting kinetics by H_2 reduction

Effect of CO production rate with CO_2 concentration for temperature range (700-1000ºC):

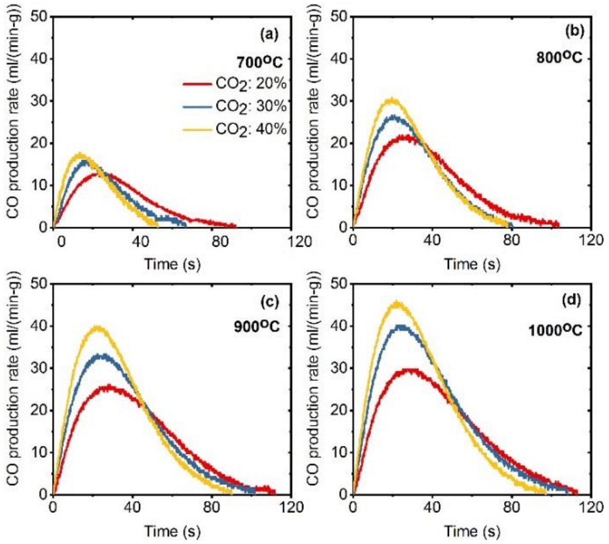

Figure 127. The comparison of CO production rate for varying concentration of CO_2 in the feed for (a) 700ºC (b) 800ºC (c) 900ºC (d) 1000ºC.

Effect of CO peak rate and total CO production with CO_2 concentration for temperature range (700-1000ºC):

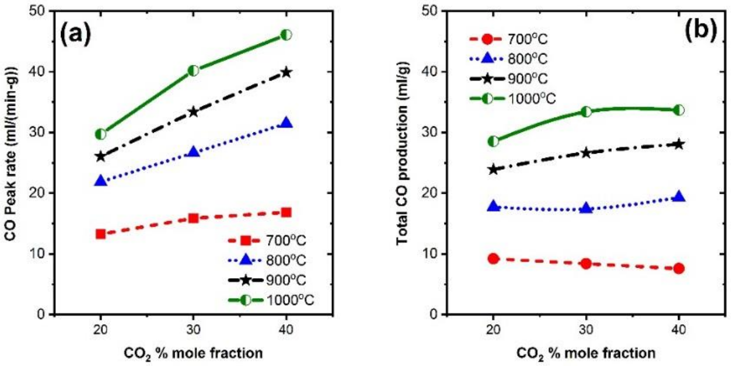

Figure 128. (a) CO peak rate (b) total production as a function of CO_2 concentration for increasing temperature range (700-1000ºC).

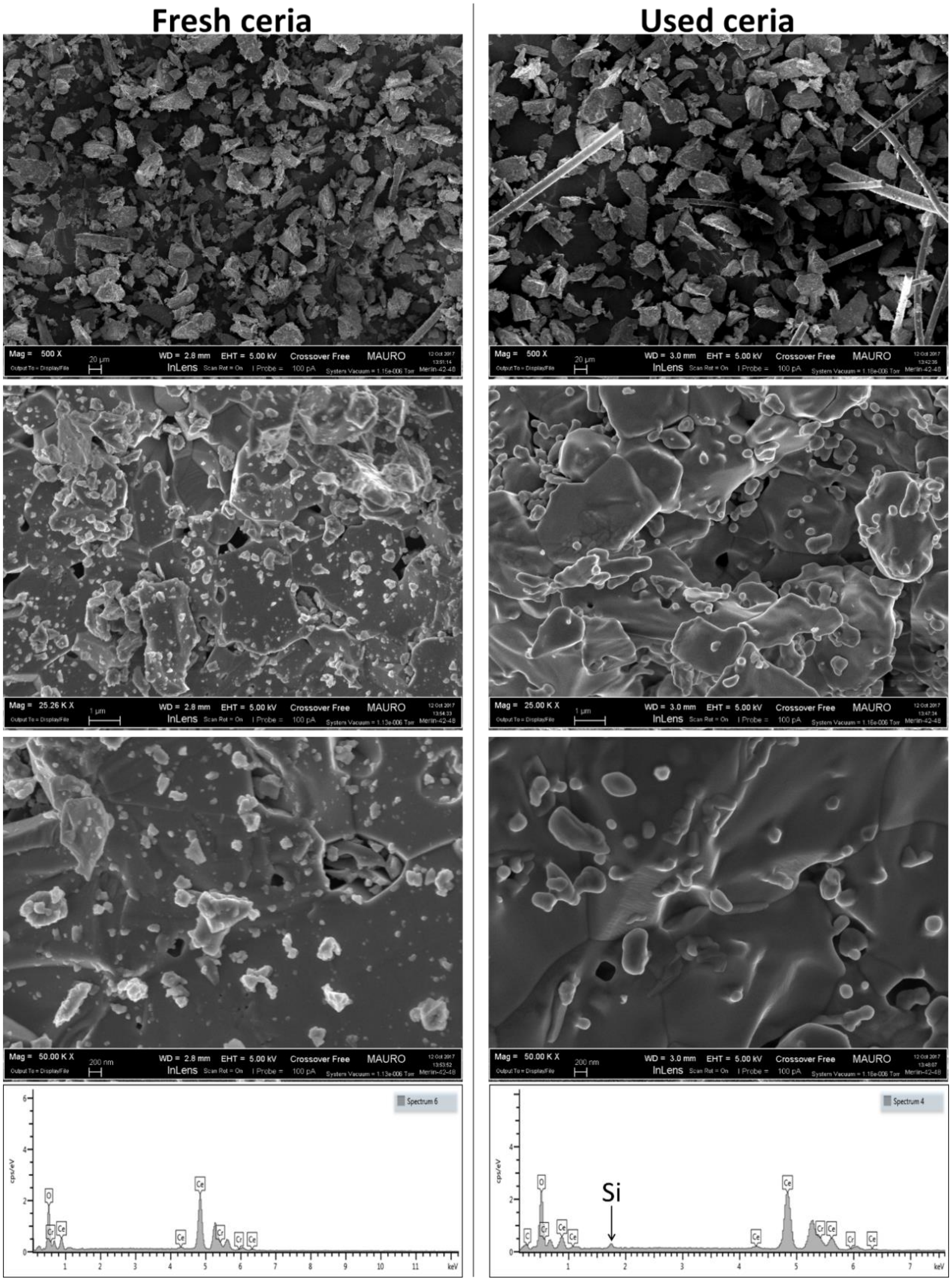

Figure 129. SEM images of the fresh and used ceria samples with EDS at different magnification with H_2 reduction and CO_2 splitting.

Akaike Information Criterion (AIC):

AIC measures the ability of a model to fit a certain set of experimental data by measuring the distance from the model and distinguishes it to be “true model”. It is an information criterion because it provides an estimation of the information lost when the model is used to represent a phenomenon that gives the reference data. AIC is based on a trade-off between the quality of fit and the complexity of the model: it indeed penalizes the increase of parameters of the models. It is not based on the acceptance or refuse of a null hypothesis: this implies that the method cannot provide an absolute view about the quality of the tested model, but only a relative comparison among models. In other words, if a set of models do not fit appropriately the data, AIC does not warn, but it only states the best among them [434].

The general formula for AIC is given by equation (A.3.1).

$$AIC = -2\ln\left(\hat{L}\right) + 2K_1 \tag{A.3.1}$$

where K_1 is the number of parameter of the model and $\hat{L}$ is the value that maximizes the likelihood function of the model. After a regression study, it is possible to use the corresponding Residual Sum of Squares in place of $\hat{L}$ to directly calculate the AIC value. With RSS the equation 1 transforms to equation (A.3.2).

$$AIC = n_1 \ln\left(\frac{RSS}{n_1}\right) + 2K_1 \tag{A.3.2}$$

where n_1 is the dimension of the data set and RSS is the Residual Sum of Squares and it can be given by equation (A.3.3).

$$RSS = \sum_{i=1}^{n_1} (\hat{u}_i)^2 = \sum_{i=1}^{n_1} \left(y_i - \hat{y}_i\right)^2 = \sum_{i=1}^{n_1} \left(y_i - f\left(x_i\right)\right)^2 \tag{A.3.3}$$

$\hat{u}_i$ are the residual, the difference between the real values and the values from the regression model.

A bias adjustment is required only in case $n_1/K_1 < 40$, then the AIC is termed as AICc meaning corrected AIC. It can be given as equation (A.3.4).

$$AICc = n_1 \ln\left(\frac{RSS}{n_1}\right) + 2K_1 + \frac{2K_1\left(K_1 + 1\right)}{n_1 - K_1 - 1} \tag{A.3.4}$$

The AICc is calculated for all the models examined and the model with the smallest value of AICc is selected.

Table 59. 20% CO_2 concentration RSS and AICc values.

20% CO_2 RSS and AICc values

method	**model**	**700°C**		**800°C**		**900°C**		**1000°C**	
		RSS	**AICc**	**RSS**	**AICc**	**RSS**	**AICc**	**RSS**	**AICc**
dX/dt-X	F1.5	0.136506	-4796.81	0.114664	-5586.85	0.099529	-6189.02	0.096052	-6253.45
	F2	0.321825	-4303.67	0.273779	-5023.75	0.2365	-5584.03	0.229694	-5640.53
	F3	2.017999	-3248.05	1.738984	-3827.62	1.490414	-4297.27	1.457004	-4341.82
	R2	0.020423	-5889.13	0.019425	-6735.57	0.016411	-7448.94	0.015734	-7525.22
	R3	0.025562	-5760.1	0.025768	-6552.74	0.022279	-7235.28	0.021302	-7312.24
	D1	10334.17	1663.084	3104.73	1016.713	11194.6	1940.702	15932.1	2195.876
	D2	20317.33	2051.794	6118.966	1455.681	22014.27	2413.407	31389.86	2672.615
	D3	0.052743	-5343.6	0.045676	-6182.37	0.041149	-6806.41	0.03937	-6880.45
	D4	45.56217	-1455.79	1728.7	637.8577	51.41858	-1822.15	65.66164	-1664.7
	AE1	0.058253	-5286.46	0.047892	-6151.71	0.041753	-6796.21	0.039987	-6869.51
	AE0.5	103864.4	2989.971	31439.93	2514.617	112340.9	3552.67	160738.2	3820.819
	AE1.5	0.001805	-7284.14	0.001432	-8422.68	0.001259	-9243.77	0.001002	-9460.86
	AE2	0.000588	-7928.65	0.000535	-9060.22	0.000394	-10055.2	0.000586	-9838.38
	AE3	0.008585	-6387.47	0.007229	-7375.06	0.005919	-8161.74	0.006608	-8135.12
	AE4	0.020025	-5900.45	0.016346	-6847.22	0.013831	-7568.5	0.014847	-7566.01
	Aen	0.000264	-8387.92	0.000221	-9628.32	0.000155	-10707.2	0.000274	-10371
	SB	0.000271	-8369.78	0.000209	-9665.28	8.94E-05	-11088.6	0.000143	-10826.9
	PT	0.033293	-5608.14	0.026461	-6535.56	0.024524	-7168.17	0.026009	-7171.88
X-t	F1.5	13.77583	-2143.59	14.89744	-2437.94	16.02001	-2637.29	16.04467	-2655.33
	F2	19.88256	-1932.6	21.69989	-2194.59	23.40284	-2372.36	23.46628	-2388.05
	F3	31.72283	-1663.97	34.88066	-1887.51	37.74722	-2038.2	37.96259	-2049.89
	R2	2.669721	-3087.13	5.017568	-3142.03	4.96974	-3455.45	5.038927	-3469.53
	R3	3.304487	-2964.48	5.857721	-3041.87	5.982661	-3325.79	6.027146	-3343.64

	D1	14.30321	-2121.98	15.7158	-2403.34	15.9027	-2642.43	16.0377	-2655.63
	D3	21.04113	-1900.04	22.59374	-2168.47	24.94229	-2327.83	25.22771	-2337.17
	AE1	8.271261	-2436.91	8.778874	-2780.1	9.309848	-3016.69	9.336122	-3035.99
	AE0.5	26.18237	-1774.34	28.65325	-2014.75	31.17742	-2171.86	31.46087	-2181.95
	AE1.5	1.52291	-3409.9	1.39592	-3969.8	1.328096	-4377.87	1.281639	-4431.97
	AE2	0.086214	-5061.04	0.18854	-5265.09	0.284452	-5454.98	0.346139	-5352.24
	AE3	8.630128	-2412.49	11.57004	-2601.48	13.23546	-2770.76	13.79469	-2761.54
	AE4	29.84552	-1699.04	38.50383	-1823.57	42.75179	-1951.17	43.92742	-1947.29
	AEn	0.290962	-4359.64	0.01741	-6804.41	0.071244	-6420.72	0.354522	-5333.42
	SB	0.257819	-4427.17	0.019789	-6719.56	0.05686	-6576.35	0.244802	-5591.75
	PT	94.11067	-1038.69	101.9002	-1193.88	112.9495	-1272.07	116.0169	-1264.54

Table 60. 30% CO_2 concentration RSS and AICc values.

30% CO_2 RSS and AICc values									
method	**model**	**700°C**		**800°C**		**900°C**		**1000°C**	
		RSS	**AICc**	**RSS**	**AICc**	**RSS**	**AICc**	**RSS**	**AICc**
dX/dt-X	F1.5	0.175298	-3239.91	0.143068	-4095.85	0.112515	-5483.32	0.108199	-5886.75
	F2	1.190957	-2440.92	0.341906	-3658.49	0.271396	-4924.2	0.263444	-5286.97
	F3	2.607614	-2114.13	2.175489	-2729.56	1.73618	-3745.73	1.712398	-4025.38
	R2	0.031284	-3958.55	0.023416	-5004.41	0.018192	-6640.36	0.017585	-7111.37
	R3	0.041091	-3844.84	0.031783	-4851.04	0.024344	-6455.39	0.023265	-6922.69
	D1	6910.6	1172.822	4300.875	1080.283	5593.848	1383.632	8344.372	1697.86
	D2	13601.07	1455.169	8485.206	1421.395	11043.52	1815.544	16536.62	2158.869
	D3	0.068785	-3630.01	0.056561	-4561.7	0.045566	-6057.31	0.043277	-6504.36
	D4	45.47257	-922.062	61.4339	-1052.52	97.58595	-1187.29	434.8028	-293.439
	AE1	0.074579	-3596.29	0.059662	-4534.91	0.046144	-6049.31	0.044003	-6493.15

	AE0.5	69587.36	2135.894	43698.9	2244.172	56860.59	2856.155	85973.13	3269.929
	AE1.5	0.002249	-5056.33	0.001953	-6251.49	0.001106	-8418.39	0.000825	-9173.51
	AE2	0.001363	-5265.29	0.000446	-6993.2	0.000619	-8787.11	0.000907	-9109.43
	AE3	0.012674	-4335.35	0.007615	-5568.3	0.007779	-7179.83	0.008642	-7590.2
	AE4	0.028321	-4000.04	0.017656	-5146.14	0.017293	-6672.52	0.018575	-7074.43
	Aen	0.000641	-5578.11	0.000206	-7379.51	0.000637	-8766.37	0.001576	-8735.28
	SB	0.000682	-5550.02	0.000122	-7639.74	0.000167	-9616.2	0.179063	-5543.21
	PT	0.046272	-3795.33	0.029538	-4887.82	0.026133	-6410.35	0.028601	-6783.51
X-t	F1.5	10.01084	-1553.17	11.8113	-1880.27	13.50007	-2443.34	14.08961	-2604.89
	F2	14.44891	-1400.15	17.1863	-1691.99	20.01124	-2193.41	20.96886	-2336.91
	F3	23.11831	-1204.16	27.6168	-1453.89	32.67143	-1882.12	34.35383	-2004.17
	R2	3.509579	-1990.26	3.792672	-2450.54	4.176569	-3188.33	4.425308	-3385.45
	R3	4.075286	-1927.94	4.523008	-2362.13	4.937489	-3082.05	5.172131	-3280.34
	D1	10.20729	-1545.06	11.89136	-1876.88	14.4761	-2399.01	15.67048	-2533.22
	D3	15.53033	-1370.05	18.27516	-1661.15	21.15403	-2158.14	22.08756	-2301.88
	AE1	6.016276	-1765.5	6.933538	-2147.68	7.67786	-2801.71	7.985043	-2987.63
	AE0.5	19.23263	-1280.89	22.78443	-1550.45	26.67535	-2010.88	27.91062	-2144.17
	AE1.5	1.034863	-2499.51	1.020688	-3109.46	0.957864	-4123.39	0.993273	-4392.47
	AE2	0.104815	-3454.37	0.202835	-3920.61	0.391186	-4692.05	0.440243	-4940.89
	AE3	6.917383	-1707.3	9.937641	-1966.98	12.85249	-2474.56	13.32706	-2642.39
	AE4	23.2206	-1202.32	32.89464	-1366.1	40.20325	-1750.4	41.30316	-1880
	AEn	0.202616	-3177.51	0.054339	-4579.82	0.612874	-4404.94	0.02961	-6758.17
	SB	0.177763	-3230.08	0.045442	-4667.58	0.416196	-4648.69	0.022145	-6951.96
	PT	70.91318	-736.77	80.65278	-915.88	95.58012	-1200.47	100.4959	-1280.7

Table 61. 40% CO_2 concentration RSS and AICc values.

40% CO_2 RSS and AICc values

method	model	700°C		800°C		900°C		1000°C	
		RSS	AICc	RSS	AICc	RSS	AICc	RSS	AICc
dX/dt-X	F1.5	0.314668	-2285.31	0.150046	-3917.27	0.131421	-4696.8	0.12229	-5134.98
	F2	0.455598	-2163.54	0.357796	-3495.79	0.313659	-4207.92	0.294337	-4604.47
	F3	2.899458	-1554.67	2.265588	-2600.66	1.987978	-3170.14	1.878695	-3484.89
	R2	0.029522	-3063.84	0.025342	-4779.83	0.021948	-5702.63	0.01993	-6230.73
	R3	0.040958	-2956.13	0.033815	-4639.93	0.029378	-5538.76	0.02666	-6055.02
	D1	3448.69	775.0487	15395.72	1678.983	8863.415	1552.1	8421.77	1593.541
	D2	6803.528	998.5867	30342.52	2008.036	17470.04	1933.448	16622.65	2004.228
	D3	0.08034	-2734.47	0.059873	-4362.84	0.052745	-5209.87	0.049505	-5681.19
	D4	54.01688	-592.424	250.8153	-317.825	51.11567	-1345.34	76.17533	-1248.6
	AE1	0.078329	-2742.81	0.062806	-4339.65	0.05486	-5187.77	0.050352	-5670.94
	AE0.5	34933.35	1536.831	155686	2801.152	71475.52	2725.232	85519.03	2993.564
	AE1.5	0.002907	-3826.51	0.001693	-6092.33	0.001555	-7190.51	0.001193	-7931.3
	AE2	0.001172	-4125.36	0.000735	-6496.7	0.000489	-7840.78	0.000638	-8309.83
	AE3	0.011059	-3386.89	0.009887	-5236.31	0.00811	-6262.14	0.008364	-6755.15
	AE4	0.024604	-3123.8	0.022575	-4835.9	0.018811	-5789.3	0.018741	-6267.9
	Aen	0.001218	-4110.58	0.00019	-7150.09	0.000194	-8357.43	0.000229	-8925.63
	SB	0.000529	-4382.81	0.000202	-7118.25	0.000105	-8700.78	0.000126	-9283.74
	PT	0.041406	-2952.55	0.036716	-4600.02	0.018789	-5789.98	0.02921	-5999.84
X-t	F1.5	7.660237	-1235.04	11.00976	-1833.9	12.59343	-2132.66	12.77403	-2327.12
	F2	11.18328	-1110.56	16.09276	-1649.8	18.45559	-1917.87	18.95862	-2088.63
	F3	18.07792	-952.55	25.96867	-1417.72	29.78506	-1648.87	30.92061	-1793.18
	R2	2.317426	-1628.39	3.578549	-2378.96	4.039308	-2771.71	3.955228	-3035.24
	R3	2.829787	-1562.68	4.21917	-2299.09	4.766812	-2678.64	4.652189	-2937.21

D1	7.504292	-1241.81	11.34986	-1819.15	13.16012	-2107.92	13.98051	-2272.61
D3	11.7914	-1093.14	17.10287	-1620.28	19.42938	-1888.97	19.85713	-2060.67
AE1	4.456986	-1413.22	6.428782	-2094.83	7.30372	-2438.83	7.239855	-2670.08
AE0.5	15.05345	-1012.78	21.38766	-1511.85	24.39154	-1761.14	25.12559	-1918.53
AE1.5	0.552021	-2100.38	0.953805	-3020.25	1.073205	-3516.6	0.933962	-3907.02
AE2	0.259887	-2348.23	0.180955	-3826.42	0.205642	-4445.17	0.327385	-4540.2
AE3	7.928515	-1223.72	8.834406	-1940.67	10.19142	-2251.59	11.53912	-2388.53
AE4	24.77719	-848.838	28.61619	-1370.64	32.99228	-1591.4	36.28956	-1696.47
AEn	0.149241	-2528.72	0.066646	-4308.87	0.169168	-4552.9	0.232672	-4744.47
SB	0.081233	-2726.84	0.060466	-4354.07	0.126473	-4714.37	0.168462	-4937.51
PT	107.6154	-365.655	77.37226	-888.227	82.99992	-1072.92	89.14751	-1153.62

Table 62. F-test for 30% CO_2 concentration.

Temperature	Method	Cases compared	F-ratio	Fcritical	Winner model
700 (°C)	dX/dt-X	AEn/AE2	1.012048	1.1738876	AE2
		SB/AE2	0.959723	0.8518703	SB
		SB/AEn	0.971285	0.8518703	SB
	X-t	AEn/AE2	0.978295	0.8521936	AEn
		SB/AE2	0.924482	0.8508872	SB
		SB/AEn	1.027557	1.1752439	AEn
800 (°C)	dX/dt	AEn/AE2	1.009323	1.1573048	AE2
		SB/AE2	0.964478	0.8640766	SB
		SB/AEn	0.955569	0.8640766	SB
	X-t	AEn/AE2	1.014999	1.1559873	AE2
		SB/AE2	0.923146	0.8631966	SB
		SB/AEn	1.009162	1.1584847	AEn
900 (°C)	dX/dt	AEn/AE2	0.993135	0.8791234	AEn
		SB/AE2	1.016131	1.1374967	AE2
		SB/AEn	1.023155	1.1374967	AEn
	X-t	AEn/AE2	0.993135	0.8791234	AEn
		SB/AE2	0.92026	0.877438	SB
		SB/AEn	1.112116	1.1396817	AEn
1000 (°C)	dX/dt	AEn/AE2	0.986339	0.8841665	AEn
		SB/AE2	0.964181	0.8841665	SB
		SB/AEn	0.977535	0.8841665	SB
	X-t	AEn/AE2	0.972644	0.8843186	AEn
		SB/AE2	0.922064	0.880823	SB
		SB/AEn	0.992663	0.880823	SB

Table 63. F-test for 40% Concentration for CO_2.

Temperature	Method	Cases compared	F-ratio	Fcritical	Winner model
700 (°C)	dX/dt-X	AEn/AE2	1.026574	1.1985095	AE2
		SB/AE2	0.961215	0.8355021	SB
		SB/AEn	0.935992	0.8355021	SB
	X-t	AEn/AE2	1.03613	1.1956132	AE2
		SB/AE2	0.930729	0.8336786	SB
		SB/AEn	1.073058	1.199503	AEn
800 (°C)	dX/dt-X	AEn/AE2	0.991252	0.8622988	AEn
		SB/AE2	1.610224	1.1807985	SB
		SB/AEn	1.63232	1.1807985	SB
	X-t	AEn/AE2	0.984244	0.8622988	AEn
		SB/AE2	0.923185	0.8609842	SB
		SB/AEn	1.010433	1.1614615	AEn
900 (°C)	dX/dt-X	AEn/AE2	0.994304	0.8709692	AEn

		SB/AE2	1.783189	1.1760923	AEn
		SB/AEn	1.808916	1.1760923	AEn
	X-t	AEn/AE2	0.989714	0.8710752	AEn
		SB/AE2	0.92178	0.8702199	SB
		SB/AEn	1.034595	1.1491348	AEn
1000 (ºC)	dX/dt-X	AEn/AE2	0.983578	0.875298	AEn
		SB/AE2	0.964337	0.8751064	SB
		SB/AEn	0.98036	0.8751064	SB
	X-t	AEn/AE2	0.965458	0.8754886	AEn
		SB/AE2	0.919702	0.8745263	SB
		SB/AEn	1.058959	1.1434762	AEn

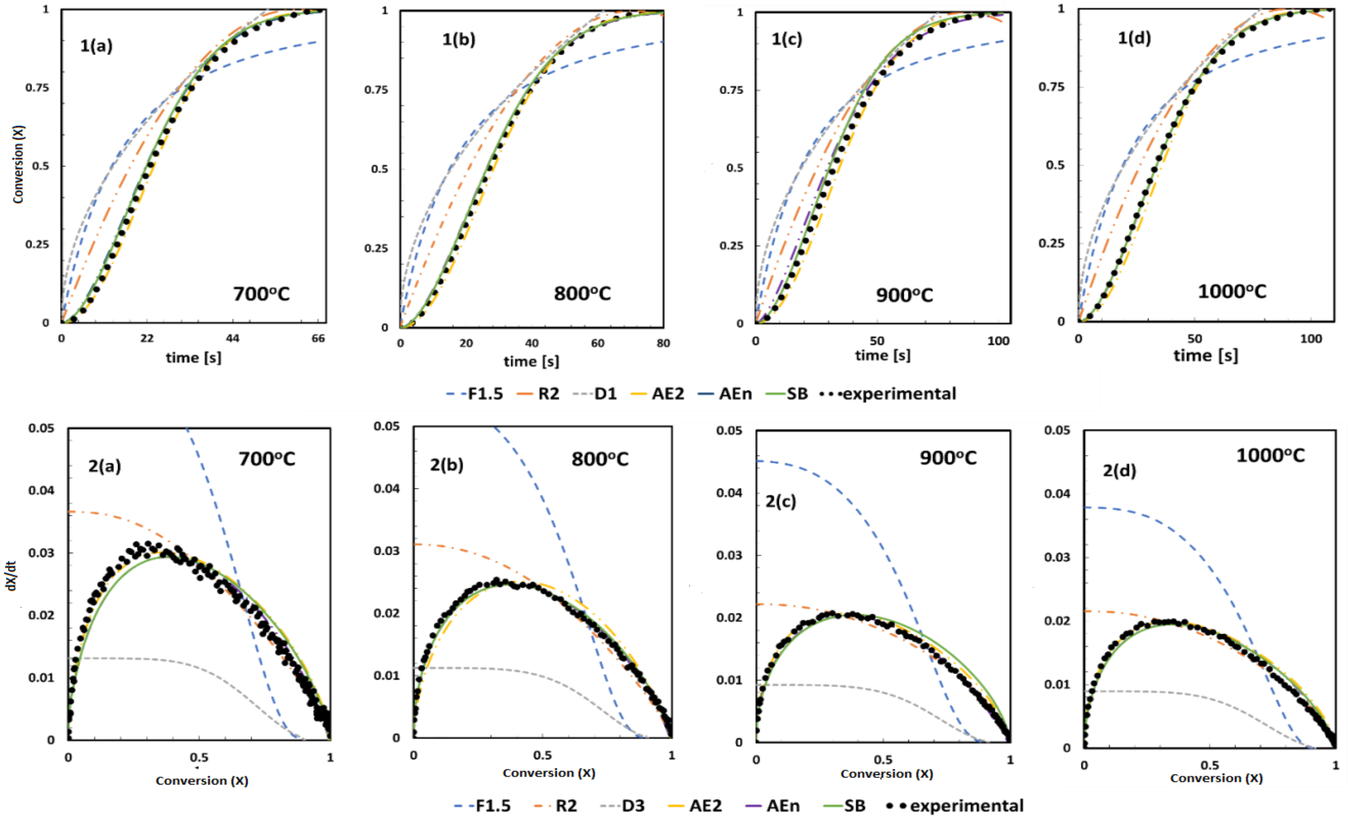

Figure 130. Comparison of X vs t between the experimental data and models with a concentration of 30% of CO_2 at different temperatures; 1(a) T=700°C, 1(b) T=800°C, 1(c) T=900°C, 1(d) T=1000°C; and dX/dt vs X between the experimental data and models with a concentration of 30% of CO_2 at different temperatures; 2(a) T=700°C, 2(b) T=800°C, 2(c) T=900°C, 2(d) T=1000°C.

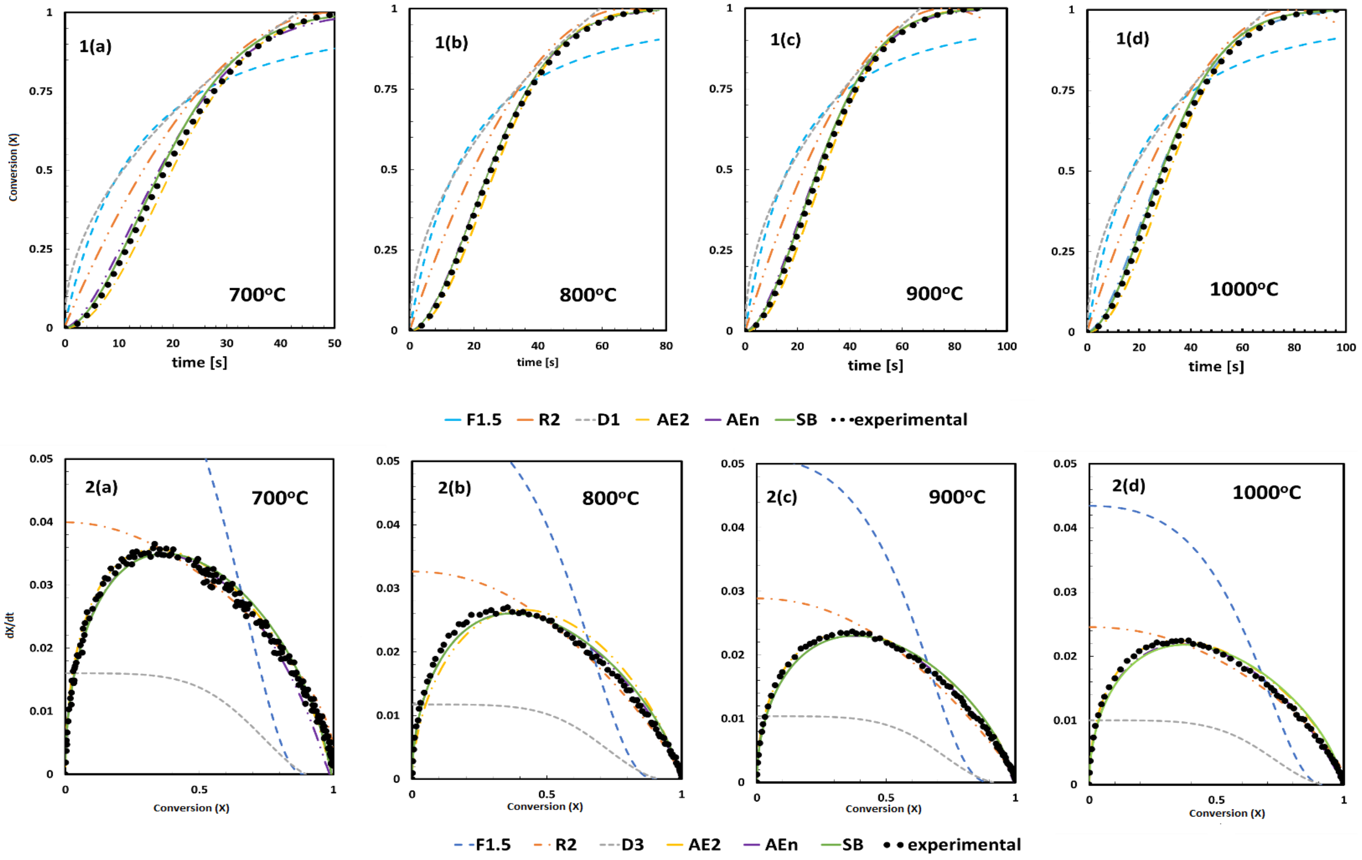

Figure 131. Comparison of X vs t between the experimental data and models with a concentration of 40% of CO_2 at different temperatures; 1(a) T=700°C, 1(b) T=800°C, 1(c) T=900°C, 1(d) T=1000°C; and dX/dt vs X between the experimental data and models with a concentration of 20% of CO_2 at different temperatures; 2(a) T=700°C, 2(b) T=800°C, 2(c) T=900°C, 2(d) T=1000°C.

A.3.2 Assessment of methane reduction and oxidation of CO_2 oxidation of non-stoichiometric ceria

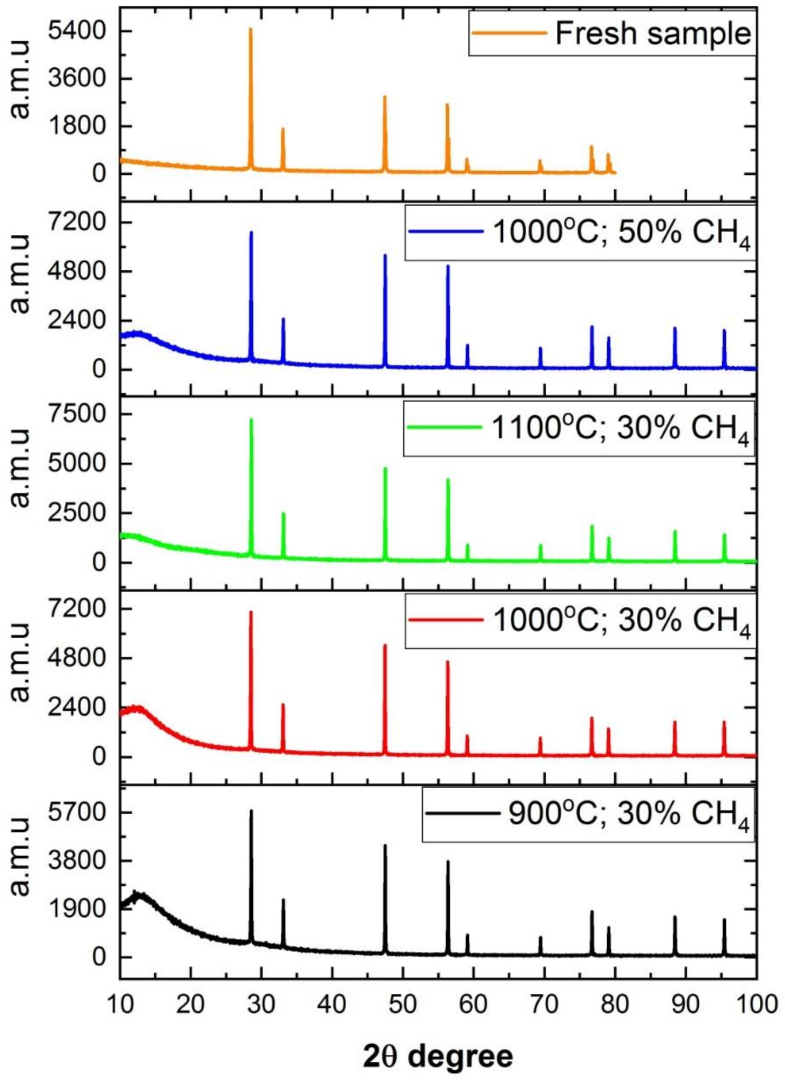

Figure 132. XRD images of fresh and used samples of ceria with methane reduction at different temperatures and concentration.

References

[1] I.E.A. IEA, Global Energy & CO2 Status Report 2017, 2018. https://www.iea.org/publications/freepublications/publication/GECO2017.pdf.

[2] IPCC, Foreword, Preface, Dedication and In Memoriam, Clim. Chang. 2014 Mitig. Clim. Chang. Contrib. Work. Gr. III to Fifth Assess. Rep. Intergov. Panel Clim. Chang. (2014) 1454. doi:10.1017/CBO9781107415416.

[3] BP Energy Economics, 2018 BP Energy Outlook 2018 BP Energy Outlook, 2018. doi:10.1088/1757-899X/342/1/012091.

[4] IPCC, IPCC special report on global warming of 1.5oC, 2019.

[5] G. Liu, J.A. Sorensen, J.R. Braunberger, R. Klenner, J. Ge, C.D. Gorecki, E.N. Steadman, J.A. Harju, CO2-Based Enhanced Oil Recovery from Unconventional Reservoirs: A Case Study of the Bakken Formation, SPE Unconv. Resour. Conf. (2014) 7. doi:10.2118/168979-MS.

[6] P.L. Spath, D.C. Dayton, Preliminary Screening -- Technical and Economic Assessment of Synthesis Gas to Fuels and Chemicals with Emphasis on the Potential for Biomass-Derived Syngas, 2003. doi:10.2172/15006100.

[7] D.R. Simbeck, A.D. Karp, R.L. Dickenson, Syngas production for gas-to-liquids applications: Technologies, issues and outlook., 1998. https://web.anl.gov/PCS/acsfuel/preprint archive/Files/Merge/Vol-45_1-0003.pdf.

[8] E.J. Sheu, E.M.A. Mokheimer, A.F. Ghoniem, A review of solar methane reforming systems, Int. J. Hydrogen Energy. 40 (2015) 12929–12955. doi:https://doi.org/10.1016/j.ijhydene.2015.08.005.

[9] B. Bulfin, J. Vieten, C. Agrafiotis, M. Roeb, C. Sattler, Applications and limitations of two step metal oxide thermochemical redox cycles; A review, J. Mater. Chem. A. 5 (2017) 18951–18966. doi:10.1039/c7ta05025a.

[10] C. Graves, S.D. Ebbesen, M. Mogensen, K.S. Lackner, Sustainable hydrocarbon fuels by recycling CO2 and H2O with renewable or nuclear energy, Renew. Sustain. Energy Rev. 15 (2011) 1–23. doi:10.1016/j.rser.2010.07.014.

[11] A.G. Konstandopoulos, C. Pagkoura, D. Dimitrakis, S. Lorentzou, G. Karagiannakis, Solar hydrogen production, in: Prod. Hydrog. from Renew. Resour., 2015: pp. 283–311.

[12] R.J. Detz, J.N.H. Reek, B.C.C. Van Der Zwaan, The future of solar fuels: When could they become competitive?, Energy Environ. Sci. 11 (2018) 1653–1669. doi:10.1039/c8ee00111a.

[13] S.E. Hosseini, M.A. Wahid, Hydrogen production from renewable and sustainable energy resources: Promising green energy carrier for clean development, Renew. Sustain. Energy Rev. 57 (2016) 850–866. doi:10.1016/j.rser.2015.12.112.

[14] R.G. Lemus, J.M. Mart?nez Duart, Updated hydrogen production costs and parities for conventional and renewable technologies, Int. J. Hydrogen Energy. 35 (2010) 3929–3936. doi:10.1016/j.ijhydene.2010.02.034.

[15] M. Ruth, M. Laffen, T. Timbario, Hydrogen Pathways: Cost, Well-to-Wheels Energy Use, and Emissions for the Current Technology Status of Seven Hydrogen Production, Delivery, and Distribution Scenarios, DoE EERE. (2009). doi:10.2172/1107463.

[16] Dimitrios A. Dimitrakis, Thermochemical Water and Carbon Dioxide Redox Splitting for Neutral Carbon Footprint Solar Fuels: From Material to Reactor, Aristotle University of Thessaloniki, 2017.

[17] J.H. Montoya, L.C. Seitz, P. Chakthranont, A. Vojvodic, T.F. Jaramillo, J.K. Nørskov, Materials for solar fuels and chemicals, Nat. Mater. 16 (2016) 70–81. doi:10.1038/nmat4778.

[18] H.L. Tuller, Solar to fuels conversion technologies: A perspective, Mater. Renew. Sustain. Energy. 6 (2017) 1–16. doi:10.1007/s40243-017-0088-2.

[19] V.N. Nguyen, L. Blum, Syngas and synfuels from H2O and CO2: Current status, Chemie-Ingenieur-Technik. 87 (2015) 354–375. doi:10.1002/cite.201400090.

[20] C. Agrafiotis, M. Roeb, A.G. Konstandopoulos, L. Nalbandian, V.T. Zaspalis, C. Sattler, P. Stobbe, A.M. Steele, Solar water splitting for hydrogen production with monolithic reactors, Sol. Energy. 79 (2005) 409–421. doi:10.1016/j.solener.2005.02.026.

[21] S. Tescari, C. Agrafiotis, S. Breuer, L. De Oliveira, M. Neises-Von Puttkamer, M. Roeb, C. Sattler, Thermochemical solar energy storage via redox oxides: Materials and reactor/heat exchanger concepts, Energy Procedia. 49 (2013) 1034–1043. doi:10.1016/j.egypro.2014.03.111.

[22] C. Agrafiotis, M. Roeb, C. Sattler, A review on solar thermal syngas production via redox pair-based water/carbon dioxide splitting thermochemical cycles, Renew. Sustain. Energy Rev. 42 (2015) 254–285. doi:10.1016/j.rser.2014.09.039.

[23] A. Steinfeld, Solar thermochemical production of hydrogen - A review, Sol. Energy. 78 (2005) 603–615. doi:10.1016/j.solener.2003.12.012.

[24] D. Yadav, R. Banerjee, A review of solar thermochemical processes, Renew. Sustain. Energy Rev. 54 (2016) 497–532. doi:10.1016/j.rser.2015.10.026.

[25] Y. Zhang, Q. Zhu, X. Lin, Z. Xu, J. Liu, Z. Wang, J. Zhou, K. Cen, A novel thermochemical cycle for the dissociation of CO2and H2O using sustainable energy sources, Appl. Energy. 108 (2013) 1–7. doi:10.1016/j.apenergy.2013.03.019.

[26] J.R. Scheffe, M. Welte, A. Steinfeld, Thermal Reduction of Ceria within an Aerosol Reactor for H_2O and CO_2 Splitting, Ind. Eng. Chem. Res. 53 (2014) 2175–2182. doi:10.1021/ie402620k.

[27] E. Alonso, M. Romero, Review of experimental investigation on directly irradiated particles solar reactors, Renew. Sustain. Energy Rev. 41 (2015) 53–67. doi:10.1016/j.rser.2014.08.027.

[28] K.J. Albrecht, G.S. Jackson, R.J. Braun, Evaluating thermodynamic performance limits of thermochemical energy storage subsystems using reactive perovskite oxide particles for concentrating solar power, Sol. Energy. 167 (2018) 179–193. doi:10.1016/j.solener.2018.03.078.

[29] J.R. Scheffe, A. Steinfeld, Thermodynamic analysis of cerium-based oxides for solar thermochemical fuel production, Energy and Fuels. 26 (2012) 1928–1936. doi:10.1021/ef201875v.

[30] B.D. Ehrhart, C.L. Muhich, I. Al-Shankiti, A.W. Weimer, System efficiency for two-step metal oxide solar thermochemical hydrogen production – Part 1: Thermodynamic model and impact of oxidation kinetics, Int. J. Hydrogen Energy. 41 (2016) 19881–19893. doi:10.1016/j.ijhydene.2016.07.109.

[31] S. Brendelberger, H. von Storch, B. Bulfin, C. Sattler, Vacuum pumping options for application in solar thermochemical redox cycles – Assessment of mechanical-, jet- and thermochemical pumping systems, Sol. Energy. 141 (2017) 91–102. doi:10.1016/j.solener.2016.11.023.

[32] B.D. Ehrhart, C.L. Muhich, I. Al-Shankiti, A.W. Weimer, System efficiency for two-step metal oxide solar thermochemical hydrogen production – Part 3: Various methods for achieving low oxygen partial pressures in the reduction reaction, Int. J. Hydrogen Energy. 41 (2016) 19904–19914. doi:10.1016/j.ijhydene.2016.07.106.

[33] I. Ermanoski, J. Grobbel, A. Singh, J. Lapp, S. Brendelberger, M. Roeb, C. Sattler, J. Whaley, A. McDaniel, N.P. Siegel, Design and construction of a cascading pressure reactor prototype for solar-thermochemical hydrogen production, AIP Conf. Proc. 1734 (2016). doi:10.1063/1.4949203.

[34] S. Lorentzou, C. Pagkoura, A. Zygogianni, G. Karagiannakis, A.G. Konstandopoulos, Thermochemical cycles over redox structured reactors, Int. J. Hydrogen Energy. 42 (2017) 19664–19682. doi:10.1016/j.ijhydene.2017.06.109.

[35] I. Ermanoski, N.P. Siegel, E.B. Stechel, A New Reactor Concept for Efficient Solar-Thermochemical Fuel Production, J. Sol. Energy Eng. 135 (2013) 031002. doi:10.1115/1.4023356.

[36] B. Wei, A Novel Solar-Driven System for Two-Step Conversion of CO2 with Ceria-Based Catalysts, KTH Royal Institute of Technology, Stockholm, 2014.

[37] K. Otsuka, E. Sunada, T. Ushiyama, I. Yamanaka, The production of synthesis gas by the redox of cerium oxide, in: M. de Pontes, R.L. Espinoza, C.P. Nicolaides, J.H. Scholtz, M.S.B.T.-S. in S.S. and C. Scurrell (Eds.), Nat. Gas Convers. IV, Elsevier, 1997: pp. 531–536. doi:https://doi.org/10.1016/S0167-2991(97)80386-2.

[38] Z. Zhao, Redox kinetics study for chemical looping combustion, water and CO2 splitting using nickel and cerium based oxygen carrier, Massachusetts institute of technology, 2016.

[39] K. Randhir, N.R. Rhodes, L. Li, N. AuYeung, D.W. Hahn, R. Mei, J.F. Klausner, Magnesioferrites for solar thermochemical fuel production, Sol. Energy. 163 (2018) 1–15. doi:10.1016/j.solener.2017.12.006.

[40] K. Saravanan, H. Ham, N. Tsubaki, J.W. Bae, Recent progress for direct synthesis of dimethyl

ether from syngas on the heterogeneous bifunctional hybrid catalysts, Appl. Catal. B Environ. 217 (2017) 494–522. doi:10.1016/j.apcatb.2017.05.085.

[41] S.C. Bayham, A. Tong, M. Kathe, L.-S. Fan, Chemical looping technology for energy and chemical production, Wiley Interdiscip. Rev. Energy Environ. 5 (2016) 216–241. doi:10.1002/wene.173.

[42] Q. Jiang, G. Zhou, Z. Jiang, C. Li, Thermochemical CO2 splitting reaction with CexM1-xO2-δ (M=Ti4+, Sn4+, Hf4+, Zr4+, La3+, Y3+ and Sm3+) solid solutions, Sol. Energy. 99 (2014) 55–66. doi:10.1016/j.solener.2013.10.021.

[43] Z. Hui, G. Nicolas, V. Franc, P. Miche, Preparation and electrical properties of a pyrochlore-related, 160 (2003) 317–326. doi:10.1016/S0167-2738(03)00207-8.

[44] Global CCS Institute, The Global Status of CCS: 2017, (2017) 43. doi:978-0-9944115-2-5.

[45] D.Y.C. Leung, G. Caramanna, M.M. Maroto-Valer, An overview of current status of carbon dioxide capture and storage technologies, Renew. Sustain. Energy Rev. 39 (2014) 426–443. doi:10.1016/j.rser.2014.07.093.

[46] T.C. Merkel, H. Lin, X. Wei, R. Baker, Power plant post-combustion carbon dioxide capture: An opportunity for membranes, J. Memb. Sci. 359 (2010) 126–139. doi:10.1016/j.memsci.2009.10.041.

[47] P. Chiesa, G. Lozza, A. Malandrino, M. Romano, V. Piccolo, Three-reactors chemical looping process for hydrogen production, Int. J. Hydrogen Energy. 33 (2008) 2233–2245. doi:10.1016/j.ijhydene.2008.02.032.

[48] IEA, Energy Technology Analysis: Prospects for CO2 Capture and Storage, (2004) 249. doi:10.1016/B978-1-85617-710-8.00010-8.

[49] M. Wang, A. Lawal, P. Stephenson, J. Sidders, C. Ramshaw, Post-combustion CO2 capture with chemical absorption: A state-of-the-art review, Chem. Eng. Res. Des. 89 (2011) 1609–1624. doi:10.1016/j.cherd.2010.11.005.

[50] B.J.P. Buhre, L.K. Elliott, C.D. Sheng, R.P. Gupta, T.F. Wall, Oxy-fuel combustion technology for coal-fired power generation, Prog. Energy Combust. Sci. 31 (2005) 283–307. doi:10.1016/j.pecs.2005.07.001.

[51] M.A. Habib, M. Nemitallah, R. Ben-Mansour, Recent development in oxy-combustion technology and its applications to gas turbine combustors and ITM reactors, Energy and Fuels. 27 (2013) 2–19. doi:10.1021/ef301266j.

[52] I. Pfaff, A. Kather, Comparative thermodynamic analysis and integration issues of CCS steam power plants based on oxy-combustion with cryogenic or membrane based air separation, Energy Procedia. 1 (2009) 495–502. doi:10.1016/j.egypro.2009.01.066.

[53] T. Lockwood, Developments in oxyfuel combustion of coal, IEA Clean Coal Centre, CCC/240, London, United Kingdom. (2014) 1–122.

[54] M. Chorowski, W. Gizicki, Technical and economic aspects of oxygen separation for oxy-fuel purposes, Arch. Thermodyn. 36 (2015) 157–170. doi:10.1515/aoter-2015-0011.

[55] M. Nemitallah, M. Habib, H. Badr, S. Said, J. Aqil, B. Rached, E.M. Mokheimer, khaled Mezghani, Oxy-fuel combustion technology: current status, applications, and trends, Int. J. Energy Res. 41 (2017) 1670–1708. doi:10.1002/er.3722.

[56] White Rose project, (n.d.). http://www.zeroco2.no/projects/developers/alstom (accessed March 1, 2018).

[57] W. Xiuzhang, Shenhua Group's carbon capture and storage (CCS) demonstration, Min. Rep. 150 (2014) 81–84. doi:10.1002/mire.201400006.

[58] R.J. Allam, M.R. Palmer, G.W. Brown, J. Fetvedt, D. Freed, H. Nomoto, M. Itoh, N. Okita, C. Jones, High efficiency and low cost of electricity generation from fossil fuels while eliminating atmospheric emissions, including carbon dioxide, Energy Procedia. 37 (2013) 1135–1149. doi:10.1016/j.egypro.2013.05.211.

[59] R. Anderson, H. Brandt, S. Doyle, F. Viteri, A demonstrated 20 MWt gas generator for a clean steam power plant, in: 28th Int. Tech. Conf. Coal Util. Fuel Syst., 2003: p. 916.

[60] R. Stanger, T. Wall, R. Spörl, M. Paneru, S. Grathwohl, M. Weidmann, G. Scheffknecht, D. McDonald, K. Myöhänen, J. Ritvanen, Oxyfuel combustion for CO2 capture in power plants, Int. J. Greenh. Gas Control. 40 (2015) 55–125. doi:http://dx.doi.org/10.1016/j.ijggc.2015.06.010.

[61] N. MacDowell, N. Florin, A. Buchard, J. Hallett, A. Galindo, G. Jackson, C.S. Adjiman, C.K. Williams, N. Shah, P. Fennell, An overview of CO2 capture technologies, Energy Environ. Sci.

3 (2010) 1645. doi:10.1039/c004106h.

[62] D.Y.C. Leung, G. Caramanna, M.M. Maroto-Valer, An overview of current status of carbon dioxide capture and storage technologies, Renew. Sustain. Energy Rev. 39 (2014) 426–443. doi:10.1016/j.rser.2014.07.093.

[63] B. Metz, D. Ogunlade, de C. Heleen, L. Manuela, M. (eds.). Leo, IPCC, 2005: IPCC Special Report on Carbon Dioxide Capture and Storage. Prepared by working Group III of the Intergovernmental Panel on Climate Change, 2005.

[64] B. Van Der Zwaan, K. Smekens, CO2 capture and storage with leakage in an energy-climate model, Environ. Model. Assess. 14 (2009) 135–148. doi:10.1007/s10666-007-9125-3.

[65] C. Doughty, B.M. Freifeld, R.C. Trautz, Site characterization for CO2 geologic storage and vice versa: The Frio brine pilot, Texas, USA as a case study, Environ. Geol. 54 (2008) 1635–1656. doi:10.1007/s00254-007-0942-0.

[66] K.Z. House, D.P. Schrag, C.F. Harvey, K.S. Lackner, Permanent carbon dioxide storage in deep-sea sediments, Proc. Natl. Acad. Sci. 103 (2006) 12291–12295. doi:10.1073/pnas.0605318103.

[67] C.R. Jenkins, P.J. Cook, J. Ennis-King, J. Undershultz, C. Boreham, T. Dance, P. de Caritat, D.M. Etheridge, B.M. Freifeld, A. Hortle, D. Kirste, L. Paterson, R. Pevzner, U. Schacht, S. Sharma, L. Stalker, M. Urosevic, Safe storage and effective monitoring of CO2 in depleted gas fields, Proc. Natl. Acad. Sci. 109 (2012) E35–E41. doi:10.1073/pnas.1107255108.

[68] M.D. Zoback, S.M. Gorelick, Earthquake triggering and large-scale geologic storage of carbon dioxide, Proc. Natl. Acad. Sci. 109 (2012) 10164–10168. doi:10.1073/pnas.1202473109.

[69] Z. Yuan, M.R. Eden, R. Gani, Toward the Development and Deployment of Large-Scale Carbon Dioxide Capture and Conversion Processes, Ind. Eng. Chem. Res. 55 (2016) 3383–3419. doi:10.1021/acs.iecr.5b03277.

[70] Q.E. Alessandra, C. Gabriele, D. Jean-Luc, P. Siglinda, Carbon Dioxide Recycling: Emerging Large-Scale Technologies with Industrial Potential, ChemSusChem. 4 (2011) 1194–1215. doi:10.1002/cssc.201100473.

[71] J.M. Tour, C. Kittrell, V.L. Colvin, Green carbon as a bridge to renewable energy, Nat. Mater. 9 (2010) 871. http://dx.doi.org/10.1038/nmat2887.

[72] R.M. Cuéllar-Franca, A. Azapagic, Carbon capture, storage and utilisation technologies: A critical analysis and comparison of their life cycle environmental impacts, J. CO2 Util. 9 (2015) 82–102. doi:10.1016/j.jcou.2014.12.001.

[73] C.H. Huang, C.S. Tan, A review: CO2 utilization, Aerosol Air Qual. Res. 14 (2014) 480–499. doi:10.4209/aaqr.2013.10.0326.

[74] M. Aresta, Carbon Dioxide: Utilization Options to Reduce its Accumulation in the Atmosphere, Carbon Dioxide as Chem. Feed. (2010) 1–13. doi:10.1002/9783527629916.ch1.

[75] C. Song, Global challenges and strategies for control, conversion and utilization of CO2 for sustainable development involving energy, catalysis, adsorption and chemical processing, Catal. Today. 115 (2006) 2–32. doi:10.1016/j.cattod.2006.02.029.

[76] N. von der Assen, J. Jung, A. Bardow, Life-cycle assessment of carbon dioxide capture and utilization: avoiding the pitfalls, Energy Environ. Sci. 6 (2013) 2721–2734. doi:10.1039/C3EE41151F.

[77] M. Peters, B. Köhler, W. Kuckshinrichs, W. Leitner, P. Markewitz, T.E. Müller, Chemical technologies for exploiting and recycling carbon dioxide into the value chain, ChemSusChem. 4 (2011) 1216–1240. doi:10.1002/cssc.201000447.

[78] V. Spallina, A. Shams, A. Battistella, F. Gallucci, M.V.S. Annaland, Chemical Looping Technologies for H2 Production with CO2 Capture: Thermodynamic Assessment and Economic Comparison, Energy Procedia. 114 (2017) 419–428. doi:10.1016/j.egypro.2017.03.1184.

[79] A.J. Traynor, R.J. Jensen, Direct Solar Reduction of CO2 to Fuel: First Prototype Results, Ind. Eng. Chem. Res. 41 (2002) 1935–1939. doi:10.1021/ie010871x.

[80] Y. Nigara, B. Cales, Production of carbon monoxide by direct thermal splitting of carbon dioxide at high temperature, Bull. Chem. Soc. Jpn. 59 (1986) 1997–2002. doi:10.1246/bcsj.59.1997.

[81] J.L. Lyman, R.J. Jensen, Chemical reactions occurring during direct solar reduction of CO2, Sci. Total Environ. 277 (2001) 7–14. doi:10.1016/S0048-9697(01)00829-4.

[82] R. Sadeghbeigi, Fluid catalytic cracking handbook: An Expert Guide to the Practical Operation, Design, and Optimization ofFCC Unit, 3rd ed., Butterworth-Heinemann, 2012. doi:10.1016/B978-0-12-386965-4.X0001-8.

[83] M. Tang, L. Xu, M. Fan, Progress in oxygen carrier development of methane-based chemical-

looping reforming: A review, Appl. Energy. 151 (2015) 143–156. doi:10.1016/j.apenergy.2015.04.017.

[84] N. Dilmaç, Ö.F. Dilmaç, E. Yardımcı, Utilization of Menteş iron ore as oxygen carrier in Chemical-Looping Combustion, Energy. 138 (2017) 785–798. doi:10.1016/j.energy.2017.07.126.

[85] P.T. Krenzke, J.H. Davidson, Thermodynamic analysis of syngas production via the solar thermochemical cerium oxide redox cycle with methane-driven reduction, Energy and Fuels. 28 (2014) 4088–4095. doi:10.1021/ef500610n.

[86] M. Welte, K. Warren, J.R. Scheffe, A. Steinfeld, Combined Ceria Reduction and Methane Reforming in a Solar-Driven Particle-Transport Reactor, Ind. Eng. Chem. Res. 56 (2017) 10300–10308. doi:10.1021/acs.iecr.7b02738.

[87] K.J. Warren, J.R. Scheffe, Kinetic insights into the reduction of ceria facilitated via the partial oxidation of methane, Mater. Today Energy. 9 (2018) 39–48. doi:10.1016/j.mtener.2018.05.001.

[88] S. Bhavsar, G. Veser, Chemical looping beyond combustion : production of synthesis gas via chemical looping partial oxidation of methane, RSC Adv. 4 (2014) 47254–47267. doi:10.1039/c4ra06437b.

[89] G.P. Smestad, A. Steinfeld, Review: Photochemical and thermochemical production of solar fuels from H2O and CO2 using metal oxide catalysts, Ind. Eng. Chem. Res. 51 (2012) 11828–11840. doi:10.1021/ie3007962.

[90] I. Vishnevetsky, A. Berman, M. Epstein, Features of solar thermochemical redox cycles for hydrogen production from water as a function of reactants' main characteristics, Int. J. Hydrogen Energy. 36 (2011) 2817–2830. doi:10.1016/j.ijhydene.2010.11.027.

[91] R.J. Carrillo, J.R. Scheffe, Advances and trends in redox materials for solar thermochemical fuel production, Sol. Energy. 156 (2017) 3–20. doi:10.1016/j.solener.2017.05.032.

[92] L. Gael, A. Stéphane, J. Jumas, J. Olivier-fourcade, Characterization of Two-Step Tin-Based Redox System for Thermochemical Fuel Production from Solar-Driven CO2 and H2O Splitting Cycle, Ind. Eng. Chem. 53 (2014) 5668–5677.

[93] Y. Zhang, T. Nie, Z. Wang, J. Liu, J. Zhou, K. Cen, Splitting of CO2 via the Heterogeneous Oxidation of Zinc Powder in Thermochemical Cycles, Ind. Eng. Chem. Res. 55 (2016) 534–542. doi:10.1021/acs.iecr.5b02407.

[94] P. Furler, J.R. Scheffe, D. Marxer, A. Steinfeld, Solar reactors for thermochemical CO2 and H2O splitting via metal oxide redox reactions, in: SFERA II SUMMER Sch. Odeillo , Fr. Fr., 2014. https://sfera2.sollab.eu/uploads/images/networking/SFERA SUMMER SCHOOL 2014 - PRESENTATIONS/Solar Reactor Reduction - Philipp FURLER.pdf.

[95] U.W. Hartley, N. Ngoenthong, K. Cheenkachorn, T. Sornchamni, CO2 to Syngas: Metal Oxides on Stainless Steel 316L for micro- channel reactor application, in: Int. Conf. Chem. Biochem. Eng. Paris (France), 20-22 July 2015, 2015: pp. 8–11. https://www.researchgate.net/profile/Mahdi_Belguidoum/publication/289540155_AbstractsBook_ICCBE2015/links/5690232b08aec14fa557e115/AbstractsBook-ICCBE2015.pdf.

[96] Q. Jiang, Z. Chen, J. Tong, M. Yang, Z. Jiang, C. Li, Catalytic Function of IrOxin the Two-Step Thermochemical CO2-Splitting Reaction at High Temperatures, ACS Catal. 6 (2016) 1172–1180. doi:10.1021/acscatal.5b01774.

[97] N. Gokon, T. Suda, T. Kodama, Oxygen and hydrogen productivities and repeatable reactivity of 30-mol%-Fe-, Co-, Ni-, Mn-doped CeO2-δfor thermochemical two-step water-splitting cycle, Energy. 90 (2015) 1280–1289. doi:10.1016/j.energy.2015.06.085.

[98] T. Nakamura, Hydrogen production from water utilizing solar heat at high temperatures, Sol. Energy. 19 (1977) 467–475. doi:10.1016/0038-092X(77)90102-5.

[99] M. Roeb, C. Sattler, R. Klüser, N. Monnerie, L. de Oliveira, A.G. Konstandopoulos, C. Agrafiotis, V.T. Zaspalis, L. Nalbandian, A. Steele, P. Stobbe, Solar Hydrogen Production by a Two-Step Cycle Based on Mixed Iron Oxides, J. Sol. Energy Eng. 128 (2006) 125. doi:10.1115/1.2183804.

[100] L.S. Darken, R.W. Gurry, The System Iron-Oxygen. II. Equilibrium and Thermodynamics of Liquid Oxide and Other Phases, J. Am. Chem. Soc. 68 (1946) 798–816. doi:10.1021/ja01209a030.

[101] M. Roeb, M. Neises, N. Monnerie, F. Call, H. Simon, C. Sattler, M. Schm??cker, R. Pitz-Paal, Materials-related aspects of thermochemical water and carbon dioxide splitting: A review, Materials (Basel). 5 (2012) 2015–2054. doi:10.3390/ma5112015.

[102] F.X. Chiron, G.S. Patience, Kinetics of mixed copper-iron based oxygen carriers for hydrogen production by chemical looping water splitting, Int. J. Hydrogen Energy. 37 (2012) 10526–10538. doi:10.1016/j.ijhydene.2012.04.052.

[103] W. Liu, J.Y. Lim, M.A. Saucedo, A.N. Hayhurst, S.A. Scott, J.S. Dennis, Kinetics of the reduction of wüstite by hydrogen and carbon monoxide for the chemical looping production of hydrogen, Chem. Eng. Sci. 120 (2014) 149–166. doi:10.1016/j.ces.2014.08.010.

[104] T. Kodama, N. Gokon, R. Yamamoto, Thermochemical two-step water splitting by ZrO2-supported NixFe3-xO4 for solar hydrogen production, Sol. Energy. 82 (2008) 73–79. doi:10.1016/j.solener.2007.03.005.

[105] F. Liu, Cerium oxide promoted oxygen carrier development and scale modeling study for chemical looping comustion, University of Kentucky, 2013. https://uknowledge.uky.edu/cgi/viewcontent.cgi?article=1029&context=me_etds.

[106] W.C. Chueh, S.M. Haile, A thermochemical study of ceria: Exploiting an old material for new modes of energy conversion and CO2 mitigation, Philos. Trans. R. Soc. A Math. Phys. Eng. Sci. 368 (2010) 3269–3294. doi:10.1098/rsta.2010.0114.

[107] S. Abanades, G. Flamant, Thermochemical hydrogen production from a two-step solar-driven water-splitting cycle based on cerium oxides, Sol. Energy. 80 (2006) 1611–1623. doi:10.1016/j.solener.2005.12.005.

[108] B. Bulfin, A.J. Lowe, K.A. Keogh, B.E. Murphy, O. Lübben, S.A. Krasnikov, I. V. Shvets, Analytical Model of CeO 2 Oxidation and Reduction, J. Phys. Chem. C. 117 (2013) 24129–24137. doi:10.1021/jp406578z.

[109] E.A. Kümmerle, G. Heger, The Structures of C-Ce2O3+δ, Ce7O12, and Ce11O20, J. Solid State Chem. 147 (1999) 485–500. doi:10.1006/jssc.1999.8403.

[110] B. Bulfin, L. Hoffmann, L. De Oliveira, N. Knoblauch, F. Call, M. Roeb, C. Sattler, M. Schmücker, Statistical thermodynamics of non-stoichiometric ceria and ceria zirconia solid solutions, Phys. Chem. Chem. Phys. 18 (2016) 23147–23154. doi:10.1039/c6cp03158g.

[111] N. Knoblauch, H. Simon, M. Schmücker, Chemically induced volume change of CeO2 − δand nonstoichiometric phases, Solid State Ionics. 301 (2017) 43–52. doi:10.1016/j.ssi.2017.01.003.

[112] N. Gokon, S. Sagawa, T. Kodama, Comparative study of activity of cerium oxide at thermal reduction temperatures of 1300-1550 C for solar thermochemical two-step water-splitting cycle, Int. J. Hydrogen Energy. 38 (2013) 14402–14414. doi:10.1016/j.ijhydene.2013.08.108.

[113] S. Abanades, A. Legal, A. Cordier, G. Peraudeau, G. Flamant, A. Julbe, Investigation of reactive cerium-based oxides for H2 production by thermochemical two-step water-splitting, J. Mater. Sci. 45 (2010) 4163–4173. doi:10.1007/s10853-010-4506-4.

[114] A. Le Gal, S. Abanades, Catalytic investigation of ceria-zirconia solid solutions for solar hydrogen production, Int. J. Hydrogen Energy. 36 (2011) 4739–4748. doi:10.1016/j.ijhydene.2011.01.078.

[115] J.R. Scheffe, A. Steinfeld, Thermodynamic analysis of cerium-based oxides for solar thermochemical fuel production, Energy and Fuels. 26 (2012) 1928–1936. doi:10.1021/ef201875v.

[116] K. Otsuka, M. Hatano, A. Morikawa, Decomposition of water by cerium oxide of δ-phase, Inorganica Chim. Acta. 109 (1985) 193–197. doi:https://doi.org/10.1016/S0020-1693(00)81768-5.

[117] R.J. Panlener, R.N. Blumenthal, J.E. Garnier, A thermodynamic study of nonstoichiometric cerium dioxide, J. Phys. Chem. Solids. 36 (1975) 1213–1222. doi:https://doi.org/10.1016/0022-3697(75)90192-4.

[118] M. Kang, X. Wu, J. Zhang, N. Zhao, W. Wei, Y. Sun, Enhanced thermochemical CO2splitting over Mg- and Ca-doped ceria/zirconia solid solutions, RSC Adv. 4 (2014) 5583–5590. doi:10.1039/c3ra45595e.

[119] A. Le Gal, S. Abanades, G. Flamant, CO2 and H2O Splitting for Thermochemical Production of Solar Fuels Using Nonstoichiometric Ceria and Ceria/Zirconia Solid Solutions, Energy & Fuels. 25 (2011) 4836–4845. doi:10.1021/ef200972r.

[120] P. Singh, M.S. Hegde, Ce0.67Cr0.33O2.11: A New Low-Temperature O2 Evolution Material and H2 Generation Catalyst by Thermochemical Splitting of Water, Chem. Mater. 22 (2010) 762–768. doi:10.1021/cm9013305.

[121] J.R. Scheffe, R. Jacot, G.R. Patzke, A. Steinfeld, Synthesis, Characterization, and Thermochemical Redox Performance of Hf4+, Zr4+, and Sc3+ Doped Ceria for Splitting CO2,

J. Phys. Chem. C. 117 (2013) 24104–24114. doi:10.1021/jp4050572.

[122] S. Ihara, On the study of hydrogen production from water using solar thermal energy, Int. J. Hydrogen Energy. 5 (1980) 527–534. doi:https://doi.org/10.1016/0360-3199(80)90059-2.

[123] A. Le Gal, S. Abanades, Catalytic investigation of ceria-zirconia solid solutions for solar hydrogen production, Int. J. Hydrogen Energy. 36 (2011) 4739–4748. doi:https://doi.org/10.1016/j.ijhydene.2011.01.078.

[124] A. Le Gal, S. Abanades, Dopant Incorporation in Ceria for Enhanced Water-Splitting Activity during Solar Thermochemical Hydrogen Generation, J. Phys. Chem. C. 116 (2012) 13516–13523. doi:10.1021/jp302146c.

[125] Y. Hao, C.K. Yang, S.M. Haile, High-temperature isothermal chemical cycling for solar-driven fuel production, Phys. Chem. Chem. Phys. 15 (2013) 17084–17092. doi:10.1039/c3cp53270d.

[126] Q. Jiang, G. Zhou, Z. Jiang, C. Li, Thermochemical CO2 splitting reaction with CexM1-xO2-δ (M=Ti4+, Sn4+, Hf4+, Zr4+, La3+, Y3+ and Sm3+) solid solutions, Sol. Energy. 99 (2014) 55–66. doi:10.1016/j.solener.2013.10.021.

[127] G.D. Takalkar, R.R. Bhosale, A. Kumar, F. AlMomani, M. Khraisheh, R.A. Shakoor, R.B. Gupta, Transition metal doped ceria for solar thermochemical fuel production, Sol. Energy. 172 (2018) 204–211. doi:https://doi.org/10.1016/j.solener.2018.03.022.

[128] G. Voitic, V. Hacker, Recent advancements in chemical looping water splitting for the production of hydrogen, RSC Adv. 6 (2016) 98267–98296. doi:10.1039/C6RA21180A.

[129] Q. Jiang, J. Tong, G. Zhou, Z. Jiang, Z. Li, C. Li, Thermochemical CO2 splitting reaction with supported LaxA1−xFeyB1−yO3 (A=Sr, Ce, B=Co, Mn; 0□x, y□1) perovskite oxides, Sol. Energy. 103 (2014) 425–437. doi:https://doi.org/10.1016/j.solener.2014.02.033.

[130] C.K. Yang, Y. Yamazaki, A. Aydin, S.M. Haile, Thermodynamic and kinetic assessments of strontium-doped lanthanum manganite perovskites for two-step thermochemical water splitting, J. Mater. Chem. A. 2 (2014) 13612–13623. doi:10.1039/c4ta02694b.

[131] S. Dey, B.S. Naidu, A. Govindaraj, C.N.R. Rao, Noteworthy performance of $La_{1-x}Ca_xMnO_3$ perovskites in generating H_2 and CO by the thermochemical splitting of H_2O and CO_2, Phys. Chem. Chem. Phys. 17 (2015) 122–125. doi:10.1039/C4CP04578E.

[132] C.N.R. Rao, S. Dey, Generation of H2 and CO by solar thermochemical splitting of H2O and CO2 by employing metal oxides, J. Solid State Chem. 242 (2016) 107–115. doi:https://doi.org/10.1016/j.jssc.2015.12.018.

[133] A.H. McDaniel, E.C. Miller, D. Arifin, A. Ambrosini, E.N. Coker, R. O'Hayre, W.C. Chueh, J. Tong, Sr- and Mn-doped LaAlO3−δ for solar thermochemical H2 and CO production, Energy Environ. Sci. 6 (2013) 2424. doi:10.1039/c3ee41372a.

[134] M.E. Gálvez, R. Jacot, J. Scheffe, T. Cooper, G. Patzke, A. Steinfeld, Physico-chemical changes in Ca, Sr and Al-doped La-Mn-O perovskites upon thermochemical splitting of CO2 via redox cycling, Phys. Chem. Chem. Phys. 17 (2015) 6629–6634. doi:10.1039/c4cp05898d.

[135] A. Demont, S. Abanades, Solar thermochemical conversion of CO2 into fuel via two-step redox cycling of non-stoichiometric Mn-containing perovskite oxides, J. Mater. Chem. A. 3 (2015) 3536–3546. doi:10.1039/c4ta06655c.

[136] S. Dey, B.S. Naidu, C.N.R. Rao, Beneficial effects of substituting trivalent ions in the B-site of La0.5Sr0.5Mn1-xAxO3(A = Al, Ga, Sc) on the thermochemical generation of CO and H2from CO2and H2O, Dalt. Trans. 45 (2016) 2430–2435. doi:10.1039/c5dt04822b.

[137] A.H. McDaniel, A. Ambrosini, E.N. Coker, J.E. Miller, W.C. Chueh, R. O'Hayre, J. Tong, Nonstoichiometric perovskite oxides for solar thermochemical H2and CO production, Energy Procedia. 49 (2013) 2009–2018. doi:10.1016/j.egypro.2014.03.213.

[138] Q. Jiang, J. Tong, G. Zhou, Z. Jiang, Z. Li, C. Li, Thermochemical CO2 splitting reaction with supported LaxA1-xFeyB1-yO3 (A=Sr, Ce, B=Co, Mn; 0≤x, y≤1) perovskite oxides, Sol. Energy. 103 (2014) 425–437. doi:10.1016/j.solener.2014.02.033.

[139] N.L. Galinsky, Y. Huang, F. Li, Iron Oxide with Facilitated O2 − Transport for Facile Fuel Oxidation and CO2 Capture in a Chemical Looping Scheme, ACS Sustain. Chem. Eng. 1 (2013) 364–373. doi:10.1021/sc300177j.

[140] D.S. Mathew, R.S. Juang, An overview of the structure and magnetism of spinel ferrite nanoparticles and their synthesis in microemulsions, Chem. Eng. J. 129 (2007) 51–65. doi:10.1016/j.cej.2006.11.001.

[141] T.A.S. Ferreira, J.C. Waerenborgh, M.H.R.M. Mendonça, M.R. Nunes, F.M. Costa, Structural and morphological characterization of FeCo2O4 and CoFe2O4 spinels prepared by a

coprecipitation method, Solid State Sci. 5 (2003) 383–392. doi:10.1016/S1293-2558(03)00011-6.

[142] V.J. Aston, B.W. Evanko, A.W. Weimer, Investigation of novel mixed metal ferrites for pure H2 and CO2 production using chemical looping, Int. J. Hydrogen Energy. 38 (2013) 9085–9096. doi:10.1016/j.ijhydene.2013.05.078.

[143] S. Cocchi, M. Mari, F. Cavani, J.M.M. Millet, Chemical and physical behavior of CoFe2O4 in steam-iron process with methanol, Appl. Catal. B Environ. 152–153 (2014) 250–261. doi:10.1016/j.apcatb.2014.01.040.

[144] Different Types of Solar Concentrators-KTH Roya Institute of Technology Energy Department, (n.d.). http://energy.kth.se/compedu/webcompedu/webhelp/S9_Renewable_Energy/B5_Solar_Energy/C3_Advanced_Solar_Thermal/ID107_files/Different_Types_of_Solar_Concentrators.htm (accessed June 2, 2018).

[145] C.N.R. Rao, S. Dey, Solar thermochemical splitting of water to generate hydrogen, Proc. Natl. Acad. Sci. 2017 (2017) 201700104. doi:10.1073/pnas.1700104114.

[146] C.L. Muhich, B.D. Ehrhart, I. Al-Shankiti, B.J. Ward, C.B. Musgrave, A.W. Weimer, A review and perspective of efficient hydrogen generation via solar thermal water splitting, Wiley Interdiscip. Rev. Energy Environ. 5 (2016) 261–287. doi:10.1002/wene.174.

[147] N.P. Siegel, J.E. Miller, I. Ermanoski, R.B. Diver, E.B. Stechel, Factors affecting the efficiency of solar driven metal oxide thermochemical cycles, Ind. Eng. Chem. Res. 52 (2013) 3276–3286. doi:10.1021/ie400193q.

[148] W.C. Chueh, M. Abbott, D. Scipio, S.M. Haile, High-flux solar-driven thermochemical dissociation of CO2 and H2O using ceria redox reactions, Science (80-.). 63 (2010) 1797–1801. doi:10.1123/science.1197834.

[149] P. Furler, J.R. Scheffe, A. Steinfeld, Syngas production by simultaneous splitting of H2O and CO2via ceria redox reactions in a high-temperature solar reactor, Energy Environ. Sci. 5 (2012) 6098–6103. doi:10.1039/C1EE02620H.

[150] A. Houaijia, C. Sattler, M. Roeb, M. Lange, S. Breuer, J.P. Säck, Analysis and improvement of a high-efficiency solar cavity reactor design for a two-step thermochemical cycle for solar hydrogen production from water, Sol. Energy. 97 (2013) 26–38. doi:10.1016/j.solener.2013.07.032.

[151] M. Chambon, S. Abanades, G. Flamant, Thermal Dissociation of Compressed ZnO and SnO2 Powders in a Moving-Front Solar Thermochemical Reactor Marc, AIChE J. 57 (2011) 2264–2273. doi:10.1002/aic.

[152] R.B. Diver, J.E. Miller, M.D. Allendorf, N.P. Siegel, R.E. Hogan, Solar Thermochemical Water-Splitting Ferrite-Cycle Heat Engines, J. Sol. Energy Eng. 130 (2008) 041001. doi:10.1115/1.2969781.

[153] J. Kim, J.E. Miller, C.T. Maravelias, E.B. Stechel, Comparative analysis of environmental impact of S2P (Sunshine to Petrol) system for transportation fuel production, Appl. Energy. 111 (2013) 1089–1098. doi:10.1016/j.apenergy.2013.06.035.

[154] T. Melchior, C. Perkins, A.W. Weimer, A. Steinfeld, A cavity-receiver containing a tubular absorber for high-temperature thermochemical processing using concentrated solar energy, Int. J. Therm. Sci. 47 (2008) 1496–1503. doi:10.1016/j.ijthermalsci.2007.12.003.

[155] J. Martinek, R. Viger, A.W. Weimer, Transient simulation of a tubular packed bed solar receiver for hydrogen generation via metal oxide thermochemical cycles, Sol. Energy. 105 (2014) 613–631. doi:10.1016/j.solener.2014.04.022.

[156] M. Roeb, M. Neises, J.P. Säck, P. Rietbrock, N. Monnerie, J. Dersch, M. Schmitz, C. Sattler, Operational strategy of a two-step thermochemical process for solar hydrogen production, Int. J. Hydrogen Energy. 34 (2009) 4537–4545. doi:10.1016/j.ijhydene.2008.08.049.

[157] M. Roeb, J.P. Säck, P. Rietbrock, C. Prahl, H. Schreiber, M. Neises, L. de Oliveira, D. Graf, M. Ebert, W. Reinalter, M. Meyer-Grünefeldt, C. Sattler, A. Lopez, A. Vidal, A. Elsberg, P. Stobbe, D. Jones, A. Steele, S. Lorentzou, C. Pagkoura, A. Zygogianni, C. Agrafiotis, A.G. Konstandopoulos, Test operation of a 100kW pilot plant for solar hydrogen production from water on a solar tower, Sol. Energy. 85 (2011) 634–644. doi:10.1016/j.solener.2010.04.014.

[158] H. Kaneko, T. Miura, A. Fuse, H. Ishihara, S. Taku, H. Fukuzumi, Y. Naganuma, Y. Tamaura, Rotary-type solar reactor for solar hydrogen production with two-step water splitting process, Energy and Fuels. 21 (2007) 2287–2293. doi:10.1021/ef060581z.

[159] Y. Tamaura, A. Steinfeld, P. Kuhn, K. Ehrensberger, Production of solar hydrogen by a novel, 2-step, water-splitting thermochemical cycle, Energy. 20 (1995) 325–330. doi:10.1016/0360-5442(94)00099-O.

[160] R. Müller, P. Haeberling, R.D. Palumbo, Further advances toward the development of a direct heating solar thermal chemical reactor for the thermal dissociation of ZnO(s), Sol. Energy. 80 (2006) 500–511. doi:10.1016/j.solener.2005.04.015.

[161] C. Muhich, A. Steinfeld, Principles of doping ceria for the solar thermochemical redox splitting of H_2O and CO_2, J. Mater. Chem. A. 5 (2017) 15578–15590. doi:10.1039/C7TA04000H.

[162] E. Koepf, S.G. Advani, A. Steinfeld, A.K. Prasad, A novel beam-down, gravity-fed, solar thermochemical receiver/reactor for direct solid particle decomposition: Design, modeling, and experimentation, Int. J. Hydrogen Energy. 37 (2012) 16871–16887. doi:10.1016/j.ijhydene.2012.08.086.

[163] E.E. Koepf, M.D. Lindemer, S.G. Advani, A.K. Prasad, Experimental Investigation of Vortex Flow in a Two-Chamber Solar Thermochemical Reactor, J. Fluids Eng. 135 (2013) 111103. doi:10.1115/1.4024965.

[164] J.R. Scheffe, M. Welte, A. Steinfeld, Thermal Reduction of Ceria within an Aerosol Reactor for H_2O and CO_2 Splitting, Ind. Eng. Chem. Res. 53 (2014) 2175–2182. doi:10.1021/ie402620k.

[165] N. Gokon, T. Mataga, N. Kondo, T. Kodama, Thermochemical two-step water splitting by internally circulating fluidized bed of NiFe2O4particles: Successive reaction of thermal-reduction and water-decomposition steps, Int. J. Hydrogen Energy. 36 (2011) 4757–4767. doi:10.1016/j.ijhydene.2011.01.076.

[166] I. Ermanoski, Cascading pressure thermal reduction for efficient solar fuel production, Int. J. Hydrogen Energy. 39 (2014) 13114–13117. doi:10.1016/j.ijhydene.2014.06.143.

[167] A. Mcdaniel, K. Randolph, High Efficiency Solar Thermochemical Reactor for Hydrogen Production (Annual progress report: 2015), 2015. https://www.hydrogen.energy.gov/pdfs/progress15/ii_c_1_mcdaniel_2015.pdf.

[168] A. Abad, P. Gayán, L.F. de Diego, F. García-Labiano, J. Adánez, Fuel reactor modelling in chemical-looping combustion of coal: 1. model formulation, Chem. Eng. Sci. 87 (2013) 277–293. doi:10.1016/j.ces.2012.10.006.

[169] M.A. Schnellmann, S.A. Scott, G. Williams, J.S. Dennis, Sensitivity of chemical-looping combustion to particle reaction kinetics, Chem. Eng. Sci. 152 (2016) 21–25. doi:10.1016/j.ces.2016.05.028.

[170] D.L.-S. Fan, Chemical Looping Partial Oxidation: Gasification, Reforming, and Chemical Syntheses, Cambridge University Press, 2017.

[171] J.G. Yates, P. Lettieri, Fluidized-Bed Reactors: Processes and Operating Conditions, 2016. doi:10.1007/978-3-319-39593-7.

[172] M. Kramp, S. Heinrich, Carbon Stripping – A Critical Process Step in Chemical Looping Combustion of Solid Fuels, Chem. Eng. Technol. 35 (2012) 497–507. doi:10.1002/ceat.201100438.

[173] A. Cuadrat, A. Abad, P. Gayán, L.F. De Diego, F. García-labiano, J. Adánez, Theoretical approach on the CLC performance with solid fuels : Optimizing the solids inventory, Fuel. 97 (2012) 536–551. doi:10.1016/j.fuel.2012.01.071.

[174] T.A. Brown, J.S. Dennis, S.A. Scott, J.F. Davidson, A.N. Hayhurst, Gasification and Chemical-Looping Combustion of a Lignite Char in a Fluidized Bed of Iron Oxide, Energy & Fuels. 24 (2010) 3034–3048. doi:10.1021/ef100068m.

[175] K. Mahalatkar, J. Kuhlman, E.D. Huckaby, T.O. Brien, CFD simulation of a chemical-looping fuel reactor utilizing solid fuel, Chem. Eng. Sci. 66 (2011) 3617–3627. doi:10.1016/j.ces.2011.04.025.

[176] Y. Zhang, Z. Chao, H.A. Jakobsen, Modelling and simulation of chemical looping combustion process in a double loop circulating fluidized bed reactor, Chem. Eng. J. 320 (2017) 271–282. doi:10.1016/j.cej.2017.03.046.

[177] R. Legros, J. Chaouki, J. Paris, Simulation of circulating fluidized bed reactors using ASPEN PLUS, Fuel. 77 (1998) 327–337. doi:10.1016/S0016-2361(97)00211-1.

[178] R. Legros, J. Chaouki, J. Paris, Simulation of circulating fluidized bed reactors using ASPEN PLUS, 77 (1998) 327–337.

[179] N. Sadhwani, P. Li, M.R. Eden, S. Adhikari, Process Modeling of Fluidized Bed Biomass-CO2 Gasification using ASPEN Plus, in: 27th Eur. Symp. Comput. Aided Process Eng. ESCAPE 27,

Elsevier B.V., Barcelona, Spain, 2017: pp. 2509–2514. doi:10.1016/B978-0-444-63965-3.50420-7.

[180] Fluidization in Aspen Plus-Aspen Technology Tutorial, (2013).

[181] R.J. Schaefer, Steady State Behaviour of Moving Bed Reactors, Chem. Eng. Sci. 29 (1974) 119–127.

[182] A. Rahimi, A. Niksiar, A general model for moving-bed reactors with multiple chemical reactions part I: Model formulation, Int. J. Miner. Process. 124 (2013) 58–66. doi:10.1016/j.minpro.2013.02.015.

[183] D.R. Parisi, M.A. Laborde, Modeling of counter current moving bed gas-solid reactor used in direct reduction of iron ore, Chem. Eng. J. 104 (2004) 35–43. doi:10.1016/j.cej.2004.08.001.

[184] E.D. Negri, O.M. Alfano, M.G. Chiovetta, Moving-Bed Reactor Model for the Direct Reduction of Hematite . Parametric Study, Ind. Eng. Chem. 34 (1995) 4266–4276. doi:10.1021/ie00039a017.

[185] B. Dussoubs, J. Jourde, F. Patisson, J.L. Houzelot, D. Ablitzer, Mathematical modelling of uranium dioxide conversion in a moving bed furnace, Powder Technol. 128 (2002) 168–177.

[186] B.W. Benjamin, Great Plains ASPEN Model Development: Gasifier Model. Final Topical Report, Sci. Des. Co., Inc., New York. (1985) 180.

[187] Aspen Plus Model for Moving Bed Coal Gasifier-Aspen Technology tutorial, 2010.

[188] A. Tong, L. Zeng, M. V Kathe, D. Sridhar, L. Fan, Application of the Moving-Bed Chemical Looping Process for High Methane Conversion, Energy & Fuels. 27 (2013) 4119–4128. doi:10.1021/ef3020475.

[189] C. He, X. Feng, K. Hoong, Process modeling and thermodynamic analysis of Lurgi fixed-bed coal gasifier in an SNG plant, Appl. Energy. 111 (2013) 742–757. doi:10.1016/j.apenergy.2013.05.045.

[190] S. Mukherjee, Chemical looping combustion for solid fuels – Development and optimisation of industrial scale flowsheet models for power generation, University of Surrey, 2015. doi:10.13140/2.1.2554.1442.

[191] R. Porrazzo, G. White, R. Ocone, Techno-economic investigation of a chemical looping combustion based power plant, Faraday Discuss. 192 (2016) 437–457. doi:10.1039/C6FD00033A.

[192] E. Gençer, D.S. Mallapragada, F. Maréchal, M. Tawarmalani, R. Agrawal, Round-the-clock power supply and a sustainable economy via synergistic integration of solar thermal power and hydrogen processes, Proc. Natl. Acad. Sci. 112 (2015) 15821–15826. doi:10.1073/pnas.1513488112.

[193] A. de la Calle, A. Bayon, Annual Performance of a Solar-Thermochemical Hydrogen Production Plant Based on CeO2 Redox Cycle, in: Proc. 12th Int. Model. Conf. May 15-17, 2017, Prague, Czech Repub., 2017: pp. 857–866. doi:10.3384/ecp17132857.

[194] A.W. Zimmermann, R. Schom, Assessing Early-Stage CO 2 utilization Technologies — Comparing Apples and Oranges ?, (2017) 850–860. doi:10.1002/ente.201600805.

[195] F.D. Meylan, V. Moreau, S. Erkman, CO 2 utilization in the perspective of industrial ecology , an overview, Biochem. Pharmacol. 12 (2015) 101–108. doi:10.1016/j.jcou.2015.05.003.

[196] M. Aresta, A. Dibenedetto, A. Angelini, The changing paradigm in CO2utilization, J. CO2 Util. 3–4 (2013) 65–73. doi:10.1016/j.jcou.2013.08.001.

[197] A.E. Farooqui, A.M. Pica, P. Marocco, D. Ferrero, A. Lanzini, S. Fiorilli, J. Llorca, M. Santarelli, Assessment of kinetic model for ceria oxidation for chemical-looping CO2 dissociation, Chem. Eng. J. 346 (2018) 171–181. doi:10.1016/j.cej.2018.04.041.

[198] J.R. Scheffe, A. Steinfeld, Oxygen exchange materials for solar thermochemical splitting of H2O and CO2: A review, Mater. Today. 17 (2014) 341–348. doi:10.1016/j.mattod.2014.04.025.

[199] V.M. Wheeler, J. Zapata, P. Kreider, W. Lipiński, Effect of non-stoichiometry on optical, radiative, and thermal characteristics of ceria undergoing reduction, Opt. Express. 26 (2018) 1238–1243. doi:oe-26-10-A360.

[200] S. Li, V.M. Wheeler, P.B. Kreider, W. Lipiński, Thermodynamic Analyses of Fuel Production via Solar-driven Non-stoichiometric Metal Oxide Redox Cycling—Part I: Revisiting Flow and Equilibrium Assumptions, Energy & Fuels. (2018). doi:10.1021/acs.energyfuels.8b02081.

[201] S. Li, Vi. Wheeler, P.B. Kreider, R. Bader, W. Lipiński, Thermodynamic Analyses of Fuel Production via Solar-driven Non-stoichiometric Metal Oxide Redox Cycling—Part II: Impact of Solid–Gas Flow Configurations and Active Material Composi-tion on System Level

Efficiency, Energy & Fuels. (2018) acs.energyfuels.8b02082. doi:10.1021/acs.energyfuels.8b02082.

[202] S. Brendelberger, M. Roeb, M. Lange, C. Sattler, Counter flow sweep gas demand for the ceria redox cycle, Sol. Energy. 122 (2015) 1011–1022. doi:10.1016/j.solener.2015.10.036.

[203] A. M. Eltony, D. Gangloff, M. Shi, A. Bylinskii, V. Vuletic, I. Chuang, Technologies for trapped-ion quantum information systems, 2015. doi:10.1007/s11128-016-1298-8.

[204] C. Lu, K. Li, H. Wang, X. Zhu, Y. Wei, M. Zheng, C. Zeng, Chemical looping reforming of methane using magnetite as oxygen carrier: Structure evolution and reduction kinetics, Appl. Energy. 211 (2018) 1–14. doi:10.1016/j.apenergy.2017.11.049.

[205] S. Chuayboon, S. Abanades, S. Rodat, Syngas production via solar-driven chemical looping methane reforming from redox cycling of ceria porous foam in a volumetric solar reactor, Chem. Eng. J. 356 (2018) 756–770. doi:10.1016/j.cej.2018.09.072.

[206] S. Mukherjee, Chemical looping combustion for solid fuels – Development and optimisation of industrial scale flowsheet models for power generation, (2015). doi:10.13140/2.1.2554.1442.

[207] R. Porrazzo, G. White, R. Ocone, Techno-economic investigation of a chemical looping combustion based power plant, Faraday Discuss. 192 (2016) 437–457. doi:10.1039/C6FD00033A.

[208] N. V. Skorodumova, S.I. Simak, B.I. Lundqvist, I.A. Abrikosov, B. Johansson, Quantum origin of the oxygen storage capability of ceria, Phys. Rev. Lett. 89 (2002) 166601/1-166601/4. doi:10.1103/PhysRevLett.89.166601.

[209] L.-H. Tsui, V. Stetsovych, B. Pereda-ayo, J.R. González-velasco, Experimental control of Ce 3 + concentration in ceria based model catalysts, Charles University in Prague, 2015. doi:10.5772/55729.

[210] O. Levenspiel, Chemical reaction engineering, 1999. doi:10.1021/ie990488g.

[211] A. Abad, J. Adánez, F. García-Labiano, L.F. de Diego, P. Gayán, Modeling of the chemical-looping combustion of methane using a Cu-based oxygen carrier, Energy Procedia. 1 (2009) 391–398. doi:10.1016/j.egypro.2009.01.053.

[212] L. Chen, X. Yang, G. Li, C. Wen, X. Li, C. Snape, An Improved Form of Shrinking Core Model for Prediction of the Conversion during Reduction Process in Chemical Looping Combustion, Energy and Fuels. 31 (2017) 1993–2006. doi:10.1021/acs.energyfuels.6b03036.

[213] Z. Zhao, M. Uddi, N. Tsvetkov, B. Yildiz, A.F. Ghoniem, Redox Kinetics Study of Fuel Reduced Ceria for Chemical-Looping Water Splitting, J. Phys. Chem. C. 120 (2016) 16271–16289. doi:10.1021/acs.jpcc.6b01847.

[214] D. Arifin, Study of redox reactions to split water and carbon dioxide, University of Colorado, 2013. http://scholar.colorado.edu/chbe_gradetds/54.

[215] T. Ishida, N. Gokon, T. Hatamachi, T. Kodama, Kinetics of thermal reduction step of thermochemical two-step water splitting using CeO2 particles: Master-plot method for analyzing non-isothermal experiments, Energy Procedia. 49 (2013) 1970–1979. doi:10.1016/j.egypro.2014.03.209.

[216] B. Bulfin, Cerium dioxide redox cycle for fuel production, Trinity College, Dublin, 2015. http://hdl.handle.net/2262/79500.

[217] M.A. Panlener, R.N. Blumenthal, J.E. Garnier, A thermodynamic and electrical conductivity study of nonstoichiometric cerium dioxide, Solid State Ionics. 60 (1993) 279–298. doi:10.1016/0167-2738(93)90006-O.

[218] J.W. Dawicke, R.N. Blumenthal, Oxygen association pressure measurements on nonstoichiometric cerium dioxide, J. Electrochem. Soc. 133 (1986) 904–909. doi:10.1149/1.2108760.

[219] S. Ackermann, L. Sauvin, R. Castiglioni, J.L.M. Rupp, J.R. Scheffe, A. Steinfeld, Kinetics of CO2 Reduction over Nonstoichiometric Ceria, J. Phys. Chem. C. 119 (2015) 16452–16461. doi:10.1021/acs.jpcc.5b03464.

[220] D. Arifin, A.W. Weimer, Kinetics and mechanism of solar-thermochemical H2and CO production by oxidation of reduced CeO2, Sol. Energy. 160 (2018) 178–185. doi:10.1016/j.solener.2017.11.075.

[221] I. Ermanoski, N. Siegel, E. Stechel, A New Reactor Concept for Efficient Solar-Thermochemical Fuel Production, J. Sol. Energy Eng. 135 (2013) 31002. doi:10.1115/1.4023356.

[222] Ivan Ermanoski, Moving bed reactor for solar thermochemical fuel production, US 8.420,032 B1, 2013. https://patents.google.com/patent/US8420032.

[223] J. Fan, L. Zhu, P. Jiang, L. Li, H. Liu, Comparative exergy analysis of chemical looping combustion thermally coupled and conventional steam methane reforming for hydrogen production, J. Clean. Prod. 131 (2016) 247–258. doi:10.1016/j.jclepro.2016.05.040.

[224] CO2 Capture Project (CCP), CCS Technology Development and Demonstration Results, 2015. http://www.co2captureproject.org/reports.html?utm_medium=email&utm_campaign=CCP.

[225] P. Viebahn, D. Vallentin, S. Höller, Prospects of carbon capture and storage (CCS) in China's power sector - An integrated assessment, Appl. Energy. 157 (2015) 229–244. doi:10.1016/j.apenergy.2015.07.023.

[226] M. Tou, R. Michalsky, A. Steinfeld, Solar-Driven Thermochemical Splitting of CO2and In Situ Separation of CO and O2across a Ceria Redox Membrane Reactor, Joule. 1 (2017) 146–154. doi:10.1016/j.joule.2017.07.015.

[227] A. Farooqui, A. Bose, D. Ferrero, J. Lorca, M. Santarelli, Simulation of two-step redox recycling of non-stoichiometric ceria with thermochemical dissociation of CO2/H2O in moving bed reactors - Part II: Techno-economic analysis and integration with 100 MW oxyfuel power plant with carbon capture, Chem. Eng. Sci. (n.d.).

[228] D. Arifin, Study of redox reactions to split water and carbon dioxide, University of Colorado, 2013. http://scholar.colorado.edu/chbe_gradetds/54.

[229] A. Farooqui, A. Bose, D. Ferrero, J. Lorca, M. Santarelli, Simulation of two-step redox recycling of non-stoichiometric ceria with thermochemical dissociation of CO2/H2O in moving bed reactors - Part 1: Model development with redox kinetics and sensitivity analysis, Chem. Eng. Sci. (n.d.).

[230] K. Jana, A. Ray, M.M. Majoumerd, M. Assadi, S. De, Polygeneration as a future sustainable energy solution – A comprehensive review, Appl. Energy. 202 (2017) 88–111. doi:10.1016/j.apenergy.2017.05.129.

[231] R.W. Breault, E.R. Monazam, J.T. Carpenter, Analysis of hematite re-oxidation in the chemical looping process, Appl. Energy. 157 (2015) 174–182. doi:10.1016/j.apenergy.2015.08.015.

[232] C. Zhou, K. Shah, H. Song, J. Zanganeh, E. Doroodchi, B. Moghtaderi, Integration Options and Economic Analysis of an Integrated Chemical Looping Air Separation Process for Oxy-fuel Combustion, Energy & Fuels. 30 (2016) 1741–1755. doi:10.1021/acs.energyfuels.5b02209.

[233] C. Yin, J. Yan, Oxy-fuel combustion of pulverized fuels: Combustion fundamentals and modeling, Appl. Energy. 162 (2016) 742–762. doi:10.1016/j.apenergy.2015.10.149.

[234] D.J. Dillon, V. White, R.J. Allam, R.A. Wall, J. Gibbins, Oxy Combustion Processes for CO2 Capture from Power Plant, International Energy Agency, 2005. https://ieaghg.org/docs/General_Docs/Reports/Report 2005-9 oxycombustion.pdf.

[235] S. Mukherjee, P. Kumar, A. Yang, P. Fennell, Energy and exergy analysis of chemical looping combustion technology and comparison with pre-combustion and oxy-fuel combustion technologies for CO2 capture, J. Environ. Chem. Eng. 3 (2015) 2104–2114. doi:10.1016/j.jece.2015.07.018.

[236] K. Shah, B. Moghtaderi, J. Zanganeh, T. Wall, Integration options for novel chemical looping air separation (ICLAS) process for oxygen production in oxy-fuel coal fired power plants, Fuel. 107 (2013) 356–370. doi:10.1016/j.fuel.2013.01.007.

[237] R.P. Cabral, N. Mac Dowell, A novel methodological approach for achieving £/MWh cost reduction of CO2 capture and storage (CCS) processes, Appl. Energy. 205 (2017) 529–539. doi:10.1016/j.apenergy.2017.08.003.

[238] J.-P. Tranier, R. Dubettier, N. Perrin, Air Liquide, Air Separation Unit for Oxy-Coal Combustion Systems, 1st Int. Oxyfuel Combust. Conf. (2009).

[239] B. Moghtaderi, A Novel Chemical Looping Based Air Separation Technology for Oxy-Fuel Combustion of Coal, 2014. doi:10.1115/1.802915.ch1.

[240] M.E. Boot-Handford, J.C. Abanades, E.J. Anthony, M.J. Blunt, S. Brandani, N. Mac Dowell, J.R. Fernández, M.-C. Ferrari, R. Gross, J.P. Hallett, R.S. Haszeldine, P. Heptonstall, A. Lyngfelt, Z. Makuch, E. Mangano, R.T.J. Porter, M. Pourkashanian, G.T. Rochelle, N. Shah, J.G. Yao, P.S. Fennell, Carbon capture and storage update, Energy Environ. Sci. 7 (2014) 130–189. doi:10.1039/C3EE42350F.

[241] A. Skorek-Osikowska, Ł. Bartela, J. Kotowicz, Thermodynamic and ecological assessment of selected coal-fired power plants integrated with carbon dioxide capture, Appl. Energy. 200 (2017) 73–88. doi:10.1016/j.apenergy.2017.05.055.

[242] A.E. Farooqui, H.M. Badr, M.A. Habib, R. Ben-Mansour, Numerical investigation of

combustion characteristics in an oxygen transport reactor, Int. J. Energy Res. 38 (2014). doi:10.1002/er.3070.

[243] A.E. Farooqui, M.A. Habib, H.M. Badr, R. Ben-Mansour, Modeling of ion transport reactor for oxy-fuel combustion, Int. J. Energy Res. 37 (2013). doi:10.1002/er.2923.

[244] R. Ben-Mansour, M.A. Habib, H.M. Badr, F. Azharuddin, M. Nemitallah, Characteristics of oxy-fuel combustion in an oxygen transport reactor, in: Energy and Fuels, ACS Publications, 2012: pp. 4599–4606. doi:10.1021/ef300539c.

[245] J. Mletzko, S. Ehlers, A. Kather, Comparison of natural gas combined cycle power plants with post combustion and oxyfuel technology at different CO2 capture rates, Energy Procedia. 86 (2016) 2–11. doi:10.1016/j.egypro.2016.01.001.

[246] S. Nazir, O. Bolland, S. Amini, Analysis of Combined Cycle Power Plants with Chemical Looping Reforming of Natural Gas and Pre-Combustion CO2 Capture, Energies. 11 (2018) 147. doi:10.3390/en11010147.

[247] H. Hong, H. Jin, B. Liu, A Novel Solar-Hybrid Gas Turbine Combined Cycle With Inherent CO[sub 2] Separation Using Chemical-Looping Combustion by Solar Heat Source, J. Sol. Energy Eng. 128 (2006) 275. doi:10.1115/1.2212443.

[248] M. Jafarian, M. Arjomandi, G.J. Nathan, A hybrid solar and chemical looping combustion system for solar thermal energy storage, Appl. Energy. 103 (2013) 671–678. doi:10.1016/j.apenergy.2012.10.033.

[249] O.V. Ogidiama, M.R.M. Abu-Zahra, T. Shamim, Techno-economic analysis of a poly-generation solar-assisted chemical looping combustion power plant, Appl. Energy. 228 (2018) 724–735. doi:10.1016/j.apenergy.2018.06.091.

[250] H. Kong, Y. Hao, H. Wang, A solar thermochemical fuel production system integrated with fossil fuel heat recuperation, Appl. Therm. Eng. 108 (2016) 958–966. doi:10.1016/j.applthermaleng.2016.03.170.

[251] H. Kong, Y. Hao, H. Jin, Isothermal versus two-temperature solar thermochemical fuel synthesis: A comparative study, Appl. Energy. 228 (2018) 301–308. doi:10.1016/j.apenergy.2018.05.099.

[252] Mitsubishi Heavy Industries, Gas Turbines, (n.d.). https://www.mhi.com/products/energy/gas_turbine.html (accessed May 23, 2018).

[253] Wärtsilä, Gas Turbine for Power Generation: Introduction, (2018). https://www.wartsila.com/energy/learning-center/technical-comparisons/gas-turbine-for-power-generation-introduction (accessed May 29, 2018).

[254] A. Farooqui, A. Bose, D. Ferrero, J. Llorca, M. Santarelli, Techno-economic and exergetic assessment of an oxy-fuel power plant fueled by syngas produced by chemical looping CO2 and H2O dissociation, J. CO2 Util. 27 (2018) 500–517. doi:10.1016/j.jcou.2018.09.001.

[255] A. Mutuberria, J. Pascual, M. V. Guisado, F. Mallor, Comparison of Heliostat Field Layout Design Methodologies and Impact on Power Plant Efficiency, Energy Procedia. 69 (2015) 1360–1370. doi:10.1016/j.egypro.2015.03.135.

[256] B. Ehrhart, D. Gill, Evaluation of annual efficiencies of high temperature central receiver concentrated solar power plants with thermal energy storage, Energy Procedia. 49 (2013) 752–761. doi:10.1016/j.egypro.2014.03.081.

[257] G.P. Hammond, Engineering sustainability : thermodynamics , energy systems , and the environment, 639 (2004) 613–639. doi:10.1002/er.988.

[258] A. Bejan, Thermal Design and Optimzation, John Wiley, New York, 1996.

[259] S. Brendelberger, J. Vieten, M.J. Vidyasagar, M. Roeb, C. Sattler, Demonstration of thermochemical oxygen pumping for atmosphere control in reduction reactions, Sol. Energy. 170 (2018) 273–279. doi:10.1016/j.solener.2018.05.063.

[260] S. Sievers, T. Seifert, M. Franzen, G. Schembecker, C. Bramsiepe, Fixed capital investment estimation for modular production plants, Chem. Eng. Sci. 158 (2017) 395–410. doi:10.1016/j.ces.2016.09.029.

[261] C. Cormos, Integrated assessment of IGCC power generation technology with carbon capture and storage (CCS), Energy. 42 (2012) 434–445. doi:10.1016/j.energy.2012.03.025.

[262] Politecnico di Milano - Alstom UK, CArbon-free Electricity by SEWGS: Advanced materials, Reactor (CAESER)-, and process design; in module D 4.9: European best practice guidelines for assessment of CO2 capture technologies (FP7 - ENERGY.2007.5.1.1), 2011. https://cordis.europa.eu/project/rcn/85757_en.html.

[263] Politecnico di Milano - CAESER Project, Enabling advanced pre-combustion capture techniques and plants; in deliverable D.1.4.3: European best practice guidelines for assessment of CO2 capture technologies, 2011. https://www.sintef.no/globalassets/project/decarbit/d-1-4-3_euro_bp_guid_for_ass_co2_cap_tech_280211.pdf.

[264] Y. Zhao, H. Chen, M. Waters, D.N. Mavris, Modeling and Cost Optimization of Combined Cycle Heat Recovery Generator Systems, Vol. 1 Turbo Expo 2003. (2003) 881–891. doi:10.1115/GT2003-38568.

[265] N. Berghout, T. Kuramochi, M. van den Broek, A. Faaij, Techno-economic performance and spatial footprint of infrastructure configurations for large scale CO2 capture in industrial zones. A case study for the Rotterdam Botlek area (part A), Int. J. Greenh. Gas Control. 39 (2015) 256–284. doi:10.1016/j.ijggc.2015.05.019.

[266] Politecnico di Milano – Alstom UK (CAESAR project), European best practice guidelines for assessment of CO2 capture technologies., (2011).

[267] IEA, Executive Summary - Projected Costs of Generating Electricity, 2015. https://www.oecd-nea.org/ndd/pubs/2015/7057-proj-costs-electricity-2015.pdf.

[268] Eurostat, Natural gas price statistics, EU-28, (2016) 1–12. doi:http://ec.europa.eu/eurostat/statistics-explained/index.php/Natural_gas_price_statistics.

[269] C. Falter, V. Batteiger, A. Sizmann, Climate Impact and Economic Feasibility of Solar Thermochemical Jet Fuel Production, Environ. Sci. Technol. 50 (2016) 470–477. doi:10.1021/acs.est.5b03515.

[270] J. Apt, A. Newcomer, L.B. Lave, S. Douglas, L.M. Dunn, An Engineering-Economic Analysis of Syngas Storage, U.S. Dep. Energy's Natl. Energy Technol. Lab. (2008) 143.

[271] Capital Cost Estimates for Utility Scale Electricity Generating Plants, 2016. https://www.eia.gov/analysis/studies/powerplants/capitalcost/pdf/capcost_assumption.pdf.

[272] IRENA, Renewable Energy Technologies Cost Analysis Series: Concentrating Solar Power, Compr. Renew. Energy. 3 (2012) 595–636. doi:10.1016/B978-0-08-087872-0.00319-X.

[273] L.K. Rihko-Struckmann, P. Datta, M. Wenzel, K. Sundmacher, N.V.R.A. Dharanipragada, H. Poelman, V. V Galvita, G.B. Marin, Hydrogen and Carbon Monoxide Production by Chemical Looping over Iron-Aluminium Oxides, Energy Technol. 4 (2016) 304–313. doi:10.1002/ente.201500231.

[274] A.I. Demidov, I.A. Markelov, Thermodynamics of interaction of iron oxides and carbon monoxide, Russ. J. Appl. Chem. 84 (2011) 196–198. doi:10.1134/S1070427211020054.

[275] R. Bader, L.J. Venstrom, J.H. Davidson, W. Lipiński, Thermodynamic analysis of isothermal redox cycling of ceria for solar fuel production, Energy and Fuels. 27 (2013) 5533–5544. doi:10.1021/ef400132d.

[276] P. Furler, J. Scheffe, M. Gorbar, L. Moes, U. Vogt, A. Steinfeld, Solar Thermochemical CO2 Splitting Utilizing a Reticulated Porous Ceria Redox System, Energy & Fuels. 26 (2012) 7051–7059. doi:10.1021/ef3013757.

[277] T. Montini, M. Melchionna, M. Monai, P. Fornasiero, Fundamentals and Catalytic Applications of CeO2-Based Materials, Chem. Rev. 116 (2016) 5987–6041. doi:10.1021/acs.chemrev.5b00603.

[278] S. Chuayboon, S. Abanades, S. Rodat, Syngas production via solar-driven chemical looping methane reforming from redox cycling of ceria porous foam in a volumetric solar reactor, Chem. Eng. J. (2018). doi:10.1016/j.cej.2018.09.072.

[279] M.M. Nair, S. Abanades, Tailoring Hybrid Nonstoichiometric Ceria Redox Cycle for Combined Solar Methane Reforming and Thermochemical Conversion of H2O/CO2, Energy and Fuels. 30 (2016) 6050–6058. doi:10.1021/acs.energyfuels.6b01063.

[280] K.J. Warren, J. Reim, K. Randhir, B. Greek, R. Carrillo, D.W. Hahn, J.R. Scheffe, Theoretical and Experimental Investigation of Solar Methane Reforming through the Nonstoichiometric Ceria Redox Cycle, Energy Technol. 5 (2017) 2138–2149. doi:10.1002/ente.201700083.

[281] A. Steinfeld, P. Scherrer, P. Kuhn, J. Karni, High-Temperature Solar Thermochemistry: Production of Iron and Synthesis Gas by Fe304-Reduction With Methane, 18 (1993) 239–249.

[282] E.R. Monazam, R.W. Breault, R. Siriwardane, Kinetics of magnetite (Fe3O4) oxidation to hematite (Fe2O3) in air for chemical looping combustion, Ind. Eng. Chem. Res. 53 (2014) 13320–13328. doi:10.1021/ie501536s.

[283] K.S. Kang, C.H. Kim, K.K. Bae, W.C. Cho, S.H. Kim, C.S. Park, Oxygen-carrier selection and thermal analysis of the chemical-looping process for hydrogen production, Int. J. Hydrogen

Energy. 35 (2010) 12246–12254. doi:10.1016/j.ijhydene.2010.08.043.

[284] A. Laachir, V. Perrichon, A. Badri, J. Lamotte, E. Catherine, J.C. Lavalley, J. El Fallah, L. Hilaire, F. Normand, B. Pascal, E. Quemere, G.N. Sauvion, O. Touret, Reduction of CeO2 by Hydrogen, J. CHEM. SOC. FARADAY TRANS.,. 87 (1991) 1601–1609.

[285] M. Welte, R. Barhoumi, A. Zbinden, J.R. Scheffe, A. Steinfeld, Experimental Demonstration of the Thermochemical Reduction of Ceria in a Solar Aerosol Reactor, Ind. Eng. Chem. Res. 55 (2016) 10618–10625. doi:10.1021/acs.iecr.6b02853.

[286] V. Galvita, K. Sundmacher, Hydrogen production from methane by steam reforming in a periodically operated two-layer catalytic reactor, Appl. Catal. A Gen. 289 (2005) 121–127. doi:10.1016/j.apcata.2005.04.053.

[287] V. Collins-Martinez, M. Escobedo Bretado, M. Meléndez Zaragoza, J. Salinas Gutiérrez, A.L. Ortiz, Absorption enhanced reforming of light alcohols (methanol and ethanol) for the production of hydrogen: Thermodynamic modeling, Int. J. Hydrogen Energy. 38 (2013) 12539–12553. doi:10.1016/j.ijhydene.2012.11.146.

[288] C.C. Cormos, Evaluation of syngas-based chemical looping applications for hydrogen and power co-generation with CCS, Int. J. Hydrogen Energy. 37 (2012) 13371–13386. doi:10.1016/j.ijhydene.2012.06.090.

[289] S.M. Nazir, O. Bolland, S. Amini, Full Plant Scale Analysis of Natural Gas Fired Power Plants with Pre-Combustion CO2 Capture and Chemical Looping Reforming (CLR), Energy Procedia. 114 (2017) 2146–2155. doi:10.1016/j.egypro.2017.03.1350.

[290] D.P. Harrison, Sorption-Enhanced Hydrogen Production : A Review, Ind. Eng. Chem. Res. 47 (2008) 6486–6501. doi:10.1021/ie800298z.

[291] HYGHSPIN screw pumps for flexible use to acheive maximum efficiency, Jung Process Syst. (2009) 17. http://www.alflow.dk/Files/Files/eCom/jung/brochure-hyghspin-en.pdf.

[292] M.N. Khan, T. Shamim, Influence of Specularity Coefficient on the Hydrodynamics and Bubble Statistics of an Annular Fluidized Bed Reactor, Energy Procedia. 105 (2017) 1998–2003. doi:10.1016/j.egypro.2017.03.573.

[293] CAESAR project - European best practice guidelines for assessment of CO2 capture technologies., 2011. https://www.sintef.no/globalassets/project/decarbit/d-1-4-3_euro_bp_guid_for_ass_co2_cap_tech_280211.pdf.

[294] A. Steinfeld, Chapter 8 Thermochemical production of syngas using concentrated solar energy, Annu. Rev. Heat Transf. (2012) 255–275. doi:10.1615/AnnualRevHeatTransfer.2012004537.

[295] S. Mukherjee, P. Kumar, A. Yang, P. Fennell, Energy and exergy analysis of chemical looping combustion technology and comparison with pre-combustion and oxy-fuel combustion technologies for CO 2 capture, J. Environ. Chem. Eng. 3 (2015) 2104–2114. doi:10.1016/j.jece.2015.07.018.

[296] G.P. Hammond, A.J. Stapleton, Exergy analysis of the United Kingdom energy, 215 (2001) 141–162.

[297] T.J. Kotas, The Exergy Method of Thermal Plant Analysis, Butterworths, 1985.

[298] J. Szargut, Chemical Exergies of the Elements, Appl. Energy. 32 (1989) 269–286.

[299] M.N. Khan, T. Shamim, Exergoeconomic analysis of a chemical looping reforming plant for hydrogen production, Int. J. Hydrogen Energy. 42 (2017) 4951–4965. doi:10.1016/j.ijhydene.2016.11.098.

[300] J.Y. Xiang, M. Cal, M. Santarelli, Calculation for physical and chemical exergy of flows in systems elaborating mixed-phase flows and a case study in an IRSOFC plant, 115 (2004) 101–115. doi:10.1002/er.953.

[301] M.M. Mekonnen, P.W. Gerbens-Leenes, A.Y. Hoekstra, The consumptive water footprint of electricity and heat: a global assessment, Environ. Sci. Water Res. Technol. 1 (2015) 285–297. doi:10.1039/C5EW00026B.

[302] A.D. Martin, A. Delgado, A. Delgado Martin, Water Footprint of Electric Power Generation : Modeling its use and analyzing options for a water-scarce future, 2012. doi:10.1021/es802162x.

[303] N. Florin, P. Fennell, CCR Land Footprint Review, IC 26, (2006) 1–30. https://www.gov.uk/government/uploads/system/uploads/attachment_data/file/43615/CCR_guidance_-_Imperial_College_review.pdf.

[304] M. Ishida, H. Jin, A novel chemical-looping combustor without NOx formation, Ind. Eng. Chem. Res. 35 (1996) 2469–2472. doi:10.1021/ie950680s.

[305] M. Pan, F. Aziz, B. Li, S. Perry, N. Zhang, I. Bulatov, R. Smith, Application of optimal design

methodologies in retrofitting natural gas combined cycle power plants with CO2capture, Appl. Energy. 161 (2016) 695–706. doi:10.1016/j.apenergy.2015.03.035.

[306] Quarterly report on Europeon Electricity Markets, Brussels, 2018. https://ec.europa.eu/energy/sites/ener/files/documents/quarterly_report_on_european_gas_markets_q1_2018.pdf.

[307] Z. Khorshidi, M. Soltanieh, Y. Saboohi, M. Arab, Economic Feasibility of CO 2 Capture from Oxy-fuel Power Plants Considering Enhanced Oil Recovery Revenues, Energy Procedia. 4 (2011) 1886–1892. doi:10.1016/j.egypro.2011.02.067.

[308] E.S. Rubin, J.E. Davison, H.J. Herzog, The cost of CO 2 capture and storage, Int. J. Greenh. Gas Control. (2015). doi:10.1016/j.ijggc.2015.05.018.

[309] J. Varghese, S. Bandyopadhyay, Targeting for energy integration of multiple fired heaters, Ind. Eng. Chem. Res. 46 (2007) 5631–5644. doi:10.1021/ie061619y.

[310] C.C. Cormos, Evaluation of energy integration aspects for IGCC-based hydrogen and electricity co-production with carbon capture and storage, Int. J. Hydrogen Energy. 35 (2010) 7485–7497. doi:10.1016/j.ijhydene.2010.04.160.

[311] E.S. Spang, W.R. Moomaw, K.S. Gallagher, P.H. Kirshen, D.H. Marks, The water consumption of energy production : an international comparison, Environ. Res. Lett. 9 (2014) 105002. doi:10.1088/1748-9326/9/10/105002.

[312] A. Bose, K. Jana, D. Mitra, S. De, Co-production of power and urea from coal with CO2 capture: Performance assessment, Clean Technol. Environ. Policy. 17 (2015) 1271–1280. doi:10.1007/s10098-015-0960-7.

[313] Q. Zhang, Nurhayati, C.L. Cheng, D. Nagarajan, J.S. Chang, J. Hu, D.J. Lee, Carbon capture and utilization of fermentation CO2: Integrated ethanol fermentation and succinic acid production as an efficient platform, Appl. Energy. 206 (2017) 364–371. doi:10.1016/j.apenergy.2017.08.193.

[314] C. Graves, S.D. Ebbesen, M. Mogensen, K.S. Lackner, Sustainable hydrocarbon fuels by recycling CO2 and H2O with renewable or nuclear energy, Renew. Sustain. Energy Rev. 15 (2011) 1–23. doi:10.1016/j.rser.2010.07.014.

[315] S.M. Jarvis, S. Samsatli, Technologies and infrastructures underpinning future CO2value chains: A comprehensive review and comparative analysis, Renew. Sustain. Energy Rev. 85 (2018) 46–68. doi:10.1016/j.rser.2018.01.007.

[316] K. Jana, A. Ray, M.M. Majoumerd, M. Assadi, S. De, Polygeneration as a future sustainable energy solution – A comprehensive review, Appl. Energy. 202 (2017) 88–111. doi:10.1016/j.apenergy.2017.05.129.

[317] Y.K. Salkuyeh, T.A. Adams, A new power, methanol, and DME polygeneration process using integrated chemical looping systems, Energy Convers. Manag. 88 (2014) 411–425. doi:10.1016/j.enconman.2014.08.039.

[318] L. Qun, Yi; Yan-Hong, Hao; Ji-Long, Zhang; Wen-Ying, Energy Polygeneration Systems and CO2 Recycle in: Advances in Energy Systems Engineering, Springer-Verlag, 2017. doi:10.1021/ie101383h.

[319] S. Li, L. Gao, H. Jin, Realizing low life cycle energy use and GHG emissions in coal based polygeneration with CO2 capture, Appl. Energy. 194 (2017) 161–171. doi:10.1016/j.apenergy.2017.03.021.

[320] K. Jana, S. De, Environmental impact of biomass based polygeneration – A case study through life cycle assessment, Bioresour. Technol. 227 (2017) 256–265. doi:10.1016/j.biortech.2016.12.067.

[321] A. Farooqui, A. Bose, D. Ferrero, J. Llorca, M. Santarelli, Techno-economic and exergetic assessment of an oxy-fuel power plant fueled by syngas produced by chemical looping CO2 and H2O dissociation, J. CO2 Util. (2018). doi:10.1016/j.jcou.2018.09.001.

[322] R. Stanger, T. Wall, R. Spörl, M. Paneru, S. Grathwohl, M. Weidmann, G. Scheffknecht, D. McDonald, K. Myöhänen, J. Ritvanen, S. Rahiala, T. Hyppänen, J. Mletzko, A. Kather, S. Santos, Oxyfuel combustion for CO2capture in power plants, Int. J. Greenh. Gas Control. 40 (2015) 55–125. doi:10.1016/j.ijggc.2015.06.010.

[323] V.N. Nguyen, L. Blum, Syngas and synfuels from H2O and CO2: Current status, Chemie-Ingenieur-Technik. 87 (2015) 354–375. doi:10.1002/cite.201400090.

[324] G.P. Smestad, A. Steinfeld, Review: Photochemical and thermochemical production of solar fuels from H 2O and CO 2 using metal oxide catalysts, Ind. Eng. Chem. Res. 51 (2012) 11828–

11840. doi:10.1021/ie3007962.

[325] B. Moghtaderi, Review of the recent chemical looping process developments for novel energy and fuel applications, Energy and Fuels. 26 (2012) 15–40. doi:10.1021/ef201303d.

[326] J. Kim, C.A. Henao, T.A. Johnson, D.E. Dedrick, J.E. Miller, E.B. Stechel, C.T. Maravelias, Methanol production from CO2 using solar-thermal energy: process development and techno-economic analysis, Energy Environ. Sci. 4 (2011) 3122. doi:10.1039/c1ee01311d.

[327] J. Kim, T.A. Johnson, J.E. Miller, E.B. Stechel, C.T. Maravelias, Fuel production from CO2 using solar-thermal energy: system level analysis, Energy Environ. Sci. 5 (2012) 8417. doi:10.1039/c2ee21798h.

[328] T.C. Davenport, C.K. Yang, C.J. Kucharczyk, M.J. Ignatowich, S.M. Haile, Maximizing fuel production rates in isothermal solar thermochemical fuel production, Appl. Energy. 183 (2016) 1098–1111. doi:10.1016/j.apenergy.2016.09.012.

[329] C. Falter, R. Pitz-Paal, Energy analysis of solar thermochemical fuel production pathway with a focus on waste heat recuperation and vacuum generation, Sol. Energy. 176 (2018) 230–240. doi:10.1016/J.SOLENER.2018.10.042.

[330] T.A. Semelsberger, R.L. Borup, H.L. Greene, Dimethyl ether (DME) as an alternative fuel, J. Power Sources. 156 (2006) 497–511. doi:10.1016/j.jpowsour.2005.05.082.

[331] G. Olah, G. Alain, S.P. GK, Beyond oil and gas: the methanol economy, 2nd and up, WILEY - VCH, 2009. doi:10.1002/9783527627806.

[332] T. Ogawa, N. Inoue, T. Shikada, Y. Ohno, Direct Dimethyl Ether Synthesis, J. Nat. Gas Chem. 12 (2003) 219–227.

[333] G. M, K. R, J. E, Production of methanol and dimethyl ether from biomass derived syngas: a comparison of the different synthesis pathways by means of flowsheet simulation, in: 23rd Eur. Symp. Comput. Aided Process Eng. (ESCAPE 23) 9-12 June, 2013, 2013: p. 2013. doi:10.1016/B978-0-7506-3560-8.50001-9.

[334] F. Ren, J.-F. Wang, H.-S. Li, Direct mass production technique of dimethyl ether from synthesis gas in a circulating slurry bed reactor, Stud. Surf. Sci. Catal. 159 (2006) 489–492. https://www.scopus.com/inward/record.uri?eid=2-s2.0-33745792734&partnerID=40&md5=25145520ec4d439b01fe6100b67846b8.

[335] T.A. Adams, J.H. Ghouse, Polygeneration of fuels and chemicals, Curr. Opin. Chem. Eng. 10 (2015) 87–93. doi:10.1016/j.coche.2015.09.006.

[336] K. Li, H. Wang, Y. Wei, Syngas generation from methane using a chemical-looping concept: A review of oxygen carriers, J. Chem. (2013). doi:10.1155/2013/294817.

[337] S. Luo, L. Zeng, D. Xu, M. Kathe, E. Chung, N. Deshpande, L. Qin, A. Majumder, T.L. Hsieh, A. Tong, Z. Sun, L.S. Fan, Shale gas-to-syngas chemical looping process for stable shale gas conversion to high purity syngas with a H2:CO ratio of 2:1, Energy Environ. Sci. 7 (2014) 4104–4117. doi:10.1039/c4ee02892a.

[338] A. Hankin, N. Shah, Process exploration and assessment for the production of methanol and dimethyl ether from carbon dioxide and water, Sustain. Energy Fuels. 00 (2017) 1–16. doi:10.1039/C7SE00206H.

[339] Y.K. Salkuyeh, T.A. Adams, A new power, methanol, and DME polygeneration process using integrated chemical looping systems, Energy Convers. Manag. 88 (2014) 411–425. doi:10.1016/j.enconman.2014.08.039.

[340] A. Lerner, M.J. Brear, J.S. Lacey, R.L. Gordon, P.A. Webley, Life cycle analysis (LCA) of low emission methanol and di-methyl ether (DME) derived from natural gas, Fuel. 220 (2018) 871–878. doi:10.1016/j.fuel.2018.02.066.

[341] H.M. Shim, S.J. Lee, Y.D. Yoo, Y.S. Yun, H.T. Kim, Simulation of DME synthesis from coal syngas by kinetics model, Korean J. Chem. Eng. 26 (2009) 641–648. doi:10.1007/s11814-009-0107-9.

[342] G.H. Graaf, J.G.M. Winkelman, Chemical Equilibria in Methanol Synthesis Including the Water-Gas Shift Reaction: A Critical Reassessment, Ind. Eng. Chem. Res. 55 (2016) 5854–5864. doi:10.1021/acs.iecr.6b00815.

[343] M.K. Cohce, I. Dincer, M.A. Rosen, Energy and exergy analyses of a biomass-based hydrogen production system, Bioresour. Technol. 102 (2011) 8466–8474. doi:10.1016/j.biortech.2011.06.020.

[344] A.M. Eltony, H.G. Park, S.X. Wang, J. Kong, I.L. Chuang, Motional heating in a graphene-coated ion trap, Nano Lett. 14 (2014) 5712–5716. doi:10.1021/nl502468g.

[345] D.-Y. Peng, D.B. Robinson, A New Two-Constant Equation of State, Ind. Eng. Chem. Fundam. 15 (1976) 59–64. doi:10.1021/i160057a011.

[346] L. Fanxing, Z. Liang, V.L. G., Y. Zachary, F. Liang-Shih, Syngas chemical looping gasification process: Bench-scale studies and reactor simulations, AIChE J. 56 (2009) 2186–2199. doi:10.1002/aic.12093.

[347] I. Barin, Thermochemical data of pure substances, (1995) 1885. doi:10.1002/9783527619825.

[348] M.B. Berkenpas, J.J. Fry, K. Kietzke, E.S. Rubin, IECM User Documentation : User Manual IECM User Documentation : User Manual, (2018) 509–515.

[349] M.N. Khan, T. Shamim, Influence of Specularity Coefficient on the Hydrodynamics and Bubble Statistics of an Annular Fluidized Bed Reactor, Energy Procedia. 105 (2017) 1998–2003. doi:10.1016/j.egypro.2017.03.573.

[350] D.K. Bhunya, Simulation Study of Cryogenic Air Separation Unit Using Aspen Hysys At Rourkela Steel Plant Master of Technology in (Cryogenic and Vacuum Technology) National Institute of Technology Rourkela, National Institute of Technology Rourkela, 2014. http://ethesis.nitrkl.ac.in/5971/1/E-138.pdf.

[351] J. Aprilia, K. Kolmetz, Air seperation units (Engineering design guideline) KLM Technology Group-Practical Engineering Guidelines for Processing Plant Solutions, 2013. http://kolmetz.com/pdf/EDG/ENGINEERING_DESIGN_GUIDELINE_Air_Seperation_Units_Rev01web.pdf.

[352] V. Raibhole, S. Sapali, Simulation of Medium Purity Gaseous Oxygen Cryogenic Plant for Biomass Gasification by Aspen Plus, Open Access Sci. Reports. 1:343 (2012). doi:10.4172/scientificreports.343.

[353] B.J.P. Buhre, L.K. Elliott, C.D. Sheng, R.P. Gupta, T.F. Wall, Oxy-fuel combustion technology for coal-fired power generation, Prog. Energy Combust. Sci. 31 (2005) 283–307. doi:10.1016/j.pecs.2005.07.001.

[354] M. Pozzo, A. Lanzini, M. Santarelli, Enhanced biomass-to-liquid (BTL) conversion process through high temperature co-electrolysis in a solid oxide electrolysis cell (SOEC), Fuel. 145 (2015) 39–49. doi:10.1016/j.fuel.2014.12.066.

[355] K.L. Ng, D. Chadwick, B.A. Toseland, Kinetics and modelling of dimethyl ether synthesis from synthesis gas, Chem. Eng. Sci. 54 (1999) 3587–3592. doi:10.1016/S0009-2509(98)00514-4.

[356] F. Dadgar, R. Myrstad, P. Pfeifer, A. Holmen, H.J. Venvik, Direct dimethyl ether synthesis from synthesis gas: The influence of methanol dehydration on methanol synthesis reaction, Catal. Today. 270 (2016) 76–84. doi:10.1016/j.cattod.2015.09.024.

[357] C. Arcoumanis, C. Bae, R. Crookes, E. Kinoshita, The potential of di-methyl ether (DME) as an alternative fuel for compression-ignition engines: A review, Fuel. 87 (2008) 1014–1030. doi:10.1016/j.fuel.2007.06.007.

[358] J. Sun, G. Yang, Y. Yoneyama, N. Tsubaki, Catalysis chemistry of dimethyl ether synthesis, ACS Catal. 4 (2014) 3346–3356. doi:10.1021/cs500967j.

[359] R.S. Treptow, Le Chatelier's Principle, J. Chem. Educ. 57 (1980) 417–419. doi:10.1021/ed057p417.

[360] F. Pontzen, W. Liebner, V. Gronemann, M. Rothaemel, B. Ahlers, CO2-based methanol and DME - Efficient technologies for industrial scale production, Catal. Today. 171 (2011) 242–250. doi:10.1016/j.cattod.2011.04.049.

[361] K.M. Vanden Bussche, G.F. Froment, A Steady-State Kinetic Model for Methanol Synthesis and the Water Gas Shift Reaction on a Commercial Cu/ZnO/Al2O3Catalyst, J. Catal. 161 (1996) 1–10. doi:10.1006/jcat.1996.0156.

[362] G. Berčič, J. Levec, Catalytic Dehydration of Methanol to Dimethyl Ether. Kinetic Investigation and Reactor Simulation, Ind. Eng. Chem. Res. 32 (1993) 2478–2484. doi:10.1021/ie00023a006.

[363] R.S. Schiffino, R.P. Merrill, A mechanistic study of the methanol dehydration reaction on .gamma.-alumina catalyst, J. Phys. Chem. 97 (1993) 6425–6435. doi:10.1021/j100126a017.

[364] G.W. K. Klier, Simmons, Catalytic Synthesis of Methanol from CO / H2, J. Catal. 360 (1982) 343–360. doi:https://doi.org/10.1016/0021-9517(82)90040-9.

[365] G.R. Moradi, F. Yaripour, P. Vale-Sheyda, Catalytic dehydration of methanol to dimethyl ether over mordenite catalysts, Fuel Process. Technol. 91 (2010) 461–468. doi:10.1016/j.fuproc.2009.12.005.

[366] I.C. Kemp, Pinch analysis and process integration: A user guide on process integration for the efficient use of energy, Pinch Anal. Process Integr. (2007) 416.

doi:http://dx.doi.org/10.1016/B978-075068260-2.50003-1.

[367] T.J. Kotas, Chapter 2 - Basic exergy concepts BT - The Exergy Method of Thermal Plant Analysis, in: Butterworth-Heinemann, 1985: pp. 29–56. doi:https://doi.org/10.1016/B978-0-408-01350-5.50009-X.

[368] Kristen Gerdes, John Haslbeck, Norma Kuehn, Eric Lewis, Lora L. Pinkerton, Mark Woods, James Simpson, Marc J. Turner, Elsy Varghese, Cost and Performance Baseline for Fossil Energy Plants Volume 1: Bituminous Coal and Natural Gas to Electricity, Doe/Netl-2010/1397. 1 (2010). doi:DOE/NETL-2010/1397.

[369] K. Gerdes, W.M. Summers, J. Wimer, Cost Estimation Methodology for NETL Assessments of Power Plant Performance, Doe/Netl-2011/1455. (2011) 26. http://www.netl.doe.gov/File Library/research/energy analysis/publications/QGESSNETLCostEstMethod.pdf.

[370] J.A.S. Richard Turton, Richard C. Bailie, Wallace B. Whiting, Analysis, Synthesis and Design of Chemical Processes Third Edition, 2013. doi:10.1017/CBO9781107415324.004.

[371] Y. Zhao, H. Chen, M. Waters, D.N. Mavris, Modeling and Cost Optimization of Combined Cycle Heat Recovery Generator Systems, Vol. 1 Turbo Expo 2003. (2003) 881–891. doi:10.1115/GT2003-38568.

[372] L.E. D., J. Haiming, C.F. E., Large-scale gasification-based coproduction of fuels and electricity from switchgrass, Biofuels, Bioprod. Biorefining. 3 (2009) 174–194. doi:doi:10.1002/bbb.137.

[373] IPIECA, (n.d.). http://www.ipieca.org/resources/energy-efficiency-solutions/power-and-heat-generation/turbo-expanders/.

[374] Statista wabe page, (n.d.). https://www.statista.com/statistics/450146/global-reo-cerium-oxide-price-forecast/.

[375] M. Yang, International Energy Agency Working Paper Series Modeling Investment Risks and Uncertainties with Real Options Approach Modeling Investment Risks and Uncertainties with Real Options Approach, Structure. 13 (2007) 1120–37. http://www.iea.org/Textbase/publications/free_new_Desc.asp?PUBS_ID=1857.

[376] F. Watson, EU CO2 price to hit Eur30/mt by end 2019: Bank of America, Spglobal.Com. (2018). https://www.spglobal.com/platts/en/market-insights/videos/market-movers-europe/112618-oil-price-decline-takes-center-stage (accessed December 4, 2018).

[377] S. Ambrogi, EU carbon prices could double by 2021 and quadruple by 2030, Https://Www.Carbontracker.Org. (2018). https://www.carbontracker.org/eu-carbon-prices-could-double-by-2021-and-quadruple-by-2030/ (accessed December 4, 2018).

[378] P.N. Dyer, R.E. Richards, S.L. Russek, D.M. Taylor, Ion transport membrane technology for oxygen separation and syngas production, Solid State Ionics. 134 (2000) 21–33. doi:10.1016/S0167-2738(00)00710-4.

[379] C. Falter, R. Pitz-Paal, Water Footprint and Land Requirement of Solar Thermochemical Jet-Fuel Production, Environ. Sci. Technol. 51 (2017) 12938–12947. doi:10.1021/acs.est.7b02633.

[380] M. Egan, The Water Footprint Assessment Manual. Setting the Global Standard, Soc. Environ. Account. J. 31 (2011) 181–182. doi:10.1080/0969160X.2011.593864.

[381] A.D. Martin, A. Delgado, A. Delgado Martin, Water Footprint of Electric Power Generation : Modeling its use and analyzing options for a water-scarce future, Int. Congr. Adv. Nucl. Power Plants. 44 (2012) 117. doi:10.1021/es802162x.

[382] M. Martín, Artificial versus Natural Reuse of CO2 for DME Production: Are We Any Closer?, Engineering. 3 (2017) 166–170. doi:10.1016/J.ENG.2017.02.002.

[383] P.T. Krenzke, J.R. Fosheim, J.H. Davidson, Solar fuels via chemical-looping reforming, Sol. Energy. 156 (2017) 48–72. doi:10.1016/j.solener.2017.05.095.

[384] K. Otsuka, T. Ushiyama, I. Yamanaka, Partial Oxidation of Methane Using the Redox of Cerium Oxide, Chem. Lett. 22 (1993) 1517–1520. doi:10.1246/cl.1993.1517.

[385] D. Arifin, A.W. Weimer, Kinetics and mechanism of solar-thermochemical H2 and CO production by oxidation of reduced CeO2, Sol. Energy. 160 (2018) 178–185. doi:10.1016/j.solener.2017.11.075.

[386] F.J. Gotor, José, M. Criado, J. Malek, N. Koga, Kinetic analysis of solid-state reactions: The universality of master plots for analyzing isothermal and nonisothermal experiments, J. Phys. Chem. A. 104 (2000) 10777–10782. doi:10.1021/jp0022205.

[387] A. Khawam, D.R. Flanagan, Solid-State Kinetic Models: Basics and Mathematical Fundamentals, J. Phys. Chem. B. 110 (2006) 17315–17328. doi:10.1021/jp062746a.

[388] S. Abanades, P. Charvin, F. Lemont, G. Flamant, Novel two-step SnO2/SnO water-splitting

cycle for solar thermochemical production of hydrogen, Int. J. Hydrogen Energy. 33 (2008) 6021–6030. doi:10.1016/j.ijhydene.2008.05.042.

[389] S. Abanades, G. Flamant, Thermochemical hydrogen production from a two-step solar-driven water-splitting cycle based on cerium oxides, Sol. Energy. 80 (2006) 1611–1623. doi:10.1016/j.solener.2005.12.005.

[390] A. Pappacena, M. Rancan, L. Armelao, J. Llorca, W. Ge, B. Ye, A. Lucotti, A. Trovarelli, M. Boaro, New Insights into the Dynamics That Control the Activity of Ceria-Zirconia Solid Solutions in Thermochemical Water Splitting Cycles, J. Phys. Chem. C. 121 (2017) 17746–17755. doi:10.1021/acs.jpcc.7b06043.

[391] N.B. Goikoetxea, M.B. Gómez-Mancebo, R. Fernández-Saavedra, F. García-Pérez, J.A. Jiménez, J. Rodríguez, I. Rucandio, A.J. Quejido, Study of the performance of Co and Ni ferrites after several cycles involved in water-splitting thermochemical cycles, Int. J. Hydrogen Energy. 41 (2016) 16696–16704. doi:10.1016/j.ijhydene.2016.07.085.

[392] S. Abanades, P. Charvin, G. Flamant, P. Neveu, Screening of water-splitting thermochemical cycles potentially attractive for hydrogen production by concentrated solar energy, Energy. 31 (2006) 2469–2486. doi:10.1016/j.energy.2005.11.002.

[393] S. Abanades, A. Legal, A. Cordier, G. Peraudeau, G. Flamant, A. Julbe, Investigation of reactive cerium-based oxides for H2 production by thermochemical two-step water-splitting, J. Mater. Sci. 45 (2010) 4163–4173. doi:10.1007/s10853-010-4506-4.

[394] S. Abanades, G. Flamant, Thermochemical hydrogen production from a two-step solar-driven water-splitting cycle based on cerium oxides, Sol. Energy. 80 (2006) 1611–1623. doi:https://doi.org/10.1016/j.solener.2005.12.005.

[395] A. Pappacena, M. Boaro, L. Armelao, J. Llorca, A. Trovarelli, D. Chimica, F. Ambiente, Water splitting reaction over Ce 0 . 15 Zr 0 . 85 O 2 driven by surface heterogeneity, (n.d.).

[396] F.P. Bernardo, P.M. Saraiva, A novel CeO2 – xSnO2 / Ce2Sn2O7 pyrochlore cycle for enhanced solar thermochemical water splitting, Am. Inst. Chem. Eng. J. 61 (2014) 1–15. doi:10.1002/aic.

[397] J.R. Scheffe, J. Li, A.W. Weimer, A spinel ferrite/hercynite water-splitting redox cycle, Int. J. Hydrogen Energy. 35 (2010) 3333–3340. doi:https://doi.org/10.1016/j.ijhydene.2010.01.140.

[398] A. Le Gal, S. Abanades, G. Flamant, CO 2 and H 2 O Splitting for Thermochemical Production of Solar Fuels Using Nonstoichiometric Ceria and Ceria/Zirconia Solid Solutions, Energy & Fuels. 25 (2011) 4836–4845. doi:10.1021/ef200972r.

[399] S. Abanades, A. Le Gal, CO2 splitting by thermo-chemical looping based on ZrxCe1−xO2 oxygen carriers for synthetic fuel generation, Fuel. 102 (2012) 180–186. doi:10.1016/j.fuel.2012.06.068.

[400] S.G. Rudisill, L.J. Venstrom, N.D. Petkovich, T. Quan, N. Hein, D.B. Boman, J.H. Davidson, A. Stein, Enhanced Oxidation Kinetics in Thermochemical Cycling of CeO 2 through Templated Porosity, J. Phys. Chem. C. 117 (2013) 1692–1700. doi:10.1021/jp309247c.

[401] P. Furler, J. Scheffe, D. Marxer, M. Gorbar, A. Bonk, U. Vogt, A. Steinfeld, Thermochemical CO 2 splitting via redox cycling of ceria reticulated foam structures with dual-scale porosities, Phys. Chem. Chem. Phys. 16 (2014) 10503–10511. doi:10.1039/C4CP01172D.

[402] L.J. Venstrom, R.M. De Smith, Y. Hao, S.M. Haile, J.H. Davidson, Efficient Splitting of CO 2 in an Isothermal Redox Cycle Based on Ceria, Energy & Fuels. 28 (2014) 2732–2742. doi:10.1021/ef402492e.

[403] B. Zhao, C. Huang, R. Ran, X. Wu, D. Weng, Two-step thermochemical looping using modified ceria-based materials for splitting CO2, J. Mater. Sci. 51 (2016) 2299–2306. doi:10.1007/s10853-015-9534-7.

[404] S. Ackermann, L. Sauvin, R. Castiglioni, J.L.M. Rupp, J.R. Scheffe, A. Steinfeld, Kinetics of CO 2 Reduction over Nonstoichiometric Ceria, J. Phys. Chem. C. 119 (2015) 16452–16461. doi:10.1021/acs.jpcc.5b03464.

[405] Z. Zhao, M. Uddi, N. Tsvetkov, B. Yildiz, A.F. Ghoniem, Enhanced intermediate-temperature CO 2 splitting using nonstoichiometric ceria and ceria–zirconia, Phys. Chem. Chem. Phys. 19 (2017) 25774–25785. doi:10.1039/C7CP04789D.

[406] L.J. Venstrom, N. Petkovich, S. Rudisill, A. Stein, J.H. Davidson, The Effects of Morphology on the Oxidation of Ceria by Water and Carbon Dioxide, J. Sol. Energy Eng. 134 (2012) 011005. doi:10.1115/1.4005119.

[407] L. Zhu, Y. Lu, Reactivity and efficiency of ceria-based oxides for solar CO2 splitting via isothermal and near-isothermal cycles, Energy & Fuels. (2017) acs.energyfuels.7b03284.

doi:10.1021/acs.energyfuels.7b03284.

[408] N. Knoblauch, L. Dörrer, P. Fielitz, M. Schmücker, G. Borchardt, J.R. Scheffe, A. Steinfeld, P.S. Manning, J.D. Sirman, J.A. Kilner, M. Kamiya, E. Shimada, Y. Ikuma, M. Komatsu, H. Haneda, M. Katsuki, S. Wang, K. Yasumoto, M. Dokiya, M. Stan, Y.T. Zhu, H. Jiang, E.N. Armstrong, K.L. Duncan, D.J. Oh, J.F. Weaver, E.D. Wachsman, B. Bulfin, A.J. Lowe, K.A. Keogh, B.E. Murphy, O. Lübben, S.A. Krasnikov, I. V. Shvets, S. Ackermann, J.R. Scheffe, A. Steinfeld, C.B. Gopal, S.M. Haile, J. Rutman, M. Kilo, S. Weber, I. Riess, J. Maier, R.A. De Souza, E.N. Armstrong, K.L. Duncan, E.D. Wachsman, H. Dünwald, C. Wagner, E. Fischer, J.L. Hertz, E.W. Hart, A.J. Mortlock, Q.-L. Meng, C. -i. Lee, T. Ishihara, H. Kaneko, Y. Tamaura, I. Ermanoski, N.P. Siegel, E.B. Stechel, R.J. Panlener, R.N. Blumenthal, J.E. Garnier, P. Fielitz, G. Borchardt, X.-D. Zhou, W. Huebner, I. Kosacki, H.U. Anderson, P. Fielitz, G. Borchardt, M. Schmücker, H. Schneider, P. Willich, J.A. Lane, J.A. Kilner, M.A. Panhans, R.N. Blumenthal, C.C. Kan, H.H. Kan, F.M.V.A. IV, E.N. Armstrong, E.D. Wachsman, Surface controlled reduction kinetics of nominally undoped polycrystalline CeO $_2$, Phys. Chem. Chem. Phys. 17 (2015) 5849–5860. doi:10.1039/C4CP05742B.

[409] E. V. Ramos-Fernandez, N.R. Shiju, G. Rothenberg, Understanding the solar-driven reduction of CO $_2$ on doped ceria, RSC Adv. 4 (2014) 16456–16463. doi:10.1039/C4RA01242A.

[410] N. Knoblauch, H. Simon, L. Dörrer, D. Uxa, P. Fielitz, J. Wendelstorf, K.-H. Spitzer, M. Schmücker, G. Borchardt, Ceria: Recent Results on Dopant-Induced Surface Phenomena, Inorganics. 5 (2017) 76. doi:10.3390/inorganics5040076.

[411] M. Tou, R. Michalsky, A. Steinfeld, Solar-Driven Thermochemical Splitting of CO2and In Situ Separation of CO and O2across a Ceria Redox Membrane Reactor, Joule. 1 (2017) 146–154. doi:10.1016/j.joule.2017.07.015.

[412] Z. Zhao, M. Uddi, N. Tsvetkov, B. Yildiz, A.F. Ghoniem, Redox Kinetics and Nonstoichiometry of Hydrogen Production, (n.d.).

[413] S. Ackermann, J.R. Scheffe, A. Steinfeld, Diffusion of oxygen in ceria at elevated temperatures and its application to H2O/CO2 splitting thermochemical redox cycles, J. Phys. Chem. C. 118 (2014) 5216–5225. doi:10.1021/jp500755t.

[414] W.C. Chueh, C. Falter, M. Abbott, D. Scipio, P. Furler, S.M. Haile, A. Steinfeld, High-Flux Solar-Driven Thermochemical Dissociation of CO2 and H2O Using Nonstoichiometric Ceria, Science (80-.). 330 (2010) 1797–1801. doi:10.1126/science.1197834.

[415] A. Stamatiou, P.G. Loutzenhiser, A. Steinfeld, Solar Syngas Production via H 2 O/CO 2 - Splitting Thermochemical Cycles with Zn/ZnO and FeO/Fe 3 O 4 Redox Reactions †, Chem. Mater. 22 (2010) 851–859. doi:10.1021/cm9016529.

[416] P. Furler, J.R. Scheffe, A. Steinfeld, Syngas production by simultaneous splitting of H2O and CO 2 via ceria redox reactions in a high-temperature solar reactor, Energy Environ. Sci. 5 (2012) 6098–6103. doi:10.1039/C1EE02620H.

[417] C. Muhich, A. Steinfeld, Principles of doping ceria for the solar thermochemical redox splitting of H2O and CO2, J. Mater. Chem. A. 5 (2017) 15578–15590. doi:10.1039/C7TA04000H.

[418] M. Hoes, C.L. Muhich, R. Jacot, G.R. Patzke, A. Steinfeld, Thermodynamics of paired charge-compensating doped ceria with superior redox performance for solar thermochemical splitting of H $_2$ O and CO $_2$, J. Mater. Chem. A. (2017). doi:10.1039/C7TA05824A.

[419] M. Avrami, Kinetics of Phase Change. I General Theory, J. Chem. Phys. 7 (1939) 1103–1112. doi:10.1063/1.1750380.

[420] M. Avrami, Kinetics of Phase Change. II Transformation-Time Relations for Random Distribution of Nuclei, J. Chem. Phys. 8 (1940) 212–224. doi:10.1063/1.1750631.

[421] M. Avrami, Granulation, Phase Change, and Microstructure Kinetics of Phase Change. III, J. Chem. Phys. 9 (1941) 177–184. doi:10.1063/1.1750872.

[422] Erofe'ev BN, Generalized chemical kinetics equation and its application to reaction with solid participants., Dokl. Akad. Nauk SSSR. 52 (1946) 515.

[423] S.K. Bhatia, D.D. Perlmutter, A random pore model for fluid-solid reactions: I. Isothermal, kinetic control, AIChE J. 26 (1980) 379–386. doi:10.1002/aic.690260308.

[424] J. Šesták, G. Berggren, Study of the kinetics of the mechanism of solid-state reactions at increasing temperatures, Thermochim. Acta. 3 (1971) 1–12. doi:10.1016/0040-6031(71)85051-7.

[425] F. Prout, EG; Tompkins, The thermal decomposition of potassium permanganate, Trans. Faraday Soc. 40 (1944) 488–98.

[426] M. Galwey, AK;Brown, Chapter 3 Kinetic models for solid state reactions, in: 1999: pp. 75–115. doi:10.1016/S0167-6881(99)80004-4.

[427] B. Janković, B. Adnađević, S. Mentus, The kinetic study of temperature-programmed reduction of nickel oxide in hydrogen atmosphere, Chem. Eng. Sci. 63 (2008) 567–575. doi:10.1016/j.ces.2007.09.043.

[428] L. Han, Z. Zhou, G.M. Bollas, Heterogeneous modeling of chemical-looping combustion. Part 1: Reactor model, Chem. Eng. Sci. 104 (2013) 233–249. doi:10.1016/j.ces.2013.09.021.

[429] J.D. HANCOCK, J.H. SHARP, Method of Comparing Solid-State Kinetic Data and Its Application to the Decomposition of Kaolinite, Brucite, and BaCO3, J. Am. Ceram. Soc. 55 (1972) 74–77. doi:10.1111/j.1151-2916.1972.tb11213.x.

[430] S.R. Son, K.S. Go, S.D. Kim, Thermogravimetric Analysis of Copper Oxide for Chemical-Looping Hydrogen Generation, Ind. Eng. Chem. Res. 48 (2009) 380–387. doi:10.1021/ie800174c.

[431] Galwey AK; Brown ME, Kinetic background to thermal analysis and calorimetry, in: Handb. Therm. Anal. Calorim. Vol. 1 Princ. Pract., 1998: pp. 147–216.

[432] D.R. Burnham, Kenneth P., Anderson, Model selection and multi-model inference: a practical information-theoretic approach, 2nd ed., Springer-Verlag, New York, 2002.

[433] M. AM, Introduction of the theory of statistics, 3rd ed., McGraw-Hill, 1974.

[434] T.M. Ludden, S.L. Beal, L.B. Sheiner, Comparison of the Akaike Information Criterion, the Schwarz criterion and the F test as guides to model selection, J. Pharmacokinet. Biopharm. 22 (1994) 431–445. doi:10.1007/BF02353864.

[435] H.-V. Richard G, Lomax; Debbie L, Statistical concepts, a second course, 4th editio, Routledge, Taylot and Francis Group, New York, New York, 2012.

[436] K. Otsuka, Y. Wang, E. Sunada, I. Yamanaka, Direct partial oxidation of methane to synthesis gas by cerium oxide, J. Catal. 175 (1998) 152–160. doi:10.1006/jcat.1998.1985.

[437] Y. Kiyoshi, Otsuka; Tetsuya, Ushiyama; Ichiro, Partial oxidation of methane using the redox of cerium oxide, Chem. Lett. (1993) 1517–1520.

[438] K.J. Warren, J. Reim, K. Randhir, B. Greek, R. Carrillo, D.W. Hahn, J.R. Scheffe, Theoretical and Experimental Investigation of Solar Methane Reforming through the Nonstoichiometric Ceria Redox Cycle, Energy Technol. 5 (2017) 2138–2149. doi:10.1002/ente.201700083.

[439] C.K. Yang, Y. Yamazaki, A. Aydin, S.M. Haile, J.R. Scheffe, J. Li, A.W. Weimer, K. Otsuka, M. Hatano, A. Morikawa, E.S. Material, M.C.A. This, T.R. Society, M. Kang, X. Wu, J. Zhang, N. Zhao, W. Wei, Y. Sun, J.R. Scheffe, R. Jacot, G.R. Patzke, A. Steinfeld, A. Le Gal, S. Abanades, Y. Hao, C.K. Yang, S.M. Haile, M.E. Gálvez, R. Jacot, J.R. Scheffe, T. Cooper, G.R. Patzke, A. Steinfeld, I. Ermanoski, J.E. Miller, M.D. Allendorf, S. Dey, B.S. Naidu, C.N.R.R. Rao, A. Govindaraj, C.N.R.R. Rao, A. Demont, S. Abanades, T.C. Davenport, M. Kemei, M.J. Ignatowich, S.M. Haile, P. Singh, M.S. Hegde, S. Dey, B.S. Naidu, A. Govindaraj, C.N.R.R. Rao, L. Zhu, Y. Lu, W.C. Chueh, M. Abbott, D. Scipio, S.M. Haile, A. Le Gal, S. Abanades, R. Fernández-Saavedra, M.B. Gómez-Mancebo, C. Caravaca, M. Sánchez, A.J. Quejido, A. Vidal, F. Fresno, R. Fernández-Saavedra, M. Belén Gómez-Mancebo, A. Vidal, M. Sánchez, M. Isabel Rucandio, A.J. Quejido, M. Romero, T.C. Davenport, M. Kemei, M.J. Ignatowich, S.M. Haile, L. Nalbandian, A. Evdou, V. Zaspalis, A. Steinfeld, V.M. Wheeler, R. Bader, P.B. Kreider, M. Hangi, S. Haussener, W. Lipiński, T. Kodama, S. Bellan, N. Gokon, H.S. Cho, C.P. Falter, A. Sizmann, R. Pitz-Paal, C. Jarrett, W.C. Chueh, C. Yuan, Y. Kawajiri, K.H. Sandhage, A. Henry, N. Gokon, H. Murayama, A. Nagasaki, T. Kodama, I. Alxneit, T. Kodama, Y. Kondoh, R. Yamamoto, H. Andou, N. Satou, H. Kaneko, T. Kodama, N. Gokon, Y. Tamaura, K. Lovegrove, A. Luzzi, K. Ehrensberger, A. Frei, P. Kuhn, H.R. Oswald, P. Hug, D. Arifin, A.W. Weimer, S. Abanades, G. Flamant, A. Le Gal, S. Abanades, G. Flamant, Q. Jiang, G. Zhou, Z. Jiang, C. Li, C. Agrafiotis, M. Roeb, C. Sattler, W.C. Chueh, S.M. Haile, N. Gokon, S. Sagawa, T. Kodama, Q. Jiang, J. Tong, G. Zhou, Z. Jiang, Z. Li, C. Li, A. Le Gal, S. Abanades, P. Furler, J.R. Scheffe, A. Steinfeld, R. Bala Chandran, J.H. Davidson, E.N. Coker, J.A. Ohlhausen, A. Ambrosini, J.E. Miller, A.H. McDaniel, A. Ambrosini, E.N. Coker, J.E. Miller, W.C. Chueh, R. O'Hayre, J. Tong, T. Nakamura, S. Abanades, Interplay of material thermodynamics and surface reaction rate on the kinetics of thermochemical hydrogen production, Sol. Energy. 17 (2015) 16932–16945. doi:10.1016/j.ijhydene.2017.05.184.

[440] F. Lin, M. Rothensteiner, I. Alxneit, J.A. van Bokhoven, A. Wokaun, First demonstration of direct hydrocarbon fuel production from water and carbon dioxide by solar-driven

thermochemical cycles using rhodium–ceria, Energy Environ. Sci. (2016). doi:10.1039/C6EE00862C.

[441] F. Lin, A. Wokaun, I. Alxneit, Rh-doped Ceria: Solar Organics from H2O, CO2 and Sunlight?, in: Energy Procedia, 2015. doi:10.1016/j.egypro.2015.03.151.

[442] T. Kodama, N. Gokon, Thermochemical cycles for high-temperature solar hydrogen production, Chem. Rev. 107 (2007) 4048–4077. doi:10.1021/cr050188a.

[443] S. Lorentzou, D. Dimitrakis, A. Zygogianni, G. Karagiannakis, A.G. Konstandopoulos, Thermochemical H2O and CO2splitting redox cycles in a NiFe2O4structured redox reactor: Design, development and experiments in a high flux solar simulator, Sol. Energy. 155 (2017) 1462–1481. doi:10.1016/j.solener.2017.07.001.

[444] J. Lapp, Thermal modeling and design of a solar non-stoichiometric redox reactor with heat recovery, (2013). http://conservancy.umn.edu/handle/11299/159856.

[445] M. Roeb, C. Sattler, R. Klüser, N. Monnerie, L. de Oliveira, A.G. Konstandopoulos, C. Agrafiotis, V.T. Zaspalis, L. Nalbandian, A. Steele, P. Stobbe, Solar Hydrogen Production by a Two-Step Cycle Based on Mixed Iron Oxides, J. Sol. Energy Eng. 128 (2006) 125. doi:10.1115/1.2183804.

[446] M. Welte, K. Warren, J.R. Scheffe, A. Steinfeld, Combined Ceria Reduction and Methane Reforming in a Solar-Driven Particle-Transport Reactor, Ind. Eng. Chem. Res. 56 (2017). doi:10.1021/acs.iecr.7b02738.

[447] J.R. Scheffe, A.H. McDaniel, M.D. Allendorf, A.W. Weimer, Kinetics and mechanism of solar-thermochemical H2 production by oxidation of a cobalt ferrite–zirconia composite, Energy Environ. Sci. 6 (2013) 963. doi:10.1039/c3ee23568h.

[448] W.C. Chueh, M. Abbott, D. Scipio, S.M. Haile, High-flux solar-driven thermochemical dissociation of CO 2 and H 2 O using ceria redox reactions, Science (80-.). 63 (2010) 2010. doi:10.1123/science.1197834.

[449] P. Pantu, K. Kim, G.R. Gavalas, Methane partial oxidation on Pt/CeO2–ZrO2 in the absence of gaseous oxygen, Appl. Catal. A Gen. 193 (2000) 203–214. doi:10.1016/S0926-860X(99)00429-9.

[450] R.J. Carrillo, K.J. Warren, J. Scheffe, Experimental framework for evaluation of the thermodynamic and kinetic parameters of metal-oxides for solar thermochemical fuel production, J. Sol. Energy Eng. (2018). doi:10.1115/1.4042088.

[451] A. Steinfeld, A. Frei, P. Kuhn, D. Wuillemin, Solar thermal production of zinc and syngas via combined ZnO-reduction and CH4-reforming processes, Int. J. Hydrogen Energy. 20 (1995) 793–804. doi:10.1016/0360-3199(95)00016-7.

[452] X. Zhu, H. Wang, Y. Wei, K. Li, X. Cheng, Hydrogen and syngas production from two-step steam reforming of methane using CeO2as oxygen carrier, J. Nat. Gas Chem. 20 (2011) 281–286. doi:10.1016/S1003-9953(10)60185-5.

[453] J. Adanez, A. Abad, F. Garcia-Labiano, P. Gayan, L.F. De Diego, Progress in chemical-looping combustion and reforming technologies, Prog. Energy Combust. Sci. (2012). doi:10.1016/j.pecs.2011.09.001.

[454] Y.K. Salkuyeh, T.A. Adams, Co-production of olefins, fuels, and electricity from conventional pipeline gas and shale gas with near-zero CO2emissions. Part II: Economic performance, Energies. 8 (2015) 3762–3774. doi:10.3390/en8053762.

[455] D. Cocco, A. Pettinau, G. Cau, Energy and economic assessment of IGCC power plants integrated with DME synthesis processes, Proc. Inst. Mech. Eng. Part A J. Power Energy. 220 (2006) 95–102. doi:10.1243/095765006X76027.

[456] C.M. Quintella, S.A. Hatimondi, A.P.S. Musse, S.F. Miyazaki, G.S. Cerqueira, A. De Araujo Moreira, CO2 capture technologies: An overview with technology assessment based on patents and articles, Energy Procedia. 4 (2011) 2050–2057. doi:10.1016/j.egypro.2011.02.087.

[457] J. Werther, Wein. J, Expansion Behavior of Gas Fluidized Beds in the Turbulent Regime, AIChE Symp. Ser. 90 (1994) 31–44.

[458] D. Kunii, O. Levenspiel, Fluidization Engineering, Butterworth-Heinemann, 1991. https://www.elsevier.com/books/fluidization-engineering/brenner/978-0-08-050664-7.

[459] J. Werther, Fluidized-Bed Reactors, Ullmann's Encycl. Ind. Chem. 29 (2007) 1–41. doi:doi:10.1002/14356007.b04_239.pub2.

[460] C. Chan, J.P.K. Seville, J. Baeyens, The transport disengagement height (TDH) in a bubbling fluidized bed, 13th Int. Conf. Fluid. - New Paradig. Fluid. Eng. (2010) 1–8.

[461] A. Cahyadi, A.H. Neumayer, C.M. Hrenya, R.A. Cocco, J.W. Chew, Comparative study of Transport Disengaging Height (TDH) correlations in gas-solid fluidization, Powder Technol. 275 (2015) 220–238. doi:10.1016/j.powtec.2015.02.010.

[462] A. Brems, C.W. Chan, J.P.K. Seville, D. Parker, J. Baeyens, Modelling the transport disengagement height in fluidized beds, Adv. Powder Technol. 22 (2011) 155–161. doi:10.1016/j.apt.2010.07.012.

[463] A.B. Fournol, M.A. Bergougnou, C.G.J. Baker, Solids entrainment in a large gas fluidized bed, Can. J. Chem. Eng. 51 (2018) 401–404. doi:10.1002/cjce.5450510402.

[464] S.E. George, J.R. Grace, Entrainment of particles from aggregative fluidized beds, Am. Inst. Chem. Eng. Symp. Ser. 74 (1978) 67–74.

[465] I.H. Chan, T.. Knowlton, The effect of pressure on entrainemt from bubbling gas fludized bed, in: D. Kunii, R. Toei (Eds.), Fluidization, Engineering Foundation, New York, 1984: pp. 283–290.

[466] M. Sciążko, J. Bandrowski, J. Raczek, On the entrainment of solid particles from a fluidized bed, Powder Technol. 66 (1991) 33–39. doi:https://doi.org/10.1016/0032-5910(91)80078-W.

[467] A.S. Fung, F. Hamdullahpur, Effect of bubble coalescence on entrainment in gas fluidized beds, Powder Technol. 77 (1993) 251–265. doi:https://doi.org/10.1016/0032-5910(93)85018-5.

[468] F. Systems, Hadbook of fluidization and fluid- particle systems, 2003. doi:10.1016/S1672-2515(07)60126-2.

[469] C.Y. Wen, L.H. Chen, Fluidized bed freeboard phenomena: Entrainment and elutriation, AIChE J. 28 (1982) 117–128. doi:10.1002/aic.690280117.

[470] V. Stojkovski, Z. Kosti, Empirical correlation for prediction of the elutriation rate constant, Therm. Sci. 7 (2003) 43–58. doi:10.2298/TSCI0302043S.

[471] S.M. Tasirin, D. Geldart, The entrainment of fines and superfines from fluidized beds, Powder Handl. Process. 10 (1998) 263–268. https://ukm.pure.elsevier.com/en/publications/the-entrainment-of-fines-and-superfines-from-fluidized-beds.

[472] F.A. Zenz, N.A. Weil, A theoretical-empirical approach to the mechanism of particle entrainment from fluidized beds, AIChE J. 4 (2018) 472–479. doi:10.1002/aic.690040417.

[473] M. Colakyan, O. Levenspiel, Elutriation from fluidized beds, Powder Technol. 38 (1984) 223–232. doi:https://doi.org/10.1016/0032-5910(84)85005-6.

[474] D. Geldart, S. Cullinan, S. Georghiades, D. Gilvray, D.. Pope, The effect of fines on entrainment from gas fluidized beds, Trans. Inst. Chem. Eng. 57 (1979) 269–275.

[475] AspenTech. Jump Start: Solids Process Modeling in Aspen Plus, (2014).

[476] S. Lenzini, W.S. Choe, F. You, O. Components, Reactors for process design, 2018. https://processdesign.mccormick.northwestern.edu/index.php/Reactor#Aspen_Plus_Fluidized_Bed_Reactor_Simulation_2.

[477] Aspen plus tutorial on: Reaction in Fluidized Beds, 2013.

[478] Kamil Kubinski, The concept of electricity storage - a review of technology with particular emphasis on storage in compressed air, 2017.

[479] M. Hamzehei, H. Rahimzadeh, G. Ahmadi, Study of Heat Transfer and Hydrodynamics in a Gas-Solid Fluidized Bed Reactor Experimentally and Numerically, Appl. Mech. Mater. 110–116 (2011) 4187–4197. doi:10.4028/www.scientific.net/AMM.110-116.4187.

[480] M. Hamzehei, H. Rahimzadeh, G. Ahmadi, Computational and Experimental Study of Heat Transfer and Hydrodynamics in a 2D Gas-Solid Fluidized Bed Reactor, Ind. Eng. Chem. 49 (2010) 5110–5121. doi:10.1021/ie900510a.

[481] G. Tsatsaronis, Definitions and nomenclature in exergy analysis and exergoeconomics, Energy. 32 (2007) 249–253. doi:10.1016/j.energy.2006.07.002.

[482] G. Tsatsaronis, Computer-aided energy systems analysis: presented at the winter annual meeting of the American Society of Mechanical Engineers, Dallas, Texas, November 25-30, 1990, Amer Society of Mechanical, 1990.

[483] A. Lazzaretto, R. Andreatta, Algebraic formulation of a process-based exergoeconomic method, Am. Soc. Mech. Eng. Adv. Energy Syst. Div. AES. 35 (1995) 2018.

[484] M. Khaljani, R. Khoshbakhti Saray, K. Bahlouli, Comprehensive analysis of energy, exergy and exergo-economic of cogeneration of heat and power in a combined gas turbine and organic Rankine cycle, Energy Convers. Manag. 97 (2015) 154–165. doi:10.1016/j.enconman.2015.02.067.

[485] A. Lazzaretto, G. Tsatsaronis, SPECO: A systematic and general methodology for calculating

efficiencies and costs in thermal systems, Energy. 31 (2006) 1257–1289. doi:10.1016/j.energy.2005.03.011.

[486] M.A. Lozano, A. Valero, Theory of the exergetic cost, Energy. 18 (1993) 939–960. doi:10.1016/0360-5442(93)90006-Y.

[487] A. Valero, M. Lozano, M. Munoz, A general theory of exergy saving I. On the exergetic cost, 1986.

[488] R. Dindorf, Estimating potential energy savings in compressed air systems, Procedia Eng. 39 (2012) 204–211. doi:10.1016/j.proeng.2012.07.026.

Curriculum Vitae

Azharuddin was born on the 6th of December in 1986 in Hyderabad, India. He received his Bachelors in Mechanical Engineering from Osmania University, Hyderabad in 2008. He worked as a Rotating equipment engineer in Reliance Industries Limited from 2008-2009. He received Ministry of Higher Education fellowship from Saudi Arabia to pursue Masters of Science in Mechanical Engineering from King Fahd University of Petroleum and Minerals (KFUPM). During this period, he worked on oxygen transport membranes with Massachusetts Institute of Technology (MIT) for his master thesis. After graduating in 2011, he worked as sustainability engineer at KFUPM and at Technology Innovation Center -Carbon capture and sequestration (TIC-CCS) till September 2014. Thereafter, he joined Erasmus Mundus Joint Doctorate Program under Environomical Pathways for Sustainable Energy Services at Politecnico di Torino, Italy and Universitat Politècnica de Catalunya, Spain. He was visiting scholar at Eindhoven University of Technology, the Netherlands from February to March 2018.